PROCEEDINGS
OF

NOISE
SHOCK
and
VIBRATION
CONFERENCE

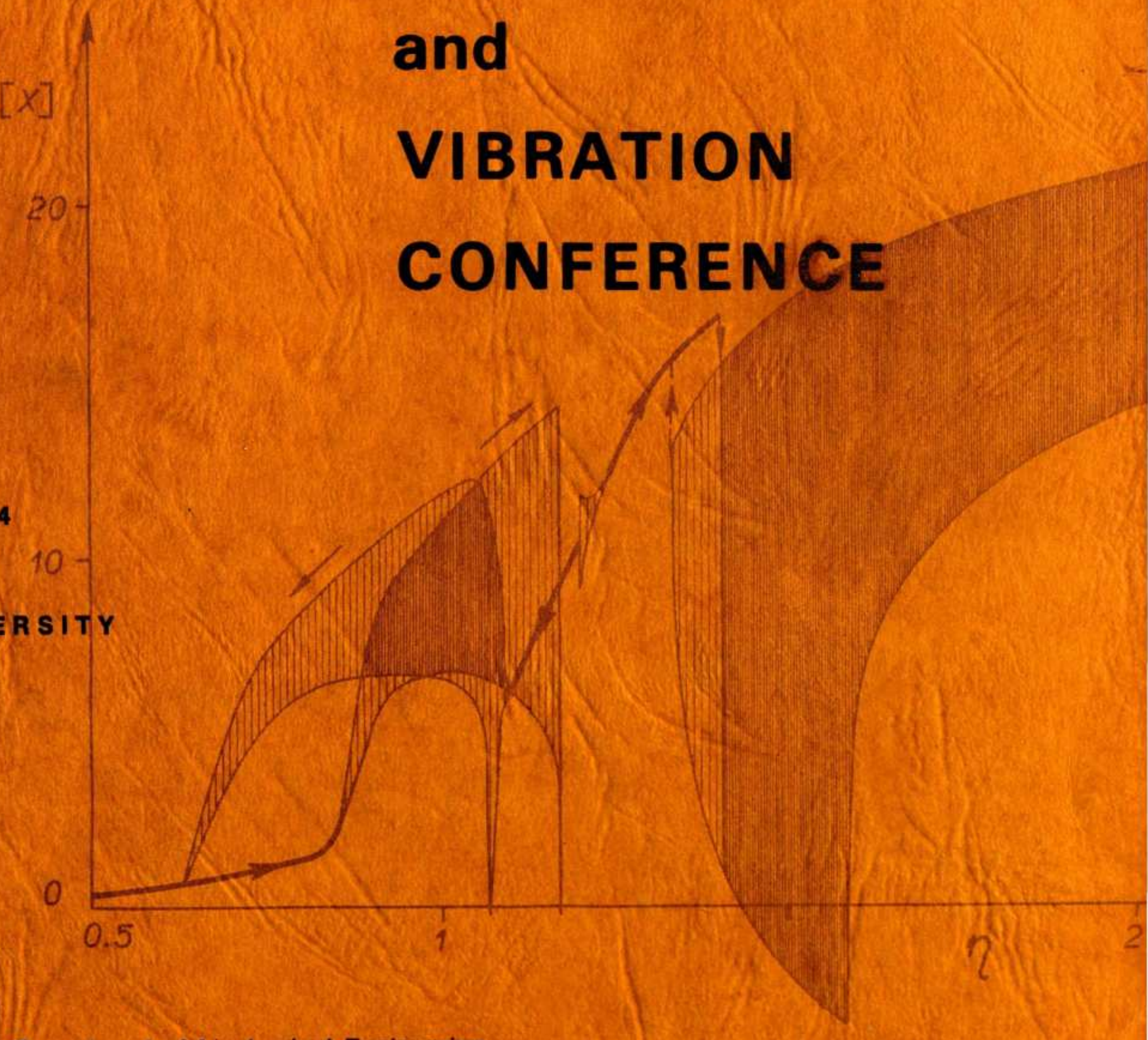

HELD DURING
MAY 22-25 1974
AT
MONASH UNIVERSITY
MELBOURNE

Sponsored by:

Monash University, Department of Mechanical Engineering

Australian Acoustical Society, Victoria Division

The Institution of Engineers, Australia (The National Committee on Applied Mechanics)

P. BS

PROCEEDINGS
OF

NOISE
SHOCK
and
VIBRATION
CONFERENCE

HELD DURING

MAY 22-25 1974

AT

MONASH UNIVERSITY

MELBOURNE

Sponsored by:

Monash University, Department of Mechanical Engineering

Australian Acoustical Society, Victoria Division

The Institution of Engineers, Australia (The National Committee on Applied Mechanics)

Published by

THE CONFERENCE ORGANISING COMMITTEE

of the

NOISE, SHOCK AND VIBRATION CONFERENCE

at the Department of Mechanical Engineering
Monash University, Clayton, Australia, 3168

Edited by

THE CONFERENCE PROGRAMME AND EDITORIAL COMMITTEE

J. D. C. Crisp (Convenor)
R. G. Barden
R. J. Alfredson
H. Nolle

Printed in Melbourne by Chas E. Tully Pty. Ltd., 35 Clifford Street, Huntingdale

Preface

The Conference Organising Committee was pleased to have attracted Professor K. H. Hunt, Dean of the Faculty of Engineering, Monash University to welcome the delegates and to invite them to make effective use of the facilities that the University provides.

The Committee was also keenly appreciative of the most generous support afforded by several organisations which made it possible to subsidise, in some cases in a very substantial way, the visit to Australia of distinguished colleagues from abroad. These organisations included Repco Limited, The Broken Hill Associated Smelters Pty. Ltd., Esso Australia Ltd., ACI Australian Fibreglass Pty. Ltd., ICI Australia Limited, the Colonial Sugar Refinery Co. Ltd., Ford Motor Company of Australia Ltd., and Silentbloc (Australia) Proprietary Limited.

The Committee acknowledges with pleasure the significant contribution to the proceedings of the Conference of the various and novel displays arranged by manufacturers of equipment, instrumentation and data systems: they were Bruel & Kjaer, General Radio, Time/Data, Dynamics Corporation, Data Laboratories, Saicor-Honeywell, Biomation and Ithaco, Dawe Instruments Limited, Ling Electronics, I.M.V. Lab. Co. and Federal Scientific Corp.

A particular feature of the Conference was the Instrumentation Forum which brought together in confrontation both manufacturers and users. The panel that focused the discussion consisted of —

A. J. Carolan
Specialist
Bruel & Kjaer
Naerum, Denmark

R. L. Eshleman
Science Advisor
I.I.T. Research Institute
Chicago

H. G. Platzke
Impulsphysik GmbH
West Germany

R. A. Piesse
Director
National Acoustic Laboratories
Sydney

D. H. Edwards
Senior Technical Officer
Aeronautical Research Laboratories
Melbourne

J. A. Macinante
Senior Principal Research Scientist
C.S.I.R.O.
National Standards Laboratory
Chippendale

W. R. Raymond
Product Marketing Manager
Acoustics/Signal Analysis
General Radio
Concord, USA

Finally, mention should be made of the Workshop on Codes, Specification and Practice in Vibration which was managed by Mr. T. Silverson with the assistance of Mr. J. A. Macinante and Dr. H. Nolle; and of the displays of books, texts and bibliographics mounted by the Hargrave Library of Monash University, by the Monash Bookshop on behalf of many publishers, and by the Shock & Vibration Centre, Naval Research Laboratory, Washington, D.C.

JOHN D. C. CRISP
Editor

Conference Organising Committee

Professor R. G. Barden, Co-Chairman

Department of Mechanical Engineering, Monash University

Professor J. D. C. Crisp, Co-Chairman

Department of Mechanical Engineering, Monash University
Member, National Committee on Applied Mechanics, I.E. Aust.

Mr. J. F. M. Bryant

Australian Road Research Board
Australian Acoustical Society

Mr. F. W. Hooton

Aeronautical Research Laboratories, Department of Supply

Mr. J. A. Macinante

National Standards Laboratory, C.S.I.R.O.
Member, National Committee on Applied Mechanics, I.E. Aust.

Mr. G. A. B. Riley

Australian Acoustical Laboratory
Chairman, Australian Acoustical Society (Victorian Division)

Mr. T. Silverson

Imperial Chemical Industries, Australia, Ltd.
Chairman, National Committee on Applied Mechanics, I.E. Aust.

Dr. R. J. Alfredson, Co-Secretary

Department of Mechanical Engineering, Monash University

Dr. H. Nolle, Co-Secretary

Department of Mechanical Engineering, Monash University

ERRATA

1. Add page numbers to pages 162, 176, 304, 379, 420(a), 428(a).
2. Page 259. first equation is number (5).
3. Page 374, section 3 (1st and 3rd line): Fig. 3b should read Fig. 4b.
4. Page 449. figure captions are for top figure: Fig. 12. Industrial Vibration Monitor; bottom figure: Fig. 2. Portable Vibration Set.
5. In "CONTENTS" replace the respective two existing sections by the ones below:

VIBRATION MEASUREMENT TECHNIQUES

NOISE, SHOCK AND VIBRATION MEASUREMENT

Contents

*Keynote speakers.

*Keynote speakers.

Noise, Shock & Vibration Conference, 1974 Monash University, Melbourne

PROTECTION OF THE PUBLIC HEALTH AND WELFARE FROM THE EFFECTS OF ENVIRONMENTAL NOISE

L. L. Beranek
Bolt Beranek and Newman Inc.
Cambridge, Mass.,
U.S.A.

SUMMARY - Noise of sufficiently high level may impair hearing, affect speech communication and interfere with various human activities such as sleep and thought. An "equivalent noise level, L_{eq}" in decibels is defined to rate noises. By imposing a ten-decibel penalty on nighttime noise a day/night equivalent noise level, L_{dn} is used to rate community annoyance to regularly occurring noise. Workers are exposed to 8-hour long levels which are labeled $L_{eq(8)}$. The findings are:

1. Complete protection of workers' hearing after many years of exposure to noise requires that $L_{eq(8)}$ not exceed 75 dB(eq-8).
2. Protection of workers' ability to understand speech satisfactorily after many years of exposure to noise requires that $L_{eq(8)}$ not exceed 90 dB(eq-8).
3. Protection of inhabitants' ability to converse and listen to radio and television comfortably in their homes with open windows requires that L_{eq} not exceed 55 dB(eq) outdoors.
4. The dividing level between "no overt community reaction" to noise and "sporadic complaints about the noise to someone in power" is about 55 dB(dn).

INTRODUCTION

The international definition of noise is "unwanted sound". But, who is to make the judgment of unwantedness? An old French proverb says, "I do not like noise unless I make it myself". Thus, the airlines, the trucking (lorry) operators, the drop-forge industry and children on the playground fail to appreciate the complaints of people whose sleep, thinking, or enjoyment of television is shattered by their racket. Unfortunately, a person who is affected by noise doesn't have very much power to control it. Transportation is authorized by national government; industry is authorized by municipal government; and playgrounds are concomitants of neighborhood schools. Only if the people of a nation rise up together against an ever-increasing din will a reversal of the scourge of noise on their lives be brought about.

In many countries lawmakers have seriously begun to wrestle with the problem of environmental noise. In the United States of America several large cities and states have led the way to lower noise levels by passing laws that primarily limit transportation and recreational vehicle noise. About six years ago the United States Department of Labor appended a safety regulation on industrial noise exposure to an earlier general safety act that applied only to Federal contractors. Four years ago, this hearing safety regulation was extended to all industries through the Occupational Safety and Health Act of 1970. Two years ago, the Noise Control Act of 1972 was passed in the United States with the general requirement that limits to noise levels should be set which "protect the public health and welfare with an adequate margin of safety". By "health and welfare" is meant "complete physical, mental and social well being, not merely absence of disease and infirmity". By "public" is meant "all parts of the population including that which is medically susceptible to noise".

We must emphasize that large-scale studies of the population at large are needed to give us more accurate information on the relations between cumulative noise exposure of individuals and the effects on their health. This statement is even true for the effects of noise on hearing acuity, about which a great body of knowledge exists. We are hardly informed at all on the effects of long exposures of noise on the general well-being of individuals. I shall attempt today to survey what is known on these subjects.

SOME DEFINITIONS

Many of those at this conference likely are not specialists in the human aspects of noise and its control. Thus, some definitions are in order.

Noise induced hearing impairment: Any person's hearing should be protected so that he can converse socially and enjoy music, drama, motion pictures, radio, television, assemblies and sports, both in auditoriums and at home. A person's hearing may degenerate because of age, disease, accident, or it may degenerate because of exposure to noise levels. If the noise is very intense, such as a nearby explosion, noise-induced hearing impairment may result instantaneously. Industrial-type noises, if intense enough, may result in noise-induced permanent hearing impairment in a matter of a few months or after many years of exposure. Obviously noise induced hearing impairment is a degradation in the "health and welfare" of those affected.

Annoyance: The phrase "effects of noise on health and welfare" also includes an understanding of how noise causes "annoyance". Annoyance relates to a person's mental anguish, personal comfort, and well being. In the courts of law of most countries, "annoyance" *per se* is not a recognized legal concept. Annoyance is a subjective human reaction to something, like noise, that interferes with a desired human activity. Common law has recognized only interference with a personal right or a property right. By contrast, hearing damage has been recognized legally because a person has a right to hear and the amount of his hearing degradation and its effect on his ability to understand speech can be measured at any time. If annoyance can be related directly to interference with some human activity like work performance, ability to understand speech, or ability to drive an automobile, there probably is no fundamental difficulty in encompassing it as part of the common law.

Environmental noise: The term "environmental noise" means "the intensity, duration, and character of sounds from all sources". This definition is embodied in Section 3(11) of the U.S. Noise Control Act of 1972.

DOMINANT CHARACTERISTICS OF NOISE

We need a rating system for condensing all of the characteristics of environmental noise into one number which can be used to judge the effects of noise on human beings -- one glorified type of decibel, if you please. Let us tabulate the dominant characteristics of environmental noise that must be squeezed into such a single-number indicator. There are three characteristics:

1. Magnitude of the noise: The primary factor in the physical description of environmental noise is its magnitude. A physical measurement of magnitude should be based on: (a) satisfactory correlation with the human responses of hearing loss, speech interference, annoyance and loss of sleep owing to noise; (b) cumulative effects of all noise exposures over long periods of time; (c) satisfactory application to all commonly experienced noise environments; (d) measurability by available and simple instruments; and (e) predictability from knowledge of those physical events that produce the noise.

2. Frequency compositon: A second dominant characteristic is the combination of low-pitched, medium-pitched and high-pitched sounds (frequency components) in the overall noise. People distinguish not only high-frequency components from low-frequency components in a complex noise, but they find high frequency noises much more annoying than low frequency noises of the same physical magnitude.

3. Fluctuation of the noise both in short term and in longer periods: The third dominant characteristic of noise is that it is not steady. To describe the property of fluctuation in noise requires a statistical approach, yielding the magnitude both as a function of time and as a function of frequency.

BASIC NOISE DOSE SITUATIONS

An ideal approach to specifying acceptable noise levels in terms of their effect on public health and welfare would be to start with an analysis of the noise doses received by individuals. Each noise dose, however, is a function of the recipient's life style. For example, exposures to noise vary greatly among factory workers, office workers, housewives and school children.

(See Figs. 1 - 5). Even two individuals working in the same office might accumulate different total noise doses if they use different modes of transportation, live in different areas and have different television habits. To bring the array of possible alternatives into some kind of perspective, we list three basic situations:

A. Defined areas and conditions in which people are exposed to environmental noise for limited periods of time, such as work situations, school classrooms, or vehicles.

B. Defined areas and conditions in which people are exposed to environmental noise for extended periods of time, such as residential dwellings in urban areas, or near airports, highways or factories.

C. Total noise exposure dose of an individual, irrespective of area or condition.

DEVELOPMENT OF EQUIVALENT SOUND LEVEL (L_{eq})

The three dominant characteristics of noise described above (Nos. 1 to 3) are now to be developed into one unit of measurement (See Fig. 6).

Magnitude: When a sound wave travels through the air it causes a fluctuation in the pressure in the air which can be measured in Newtons per square meter (or pounds per square inch). However, the range between the faintest audible sounds and the crash of thunder can be a ratio of 1,000,000,000,000 to 1, so that some means of compressing the scale must be sought. International standards express the magnitude of sound logarithmically as sound pressure level, defined as twenty times the common logarithm of the ratio of the sound pressure in question to a reference sound pressure of 0.00002 Newton per square meter. The unit is the decibel.

Frequency Characteristics: It is well known that the higher frequencies in noise affect the intelligibility of speech and are more annoying than the lower frequencies. Many schemes, some of them very elaborate, have been devised to take account of this fact. For most types of noise, however, the "A-weighted sound level", L_A, a quantity whose units are "A-weighted decibels, i.e., dB(A)" has already found wide acceptance internationally in describing the noise of transportation and urban activities as well as relating to the loudness level of a noise. This quantity, A-weighted sound level in dB(A), can be read directly from all standard sound level (noise) meters. In these meters an electrical network is used partially to suppress the frequencies below 500 Hz and above 5,000 Hz.

Time Characteristics: A method for averaging continuously fluctuating or more slowly changing A-weighted sound levels over a long period of time has been accepted by a number of nations. The procedure results in an "Equivalent Sound Level, (L_{eq})" measured in units of db(eq). It is defined as the equivalent steady sound level L_{eq}, that, in a stated period of time, contains the same sound energy as the time-varying noise under measurement contains in that same period of time. This quantity has been found to correlate well with the subjective reaction of people to traffic noise of all kinds. Commercial instrumentation is currently becoming available for measuring L_{eq} directly.

The concept of representing a fluctuating sound (noise) level in terms of an equivalent steady sound level, L_{eq}, has been satisfactorily validated as a procedure to describe the onset and progression of permanent noise-induced hearing loss. There is also considerable evidence to show that it applies to the prediction of annoyance in various community noise situations.

As an example, if there was a sound of 80 dB(A) present in a location for half an hour which then decreased to a sound level of 74 dB(A) in the next half hour, what would be the equivalent sound level L_{eq}? A sound that has a level 6 dB(A) lower than another, has one-fourth the A-weighted energy. Hence the energy in the two half-hours averaged over the hour would be (1 + 0·25) divided by 2, or 0·625 of the energy in the larger sound. A decrease in sound energy by a factor of 0·625, means a decrease of 2 decibels. Hence, the equivalent A-weighted sound level L_{eq} = 80 - 2 = 78 dB(eq) would be the "average" for the hour.

Daytime/Nighttime Equivalent Sound Levels: It is well known that to the vast majority of people (those who sleep, approximately between the hours 10:00 p.m. and 7:00 a.m.) nighttime noise is more annoying than daytime noise of the same energy. Most nations have come to the conclusion that nighttime noise levels must be about 10 decibels lower than daytime levels to be judged as having the same annoyance as daytime levels.

By international agreement, daytime extends from 7:00 a.m. to 10:00 p.m. (0700 to 2200) and nighttime extends from 10:00 p.m. to 7:00 a.m. (2200 to 0700) the next day. The symbol for the 15-hour, daytime, A-weighted, equivalent sound level is L_d and that for the 9-hour nighttime level is L_n. The units for A-weighted noise levels in these periods respectively are dB(d) and dB(n).

The measure for a 24-hour day is the Day/Night Sound Level (L_{dn}). It is defined as the A-weighted, equivalent sound level during the 24-hour time period with a 10 dB penalty applied to nighttime sound levels. (See Fig. 7). The unit is dB(dn).

Twenty-Four-Hour Equivalent Sound Level: This level is simply the equivalent noise level over a 24-hour period without any nighttime penalty. It is called the A-weighted, 24-hour, equivalent sound level ($L_{eq(24)}$) in units dB (eq-24).

Eight-Hour Equivalent Sound Level: The typical worker spends 8 hours per day, 5 days a week at his job. The equivalent, A-weighted noise level associated with his occupation is $L_{eq(8)}$ in units of dB(eq-8).

MAXIMUM EXPOSURE LEVELS TO AVOID SIGNIFICANT ADVERSE EFFECTS ON HEARING

If one looks at those daily functions related to hearing that are necessary to economic and social survival in our complex civilization, it seems reasonable to conclude that communication by speech is by far the most important. Thus, at least in the United States and some other countries, maximum permissible noise levels for workers, called damage-risk criteria for workers, have been chosen to protect exposed persons against loss of hearing for everyday speech. This loss, by agreement, relates specifically to the arithmetic average of the hearing losses for an individual at the three frequencies, 500, 1000 and 2000 Hz. By hearing loss we mean the amount by which a person's hearing is worse than the standardized normal for young persons as measured by a standardized audiometer (ISO Standards/R-384-1964). We must point out that the hearing loss induced by noise at 4000 Hz is much greater than that at any of the three frequencies just mentioned. For example, tests on a group of 500 people showed that, after 20 years of exposure to a noise of about 95 dB(A), the average of their hearing losses was 50 dB at 4000 Hz, and only 20 dB for the average of the losses at 500, 1000 and 2000 Hz. This study also confirmed that people differ greatly in their susceptibility to hearing loss. After 10 years of exposure, the spread in hearing loss among individuals at frequencies of 3000 Hz or more was about 15 dB. After 25 years, the spread increased to about 30 dB.

Obviously, one doesn't need the "perfect" hearing of the young to understand speech satisfactorily. For practical purposes, a hearing loss (as defined above) of up to 25 decibels will permit speech to be understood satisfactorily. In the United States a person whose hearing loss is in excess of 25 dB is said to be handicapped or damaged. As the loss of hearing increases above 25 dB, the degree of handicap increases. By definition, in the United States, the degree of hearing handicap, also called the percentage impairment of hearing begins from a hearing loss of 25 dB (average at 500, 1000 and 2000 Hz) which is called "zero hearing handicap", and increases at the rate of 1·5 percentage points for each decibel of average hearing loss until a loss of 92 dB is achieved (called "100% hearing handicap".)

Let us now investigate the risk of a person's experiencing a hearing handicap by continuous exposure to various noise levels, 8 hours a day at work, for various number of years. Reference should be made to Table 1. Here we see the percentage risk of developing a hearing handicap. For each noise exposure level in dB(A), two rows of percentages are given. The upper row, labeled "total", gives the percentage of people who have hearing impairment owing to the combination of noise and age, as a function of years of exposure. The lower row, labeled "due to noise", takes out the effects of normal aging.

It is obvious that if we are to assume no risk of hearing handicap owing to noise for speech whatsoever, the noise exposure levels must be 80 dBA or lower. A noise level of 90 dBA, for example, is expected to cause a hearing handicap, owing to the noise alone, after 30 years of exposure, in about 15 per cent of workers. Actually, because of the effects of age, about one-fourth of the noise-exposed workers will suffer a hearing handicap. Remember, that "no hearing handicap" means no more than 25 dB hearing loss, averaged at the frequencies 500, 1000 and 2000Hz.

There are a number of ways to view the question of allowable noise exposure levels to protect hearing. One viewpoint is that 97 per cent of the population should be protected from any measurable noise-induced permanent shift in hearing threshold at all frequencies even after 40 years of exposure, 8 hours a day, 250 days a year. We also observe that hearing losses at or near 4000 Hz owing to noise are greater than at any other frequency.

If one assumes that for about 10% of each 8-hour working day, the worker is out of the area of maximum noise (owing to visits to other areas) and further that if he or she is exposed to noise levels which are over 5 decibels lower during the remaining 16 hours of the day, then studies worldwide show that for 97% protection at all frequencies:

$L_{eq(8)}$ must not exceed 75 db(eq-8)

If the workers were to be exposed to the noise level 24 hours per day, then the permissible level would have to be 5 decibels lower to provide the same protection for his hearing, that is to say:

$L_{eq(24)}$ must not exceed 70 dB(eq-24).

The U.S. Occupational Safety and Health Agency (OSHA) permits companies to have greater noise levels in their working areas, namely up to 90 dB(eq-8) because that regulation permits noise-induced hearing loss to reach 25 dB as determined by averaging the hearing loss of an individual at 500, 1000 and 2000 Hz. As we said before, losses at these frequencies are considerably less than at 4000 Hz which is where the ear is most susceptible to noise-induced damage. Full protection at 4000 Hz requires that $L_{eq(8)}$ not exceed 75 dB(eq-8). To protect 92% of the people from having 25 dB or more loss averaged at the three frequencies above after 40 years of exposure, 8 hours a day, 250 days a year, with 10% of workers' time spent in lower noise levels:

$L_{eq(8)}$ must not exceed 90 dB(eq-8)

EFFECTS OF NOISE ON LISTENING, THINKING, RELAXATION AND SLEEP

When two people converse outdoors or in an acoustically "dead" space, three factors determine how well they understand each other: (1) the noise level; (2) their distance apart; and (3) their voice level. Other factors may also be of importance, for example, whether the noise fluctuates, whether the persons do some lip reading, whether they anticipate what is about to be said, or whether their accents are bothersome.

Under the conditions that the noise is steady, the talkers have average voice strengths, accents play no part and there is no lip reading, voice communication will be acceptable (95% sentence intelligibility) for each A-weighted noise level L_{eq} given in the body of Table 2, provided the voice level and distance apart are appropriate. For example, two people may converse satisfactorily at normal voice level in a 60 dB(A) noise if they are 2 meters or less apart (mouth to ear separation), facing each other. If the noise level were to increase 6 dB(A), the talkers would either have to raise their voice levels or reduce their separation to 1 meter or less.

Fluctuating noise of the same equivalent noise level L_{eq} makes speech easier to understand, because one can hear in the lulls between the peaks of the noise. If one assumes normal voices at 2 meters separation, the permissible equivalent noise level, L_{eq}, for aircraft or urban noises may be up to 5 dB(eq) greater than for a steady noise.

Many countries have sponsored studies of acceptable noise levels for listening to radio and television in dwellings. The results indicate that for satisfactory listening by the average person the indoors L_{eq} must not exceed 45 to 50 dB(eq) -- the lower level applying to steady noise. Of course, indoor noise levels that are 5 dB(eq) or more lower are more comfortable and are desirable where possible. Thus, acoustical consultants generally recommend that noise levels not exceed 40, or at most 45 dBA in living rooms.

Because aircraft and urban noise are the principal sources of the loudest noises found indoors, we must have knowledge of the noise reduction provided by homes, both with open and closed windows.

Aircraft noise generally reaches homes from planes in flight. Thus, an angle of elevation is involved. Surface traffic noise generally impinges on windows horizontally. Two different studies reveal the following: For aircraft noise, the national average of noise level reduction of a house with windows open is about 15 dB(A) and closed about 25 dB(A). In the second study, for traffic noise impinging horizontally on a house, the reductions are for open windows about 10 dB(A) and for closed windows about 20 dB(A). Of course, there is considerable variability from house to house. Lightweight construction in warm climates is 3 to 5 dB(A) less effective in reducing noise than heavy construction typical of colder areas. The number of windows and the amount of rugs and draperies and the average ceiling height in the room also affect the noise levels inside. It is reasonable to assume that a 10 db(A) difference between indoor and outdoor noise levels should be chosen when setting acceptable outdoor levels.

Based on the above, continuous outdoor levels should not exceed 55 dB(eq) if satisfactory listening conditions are to be maintained indoors with open windows.

In many countries surveys have been conducted of the effects of noise on various activities in everyday life. Aircraft noise (affecting people who live near airports) has its greatest effect on speech communication in the home (television, radio, telephone, conversation) with a much lower effect on relaxation, reading and sleep. Traffic noise has its greatest effect on sleep, with effects on speech communication (as above) following next and mental activity (reading, thinking) third.

Unfortunately, most studies have not arrived at numerical relations between noise levels and degree of effect on sleep, reading, thinking and relaxing. However, clear relations between noise and speech communications do exist, as described above.

We are forced to the conclusion that until much more is learned about numerical relations between noise and human activities like sleep and thinking, interference with speech communication must serve as the surrogate for interference with other human activities.

OVERT COMMUNITY REACTION TO NOISE

Noise that seriously affects human activities, or is sufficiently aggravating, often leads to public complaints, lawsuits, or demonstrations. Such actions are commonly associated with aircraft noise where airports are closely surrounded by residential areas. Actions of this kind have sometimes been directed against rail transportation, traffic and industrial noises, the principal determinants of urban environmental noise.

The customary means for measuring community environmental noise is the day/night level, L_{dn}, which was defined earlier. The day/night noise level differs from the straighforward equivalent noise level, in that nighttime noise is penalized 10 dB see Fig. 7).

Overt community reaction is dependent on other factors than the day/night level L_{dn}. In the colder climates, people are bothered more by noise in the summer because they are less accustomed to noise through open windows. Quiet communities are bothered more by an occasional loud noise than are noisy ones. In a very noisy community, a large percentage of those people most affected by noise eventually move away. Thus, if there is a long history of high noise levels in a community, complaints against a new, even higher, level will not be as many as in a community less accustomed to noise. Finally, noises with a particularly raucous character, or with a singing (pure) tonal content are more disturbing than more uniform noises.

For example, a certain noise in a quiet suburban community might be just as offensive to the inhabitants as a 20 decibel louder noise in a very noisy urban community. Similarly, a new noise in a community might be as annoying as a familiar noise that is 10 decibels more intense. People are also more tolerant (by 10 or so decibels) to a noise that they know is very necessary and will not continue indefinitely. The summer/winter difference is worth 5 to 10 decibels (open vs closed windows) and a pure tone or raucous noise is equivalent to an increase of 5 to 10 decibels L_{dn}.

Several conclusions have been deduced from studies of overt neighborhood complaint situations:

1. There appears to be no community reaction to an intruding noise when its L_{dn} level is more than 5 dB less than the otherwise prevailing L_{dn} noise level.

2. A significant number of complaints may be expected when the day/night noise level L_{dn} of the intruding noise exceeds that existing without the intruding noise by 5 to 8 dB(dn).

3. Vigorous community reaction may be expected when the excess approaches 20 dB(dn).

4. There is no evidence in many cases studied in the United States that even sporadic complaints result from day/night levels of less than 50 dB(dn).

5. The dividing line between "no reaction" and "sporadic complaints" appears to be at about 55 dB(dn) in the U.S. cases studied.

EXPRESSIONS OF ANNOYANCE WHEN QUESTIONED

Social surveys in which people were asked to express their annoyance with environments of varying noisiness have been made in many countries. Some surveys constructed a scale of annoyance; others simply report the responses to the direct question of "how annoying is the noise". Those studies have also given a relationship between the number of people who say they are "highly annoyed" and the number of people who indicate that they have ever complained about the noise to anyone in authority.

The results of these studies, all of which involved some degree of aircraft noise, are shown in Fig. 8.

The abscissa gives the day/night, outdoor noise level (L_{dn}) in dB(dn) as measured in the region where each person questioned lived. The left ordinate gives the percentage of those who say that they have ever complained to someone in authority about the noise. The right-hand ordinate gives the percentage of those who claim, when questioned in the survey, to be highly annoyed with the noise.

The three circles on the graph give the points of average "community reaction" and serve to demark four regions of the graph: (1) no reaction; (2) some reaction; (3) complaints and threats of legal action; and (4) vigorous action by the community.

The top abscissa gives the relative importance of aircraft noise as a factor causing persons questioned to dislike the area or to want to move from the area. For example, below 54 dB(dn), noise is the least important of all factors (area is dirty/overcrowded, desire better climate, desire better living conditions, undesirable neighbors, want to be nearer work, want change, too much other noise) in causing people to want to move or to like their area less now than in the past. Above 68 dB(dn) aircraft noise is the most important factor.

CONCLUSIONS ON INTERFERENCE OF NOISE WITH HUMAN ACTIVITIES

The primary effect of noise on human health and welfare owing to interference with human activity is interference with speech communication. In the home, the noise level below which speech interference is not affected is 45 dB(A). This level corresponds to an outdoor day/night level of 55 dB(dn). Also 45 dB(A) is consistent with the background noise levels inside the home that exist with people's activity.

Reference to Fig. 8 shows that a L_{dn} of 55 dB(dn) is that level below which expected community reaction is zero. It, therefore, may be identified as the highest level outdoors in residential areas that is compatible with the protection of public health and welfare. A level of 55 dB(dn) is also compatible with adequate speech communication indoors and outdoors.

One must remember, of course, that local situations, attitudes and conditions may make lower levels desirable for some locations or may permit higher levels. A noise environment that will not be annoying to some small percentage of the population cannot be identified by specifying noise level alone, at least at the present time.

ACKNOWLEDGMENT

The author has drawn primarily on two summary documents in preparing this paper. These documents, in turn,are based on hundreds of scientific papers which have appeared in the technical press, many of which are listed in the documents so they will not be referenced here. The two documents are (1) Revised Draft Document of the U.S. Environmental Protection Agency, "Information on Levels of Environmental Noise Requisite to Protect Public Health and Welfare with an Adequate Margin of Safety", January 1974; and (2) Leo L. Beranek, Editor, "Noise and Vibration Control", McGraw-Hill Book Co., New York, New York, 1971.

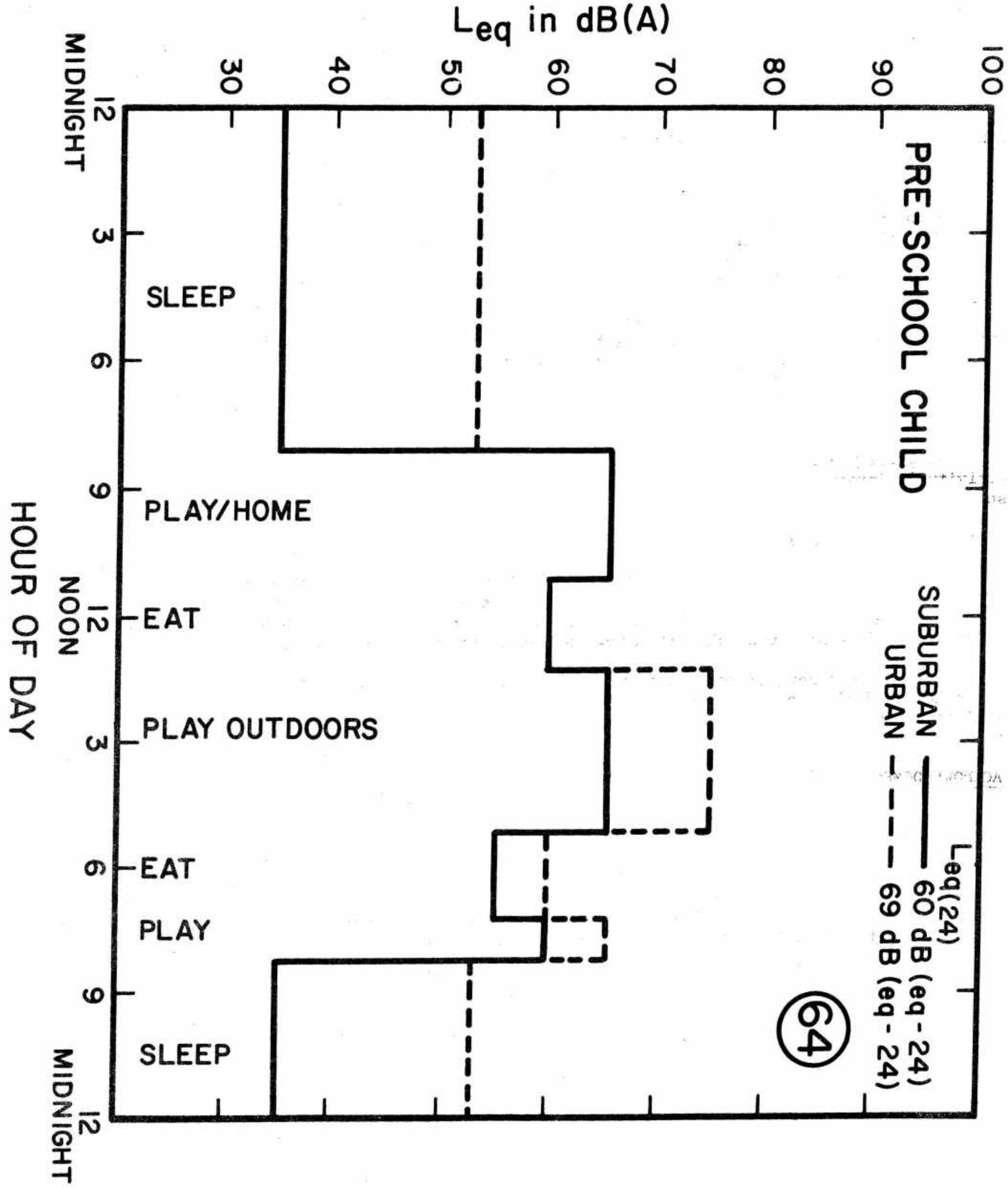

Fig. 1 Typical Daily Noise Exposure Pattern of a Pre-school Child.

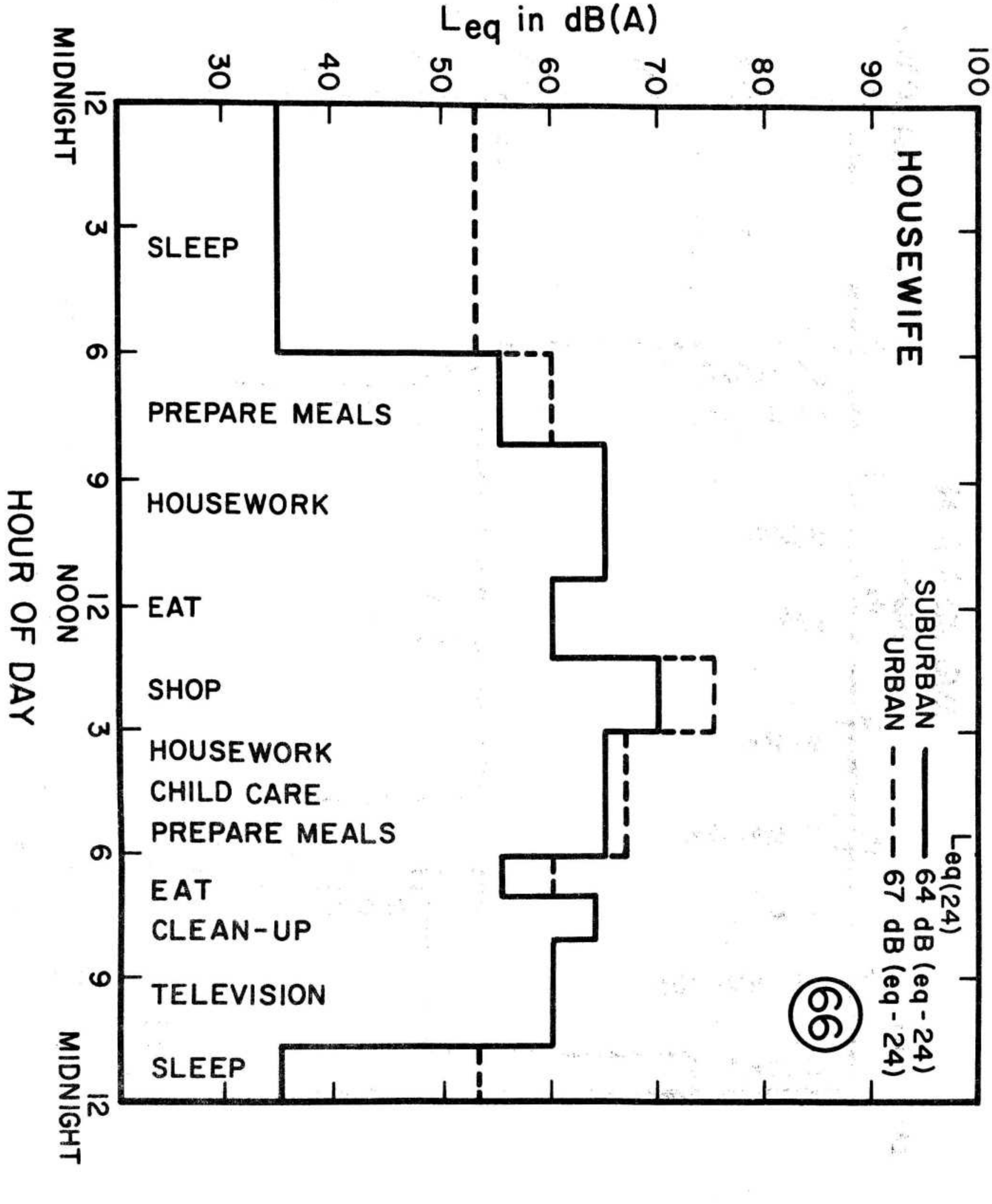

Fig. 2 Typical Daily Noise Exposure Pattern of a Housewife.

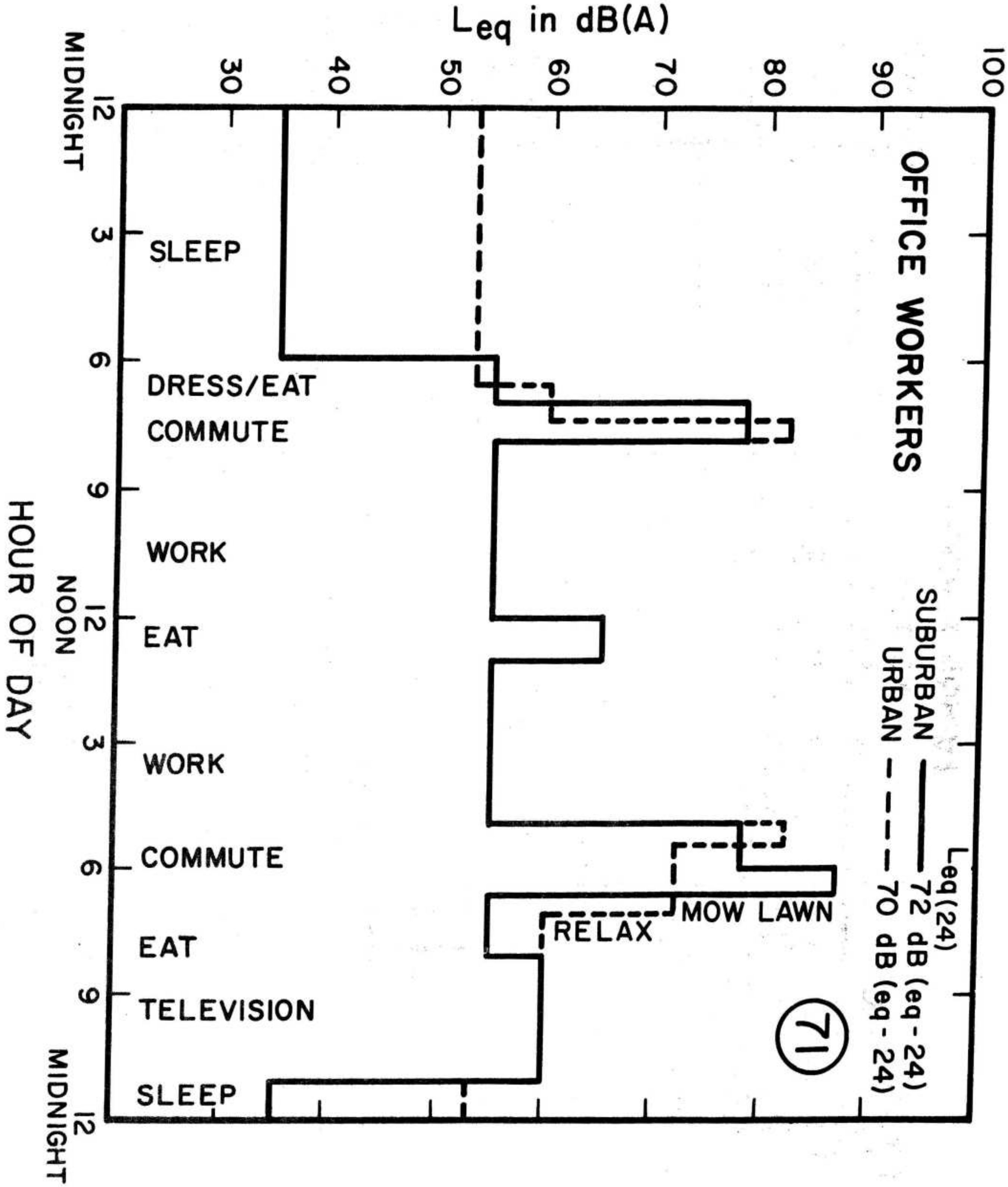

Fig. 3 Typical Daily Noise Exposure Pattern of an Office Worker.

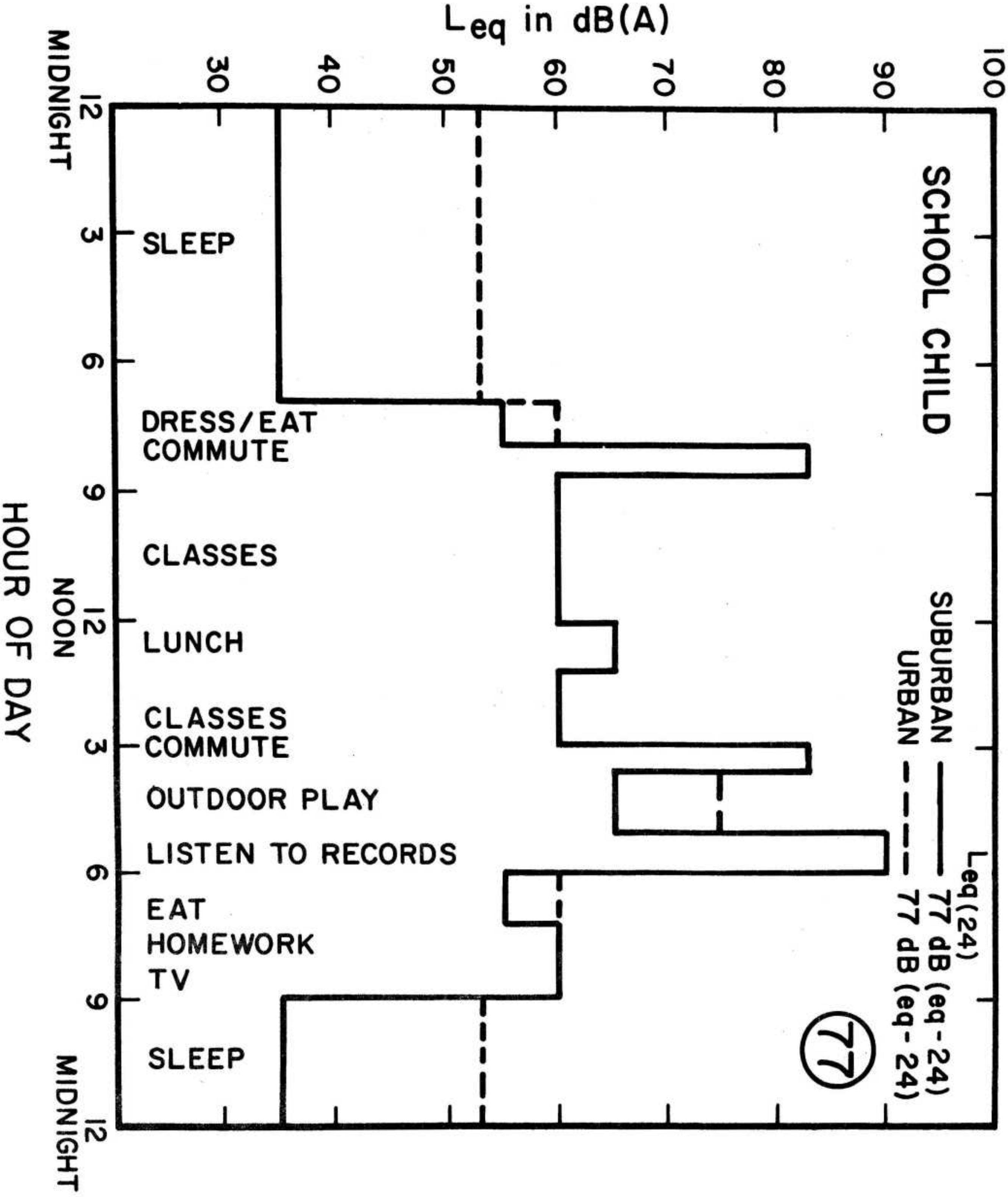

Fig. 4 Typical Daily Noise Exposure Pattern of a School Child.

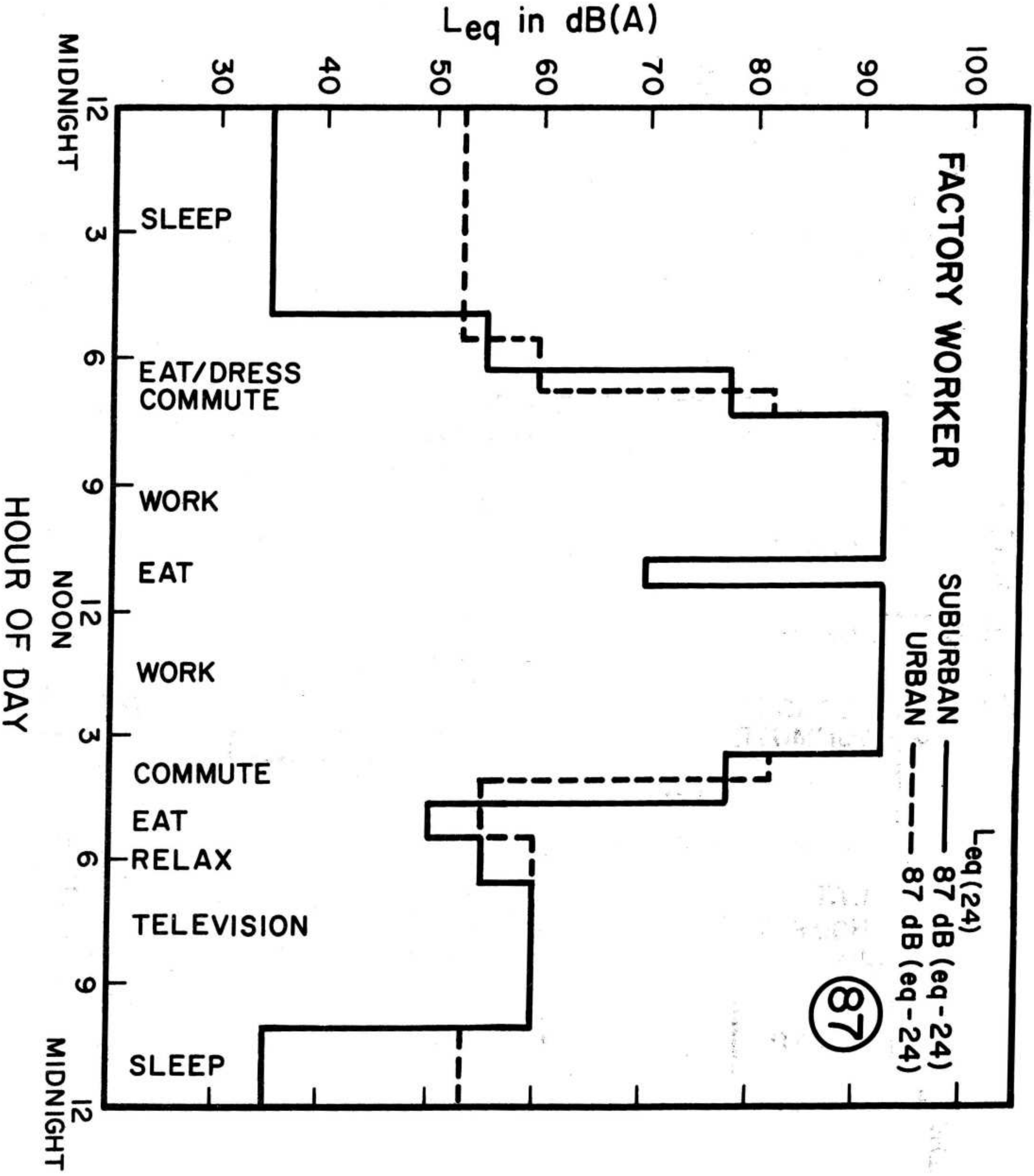

Fig. 5 Typical Daily Noise Exposure Pattern of a Factory Worker.

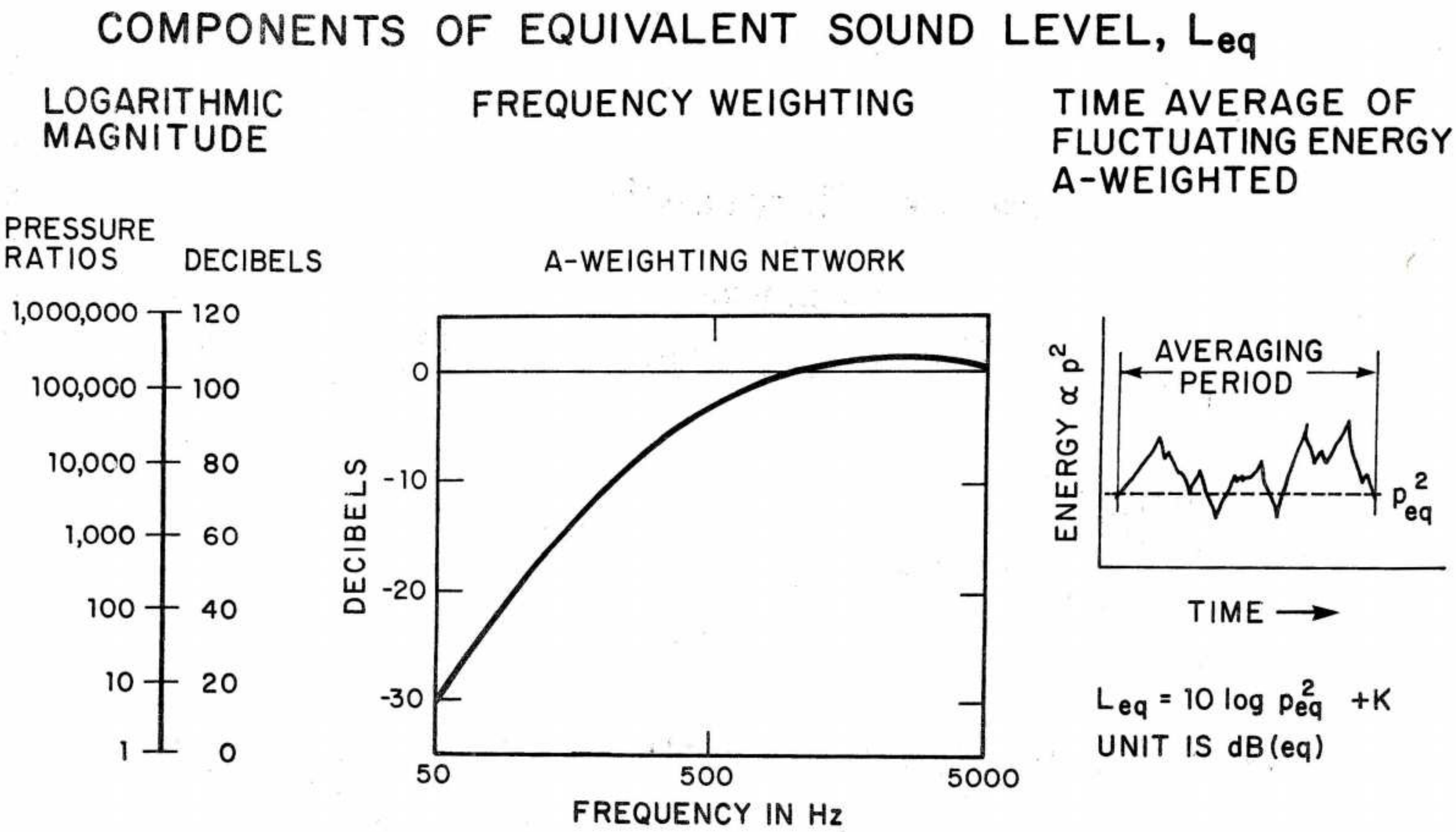

Fig. 6 Illustration of the Three Basic Factors that Comprise Equivalent Sound Level, L_{eq} in dB(eq).

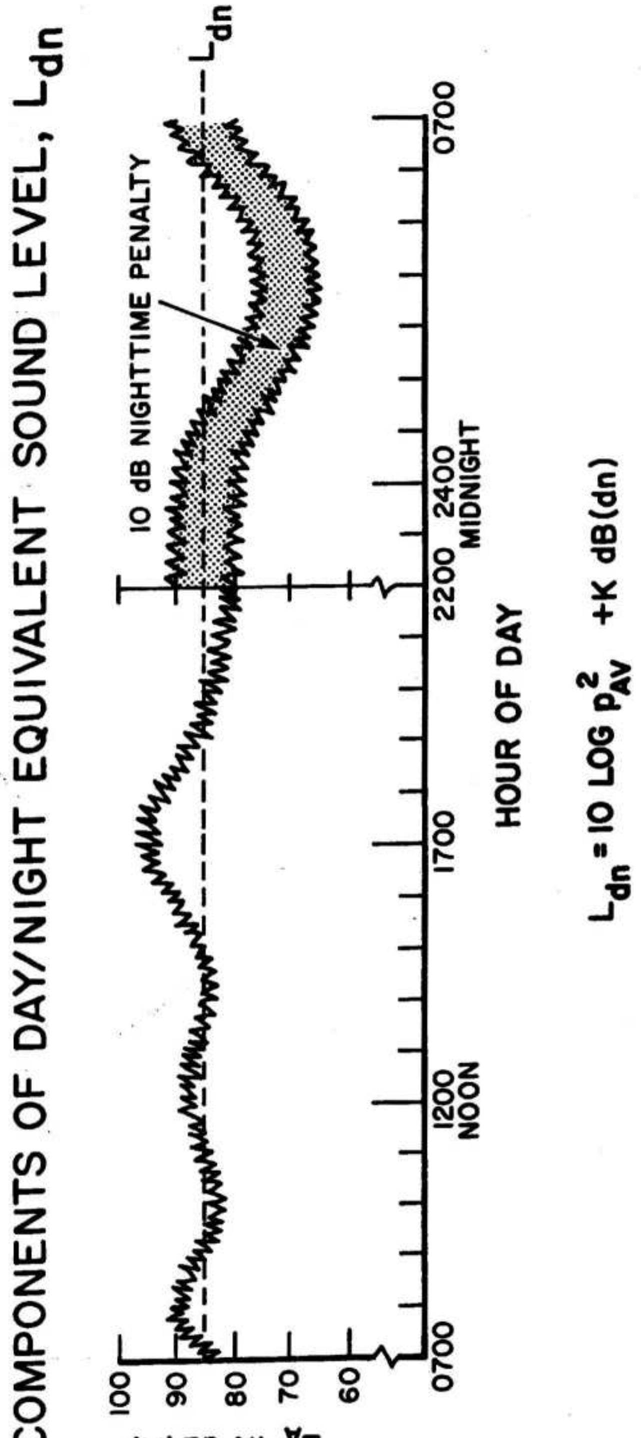

Fig. 7 Illustration of the Method Used to Derive the Daytime/Nighttime Equivalent Sound Level, L_{dn} in dB(dn) from the Day-long Fluctuating Noise Level. Note that the antilog of $(L_A/10)$ Must Be Taken to Obtain p^2. Then p^2 is Averaged to Obtain p^2_{av}. Finally $10 \log p^2_{av}$ is taken to get L_{dn}.

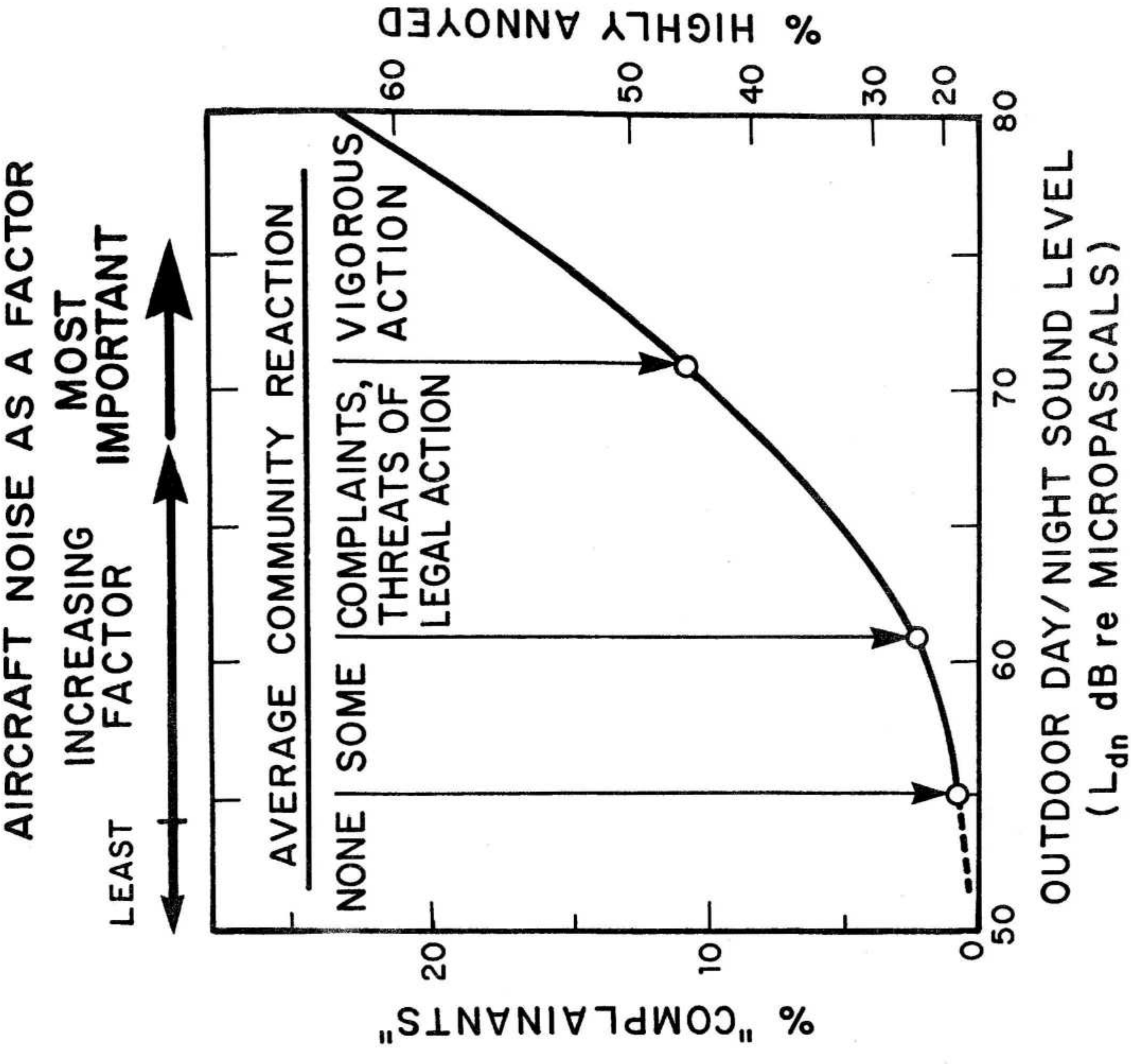

Fig. 8 Chart showing interrelations among percentage who complain, percentage who are highly annoyed, L_{dn} noise levels, regions of various degrees of community reaction and the relative importance of various levels of aircraft noise.

PERCENTAGE RISK OF DEVELOPING A HEARING HANDICAP, 8 HR DAY EXPOSURE

Exposure level in dBA	Age, years	20	25	30	35	40	45	50	55	60	65
	Exposure, years (re age 20)	0	5	10	15	20	25	30	35	40	45
80	Total	0.7%	1.0	1.3	2.0	3.1	4.9	7.7	13.5	24.0	40.0
80	Due to noise	No increase in risk at this level of exposure									
85	Total	0.7%	2.0	3.9	6.0	8.1	11.0	14.2	21.5	32.0	46.5
85	Due to noise	0.0	1.0	2.6	4.0	5.0	6.1	6.5	8.0	8.0	6.5
90	Total	0.7%	4.0	7.9	12.0	15.0	18.3	23.3	31.0	42.0	54.5
90	Due to noise	0.0	3.0	6.6	10.0	11.9	13.4	15.6	17.5	18.0	14.5
95	Total	0.7%	6.7	13.6	20.2	24.5	29.0	34.4	41.8	52.0	64.0
95	Due to noise	0.0	5.7	12.3	18.2	21.4	24.1	26.7	28.3	28.0	24.0
100	Total	0.7%	10.0	22.0	32.0	39.0	43.0	48.5	55.0	64.0	75.0
100	Due to noise	0.0	9.0	20.7	30.0	35.9	38.1	40.8	41.5	40.0	35.0
105	Total	0.7%	14.2	33.0	46.0	53.0	59.0	65.5	71.0	78.0	84.5
105	Due to noise	0.0	13.2	31.7	44.0	49.9	54.1	57.8	57.5	54.0	44.5
110	Total	0.7%	20.0	47.5	63.0	71.5	78.0	81.5	85.0	88.0	91.5
110	Due to noise	0.0	19.0	46.2	61.0	68.4	73.1	73.8	71.5	64.0	51.5
115	Total	0.7%	27.0	62.5	81.0	87.0	91.0	92.0	93.0	94.0	95.0
115	Due to noise	0.0	26.0	61.2	79.0	83.9	86.1	84.3	89.5	70.0	55.0

Percentage of Population

STEADY A-WEIGHTED NOISE LEVELS THAT WILL ALLOW COMMUNICATION WITH 95 PERCENT SENTENCE INTELLIGIBILITY OVER VARIOUS DISTANCES OUTDOORS FOR DIFFERENT VOICE LEVELS

VOICE LEVEL	COMMUNICATION DISTANCE (METERS)					
	0.5	1	2	3	4	5
NORMAL VOICE	72	66	60	56	54	52 dB(A)
RAISED VOICE	78	72	66	62	60	58 dB(A)

MAXIMUM L_{dn} VALUES IN dB(dn) IDENTIFIED WITH THE ONSET OF HEALTH AND WELFARE EFFECTS ON PEOPLE

FOR ALL TYPES OF AREAS* THE $L_{eq(8)}$ LEVELS FOR PROTECTION AGAINST ANY HEARING LOSS AT ALL FREQUENCIES AFTER 40 YEARS OF EXPOSURE, 8 HOURS A DAY, 250 DAYS PER YEAR IS 75 dB(eq-8)

PARTICULAR OCCUPIED AREAS	MEASURE	INDOOR	OUTDOOR
RESIDENTIAL	L_{dn}	45	55
HOSPITALS (OPEN WINDOWS)	L_{dn}	45	55
HOSPITALS (AIRCONDITIONED)	L_{dn}	45	65-75
EDUCATIONAL (OPEN WINDOWS)	L_{dn}	45	55
EDUCATIONAL (AIRCONDITIONED)	L_{dn}	45	65-75
OFFICES (OPEN WINDOWS)	L_{dn}	45	55
OFFICES (AIRCONDITIONED)	L_{dn}	45	65-75

*e.g., TRANSPORTATION, INDUSTRY, COMMERCIAL, RECREATIONAL, AND FARM MACHINERY.

Noise, Shock & Vibration Conference, 1974 Monash University, Melbourne

THE 'SAFE' WORKDAY NOISE DOSE

D. Ward
Hearing Research Laboratory
University of Minnesota

The rationale and data base underlying the major alternative proposals for a permissible 8-hr exposure to industrial noise, which range from the present 90 dBA down to 55 dBA, are discussed. The present evidence indicates that for ordinary industrial noises, 90 dBA will lead to measurable noise-induced permanent threshold shifts in some susceptible individuals, 80 dBA can be considered completely safe, 70 dBA is unnecessarily over-protective, and anything lower is absurd. If a fixed trading relation between level and exposure time must be used, experiments using temporary threshold shifts show that the 5-dB-per-halving-time relation of the present American regulation is more accurate than the 3-dB trading relation of the total-energy (immission) theory supported by ISO and under consideration by the Environmental Protection Agency of the USA. It is contended that the over-protective proposals, and indeed the total-energy hypothesis in any form, are based on the erroneous assumption that noise is analogous to real environmental pollutants such as radiation, sulphur oxides, lead, and so on. What appears to have been forgotten is the fact that the normal function of the ear is the reception of sound.

In the field of hearing loss induced by noise, the question of who is to be protected from what, and by whom, has undergone some interesting changes in the past few decades, changes parallelling a general shift of governmental policy. From support of exploitation of the weak by the powerful, the tendency has been progressing toward the legitimate function of government: protection of the citizen against damage from his neighbors. Unfortunately, the reformers producing this change cannot seem to stop when they succeed in protecting us against others, but go on to protect us against ourselves (as, for example, in the matter of mandatory seat-belt wearing). As a result, governmental agencies all over the world charged with developing standards for noise exposure are under pressure to protect the most sensitive people from the slightest change in physiological function, even when this is due to noises to which they choose to expose themselves. This partly explains why suggested permissible 8-hr exposures to noise supported by various individuals or groups range from 55 to 90 dBA. I should like to discuss the reasons for this great range in more detail today.

Half a century ago, the original purpose of Workmen's Compensation Laws was to indemnify a worker for loss of earning capacity. In the field of hearing loss, this could hardly occur except following acoustic trauma--a single exposure that produced so much loss that in the worker's normal work environment he was handicapped in not being able to hear what others hear, and so would have to be shifted to a less responsible (and less remunerative) job. The hearing loss that developed gradually over a period of several years seldom became so severe that the worker could not hear nearly as well as a normal-hearing person in his own noise environment, even though he might have trouble elsewhere. Thus the economic consequences of such indemnification were not very severe, because few workers were involved.

Gradually, however, public indignation over early deaths and obvious impairment in mines and mills because of employer disregard for the health of employees led to the consensus that no person should suffer impairment in health because of his employment. In our field, this shift of opinion meant that loss of earning power was no longer a requirement for compensation; instead, the criterion was taken to be "handicap": a loss of hearing so severe that the individual was aware of difficulty in hearing speech. Therefore a group of otologists, audiologists and speech scientists examined the relevant data and came to the conclusion that handicap existed (that is, people complained) when the average Hearing Level (ASA 1951) at 500, 1000 and 2000 Hz was 15 dB or greater; the magnitude of the losses at 4 and 8 kHz seemed almost irrelevant. Thus was born the "low fence" that lives on in the USA, now grown to 26 dB HL (ISO) because of the change in audiometric standards.

Handicap seemed to be complete--i.e., the patient understood practically nothing--when the average loss, still at 500, 1000 and 2000 Hz, was about 65 dB higher. So for ease of calculation, the committee decided that if one postulated that there was an increase in handicap of 1.5% for each 1-dB increase in loss (15% for each 10 dB), then 100% handicap would occur when this average HL reached $15+(100/1.5)=82$ dB(ASA) or about 93 dB (ISO). This low fence and impairment scale is generally known as the AAOO (American Academy of Ophthalmology and Otolaryngology) formula.

Although there has never been agreement among scientists that impairment in hearing speech under all circumstances was independent of the HLs at 4 and 8 kHz, nor that the low fence really is 26 dB HL (ISO), nor that complete impairment was reached only at 92 dB--nor, for that matter, that handicap even does grow linearly with HL in the first place--the prestige of the medical societies has been great enough that the AAOO formula has been adopted in a majority of the states in the USA. Indeed, the AAOO has just reaffirmed their support of these principles in their revised Guide for Conservation of Hearing.

It was only natural, therefore, that when it came to setting up noise-exposure limits for workers, considerable weight has been attached to this AAOO low-fence criterion. The "risk" associated with a given habitual noise exposure is defined as the difference between the probability that the hearing of the exposed worker would exceed the low fence after 20 years of daily exposure and the probability that the low fence would have been exceeded had he not worked in the noise. Thus if, of 100 45-year-old colliery workers, 25 were found to have handicapping losses, while a group of matched controls (i.e., men who were exposed to the same auditory hazards outside the work situation--the same average exposure to gunfire, illnesses, chain saws, firecrackers, head blows--as the colliery workers, but who worked in quiet) showed only 10 men out of 100 exceeding the low fence, then the "risk" associated with the typical exposure involved would be taken to be 25-10=15%. Said again, the worker who already had a 10% chance of exceeding the handicap threshold at age 45 due to the joint action of presbyacusis (the loss of hearing due to aging processes) and to sociacusis (that attributable to the vicissitudes of modern life) would now have a 25% chance when these hazards are combined with those occasioned by his noise exposure at work, so that the risk "caused" by the exposure at work is 15%.

If this definition of impairment is accepted, the job of setting standards reduces to simply determining what noise exposures just produce a specified degree of risk. Zero risk, with this definition, would exist when the incidence of handicap is no higher than that attributable to presbyacusis and sociacusis in a non-exposed population.

Our Congress, however, in the passage of the Noise Control Act of 1972, was clearly not content with such a lenient standard. The Act charged the Environmental Protection Agency with ultimately developing standards that would protect all citizens against any deleterious effects on their "health and welfare"--with even an "adequate margin of safety" thrown in for good measure. In this context, permitting unlimited amounts of hearing loss at 4000 Hz, just because the redundancy of speech is such that most people can understand--at least in quiet--speech out of which all the spectral elements above 2000 Hz had been filtered, was unwarranted. On the other hand, everyone except our Congressmen realized that the goal of protecting even the most susceptible individual from any loss whatsoever was somewhat impractical. At any rate, some new "low fence" was indicated.

The Office of Noise Abatement and Control (ONAC) of EPA, following a recommendation made by their scientific advisers from Wright-Patterson Air Force Base under Henning von Gierke, has suggested that this low-fence criterion be a 5-dB change in threshold at the frequency most sensitive to noise damage, 4000 Hz, in the most susceptible 10% of the workers exposed. Since 5 dB is the size of the smallest step on most audiometers, it might seem at first glance that a more stringent criterion could hardly be suggested, unless of course one attempted to protect the most susceptible 1% (or 0.1%, etc.) instead of the most susceptible 10%. However, if a proposed exposure limit is based not on hearing loss at all but on auditory fatigue (temporary threshold shift, or TTS), even lower exposures could be indicated. One might take the view, as indeed one American as well as several Russian investigators have, that any measurable auditory fatigue indicates a situation that is hazardous when repeated daily for 40 years.

It is no wonder, then, that currently-espoused limits of exposure for the standard 8-hr workday range all the way from 55 dBA to 90 dBA. Almost all of these suggestions are "correct"--that is, they protect some fraction of the population against something--but since the goals differ, so do the permissible levels. A further complicating factor is that exposure levels are nearly all specified in terms of dBA, but the fact of the matter is that two noises equal in dBA are not necessarily equal in hazard to hearing; if all the energy of a noise whose level has a given dBA rating is concentrated in the 2-4-kHz region, considerably greater TTS, at least, will be produced than by a more typical industrial noise at the same dBA level whose energy is spread over many octaves.

Let us begin at the top, so to speak, and work down. The present "Walsh-Healey" or "OSHA" exposure standard for 8 hr is, as everybody knows, 90 dBA. As far as I have been able to tell, this limit was not really designed to meet any specific criterion, but represents a political compromise between scientists and conservationists who really wanted a lower limit, on the one hand, and representatives of industry, who knew that the lower the limits were set, the more it would cost to comply, on the other. No data I know of imply that 8 hr of 90 dBA of typical steady industrial noise day after day is completely innocuous; instead, this exposure represents a degree of risk that was acceptable to the designers of the rule.

The three sets or collections of data most often cited in discussion of damage-risk criteria are those of Baughn (1966, 1973), Robinson (1968), and Passchier-Vermeer (1968). It may be worthwhile to review their results briefly at this point, in order to understand some of the suggested standards. Baughn's data on 6835 workers are summarized in Fig. 1. Here the percentages of right ears with AAOO impairment are shown as a function of age for three relatively-steady-state-noise exposure levels: 92, 86 and 78 dBA. The curves are all idealized; Baughn, not unlike other workers in this area, does not publish the raw data. The percentages are known to be inflated by the presence of TTS (no attempt was made to test men only at the beginning of the shift) and probably by masking of the more sensitive ears at 500 Hz. Furthermore, no control data were gathered. With these reservations, however, the implication of Fig. 1 is that 86 dBA is more hazardous than 78 dBA, so that, unless TTS can explain all the difference, a standard can be no higher than about 80 dBA if it seeks to prevent all risk.

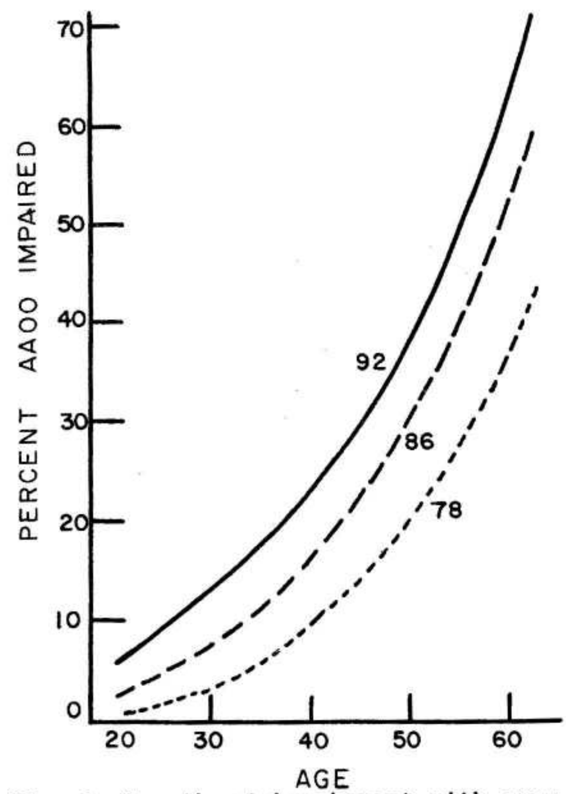

Fig. 1. Growth of impairment with age; dBA is the parameter. (Baughn, 1966).

A similar conclusion can be reached by considering the results obtained by Robinson on both ears of 759 noise workers and 97 controls. Robinson, a physicist, fits his data to fancy equations and, like Baughn, prefers to show us smoothed curves rather than actual data. Be that as it may, Fig. 2 shows the implication of Robinson's analysis. Here the rise of the median HL at 4 kHz with years of work (presuming the worker began at age 20) is plotted, with level the parameter. Again it appears that if one were to extrapolate downward from the curves shown for 95, 90, and 85 dBA, the "no noise" condition should agree with a curve of just below 80 dBA. That is, habitual exposure to 80 dBA for 8 hr should give only a slight increase in the hearing loss at 4 kHz over that ascribable to the combined action of presbyacusis and sociacusis.

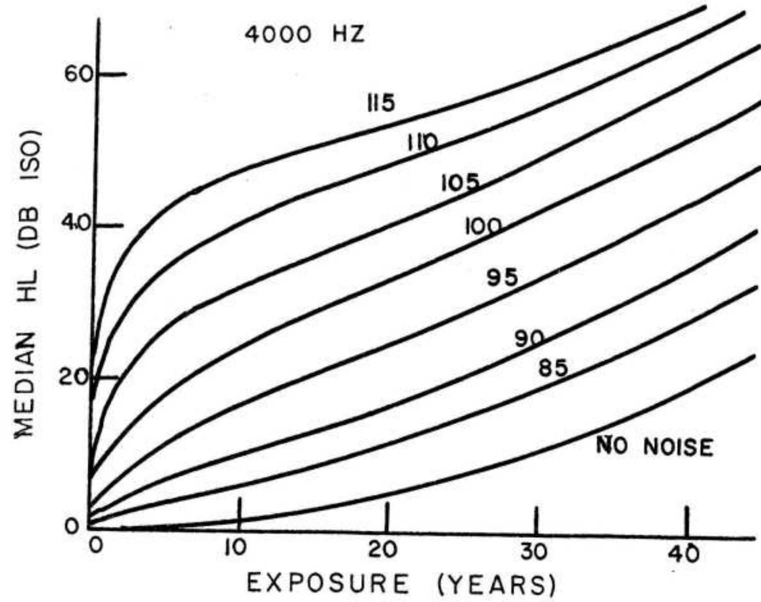

Figure 2. Increase of HL at 4 kHz with years of exposure; the parameter is A-weighted sound level. After Robinson, 1968.

Passchier-Vermeer put together the results of 8 different studies involving continuous exposure to noises ranging from 84 to 102 dBA (there was one datum at 79 dBA, from a survey by Kylin (1960), but this was a group of only 7 men, so one can hardly attach much weight to it). She plotted a series of graphs showing the relations between median noise-induced permanent threshold shift (NIPTS--the number of dB by which the HLs of the population concerned exceeded those of a non-noise-exposed group, according to a synthesis of normal data by Spoor) and the level of the noise. Figure 3 shows the collected data at 4000 Hz for persons exposed for 10 yr or more (NIPTS generally grows swiftly in the first years of exposure, reaching an asymptote at 10 yr or so). Although Passchier-Vermeer made her line of fit to the data veer off to the left as shown by the dashed line, if one instead ignores the one point at which her curve ends (which, as I said, was based on 14 ears of 7 workers), and fits a straight line to the data (the solid curve), it is clear that 80 dBA will just fail to produce a NIPTS, that 85 dBA will produce a median 10-dB NIPTS, and 90 dBA a median shift of 20 dB. Similar figures for other frequencies show that 0, 10 and 20 dB of NIPTS, respectively, would be caused by: 77, 86 and 94 dBA at 6000 Hz; by 84, 93 and 102 dBA at 8000 Hz; and by 80, 85 and 90 dBA at 3000 Hz (just as at 4 kHz). At 1000 and 500 Hz, no change was observed at levels up to 90 dBA; a 5-dB NIPTS at 1000 Hz required a level of at least 95 dBA, and at 500 Hz, about 100 dBA.

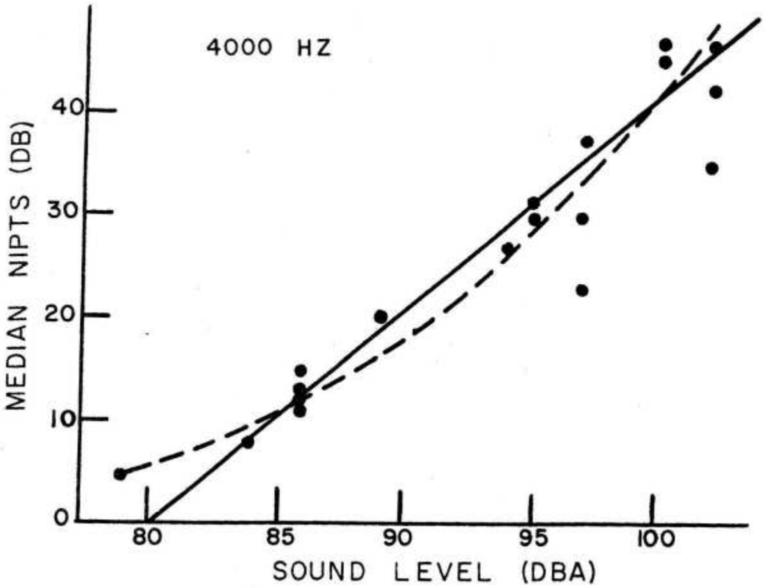

Figure 3. Growth of NIPTS with level in persons exposed about 10 years. After Passchier-Vermeer, 1968.

The analysis of Passchier-Vermeer provides some sort of justification for the 90-dBA standard. If one were trying to protect only against an excessive proportion of AAOO impairment, and not worrying about the most sensitive frequency, then a 90-dBA standard is not unreasonable. Only very small median losses would be produced at 500 and 1000 Hz, perhaps 10 dB at 2000 Hz, and some 20 dB at 4000 Hz. Thus the percentage of workers pushed over the low fence by the noise should not be very large. But if one accepts the viewpoint that the average person should not suffer any significant change in threshold sensitivity due to industrial noise, then it is clear that less severe exposures are indicated. Thus NIOSH (National Institutes for Occupational Safety and Health), in a document released in

1972, proposed that the 8-hr exposure level be lowered to 85 dBA. Again, this was considered to permit some risk as a balance against the rather large sums of money required to reduce exposure levels below this point. However, this recommendation has not been implemented by any agency except the USA Army and Air Force. In civilian government circles, apparently enough influence has been brought to bear that the level remains at 90 dBA. For example, consider the committee of 15 persons, mostly laymen, appointed by the Occupational Safety and Health Administration to advise the Department of Labor on exposure limits. Although an early version of their recommendation provided for a gradual reduction of the limit from 90 to 85 dBA over a period of years, that provision is missing from what will apparently be their final version.

It may be noted that within the last few years, additional studies have tended to support the view that 85 dBA for 8 hr constitutes a near-negligible risk. For example, Roth (1970) measured the hearing of persons working in just about exactly 85-dBA noise generated by grinding operations in a ceramic shop. Although he concludes that the existence, in this group of 106 workers, of 19 persons with HLs of 20 dB or above at some test frequency in either ear means that 85 dBA is hazardous, this conclusion rests on the naive assumption that all of the observed hearing losses had to be due to the noise. A similar disregard of sociacusic influence led Maksimova et al. (1966) to the same conclusion in regard to the hearing of 220 female workers in a candy factory generating a noise somewhere between 85 and 90 dBA, where they found that 15% of these women had HLs of 15 dB or more at some frequency. I cannot imagine that with such a low value of HL as the cutting score, a control group would show any smaller percentage.

What grounds, however, do exist for suggesting limits even lower than the 80 dBA for 8 hr implied by the evidence presented thus far as representing zero risk? There are at least three possibilities:

(1) To protect against noises whose spectra make them more hazardous than ordinary industrial noises having the same A-weighted sound level.
(2) To protect the most sensitive individual instead of just the average worker.
(3) To provide a margin of safety.

The first reason is unquestionably a good one, if one's desire is to set the basic limits on the basis of the worst of all possible conditions, and then to apply correction factors that raise the limit when conditions are less severe. Unfortunately, no human data involving NIPTS from noises in which all the energy is concentrated in the 2-4-kHz region is yet available. If, however, one can assume that the hearing loss at 4 kHz <u>is</u> caused by noise in that region, then a study of the spectra of the noises whose effects are summarized by Passchier-Vermeer indicates that the average difference between the overall dBA value of the noise and the octave-band SPL in the 2-4-kHz region is 6 dBA. In other words, one could predict that the same effect on the sensitivity at 4000 Hz would be produced by a 74-dB-SPL octave band of noise centered at 3 kHz as by an 80-dBA pink noise. And because the process of A-weighting actually increases the indicated value of a noise at this frequency, the 74-dB SPL would be equivalent to 75 dBA. In short, this analysis suggests that the basic exposure limit should be dropped to 75 dBA for 8 hr, but with a 5-dB correction (i.e., to 80 dBA) if the noise is reasonably broad in spectrum, which of course is usually the case.

By a strange coincidence, this figure of 75 dBA for 8 hr is the value proposed by ONAC in the second draft (the latest draft at the time I am writing this) of its "limits" document. (This document is one prepared in conformance with the mandate of the Noise Control Act of 1972 that EPA shall publish "information on the levels of environmental noise the attainment and maintenance of which in defined areas under various conditions are requisite to protect the public health and welfare with an adequate margin of safety." You will note that this is impossible, because health, at any rate, if not also welfare, depends not on levels but on <u>exposures</u>, which are joint functions of level <u>and time</u>. ONAC, faced with the alternatives of either telling Congress to go fly a kite or pretending that levels are synonymous with exposures, has chosen the latter course, which is probably prudent although it leads to some confusion in the document!) I say "strange coincidence" because they arrived at the 75-dBA figure on the basis of speculations regarding the most susceptible individual (rather than by taking spectrum of the noise into consideration--indeed, spectrum is not considered at all) and then finally allowing a correction for intermittency.

I contend, however, that no further correction for individual differences in susceptibility need be applied to the data cited above, in that the effect of the noise on the most susceptible individuals is already reflected in the curves: it is precisely the most susceptible individuals who are responsible for the first shifts in the distribution of HLs as noise exposure increases! Nearly everyone will be affected by 100 dBA for 8 hr over a period of years, fewer by 95 dBA, fewer yet at 90 dBA, and so on, until at 80 dBA or thereabouts nobody is affected, and therefore the difference between the HL distributions in 80-dBA workers and those of groups of persons who worked in anything lower becomes zero. This line of reasoning will be fallacious only if the most susceptible individuals are those who have either the best or the worst hearing initially, so that even when the median is unaffected, the 10%ile or 90%ile might be. For example, one might argue that it is the people with the most sensitive hearing who will be most susceptible. It is known that workers with lower (better) hearing thresholds show more TTS from a given day's exposure than those with elevated thresholds (Ward, 1963). So if TTS has any relation to NIPTS, one should look for changes in the most sensitive percentiles, say the 10%ile.

On the other hand, if one assumes that the existence of loss in a given ear proves that it is unusually susceptible, then perhaps one should look at the 90%ile. (Such an assumption is often tacitly made, and was indeed employed by one of the scientific advisers of ONAC (Johnson, 1973), but there really is no convincing evidence that it is correct. To even test the notion, it would be necessary to insure that all the persons whose hearing was being compared had had exactly the same noise exposure, not just "approximately" the same, which is all that can be said about all present NIPTS data.)

Accordingly, the question is, what do the actual distributions of noise-exposed and non-noise-exposed populations look like? Passchier-Vermeer collected all the appropriate data from the studies she analyzed, and concluded that the behavior of the 25 and 75%iles was indistinguishable from that of the median, which implies that a given noise is just as likely to produce a measurable loss in the best-hearing half of the population as in the worst-hearing half. If, then, susceptibility--in any operationally-useful sense of the word--is not dependent on HL per se, then it must be concluded that if a noise has no effect on the median, it will have no effect on any other decile, and so the 80-dBA value does take the most susceptible ears into consideration.

What about a possible "margin of safety"? ONAC's task was to consider not just industrial noise exposure alone, but rather the total noise exposure a citizen might be subjected to both at work and elsewhere. Work exposures and voluntary exposures to loud sounds must add together in some way; if the total permissible daily noise dose were the equivalent of 80 dBA for 8 hr, then one might expect that for the 80-dBA worker, even attending a symphony concert could constitute an increment large enough to produce some loss of hearing. Assuming it to be unreasonable to require that a person avoid loud music, refrain from shouting at other motorists, wear ear plugs while mowing his lawn, etc. (and at least it still is at the moment), perhaps industrial noise limits should be shifted down by 5 dBA to guard against such summative or at least interactive effects.

However, the same argument used to counter the necessity of making an allowance for susceptibility applies here. The industrial data of Passchier-Vermeer are based on real people, exposed to sociacusic influences, even though in some cases, efforts were made to exclude major ones. A failure of the distributions of persons exposed to 80-dBA noise at work to differ from that of those who do not work in noise at all means that, even added to the hazards of everyday living, an 8-hr exposure at 80 dBA is safe.

Thus if the implications of the charts of Passchier-Vermeer and Robinson hold up as more data is gathered (especially on workers in the 80-90-dBA range), a 75-dBA limit for continuous exposure for 8 hr/day, with a 5-dBA correction when the noise is broad in spectrum, seems to be correct for complete protection. It could be, of course, that that one point of Kylin's on Passchier-Vermeer's charts is actually correct, and that the line describing NIPTS as a function of level does bend to the left as Passchier-Vermeer drew it, because of sociacusic influences acting in conjunction with noise. An investigation is now underway in the USA in which workers who have spent many years in constant noise levels between 80 and 90 dBA will be intensively studied. Since ear protection is not yet required for these people, it may be our last chance to get clear data on humans. Even at worst, however, it is difficult to see how this 80-dBA 8-hr limit for broad-band noise could be in error by more than 5 dB, based on present data.

It is true, of course, that Kryter (1970, 1973) has been touting 55 dBA as the threshold level for damage. However, his contentions are based on rejection of the data cited here, speculative extrapolation of TTS data, and on a curious yet consistent assumption that NIPTSs are merely the same as raw HLs. Suppose that a worker at the age of 40 has a HL of 20 dB, while the average non-noise-exposed worker of that age has a 15-dB HL. Most of us would then agree that the NIPTS of the worker in question is 20-15=5 dB. Not Kryter, however; he contends that the NIPTS is 20 dB. It is no wonder that the losses associated with 80 dBA (as, for example, implied by Baughn's data) are judged by Kryter to be unacceptable--the amazing thing is how he even concludes that 55 dBA is innocuous, since some persons working in that level will surely be found to have crossed any low fence employed.

Before going on, let me return to the question of the role of TTS here. While I do not believe that TTS data should take precedence over PTS data in establishing limits that will prevent development of NIPTS, nevertheless I feel that TTS data do have some relevance. For example, what TTS is caused by an 8-hr exposure to 75 dB of high-frequency octave-band noise, the most severe possible with a 75-dBA limit? Figure 4 shows the growth of TTS_2 (TTS 2 min after cessation of exposure) at 4 kHz caused by a 2800-5600-Hz band of noise, for the median, 10%ile and 90%ile of the group of 20 young normal ears tested. The median at the end of 8 hr was 6 dB, the 90%ile 12 dB. If this can be regarded as a representative sample of ears, only one ear in 500 would display a TTS_2 of 20 dB or greater at the end of the day. Perhaps it will eventually be shown that a 20-dB TTS_2 repeated day after day will ultimately produce a PTS. In that case, a reduction of 5 dB to protect this most sensitive person would be in order. Until then, however, it seems to me that the 75-dBA level for this octave band of noise is a reasonable standard on both PTS and TTS grounds. I certainly see no reason to conclude that if any TTS is produced, then there is a finite hazard, as a couple of Russian investigators have assumed recently (Gel'tischcheva and Ponomarenko, 1968). They propose a limit of 60 dBA for a 4-kHz octave band of noise because in their subjects a 3-dB TTS was produced after a 1-hr exposure.

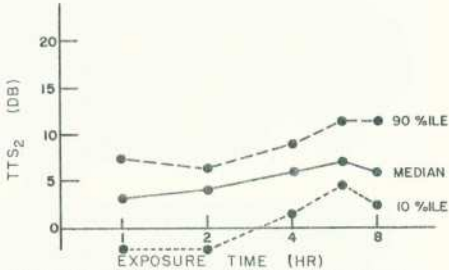

Figure 4. Growth of TTS_2 at 4 kHz with time in octave band of noise (2800-5600 Hz) at 75 dB SPL (20 ears).

So much for the basic standard. What now of shorter, interrupted, or irregular exposures, which are probably more typical of industry than the continuous ones involved in all the NIPTS data at hand? As you know, Robinson champions the "total immission" theory, which proposes that the NIPTS depends only on the integral of the A-weighted power entering the ear--the total A-weighted energy, so to speak. However, since Robinson's data, like those of Baughn and Passchier-Vermeer, concerned only persons with continuous exposures (those with intermittent exposures were carefully eliminated), there is no compelling reason to subscribe to that theory.

Some evidence does exist that implies that an intermittent exposure produces much less PTS than a steady one of the same energy. This evidence comes largely from miners. In the USA, Sataloff et al. (1969) showed that miners exposed for a total of nearly 3 hr daily to drilling noise of 115 to 122 dBA, but with some 5 min of quiet, on the average, between 3-min bursts of noise, had only about the percentage of ears with AAOO handicap as the Baughn and Robinson data would predict to occur in 100 dBA, which is at least 15 dB below the "effective level" L_{eq} of the exposure--that is, that level which, had it been constant throughout the 8 hr, would have contained the same energy as the intermittent exposure. A similar low incidence of handicapping losses has been reported by studies of miners in other countries (Bláha and Slepicka, 1967; Jönsson, 1967; Motta and Tarsitani, 1969). Also, remarkably small PTSs are produced in rock-and-roll musicians, despite their near-daily exposure to several hours of intermittent 110-dBA music (Speaks et al., 1969; Reddell and Lebo, 1972).

It is also well known that the TTS from intermittent exposures is much reduced relative to that from steady noise; indeed, if the noise bursts and intervening quiet periods are quite short (up to a minute), then the TTS from an 8-hr exposure when the noise is "on" half the time is less than half as great as when it is on continuously, a value well below that produced by an 8-hr L_{eq} (a continuous noise 3 dB lower).

Because of this information, the Walsh-Healey compromise, in addition to a basic 90-dBA 8-hr exposure, postulated a trading relation of 5 dB per halving of the exposure time instead of the 3-dB relation that is a corollary of the total-energy hypothesis, on the grounds that most exposures are intermittent. This trading relation of 5 dB seems to be reasonable, as it permits exposures up to 115 dBA for 15 minutes. However, the scientific advisers to ONAC have long been enamored of the total-energy principle (von Gierke was instrumental in getting it built into Air Force Regulation 160-3, a 1956 standard set for the Air Force), and so it is firmly esconced in the "Limits" document, lock, stock and barrel, except that a flat 5-dB correction factor is allowed if the noise is intermittent. Thus ONAC's suggested limit of 70 dBA for 8 hr of steady exposure is translated to an intermittent exposure of 75 dBA for 8 hr and thence to a 24-hr L_{eq} of 70 dBA, which means that 80 dBA would be permitted for 2.4 hr, 90 dBA for 0.24 hr (15 minutes), 100 dBA for 1.5 min, or 110 dBA for 9 seconds. I would hazard a guess that nobody except perhaps Kryter and Ponomarenko would contend that such a limit for total daily dose as this would be under-conservative for even the most susceptible of persons. You will note that this proposal is several orders of magnitude different from the Walsh-Healey provisions, 115 dBA being permitted for only about 3 seconds instead of 15 minutes. To my mind, such a limit is merely ridiculous. There is no substantial support to be found for the total-energy hypothesis, yet merely because it is a simple rule it is being seriously proposed. This shows how a small band of determined advocates can force their personal opinions on a government agency that is forced to do a complicated job without adequate funding.

While the merits of these fantastic limits are being debated, we at the Hearing Research Laboratory have been plodding along trying to determine, using TTS, whether the temporal trading relation should be 3 or 5 dB per halving time (or even 4 dB, as Pfander (1965) has long championed, and which has been adopted by the Air Force in a revision of AFR 160-3 as a "compromise" between 3 and 5 dB). While we hope eventually to determine NIPTSs in chinchillas exposed to various patterns of noise, at the moment we must study TTSs in man, and hope that if two 8-hr noise exposures produce the same TTS, they will eventually be shown to be equally hazardous.

Table 1 shows some of our results gathered last year, using a 4-kHz octave band of noise (2800-5600 Hz). The entries show the mean TTS_2s (in 20 ears) measured at 4 and 6 kHz at the end of 8 hr of exposure. In addition to continuous exposure (top line), 3 different on-fractions R were used (1/2, 1/4 and 1/8) and 3 different periods T (1.5, 9 and 40 min). Thus the Table indicates, for example, that the mean TTS_2 after 8 hr of exposure to 75 dB SPL was 6.4 dB (the TTS_2s at 4 and 6 kHz were always nearly equal), in agreement with Fig. 4.

It can be seen that the 5-dB-per-halving-time relation is supported by the data: a TTS_2 of about 8 dB is produced, for example, when the period is 1.5 min, by 45-sec bursts at 85 dB, by 22.5-sec bursts at 90 dB, and by 11.3-sec bursts at 95 dB. The reduction of TTS depends on the cycle duration, it is clear, but if that is held constant, then a 5-dB increase just about balances out a 50% reduction in cumulative exposure time.

TABLE 1

R	T (min)	Exposure Level (dB SPL) 75	80	85	90	95	100
1	cont	6.4	14.5	23.3			
1/2	1.5			8.6	14.0		
1/2	9			15.2			
1/2	40			18.1			
1/4	1.5				8.5	13.3	
1/4	9				14.7		
1/4	40				18.8		
1/8	1.5					8.6	19.7
1/8	9					10.5	
1/8	40				12.5	(20)	

Results using a 1000-Hz octave band of noise were quite similar, except that the trading relation implied is even greater than 5 dB--perhaps 6 dB per halving time. When we employed a 250-Hz octave band, an on-fraction of 1/2 gave less TTS_2 at 115 dB than did 95 dB of steady noise. The recuperative powers of the ear are clearly reflected by this result.

At any rate, even in this most hazardous auditory area, a trading relation of 5 dB appears adequate. Perhaps TTS data are not completely appropriate, but if they are all we have, it seems to me that some attention should be paid to them.

Actually, I would argue that the total-energy hypothesis, apart from having little empirical support, makes a false basic assumption, in postulating that every bit of energy contributes to the eventual demise of a hair cell. In a public hearing on the Levels document, the proponents of the total-energy theory repeatedly drew an analogy to the problem of radiation damage. Now as a first approximation, it is true that damage from X-radiation does tend to cumulate over a day or week; if it did not, then the photographic-plate radiation dosimeter would be useless, since it does integrate over time, regardless of the pattern of exposure. It is probably true that each high-energy particle penetrating the skull destroys a brain cell or two. But damage to hair cells from noise is, I feel, quite a different kettle of fish. After all, the brain is not normally a receptor for the identification of X-radiation, but the ear's customary job is detection of sound. For this reason, I cannot help believing that there is a reasonably high level, different for different people, below which no deleterious effect will be observed, no matter how long the exposure, any more than a long exposure of the eye to moderate levels of illumination will eventually produce destruction of rods and cones. Similarly, even for levels higher that this, there must be a critical duration below which, again, not the slightest permanent damage results. McRobert and I (1973) have gathered TTS data that imply that this is the case for impulse noise, at least. That is, if one determines the level of simulated gunfire that just produces a cumulative TTS, so that 20 such pulses will produce say 10 dB of TTS, and one then reduces the level by 9 dB, one can listen to over 600 of them with no resulting TTS (boredom ended the experiment at 600 pulses), although 80 of them should have produced the 10-dB TTS, according to the total-energy hypothesis.

* * * * *

In summary, it appears that octave-band levels below about 70 to 75 dB cannot produce a TTS that grows with exposure time (a conclusion we had already reached 15 years ago--cf. Ward, Glorig and Sklar, 1958, 1959), so that, when ordinary broad-band noises are concerned, for overall levels of 80 dBA or less, negligible hazard to hearing exists from an 8-hr exposure even for the most sensitive test frequency, 4 kHz; this conclusion is seen to be in agreement with NIPTS results. Risk criteria lower than this are based on simple fudge factors, extrapolations of questionable validity, or on the assumption that where a TTS is found, PTS will eventually occur. On the other hand, limits higher than this are compromises between risk of measurable NIPTS and the costs of noise control.

I do hope that the total-energy hypothesis based on a daily tolerable dose of 75 dBA for 8 hr does not replace our present Walsh-Healey (OSHA) regulation. I personally believe that an 85-dBA 8-hr criterion, with a 5-dB trading relation, is what should be aimed for, even though requiring ear protection for every person who works in 85 dBA will be a waste of effort for all but the most susceptible workers. I also hope we can somehow eliminate the silly notion that 116 dBA even for a second or two is forbidden; perhaps an equal-energy-based trading relation (i.e., 3 dB per halving time) for levels above 110 dBA should be used. At any rate, the relations among level, duration and pattern of exposure for constant risk are clearly complex; so the best solution, I am still convinced, is to continue to try to develop risk criteria that are accurate even though intricate, as we attempted to do in the CHABA criteria proposed 8 years ago (Kryter, Ward, Miller and Eldredge, 1966), and then try to simplify them, rather than starting with a simplistic principle and then trying to force the data to justify it.

Acknowledgment

The research reported herein was supported by a grant from the National Institute for Occupational Safety and Health (NIOSH) of the Public Health Service, Dept. of Health, Education, and Welfare (Grant #5 R01 OH 00350).

REFERENCES

Anon. Noise and Conservation of Hearing. Technical Bulletin TB Med 251, Department of the Army, Washington, D. C., March 1972.

Anon. Occupational Exposure to Noise....criteria for a recommended standard. US Dept. of Health, Education and Welfare, National Institute for Occupational Safety and Health, 1972.

Baughn, W. L. Noise control--percent of population protected. Int. Audiol. 5, 331-338 (1966).

Baughn, W. L. Relation between daily noise exposure and hearing loss as based on the evaluation of 6835 industrial noise exposure cases. Report AMRL-TR-73-53, Aerospace Medical Research Laboratory, Wright-Patterson AFB, Ohio, 1973.

Bláha, V. and J. Slepicka. Klinický a hygienický Rozbor Rizika Hluku v Kamenouhelných Dolech. Cs. Hyg. 12, 521-527 (1967).

Gel'tishcheva, E. A. and I. I. Ponomarenko. Noise standards for adolescents. Hygiene and Sanitation 33, Nos. 10-12, 199-203 (1968).

Johnson, D. L. Prediction of NIPTS due to continuous noise exposure. Report AMRL-TR-73-91 (also EPA-550/9-73-001-B), Aerospace Medical Research Laboratory, Wright-Patterson AFB, Ohio, 1973.

Jönsson, M. Siebaudiometrische Untersuchungen von Lärmarbeitern. Dtsch. Gesund.-wes. 22, 2286-2289 (1967).

Kryter, K. D. The Effects of Noise on Man. Academic Press, New York, 1970.

Kryter, K. D. Impairment to hearing from exposure to noise. J. Acoust. Soc. Am. 53, 1211-1234 (1973).

Kryter, K. D., W. D. Ward, J. D. Miller and D. H. Eldredge. Hazardous exposure to intermittent and steady-state noise. J. Acoust. Soc. Am. 39, 451-464 (1966).

Kylin, B. Temporary threshold shift and auditory trauma following exposure to steady-state noise. Acta Oto-laryngol. Suppl. 152 (1960).

Maksimova, L. I., P. S. Kublanova, V. B. Maiorov and K. A. Dmitrieva. Hearing loss in factory workers exposed to permitted levels of noise for prolonged periods. Hygiene and Sanitation 31:1, 167-172 (1966).

McRobert, H. and W. D. Ward. Damage-risk criteria: the trading relation between intensity and the number of nonreverberant impulses. J. Acoust. Soc. Am. 53, 1297-1300 (1973).

Motta, G. and D. Tarsitani. Il trauma acustico professionale dei lavoratori delle miniere di carbone. Clin. Otorinolaring. 21, 83-109 (1969).

Passchier-Vermeer, W. Hearing loss due to exposure to steady-state broadband noise. IG-TNO Report 35, April 1968. (Delft, Netherlands).

Pfander, F. Über die Toleranzgrenze bei akustischen Einwirkung. HNO (Berlin) 13, 27-28 (1965).

Reddell, R. C. and C. P. Lebo. Ototraumatic effects of hard rock music. California Med. 116, 1-4 (1972).

Robinson, D. W. The relationships between hearing loss and noise exposure. National Physical Laboratory Aero Report AC 32 (1968). (Teddington, England).

Roth, A. Untersuchungen über die gehörschädigende Wirkung von Industrielärm unterhalb der Grenznormative. Z. ges. Hyg. 16, 760-763 (1970).

Sataloff, J., L. Vassallo and H. Menduke. Hearing loss from exposure to interrupted noise. Arch. Env. Health 18, 972-981 (1969).

Speaks, C., D. Nelson and W. D. Ward. Hearing loss in rock-and-roll musicians. J. Occup. Med. 12, 216-219 (1970).

Spoor, A. Presbycusis values in relation to noise induced hearing loss. Int. Audiol. 6, 48-57 (1967).

Ward, W. D. Auditory Fatigue and Masking. In: Modern Developments in Audiology, J. Jerger, Ed. Academic Press, New York, 1963.

Ward, W. D., A. Glorig and D. L. Sklar. Dependence of temporary threshold shift at 4 kc on intensity and time. J. Acoust. Soc. Am.30, 944-954 (1958).

Ward, W. D., A. Glorig and D. L. Sklar. Temporary threshold shift from octave-band noise: applications to damage-risk criteria. J. Acoust. Soc. Am. 31, 522-528 (1959).

DAMAGE RISK CRITERIA FOR IMPULSE AND IMPACT NOISE

C. G. Rice
Institute of Sound and Vibration Research
The University, Southampton
Hampshire, U.K.

SUMMARY -

The historical development and current states of knowledge regarding impulse and impact noise damage risk criteria are critically reviewed.

Definitions of impulse and impact noise are given, from which it is possible to formulate two criteria so that such noises may be separately assessed for hearing hazard. The problems associated with the formulation of these criteria are stated, together with the difficulties likely to be caused by over-extrapolation of the experimental data upon which they were based.

Progress towards the unification of impulse and impact damage risk criteria with steady state noise exposure standards is discussed, although it is felt that further research will be necessary before this becomes possible in a form acceptable to, and implementable by, governmental agencies.

INTRODUCTION

The hazardous effects of high intensity impulse noise on hearing have long been recognised, and when reviewing the documented researches it is impossible to proceed far without reference to the classic work of Murray and Reid (1, 2). There is also little doubt that many of the fundamental problems which beset Murray and Reid when trying to quantify these hazardous effects still exist today.

In addition however, we currently have to placate the legal and political administrators of our noise polluted environments. This factor creates new problems, because the demands of society require that noise criteria must be readily understood and easily applied. In striking the correct balance between research and application therefore, care must be taken not to over simplify and extrapolate data out of the context in which it was obtained.

These problems are discussed in the context of damage risk criteria for impulse and impact noise.

DEFINITIONS OF IMPULSE AND IMPACT NOISE

Confusion seems to occur in the use of these terms; in the present discussion their broad definition will be taken as follows.

IMPULSE NOISE

A short duration sound particularly characterised by a shock front pressure waveform (i.e., virtually instantaneous rise time), usually created by sudden releases of energy; for example as encountered with explosives or in gunblast situations.

Such a characteristic impulse pressure waveform is often referred to as a Friedlander wave and is illustrated in figure 1a. This single impulse waveform is typically generated in free field environments where the sound reflecting surfaces which create reverberation are absent. In the gunfire situation additional mechanically generated noise is also present in addition to the shock pulse. In these situations the waveform envelope can take the form illustrated in figure 1b.

The duration of such noises vary from microseconds to several milliseconds (up to 50 ms), although in confined spaces the reverberation characteristics may cause the duration to extend up to about one-half second or so. In all cases however, the shock front waveform characteristic is present.

In general people are not habitually exposed to such noises and typical estimates of the number of pulses likely to be received on any one occasion vary between 10 and 100, although up to 1000 pulses can be anticipated.

IMPACT NOISE

Impact noises are normally produced by non-explosive means, such as metal to metal impacts in industrial plant processes. In such cases the shock front waveform characteristic is not always present, and due to the reverberant industrial environments in which they are heard, the durations are often longer than those usually associated with impulse noise. The background noise present in such situations, coupled with the regularity with which they occur, often causes the impacts to give the appearance of running into each other.

People in industrial situations are usually habitually exposed to such noises and the number of pulses heard on any one occasion often runs to several thousand.

The cases in favour or otherwise of the 'impulse' - 'impact' noise distinction may be variously made. It is becoming increasingly clear however that until we know considerably more than we do at present about the roles played by the numerous parameters involved in the establishment of damage risk criteria, it would be incautious to turn a blind eye to this distinction. Some of those factors currently thought to be important and worthy of incorporation into impulse/impact damage risk criteria are: peak sound pressure level, rise time of the initial shock front, waveform envelope characteristic, effective duration, spectrum content, critical level for the onset of hearing threshold shift effects, rate of occurrence of the pulses, total number of pulses in exposure, individual susceptibility to hearing impairment, orientation of the ear with respect to the noise source, acoustic reflex actions, total noise exposure history, etc.

DAMAGE RISK CRITERIA FOR IMPULSE NOISE

Murray and Reid (1, 2) in 1946 were aware of the problems involved in establishing quantitative damage risk criteria. Examination of many of the factors previously mentioned led them to formulate a relationship between 'blast pressure' and 'ten round hearing loss'. This is shown in figure 2, and remained unchallenged until about the mid 1960's. At that time researchers felt that Murray and Reid's basic concepts needed extension in order to take account of the durational characteristics of the noise, and of a trading relationship between these factors and the total number of pulses received per exposure. In fact we have progressed little further than that in the last decade, and many other factors still remain unsolved.

In review, therefore, the steady state noise damage risk criteria in existence in the early 1960's, only referred obliquely to the problem by including an upper limit of about 135 dB for unprotected noise exposure of any duration, however short. However, it was considered that this limit was unnecessarily conservative, particularly with respect to exposure to many types of gunfire noise. In the UK a programme of research was undertaken in which methods of measuring and specifying the physical characteristics of impulse noise were compared with the temporary threshold shifts which such noises produced in volunteer subjects. The results of these investigations were initially presented in 1965 in a Medical Research Council's Royal Naval Personnel Research Committee Report (3) and extended to include safe limits for certain types of impulse-noise exposure in a paper (4) presented at the Fifth International Congress of Acoustics in Liege. At the same Congress, USA data presented by Kryter and Garinther showed that they had been conducting simultaneous but independent studies (5, 6) and had arrived at remarkably similar conclusions. Combination of these data supplemented by further research in both laboratories led to the formulation in 1968 by Coles, Garinther, Hodge and Rice (7) of what is thought to be the first authoritative DRC for exposure to gunfire noise. This applied the limits of acceptance TTS to protect 75% of the exposed population recommended by the NAS-NRC committee on Hearing, Bioacoustics and Biomechanics (CHABA). This specified that "end of day" TTS should not exceed 10 dB at or below 1000 Hz, 15 dB at 2000 Hz, and 20 dB at or above 3000 Hz in 75% of the normally-hearing persons exposed. An approximation to the 90th percentile could be made by reducing the criterion peak pressure levels by 5 dB.

The peak pressure and duration exposure limits proposed in the criterion are shown in figure 3 where the A and B durations are defined in figure 1, waveform specification by oscilloscopic techniques being the preferred method of measurement (7). At the time of publication these authors considered that it was too cumbersome to express damage risk from exposure to heavy weapons, small arms or sporting guns in terms of the number of rounds fired or the repetition rate. Therefore certain general qualifications or corrections were placed on the criterion:

(i) the total number of impulses would be limited <u>on average</u> to 100 per exposure,
(ii) the anticipated average number of exposures per year was 10-20,
(iii) the repetition rate was of the order 6-30 impulses per minute,
(iv) the criterion should be lowered by 5 dB for normal sound incidence,
(v) when exposure is to be occasional, single impulses only, the criterion could be relaxed by 10 dB,
(vi) protection for the more susceptible person (>95%) can be achieved by lowering the curves by 10 dB.

In 1967 Forrest (8) extended these ideas to include the use of a trading relationship between B duration and the number of pulses per exposure. This data provides for approximately 2.7 dB reduction in peak level per doubling of B duration, compared with the Coles et al (7) criterion slope of 2 dB reduction per doubling.

In 1968 the NAS-NRC committee on Hearing, Bioacoustics and Biomechanics proposed a damage-risk criterion for gunfire noise (9) based on the previously discussed criterion (7). Whilst certain modifications in presentation were proposed, for example a 5 dB lowering of the curves for 95th percentile protection and 5 dB lowering for normal incidence, more substantive modifications were also incorporated. The first was the termination of the basic DRC at 164 dB which meant that under no circumstance should any ear be exposed to a peak level in excess of 179 dB (this corresponds to the limit for a single pulse (+10 dB) at grazing incidence (+5 dB) with a 25 microsecond duration. The second modification was the 138 dB "floor" for B-durations of 200 to 1000 milliseconds in order to take account of the protection afforded by the reflex contractions of the middle-ear muscles. Thirdly corrections for the number of pulses per exposure were established, based on the Coles et al (7) opinion that "Where exposure is to occasional single impulses only, it seems reasonable to raise the limits somewhat, and an estimate of 10 dB has been agreed upon for this".

The CHABA criterion is shown in figure 4 and it must be stressed that it consolidated the first attempt at a reasonable impulse noise damage risk criterion. The limitations were clearly stated (7, 9), and most importantly it should be remembered that the interpretation of the experimental data rested heavily on the conclusively unproven assumption of a consistent relationship between TTS and PTS. Furthermore, the empirical nature of the specification of the noise was clearly stressed.

CORRECTION FACTORS FOR THE NUMBER OF IMPULSES

The data on which the Coles et al (7) and subsequent CHABA (9) criteria were based was distinctly limited to impulses having 'A' or 'B' durations of less than about 500 milliseconds, and with an average of 100 impulses per exposure. The CHABA correction factors for the number of impulses are shown in figure 5, and it can be seen that the original data is extrapolated to 1000 impulses. In fact for gunfire noise only the normal and grazing incidence correction factors for single impulses (and by implication up to 100 impulses) have been validated; this was done by Hodge and Garinther (10) in 1970. More recently McRobert and Ward (11) using high intensity artificially generated impulses have produced data which support the '5 dB decrease per 10 fold increase in the number of impulses' hypothesis.

It would therefore seem clear that for short duration high intensity shock front impulse noises the CHABA (9) criterion is probably the most authoritative document to date. This is for use with impulses having 'B' durations of up to about 250 ms and up to 1000 impulses per daily exposure.

Expression of the possible combinations of 'B' duration and Number of impulses (N) within these limits for the 75th percentile protection and grazing incidence is shown in figure 6, based on a recent paper by Rice and Martin (12). It appears that no great loss of accuracy is admitted by this method of treatment and expression of the B-N trading relationship is much easier to follow.

In support of the United States Environmental Protection Agency (EPA) Guignard (13) has prepared guidelines for evaluating impulse noise exposure. This data is a modification of the CHABA criterion and uses an equal energy trading relationship to extrapolate for exposures of up to 10,000 pulses with hearing impairment not to exceed 5 dB at 4 kHz in more than 10% of the population. (See figure 7.)

Limitations to this approach are voiced by Guignard with respect to the underestimation of the likely hazard for smaller exposures. However, further caution should be advocated if this method is adopted by the EPA (14). By invoking an equal energy concept it would seem implicit that equal 'B' duration - number of pulses (N) products should predict equal peak level of hazard. Reference to table 1 shows that this is not the case, and whilst the mean predicted values differ considerably in many cases from the CHABA limits, the ranges of peak levels for a given BN product are additionally wider using the Guignard approach.

Table 1. Tolerable mean peak levels (with their ranges) for various BN Products as calculated by two methods.

	CHABA (9)		Guignard (13)	
BN ms	Mean Peak dB	Range dB	Mean Peak dB	Range dB
0.1	158		168	
1	152	2	159.5	3
10	146	3.5	151	6.5
100	140.5	5	143	10
1,000	135	3	135.5	18
10,000	129.5	3	127.5	15
100,000	124.5	3	119.5	11.5
1,000,000	121		112	8

It is suggested that such wide ranges as those indicated in table 1 will probably be untenable in practice. The approach is felt also to show the dangers of the over extrapolation of limited data.

DAMAGE RISK CRITERIA FOR IMPACT NOISE

Following publication of the CHABA criterion (9) interest in its application to the industrial environment obviously grew. The repeated impact situation led Coles and Rice (15) to extrapolate their earlier data (7) to try and meet this new requirement. Based on additional data by Cohen, Kylin and La Benz (16) and Walker (17) the revised correction factors are compared in figure 8 with the proposals of CHABA and Guignard (13).

Whilst the Coles and Rice corrections appeared to fit situations involving reverberant repeated impacts, they are clearly at variance with the more recent impulse noise data of McRobert and Ward (11). If the data has been correctly interpreted therefore it seems that, as discussed earlier, separate criteria are required for impulse and impact noise, once the number of pulses exceeds about 1000.

Further evidence for this comes from the work of Martin and Atherley (18, 19). Following studies of industrial impact noise, methods were evolved by which the effects upon hearing could be evaluated in terms of the "equivalent-continuous noise level" concept. Different procedures for evaluating the noise characteristics are recommended depending upon the peak height, repetition rate and decay time constant of the impact waveform envelope (19). In addition the method fits with the British Occupational Hygiene Society and Department of Employment practices for exposure to wide band steady state noise (20, 21). Contemporary with, but in the absence of the McRobert and Ward (11) observations, Rice and Martin (12) reviewed the impulse-impact noise damage risk criteria and suggested that the unification of them might be possible using the immission principle of equivalent 'A' weighted sound energy for continuous noise exposure. Figure 6 compares this equal energy approach with the CHABA criterion and the Coles and Rice (15) data (for upwards of 1000 pulses).

UNIFICATION OF IMPULSE-IMPACT DAMAGE RISK CRITERIA

The case for unification on an equal energy basis (12) would demand that the CHABA impulse criterion be considerably tightened for BN products greater than about 10 ms. On reflection it is felt that considerably more research is required before this matter can be resolved, and until that time two separate approaches are recommended. For impulse noise of up to 1000 pulses per occasion the CHABA criterion (9) is recommended, whereas for impact noises over 1000 pulses per occasion the method of Martin and Atherley (19) is recommended. This view now supports that of McRobert and Ward (11) who said that '... it may be wrong to have a single curve to represent the trading relationship between level and number of pulses for both impulse and impact noise.'

Figure 9 shows the recommended impulse and impact criteria over a wide range of peak level and 'B' duration times number of impulse values. Also marked is the equivalent point for an 8 hour daily exposure to 90 dBA. It is interesting to note that if instead of using the equal energy concept (as is current European Practice), a 5 dB per halving of exposure is used (as is current USA practice), the criteria essential resolve themselves.

Quite obviously considerably more research needs to be undertaken in order to resolve, as Murray and Reid originally pointed out, the complex relationships between those features in the noise which are most important in relation to the hearing loss caused.

REFERENCES

1. N.E. Murray and G. Reid 1946 J. Laryngol. Otol. 61, 92-130. Temporary deafness due to gunfire.

2. N.E. Murray and G. Reid 1946 Med. J. Australia 1, 611-617. Experimental observations on the aural effects of gunblast.

3. R.R.A. Coles and C.G. Rice 1965 Medical Research Council, London, Report RNP65/1049. The pure-tone, speech and impulse noise attenuating properties of Selectone-K and V-51R earplugs.

4. C.G. Rice and R.R.A. Coles 1965 Proceedings of the 5th International Congress on Acoustics, Liege, Belgium, Paper R67. Impulse noise studies and temporary threshold shift.

5. U.S. Army Human Engineering Laboratories, Aberdeen Proving Grounds, Maryland. 1965 HEL Standard S-1-63B. Maximum noise level for Army material command equipment.

6. K.D. Kryter and G.R. Garinther 1965 Acta-Otolaryngologica (Stockholm) Supplement 211. Auditory effects of impulses from firearms.

7. R.R.A. Coles, G.R. Garinther, D.C. Hodge and C.G. Rice 1968 Jn. Acoust. Soc. Amer. 43, 336-346. Hazardous exposure to impulse noise.

8. M.R. Forrest 1967 M.Sc. Dissertation, University of Southampton. The effects of high intensity impulsive noise on hearing.

9. NAS-NRC Committee on Hearing, Bioacoustics and Biomechanics 1968 Report of Working Group 57. Proposed damage-risk criterion for impulse noise (gunfire).

10. D.C. Hodge and G.R. Garinther 1970 Jn. Acoust. Soc. Amer. 48, 1429-30. Validation of the single-impulse correction factor of the CHABA impulse-noise damage risk criterion.

11. H. McRobert and W.D. Ward 1973 Jn. Acoust. Soc. Amer. 53, 1297-1300. Damage risk criteria: The trading relation between intensity and the number of non-reverberant impulses.

12. C.G. Rice and A.M. Martin 1973 Jn. Sound Vib. 28, 359-67. Impulse noise damage risk criteria.

13. J.C. Guignard 1973 UDRI-TR-73-42. Interim Technical Report under Contract F33615-72-C-1488. University of Dayton Research Institute, Ohio. Some guidelines for evaluating impulse noise exposure.

14. Second EPA ONAC Preliminary Draft 1974 Information on levels of environmental noise requisite to protect public health and welfare with an adequate margin of safety. (This document has not been formally released by EPA and does not represent agency policy.)

15. R.R.A. Coles and C.G. Rice 1970 Annals of Occupational Hygiene 13, 43-50. Towards a criterion for impulse noise in industry.

16. A. Cohen, B. Kylin and P.J. La Benz 1966 Jn. Acoust. Soc. Amer. 40, 1371-80. Temporary threshold shifts in hearing from exposure to combined impact/steady-state noise conditions.

17. J.G. Walker 1970 Annals of Occupational Hygiene 13, 51-58. Temporary threshold shift from impulse noise.

18. G.R.C. Atherley and A.M. Martin 1971 Annals of Occupational Hygiene 14, 11-28. Equivalent-continuous noise level as a measure of injury from impact and impulse noise.

19. A.M. Martin and G.R.C. Atherley 1973 Annals of Occupational Hygiene 16, 19-26. A method for the assessment of impact noise with respect to injury to hearing.

20. British Occupational Hygiene Society 1971 Hygiene Standard for Wide Band Noise. Pergamon Press.

21. Department of Employment 1972 Code of Practice for reducing the explosure of employed persons to noise. London: Her Majesty's Stationery Office.

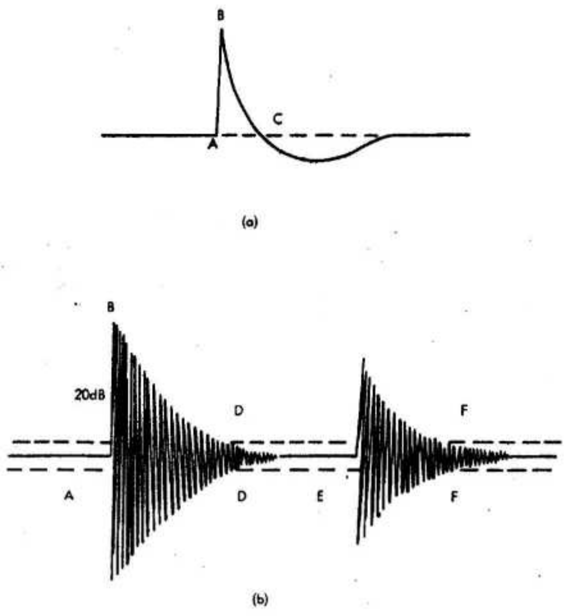

FIG 1. IDEALIZED OSCILLOSCOPIC WAVEFORMS OF IMPULSE NOISES.
PEAK LEVEL: PRESSURE DIFFERENCE AB. RISE TIME : TIME DIFFERENCE AB.
(a) A DURATION : TIME DIFFERENCE AC. (b) B DURATION: TIME DIFFERENCE AD.
(+ EF WHEN A REFLECTION IS PRESENT). (COLES et al. [7])

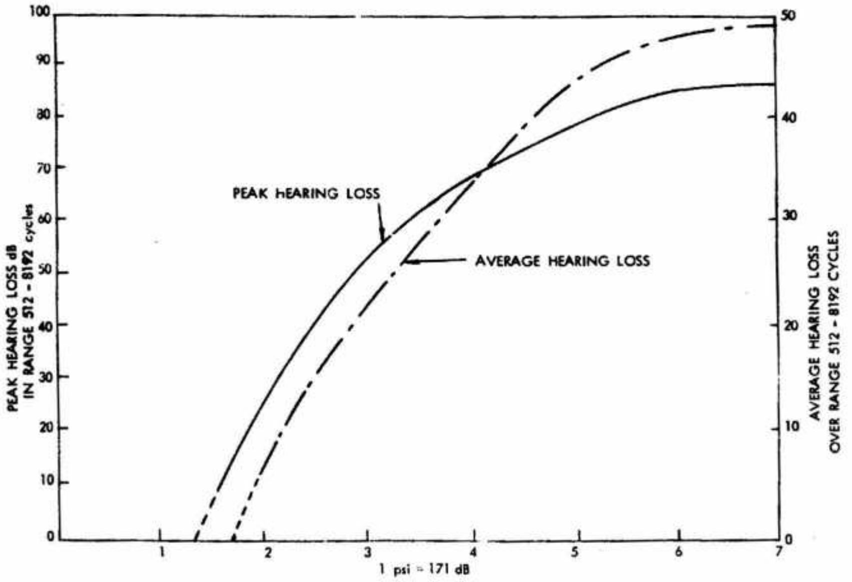

FIG 2. BLAST PRESSURES vs TEN ROUND HEARING LOSS (MURRAY & REID [1]

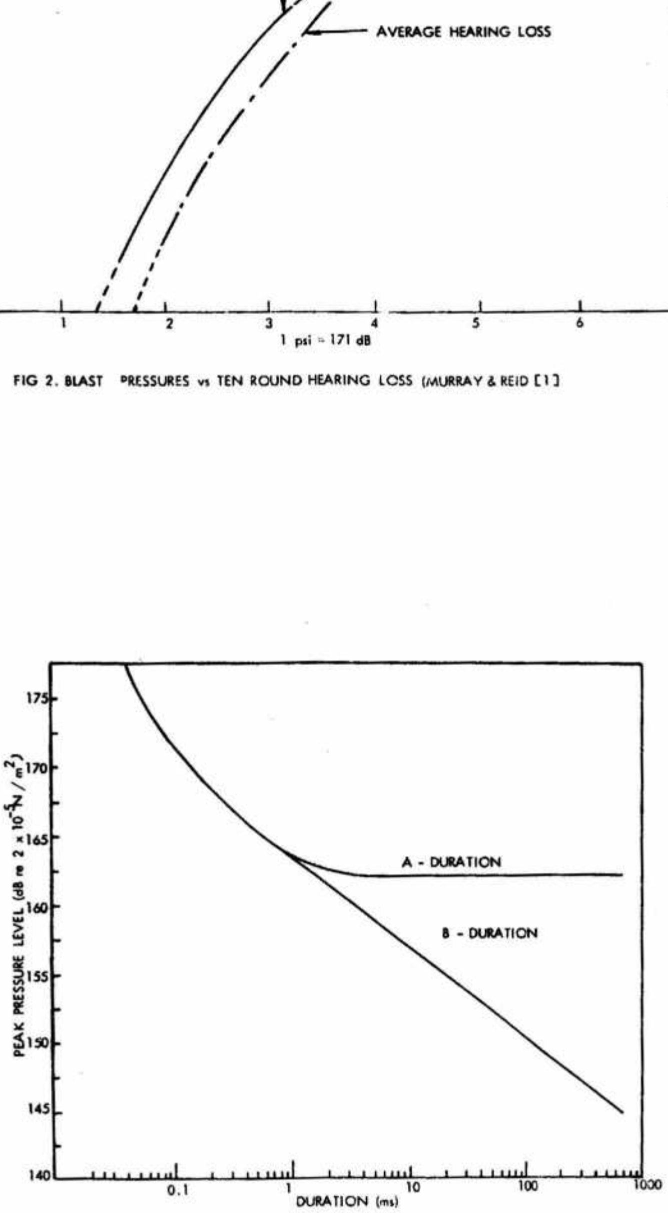

FIG 3. PEAK PRESSURE LEVEL AND DURATION LIMITS FOR IMPULSES HAVING NEAR - INSTANTANEOUS RISE TIMES (COLES et al. [7])

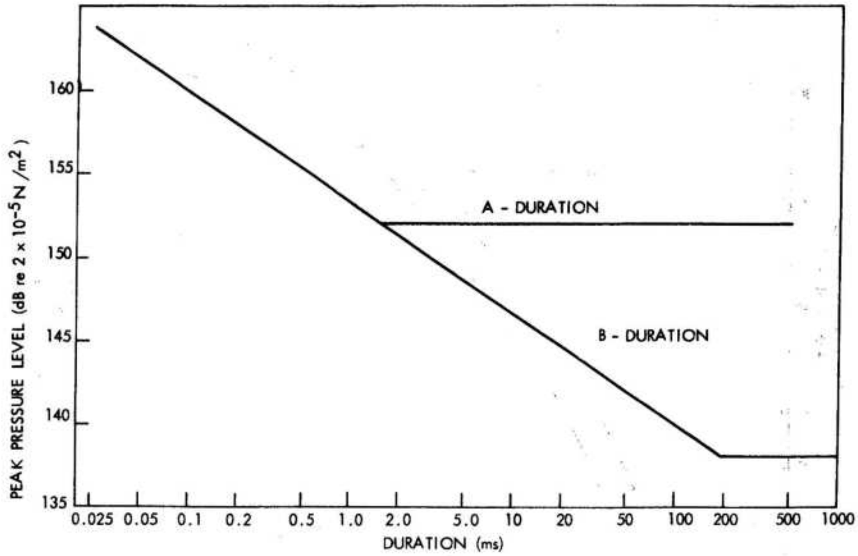

FIG 4 DAMAGE RISK CRITERION FOR IMPULSE (GUNFIRE) NOISE (CHABA [9])

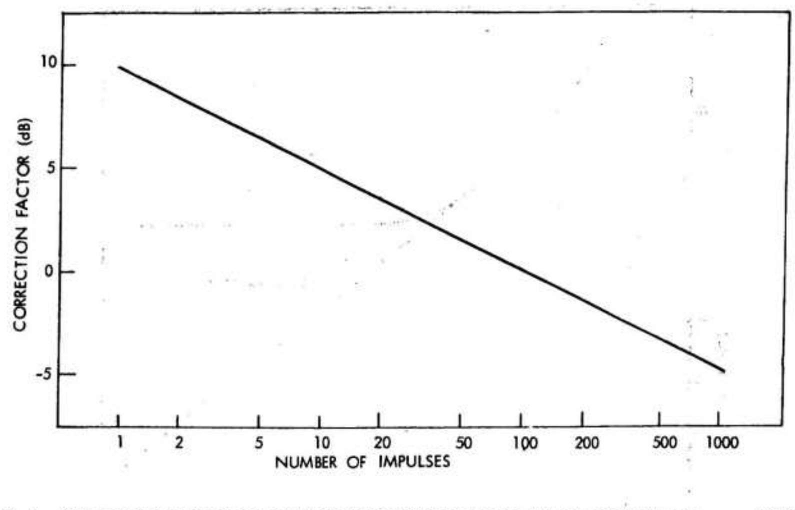

FIG 5 CORRECTION FACTOR TO DAMAGE RISK CRITERION FOR NUMBER OF IMPULSES (CHABA [9])

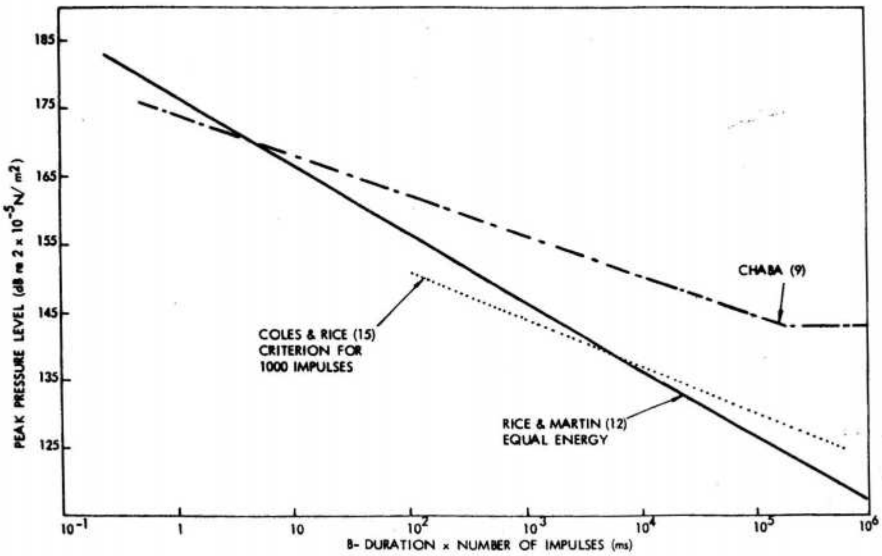

FIG 6 COMPARISON OF DAMAGE RISK CRITERIA FOR GUNFIRE NOISE WITH AN EQUIVALENT CONTINUOUS NOISE LEVFL OF 9U Jb(A) CALULATED BY FOLLOWING THE METHOD OF MARTIN & ATHERLEY [19]. ALL CURVES CORRECTED FOR 75% PROTECTED AND GRAZING INCIDENCE MAXIMUM NUMBER OF IMPULSES IS 1000 FOR GUNFIRE CRITERIA

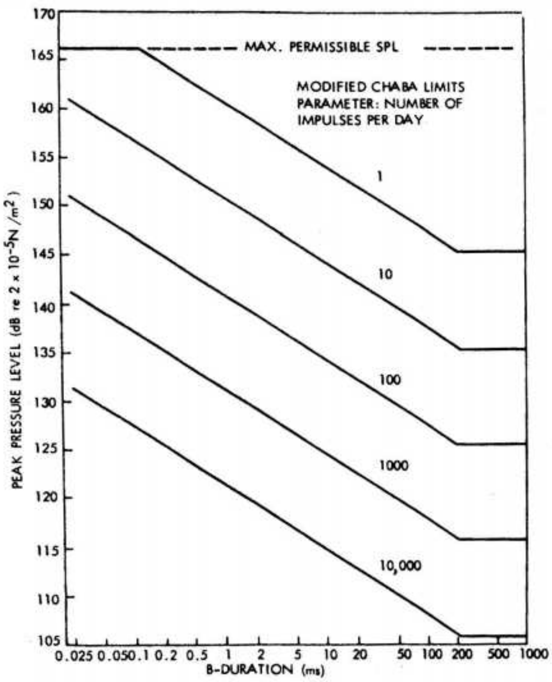

FIG 7 SET OF MODIFIED CHABA LIMITS. PARAMETER: NUMBER OF IMPULSES PER DAILY EXPOSURE. CRITERION OF CONSERVATION: NIPTS NOT TO EXCEED 5 dB AT 4 kHz IN MORE THAN 10% OF POPULATION. (GUIGNARD [13])

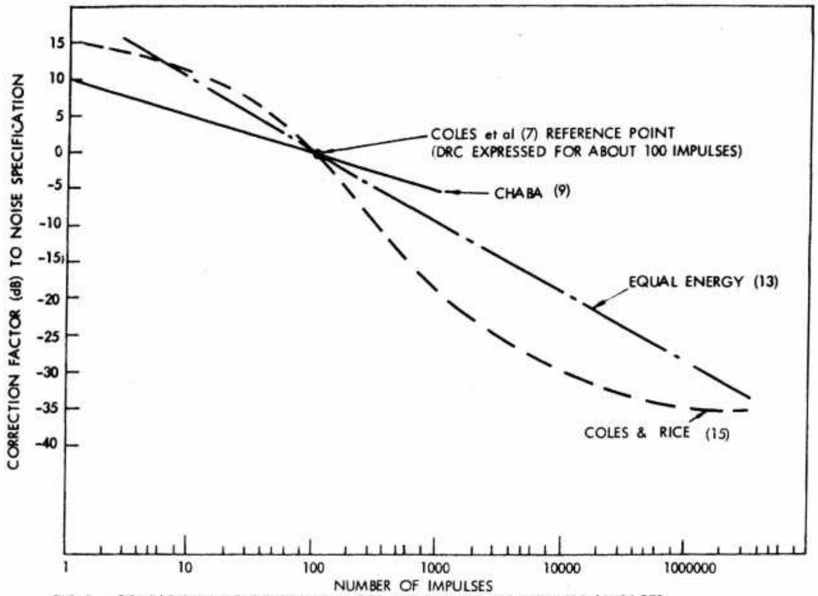

FIG 8 COMPARISON OF CORRECTIONS FOR THE NUMBER OF IMPULSES / IMPACTS

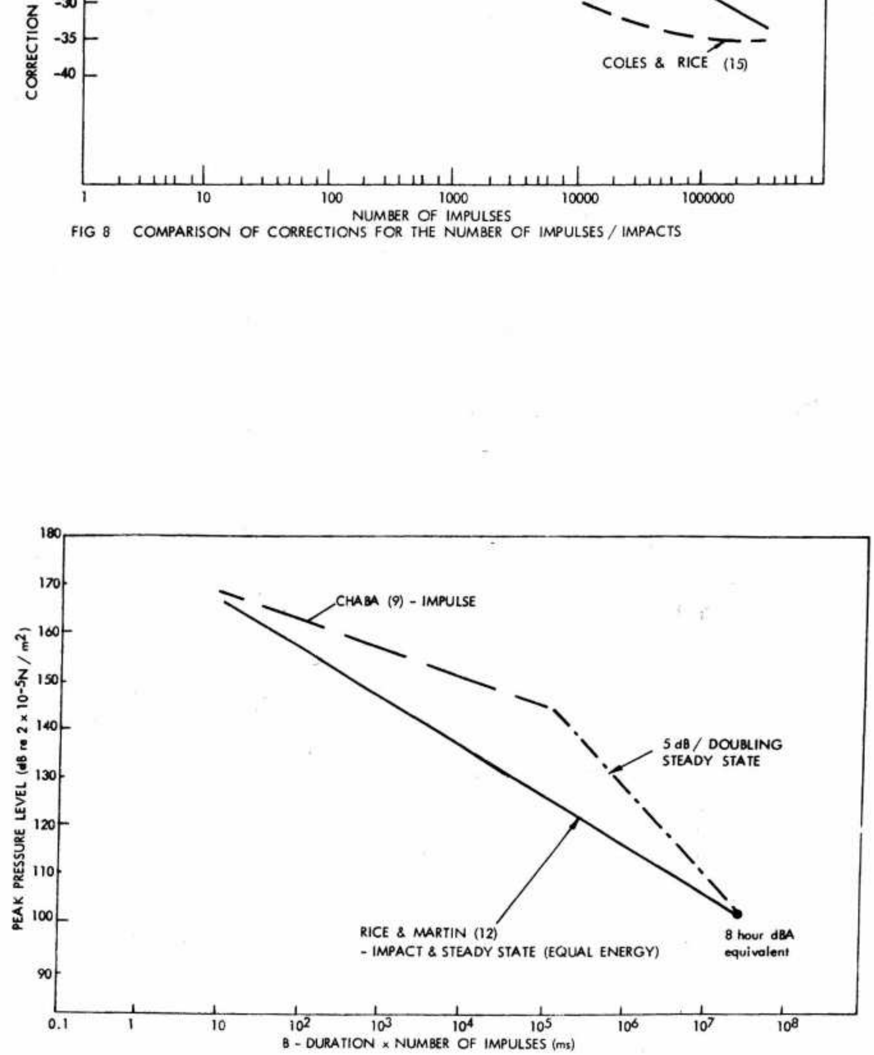

FIG 9 COMPARISON OF IMPULSE AND IMPACT DAMAGE RISK CRITERIA WITH STEADY STATE CRITERIA
(75% PROTECTION, GRAZING INCIDENCE)

A REVIEW OF RECENT COMMUNITY NOISE RESEARCH IN THE UNITED STATES

S. A. Fidell
Bolt Beranek and Newman Inc.
Canoga Park
California, U.S.A.

SUMMARY - In the United States, noise has become the controlling factor in the design of commercial aircraft and airport facilities. Research into methods for assessing individual and community response to noise exposure, quantification of the noise produced by present and future air carrier systems, and methods for alleviating noise exposure have been undertaken recently by a number of Federal agencies, including The Environmental Protection Agency, The Department of Transportation, The National Aeronautics and Space Administration, and The Federal Aviation Agency. The results of a number of these projects, dealing with a nationwide noise survey, sleep interference, effects of noise exposure, and public opinion polls will be discussed.

Traffic noise has also become a major concern as traffic has been increasingly recognized as the principal source of background noise levels in urban environments. Efforts to reduce traffic noise by source control and highway design, as well as the effects of time varying traffic noise on speech intelligibility will be discussed.

Within the last few years noise has become a principal determinant of the growth of air transportation in the United States. New aircraft are being designed as much for noise reduction as for traditional goals such as payload, speed, and range. The last major airport to open in the United States (Dallas-Ft. Worth) required a 160 km^2 site to contain the anticipated NEF 40 contour. The lack of noise-compatible sites makes it doubtful that a major new airport will open elsewhere in the United States within the next decade.

Similarly, ground transportation has lately been recognized as responsible for the ambient noise levels to which most of the country's population is exposed. Legislation and regulations now compel highway design engineers in the United States to design inherently quieter roads, and truck and automobile manufacturers to produce quieter vehicles. Environmental impact statements for new construction of roads require study of the effects of traffic noise on exposed populations.

The focussing of attention on noise pollution created by the Federal Noise Control Act of 1972 has accelerated study of the effects of noise on people, particularly in the areas of annoyance, speech interference, and sleep interference. This paper discusses the results of recent research conducted in the United States in these areas.

I. Annoyance

Annoyance is perhaps the most pervasive effect of noise on people, since it is a frequent concommitant of speech, sleep, and activity interference. Attempts to relate annoyance to noise exposure levels have not been very successful, since annoyance does not seem to be very strongly related to physical characteristics of noise over any appreciable range of values. In the amplitude domain, for example, a faucet dripping at night and an aircraft flyover could be judged equally annoying in the appropriate contexts, even though the noise levels of these events differ enormously.

Individual differences do not seem to be the problem in relating noise exposure to annoyance; large scale social surveys in which data from thousands of respondents are pooled have proven little more successful in relating exposure to annoyance than have laboratory studies of small samples. In fact, correlations between even the most intricate noise ratings developed from social surveys and noise exposure data are on the order of 0.4, accounting for only about 16% of the variability in the data.

One potential explanation for the inadequacy of current prediction methods is that they are all based on delayed self report, whether in the form of social surveys or examination of other post hoc records such as complaint files. These traditional methods contain the inherent flaw that human response, noise exposure, and relationships between human response and noise exposure must be reconstructed after the fact, on the basis of uncertain information.

The American Environmental Protection Agency and Department of Transportation recently sponsored a research program (1) to evaluate a novel procedure for assessment of noise-induced annoyance in residential settings. The procedure employed to record noise exposure and annoyance simultaneously was fairly simple. Test participants were supplied a wrist-wearable signalling device (an FM transmitter) which provided an event mark on paper or magnetic analog records of noise exposure. The event marks indicated annoyance, while the analog records provided the continuous information about noise exposure. Subjects in this experiment were instructed to push a button on their "wristwatch" whenever they heard a sound they would rather not have heard.

Data were collected at airport, highway, inner city, suburban, and rural sites. The average hourly response rates over a week long period ranged from almost 12 responses per hour at the airport site to less than half a response per hour at the rural site. The rank ordering of noise neighborhoods by average response rates corresponded well with intuition; airport, inner city, highway, and rural neighborhoods, in diminishing order of annoyance.

An analysis of the relationship between annoyance responses and instantaneous noise levels demonstrated that higher rates of annoyance were in fact related to higher noise exposure levels. The strength of the relationship, however, remains to be determined in a full scale implementation of the procedure.

II. Speech Interference

One of the best understood effects of noise on people is its interference with communications. Transportation noise is known to impede verbal communication in face to face conversations, telephone use, listening to television and radio, and so forth. About 90% of the residents in a high noise exposure area near Los Angeles International Airport reported such interference in an aircraft noise survey last spring (2).

Several good measures were developed years ago to permit estimation of the intelligibility of speech in steady state noise environments. Unfortunately, most community noise from transportation varies greatly in time. Thus, until recently, it was not known how to predict speech interference effects in real life environments such as traffic noise. The Highway Research Board of the American National Academy of Science is sponsoring on-going research into this problem (3). One experiment in this series resulted in a preliminary finding that the median of a traffic noise distribution is capable of serving as a useful statistic in predicting speech interference.

The experiment was designed such that panels of four observers seated in an anechoic chamber were required to indicate which of six words in ten groups of spondee (two syllable) words was annunciated at any given time. The background in which the listening was accomplished was recorded traffic noise. Speech levels were varied systematically to determine percentage intelligibility at various speech to noise ratios.

The dependent variable was the peak speech level required for the panels of subjects to obtain a 70% correct detection rate. The 70% correct detection level was selected for close attention mainly because it provided a level of speech intelligibility sufficiently high to promote consistent performance by the test panels, yet sufficiently low to avoid ceiling effects associated with very high correct detection levels. The 70% correct point was estimated for each word list in each traffic background (a total of 268 tests) both by linear regression and interpolation of the psychometric function relating percent correct detections to speech levels.

The most significant finding was that the median of a traffic noise distribution (L_{50}) is an excellent predictor of the peak speech level necessary to achieve a 70% correct detection level of spondee words heard in traffic noise. The L_{30} and the energy mean (L_{eq}) measures were also capable of serving as estimators of this speech level, but L_{10}, which reflects the peaks of a traffic noise distribution, was not a good predictor.

Further analysis of the effect of traffic noise variation on perception of speech indicated that increased variation (greater L_{10}-L_{50}) permits a lower peak speech level for 70% correct detection with traffic noise samples of equal L_{eq}. This finding coupled with the fact that L_{eq} affords reasonably good prediction of the target speech level suggests that criteria expressed in terms of L_{eq} may provide the basis for traffic noise criteria. This is so because a criterion expressed in terms of L_{eq} for the steady state noise of freely flowing traffic will guarantee lesser amounts of speech interference from the more variable noise produced by reduced flow or increased ratios of trucks to cars.

III. Sleep Interference

Even though speech interference is the most frequently mentioned effect of community noise on peoples' lives, sleep interference is a potentially more significant effect. Indeed, laboratory studies of nocturnal noise intrusions have suggested that exposure to moderate noise levels (on the order of 70 dB(A)) can awaken or disturb the sleep of a substantial proportion of test subjects. Despite the acknowledged importance of sleep interference effects, little research has been conducted to quantify how sleep interference depends on the quantity and quality of noise exposure and to relate physical parameters of exposure to the degree of sleep interference.

Laboratory studies of sleep quality, moreover, do not provide compelling evidence of sleep interference effects in the world at large. Small numbers of test subjects are usually employed; the electrodes and recording equipment used to measure sleep electrophysiology may disturb sleep of themselves; test subjects spend only a few nights in novel sleeping quarters; and there is little opportunity for habituation to the simulated noise environment.

The National Aeronautics and Space Administration has sponsored two studies to further understanding of the effects of aircraft noise on sleep quality in residential settings (4). The first study was conducted in two metropolitan neighborhoods several miles apart. One was adjacent to Los Angeles International Airport; the other neighborhood was of similar socioeconomic level, home construction, and traffic noise exposure. Six middle aged couples served as subjects in the airport area, while five middle aged couples served as controls in the other neighborhood, for a total of 22 test subjects.

A modified four track analog tape recorder acquired both the physiological and acoustic data. The physiological data consisted of multiplexed FM recordings of EEG and EOG, recorded on separate channels for husband and wife. The acoustic data consisted of a continuous direct recording of noise exposure in the sleeping quarters. A WWV receiver provided time of day information on the remaining track at a number of sites.

Digital records of noise exposure were kept by means of an automatic noise monitoring unit. This unit provided event marking information on the physiological channels during the time a noise threshold (usually set about six dB above ambient levels) was exceeded.

The general hypothesis that intense noise exposure degrades the quality of sleep was supported to some extent, in that subjects in the airport area spent a smaller percentage of their time in deep sleep than subjects in the control area. Although a number of differences in the microstructure of sleep (time spent in various stages, shifts in sleep stages associated with specific noise intrusions, etc.) were statistically significant, the effects of noise were generally small.

A second study in progress at the time of writing is intended to assess the effects on sleep of a sudden cessation of nocturnal noise intrusions. Sleep patterns and noise exposure of test subjects in the same aircraft noise neighborhood were monitored immediately before and after a change in flight paths re-routed aircraft away from their homes. Although data collected in this study have not yet been fully analyzed, it appears that differences in sleep quality before and after the cessation of intense noise exposure will not be great.

Yet a third study conducted at the same time required test subjects to push a button on their bedsteads (in their own homes) whenever they awoke during the night. A laboratory computer logged their times of awakening over special telephone lines. Differences in this "behavioral awakening" method of assessing sleep quality in the time periods before and after cessation of overflights were also very small.

In short, although it remains possible that certain segments of the population may suffer profound sleep disturbance from nocturnal noise, it seems likely that human beings are sufficiently adaptable to learn to sleep tolerably well even in high noise environments. Whether people should have to sleep in such noisy environments, and what long term costs may result from slight chronic sleep disturbances, are issues that go beyond scientific studies of sleep disturbance.

IV. Summary

Community response to noise exposure is becoming increasingly well understood as research into the effects of noise on people progresses. Certain effects are already well appreciated (speech interference, for example), while others are only now being appreciated (i.e., annoyance). Better understanding of some noise effects such as hearing damage risk, physiological stress, and sleep interference has alleviated exaggerated fears of extensive health hazards of noise exposure (5, 6, 7). Better understanding of other noise effects (primarily annoyance) is indicating a more substantial problem than had been previously expected.

Understanding of effects of noise on individuals remains more advanced than understanding of the effects of noise on groups of people. Information about noise effects from research already in progress or currently planned should make it possible, however, to propose models in the near future that will bridge the gap between individual and community reaction to noise exposure.

REFERENCES

1. Department of Transportation Contract DOT-OS-20103, culminating in two reports; DOT-TST-74-3, Fidell, Sanford, Glenn Jones and Karl S. Pearsons, "Feasibility of a Novel Technique for Assessing Noise Induced Annoyance" and DOT-TST-74-4, Bishop, Dwight E., "Program for the Measurement of Environmental Noise", September, 1973.

2. Fidell, S. and G. Jones, "Effects of Discontinuation of Noctornal Aircraft Noise", presented at the 86th meeting of the Acoustical Society of America, November, 1973.

3. Pearsons, Karl and Sanford Fidell, "Speech Intelligibility in the Presence of Time Varying Traffic Noise", presented at the Human Factors Society Meeting, Washington, D. C., October, 1973.

4. Pearsons, Karl S. and Sanford Fidell, "The Effects of Aircraft Noise on Sleep Electrophysiology as Recorded in the Home", Contract No. NAS1-9559-19, August 8, 1973.

5. Nagel, David C. and John E. Parnell, "On The Hearing of Residents Near Airports", presented at the 86th meeting of the Acoustical Society of America, November, 1973.

6. Environmental Protection Agency, "Public Health and Welfare Criteria for Noise", NCD 73.1, July 27, 1973.

7. Southwest Research Institute, "An Exploratory Study of Physiologic and Subjective Reactions Evoked by Aversive and Non-Aversive Sounds", Contract No. HSM 099-71-39, June, 1972.

Noise, Shock & Vibration Conference, 1974 Monash University, Melbourne

ON THE SLOWNESS OF A SMALL DEPARTURE FROM STEADY FLOW

R. E. D. Bishop
Department of Mechanical Engineering
University College
London, U.K.

W. G. Price
Department of Mechanical Engineering
University College
London, U.K.

SUMMARY - A slow departure of a flow around or through a solid body from steady conditions has to be represented analytically when the stability of the motion is investigated. In such a representation, the concept of a "slow" perturbation of the flow (under conditions of "quasi-steady flow") is usually employed. The nature of this assumption is examined and a method of relaxing it is explained.

INTRODUCTION

Aircraft, ships and other marine craft, pipes, buildings and sea-bed rigs are all examples of mechanical structures that are subjected to loading actions caused by fluid flow around or through them. These loading actions commonly pose questions of two sorts (aside from those associated with manoeuvring):

(a) questions of strength

(b) questions of stability.

Both require specification of the fluid actions.

At least for problems in which the flow is steady, questions of strength are dealt with in a huge literature. They represent one of the classical fields of fluid mechanics. Stability is a much more subtle matter, though of course it is sometimes crucially important. This latter is the subject of the present paper.

Typically, we shall enquire into the time variation of a loading action (i.e. a force, a moment or more generally a generalised force), ΔF say, that is associated with a small variation of the flow about a steady state when this perturbation is brought about by a small disturbance of a structure. To do this we shall outline some recent research and, in doing so, attempt to frame an answer to a question whose significance will first be explained: What exactly is implied by the concept of quasi-steady flow that is usually adopted in the linear theory of unsteady flow?

That there is a serious problem here can be seen from the following argument. The fluid action, and hence the deviation ΔF of that action, is determined by the flow (and hence by the flow deviation) at any instant. But the flow deviation at any instant t is determined by the disturbance, $\Delta\xi$ say, of the structure not merely at that time but at all previous instants; this is because the flow is only adjusted gradually when the structure moves. It is not strictly true, therefore, that $\Delta F(t)$ depends simply on $\Delta\xi(t)$.

'RAPID' AND 'SLOW' ADJUSTMENT OF FLOW

Consider the motion of a vertical elastic tube that is clamped at its upper end and free at its lower. If water flows down the tube, conditions may arise in which the system becomes unstable and oscillates messily from side to side.(1) If, here, ΔF represents some form of generalised horizontal force exerted by the water on the tube we should intuitively assume that $\Delta F(t)$ depends accurately on the disturbance of the tube (in some sense) at time t. In other words, we should expect the flow to adjust 'rapidly' to the disturbance of the tube. In fact if this assumption is made, the predictions of theory are quite accurate.(1)

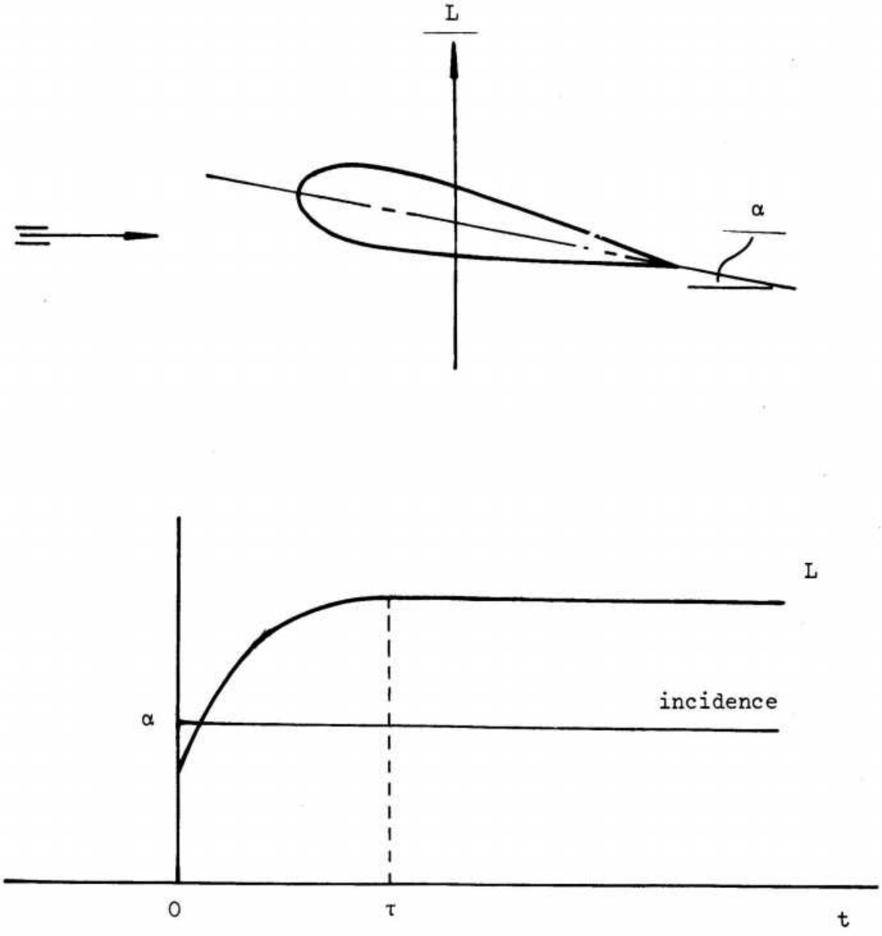

Figure 1. 'Slow' adjustment of a fluid flow

(a) A symmetrical aerofoil placed in a steady airstream showing the direction of the lift force L. At the instant $t = 0$, the angle of incidence is suddenly changed from zero to the small finite value α.

(b) Sketch showing the variation of L and of the angle of incidence with time.

At the other extreme consider a symmetric aerofoil placed in a steady airstream, as in fig. 1(a). Suppose that, at the instant $t = 0$, the angle of incidence is increased from zero to some value α. The lift force L might vary somewhat as shown in fig. 1(b), only settling down gradually to its steady value. This is because the sudden alteration of incidence demands a change of circulation in order that the after stagnation point may be held at the trailing edge. A vortex is shed into the wake and it materially affects the flow around the foil (and hence L) until it is well downstream.

We have here a system in which the flow adjustment is 'slow'. In effect the flow may be said to possess a 'memory'; for during the interval $0 < t < \tau$ (fig. 1(b)) the fluid 'remembers' that there was a previous condition ($t < 0$) in which there was no angle of incidence.

Evidently, a flow may or may not possess a memory in this sense. Now it is common, when analysing such problems as these, to assume that the flow does not possess one. It is argued that provided the motion deviations $\Delta\xi$ all occur sufficiently slowly, the deviation of a fluid action ΔF at any instant will be determined by the prevailing deviation $\Delta\xi$. The argument is a loose one but it appears to be tenable. The purpose of this paper is to examine this argument, to attempt to place it on an analytical footing and to point out an alternative approach that appears to be much less vulnerable.

It should be mentioned that in one type of analysis this assumption of quasi-steady flow has long been discarded. This is in the aeronautical context of sinusoidal motions exactly at a flutter boundary.(2)

SLOW MOTION DERIVATIVES

For the sake of definiteness consider a ship model that is towed along a towing tank with constant velocity $\bar{U}$. As it progresses down the tank, suppose the model is given a small parasitic motion of drift (or 'sway'), the velocity being v measured positive to starboard. The sway motion will cause the model to be subjected to various hydrodynamic loading actions, perhaps the most obvious of which is a net force ΔY exerted upon the hull in the athwartships direction. Let ΔY be positive when measured in the positive direction of v.

Taking $\Delta Y(t)$ and $v(t)$ as typical deviations of loading action and disturbance we may note that

$$\Delta Y(t) \;=\; \Delta Y(v,\, t;\ \text{previous values of } v;\ \bar{U} \text{ and other constant parameters}).$$

Suppose that the value of v at any instant $t - \tau$ may validly be expressed in the form of a Taylor series:

$$v(t-\tau) \;=\; v(t) - \tau\dot{v}(t) + \frac{\tau^2}{2!}\ddot{v}(t) - \frac{\tau^3}{3!}\dddot{v}(t) + \ldots..$$

Thus we may write in this event

$$\Delta Y(t) \;=\; f(v,\, \dot{v},\, \ddot{v},\, \ldots,\, t)\ ,$$

where the form of the function f( ) depends in part on the value of $\bar{U}$ and the other constant parameters.

If the expression for $\Delta Y(t)$ is now expanded as a Taylor series it is found that

$$\Delta Y(t) \;=\; Y_v v(t) + Y_{\dot{v}}\dot{v}(t) + Y_{\ddot{v}}\ddot{v}(t) + \ldots. \tag{1}$$

where

$$Y_v \;=\; \left|\frac{\partial \Delta Y}{\partial v}\right|_{\dot{v}=0=\ddot{v}=\dddot{v}=\ldots}$$

$$Y_{\dot{v}} \;=\; \left|\frac{\partial \Delta Y}{\partial \dot{v}}\right|_{v=0=\ddot{v}=\dddot{v}=\ldots}$$

etc.

In writing this series we ignore, for example, the practical objection that it is unclear how one can vary $\dot{v}$ while holding v at the zero value in forming $Y_{\dot{v}}$.

At this point we adopt the heuristic argument that, if the parasitic motion is 'slow', the time $L/\bar{U}$ for the model to travel its own length L is much less than L/v, $v/\dot{v}$, $\dot{v}/\ddot{v}$, ... ; whence

$$v \ll \bar{U}\ ; \quad \dot{v} \ll \frac{v\bar{U}}{L}\ ; \quad \ddot{v} \ll \frac{\dot{v}\bar{U}}{L}\ ; \ \ldots. \tag{2}$$

Under these conditions it seems reasonable to curtail the Taylor series so that, for slow motions,

$$\Delta Y(t) \;=\; Y_v v(t) + Y_{\dot{v}}\dot{v}(t)\ . \tag{3}$$

It is not suggested that the derivation of this result will withstand close scrutiny – only that a partial justification has been given for a relationship that can be regarded as purely empirical. The constants of proportionality Y_v, $Y_{\dot{v}}$ are known as 'fluid derivatives'.

It will be noted that, in this formulation, the force deviation ΔY at any instant is determined by the parasitic motion at that instant. That is, there is no 'fluid memory'. It is worth recording that in practice, where a linear representation is in order this type of result is very satisfactory when memory effects are obviously negligible.(1),(2)

It is a relatively simple matter to measure the value of Y_v for a model. The model has merely to be towed along the tank with a slight (constant) angle of yaw, so that $\dot{v}$ is zero while v is not. Unfortunately there is no known practical method of measuring $Y_{\dot{v}}$ directly and it is largely to meet such deficiencies as this that the Planar Motion Mechanism (PMM) was developed. (3),(4)

USE OF THE PLANAR MOTION MECHANISM

For our present purposes, a planar motion mechanism may be regarded as a device that will impart a sinusoidal variation of v on the model as it progresses along the towing tank and will measure the corresponding sway force ΔY while it does so. The method by which $Y_{\dot{v}}$ is measured, as it was originally conceived,(3) may be explained in terms of equation (3). A somewhat more complete discussion (starting from equation (1) and leading to the same conclusions) in which an attempt is made to explain the role of memory effects is given in reference 4.

If the lateral displacement is

$$y = y_0 \sin \omega t ,$$

so that

$$v = v_0 \cos \omega t = \omega y_0 \cos \omega t ,$$

equation (1) becomes

$$\Delta Y(t) = v_0(Y_v - \omega^2 Y_{\ddot{v}} + \omega^4 Y_{\ddddot{v}} - \ldots) \cos \omega t$$

$$- \omega v_0(Y_{\dot{v}} - \omega^2 Y_{\dddot{v}} + \omega^4 Y_{\overset{(5)}{v}} - \ldots) \sin \omega t$$

$$= \tilde{Y}_v v_0 \cos \omega t - \tilde{Y}_{\dot{v}} \omega v_0 \sin \omega t , \quad (4)$$

where $\tilde{Y}_v$, $\tilde{Y}_{\dot{v}}$ are 'oscillatory coefficients'. The PMM is a device that will permit $\tilde{Y}_v$, $\tilde{Y}_{\dot{v}}$ to be measured (5), since it embodies force transducers that measure components of force in phase with, and in quadrature with the displacement y.

The oscillatory coefficients are dependent upon ω, the driving frequency, and if they are measured and plotted as functions of ω, they might have some such forms as those shown in fig. 2. Notice that practical difficulties attend measurements at very low and very high frequencies ω but that, as we have already mentioned, an independent measurement may be made of Y_v for $\omega = 0$ by means of an oblique towing test.

To find $Y_{\dot{v}}$ we make use of the fact that, according to equation (4),

$$Y_{\dot{v}} = \lim_{\omega \to 0} \tilde{Y}_{\dot{v}} \quad (5)$$

In other words the required derivative is found by extrapolating the $\tilde{Y}_{\dot{v}}$ curve and finding its intercept with the axis $\omega = 0$ as indicated in fig. 2(b). Aside from permitting this extrapolation, the curve of $\tilde{Y}_{\dot{v}}$ is held to contain much valueless information. This view is sometimes buttressed by the assertion that ships are essentially "low frequency devices" and the "high frequency content" of any manoeuvres of which they are capable is very small.

By means similar to this, expressions may be found for the fluid actions associated with small disturbances. The theory is linear and the disturbances are 'slow'. If in fact the disturbances are rapid, so that adjustment of the fluid flow does not follow the disturbance even approximately, then this form of representation breaks down. The theory has the attraction of simplicity and is apparently logical even though the criterion of 'slowness' (2) seems to lack precision.

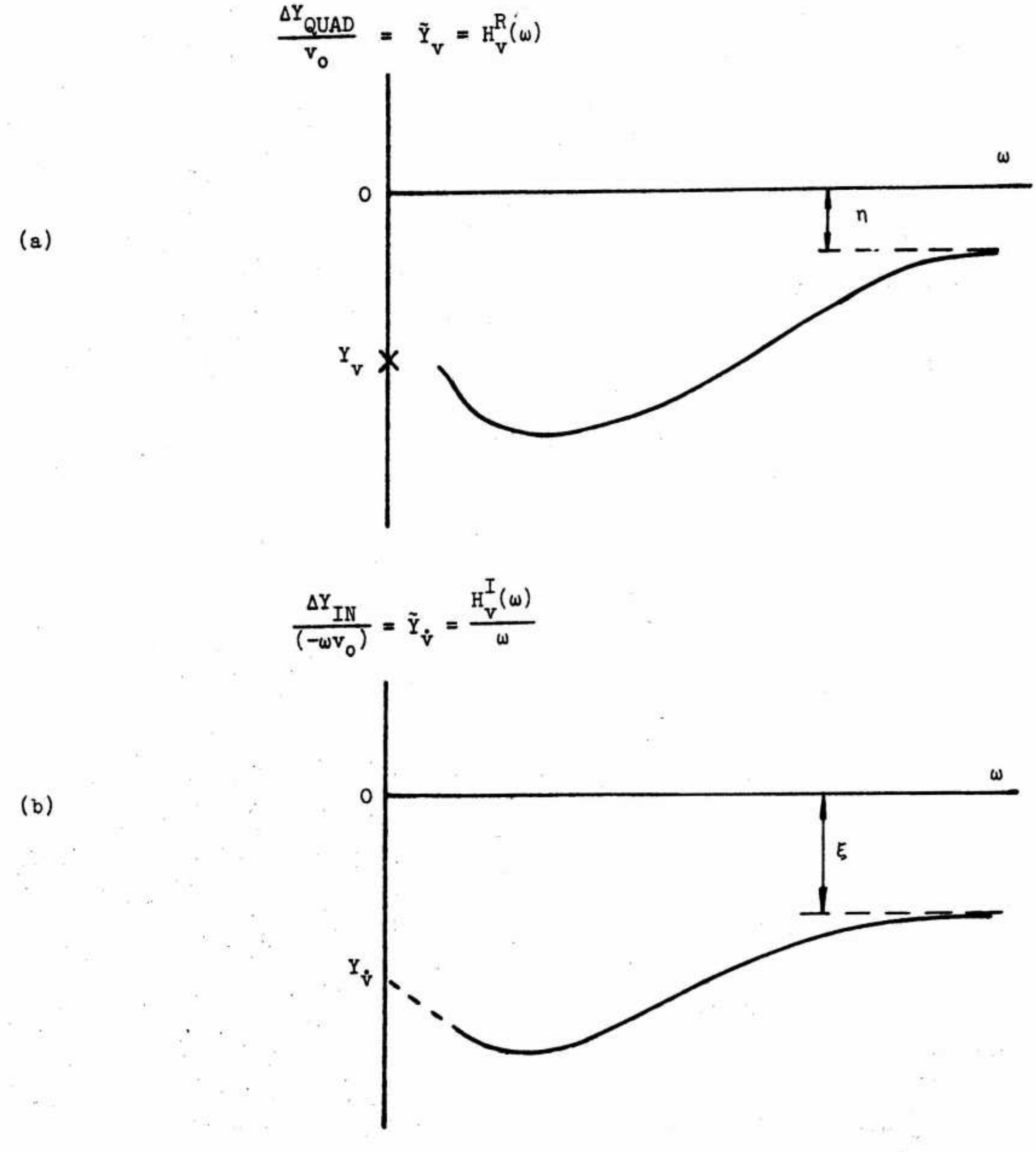

Figure 2. Sketches showing the variations of the oscillatory coefficients $\tilde{Y}_v$ and $\tilde{Y}_{\dot{v}}$ with frequency.

(a) Typical curve obtained from the measurement of sway force component in phase with sway velocity.

(b) A curve for sway force component in phase with sway displacement.

LINEAR THEORY OF FUNCTIONALS

The theory of 'functionals' permits account to be taken of memory effects (6) and it gives rise to a simple linear approximation based on the familiar technique of convolution (7). To illustrate what is implied we may again examine a parasitic sway motion of a ship model.

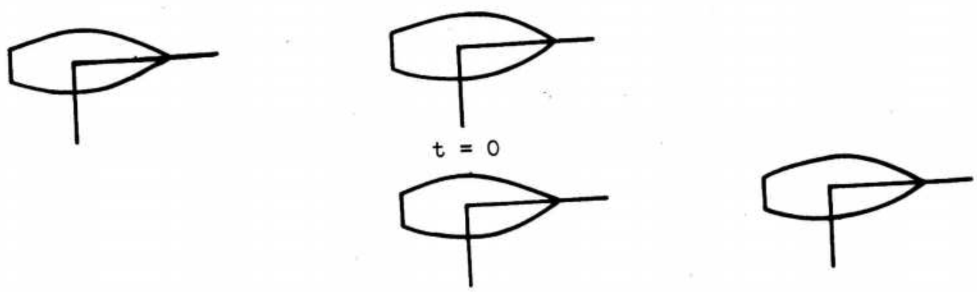

Figure 3. Step displacement of a ship model which is under way.

Suppose that the model follows its straight path with velocity $\bar{U}$ until, at the instant $t = 0$, it suddenly makes a unit step to starboard. Thereafter the model proceeds with its reference motion again (fig. 3). The parasitic sway motion may be expressed in the form

$$v(t) = \delta(t),$$

where $\delta(t)$ is the Dirac delta function. The variation of $v(t)$ is as in fig. 4(a) while that of the athwartships fluid force $\Delta Y(t)$ might be as sketched in fig. 4(b). The function $h_v(t)$ is the special form of $\Delta Y(t)$ which is generated by the unit step sideways.

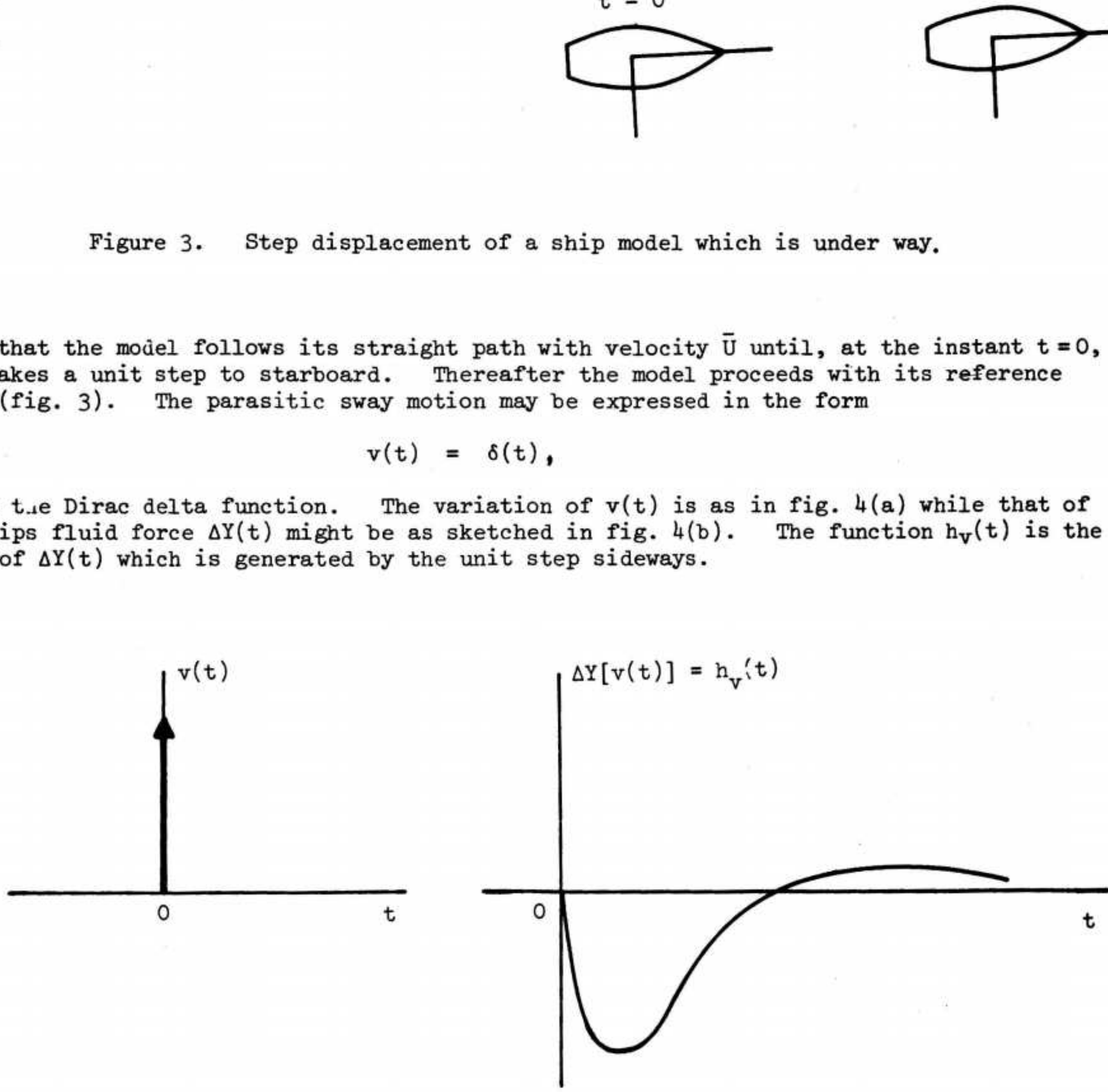

Figure 4. Variation of quantities during the motion illustrated in figure 3.

(a) Sway velocity to starboard.

(b) Fluid sway force acting to starboard.

In point of fact the curve of fig. 4(b) is a gross oversimplification. Although it is not possible to measure $h_v(t)$ directly, because the corresponding motion $v(t)$ cannot be imposed accurately, it is possible to measure its Fourier transform $H_v(\omega)$. This is really what the PMM does.(8) The curve shown in fig. 2(a) as that of $\tilde{Y}_v$ can be interpreted as that of the real part of $H_v(\omega)$, $H_v^R(\omega)$ say. Similarly the curve in fig. 2(b) for $\tilde{Y}_{\dot{v}}$ is also that of $H_v^I(\omega)/\omega$, or $1/\omega$ times the imaginary part of $H_v(\omega)$.

The non-zero asymptotes in fig. 2 imply that there are delta functions in $h_v(t)$ and in fact (7)

$$\left.\begin{aligned} h_v(t) &= -\xi\delta(t)\frac{d}{dt} + \eta\,\delta(t) + h_v^*(t) \\ &= \xi\dot{\delta}(t) + \eta\,\delta(t) + h_v^*(t), \end{aligned}\right\} \qquad (6)$$

where $h_v^*(t)$ is a well behaved function without delta functions (although it still may not resemble that of fig. 4(b) at all closely). The term $\xi\dot{\delta}(t)$ tells us that the variation of ΔY that is associated with the sudden unit step to starboard is dependent partly on the instantaneous sway accelerations of the model. The term $\eta\delta(t)$ indicates that the variation of ΔY depends partly on the instantaneous sway velocity. Finally, $h_v^*(t)$ embodies the memory effect.

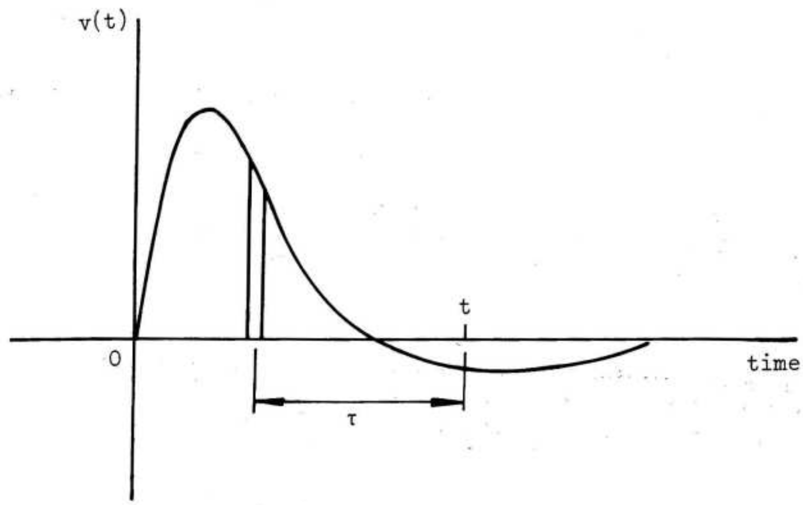

Figure 5. A possible variation of sway velocity with time.

Suppose that the ship model executes some sway motion such as is represented in fig. 5. The corresponding variation of ΔY may now be written down in the form of a convolution integral on the assumption of linearity. That is to say

$$\Delta Y[v(t)] = \int_0^t h_v(\tau)v(t-\tau)d\tau = \int_{-\infty}^{\infty} h_v(\tau)v(t-\tau)d\tau . \qquad (7)$$

With the expression (6) for $h_v(t)$, this becomes

$$\Delta Y[v(t)] = \xi\,\dot{v}(t) + \eta\,v(t) + \int_{-\infty}^{\infty} h_v^*(\tau)v(t-\tau)d\tau . \qquad (8)$$

INSTANTANEOUS FLUID ACTIONS

This consideration of the form of $h_v(t)$ leads to a fresh approach to 'slow motions'. We have seen that large memory effects are associated with rapid disturbance of the structure and/or with slow adjustment of the flow. If the disturbance of the structure is slow, or the flow adjustment is rapid, then the concept of a slow motion derivative is invoked.

The criterion used when derivatives are introduced is the somewhat unsatisfactory one quoted in equation (2) and it refers of course to the slowness of the structural disturbance. It has been suggested (6) that a more appropriate criterion would relate to the rapidity of the flow adjustment. In the terms of the special case we have discussed we can specify instantaneous adjustment of the flow by the requirement that

$$h_v^*(t) = \zeta\delta(t). \tag{9}$$

If the flow has no memory (i.e. if it adjusts instantaneously to a small structural disturbance) then equation (6) leads to the result

$$\Delta Y[v(t)] = \xi\,\dot{v}(t) + (\eta + \zeta)v(t). \tag{10}$$

The PMM results are then of the form sketched in fig. 6 and if equations (3) and (10) are compared it is seen that the constants of proportionality in the former are given by

$$Y_v = \eta + \zeta \quad ; \quad Y_{\dot{v}} = \xi. \tag{11}$$

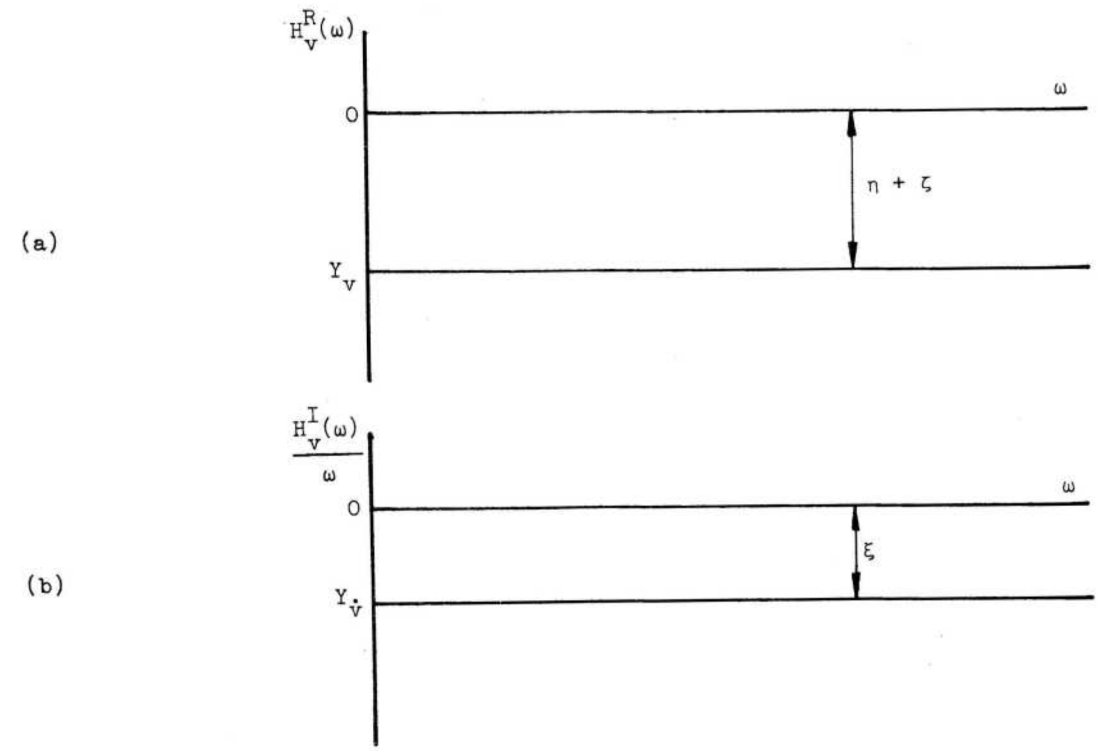

Figure 6. The special forms of the functions of figure 2 when there is no fluid memory.

(a) Sway force in phase with sway velocity

(b) Sway force in phase with sway displacement

The advantages that might perhaps be claimed for this approach are that a straightforward and unambiguous criterion of instantaneous loading is employed, that there is no necessity to invoke the Taylor series when it is not strictly valid and that the dependence on $\dot{v}(t)$ and $v(t)$ is shown to be a physical truth rather than an inspired guess.

AN ALTERNATIVE DEFINITION OF 'SLOW MOTION'

Once again suppose that the value of v at any instant $(t-\tau)$ may be validly expressed in the form of the Taylor series

$$v(t-\tau) = v(t) - \tau\dot{v}(t) + \frac{\tau^2}{2!}\ddot{v}(t) + \ldots + \frac{(-1)^n\tau^n}{n!}v^n(t) + \ldots \qquad (12)$$

so that the sway force (8) is expressible as

$$\Delta Y[v(t)] = \left[\eta + \int_{-\infty}^{\infty} h_v^*(\tau)d\tau\right]v(t) + \left[\xi - \int_{-\infty}^{\infty} \tau h_v^*(\tau)d\tau\right]\dot{v}(t) + \frac{\ddot{v}(t)}{2!}\int_{-\infty}^{\infty}\tau^2 h_v^*(\tau)d\tau - \ldots$$

$$\ldots + \frac{(-1)^n v^n(t)}{n!}\int_{-\infty}^{\infty}\tau^n h_v^*(\tau)d\tau + \ldots \qquad (13)$$

The first two terms of this series have been examined under the special condition $h_v^*(t) = \delta(t)$, and shown to correspond to the slow motion derivatives. The other terms associated with the higher time derivatives of the motion can be shown to correspond to the oscillatory coefficients of reference 4.

It is reasonable to assume that $h_v^*(\tau)$ decays, so that after a time, τ^* say, the response function is zero. This makes it possible to find an allowance for a limited memory effect. The previous series may be written in the form

$$\Delta Y[v(t)] = \left[\eta + \int_{-\infty}^{\infty} h_v^*(\tau)d\tau\right]v(t) + \left[\frac{\xi}{\tau^*} - \int_{-\infty}^{\infty}\frac{\tau}{\tau^*}h_v^*(\tau)d\tau\right]\tau^*\dot{v}(t)$$

$$+ \frac{\tau^{*2}}{2!}\ddot{v}(t)\int_{-\infty}^{\infty}\left(\frac{\tau}{\tau^*}\right)^2 h_v^*(\tau)d\tau - \ldots + \frac{(-1)^n(\tau^*)^n}{n!}v^n(t)\int_{-\infty}^{\infty}\left(\frac{\tau}{\tau^*}\right)^n h_v^*(\tau)d\tau + \ldots \qquad (14)$$

where the integrals all have finite values because

$$h_v^*(\tau) = 0 \qquad \text{for } \tau > \tau^*,$$

and

$$(\tau/\tau^*) < 1 \qquad \text{for } h_v^*(\tau) > 0.$$

The convergence of the series depends on the motion $v(t)$ and is seen to require that

$$v(t) > \tau^*\dot{v}(t) > \tau^{*2}\ddot{v}(t) > \ldots \qquad (15)$$

Thus it is seen that the assumption of slow motion in PMM tests is justified provided that the driving frequency ω is less than $1/\tau^*$.

The application of slow motion theory is therefore very dependent on the 'life', τ^*, of the impulse response function $h_v^*(\tau)$. If the life is very short, it can safely be assumed that the fluid force is determined at any instant by the prevailing motion. If the life is long, the assumption that the motion is 'slow' is of very limited value and can only be made with confidence when the disturbed motion is truly steady, as in the oblique tow test.

REFERENCES

1. I.F.A. Wahed, "Dynamic Instability of Hanging Flexible Tubes Conveying Fluid at High Speed" Unpublished Ph.D. thesis, University of London, 1969.

2. W.J. Duncan, "Introductory Survey" AGARD Manual on Aeroelasticity, 1, chap.1, 1959.

3. M. Gertler, "The DTMB Planar-Motion Mechanism System" Symp. on Towing Tank Facilities, Instrument and Measuring Techniques, Zagreb, paper 6, 1959.

4. R.E.D. Bishop and A.G. Parkinson, "On the Planar Motion Mechanism used in Ship Model Testing" Phil. Trans. Roy. Soc., A.266, 35-61, 1970.

5. T.B. Booth and R.E.D. Bishop, "The Planar Motion Mechanism" AEW Report, Haslar, 1973.

6. R.E.D. Bishop, R.K. Burcher and W.G. Price, "The Uses of Functional Analysis in Ship Dynamics" Proc. Roy. Soc., A.332, 23-35, 1973.

7. R.E.D. Bishop, R.K. Burcher and W.G. Price, "On the Linear Representation of Fluid Forces and Moments in Unsteady Flow" J. Sound Vib., 29, 113-28, 1973.

8. R.E.D. Bishop, R.K. Burcher and W.G. Price, "Application of Functional Analysis to Oscillatory Ship Model Testing" Proc. Roy. Soc., A.332, 37-49, 1973.

ON THE HYDRODYNAMIC FLUTTER ANOMALY

J. D. C. Crisp
Department of Mechanical Engineering
Monash University
Clayton, Victoria

T. F. Berreen
Department of Mechanical Engineering
Monash University
Clayton, Victoria

There has long been an unexplained discrepancy between the experimentally observed behaviour of fluttering hydrofoils and the theoretical descriptions of it, based in extensive and successful aeroelastic experience. We demonstrate some basic limitations of the classical bending-torsion flutter theory by reformulating the problem to include a third degree-of-freedom that caters for cambering distortions of the hydrofoil; and we establish, on the basis of the available incompressible two-dimensional, potential flow flutter derivatives, that this new coupling is dominant for a realistic range of geometrical and structural parameters in the regime of very low mass ratio. The results apply to any appropriate fluid.

NOTATION

$C(k)$	complex Theodorsen function representing flow unsteadiness
C^{**}	square matrix of circulatory fluid force coefficients
E	total energy, sum of kinetic and potential
F	real part of $C(k)$
$\mathcal{F}$	Rayleigh Dissipation Function
L_i	lift force coefficients for displacement modes i
M_i	pitching force coefficients for displacement modes i
N_i	camber force coefficients for displacement modes i
U	fluid speed
a	positive nondimensional distance of pitch axis aft of midchord
b	semichord (Fig.2)
h	translational motion coordinate
k	reduced frequency, $\omega b/U$
k_i	reduced modal frequency, $\omega_i b/U$
m	mass of foil section of unit span
x	streamwise coordinate (Fig.2)
x_α	nondimensional separation of section centroid aft of pitch axis
z	downward displacement coordinate (Fig.2)
α	angle of pitch motion coordinate (Fig.2)
λ_i	modal stiffness parameter, $(\omega_i/\omega_\alpha)^2$
μ	mass ratio, $m/\pi\rho b^2$
ρ	fluid density
ζ	camber motion coordinate
ω	frequency of vibration
ω_i	frequency of vibration in mode i

INTRODUCTION

The art of predicting the occurrence and nature of flutter instabilities of aerofoils and related aeronautical structures is very finely developed and both the practitioner and the scientist profess it, each according to his need, with confidence and success. In particular, its parametric vagaries and sensitivities are well understood. It is disappointing, then, that aeroelastic theory, so extensively tested, fails to describe convincingly the seemingly similar dynamic behaviour of the hydrofoil. And this is the more puzzling in that the discrepancies between conventional flutter theory and hydrodynamic reality are not simply quantitative but rather phenomenological. The easily identifiable differences between the fluttering aerofoil and hydrofoil are three: the hydrofoil normally is subject to the influence of a liquid interface; it is also prone to cavitation; and it operates in a fluid that is relatively very dense. For the purposes of formulating an effective test of theory, the first two factors can be eliminated so that conceptually the two foils have exactly the same perspective, differing only in the magnitude to be assigned to a parameter that describes the density of structure relative to that of fluid. Yet the discrepancy remains: even in the best of all comparisons theory fails to account for reality. Figure 1(a) illustrates the essential anomaly: the experimental data obtained by Woolston and Castile (1) for a range of the mass ratio $\mu = m/\pi\rho b^2$, a nondimensional parameter used as an index of relative fluid density (actually the ratio of the structural mass to that of a circumscribing cylinder of fluid for a representative spanwise section of unit extent), is not described at all well by classical "bending-torsion flutter" theory, at those values of μ appropriate to hydrodynamic conditions. In that figure the regime shaded pertains to unstable oscillations (which, in practice, are rapidly destructive), the boundary delineating the critical flutter state of self-excited vibration, according to Henry et al (3). Vigorous and thorough attempts have been made over 23 years to account for the anomaly, with only partial success. The effect of more realistic representations of the effects of viscosity, of finite span, of foil geometrical parameters such as sweep angle, and so on have been widely and rigorously examined without revealing essential, qualitatively new insights. These efforts are most recently reviewed by Abramson (2) who remarks, *inter alia*, on the sensitivity of flutter calculations to extremely small changes in system parameters in the regime of μ of hydrodynamic interest, as well as on the intensive efforts to refine the basic dynamic formulation of the flutter phenomenon. The former fact is well exemplified in the account given by Martin and Tulin (4) who describe the remarkable sensitivity of flutter behaviour to the most minute changes in the sweep angle of an hydrofoil. The matter of dynamic formulation of the flutter problem, too, is much discussed and it is this aspect to which we now direct particular attention and in respect of which we now offer what seem to be new insights.

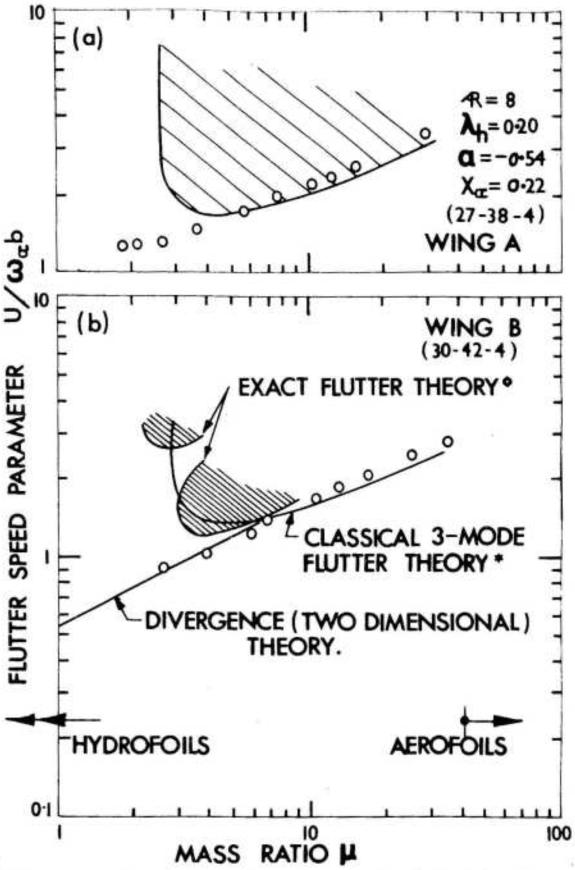

FIGURE 1. (a) The hydrodynamic flutter anomaly, illustrating the incompatibility between classical aeroelastic theory (full line) and measured data (Woolston and Castile [1]) in the region of low values of mass ratio.

(b) Some features of the hydroelastic anomaly illustrating, firstly, the sensitivity (at low values of mass ratio) of the flutter theory to modal representation and secondly, the relevance of divergence instability to the experimental data (of Woolston and Castile [1] - adapted from Fig. 9 of Henry, Dugundji and Ashley [3].

* The exact theory results from the solution of the bending-torsion differential equation. The 3-mode theory relies on a Rayleigh-Ritz formulation using two bending modes and a torsional mode.

MODAL CONVERGENCE

In Figure 1(b) are compared the like experimental data with two theoretical statements the first of which, the classical 3-mode flutter theory, represents the most primitive refinement of the classical bending torsion flutter in which a bending deformation of the foil couples, through the classical circulatory forces of steady-state vibration, with a torsional (or pitching) mode of deformation to permit the transfer of energy from the fluid stream to the foil structure to sustain oscillatory motion. The refinement consists of the addition of a third mode, in this case the first harmonic bending mode, as a possible candidate as a third degree of freedom in the dynamic representation of the flutter motion of the foil. But the qualitative difference is effectively nil - the anomaly remains. Also shown in that Figure is the result of the exact theory, which is exact in the dynamic sense only, inasmuch as the approximate modal type of representation is not used at all, but rather the foil is represented, as to its deformation state at flutter, in exact continuous form by partial differential equations of motion on the assumption that whereas no restriction is placed upon spanwise deformation, chordwise sections remain structurally rigid - so that no camber is tolerated. Up to ten modes (4) have been used as approximations to this exact representation but, like the exact dynamic formulation, these efforts do not match the experimental data. But they do reveal a significant sensitivity of the location of the flutter boundary to the modal formulation in the region of $2<\mu<5$; and the hydrofoil has $\mu < 0{\cdot}5$ approximately. That the hydrodynamic flutter phenomenon is dependent, in explanation, on a proper statement of its dynamic or modal representation has been noticed before, first by Henry et al (3) who referred to the "peculiar couplings" related to the asymptotic behaviour of Figure 1(a). But this dependence does not seem systematically to have been explored; and efforts have been concentrated on the incorporation of the higher spanwise modes, after aeroelastic practice. In this work, we show that chordwise or camber deformations of the foil section are influential, if not definitive, at low values of the mass ratio, $\mu < 1$. But this is demonstrated for a two-dimensional foil section in the expectation that finite span effects do not materially change the phenomenon.

Thus, the critical flutter motion, a sustained linear harmonic oscillation is assumed, as in the classical Rayleigh-Ritz manner, to be a linear combination of three modes of natural vibration of the two-dimensional section,

$$z(x,t) = \sum_{i=1}^{3} K_i \, z_i(x,t) = K_j \sum_{i=1}^{3} r_i \, z_i(x,t) \tag{1}$$

where the oscillatory constituent modes z_i are

$$z_1 = h(t) = H\,e^{i\omega t}$$

$$z_2 = \alpha(t) = P\,(x-ab)\,e^{i\omega t}$$

$$z_3 = \zeta(t) = Q\,[1-(x/b)^2]\,e^{i\omega t}\ ,$$

in which H, P, Q are the modal amplitudes, respectively, of vertical translation h, of pitching α and of chordwise parabolic cambering ζ - Figure 2.

Of these, the first two modal coordinates h, α (modes 1 and 2) correspond in a finite foil to bending and torsional modes of deformation, the section remaining rigid chordwise. The third camber mode 3 we introduce newly as a means of testing the modal convergence of a two-mode representation of the dynamic state. In other words, we expect the flutter boundaries predicted by the two-mode (binary) formulation to be significantly different from those arising out of the three-mode (ternary) formulation based on the inclusion of a camber mode - in which case, the question of the relevance of higher camber modes is raised; and the relevance of higher spanwise modes becomes questionable, as to the essence of the phenomenon.

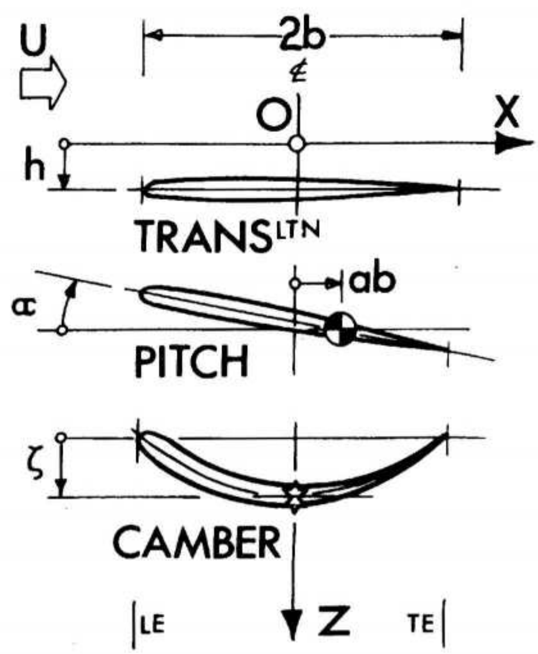

FIGURE 2. Representation of displacement and distortion of the two-dimensional foil section by vibration modes of translation, pitching and chordwise camber.

Finally, the intrusion of divergence instability (in which the foil suffers an unbounded aperiodic displacement when disturbed rather than the unbounded oscillatory response of the flutter condition) at low mass ratios is highlighted by Figure 1(b). We have further comments to offer on this, below, as it may be influenced too by camber effects.

CAMBER AND OSCILLATORY FORCES

The modal formulation of the flutter equations of motion requires access to expressions for the oscillatory fluid forces as functions of the flow regime. These are available in standard form for classical modal couplings, and they are available through the work of Spielberg (5) for two-dimensional, incompressible potential flows around parabolically cambering aerofoils and are tabulated by him, specifically, for the three modes - Figure 2 - of interest here, as functions of the degree of unsteadiness of flow expressed by the reduced frequency $k = \omega b/U$, the regime Strouhal number. He applied his flutter force coefficients tentatively to ternary aerodynamic flutter without conclusive result, and his work lay neglected for nearly a decade until applied to hydrodynamic flutter by Bendavid (6), under the direction of one of the present authors, again with very limited and inconclusive results.

In applying Spielberg's derivations now we use directly his statement of forces L, M, N resulting from unsteady fluid pressures around a flat-plate representation of the foil (so that foil profile is ignored) for each of the three modal harmonic motions. Thus

$$L_h = 1 - i\,(2/k)\,C(k)$$

$$L_\alpha = \tfrac{1}{2} - (2/k^2)\,C(k) - i\,[1 + 2\,C(k)]/k$$

$$L_\zeta = {}^3/_4 + (2/k^2)\,C(k) - i\,[C(k)]/k$$

$$M_h = \tfrac{1}{2}$$

$$M_\alpha = {}^3/_8 - i/k$$

$$M_\zeta = {}^3/_8 + 1/k^2 + i/2k$$

$$N_h = {}^3/_4 - i\,[C(k)]/k$$

$$N_\alpha = {}^3/_8 - (1/k^2)\,C(k) - i\,[1 + C(k)]/k$$

$$N_\zeta = \frac{7}{12} + (\tfrac{1}{2}k^2) + (1/k^2)\,C(k) - i\,[C(k)]/2k,$$

are, in three triads, the constituents respectively of L, M, N as governed by the three motions h, α, ζ; each is frequency dependent through the reduced frequency k; and C(k) is the frequency dependent Theodorsen function which describes amplification and phase deviations from steadiness. These force coefficients are incorporated, in the standard way, into the equations of motion for sustained harmonic motion at flutter.

THE EQUATIONS OF MOTION

A perfectly conventional analysis of the motion of the foil having the three degrees of freedom of Figure 2 and of equation (1) results in the three non-dimensional equations of dynamic force equilibrium below, exposing the balance between inertial forces, elastic forces and, on the right-hand side, fluid forces:

$$\mu \begin{bmatrix} 1 & -a & \frac{2}{3} \\ -a & \frac{1}{3}+a^2 & -\frac{2}{3}a \\ \frac{2}{3} & -\frac{2}{3}a & \frac{8}{15} \end{bmatrix} \begin{bmatrix} \ddot{h}/b\omega^2 \\ \ddot{\alpha}/\omega^2 \\ \ddot{\zeta}/\omega^2 \end{bmatrix} + \mu \begin{bmatrix} \omega_h^2/\omega^2 & 0 & 0 \\ 0 & (\frac{1}{3}+a^2)\omega_\alpha^2/\omega^2 & 0 \\ 0 & 0 & \frac{8}{15}\omega_\zeta^2/\omega^2 \end{bmatrix} \begin{bmatrix} h/b \\ \alpha \\ \zeta/b \end{bmatrix}$$

$$= \begin{bmatrix} L_h & L_\alpha-(\frac{1}{2}+a)L_h & L_\zeta \\ M_h-(\frac{1}{2}+a)L_h & M_\alpha-(\frac{1}{2}+a)(L_\alpha+M_h)+(\frac{1}{2}+a)^2L_h & M_\zeta-(\frac{1}{2}+a)L_\zeta \\ N_h & N_\alpha-(\frac{1}{2}+a)N_h & N_\zeta \end{bmatrix} \begin{bmatrix} h/b \\ \alpha \\ \zeta/b \end{bmatrix} \qquad (2)$$

in which the unknown flutter frequency is ω; and the unknown fluid stream speed U at which a sustained oscillation becomes possible - the critical flutter speed that is transitional between stability and instability - is implicit in the matrix of fluid forces of the right-hand side.

This becomes explicit, for the sake only of illustration but not of solution, if equations (2) are developed in particular form for the case a = -0·5 (the pitching axis being then at the quarter-chord station) and under the approximation C(k) = F(k), the imaginary component G(k) of C(k) being ignored. Then equation (2) can be wrought as the matrix equation

$$A\ddot{q} + B\dot{q} + Cq = 0, \qquad (3)$$

where q is the column {h/b, α, ζ} of modal amplitudes and A, B, C are square matrices of force coefficient elements. Precisely,

$$A = \mu \begin{bmatrix} 1 & {}^1/_2 & {}^2/_3 \\ {}^1/_2 & {}^7/_{12} & {}^1/_3 \\ {}^2/_3 & {}^1/_3 & {}^8/_{15} \end{bmatrix} + \begin{bmatrix} 1 & {}^1/_2 & {}^3/_4 \\ {}^1/_2 & {}^3/_8 & {}^3/_8 \\ {}^3/_4 & {}^3/_8 & {}^7/_{12} \end{bmatrix} \qquad (4)$$

is the symmetric inertia matrix having a structural component directly related to the mass ratio μ, and a virtual (fluid) inertia component which (for low μ) is always significant if not dominant (unlike the aerodynamic case for high μ);

$$B = (U/b) \begin{bmatrix} 2F & 1+2F & F \\ 0 & 1 & -\frac{1}{2} \\ F & 1+F & \frac{1}{2} \end{bmatrix} \qquad (5)$$

is the asymmetric fluid damping matrix, approximately representative of $k \to 0$ if $F \to 1$, and of $k \to \infty$ if $F \to \frac{1}{2}$ because of the properties of $C(k)$;

$$C = (U/b)^2 \begin{bmatrix} \mu k_h^2 & 2F & -2F \\ 0 & \frac{7}{12}\mu k_\alpha^2 & -1 \\ 0 & F & \frac{8}{15}\mu k_\zeta^2 - (F+\frac{1}{2}) \end{bmatrix}$$

which includes both structural stiffness components, on the diagonal, and asymmetric "fluid stiffness" components (the circulatory terms) appearing as simple functions of F.

The forms of the matrices A, B, C are of peculiar significance, as is later made clear; but the more general equations (2) we have solved in the standard fashion, particular care having been taken, through comparative and interpolation procedures, to ensure that the fluid forces on the right-hand side are properly and exactly matched (as to dependence on frequency parameter k) to the eigen-values k that the solutions yield.

TERNARY FLUTTER

The harmonic solutions of equations (2) we present for two values of a, which prescribes the chordwise station of the pitch (or "elastic") axis, in each case for a foil section that is inertially symmetric about its midchord and, moreover, that has a uniform chordwise distribution of structural mass; and, throughout, for a fixed ratio of stiffness in the translational freedom (mode 1) to that in the pitching freedom (mode 2), the parameter $\lambda_h = (\omega_h/\omega_\alpha)^2$ being then fixed at a practically relevant value, namely, 0·7. On the other hand, the sensitivity of the flutter stability boundary is tested, as a function of mass ratio μ, for a wide range - see Figure 3(a) - of the stiffness parameter $\lambda_\zeta = (\omega_\zeta/\omega_\alpha)^2$ which defines the camber mode 3 stiffness in ratio to that of the pitch mode 2. Each curve of Figure 3(a) delineates, for the designated λ_ζ, a flow speed regime such that points $(\mu, U/\omega_\alpha b)$ located above the boundary represent a state of divergent oscillatory instability.

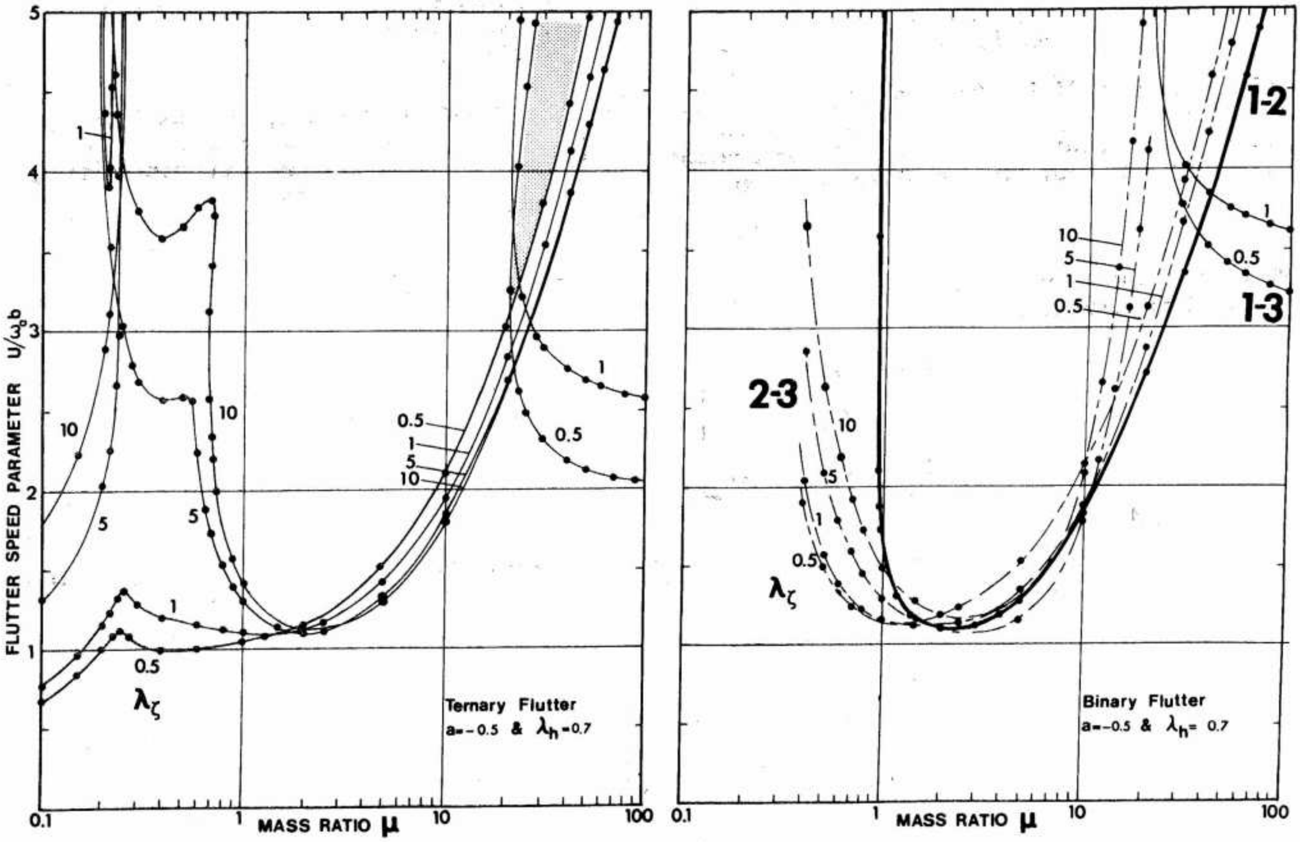

(a) (b)

FIGURE 3. (a) The dependence of flutter stability boundaries on the mass ratio according to the ternary formulation based on translation (mode 1), pitching (mode 2) and section camber (mode 3) for a variety of chorwise section stiffnesses designated through the structural frequency parameter $\lambda_\zeta = (\omega_\zeta/\omega_\alpha)^2$. The pitch axis is at the quarter-chord station (a = -0.5).
(b) The several constituent binary formulations, each involving coupling only of two of the three modes.

The Figure reveals three characteristic and discrete branches:

Branch 1 exists for high μ and low λ_ζ

Branch 2 exists for intermediate μ and for all λ_ζ

Branch 3 exists for very low μ and for all λ_ζ

some pairs of branches mutually intruding (as do Branches 1 and 2), some mutually coalescing (as do Branches 2 and 3); and some displaying less lucid features. Wherever mutual intrusion occurs, a region of double-instability exists by which is meant a regime in which either one of two distinct unstable flutter modes is possible. One such regime is shown shaded in Fig.3(a).

CLASSICAL AND BINARY FLUTTER

An interpretation of the ternary boundaries is provided by viewing the corresponding binary (two degree-of-freedom) solutions which are obtained by the repeated solution of the equations (2) taken two at a time. The three binary solutions, each representing a characteristic modal coupling duet, we display in Figure 3(b), and each has practical meaning if the third, supernumary mode can realistically be suppressed. The superficial resemblances between parts (a) and (b) of the Figure make it easy to link the ternary Branch 1 with the binary coupling 1-3; much (but not all) of the ternary Branch 2 with the binary coupling 1-2; and the ternary Branch 3, at very low μ, with no binary counterpart. Further, for the binary 2-3 coupling we find no ternary correspondence. These similarities and disparities are reinforced by comparisons of corresponding flutter frequencies along the critical boundaries and, likewise, of corresponding amplitude ratios. The latter, r_i of equation (1), are the ratios of the oscillatory flutter amplitudes of each of the constituent modal coordinates which, in combination, form the total flutter deformation z. The ratios r_i are indicators of the significance of the involvement of a mode in the flutter coupling.

The binary flutter boundary 1-2 of Figure 3(b) has, of course, a second significance inasmuch as it is the classical primitive solution - and the ternary deviations from that single binary branch constitute the effect of adding the third, camber degree-of-freedom to the conventional analysis. The two analyses become identical when that mode is suppressed and this we attain, conceptually, by considering increasingly high values of the parameter λ_ζ so that, in the limit, the camber stiffness is infinitely great the chordwise section becoming then rigid. Indeed, for relatively small values of $\lambda_\zeta>1$, the ternary Branch 1 of Figure 3(a) becomes upwardly very far removed so that the Branch 2 dominates behaviour, offering then the least critical flutter speed. And, for the larger μ appropriate to aerodynamic flutter, this ternary Branch 2 is indistinguishable from the classical binary boundary. But for yet realistic values of λ_ζ, there persist, for the lower μ, flutter branches that the classical formulation cannot reveal and that cannot be approximated by alternative binary couplings embracing the newly introduced camber mode. This suggests that whereas modal convergence is satisfactorily attained for larger μ, the uncertainties of modal convergence inherent in the Rayleigh-Ritz dynamic formulation that we earlier remarked upon at the binary limit, $\mu\simeq 1$, remain and extend even to very low μ. The refinement afforded by the relaxation of the chordwise rigidity of the foil section is still probably gross.

Figure 4, showing the ternary regimes for a section pitching about the midchord point, generally confirms these notions and serves also to highlight, by the shading of the classical 1-2 binary region, the persistence of a dominant flutter branch down to the lowest values of mass ratio.

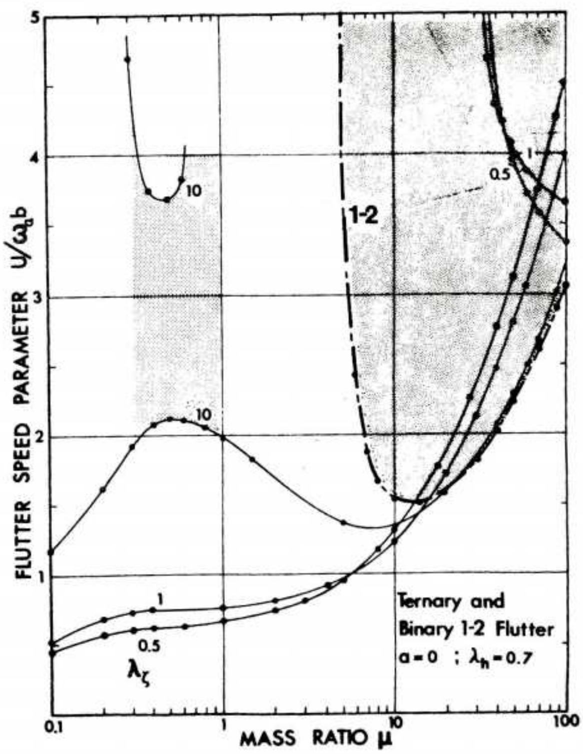

FIGURE 4. The dependence of the critical flutter boundaries on mass ratio for a pitching axis at the mid-chord station (a = 0) of the foil section. Full lines - ternary flutter; chain line - classical binary (1-2) flutter.

DIVERGENCE INSTABILITY

The equations (2) have nonperiodic solutions, ω=o and so k=o, which can be extracted immediately from the singularity condition applied to the determinantal minors of the matrix of equations (6). For then C(k) = F = 1 exactly; and the vanishing of any determinantal minor corresponds to the total potential energy of the system becoming non-positive definite. The associated static instabilities are the divergences.

Because of the zeros in the matrix the ternary singularity is coincident with that of the 2x2 for coupling of modes 2 and 3. It follows that the critical divergence speeds are given by

$$U/\omega_\alpha b = (\mu\psi)^{\frac{1}{2}}, \tag{7}$$

where ψ is a root of the quadratic equation

$$\psi^2 - {}^7/_8\psi + {}^{14}/_{45}\lambda_\zeta = 0.$$

The speeds (7), which do not involve the mode 1 and so are independent of the stiffness parameter λ_h, are plotted in Figure 5 being there labelled "1-2-3 and 2-3". Because ψ above is double-valued for any λ_ζ, there exist in general two bounds on the region of divergent instability, as illustrated in the Figure for λ_ζ=0·5. For lower values the region of instability is more extensive, reaching the horizontal axis $U/\omega_\alpha b$=0, for λ_ζ=0. There is an upper limit to λ_ζ which causes the instability to vanish completely and this is easily found as λ_ζ=0·615 being that value that first renders the roots of the above quadratic complex. Real foils will normally have λ_ζ ·1 so that the coupled 2-3 divergence condition is then dominated by a second divergent instability, labelled 1-3 in Figure 5 which is actually a divergence in the single camber mode. Thus, the critical speeds are

$$U/\omega_\alpha b = \frac{4}{3}(\mu\lambda_\zeta/5)^{\frac{1}{2}}, \tag{8}$$

and they exist because the direct circulatory hydrodynamic force coefficient ("fluid stiffness") for the parabolically cambering section is negative.

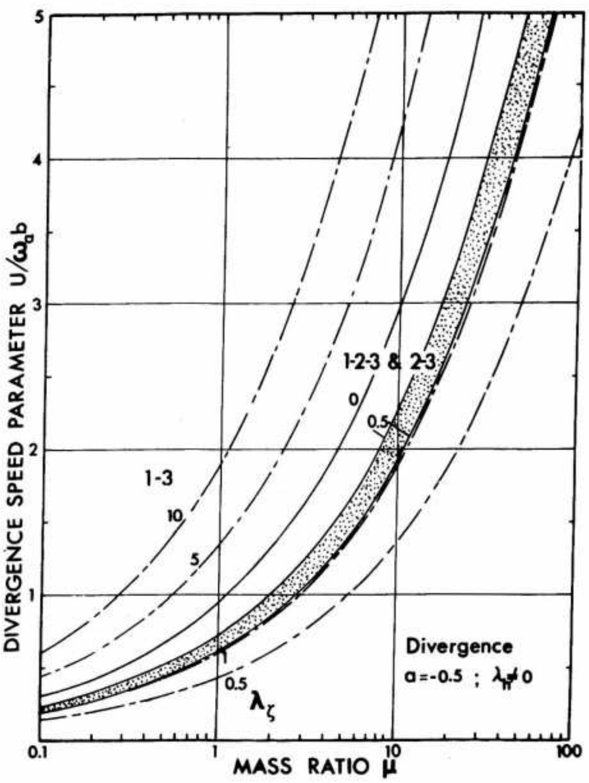

FIGURE 5. The sensitivity to mass ratio of the boundaries of divergence instability, for various modal representations, corresponding to the flutter boundaries of Fig. 2. Full lines - the ternary (1-2-3) and pitch/camber binary (2-3), which are identical; chain lines - the translation/camber binary (1-3); the translation/pitch binary instability is nonexistent.

THE DYNAMIC COUPLINGS

That the camber mode is vital at low values of mass ratio the plots make clear, and we seek now some further insight into the nature of its coupling with the classical modes. This we attempt through the equation of total power (7)

$$\dot{E} = -2F - \dot{q}^T C^{**}q, \tag{9}$$

which is a statement of the rate of change of total energy of the vibrating system. The Rayleigh Dissipation Function $2F = \dot{q}^T Bq$, in which $\dot{q}^T$ is the transpose of $\dot{q}$, measures the rate of energy loss due to the fluid damping forces represented in the damping matrix B, equation (5). And all seven principal discriminants of the determinant |B| are positive for any F>0, so that the function F is positive definite. It follows, by (9), that no mechanism of oscillatory instability is directly attributable to the damping couplings introduced by the camber mode, because E can only be diminished by them.

The second "quadratic form" in equation (9) has as its coefficients the skew-symmetric or circulatory components $c^{**}_{ij} = (c_{ij} - c_{ji})/2$ of the stiffness matrix C, equation (6), which can be decomposed as

$$C = \begin{bmatrix} \mu k^2_h & F & -F \\ F & \frac{7}{12}\mu k^2_\alpha & \frac{1}{2}(F-1) \\ -F & \frac{1}{2}(F-1) & \frac{8}{15}\mu k^2_\zeta - (F+\frac{1}{2}) \end{bmatrix} + \begin{bmatrix} 0 & F & -F \\ -F & 0 & \frac{1}{2}(F+1) \\ F & \frac{1}{2}(F+1) & 0 \end{bmatrix}$$

of which the first symmetric part contributes nothing to the energy balance, and of which the second contains the elements c^{**}_{ij} of C^{**} of equation (9). It is necessary for any self-excited oscillation to exist, that at least one off-diagonal element of that matrix be nonzero: and the magnitude of those elements may be taken as an indicator of the degree of coupling between the several modes for they directly influence the accessibility of the vibrating section to the energy of the fluid stream. In the vicinity of F=1, all the circulatory terms are of the same magnitude so that all couplings are significant.

CONCLUSION

We have established that a chordwise deformation of a foil section and its associated dynamic couplings are significant in determining both flutter and divergence instabilities, and that at low values of mass ratio this mode is dominant. Figure 6 exposes both the aeroelastic (high μ) and the hydroelastic (low μ) phenomena, highlighting the limitations of the classical bending-torsion formulation (1-2). We cannot claim to have resolved the hydrodynamic flutter anomaly but we do insist that our calculations suggest the need to scrutinise again the question of modal convergence and of the selection of appropriate modes.

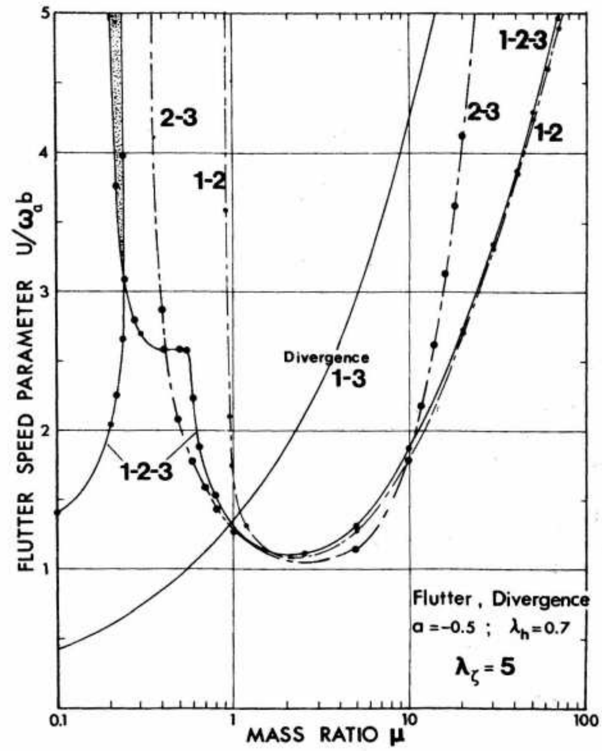

FIGURE 6. The relationship between the new ternary flutter boundaries (full lines labelled 1-2-3) and the classical flutter boundary (chain line labelled 1-2), showing also the new constituent 2-3 binary coupling of pitch and camber as well as the only divergence boundary relevant to this configuration (λ_ζ =5).

REFERENCES

(1) WOOLSTON D., & CASTILE G.E., Some effects on variation in several parameters including fluid density on the flutter speed of light uniform cantilever wings, NACA TN 2558, 1951.

(2) ABRAMSON H.N., Hydroelasticity: A review of hydrofoil flutter, AMR, 22, No.2, 115, 1969.

(3) HENRY, C.J., DUGUNDJI J., & ASHLEY H., Aeroelastic stability of lifting surfaces in high-density fluids, J.Ship Res.,2,No.4,10,1959.

(4) MARTIN M., & TULIN M.P., "Hydroelasticity of Hydrofoils", Fluid-solid Interaction, ASME, NY, 241, 1967.

(5) SPIELBERG I.M., The two-dimensional incompressible aerodynamic coefficients for oscillatory changes in airfoil camber, WADC TN/WCNS 52-7, 1952.

(6) BENDAVID D., Flutter in high density fluids, Polytech. Inst. Brooklyn, PIBAL Rep. No. 293, 1961.

(7) CRISP J.D.C., On revealing the mechanism of flutter, Jnl. Aero. Soc. India, 22, No.1, 10, 1970.

THE EFFECT OF TREAD PATTERN ON TYRE NOISE

S. E. Samuels
Department of Mechanical Engineering
Monash University
Clayton, Victoria

R. J. Alfredson
Department of Mechanical Engineering
Monash University
Clayton, Victoria

SUMMARY - A mathematical model has been developed to predict the directivity patterns produced by some radial ply tyres of simple tread design. The predictions show reasonably good agreement with measured values, and thus the model is probably suitable for adaption to commercially available tread patterns. Tread design and tyre operating parameters are used in the model, which therefore describes the way in which a tyre and its tread generates noise.

INTRODUCTION

Automobile safety and pollution control constitute two of the major research efforts currently being undertaken by both manufacturing concerns and government instrumentatilites throughout the world. Automobile noise can fairly be described as a significant source of pollution of our environment, and, as such, has rightly been included in pollution research programmes. Recent studies [1,2,3] have indicated that tyre noise represents a significant contribution to the overall noise produced by a moving automobile. Therefore, it is of interest to investigate the nature of tyre noise production, with the view to its eventual reduction to an acceptable minimum.

In a recent report to the President and Congress on transportation and engine noise [3], the United States Environmental Protection Agency (USEPA) stated that the noise produced by highway vehicles results from three major sources - tyres and gearing; engine and related accessories; and aerodynamic and body noise. Figures quoted by the USEPA to substantiate this claim are listed in Fig. 1.

Noise level at 50ft from vehicle, travelling at 35 mph. (dBA)	Source of noise
85	Engine/Mechanical
82	Exhaust
80	Intake
81	Cooling Fan
79	Tyres (55-56 mph)
89	Total

Fig. 1: USEPA Data

Regarding the tyre noise component, USEPA remarks that "tyre noise increases with speed, and, at about 50 mph becomes the principal source of noise". Thus it concludes that tyre noise levels must be substantially reduced. However, USEPA casually observes that, assuming a continuing advance in noise control technology, the elimination of tyre noise, except in the case of noisy truck tyre retreads, represents a major technical challenge. Similar remarks and conclusions re the importance of tyre noise have been made by other workers, such as D.C. Harland [4] of the U.K. Road Research Laboratory, and W.V. Galloway et al [2] of the U.S. Highway Research Board.

Broadly speaking, it is possible to divide tyre noise into two categories, the first of which is noise radiated by the tyre into the surrounding atmosphere. The second category results from tyre vibrations, which, when transmitted through a vehicle's suspension and chasis to its body panels are perceived by the vehicle's occupants as tyre noise. (These vibrations may be due to the inherent dynamic properties of the tyre, or due to a tyre/road interactive effect, or both). It is noise of the former of these two categories, and the methods by which it is generated, that this paper is concerned.

To date, very few treatises dealing with the mechanisms of tyre noise generation have **appeared.** Indeed, within the tyre industry itself, the approach seems to have have been rather ad hoc. Typically, measurements (often obtained by the "pass by" techniques) of noises associated with tyres of different tread designs would be made. Manufacturers would then adopt tread design similar to those which had been measured as the "quietest" [5,10]. Another technique well known to tyre designers is that of empirically varying the tread pattern pitch sequence* [12]. While both these techniques have shared some success in reducing tyre noise, they have provided little or no information on the actual mechanisms involved in tyre noise production.

There have, however, appeared in the literature, four source mechanisms of air radiated noise. These are squeal, tyre vibration, aerdoynamic effects and "air pumping" from the tread. Squeal [16,17] is currently attributed to tread element vibrations, and is the noise generated by a tyre during severe cornering, braking or acceleration. Road roughnesses and tyre dynamic properties may excite a tyre into complex vibrations which thereupon radiate sound [6,13]. The aerodynamic source [13] is claimed to be similar to the mechanism induced in rotating disc noise. Finally, air pumping [6,13] refers to the theory that tyres produce noise by the enclosure and subsequent release of air in the cavities between adjacent tread elements. The theory derives its name from the air release process, which is likened to a pumping phenomenon.

A comparison of each of these source mechanisms has been attempted by Hayden [13]. While this comparison required the extrapolation and manipulation of available data, it does give a reasonable indication of the contribution of each of these mechanisms to tyre noise. The comparison is presented in Fig. 2. below.

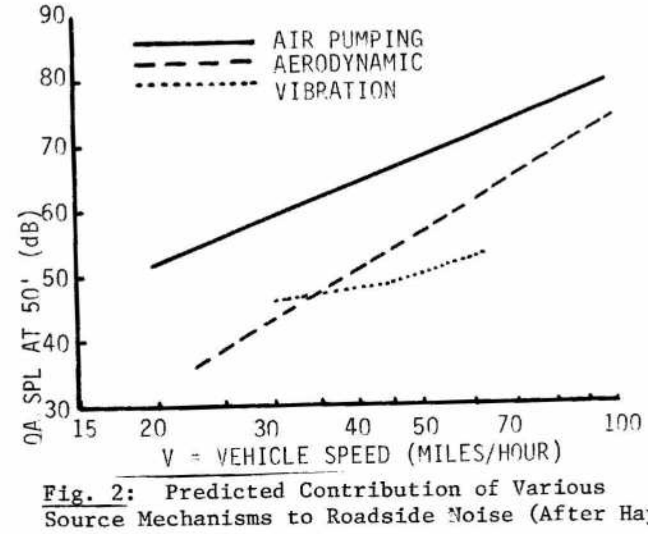

Fig. 2: Predicted Contribution of Various Source Mechanisms to Roadside Noise (After Hayden [13]).

AIR PUMPING - MONOPOLE SOURCE

Of the four sources, air pumping has appeared to be the most important. Hayden [13] presented a detailed discussion of air pumping theory. He maintained that there is an unsteady volumetric flow rate of air from and into the cavities that are enclosed between the tyre tread and the road surface. He attributes this to three postulations concerning a rolling tyre:

A. The displacement of some of the air in the tread cavities when the tread contacts the road,
B. The displacement of some of the air in the road surface cavities when the tyre rolls over and partially fills these cavities,
C. An inflow of air into the expanding cavities, enclosed by the tyre and road surface, as the tread leaves the contact area.

Thus Hayden concludes that there is an acoustic monopole source in operation, which can be described mathematically as an omnidirectional point source of noise. By employing some basic geometric calculations on a simple hypothetical tread pattern to determine the fluctuating volumetric flow rate of air from the source, Hayden arrives at the following equation, which, he maintains, is valid "only for the case of a non directional source and hemispherical spreading". Fig. 3 shows the appropriate arrangement and dimensions.

*"Pitch sequence" is the term used by tyre technologists to describe the circumferential variation in the order of repetition of identically shaped tread elements.

$SPL(r) = 68.5 + 20 \log (gw/s) + 10 \log n + 20 \log (fc) + 40 \log (V) - 20 \log (r)$

Where SPL(r) = Overall sound pressure level re 2×10^{-5} Nm^{-2}, generated by the source, measured at the observation point.

- g = Tread Depth. w = Width of a single tread cavity
- s = Circumferential distance between tread grooves
- n = Number of cavities per tyre width
- fc = Fractional change in cavity volume
- V = Forward velocity of tyre (mile/hour)
- r = Distance from contact patch to observation Point (Ft).

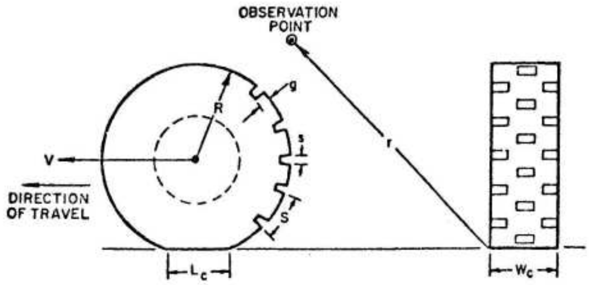

Fig.3: Hayden's Hypothetical Arrangement

Having assumed a value of 10% for fc, he then attempted correlations with some passby data obtained by Tetlow [15], and some of his own measured data. These correlations were only partly successful - in the first case the predicted levels did not agree with the measured data and in the second there was insufficient realistic data to render any agreement meaningful.

Hayden's theory, although reasonable in parts, must be questioned on several accounts.

1. Is, in fact, only one monopole source operating?
2. Is the air pumping tyre noise directional?
3. What is a realistic value of (fc) and can this be verified?
4. Is his theory applicable to tyres of different tread design?

MULTI-SOURCE AIR PUMPING

As an improvement to Hayden's theory, it is suggested that there is within the tyre contact patch, an array of point monopole sources operating via an air pumping mechanism. The shape and structure of this array will depend in the main upon the tread pattern design. Parameteres such as inflation pressure, load and speed will, of course, influence the operation of any given source array. This theory states that there is a set of monopole point sources in operation in those regions where the tread enters and exits the contact patch. While the concepts of an inrush of air into the exiting cavities and an outflow of air from the entering cavities is still retained, the theory utilises the mathematical jusitification of modelling these phenomena as steady state sinusoidal air flow fluctuations. Sound pressure waves radiated by these array sources interact to produce a directional sound field. The extent to which the radiated field is directional is principally determined by both the relative strengths of the entering and exiting sources, and the phase difference between them.

It is apparent that the model is involved with the mechanisms occuring in the tyre contact patch. Simply, we are concerned with determining an array shape and the relationships between elements of this array. These relationships can be determined once the tyre operating parameters and tread properties are known. Given an array shape and the appropriate relationships, it is possible to calculate the directivity pattern, at a particular frequency, produced by the source array. The intersource relationships are, in a sense, frequency dependent. For the rolling radius of a tyre varies with speed and consequently the length and breadth of the contact patch vary similarly. It is the length dimension that is one of the main determinants of the phase difference between entering and exiting sources. In turn, this phase difference is a critical parameter in the directivity pattern calculation. Further, a variation in rolling radius, at constant load and inflation pressure, will alter the deformation of the contact patch, and therefore vary the strengths of the source elements. In fact, the other two externally variable parameters, load and inflation pressure, have a similarly important role in determining the relative strengths and phases of the array sources.

If we consider a tyre of simple, but not too unrealistic, tread design, the approach is as follows. The tread may consist of a set of 78 lateral and 4 longitydinal (i.e. circumferential) grooves, each of equal depth and equal width, cut into an otherwise smooth tread. The lateral grooves are uniformly and equally spaced around the circumference of the tyre, while the longitudinal grooves are equi-spaced across the width of the tread. Figure 4 shcws a sketch of this design. The noise sources are assumed to be at the intersections of the lateral and longitudinal grooves that occur at the entry and exit of the contact patch. Further it is assumed that the four sources along the entry line are of equal strength and are all in phase with one another. A similar assumption applies to the sources along the exit line. Note that the entry sources and the exit sources may have any relative stengths and phase differences. We now calculate the total acoustic pressure fluctuations at an observation point a distance r from the centre of the contact patch. The only other assumption required is that any shielding effects are negligible. Further, at this stage, the calculation is limited to the case of a freely rolling tyre. Figure 5 illustrates the arrangement.

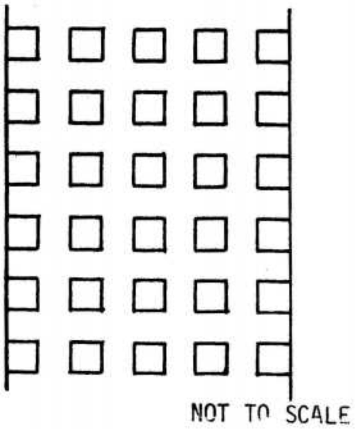

Fig.4: Tread Design

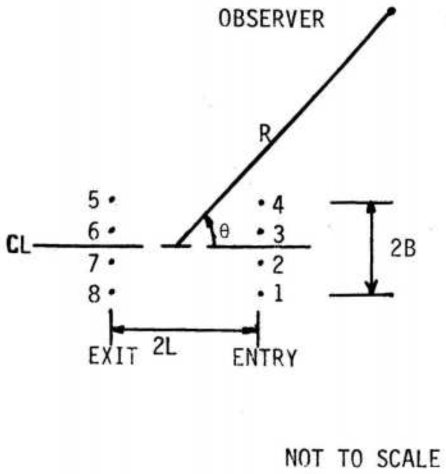

Fig.5: Arrangement for Calculation

The acoustic pressure fluctuations at the observation point due to any one of the sources, is, in complex number notation, of the form,

$$p' = \mathrm{Re}\left\{\frac{A_n}{r_n} e^{i(\omega t - kr_n - \phi_n)}\right\} \qquad \ldots(1)$$

Where, A_n = Strength of n^{th} source
r_n = Distance of n^{th} source to observer (m)
ω = Angular frequency (rad/sec)
t = Time (sec)
k = Wave number
$= \frac{2\pi}{\lambda}$, where λ = wavelength (m)
ϕ_n = Phase difference between n^{th} source and entry sources (Rad).

Thus, when n sources operate simultaneously, the total acoustic pressure fluctuations are tiven by

$$p' = \mathrm{Re}\left\{\sum_n \frac{A_n}{r_n} e^{i(\omega t - kr_n - \phi_n)}\right\} \qquad \ldots(2)$$

In regard to the directivity pattern, it is the amplitude of the above expression only that is required. Note that ϕ_n will be zero for the entry sources, and may assume any value from zero to π radians for the exit sources. The values of r_n may be calculated from the geometry of the arrangement shown in Fig. 5 . Typically they appear similar to that for source 1, which is quoted below:

$$r_1 = (r^2+B^2+L^2-2rL\cos\theta+2rB\sin\theta)^{\frac{1}{2}} \qquad \ldots(3)$$

Now, on substituting the eight values of r_n into (2) and manipulating, (2) reduces to

$$|P'| = (X^2+Y^2)^{\frac{1}{2}} \qquad \ldots(4)$$

Where $\quad X = \sum_n \frac{A_n}{r_n} \cos\,(k\,r_n - \phi_n) \quad$ and $\quad Y = \sum_n \frac{A_n}{r_n} \sin\,(kr_n - \phi_n) \qquad \ldots(5)$

The directivity pattern required is determined by evaluating (4) over the appropriate range of θ.

To predict the directivity pattern at a given tyre speed, and a given observation radius, it is necessary, then, to know the exact tyre speed, the number of elements in the tread, the dynamic dimensions of the contact patch (2L and 2B) and the phase difference and strengths of the entry and exit sources. A number of such calculations over a range of these parameters has been performed using the University's Burroughs B6700 computer.

EXPERIMENTAL APPROACH

In order to verify the above theory and to build up a more comprehensive understanding of air pumping, a series of directivity patterns for a set of tyres of differing simple tread patterns has been obtained. The measurement have been taken inside the Department's Anechoic Chamber. A steel structure that provides a mounting for a rotating drum has been installed into the chamber. The structure, which has facilities for mounting and loading a tyre which is driven by the drum, is powered by a variable speed electric motor. A microphone capable of scanning around the tyre in a horizontal plane through its contact patch with the drum is also provided in the chamber. Output signals from this microphone are fed directly into a Bruel and Kjaer Constant Bandwith Analyser. Fig.6 shows a sketch of this arrangement, while Fig.7 shows a photograph.

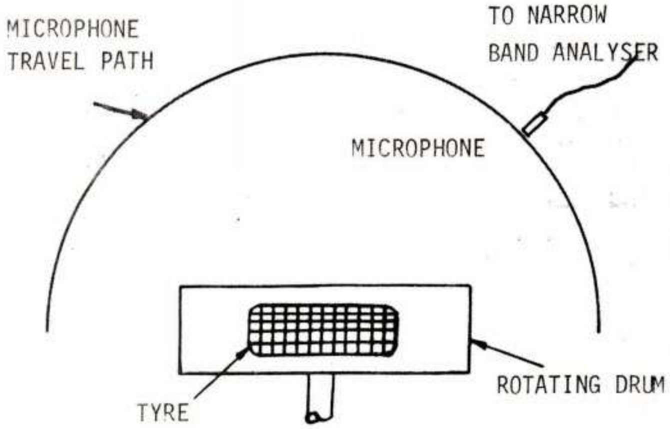

Fig.6: Schematic Diagram of Setup in Anechoic Chamber

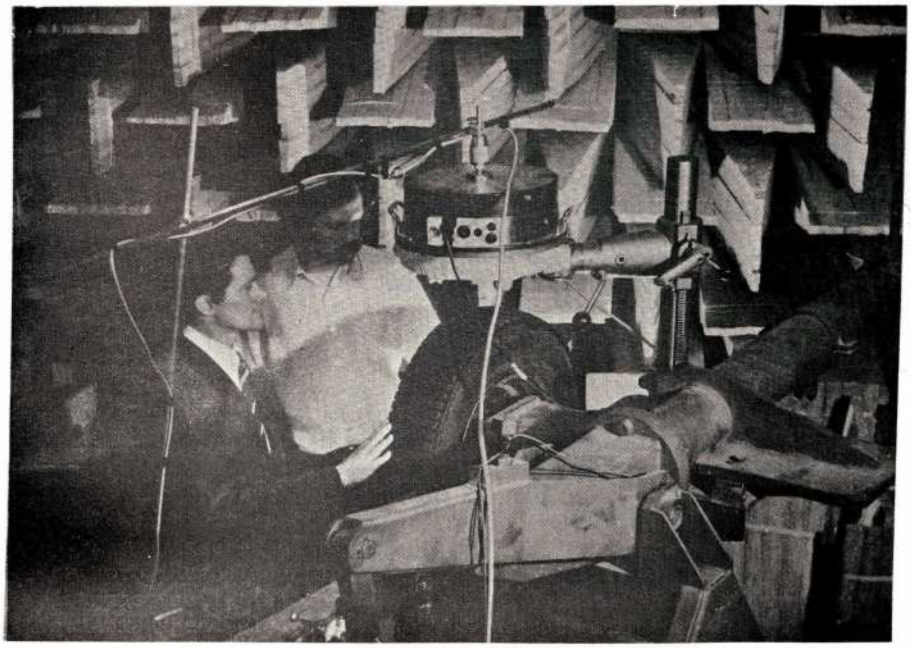

Fig.7: Photo of Setup in Anechoic Chamber

A set of experimental tyres - 185x14 radial ply - was obtained. These were retreaded with a patternless tread and then, special patterns of interest were hand cut into these treads. The patterns included one as described in the above theory, this first pattern minus the longitudinal grooves, the first pattern minus the lateral grooves, and finally, one tyre was left bald.

Each of the tyres was run in the chamber over a set of inflation pressures and speeds. At each condition, spectral analyses were performed to identify the tread noise frequencies of interest. Then, where possible, directivity patterns of the fundamental tread noise frequency were obtained. By matching these patterns with those predicted by the model, it is possible to use the model to obtain information concerning the strengths and phases of the various source arrays.

As mentioned previously, it is necessary to know accurately the dynamic dimensions of the contact patch prior to applying the model. This problem is further complicated by the variation in contact patch dimensions with load, pressure, and, in particular, speed. Tyres exhibit a centrifugal growth that is dependent on speed, and it is for this reason that the dynamic dimensions at constant speed must be measured. To do this, high speed photographs of the relevant contact patches were taken, using a high speed flashing technique.

Some typical data is presented below. It includes spectral analyses of each of the four tyres and directivity patterns for the tyre with lateral and longitudinal grooves and the tyre with only laterally grooved. Also presented is a sample side view photograph of the laterally grooved tyre. Superimposed on the directivity patterns are the shapes predicted by the model. In fact, to obtain these theoretical shapes, it was necessary to obtain optimum values of the source element strengths and phases. An existing computer optimisation programme was used to do this.

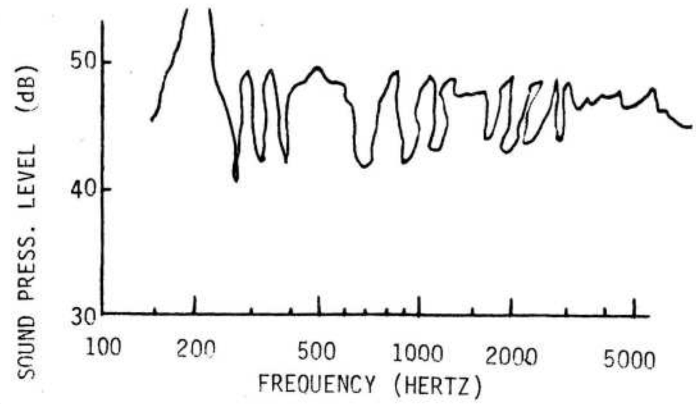

Fig.8: Spectral Analysis of Bald Tyre or of Longitudinally Grooved Tyre

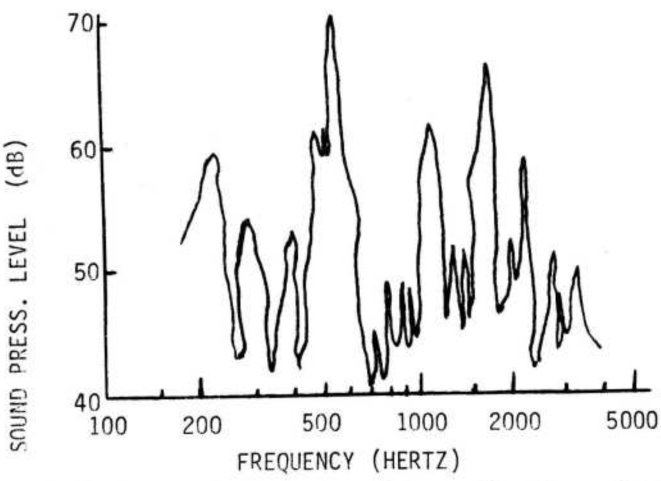

Fig.9: Spectral Analysis of Laterally Grooved Tyre or Longitudinally Plus Laterally Grooved Tyre

These results are presented in a lumped manner, as there was no observable difference between the bald tyre and the longitudinally grooved tyre. Similarly, with the laterally grooved tyre and the tyre with both lateral and longitudinal grooves, there were slight differences in the directivity patterns observed, but these were of little practical interest.

The spectral analyses of Fig.8 are of a broadband nature and are, in fact, indistinguishable from the background noise spectrum within the chamber with the rig in operation. Fig.9 shows the tonality of the noise associated with air pumping. The fundamental frequency shown in Fig.9 corresponds to the frequency with which the lateral grooves pass through the contact patch, at that

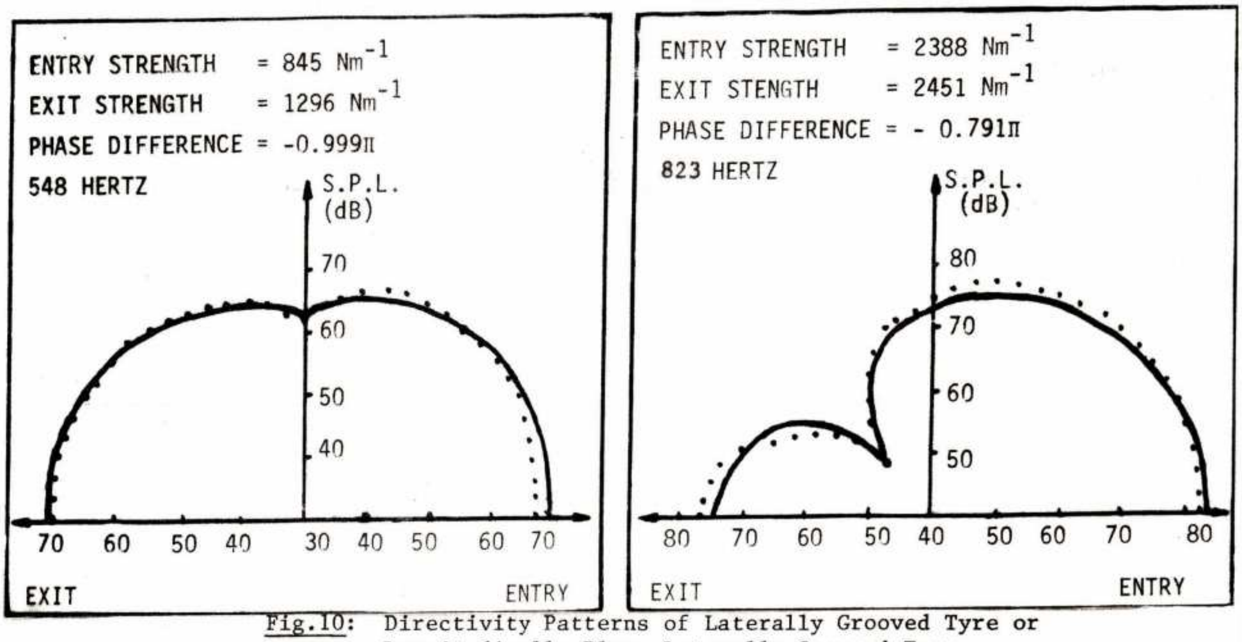

Fig.10: Directivity Patterns of Laterally Grooved Tyre or Longitudinally Plus Laterally Grooved Tyre

particular tyre speed. It is observed that there are higher harmonics of this fundamental frequency. These indicate that the nature of the air pumping process is probably similar to a sawtooth function, or a function whose Fourier transform contains harmonics.

Finally Fig.11 shows a photograph of the laterally grooved tyre operating under the conditions that produced the Directivity Patterns of Fig. 10.

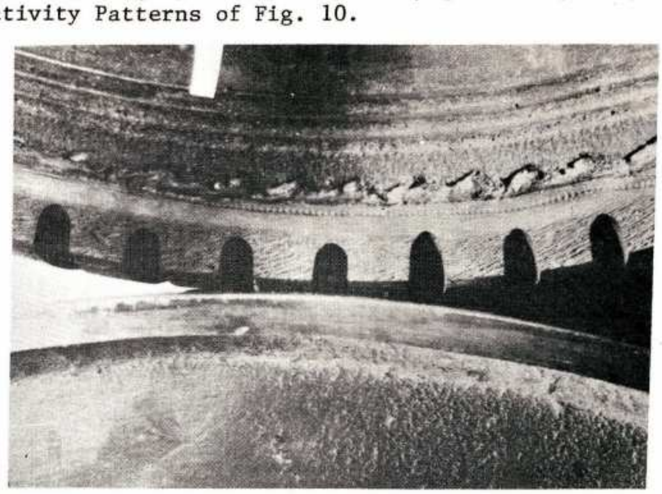

Fig.11: Photograph of Contact Path at Speed

FURTHER COMMENTS

In regard to the spectral analyses, it is seen that the bald tyre produced no noise that was distinguishable above the existing background levels. This observation verifies that the major source of tyre noise is the tread/road interaction. Further, the experiences with the plain longitudinal grooved tyre has shown that a variation or fluctuation in the tread pattern is required to generate noise. (Air pumping noise results from a fluctuating volumetric air flow rate). An interesting observation was that, at the pressure shown,no difference in shape was between the directivity patterns of the two laterally grooved tyres. This indicates a similarity of air pumping mechanisms, and further justifies the use of a multi-point source array model.

It is apparent in Fig.10 that a reasonably good agreement has been achieved in matching the model's predicted values with those measured in the chamber. The fit is as good as can be expected, with the maximum deviation being in the order of 2 to 3 dB. Several reasons help to explain the slight scatter in the experimental data. The first, and most likely, is the effect of interferences in the sound field brought about by both the rig and the chamber itself. Many plane steel surfaces suitable for sound reflection are presented by the rig. Also, the chamber in its present state is probably not perfectly anechoic, since it was necessary to remove several of the wedges on the chamber's floor and near its door. Prior to measuring the directivity patterns, it was found necessary to select an optimum microphone radius. Originally a radius as large as possible was used, but it was subsequently discovered that at this radius the microphone passed too close to the wall wedges, where the process of sound absorption generates some localised reflections. These were found to interact with the sound monitored by the microphone and produce some significant interference, which was reduced when the microphone radius was shortened.

Any effects that may result from shielding of the sound by the tyre or drum have to be accepted, as, at this stage, there is very little that can be done to overcome them. One other factor that could lead to some random data scatter is produced by the electric motor driving the rig. Occasionally, this motor exhibits variations (sometimes very large) in its output speed. Generally, these produce changes in the tyre radiated sound frequency that remain within the 10 Hertz Bandwidth of the Analyser used to monitor this noise. While these variations will have little effect on the strength of the contact patch sources, they will have some effect on the phase difference between these sources. Since these phase differences have a critical effect on the directivity patterns, it is probable that the motor speed changes will produce some scatter in the data, in the form of directivity pattern shape changes.

CONCLUDING REMARKS.

Our investigations have shown that a repeatative tread pattern design is required to produce an air radiated tyre noise that was measurable by our setup. It has been shown that this radiated noise is directional and that the relevant directivity patterns obtained so far can be predicted reasonably well by a comparatively simple mathematical model. The model embodies tread dimensions and tyre parameters and may be used to explain the noise generation process that occurs within the tyre's contact patch.

At the time of writing, insufficient data was available to test the model over a wider range of conditions and tread designs. It is planned to do this and to, hopefully, adapt the model to commercial tread pattern designs. In order to relate the source strengths and phase differences to tread parameters such as stiffness etc., it is proposed to investigate both dynamic and static tyre tread deflections under various operating conditions.

REFERENCES

1. C.H.G. MILLS & D.T. ASPINALL, "Some Aspects of Commerical Vehicle Noise" Applied Acoustics, Vol. 1, 1968, p47.
2. W.J. GALLOWAY, W.E. CLARK & J.S. KERRICK, "Highway Noise Measurement, Simulation and Mixed Reactions", Highway Research Board, U.S.A. Continuing Project. 1972.
3. ANON, "EPA Analysis of Noise Problems Points Way to Future Legislation", Automotive Engineering April 1972, p28-35.
4. D.G. HARLAND, "Noise Research and the Road Research Laboratory", Traffic and Engineering Control, July 1970, p122-125
5. R.K. HILLQUIST & R.A. BETTIS, "Measurement of Automotive Passby Noise", SAE Paper 720275, Jan 1972.
6. W.F. FLANAGAN, "Recent Studies Give Unified Picture of Tyre Noise", Automotive Engineering, April 1972, p15-19.
7. H.P. ZOEPPRITZ, "Possibilties and Limiations in Reducing Tyre Noise", ATZ, Vol. 74, No.1, 1972 p13-16 (Photostat from MIRA Document Copying Service).
8. G. ENGLER, "Factors Contributing to Wheel Noise", MIRA TRANSLATION 21/65, 1965.
9. S.A. LIPPMAN & K.A. FERGUSON, Electronics, Nov 1950, p84-87.
10. T.A. ROBERTSON, "Truck Tyre Noise", Preprint of paper presented at SAE Detroit Meeting, Feb. 1957.
11. A.L. NEDLEY, "Combining Experimental and Computer Techniques for Reducing Fan and Blower Tonal Noise", SAE Paper B25D, April 1964.
12. H. VARTERASIAN, "Quietening Noise Mathematically. Its Application to Snow Tyres". SAE Paper 690520, 1969.
13. R.E. HAYDEN, "Roadside Noise from the Interaction of a Rolling Tyre with the Road Surface", Proc. Purdue Noise Control Conference, Purdue Univ. 1971. p62-67.
14. W.A. LEASURE, "Truck Tyre Noise - Preliminary Results of a Field Measurement Programme", Proc. Purdue Noise Control Conference, Purdue Univ. 1971, p41-48.
15. D.A. TETLOW, "Truck Tyre Noise", Sound and Vibration, August 1971, Vol. 5., No. 8, p17-23.
16. N.M. TRIVISONNO, J.R. BEATTY & R.F. MILLER, "Origin of Tyre Squeal", Rubber Chem. and Technology, Vol. 41, No.4, Sept. 1968, p953-976.
17. R.F. MILLER & J.G. SLABY, "Mechanics of Tyre Squeal", SAE Preprint 186D, June 60.
18. A. CHIESA, L. OBERTO & L. TAMBURNI, "Transmission of Tyre Vibrations", Automobile Engineer, Vol. 54, 1964, p520-530.
19. J.A. OVERTON, B. MILLS, C. ASHLEY, "The Vertical Response Characteristics of the Non-Rolling Tyre". Proc. Auto Div., I. Mech.E. Vol. 184, Part 2A, 1969-70, p25-29.

20. B. MILLS & J.W. DUNN, "The Mechanical Mobility of Rolling Tyres", Proc. Auto. Div., I. Mech. Eng., Vol. 185 Part 2A, 1971, p89-101.
21. C.W. BARSON, V.E. GOUGH, J.C. HUTCHINSON, D.H. JAMES, "Tyre and Vehicle Vibration" Proc. Auto Div., I. Mech. Eng. Vol. 179, Part 2A, 1964-1965, p213-229.
22, S. ISHIKAMA, T. KUROBE & K. KAWASKI, "An Analysis of Road Noise - The Effect of Tyre and Suspension Vibrations", Bulletin of Japanese Society of Auto. Engrs., 1970, No.2, p190-199.
23. ANON, "Road Noise", Automobile Engineer, Vol. 59, 1969, p409.
24. R.C. CHANAUD, "Experimental Study of Aerodynamic Sound from a Rotating Disc", J. Acoustical Soc., America, Vol. 45, 1969, No. 2, p392.

ACKNOWLEDGEMENTS

Our thanks must go to the Olympic Tyre and Rubber Co. Pty Ltd., for its sponsorship of the project and to the staff of both the Company and the Mechanical Engineering Department for their assistance.

THE PREDICTION OF NOISE LEVELS FROM AUSTRALIAN FREEWAYS

R. J. Alfredson
Department of Mechanical Engineering
Monash University
Clayton, Victoria

SUMMARY - Measurement of noise in areas adjacent to freeways in Melbourne has indicated that existing methods for predicting freeway noise are not particularly reliable. A method has been developed based on experimental and theoretical considerations which produces entirely satisfactory results for freeways at ground level but somewhat less accurate results when the freeways are elevated or depressed. Further evaluation and development is continuing but the method appears to be at present the most suitable for predicting freeway noise levels in Australia.

1.0 Introduction

There is little doubt that road traffic noise is a potentially major source of annoyance within the community, Ref. [1]. Consequently the ability to predict noise levels from proposed freeways at the design stage is highly desirable.

Several different procedures exist for predicting freeway noise, e.g. Ref. [2] - [11] and it is not intended to discuss these in any detail. Surprisingly the methods differ significantly in their predictions and they have been found to be not particularly suitable for Australian conditions. Consequently a method has been developed for this report based on measurements along side freeways within the Melbourne area. The method, while still requiring further evaluation and development, has proved very reliable for freeways at ground level but somewhat less accurate for elevated and depressed freeways.

2.0 Existing Methods

As noted above a number of methods exist for predicting freeway noise. It is proposed however only to outline briefly what appears to b e the most widely used British and American procedures, namely those of Johnson, Ref. [2] and Gordon et al, Ref. [11]. In each case the procedure allows both the mean value and standard deviation of the traffic noise to be predicted in terms of the A weighted levels. Existing community annoyance parameters can all be evaluated from these 2 basic quantities.

On the assumption of a Normal distribution, the equation used by Jounson to calculate the mean noise level is:

$$L_{50} = 51.5 + 10 \text{ Log } \frac{Q}{d} + 30 \text{ Log } \frac{v}{40} \qquad \ldots(1),$$

where L_{50} is the mean noise level (dB(A)),
Q is the traffic flow rate (vehicles/hour),
d is the distance to the traffic flow (feet),
v is the mean traffic speed (miles/hr).

For the purpose of predicting the standard deviation, σ, of the traffic noise, Johnson et al produced a graph which showed a unique relation between σ and the product Q_{40} x d. The quantity Q_{40} is related to Q and v above by the equation

$$Q_{40} = Q \times \frac{40}{v}$$

The standard deviation decreased monotonically for increasing values of the product $Q_{40} \times d$, Fig. 9 of Ref. [2].

More recent work has indicated that a correction to the standard deviation of -1 to +1dB(A) is required for 0% and 40% heavy vehicles respectively, e.g. Ref. [7].

The method of Gordon et al is similar in principle to that of Johnson but differs significantly in detail due to the greater effect attributed to truck noise on both the mean level and the standard deviation. These quantities are calculated independently for cars and for trucks and the results are combined to produce the overall mean level and standard dev iation.

The equation developed by Gordon et al for predicting mean noise levels for cars is:

$$L_{50} = 10 \text{ Log } Q - 15 \text{ Log } d + 30 \text{ Log } v + 10 \text{ Log } \{\tanh (1.19 \times 10^{-3} Qd/v)\} + 29 \qquad \ldots(2)$$

where the symbols have the same meaning as in equation (1) except that they refer to cars alone.

For trucks, the mean noise level is calculated by:

$$L_{50} = 10 \text{ Log } Q - 10 \text{ Log } v - 15 \text{ Log } d + 10 \text{ Log } \{\tanh (1.19 \times 10^{-3} Qd/v)\} + 95 \qquad \ldots(3)$$

The method for predicting the standard deviation is similar in form to that used by Johnson except that, as previously indicated, cars and trucks are treated independently and the final value obtained by combining the two results.

The differences between the two methods are quite significant as can be seen from the following table. The table has been prepared assuming, for the sake of simplicity, a single lane of traffic 40 m from the observer with a mean traffic speed of 25 m/s.

TABLE 1
Comparison of Results due to Johnson and Gordon

No Vehicles/hr.	% Heavies	Mean Level dB(A)		Standard Deviations dB(A)	
		Johnson Ref.2	Gordon Ref.11	Johnson Ref.2	Gordon Ref.11
2000	10	68	68	3	5½
2000	30	69	74	4	5
4000	10	71	73	2½	4½
4000	30	72	77	3½	3

The differences are larger than might have been anticipated. It was recognised that there was an obvious need to establish which if either of these methods would predict results in reasonable agreement with measured levels produced by freeways in the Melbourne area.

2.1 Comparison of Measured and Predicted Noise Levels

Measurements of traffic noise were made at a number of sites on the Tullamarine and South Eastern Freeways. The sites were chosen to be representative of freeways at ground level (as well as freeways in cuttings and on elevated structures required for later work). In each case tape recordings were made simultaneously at 3 or 4 distances from the freeway extending over a range of about 15 to 70 m. The recordings which were made using the 'A' weighted filter extended over a period of approximately 15 minutes during which time a traffic count and speed check were also carried out.

A Bruel and Kjaer statistical distribution analyser type 4420 was subsequently used in conjunction with a Bruel and Kjaer level recorder type 2305 to determine the mean noise level and standard deviation.

The following table summarises the range of parameters encountered or used during the recordings.

TABLE 2

Summary of Parameters

Feature	Minimum Value	Maximum Value
Mean Traffic Speed	11 m/s	25 m/s
Total Flow Rate	1146 veh/hr	3528 Veh/hr
Distance to Centre Line	15m	70 m
Percentage of Heavy Vehicles	3	15
Elevation of Freeway	-8 m	10.5 m

The predicted noise levels and standard deviations were computed using both the method of Johnson et al and Gordon et al. Attention was concentrated in the first instance on comparing measured and predicted results for the ground level freeway situation. The results for the method of Johnson et al are shown in Fig. 1(a). It is seen that the predicted mean level is about 1dB(A) low and there is some scatter. The average predicted levels for the standard deviations are marginally high but there is significant scatter.

The results for the method of Gordon et al are given in Fig. 1(b). The predicted mean levels are some 2 to 3 dB(A) high. Similarly the predicted values for standard deviation are, on the average, also high and there is an unacceptable amount of scatter. These results and others suggested that there was a need to develop a new method for predicting freeway noise levels which would give more accurate results for Australian freeways. This is discussed below.

3.0 Proposed Method for Predicting Freeway Noise

The method developed for this study involved setting up on a digital computer two arrays of vehicles each array moving with a given mean speed in a given lane. The two lanes corresponded to the mid near side lane and the mid far side lane and the separation between these two lanes was specified.

It was assumed that each lane consisted of a random mix of cars and heavy vehicles the exact ratio being specified by the situation being simulated. Measurements of individual vehicle noise at freeway speeds have shown that typically the distribution of noise levels for individual cars and heavy vehicles are as given in Fig.2(a).Additional limited measurements have suggested that the standard deviation of the distribution for individual vehicle noise levels is not strongly influenced by changes in the mean speed. However it was found that the mean noise level for individual vehicles increased by about 9 dB(A) per doubling of vehicle speed.

The headway of the vehicles in each of the two lanes was considered to be random although the mean value would clearly depend, for each lane of traffic, on the flow rate. A number of headway distributions were investigated including the Pearson type III, Semi-Random and Gaussian, Ref.[12]. The effect of different types of distributions did not appear to be particularly significant and the Gaussian distribution was eventually used.

The overall 'A' weighted sound pressure level at any given observation position was calculated for the two arrays of vehicles at one second intervals for a period of at least 5 minutes. The sampling interval and the observation period could be easily varied by these were chosen from the experience gained in analysing the measured data. An excess attenuation of 4 dB(A) per 100 m was used and it was assumed to be a function of the mean height above ground level in accordance with the results of Ref. [7]. The mean value and standard deviation were finally calculated from 300 values obtained for the traffic noise at 1 second intervals.

This procedure was used to predict mean levels and standard deviations for the previously measured traffic situations. The comparison between the measured and predicted values is given in Fig. 2(b). The agreement is good and it would be possible to calculate community response parameters with a reasonable degree of accuracy. The range of values over which the prediction method could be checked was however obviously limited and further evaluation is needed before the method could be used with confidence.

Approximately one half of a minute of computer time was needed for each prediction using the Burroughs 6700 computer. This was significantly longer than the previously discussed methods and it was decided therefore to carry out a regression analysis to see if an equation of the form of equation (1) could be developed for both the mean value and the standard deviation. To reduce computational time it was assumed that the total number of vehicles, and the percentage of heavy vehicles, p, were the same in the near side and far side lane. The separation of these two lanes was taken as 10 m and the observers height above ground level was taken to be 1 m. The following constraints were imposed on the variables;

$$1000 \leqslant Q \leqslant 3000 \text{ Veh/hr}$$
$$20 \leqslant d \leqslant 80 \text{ m}$$
$$15 \leqslant v \leqslant 30 \text{ m/s}$$
$$5 \leqslant p \leqslant 30 \text{ \%}$$

Conventional regression analysis gave the following equations.

$$L_{50} = 5.2 + 16.4 \text{ Log } Q - 14.3 \text{ Log } d + 17.4 \text{ Log } v + 0.16 \text{ p} \quad \text{...(4)}$$

and

$$\sigma = 10.8 - 2.1 \text{ Log } Q - 3.7 \text{ Log } d + 3.84 \text{ Log } v + 0.04 \text{ p} \quad \text{...(5)}$$

The standard deviation of the error for each of these two simplified equations was less than 3/4 dB(A). Thus the above equations give a reasonable first approximation to the noise levels that could be expected from conventional 4 lane freeways at ground level.

4.0 Elevated and Depressed Freeways

The feature of elevated and depressed freeways (as well as the use of barriers) is that some shielding is provided which will affect the mean level as well as the standard deviations of the noise. It is customary to assume that there is a rough equivalence between elevated and depressed freeways as well as barriers as indicated in Fig. 3(a). The performance is dependent on the path difference.

The original investigation of Ref. [13] showed that for long barriers and steady sound sources the excess attenuation could be expressed in the form given in Fig. 3(b).

The mean 'A' weighted spectrum for normal freeway noise was found to take the form given in Fig 3(c). This spectrum was derived from measurements made at 7½ m from the mid near lane. Using this spectrum and the excess attenuation of Fig. 3(b) it was a simple matter to express the excess attenuation of traffic noise as a function of path difference as shown in Fig. 4 (a). The experience of Gordon et al, Ref. [11] was that this type of approach overestimated the excess attenuation for small and large path differences. A maximum value of 15 dB(A) was thus used and the remaining curve was linearised as shown by the dotted line in Fig. 4(a). Thus at each one second interval, the path difference for each car or truck was calculated, the respective excess attentuations were determined and the final level at the observer computed in the normal manner. The calculation of the path difference requires a knowledge of the height above the freeway of the centre of noise for each vehicle. There was no obvious method for determining this figure which would vary from vehicle to vehicle. It was assumed to take a value of 0.75 m for cars and 1.5 m for heavy vehicles. The final values for mean and standard deviation did not appear in general to be very sensitive to small changes in these assumed heights.

A comparison between the measured and predicted values for elevated and depressed freeways is given in Fig. 4(b). It is immediately obvious that the agreement between measured and predicted mean levels is not as good as with the freeway at ground level. The agreement however is still sufficient to give a first approximation.

The predicted values for the standard deviation also show some scatter when compared with the measured values. As with the mean levels this scatter is considered to be due in part to the assumption of equivalence between barriers and elevated and depressed freeways. Some error would also occur due to the assumption of two lanes rather than four. The situation is clearly much more complex than that used in this simplified approach. Further detailed study is needed to improve the accuracy and consequently simple prediction equations similar to (4) and (5) have not been produced. For the present the method developed allows a first approximation to be made of the mean and standard deviation of the traffic noise.

5.0 Concluding Remarks

Existing methods for predicting freeway noise generally do not produce results which are in good agreement with measured values. The method developed here appears to be reliable for freeways at ground level. Some further work is needed to establish positively what effect elevation of the observer has on noise levels. The effect of atmospheric conditions needs to be considered in more detail.

The accuracy of predicting noise levels from elevated or depressed freeways is adequate for a first approximation. There is scope however for refinement to the method and a need for further field measurements.

References

1. T. Priede, 'Origins of Automotive Vehicle Noise', J. Sound & Vib., Vol. 15, No. 1, 1971, p.61-73.

2. D.R. Johnson, E.G. Saunders, 'The Evaluation of Noise from Freely Flowing Traffic', J. Sound & Vib., Vol. 7, No.2, 1968, p.287-309.

3. R.J. Stephenson, F.H. Vulkan, 'Traffic Noise', J. Sound & Vib., Vol. 7, No.2, 1968, p.247-262.

4. J. Foxan, F.J. Pearson, 'A Statistical Model of Traffic Noise', Appl. Acoustics., Vol.1, 1968, p.175-188.

5. R.S. Millard (Ed), 'A Review of Road Traffic Noise', Road Research Laboratory Report, LR 357, Min. of Transp. Berkshire, U.K. 1970.

6. W. Galloway, W. Clark, 'Prediction of Noise from Motor Vehicles in Freely Flowing Traffic, Fourth Int. Cong. on Acoustics, Copenhagen, L28, 1962.

7. W.E. Scholes, J.W. Sargent, 'Designing Against Noise from Road Traffic', App. Acoustics, Vol.4 1971, p.203-234.

8. M.E. Delaney, 'A Practical Scheme for Predicting Noise Levels L_{10} Arising from Road Traffic, NPL Acoustics Report AC57, July 72.

9. M.E. Delaney, W.C. Copeland, R.C. Payne, 'Propagation of Traffic Noise in Typical Urban Situations', NPL Acoustics Report, AC54, Oct.1971.

10. M.E. Delaney, 'Prediction of Traffic Noise Levels', NPL Acoustics Report AC56, April. 1972.

11. C.G. Gordon, W.J. Galloway, B.A. Kugler, D.L. Nelson, 'Highway Noise - A Design Guide for Engineers', Highway Research Board, Nat. Acad. Sciences, Wash. D.C. 1971.

12. D.J. Buckley, 'Road Traffic Headway Distributions', Aust. Road Res. Board Prac. 7(1), 1962, p.153-183.

13. Z. Maekawa, 'Noise Reduction by Screens', App. Acoustics, Vol. 1, 1968, p157-173.

COMPARISON OF MEASURED AND PREDICTED VALUES

METHOD DUE TO JOHNSON. Ref.[2]

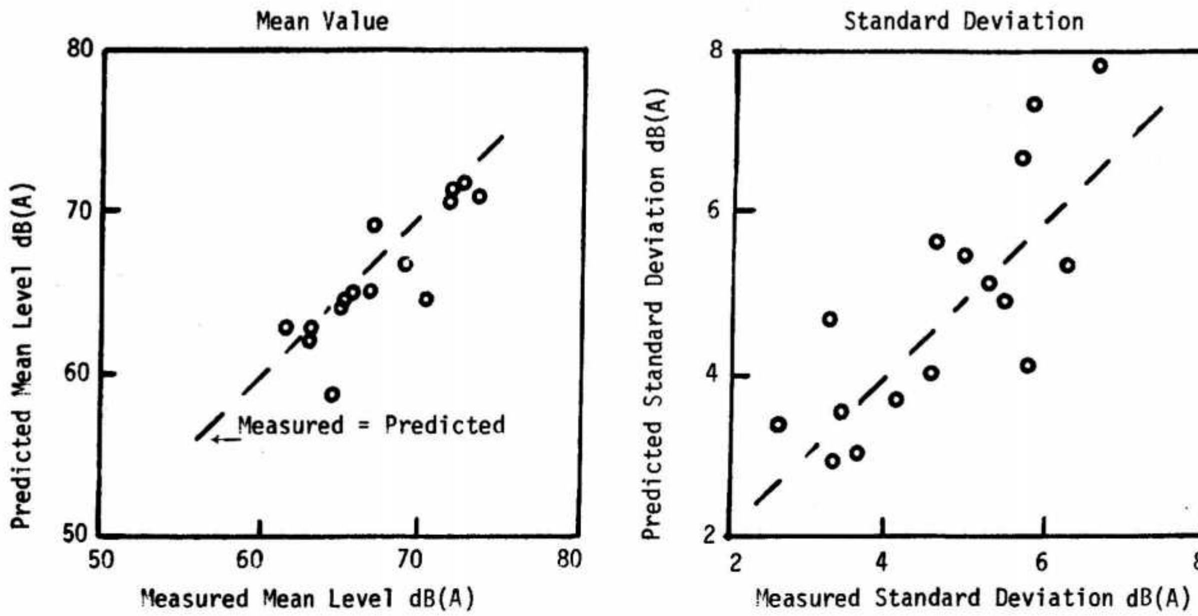

(a)

METHOD DUE TO GORDON. Ref.[11]

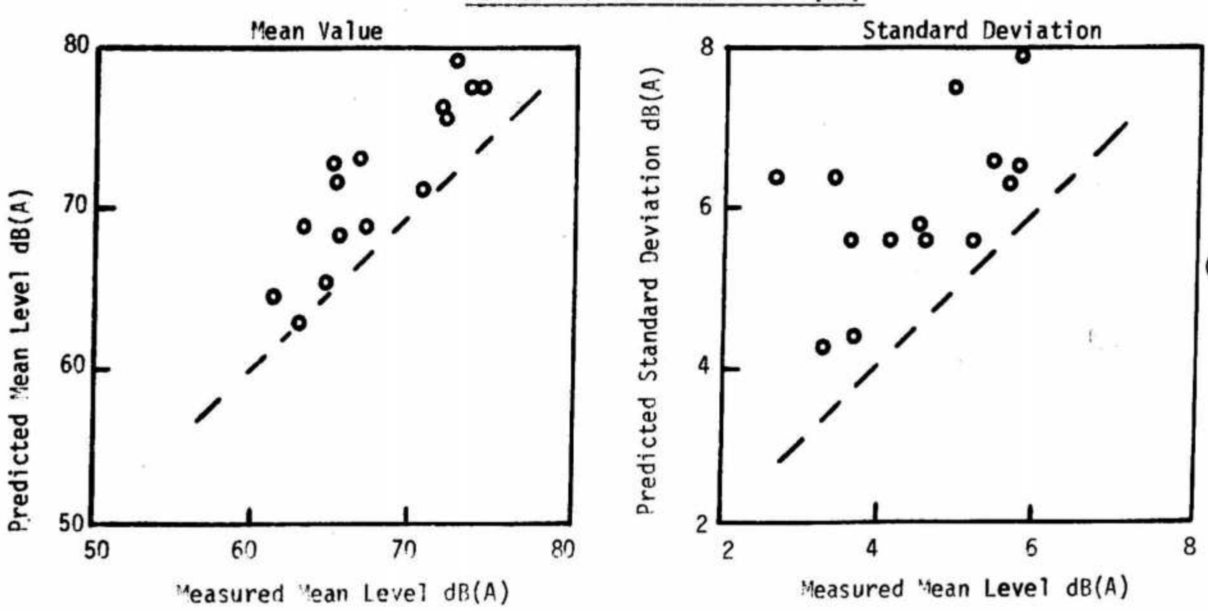

(b)

Fig.1.

NOISE LEVELS OF INDIVIDUAL VEHICLES

MEASURED AT 7½ M FROM CENTRE LINE OF VEHICLE

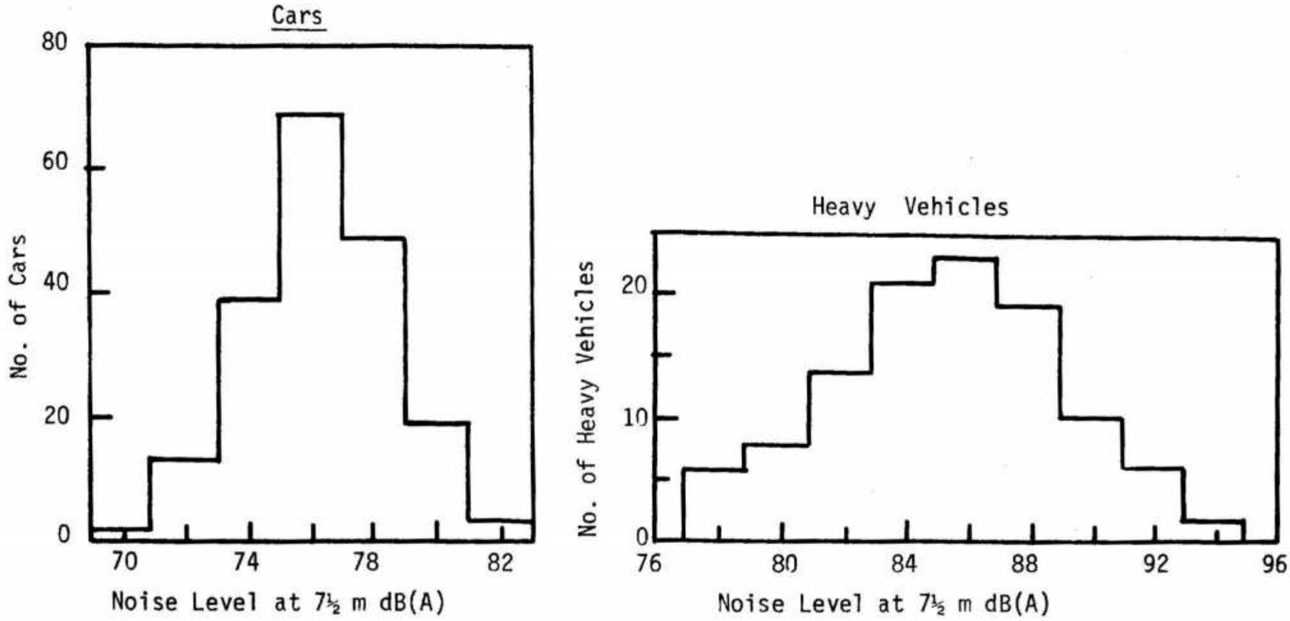

(a)

COMPARISON OF MEASURED AND PREDICTED VALUES - (GROUND LEVEL)

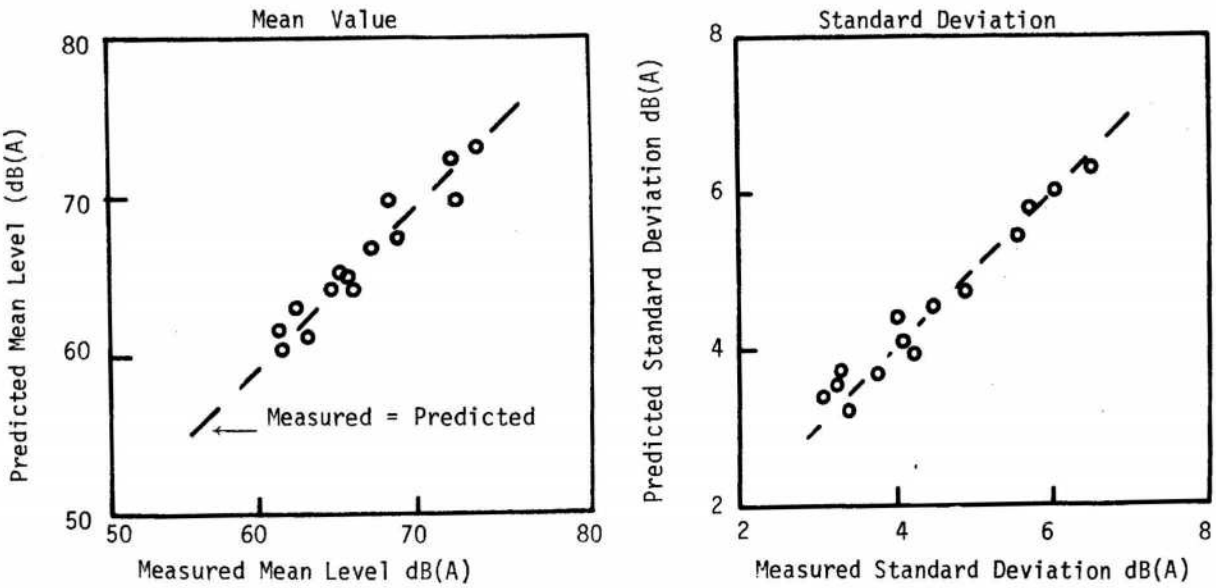

(b)

Fig.2

ACOUSTIC SHIELDING DUE TO BARRIERS AND ELEVATED AND DEPRESSED FREEWAYS

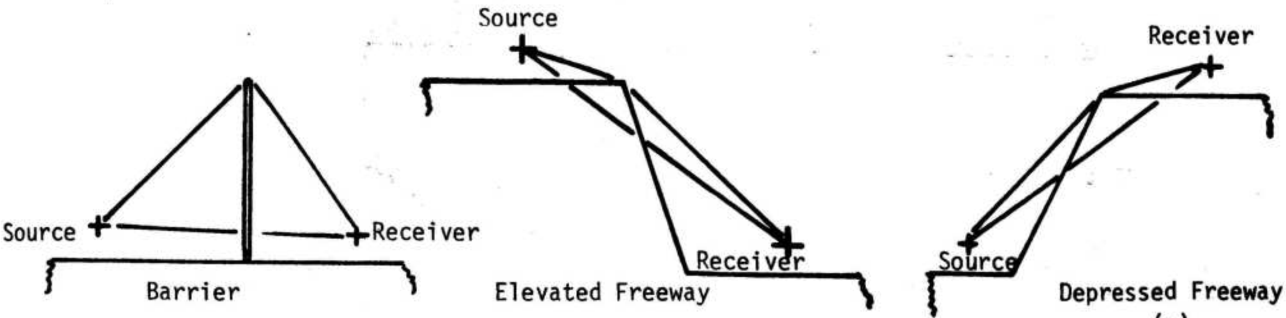

(a)

ATTENUATION OF A NOISE SOURCE BY A BARRIER (Ref.13)

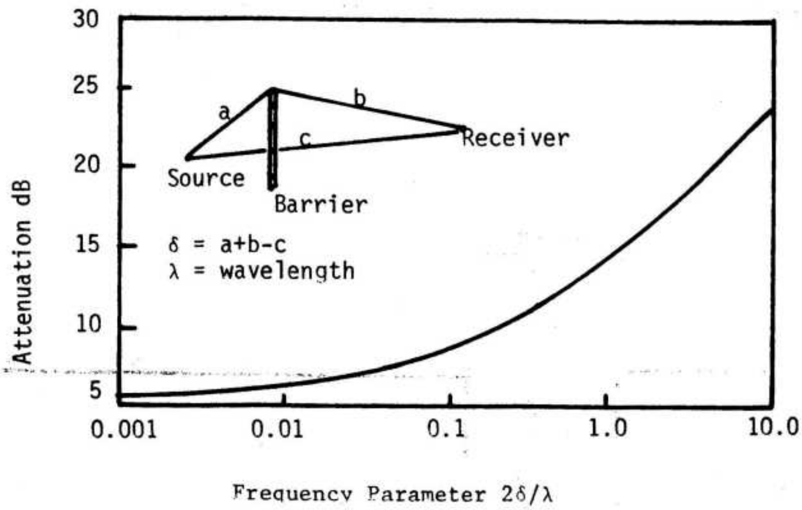

(b)

'A' WEIGHTED SPECTRUM OF FREEWAY NOISE

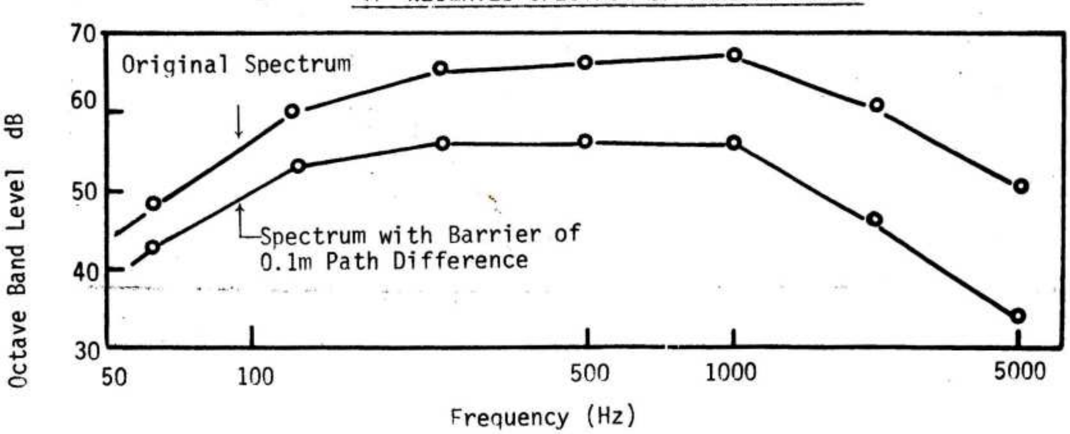

(c)

Fig.3

ATTENUATION OF VEHICLE NOISE DUE TO A BARRIER

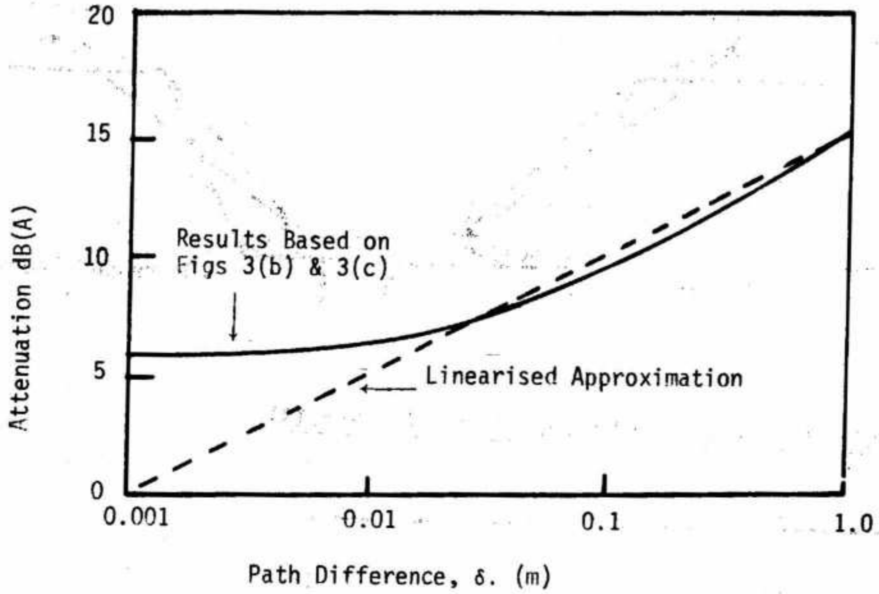

(a)

COMPARISON OF MEASURED AND PREDICTED VALUES
ELEVATED AND DEPRESSED FREEWAYS

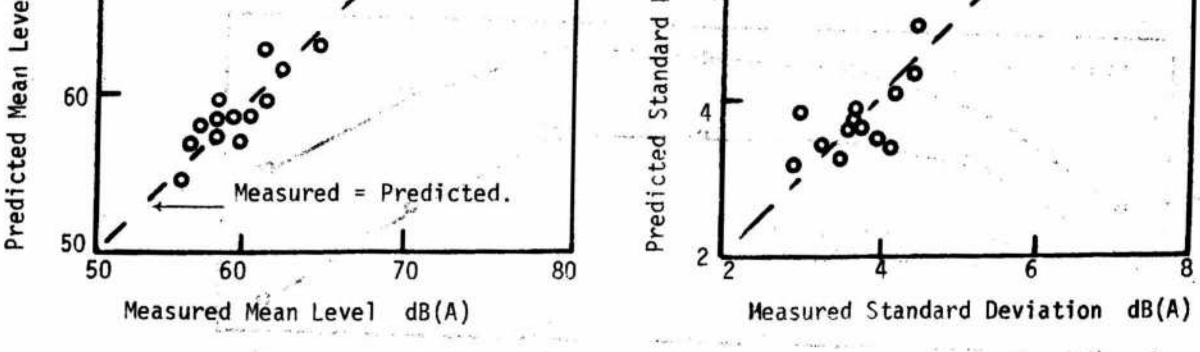

(b)

Fig.4

A DATA BASE OF TRAFFIC NOISE IN MELBOURNE STREETS

R. Saunders
Melbourne and Metropolitan Board of Works
Melbourne, Victoria

I. Taylor
Environment Protection Authority
Melbourne, Victoria

SUMMARY -

Records of traffic noise from certain Melbourne streets are presented as an information base. Three sites have been chosen which give a representative sample of streets with a variety of traffic volumes. At each site traffic counts have been made for cars and trucks. Noise levels were recorded at up to three positions at each site, and are presented graphically.

DESCRIPTION OF SITES

The three sites are in or adjacent to the suburb of North Melbourne, some two miles from Melbourne's central business district. Cycle times for traffic lights were generally of the order of two minutes.

Delhi Court is adjacent to Tullamarine Freeway, a four lane divided freeway with an eight foot central median (see Fig. 1). Observations were made at two positions about six hundred metres from the city end of the freeway. The connection to Flemington Road is controlled by traffic lights and northbound vehicles were still in platoons. All but heavy trucks had reached their cruising speed by the time the recording positions were passed. The observations were made from 7 a.m. to 7 p.m. on Monday 9th April 1973, and from 7 p.m. to 7 a.m. over Thursday night and Friday morning 2nd and 3rd August 1973.

Debney Estate is off Racecourse Road, a major four lane arterial road with trams in the centre (see Fig. 2). Observations were made at three positions from 7 a.m. to 7 p.m. on Friday 6th April 1973, and from 7 p.m. to 7 a.m. over Thursday night and Friday morning 7th and 8th June 1973. The Housing Commission Estate contains four twenty storey blocks and is situated some 150 metres west of the elevated Upfield railway line.

Hotham Estate is off Boundary Road, a secondary road which acts as a by-pass for commercial vehicles in the area (see fig. 3).

Data was collected at two other sites, but has not been presented in the interest of brevity. Detailed information is available on request.

METHOD

The field measurements were made with a Bruel and Kjael 2209 impulse sound meter fitted with a wind shield, using slow response and the 'A' weighting. A Nagra portable battery driven tape recorder 4.2L.S.P. was used to record two minute samples at each position every half hour over the twelve hour period. A calibration signal was recorded on each tape using a B & K pistophone.

The tapes were played back in a laboratory on a Plessey 77MK III tape-recorder, and the signal was fed through a B & K 2305 chart recorder coupled to a B & K Type 4420 statistical distribution analyser set to cumulative distribution. Each bin covered a range of 2.5 dB(A). L10 and L90 levels were then calculated.

Traffic volumes were counted manually, and vehicles larger than panel vans were considered to be trucks. Separate counts were made for trucks, semi-trailers, buses, trams and others, but all these categories have been classified as trucks for simplicity. Speeds varied considerably at each location over any particular quarter hour. Vehicles were timed over a measured distance and representative speeds have been recorded. At controlled intersections the variation of individual vehicle speeds is great.

The data is presented in graphical form (see Figs. 4 to 8). Successive values of the noise levels taken at each position each half hour have been combined to give hourly averages.

CONCLUSION

The measurements taken provide detailed information of existing traffic noise levels in an inner suburb of Melbourne. Noise prediction methods can be checked against this data, to evaluate their application to local conditions.

ACKNOWLEDGEMENTS

The field measurement and analysis was carried out by members of the Melbourne and Metropolitan Board of Works Highways Planning Branch and the Noise Control Branch of the Victorian Environment Protection Authority. Particular thanks are due to Jill Hulme, Bill Hooker, Vernon Hughes and Bill Edgar.

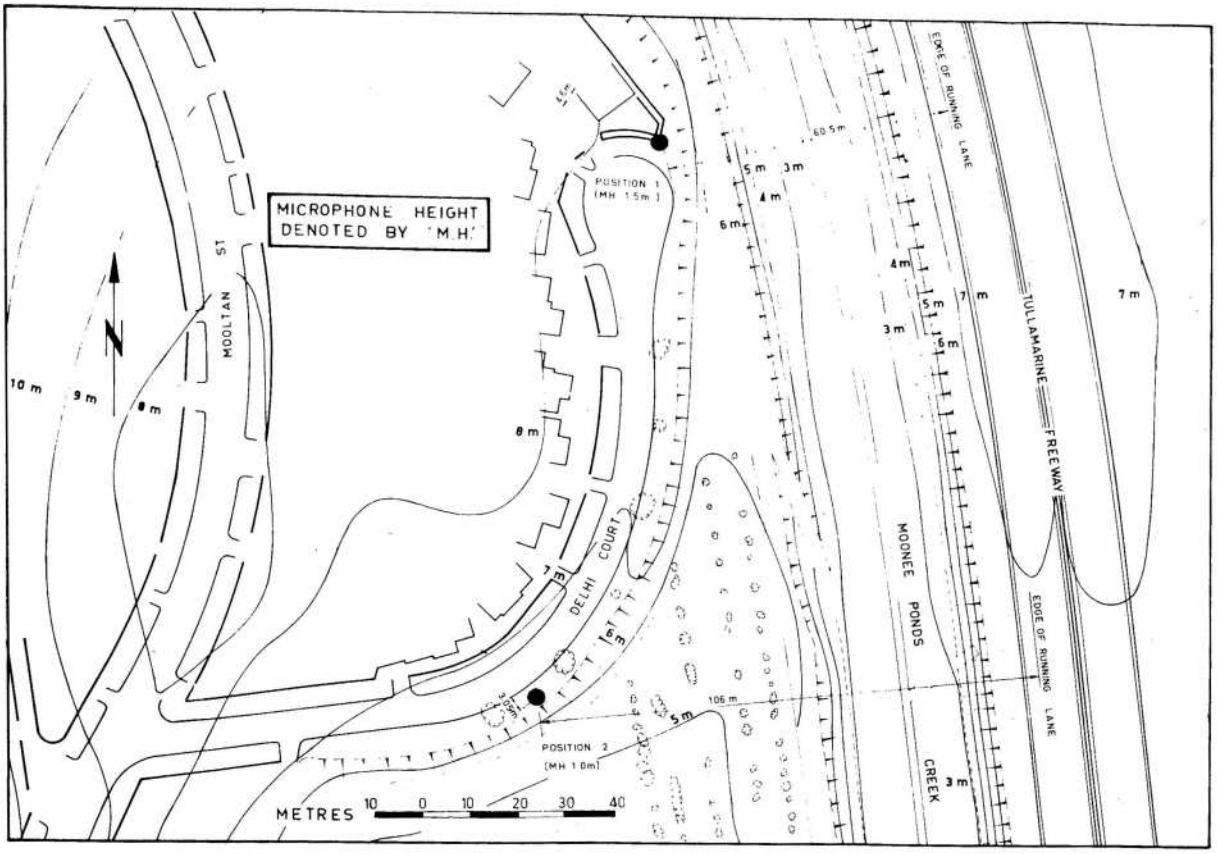

LOCATION OF RECORDING POSITIONS — TULLAMARINE FREEWAY
FIG. 1

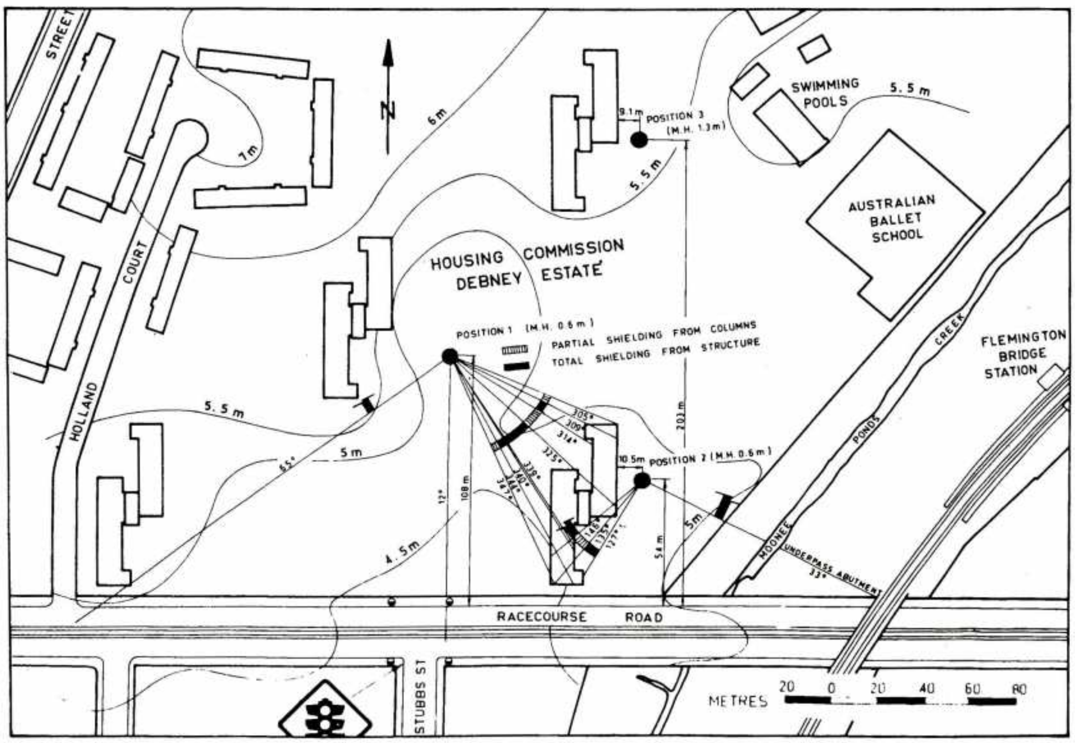

LOCATION OF RECORDING POSITIONS — DEBNEY ESTATE
FIG. 2.

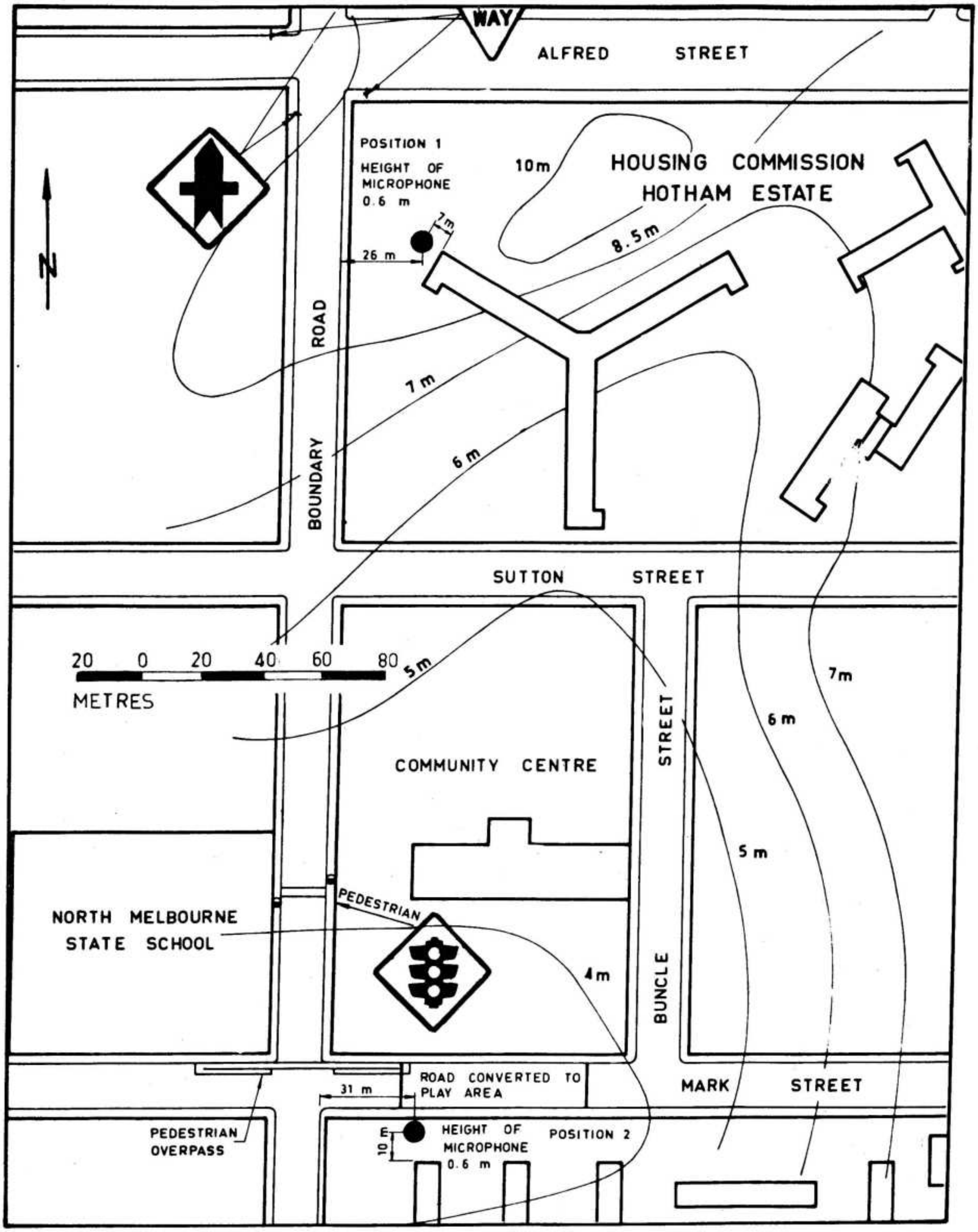

LOCATION OF RECORDING POSITIONS
HOTHAM ESTATE **FIG. 3**

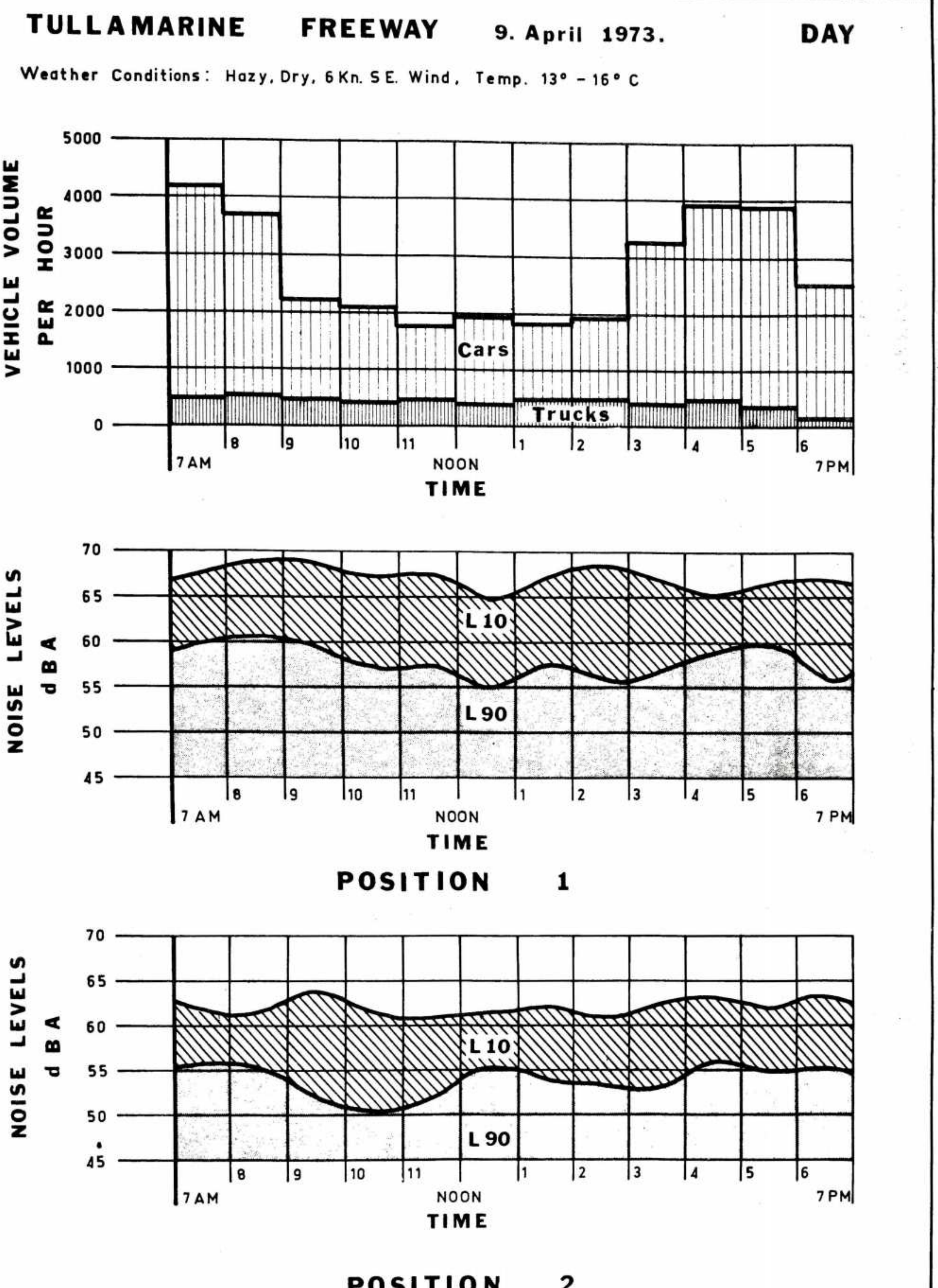
TULLAMARINE FREEWAY 9. April 1973. DAY
Weather Conditions: Hazy, Dry, 6 Kn. S E. Wind, Temp. 13° - 16° C
VEHICLE VOLUME PER HOUR
5000
4000
3000
2000
1000
0
Cars
Trucks
7 AM
8
9
10
11
NOON
1
2
3
4
5
6
7 PM
TIME
NOISE LEVELS dBA
70
65
60
55
50
45
L 10
L 90
TIME
POSITION 1
NOISE LEVELS dBA
L 10
L 90
TIME
POSITION 2

FIG. 4

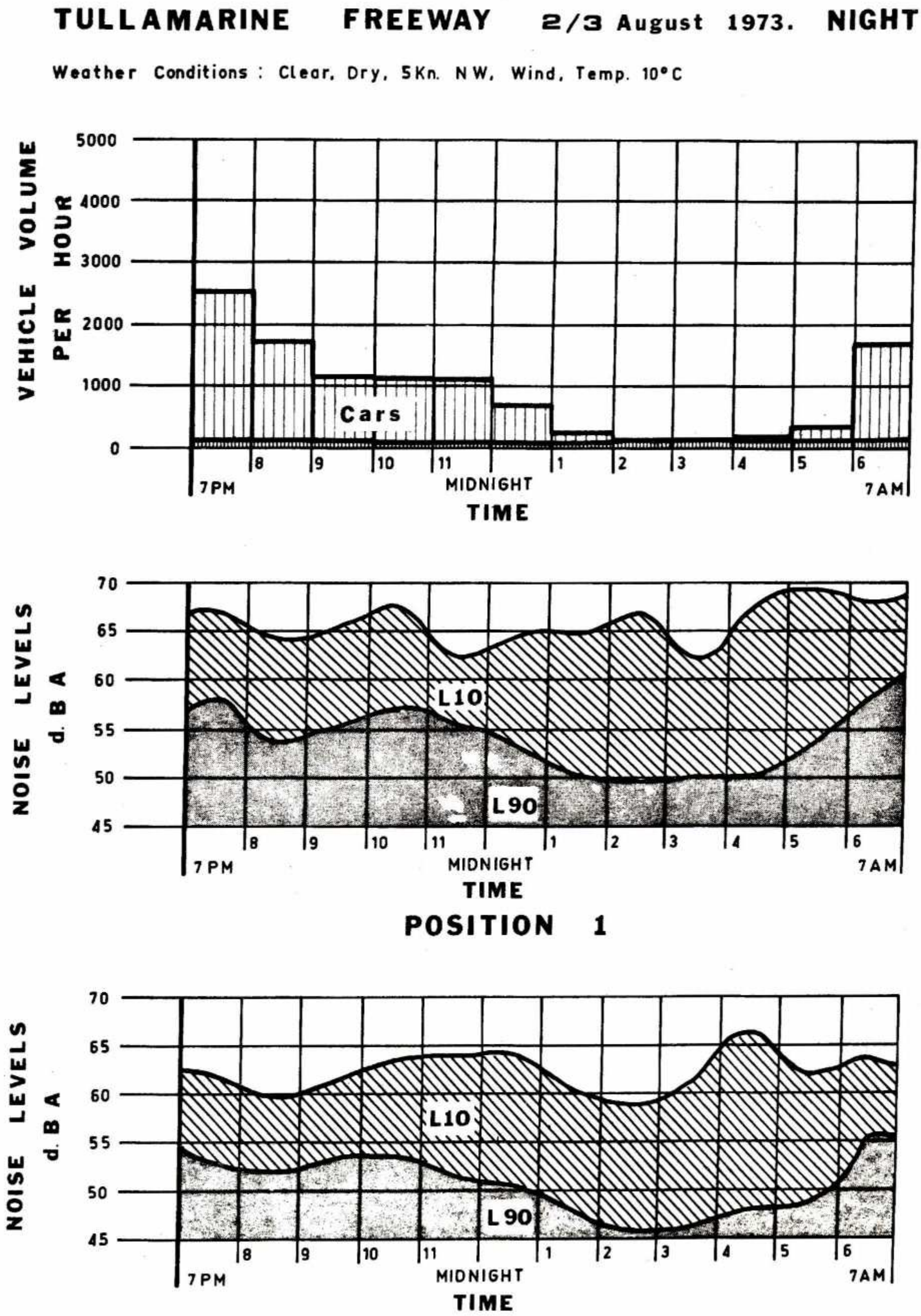
TULLAMARINE FREEWAY 2/3 August 1973. NIGHT
Weather Conditions : Clear, Dry, 5Kn. N.W. Wind, Temp. 10°C
VEHICLE VOLUME PER HOUR
5000
4000
3000
2000
1000
0
Cars
7PM
8
9
10
11
MIDNIGHT
1
2
3
4
5
6
7AM
TIME
NOISE LEVELS d.B A
70
65
60
55
50
45
L10
L90
TIME
POSITION 1
NOISE LEVELS d.B A
L10
L90
TIME
POSITION 2

FIG. 5

DEBNEY ESTATE 6. April 1973. DAY

Weather Conditions : Low cloud, Dry, 3 – 9 Kn. SW/SE Wind, Temp. 12° – 16° C

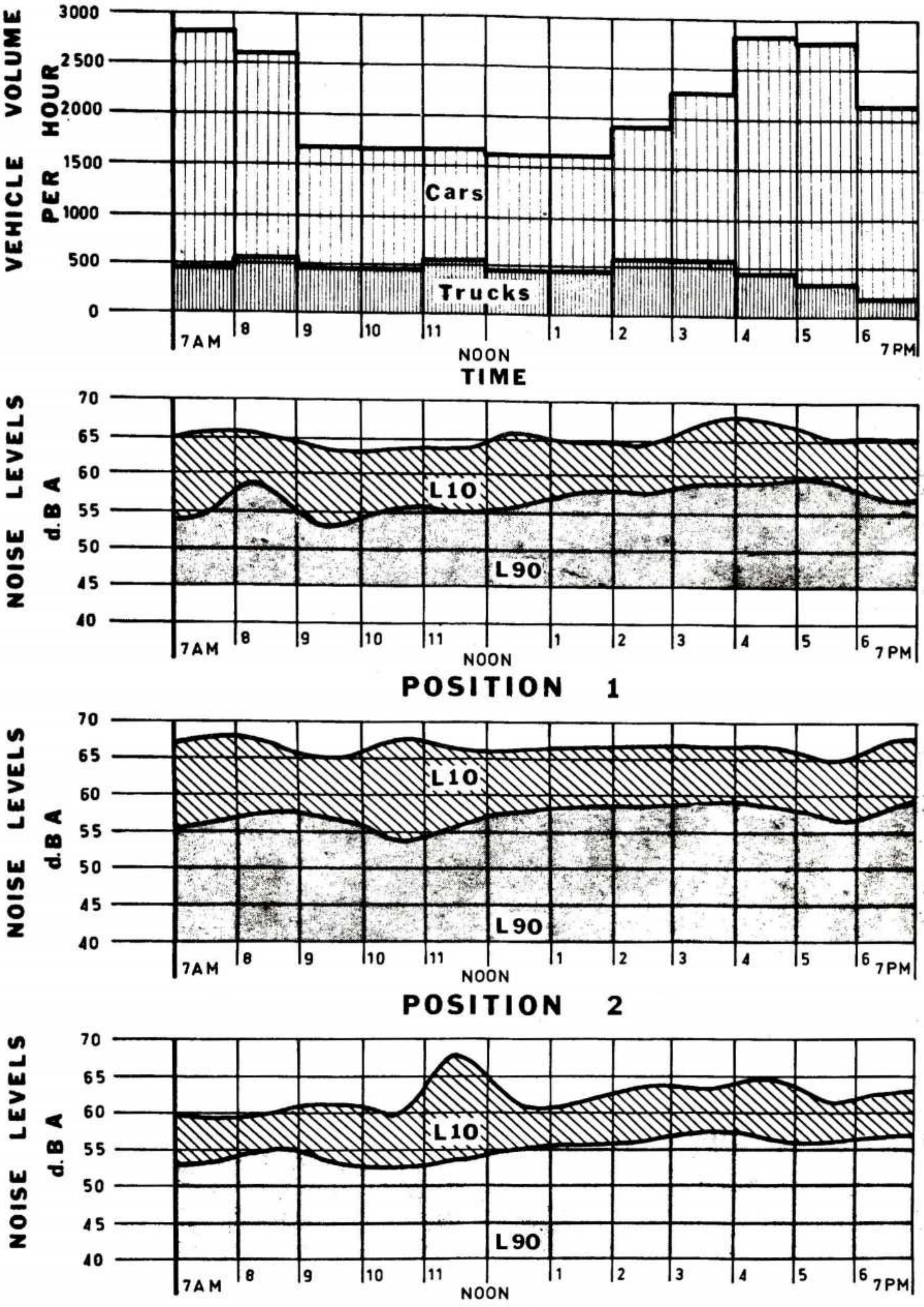

FIG. 6

DEBNEY ESTATE 7/8. June 1973. **NIGHT**

Weather Conditions : Clear, Dry, 1 Kn. N.W. Wind, Temp. 0°–4°C.

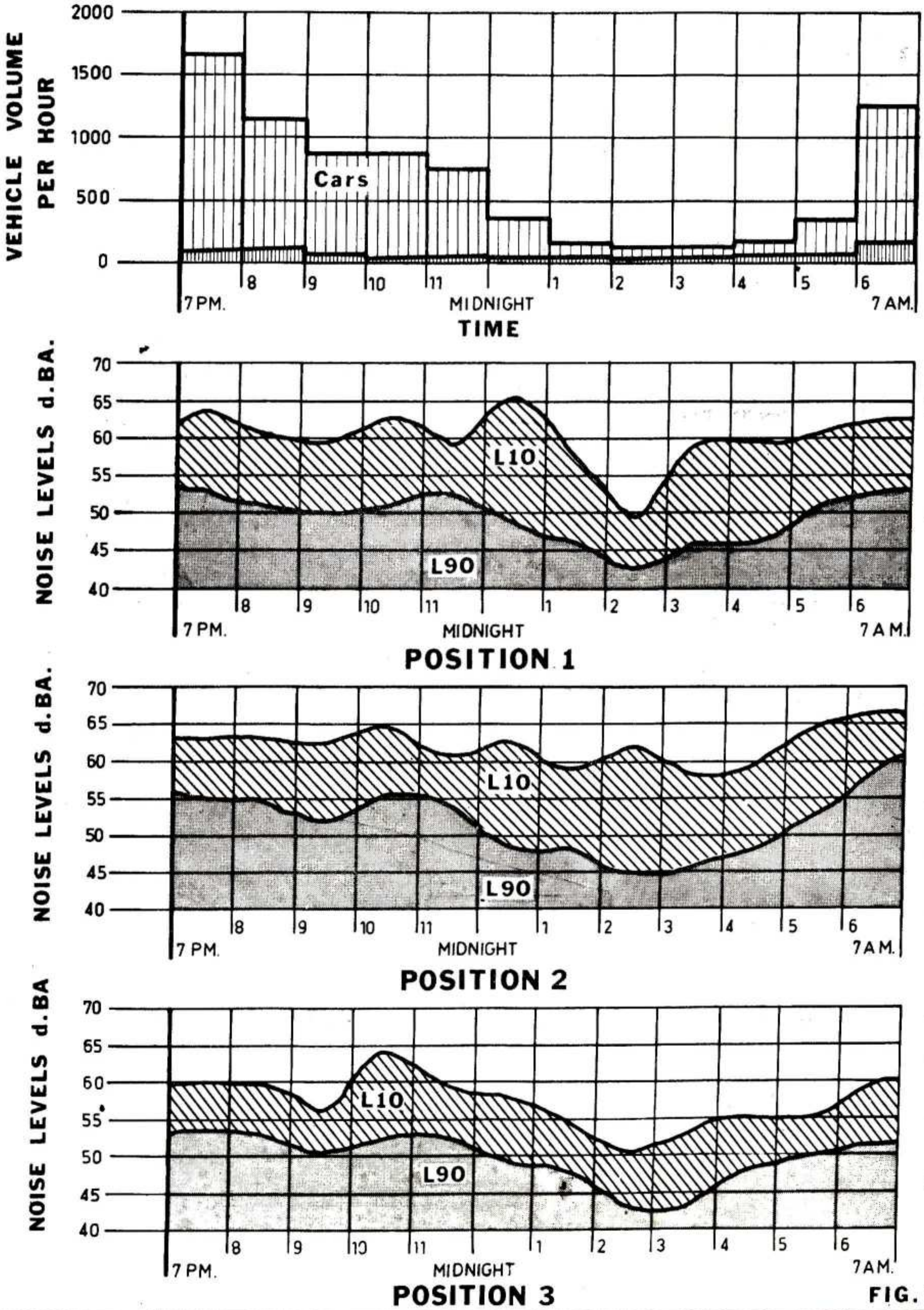

FIG. 7

HOTHAM ESTATE **7. May 1973.** **DAY**

Weather Conditions : Cloudy , Dry , 3 – 12 Kn. W. Wind , Temp 12°– 15°C.

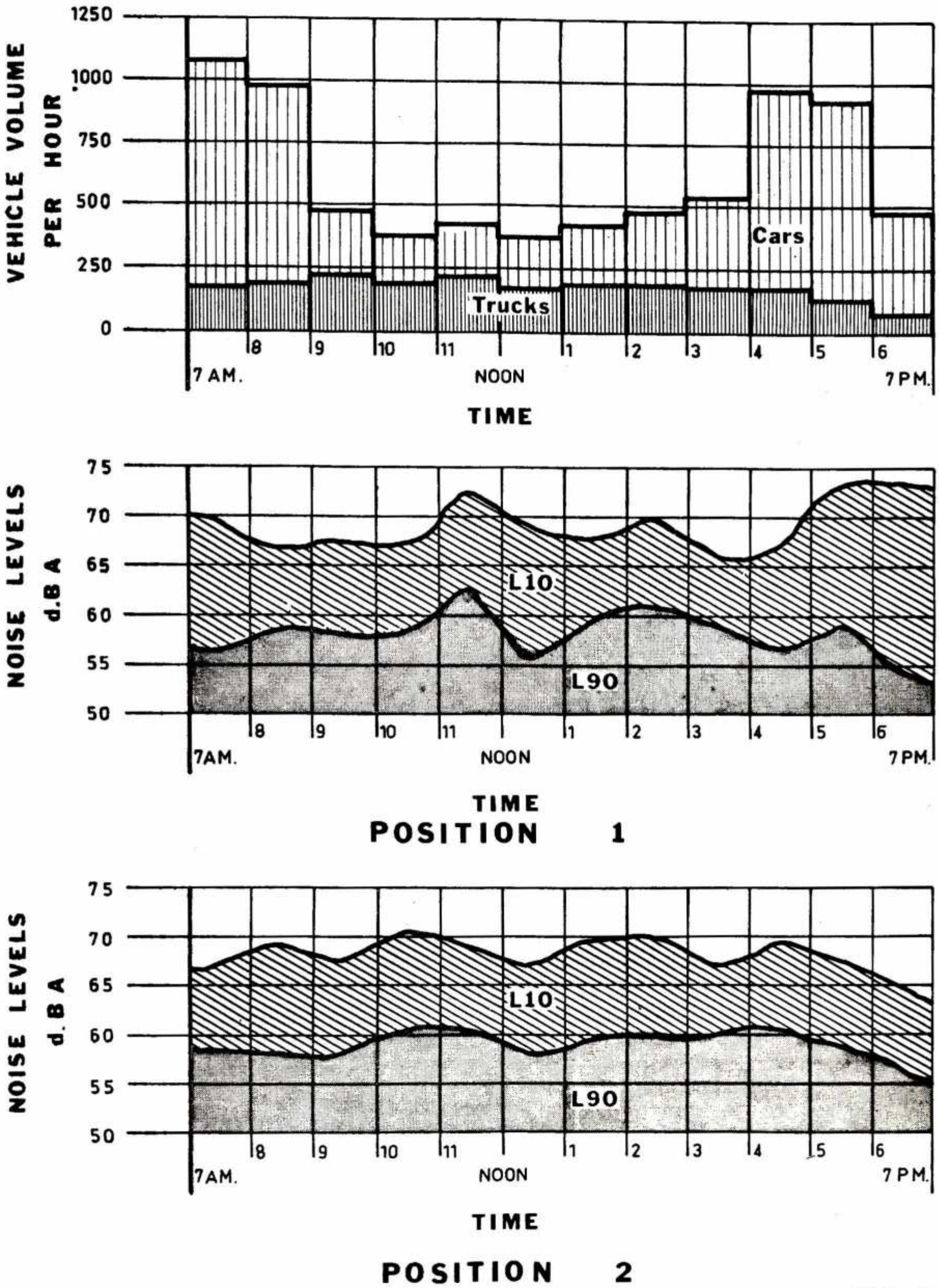

FIG. 8

FREE VIBRATION AND RESPONSE TO RANDOM PRESSURE FIELD OF ANISOTROPIC THIN CYLINDRICAL SHELLS

A. A. Lakis
Department of Mechanical Engineering
Ecole Polytechnique
University of Montreal
P. Q., Canada

R. Dore
Department of Mechanical Engineering
Ecole Polytechnique
University of Montreal
P. Q., Canada

SUMMARY

A theory is presented for the determination of the free vibration characteristics of uniform or axially non-uniform anisotropic thin cylindrical shells and the response of such shells to boundary-layer pressure fields caused by subsonic internal flow. It is a hybrid of finite-element and classical shell theories. The finite elements are cylindrical frusta and the displacement functions are determined from anisotropic shell equations. The random pressure forces are lumped at the nodes of the finite elements. The mean square response of the displacements of the shell are obtained for a boundary-layer pressure field and some calculations are conducted to illustrate the theory.

1. INTRODUCTION

A careful study of the shells used in practical applications leads to the conclusion that they are most often anisotropic (naturally or structurally) and in many cases are anisotropic and laminar. Although the problem of determining the natural frequencies of isotropic shells has produced many papers, the litterature reveals a very limited number of methods which have been generally developed for special cases of anisotropic cylindrical shells. The need is evident for a theory which can be used for the dynamic analysis of any kind of anisotropic circular cylindrical shell subjected to various boundary conditions. A practical case in point is concerned with the prediction of the natural frequencies of a double-walled steam generator [1-2].

This work attempts to fill these voids by producing a general theory with a minimum of limitations for the free vibration characteristics and the response of anisotropic cylindrical shells subjected to random pressure fields which originate from the turbulent boundary layer of an internal flow.

The analysis is based on a recently developed method for the case of isotropic cylindrical shells [4]. It is a hybrid theory based on the finite element method, with the displacement functions determined by exact solution of the equations of equilibrium of a thin cylindrical shell. The finite elements are cylindrical frusta; thus a given non-uniform shell is first subdivided into its component uniform cylindrical segments and then, generally, each segment is similarly subdivided into a number of cylindrical finite elements.

The theory for predicting the response due to random pressure fields is developed in reference [5]. The continuous pressure field is transformed to a discrete set of forces; then, the corss-correlation spectral density and the mean square values of the displacement of the shell are expressed in terms of correlation functions of the boundary-layer pressure fields.

Here the dynamics of a cylindrical shell and its response will be considered, with the following aims: (i) to extend the theory of [4] to cases where the shells are anisotropic and especially for the case of shells consisting of an arbitrary number of orthotropic layers; (ii) to use the theory of [5] to predict the response of such shells to a pressure field arising from the turbulent boundary-layer of internal flow. This generalized theory will be more directly pertinent to engineering applications, since in nearly all practical cases the shells are often anisotropic; e.g., heat exchangers and liquid metal cooled channels used in the nuclear industry. A number of assumptions are made during the course of the investigation; a compendium of these assumptions and the limitations of the theory will be given in the text.

2. FREE VIBRATION

2.1 General Theory

A given shell is subdivided into a number of finite elements, each being defined by the two nodes, i and j, and the corresponding nodal circle boundaries (Fig. 1). Then, the displacement functions may be defined by

$$[U(x,\varphi),\ W(x,\varphi),\ V(x,\varphi)]^T = [N]\,[\delta_i,\ \delta_j]^T \tag{1}$$

where $\{\delta_i\}$ and $\{\delta_j\}$ represent the nodal displacements, and the elements of [N] are in general functions of position and the shell's anisotropy.

It is noted that the finite-element method yields useful results provided that the displacement functions chosen represent adequately the true displacements; accordingly, the displacement functions should satisfy the convergence criterion of the finite-element method stating that strains within the element should be zero when the nodal displacements are generated by rigid-body motions. To this end, we shell employ the equations of thin cylindrical shells to obtain the displacement functions, instead of using the more common arbitrary polynomial forms.

Sander's theory [7] for thin cylindrical shells is used for the determination of these displacement functions. This shell theory which is based on Love's first approximation was preferred, for the following reason: in Sanders' theory all strains vanish for small rigid body motions, which is not true for Love's or Timoshenko's theories, for instance. By using such displacement functions, we automatically satisfy the convergence criterion of the finite-element method previously stated.

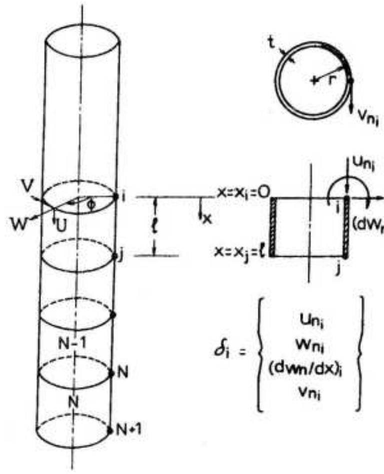

Figure 1. Definition of the finite element used and the displacement vector associated with node i, $\{\delta_i\}$.

2.2 Equations of Motion

Using Love's first approximation, we obtain the following elasticity relationships between the stress-resultant and the deformations of the middle surface for the general case of a multi-layer anisotropic shell

$$\{\sigma\} = \begin{Bmatrix} N_x \\ N_\varphi \\ \bar{N}_{x\varphi} \\ M_x \\ M_\varphi \\ \bar{M}_{x\varphi} \end{Bmatrix} = [P]\,\{\varepsilon\}\,, \tag{2}$$

$$[P] = \begin{bmatrix} p_{11} & p_{12} & o & p_{14} & p_{15} & o \\ p_{21} & p_{22} & o & p_{24} & p_{25} & o \\ o & o & p_{33} & o & o & p_{36} \\ p_{41} & p_{42} & o & p_{44} & p_{45} & o \\ p_{51} & p_{52} & o & p_{54} & p_{55} & o \\ o & o & p_{63} & o & o & p_{66} \end{bmatrix}, \tag{3}$$

the elements p_{ij} of the elasticity matrix [P] characterize the shell's anisotropy which depends on the mechanical properties of the material of the structure.

The strain vector $\{\varepsilon\}$ is the modified strain-displacement relations of Sanders [7] and is given by

$$\{\varepsilon\} = \begin{Bmatrix} \varepsilon_x \\ \varepsilon_\varphi \\ 2\varepsilon_{x\varphi} \\ \kappa_x \\ \kappa_\varphi \\ 2\bar{\kappa}_{x\varphi} \end{Bmatrix} = \begin{Bmatrix} \partial U/\partial x \\ (1/r)\ (\partial V/\partial\varphi) + (W/r) \\ \partial V/\partial x + (1/r)\ (\partial U/\partial\varphi) \\ -\partial^2 W/\partial x^2 \\ -(1/r^2)\ [(\partial^2 W/\partial\varphi^2) - (\partial V/\partial\varphi)] \\ -(2/r)\ (\partial^2 W/\partial x\partial\varphi) + (3/2r)\ (\partial V/\partial x) - (1/2r^2)\ (\partial U/\partial\varphi). \end{Bmatrix} \tag{4}$$

Upon substituting equations (2) - (4) into Sanders' shell equations of motion [7], the authors obtain the equations of equilibrium in terms of elements p_{ij} of [P] and in terms of U, V and W, namely

$$p_{11}(\partial^2U/\partial x^2)+(1/r)p_{12}(\partial W/\partial x)-p_{14}(\partial^3W/\partial x^3)+[(1/r)(p_{12}+p_{13})+(1/r^2)(p_{15}+p_{36})-(3/4r^3)p_{66}].$$
$$.(\partial^2V/\partial\varphi\partial x)+(1/r^2)[p_{33}-(1/r)p_{36}+(1/4r^2)p_{66}]\,(\partial^2U/\partial\varphi^2)-(1/r^2)\,[p_{15}+2p_{36}-$$
$$-(1/r)p_{66}](\partial^3W/\partial x\partial\varphi^2) = 0\quad ,$$

$$(1/r)[p_{33}+p_{21}+(1/r)p_{36}+(1/r)p_{51}-(3/4r^2)p_{66}](\partial^2U/\partial\varphi\partial x)+(1/r^2)\,[p_{22}+(1/r^2)p_{55}+$$
$$+(2/r)p_{25}](\partial^2V/\partial\varphi^2)+[p_{33}+(3/r)p_{36}+(9/4r^2)p_{66}]\,(\partial^2V/\partial x^2)+[p_{22}+(1/r)p_{52}](1/r^2).$$
$$.(\partial W/\partial\varphi)-(1/r^3)[p_{25}+(1/r)p_{55}](\partial^3W/\partial\varphi^3)-(1/r)\,[2p_{36}+p_{24}+(3/r)p_{66}+(1/r)p_{54}].$$
$$.(\partial^3W/\partial\varphi\partial x^2) = 0\quad , \tag{5}$$
$$-(1/r)p_{21}(\partial U/\partial x)-(1/r^2)\,[p_{22}+(1/r)p_{25}](\partial V/\partial\varphi)-(1/r^2)p_{22}W+p_{41}(\partial^3U/\partial x^3)+(1/r^2)[p_{51}+$$
$$+2p_{63}-(1/r)p_{66}](\partial^3U/\partial x\partial\varphi^2)+(1/r^3)\,[p_{52}+(1/r)p_{55}](\partial^3V/\partial\varphi^3)+(1/r)\,[p_{42}+2p_{63}+$$
$$+(1/r)p_{45}+(3/r)p_{66}](\partial^3V/\partial\varphi\partial x^2)+(2/r^3)p_{25}(\partial^2W/\partial\varphi^2)-(1/r^4)p_{55}(\partial^4W/\partial\varphi^4)+(2/r)p_{24}\,.$$
$$.(\partial^2W/\partial x^2)-p_{44}(\partial^4W/\partial x^4)-(1/r^2)(2p_{45}+4p_{66})(\partial^4W/\partial x^2\partial\varphi^2) = 0\,.$$

Here U, V and W are, respectively, the axial, circumferential and radial displacements of the middle surface of the shell, and r its mean radius (Fig. 1). The solution of these equations will give the displacement functions.

2.3 The Displacement Functions

In the continuum, we express U, V and W of the middle surface of the shell by

$$\begin{Bmatrix} U(x,\varphi) \\ W(x,\varphi) \\ V(x,\varphi) \end{Bmatrix} = \begin{bmatrix} \cos n\varphi & o & o \\ o & \cos n\varphi & o \\ o & o & \sin n\varphi \end{bmatrix} \begin{Bmatrix} u_n(x) \\ w_n(x) \\ v_n(x) \end{Bmatrix} = [T] \begin{Bmatrix} u_n(x) \\ w_n(x) \\ v_n(x) \end{Bmatrix}, \tag{6}$$

where n is the circumferential wave-number. By substituting equation (6) into equation (5) and letting

$$u_n(x) = A\ e^{\lambda x/r}\quad ,\quad v_n(x) = B\ e^{\lambda x/r}\quad ,\quad w_n(x) = C\ e^{\lambda x/r}\quad , \tag{7}$$

we obtain three simultaneous ordinary linear equations in A, B, C of the form

$$[H]\begin{Bmatrix} A \\ B \\ C \end{Bmatrix} = \{0\}. \tag{8}$$

For non-trivial solution, the determinant of [H] must vanish, leading to the following characteristic equation

$$h_8\lambda^8 - h_6\lambda^6 + h_4\lambda^4 - h_2\lambda^2 + h_o = 0\quad , \tag{9}$$

where

$$h_8 = (h_9/r^2)(p_{11}p_{44} - p_{14}^2)\quad ,$$
$$h_6 = (n^2/r^2)\,[h_9(h_1p_{44}+2p_{11}p_{45}+4p_{11}p_{66}-2h_5rp_{14})+h_7(p_{11}p_{44}-p_{14}^2) - r^2h_{11}^2p_{11} -$$
$$-h_3^2p_{44} + 2rh_3h_{11}p_{14}]+(2/r)h_9(p_{11}p_{24}-p_{14}p_{12})\quad ,$$
$$h_4 = (n^4/r^2)\,[h_1h_7p_{44}+h_9p_{11}p_{55}+(2p_{45}+4p_{66})(h_1h_9+h_7p_{11}-h_3^2)+(p_{25}+(1/r)p_{55}).$$
$$.(2h_3p_{14}-2h_{11}p_{11}r)+h_{11}r^2(2h_3h_5-h_1h_{11}) - rh_5(2h_7p_{14}+rh_5h_9)] + (n^2/r).$$
$$.[2(p_{25}+rp_{22})\,((h_3/r)p_{14}-h_{11}p_{11})-2p_{12}(h_5h_9r+h_7p_{14}-h_3h_{11}r)-2p_{24}(h_3^2 - h_1h_9 - h_7p_{11})$$
$$+2h_9p_{11}p_{25}] + h_9\,(p_{11}p_{22}-p_{12}^2)\quad ,$$
$$h_2 = (n^6/r^2)\,[h_1h_7(2p_{45}+4p_{66})+p_{55}(h_1h_9+h_7p_{11}-h_3^2)-r^2h_5^2h_7 + (p_{25}+(1/r)p_{55}).$$
$$.(-2rh_1h_{11}+2rh_3h_5-p_{11}p_{25}-(1/r)\,p_{11}p_{55})] + (n^4/r)\,[2h_1h_7p_{24}+2p_{25}(h_1h_9+h_7p_{11}-$$
$$-h_3^2)-2p_{12}(rh_5h_7-h_3p_{25}-(h_3/r)p_{55})-2(p_{25}+rp_{22})(h_1h_{11}+(1/r)p_{11}p_{25}+(1/r^2)p_{11}p_{55}-$$

$-h_3h_5)]+n^2[p_{22}(h_1h_9 + h_7p_{11} - h_3^2)-(1/r)(p_{25} + rp_{22})((1/r)p_{11}p_{25} + p_{11}p_{22} - 2h_3p_{12})-$
$-h_7p_{12}^2]$,

$$h_o = n^4h_1h_7[p_{22} + (2/r)n^2p_{25} + (n^4/r^2)p_{55}] - n^2h_1[(n^3/r)(p_{25} + (1/r)p_{55} + (n/r)(p_{25} + rp_{22})]^2$$

and the parameters h_i, $i = 1, 3, 5, 7, 9, 11$ are given by

$$h_1 = p_{33} - (1/r)p_{36} + (1/4r^2)p_{66} \quad , \quad h_3 = p_{12} + p_{33} + (1/r)(p_{15} + p_{36}) - (3/4r^2)p_{66} \quad ,$$
$$h_5 = (1/r)(p_{15} + 2p_{36} - (1/r)p_{66}) \quad , \quad h_7 = p_{22} + (1/r^2)p_{55} + (2/r)p_{25} \qquad (10)$$
$$h_9 = p_{33} + (3/r)p_{36} + (9/4r^2)p_{66} \quad , \quad h_{11} = (1/r)[2p_{36} + p_{24} + (3/r)p_{66} + (1/r)p_{54}].$$

This characteristic equation for anisotropic cylindrical shells which is a quartic in λ^2, has the same general form as equation (5) of [4] for isotropic one. The eight roots λ_i may therefore be written as follows

$$\lambda_1 = -\varkappa_1 + i\,\mu_1 \; , \quad \lambda_2 = -\varkappa_1 - i\,\mu_1 \; , \quad \lambda_3 = -\varkappa_2 + i\,\mu_2 \; , \quad \lambda_4 = -\varkappa_2 - i\,\mu_2 \; ,$$
$$\lambda_5 = \varkappa_1 + i\,\mu_1 \; , \quad \lambda_6 = \varkappa_1 - i\,\mu_1 \quad \lambda_7 = \varkappa_2 + i\,\mu_2 \quad \lambda_8 = \varkappa_2 - i\,\mu_2 \; . \qquad (11)$$

where $\varkappa_i$ and μ_i are real. Each root, λ_j, yields a solution of equation (5), the complete solution being obtained by the sum of all eight with the constants Aj, Bj and Cj, $j=1,2,..8$.

For every j, the three constants Aj, Bj and Cj are related among each other by the linear equations (8), so that u_n, v_n and w_n may be expressed in terms of only eight constants. To this end, we let

$$Aj = \alpha j\; Cj \quad , \quad Bj = \beta j\; Cj \quad , \qquad (12)$$

where αj and βj, for $j = 1$ and 3, may be expressed as follows

$$\alpha_1 = \bar\alpha_1 + i\bar\alpha_2 \; , \quad \alpha_3 = \bar\alpha_3 + i\bar\alpha_4 \; , \quad \beta_1 = \bar\beta_1 + i\bar\beta_2 \; , \quad \beta_3 = \bar\beta_3 + i\bar\beta_4 \qquad (13)$$

The real and imaginary parts of αj, βj, $j = 1$ and 3, may be obtained from the following relationships

$$\begin{bmatrix} a_{11} & a_{12} \\ a_{21} & a_{22} \end{bmatrix} \begin{Bmatrix} \alpha j \\ \beta j \end{Bmatrix} = \begin{Bmatrix} -a_{13} \\ -a_{23} \end{Bmatrix} \quad , \qquad (14)$$

where

$$a_{11} = n^2h_{11} - \lambda_j^2\, p_{11} \; , \quad a_{12} = -n\lambda_j h_3 \quad , \quad a_{13} = -\lambda_j(n^2h_5 + p_{12}) + (1/r)\lambda_j^3 p_{14} \; ,$$
$$a_{21} = a_{12} \quad , \quad a_{22} = -n^2h_7 + \lambda_j^2 h_9 \; , \quad a_{23} = -(n/r)(1+n^2)p_{25} - np_{22} - (n^3/r^2)p_{55} + $$
$$+ n\lambda_j^2 h_{11}.$$

By inspecting the coefficients of equations (8), the other αj, βj can be given by

$$\begin{array}{lll} \alpha_2 = \bar\alpha_1 - i\,\bar\alpha_2 & \alpha_5 = \bar\alpha_5 + i\,\bar\alpha_6 = -\alpha_2 & \beta_5 = \bar\beta_5 + i\,\bar\beta_6 = \beta_2 \\ \alpha_4 = \bar\alpha_3 - i\,\bar\alpha_4 & \alpha_6 = \bar\alpha_5 - i\,\bar\alpha_6 = -\alpha_1 & \beta_6 = \bar\beta_5 - i\,\bar\beta_6 = \beta_1 \\ \beta_2 = \bar\beta_1 - i\,\bar\beta_2 & \alpha_7 = \bar\alpha_7 + i\,\bar\alpha_8 = -\alpha_4 & \beta_7 = \bar\beta_7 + i\,\bar\beta_8 = \beta_4 \\ \beta_4 = \bar\beta_3 - i\,\bar\beta_4 & \alpha_8 = \bar\alpha_7 - i\,\bar\alpha_8 = -\alpha_3 & \beta_8 = \bar\beta_7 - i\,\bar\beta_8 = \beta_3 \; . \end{array} \qquad (15)$$

Upon substituting the relations (12)-(15) into equation (7) and thence into equations (6) we obtain expressions for the displacement functions in terms of eight constants $\bar C j$. These expressions may be written as

$$\begin{Bmatrix} U(x,\varphi) \\ W(x,\varphi) \\ V(x,\varphi) \end{Bmatrix} = [T]\,[R]\,\{\bar C\} \quad , \qquad (16)$$

where $[R]$ is given in appendix I and $\{\bar C\} = [\bar C_1 \;\ldots\; \bar C_8]$. The eight $\bar C j$ are the only free constants, which must be determined from eight boundary conditions, four at each edge of the finite element. The nodal displacements (Fig. 1) at nodes i, $(x = 0)$ and j, $(x = \ell)$ are defined by

$$\begin{Bmatrix} \delta_i \\ \delta_j \end{Bmatrix} = \{u_{ni},\; w_{ni},\; (dw_n/dx)_i,\; v_{ni},\; u_{nj},\; w_{nj},\; (dw_n/dx)_j,\; v_{nj}\}^T = [A]\,\{\bar C\} \; , \qquad (17)$$

where $[A]$ is given in appendix I, its elements being determined from those of $[R]$. Finally, combining equations (16) and (17), we obtain

$$\begin{Bmatrix} U(x,\varphi) \\ W(x,\varphi) \\ V(x,\varphi) \end{Bmatrix} = [T]\,[R]\,[A]^{-1} \begin{Bmatrix} \delta_i \\ \delta_j \end{Bmatrix} = [N] \begin{Bmatrix} \delta_i \\ \delta_j \end{Bmatrix} \qquad (18)$$

This equation defines the displacement functions in terms of $n\varphi$, x, the elements p_{ij} of [P] and the nodal displacements $\begin{Bmatrix} \delta_i \\ \delta_j \end{Bmatrix}$.

2.4 Determination of the Mass and Stiffness Matrices.

Substituting equations (18) into equations (4) we obtain the strain vector $\{\varepsilon\}$ in terms of $\{\delta_i\}$ and $\{\delta_j\}$ as follows:

$$\{\varepsilon\} = \begin{bmatrix} T & 0 \\ 0 & T \end{bmatrix} [Q]\,[A]^{-1} \begin{Bmatrix} \delta_i \\ \delta_j \end{Bmatrix} = [B] \begin{Bmatrix} \delta_i \\ \delta_j \end{Bmatrix} \quad , \tag{19}$$

where [Q] is given in ref.[4]. The corresponding stress-resultant matrix may be found from equation (2), i.e.,

$$\{\sigma\} = [P]\,\{\varepsilon\} = [P]\,[B] \begin{Bmatrix} \delta_i \\ \delta_j \end{Bmatrix} \quad , \tag{20}$$

where [P] is the elasticity matrix for anisotropic shells.

The stiffness and mass matrices for one finite element [3] are expressed as

$$[k] = \iint [B]^T\,[P]\,[B]\,dA\ , \quad [m] = \rho t \iint [N]^T\,[N]\,dA, \tag{21}$$

where $dA = rd\varphi dx$, ρ is the density of the shell and t its thickness. Integrating over φ and using equations (18)-(20) we obtain

$$[k] = [\,[A]^{-1}]^T\,\{\pi r \int_0^{\ell} [Q]^T\,[P]\,[Q]dx\}[A]^{-1} = [\,[A]^{-1}]^T\,[G]\,[A]^{-1} \tag{22}$$

$$[m] = \rho t\,[\,[A]^{-1}]^T\,\{\pi r \int_0^{\ell} [R]^T\,[R]\,dx\}\,[A]^{-1} = \rho t\,[\,[A]^{-1}]^T\,[S]\,[A]^{-1} \tag{23}$$

where [G] and [S] are defined by the above equations.

[G] and [S] were obtained analytically for the case of isotropic shell in reference [4] by carrying out the necessary matrix operations and integrating over x in equations (22) and (23). To do this it was found necessary to introduce several intermediate matrices, eventually obtaining expressions for the general terms k_{ij} and m_{ij} of [k] and [m], respectively.

For the case of anisotropic shells, the elements of [G] and [S] are similar to those of reference [4], for the following reason: in [4], the (i,j)th terms of [G] and [S] are determined functions of the elements of [P] and of the general terms, $\varkappa$ and μ, of the roots λ's which have the same general form as those of equation (11). Because of the complexity of the manipulations, neither the intermediate steps nor the final result will be given here. The interested reader is referred to reference [4] for details.

With [m] and [k] determined, the global mass and stiffness matrices for the whole shell, [M] and [K], respectively, may be constructed by superposition in the normal manner as described in [4]. Each of these matrices is of order 4(N+1), where N is the total number of finite elements.

2.5 Elasticity Matrix

The elasticity matrix [P] given by equation (3) is quite general, so this theory may be applied to: (i) shells consisting of single or an arbitrary number of isotropic or orthotropic layers, (ii) double-walled, gridwork or folded shells and (iii) shells with rings and stringers provided their characteristics are known. Here we limit ourselves to shells consisting of single or an arbitrary number of isotropic or orthotropic layers.

For isotropic shells, the elements p_{ij} of [P] are listed in reference [4]. In the case of an arbitrary number of orthotropic layers [8], we assume that these layers function concurrently without slippage and as previously stated that the principal directions of elasticity at each point of the shell coincide with the directions of coordinate lines; (i) for an even number of layers, 2v, the elements p_{ij} of [P] may be written in the form

$$\begin{aligned} p_{ij} &= 2 \sum_{s=1}^{v} B^s_{ij}\,(t_s - t_{s+1}),\ i = 1 \text{ to } 3, \text{ and } j = 1 \text{ to } 6, \\ p_{ij} &= (2/3) \sum_{s=1}^{v} B^s_{i-3,\,j-3}\,(t_s^3 - t_{s+1}^3),\ i = 4 \text{ to } 6, \text{ and } j = 4 \text{ to } 6. \end{aligned} \tag{24}$$

(ii) for an odd number, 2v+1, we obtain

$$p_{ij} = 2[B_{ij}^{v+1}\, t_{v+1} + \sum_{s=1}^{v} B_{ij}^{s}\, (t_s - t_{s+1})], \quad i = 1 \text{ to } 3 \text{ and } j = 1 \text{ to } 6,$$

$$p_{ij} = (2/3)[B_{i-3,j-3}^{v+1}\, t_{v+1}^{3} + \sum_{s=1}^{v} B_{i-3,j-3}^{s}\, (t_s^3 - t_{s+1}^3)], \quad i = 4 \text{ to } 6 \text{ and } j = 4 \text{ to } 6\ , \tag{25}$$

where

$$B_{11}^{s} = [E_1^s/(1-\nu_1^s\,\nu_2^s)],\ B_{22}^{s} = [E_2^s/(1-\nu_1^s\,\nu_2^s)],\ B_{12}^{s} = B_{21}^{s} = [\nu_2^s\, E_1^s/(1-\nu_1^s\,\nu_2^s)], B_{33}^{s} = 0.5G_{12}^{s}\ ,$$

t_s is the thickness of the s^{th} layer, (E_1^s, ν_1^s) and E_2^s, ν_2^s) are its young's modulus and Poisson's ratio in the x and φ directions, respectively, and G_{12}^s is the shear modulus. All other terms of B_{ij}^s are zero.

2.6 Free Vibration

For free vibration, the equation of motion may be written in the form

$$[M]\ \{\ddot{\Delta}\} + [K]\ \{\Delta\} = \{0\}\ , \tag{26}$$

where $\{\Delta\} = \{\delta_1, \delta_2, \ldots \delta_{N+1}\}^T$, N is the number of finite elements, [M] and [K] are real, symmetric matrices of order 4(N+1), and $\{\delta_{N+1}\}$ being the displacement vector associated with the lower edge of the last finite element.

In cases where the shell has rigid edge constraints, the kinematic boundary conditions must be taken into consideration. Accordingly, [K] and [M] are reduced to square matrices of order 4(N+1)--J, where J is the number of constraint equations imposed. Thus, for a shell with two edges supported, we must have $v_n = w_n = 0$ in the displacement vectors $\{\delta_1\}$ and $\{\delta_{N+1}\}$, and J=4; for a free shell, J=0; and for one with two clamped edges J=8. The solution of equation (26) now follows by standard matrix techniques, yielding the natural frequencies, ω_i , i=1, 2, ..., 4(N+1)-J, and the corresponding eigenvectors.

3. RESPONSE TO BOUNDARY-LAYER PRESSURE FIELD

3.1 General Theory

In this section we are concerned with the vibration of thin anisotropic cylindrical shells due to a pressure field arising from the turbulent boundary layer of an internal subsonic flow. It is based on a recently developped theory [5] by the author for the case of isotropic cylindrical shells. Only an outline of the theory is given here; for a detailed account the reader is referred to reference [5].

The equations of motion of the shell subjected to arbitrary load is given by

$$[M]\ \{\ddot{y}\} + [C]\ \{\dot{y}\} + [K]\ \{y\} = \{F\}, \tag{27}$$

where {y} is a nodal displacement vector, {F} is a vector of the external forces, and [M], [C] and [K] are the mass, damping and stiffness matrices, respectively.

Whereas equation (27) is quite general, the particular form of its constituent terms depends on the particular theory used. In this theory [M] and [K] are determined by equations (22) and (23), [C] is assumed to be linearly related to [M] and [K], or to either one, and the external forces {F} represent the internal random pressure field.

3.2 Assumptions

In reference [6] we have indicated how the inertial effects of a stationnary fluid contained by the shell may be taken into account. However, when the fluid is flowing, the shell is also subjected to "centrifugal" and Coriolis-type pressure forces. The former have the effect of diminishing the natural frequencies of the system, while the latter have a damping effect on vibrations in cases where one end of the shell is free. Unless we are dealing with very flexible shells, very heavy fluids, or very high velocities, the effects of these forces will be relatively small. Accordingly, for metal shells conveying fluid with flow velocity in the normal engineering range, these effects are negligible and are not taken into account.

The displacements are assumed small enough for the resultant forces to be normal to the shell's surface. It is also assumed that the pressure field is spatially continuous and that it has the properties of a weakly stationary, ergodic process. We further assume that the pressure drop in the length of the shell is sufficiently small for the mean pressure to be considered constant over the length of the shell. Finally, the continuous random pressure field of the deformable body is approximated by a finite set of discrete forces and moments acting at the nodal points [11].

3.3 Representation of Pressure Field at Nodal Points.

As previously mentioned, the shell is divided into N finite elements, each of which is a cylindrical frustum. The position of the N+1 nodal points may be chosen arbitrarily (Fig. 1).

Any pressure field is considered to be acting on an area S_e surrounding the node e of coordinate ℓ_e as shown in Figure 2(a). We define the pressure distribution acting over this area S_e by two mutually perpendicular forces per unit length. We may write, for the actual resultant force per unit length,

$$F(x,\varphi,t) = \sum_n f_{Rn}(x,t).\cos n\varphi + \sum_n f_{Cn}(x,t).\sin n\varphi \,, \tag{28}$$

where f_{Rn} and f_{Cn} are at a distance x_o from the origin of the shell as shown in figure 2(a).

These two forces acting at point A are transformed to two forces and one moment, $\mathcal{M}_r$, acting at the node e, as shown in Figure 2(b).

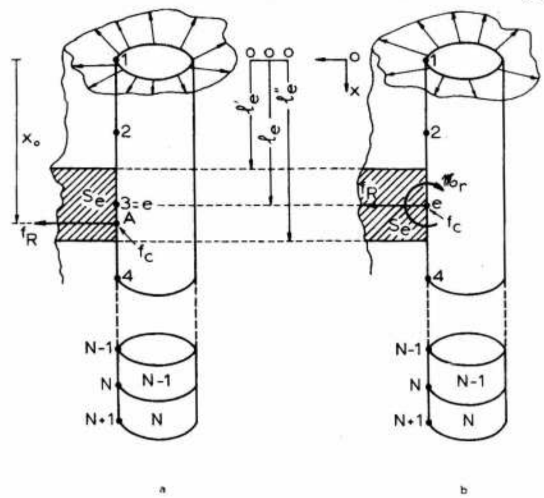

Figure 2 (a) Representation of the pressure field by a discrete force field. (b) The equivalent discrete force field acting at the node e, involving f_{Rn}, f_{Cn} and $\mathcal{M}_r$.

The external force vector associated with the n^{th} circumferential wave number at a typical node e can now be written in the following form:

$$\{F(t)\}_e = [0,\ \int_{l'i}^{l''i} [f^2_{Rn}(x_i,t)+f^2_{Cn}(x_i,t)]^{\frac{1}{2}}\ ,\ \int_{l'j}^{l''j} (x_j-\ell_j)[f^2_{Rn}(x_j,t)+f^2_{Cn}(x_j,t)]^{\frac{1}{2}}\ ,0]^T_e \quad ,(29)$$

where f_{Rn} and f_{Cn} are expressed in terms of the instantaneous pressure on the surface, $p(x,\varphi,t)$.

3.4 Mean Square Response.

We proceed by first considering the free vibration of the conservative system (26) and determining the natural frequencies ω_i and the eigenvectors $\{\Phi_i\}$, $i = 1,2,\ldots,4(N+1)-J$, where J is the number of kinematic boundaries.

We next form the modal matrix

$$[\Phi] = [\Phi_1, \Phi_2, \ldots, \Phi_{4(N+1)-J}], \text{ and define } \{y\} = [\Phi]\{Z\}. \tag{30),(31}$$

Finally the equations of motion (27) are decoupled and the mean square values of the displacements of the shell are expressed in terms of the axial and circumferential correlation functions of the pressure field, $\psi_p(\xi,o,o)$ and $\psi_p(o,\eta,o)$, respectively; see equations (10)-(25) of reference [5].

In the case of subsonic boundary-layer pressure fluctuations, the streamwise and lateral spatial correlation functions have been examined theoretically and experimentally by Bakewell et al. [9] and Clinch [10].

Bakewell measured and derived expressions for the axial and circumferential correlation functions in experiments with air flowing in a cylindrical pipe. He found the following approximate expressions for the (real) spatial correlations:

$$\psi_{p_\omega}(\xi,0,0) \simeq e^{-b|S_\xi|}\cos a S_\xi, \qquad \psi_{p_\omega}(0,\eta,0) \simeq (1+cS^2_\eta)^{-1}[2-e^{-dS^2_\eta}]^{-1}, \tag{32),(33}$$

where $S_\xi = \xi\omega/U_{conv.}$ and $S_\eta = \eta\omega/U_{\mathbf{C}}$ are the axial and circumferential Strouhal number, $\xi = |x_i - x_j|$, $\eta = |r(\varphi_i - \varphi_j)|$, ω is the center frequency, and a, b, c, d are constants to be specified; U_{conv} and $U_{\mathbf{C}}$ are, respectively, the convection and the centerline velocities.

The values of the constants used in these two expressions for axial and circumferential correlations depend on the fluid. For turbulent flow in air, the values of a, b, c and d are given in [9]

$$a = 8{\cdot}7266,\ b = 1{\cdot}0,\ \text{for } S_\xi = \xi\omega/U_{\mathbf{C}}, \qquad c = 20,\ d = 100,\ \text{for } S_\eta = \eta\omega/U_{\mathbf{C}}. \tag{34}$$

Clinch measurements in water proved that these constants are approximately the same for different fluids at the same Strouhal number, at least for sufficiently high Reynolds number.

Upon using the experimentally based relations (32)-(34), we obtain the following expression for the mean square response of the shell [5]:

$$\begin{aligned}\overline{y_q^2(t)} = \sum_{r=1}^{4(N+1)-J} \Phi_{qr}^2 \frac{r^2}{16\pi^2\omega_r^4 \mathcal{M}_r^2} \times \\ \times \left[\sum_{i=1}^{N+1}\sum_{u=1}^{N+1} \Phi_{ir}\Phi_{ur}|\Gamma_{iu}^F| + 2\sum_{i=1}^{N+1}\sum_{k=1}^{N+1} \Phi_{ir}\Phi_{kr}|\Gamma_{ki}^M| + \right. \\ \left. + \sum_{j=1}^{N+1}\sum_{k=1}^{N+1} \Phi_{jr}\Phi_{kr}|\Gamma_{jk}^{MM}| + \sum_{p=1}^{N+1}\sum_{v=1}^{N+1} \Phi_{pr}\Phi_{vr}|\Gamma_{pv}^F|\right],\end{aligned} \tag{35}$$

where Φ_{qr} is the $(qr)^{th}$ element of the modal matrix $[\Phi]$, $\mathcal{M}_r$ is the element of the generalized mass matrix, ω_r, the r^{th} natural frequency and r is the mean radius of the shell; Γ_{iu}^F, Γ_{ki}^M and Γ_{jk}^{MM} are derived analytically in reference [5].

Equation (35) is then the response of the shell to a subsonic boundary-layer pressure field at the nodal points $q(x,\varphi)$. This response is associated with a specific n, where n is the circumferential wave number (section 2.3). By repeating the analysis for a sufficient number of n, the total response for any point on the nodal circles may be obtained by superposition, in accordance with the assumption that there is no coupling between the circumferential wavenumbers.

4. CALCULATION AND DISCUSSION

The computer program of reference [5] has been modified to determine the eigenvalues, eigenvectors and the response of a given uniform or non-uniform anisotropic cylindrical shell subjected to a boundary-layer pressure field. It is written in FORTRAN V language for the IBM 360/70 computer, using double precision arithmetic throughout all the overlays.

The necessary step of the computational method may be outlined as follows: a) We first specify the imposed boundary conditions, their number, J, and the values of n ($\geqslant 2$) for which calculations should be done; b) The shell is then subdivided into a sufficient number, N, of finite elements (sufficiency in this context is related to the complexity of the structure); c) And finally the computer program, for given input data, calculated the mass and stiffness matrices for each element, assembles the global mass and stiffness matrices for the whole shell, calculates the natural frequencies and the eigenvectors, determines the damping matrix, and executes the necessary steps to obtain the response.

The necessary input data for each finite element are the mean radius, r, wall thickness, t, length of the individual element, ℓ, material density, ρ, and the elements p_{ij} of [P]

For given r, t, ℓ, ρ and p_{ij}, the computer program executes the following steps for each element: i) the eight complex roots, λ_j, of the characteristic equation (9), are calculated by Newton-Raphson iterative technique, and hence, we obtain κ_1, κ_2, μ_1, μ_2, α_j, β_j ($j = 1, 2, .., 8$), and $\bar{\alpha}_j$, $\bar{\beta}_j$; ii) the intermediate matrices are determined; iii) the displacement functions, mass and stiffness matrices, [N], [m] and [k], respectively, are computed by the relationships given by equations (18), (22) and (23).

When the stiffness and mass matrices have thus been computed for each element, the global [M] and [K] are constructed and reduced appropriately to take account of the boundary conditions.

For free vibration, the computer program proceeds to find the natural frequencies, ω_i, where $i = 1,2,\ldots\ldots,4(N+1)-J$ for each n, and the corresponding eigenvectors of a real square non-symmetric matrix of the special form $[M]^{-1}[K]$, where both [M] and [K] are real, symmetric matrices and [M] is positive definite.

Knowing the damping factor, the fluid velocity and its density at each node of the structure, equation (35) is finally executed to obtain the response to a boundary-layer pressure field.

Calculations have already been conducted to test the theory in the case of isotropic shells [5]. The free vibration characteristics of uniform and axially non-uniform shells were obtained for a variety of boundary conditions [4]. The computed natural frequencies and the response were compared with those obtained by other theories and from experiments; agreement was found to be good and, in the majority of cases, was even better with the experiments.

Here we repeat only one calculation to test the computer program and the modified theory. More results concerning the anisotropic shells will be presented and discussed at the conference.

The set of calculations undertaken here was first studied experimentally and theoretically by Clinch [12]. It is a long, simply supported cylindrical shell conveying water with flow velocities in the range 248-520 in/sec. The pertinent data are as follows: $r = 3$ in(.0762 m), $L = 240$ in(6.096 m), $t = 0.025$ in($.63 \times 10^{-3}$ m), $E = 28.5 \times 10^{6}$ lb/in^2(1.995×10^{11} N/m^2), $\nu = 0.305$, $\rho = .749 \times 10^{-3}$ lb-sec^2/in^4(8.0048×10^{3}kg/m^3). Clinch obtained the response in the frequency range of 100-1,000 Hz, approximately.

This shell was also analysed by the theory of reference [5] by subdividing the shell into 8 elements and calculating the response for $n = 2$ to 6. Here we repeat the same calculations for $n = 2$ to 12 from which the approximate "total" and the high-frequency responses of this theory are shown in Figure 3; also shown are Clinch's experimental and theoretical results.

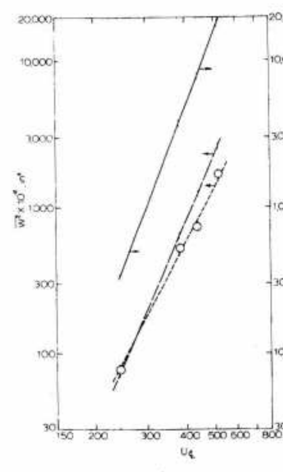

Figure 3. The mean square response of the maximum radial displacement of a shell first studied by Clinch, as a function of the centerline velocity. --- 0 ---, Clinch's experimental and theoretical results for high-frequency response; ---, theoretical results obtained by this theory ($n = 2$ to 12) for high frequency response (98-1,000 Hz); ——, "total" response obtained by this theory ($n = 2$ to 12) considering all frequency components.

It is evident from Figure 3 that the response at the high frequency range is but a small part of the total. This observation demonstrates the limitations of Clinch theory if one is interested in the total response rather than only the high-frequency range. On the other hand, the agreement between this theory and experiment, in the frequency range of 100-1,000 Hz, approximately, is quite good. This is the first and, so far, only experimental verification of this theory, as experimental data are very scarce; the results lend confidence that the values of the overall response of the shell are also reliable.

5. CONCLUSION

The hybrid finite-element, classical theory developed in this paper is used to obtain the free vibration characteristics and to predict the response, to boundary-layer pressure field of an axially non-uniform, anisotropic thin cylindrical shell. To this end the shell is subdivided into a number of cylindrical finite elements, each with two nodes, the nodal displacements being the axial, circumferential and radial displacements and a rotation. The shell equations employed, which are solved for the determination of the displacement functions, are such that the convergence criteria of the finite-element method are satisfied. The pressure field is similarly rendered discrete and is represented by two forces and a moment at each node. Finally, the pressure correlation functions used in this analysis are applicable only for flow velocities corresponding to Mach number 0.3 or less; there is no assurance that such correlation functions can be applied at higher Mach numbers when compressibility effects become important.

This theory was computerized so that if the dimensions and material properties of each finite element, and the properties and flow velocity of the fluid, are given as input, the program gives as output the natural frequencies and eigenvectors of the shell and the r.m.s. values of the nodal displacements. The analysis proceeds separately for each circumferential wavenumber, n; the total response may then be found by summing over n.

The effort involved in producing such complex theory is deemed to be justified. In this connection, it is noted that accurate knowledge of some of the high and the low frequencies is essential for the accurate determination of the response of shells to random pressure field, such as those generated by internal or external flow. Accordingly, the present method, because of its usage of classical theory for the displacement functions, may lead to the determination of the high as well as the low frequencies with high accuracy [4]. Apart from this, the main advantage of this theory is that it may be used, without modification, to obtain the free vibration characteristics and the response of any anisotropic cylindrical shell which is geometrically axially symmetric, no matter how many property discontinuities may be present, and for whatever boundary conditions.

The extension of this theory to the more general case of curved-shell finite elements is envisaged, with which shells of any shape could be analysed with enhanced precision. Another extension to this work will be to consider the effects of all the components arising from the presence of flowing or stationary fluids, on the natural frequencies for the cases of completely or partially-filled shells.

ACKNOWLEDGEMENTS

This research is supported by the National Research Council of Canada (Grant No. A8814) whose assistance is gratefully acknowledged. The author wishes to express his thanks to Dr. Nicholas Salamon for providing comments on the draft of this paper.

APPENDIX I

Matrix [R]

$$\left[\begin{array}{cccc} e^{-\psi_1}[\bar\alpha_1\cos\zeta_1-\bar\alpha_2\sin\zeta_1] & e^{-\psi_1}[\bar\alpha_2\cos\zeta_1+\bar\alpha_1\sin\zeta_1] & e^{-\psi_2}[\bar\alpha_3\cos\zeta_2-\bar\alpha_4\sin\zeta_2] & e^{-\psi_2}[\bar\alpha_4\cos\zeta_2+\bar\alpha_3\sin\zeta_2] \\ e^{-\psi_1}\cos\zeta_1 & e^{-\psi_1}\sin\zeta_1 & e^{-\psi_2}\cos\zeta_2 & e^{-\psi_2}\sin\zeta_2 \\ e^{-\psi_1}[\bar\beta_1\cos\zeta_1-\bar\beta_2\sin\zeta_1] & e^{-\psi_1}[\bar\beta_2\cos\zeta_1+\bar\beta_1\sin\zeta_1] & e^{-\psi_2}[\bar\beta_3\cos\zeta_2-\bar\beta_4\sin\zeta_2] & e^{-\psi_2}[\bar\beta_4\cos\zeta_2+\bar\beta_3\sin\zeta_2] \end{array}\right.$$

$$\left.\begin{array}{cccc} e^{\psi_1}[\bar\alpha_5\cos\zeta_1-\bar\alpha_6\sin\zeta_1] & e^{\psi_1}[\bar\alpha_6\cos\zeta_1+\bar\alpha_5\sin\zeta_1] & e^{\psi_2}[\bar\alpha_7\cos\zeta_2-\bar\alpha_8\sin\zeta_2] & e^{\psi_2}[\bar\alpha_8\cos\zeta_2+\bar\alpha_7\sin\zeta_2] \\ e^{\psi_1}\cos\zeta_1 & e^{\psi_1}\sin\zeta_1 & e^{\psi_2}\cos\zeta_2 & e^{\psi_2}\sin\zeta_2 \\ e^{\psi_1}[\bar\beta_5\cos\zeta_1-\bar\beta_6\sin\zeta_1] & e^{\psi_1}[\bar\beta_6\cos\zeta_1+\bar\beta_5\sin\zeta_1] & e^{\psi_2}[\bar\beta_7\cos\zeta_2-\bar\beta_8\sin\zeta_2] & e^{\psi_2}[\bar\beta_8\cos\zeta_2+\bar\beta_7\sin\zeta_2] \end{array}\right]$$

$$\omega_j=\kappa_j l/r,\quad \eta_j=\mu_j l/r,\quad \psi_j=\kappa_j x/r,\quad \zeta_j=\mu_j x/r;\qquad j=1,2,$$

Matrix [A]

$$\left[\begin{array}{cccccccc} \bar\alpha_1 & \bar\alpha_2 & \bar\alpha_3 & \bar\alpha_4 & \bar\alpha_5 & \bar\alpha_6 & \bar\alpha_7 & \bar\alpha_8 \\ 1 & 0 & 1 & 0 & 1 & 0 & 1 & 0 \\ -\kappa_1/r & \mu_1/r & -\kappa_2/r & \mu_2/r & \kappa_1/r & \mu_1/r & \kappa_2/r & \mu_2/r \\ \bar\beta_1 & \bar\beta_2 & \bar\beta_3 & \bar\beta_4 & \bar\beta_5 & \bar\beta_6 & \bar\beta_7 & \bar\beta_8 \\ e^{-\omega_1}[\bar\alpha_1\cos\eta_1-\bar\alpha_2\sin\eta_1] & e^{-\omega_1}[\bar\alpha_2\cos\eta_1+\bar\alpha_1\sin\eta_1] & e^{-\omega_2}[\bar\alpha_3\cos\eta_2-\bar\alpha_4\sin\eta_2] & e^{-\omega_2}[\bar\alpha_4\cos\eta_2+\bar\alpha_3\sin\eta_2] & e^{\omega_1}[\bar\alpha_5\cos\eta_1-\bar\alpha_6\sin\eta_1] & e^{\omega_1}[\bar\alpha_6\cos\eta_1+\bar\alpha_5\sin\eta_1] & e^{\omega_2}[\bar\alpha_7\cos\eta_2-\bar\alpha_8\sin\eta_2] & e^{\omega_2}[\bar\alpha_8\cos\eta_2+\bar\alpha_7\sin\eta_2] \\ e^{-\omega_1}\cos\eta_1 & e^{-\omega_1}\sin\eta_1 & e^{-\omega_2}\cos\eta_2 & e^{-\omega_2}\sin\eta_2 & e^{\omega_1}\cos\eta_1 & e^{\omega_1}\sin\eta_1 & e^{\omega_2}\cos\eta_2 & e^{\omega_2}\sin\eta_2 \\ \frac{e^{-\omega_1}}{r}[-\kappa_1\cos\eta_1-\mu_1\sin\eta_1] & \frac{e^{-\omega_1}}{r}[\mu_1\cos\eta_1-\kappa_1\sin\eta_1] & \frac{e^{-\omega_2}}{r}[-\kappa_2\cos\eta_2-\mu_2\sin\eta_2] & \frac{e^{-\omega_2}}{r}[\mu_2\cos\eta_2-\kappa_2\sin\eta_2] & \frac{e^{\omega_1}}{r}[\kappa_1\cos\eta_1-\mu_1\sin\eta_1] & \frac{e^{\omega_1}}{r}[\mu_1\cos\eta_1+\kappa_1\sin\eta_1] & \frac{e^{\omega_2}}{r}[\kappa_2\cos\eta_2-\mu_2\sin\eta_2] & \frac{e^{\omega_2}}{r}[\mu_2\cos\eta_2+\kappa_2\sin\eta_2] \\ e^{-\omega_1}[\bar\beta_1\cos\eta_1-\bar\beta_2\sin\eta_1] & e^{-\omega_1}[\bar\beta_2\cos\eta_1+\bar\beta_1\sin\eta_1] & e^{-\omega_2}[\bar\beta_3\cos\eta_2-\bar\beta_4\sin\eta_2] & e^{-\omega_2}[\bar\beta_4\cos\eta_2+\bar\beta_3\sin\eta_2] & e^{\omega_1}[\bar\beta_5\cos\eta_1-\bar\beta_6\sin\eta_1] & e^{\omega_1}[\bar\beta_6\cos\eta_1+\bar\beta_5\sin\eta_1] & e^{\omega_2}[\bar\beta_7\cos\eta_2-\bar\beta_8\sin\eta_2] & e^{\omega_2}[\bar\beta_8\cos\eta_2+\bar\beta_7\sin\eta_2] \end{array}\right]$$

REFERENCES

[1]M. P. Paidoussis and A. A. Lakis, 1973, Atomic Energy of Canada Ltd., AECL Report 4362. [2] M. P. Paidoussis and A. A. Lakis, 1972, Journal of Sound and Vibration Vol. 24, p. 51-62. [3] O. C. Zienkiewicz and Y. K. Cheung, 1968, the finite-element method in structural and continuum mechanics. [4]A. A. Lakis and M. P. Paidoussis, 1972, Journal fo Mechanical Engineering Science Vol. 14, p. 49-71. [5]A. A. Lakis and M. P. Paidoussis, 1972, Journal of Sound and Vibration, Vol. 25, p. 1-27. [6]A. A. Lakis and M. P. Paidoussis, 1971, Journal fo Sound and Vibration, Vol. 19, p. 1-15. [7]J. L. Sanders, 1959, NASA-TR-R24. [8]S. A. Ambartsumyan, 1961, NASA-TT-F-118. [9]H. P. Bakewell Jr., G. F. Carey, J. J. Libuha, H. H. Schloermer and W. A. Von Winkle, 1962, U.S. Navy Underwater Sound Lab., No. 559. [10]J. M. Clinch, 1969, Journal of Sound and Vibration, Vol. 9, p. 398-420. [11]C. A. Mercer and J. K. Hammond, 1968, Journal of Sound and Vibration Vol. 7, p. 49-61. [12]J. M. Clinch, 1970, Journal of Sound and Vibration, Vol. 12, p. 429-451.

Noise, Shock & Vibration Conference, 1974 Monash University, Melbourne

LARGE AMPLITUDE VIBRATION OF VARIABLE THICKNESS SKEW PLATES

M. Sathyamoorthy
Department of Aeronautical Engineering
Indian Institute of Technology
Madras, India

K. A. V. Pandalai
Department of Aeronautical Engineering
Indian Institute of Technology
Madras, India

SUMMARY -

The governing dynamic equations for the large amplitude flexural vibration of orthotropic skew plates of variable thickness are derived in this paper making use of a simple formulation originally proposed by Berger for the large amplitude static problems concerning rectangular plates. On the basis of an assumed vibration mode of the product form, the relationship between the amplitude and period is studied for isotropic and orthotropic skew plates of various aspect ratios and skew angles taking the variation of plate thickness to be linear along one of the co-ordinate directions. It is found that the modal equation reduces to the Duffing type of equation for which exact solution exists. The results show that the period of large amplitude vibration decreases with increasing amplitude, exhibiting hardening type of nonlinearity. Furthermore, the static problems of large deflections of skew plates are also discussed.

NOTATION -

a, b = dimensions of the plate

C = $\cos\theta$

D_1 = $\dfrac{E_1 h_o^3}{12}$

h = $h(x, y)$, thickness of plate

k^2 = $\dfrac{E_\eta}{E_\xi}$

m^2 = $\dfrac{(k^2 - q^4 - 2p^2q^2)}{p^2}$

p^2 = $\dfrac{G(1 - \nu_{\xi\eta}\nu_{\eta\xi})}{E_\xi}$

q^2 = $\nu_{\xi\eta}$

r = (a/b), plate aspect ratio

S = $\sin\theta$

t = time

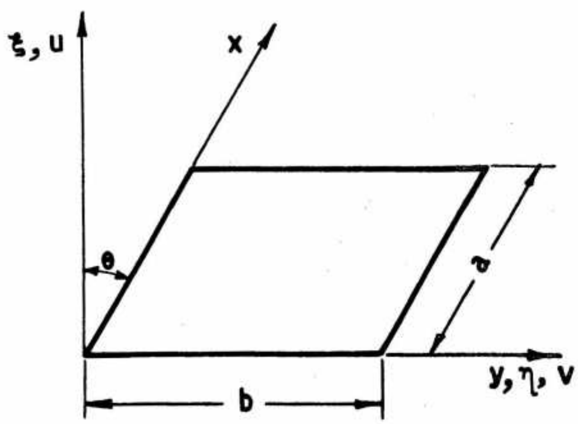

Geometry and coordinate system

FIG.1

t_1 = $(S/C) = \tan\theta$
w = lateral deflection of plate
x,y = oblique co-ordinates
ξ,η = cartesian co-ordinates
ρ = mass per unit area
τ = $\{t/a^2\sqrt{\frac{D_1}{\rho}}\}$, nondimensional time
θ = skew angle

INTRODUCTION -

Oblique panels are extensively used in modern aircraft industry and the study of large amplitude vibration of such thin panels is of practical importance because of the fact that when the flexural vibrations involve large amplitudes, the frequency of free or forced vibration is very much dependent upon the amplitude. Although the work on the flexure of rectangular plates of variable thickness was initiated as early as 1934 (3), to the authors knowledge there seems to be no literature at all on the large amplitude free flexural vibration of skew plates of variable thickness. Also, the literature available on the large amplitude flexural vibration of skew plates of constant thickness is also very limited (2,6).

This paper deals with the large amplitude free flexural vibration of thin elastic orthotropic clamped skew plates of variable thickness. The thickness is assumed to vary linearly along the x co-ordinate direction (Fig. 1). As in the previous investigations involving large amplitude flexural vibrations, the analysis is based on an assumed vibration mode of the product form and a one-term solution is considered. This is because of the significant increase in the algebraic and numerical work that is involved in working with a series of several terms. The nonlinearities investigated here arise due to the presence of nonlinear terms in the strain-displacement relations. The material constants of the orthotropic plate are with reference to the orthogonal system of axes (Fig.1).

It has been shown by the authors that the simplified formulation originally due to Berger (1) when extended to skew plates (4) yields very good results (5) and this simplified formulation is presently used to study the large amplitude vibration of variable thickness skew plates. Amplitude is plotted against period for the cases of orthotropic as well as isotropic material. In each, different aspect ratios, skew angles and taper ratios of the plate are considered. The influence of the orthotropic material constants, the effects of skew angle and taper ratio on the nonlinear response are also discussed. On specialising the present results, it is found that there is very good agreement with those available in the literature (7).

GOVERNING EQUATIONS -

The geometry of the plate and the co-ordinate system are shown in Fig. 1. x and y are oblique co-ordinates and θ is the skew angle. The nonlinear strain-displacement relations in oblique co-ordinates are (4):

$$\begin{aligned}
\epsilon_x &= \epsilon_1 - z\,w_{,xx} = C\,u_{,x} + S\,v_{,x} + \tfrac{1}{2}\,w_{,x}^2 - z\,w_{,xx} \\
\epsilon_y &= \epsilon_2 - z\,w_{,yy} = v_{,y} + \tfrac{1}{2}\,w_{,y}^2 - z\,w_{,yy} \\
\gamma_{xy} &= \gamma - 2z\,w_{,xy} = C\,u_{,y} + v_{,x} + S\,v_{,y} + w_{,x}\,w_{,y} - 2z\,w_{,xy}
\end{aligned} \tag{1}$$

The stresses are related to the strains by:

$$\begin{Bmatrix}\sigma_x\\ \sigma_y\\ \tau_{xy}\end{Bmatrix} = [a_{ij}] \begin{Bmatrix}\epsilon_x\\ \epsilon_y\\ \gamma_{xy}\end{Bmatrix} \tag{2}$$

where,

$$a_{ij} = a_{ji} \text{ and}$$

$$a_{11} = \frac{E_1}{C^3}$$

$$a_{12} = a_{21} = \frac{1}{C}(E_3 + E_1\ t_1^2)$$

$$a_{13} = a_{31} = -\ E_1\ S/C^3$$

$$a_{22} = C\ \{E_1\ t_1^4 + E_2 + 2t_1^2\ (E_3 + 2G)\}$$

$$a_{23} = a_{32} = -\ t_1\ \{E_1\ t_1^2 + E_3 + 2G\}$$

$$a_{33} = \frac{1}{C}(G + E_1\ t_1^2)$$

In the above,

$$E_1 = \frac{E_\xi}{\gamma'}\ ;\quad E_2 = \frac{E_\eta}{\gamma'}$$

$$E_3 = \frac{E_\eta \nu_{\eta\xi}}{\gamma'} = \frac{E_\xi \nu_{\xi\eta}}{\gamma'}\ ;\quad \gamma' = (1 - \nu_{\xi\eta}\nu_{\eta\xi})$$

G, E_ξ , E_η , $\nu_{\xi\eta}$ and $\nu_{\eta\xi}$ are the elastic constants of the orthotropic material in the ξ and η directions respectively. It will be recalled that only four of the above elastic constants are independant.

The stress and moment resultants can now be readily obtained from the definitions

$$N_{ij} = \int_{-h/2}^{h/2} \sigma_{ij}\ dz\ ;\qquad M_{ij} = \int_{-h/2}^{h/2} \sigma_{ij}\ z\ dz \tag{3}$$

The expression for the strain energy is given by

$$U_{strain} = U_{Ext} + U_{Bending}$$

where, the extensional strain energy is given by

$$U_{Ext} = \frac{1}{2}\int_x\int_y h\ (a_{11}\ \epsilon_1^2 + a_{22}\ \epsilon_2^2 + a_{33}\gamma^2$$
$$+ 2a_{12}\ \epsilon_1\ \epsilon_2 + 2a_{13}\ \epsilon_1\gamma + 2a_{23}\ \epsilon_2\gamma\ )\ dx\ dy \tag{4}$$

and the strain energy is bending is given by

$$U_{Bending} = \frac{1}{24}\int_x\int_y h^3\ (a_{11}\ w_{,xx}^2 + a_{22}\ w_{,yy}^2$$
$$+ 4a_{33}\ w_{,xy}^2 + 2a_{12}\ w_{,xx}\ w_{,yy} + 4a_{13}\ w_{,xx}\ w_{,xy}$$
$$+ 4a_{23}\ w_{,yy}\ w_{,xy})\ dx\ dy \tag{5}$$

The kinetic energy of the plate is given by

$$T = \frac{C\rho}{2}\int_x\int_y \left(\frac{\partial w}{\partial t}\right)^2 dx\ dy \tag{6}$$

In accordance with the Berger (1955) formulation suggested originally for static problems of rectangular plates, the expression for the extensional strain energy given by equation (4) can be written in a simplified form as (4) :

$$U_{Ext} = \frac{E_1}{2C^3} \int_x \int_y h \{\epsilon_1 + \lambda_1 \epsilon_2 + (\lambda_2 + \lambda_3)\gamma\}^2 \quad dx \quad dy \tag{7}$$

where, $\lambda_1 = \sqrt{\frac{a_{22}}{a_{11}}} = \sqrt{K_5}$

$$\lambda_2 = \sqrt{\frac{-2a_{13}}{a_{11}}} = \sqrt{\frac{-K_7}{2}}$$

$$\lambda_3 = \sqrt{\frac{-2a_{23}}{a_{11}}} = \sqrt{\frac{-K_8}{2}}$$

and $K_5 = C^4 \{K^2 + t_1^4 + 2(q^2 + 2p^2)\, t_1^2\}$

$$K_7 = -4S$$

$$K_8 = -4SC^2(t_1^2 + q^2 + 2p^2)$$

By means of Equations (5), (6) and (7) and the Hamilton's principle the following two equations governing the large amplitude flexural vibration of orthotropic skew plates can be derived:

$$h\{\epsilon_1 + \lambda_1 \epsilon_2 + (\lambda_2 + \lambda_3)\gamma\} = \frac{\delta^2 h_o^3}{12} \tag{8}$$

$$\frac{D_1 \delta^2}{C^3}\{w_{,xx} + \lambda_1 w_{,yy} + 2(\lambda_2 + \lambda_3)\, w_{,xy}\} - \rho\, C\, \frac{\partial^2 w}{\partial t^2} = L(w,h) \tag{9}$$

where,

$\delta = \delta(t)$ and h_o is the plate thickness at $x = 0$.

Also,

$$\begin{aligned} L(w,h) = {} & \frac{E_1' h^3}{3} L(w) + E_1' h\Big[\{h \frac{\partial^2 h}{\partial x^2} + 2(\frac{\partial h}{\partial x})^2\}\{w_{,xx} + K_9 w_{,yy} \\ & + \frac{K_7}{2} w_{,xy}\} + \{h \frac{\partial^2 h}{\partial y^2} + 2(\frac{\partial h}{\partial y})^2\}\{K_9 w_{,xx} \\ & + K_5 w_{,yy} + \frac{K_8}{2} w_{,xy}\} + \{h \frac{\partial^2 h}{\partial x \partial y} \\ & + 2(\frac{\partial h}{\partial x})(\frac{\partial h}{\partial y})\}\{\frac{K_7}{2} w_{,xx} + \frac{K_8}{2} w_{,yy} + K_{10} w_{,xy}\}\Big] \quad ; \end{aligned}$$

$$\begin{aligned} L(w) = {} & (w_{,xxxx} + K_5 w_{,yyyy} + K_6 w_{,xxyy} \\ & + K_7 w_{,xxxy} + K_8 w_{,yyyx}) \end{aligned}$$

$$K_6 = 2C^2(3t_1^2 + q^2 + 2p^2)$$

$$K_9 = C^2(q^2 + S^2/C^2)$$

$$K_{10} = 4C^2(p^2 + S^2/C^2)$$

and $E_1' = \frac{E_1}{4C^3}$

Equations (8) and (9) are the governing equations for the large amplitude free flexural vibration of orthotropic skew plates of variable thickness in this simplified formulation. These two equations when specialised for the case of the isotropic rectangular plate reduce to the well known Berger Equations given by Wah (7).

METHOD OF SOLUTION

For skew plates clamped along all its four edges the boundary conditions to be satisfied are:

$$w = w_{,x} = 0 \quad \text{at} \quad x = 0 \quad \text{and} \quad a$$

$$w = w_{,y} = 0 \quad \text{at} \quad y = 0 \quad \text{and} \quad b \tag{10}$$

A deflection function that satisfies all the above boundary conditions is

$$\left(\frac{w}{h_o}\right) = \frac{f(\tau)}{4}\left(1 - \cos\frac{2\pi x}{a}\right)\left(1 - \cos\frac{2\pi y}{b}\right) \tag{11}$$

When all the edges of the plate are immovable, the in-plane edge conditions are

$$u = v = 0 \quad \text{at} \quad x = 0 \text{ and } a \; ; \quad y = 0 \text{ and } b \tag{12}$$

Let us consider plates with linear taper in the x direction so that

$$h = h_o\left(1 + \frac{\alpha x}{a}\right) \tag{13}$$

in which $(1+\alpha)$ is the ratio of the plate thickness at $x = a$ to the thickness at $x = 0$. Noting that δ^2 in Equation (8) is independant of x and y, Equation (8) can be integrated to yield δ^2. Thus substituting for ϵ_1, ϵ_2 and γ in terms of displacements u, v and w from Equation (1) and for h^2 from Equation (13) and making use of the inplane edge conditions given by (12), for the assumed mode shape 'w' given by Equation (11), δ^2 is obtained as:

$$\frac{\delta^2 h_o^3}{12} = \frac{3}{32}\,\frac{f^2\,\pi^2\,h_o^3}{a^2}\,(1 + \lambda_1\, r^2)\,(1 + \alpha/2)$$

(a) Large Amplitude Vibration:

With this expression for δ^2, Galerkin method is applied on Equation (9) to obtain a modal equation of the form

$$\frac{d^2 f}{d\tau^2} + A^2 f + B^2 f^3 = \mu\,\bar{q}_n \tag{14}$$

where,

$$A^2 = \frac{16}{3}\,\frac{\pi^4}{C^4}\Big\{(1 + K_5\, r^4 + K_6\, r^2/3)\,(1 + 3\alpha/2 + \alpha^2 + \frac{\alpha^3}{4})$$
$$- 3/2\;\; \alpha^2/\pi^2(1 + K_9\, r^2)(1 + \alpha/2)\Big\}$$

$$B^2 = \frac{3\pi^4}{2C^4}(1 + \lambda_1\, r^2)^2\,(1 + \alpha/2)$$

$$\mu = \frac{16}{9} \quad \text{and} \quad \bar{q}_n = \frac{q_n\, a^4}{D_1\, h_o}$$

The exact solution to the well known modal equation (14) is given by:

$$f(\tau) = \bar{w}\; Cn\,(\omega\tau,\, g_1) \tag{15}$$

where Cn is the elliptic cosine and the nonlinear frequency,

$$\omega = \{A^2 + B^2\,(\bar{w})^2\}^{1/2}$$

The solution for f in terms of the elliptic cosine has a period

$$\left(\frac{T}{T_o}\right) = \frac{2A\;F_1(g_1)}{\pi\sqrt{A^2 + B^2(\bar{w})^2}} \tag{16}$$

where, $F_1(g_1)$ is the complete elliptic integral of the first kind and T_o is the linear period given by $T_o = 2\pi/A$.

Also, $g_1^2 = \dfrac{B^2(\overline{w})^2}{2\,\{A^2 + B^2(\overline{w})^2\}}$

It is clear from Equation (16) that the period of nonlinear vibration decreases with increasing amplitude exhibiting hardening type of nonlinearity.

Amplitude Vs. period is plotted for clamped skew plates with various skew angles, aspect ratios and taper ratios considering isotropic as well as orthotropic cases. The material constants of the plate for the two cases considered here are:

(See Figs. 2-8)

	K^2	q^2	p^2
Isotropic	1.0	0.3	0.35
Orthotropic	0.5	0.025	0.1

(b) Large Deflections:

It is interesting to note that the governing equation for the static problem involving large deflection of orthotropic skew plates subjected to uniformly distributed load $q_n = q_o$ can be readily obtained from Eqn.(14). For this purpose f has to be taken as independent of time so that $\frac{d^2 f}{d\tau^2} = 0$ and $f = (\frac{w_{max}}{h}) = w'$. Thus the load-deflection relation becomes,

$$A^2\, w' + B^2 (w')^3 = \frac{16}{9}\,\overline{q}_o \qquad (17)$$

The relationship between the load and deflection is plotted for a few cases and are shown in Figs. 9 to 11.

CONCLUSIONS

The approximate formulation originally due to Berger which is extended here for the study of orthotropic skew plates of variable thickness is found to yield results which agree well with those available in the literature for the limiting cases. The relationship between the amplitude and period exhibits hardening type of nonlinearity i.e., the period decreases with increasing amplitude for all the cases considered in this paper. The effect of taper is found to make the hardening tendency of the period versus amplitude behaviour less pronounced. The results presented here are limited in the sense that only one term is used in the series for w but in the absence of any other better method this is believed to represent an initial effort in obtaining better solutions.

REFERENCES

1. H.M. BERGER, 'A New Approach to the Analysis of Large Deflection of Plates', Jl. App. Mech., Vol. 22, 1955, p. 465.
2. J.L. NOWINSKI, 'Large Amplitude Oscillations of Oblique Panels with an Initial Curvature', AIAAJ, Vol.2, No.6, 1964, p.1025.
3. R.G. OLSSON, 'Biegung der Rechteckplatte bei linear Veranderlicher Beigungs-steifigkeit', Ingenieur-Archiv, Vol.5, 1934, p.363.
4. M. SATHYAMOORTHY and K.A.V. PANDALAI, 'Governing Equations for the Large Amplitude Flexural Vibrations of Plates and Shells', I.I.T.(M) AE Report No.19, Feb 1972.
5. M. SATHYAMOORTHY and K.A.V. PANDALAI? 'Vibration of Simply Supported - Clamped Skew Plates at Large Amplitudes', I.I.T.(M) AE Report No.29, May 1972 (Journal of Sound and Vibration, Vol.27, No.1, 8 March 1973).
6. M. SATHYAMOORTHY and K.A.V. PANDALAI, 'Nonlinear Flexural Vibration of Orthotropic Skew Plates', Journal of Sound and Vibration, Vol. 24, No.1, September 1972, p.115.
7. T. WAH, 'Large Amplitude Flexural Vibration of Rectangular Plates', Int. J. Mech. Sc., Vol.5, No.6, 1963, p. 425.

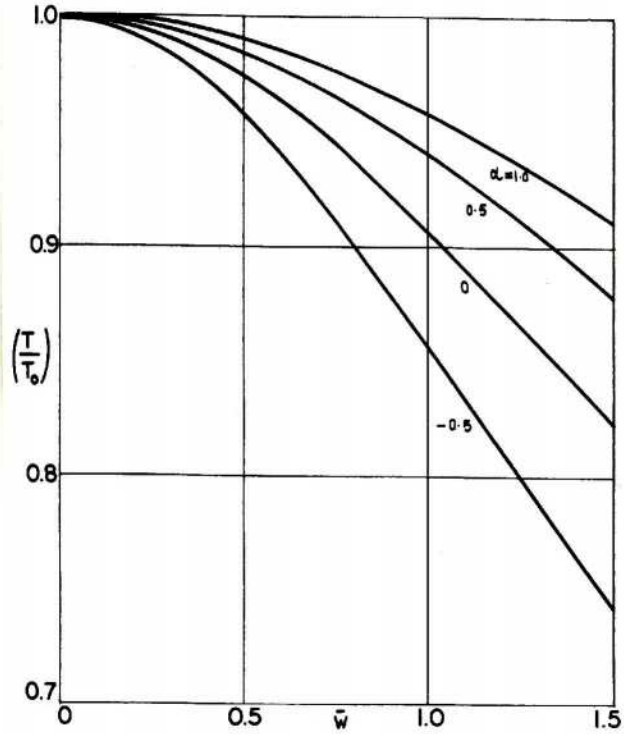

Amplitude vs period
all values of θ, r = 0, isotropic and orthotropic

FIG.2

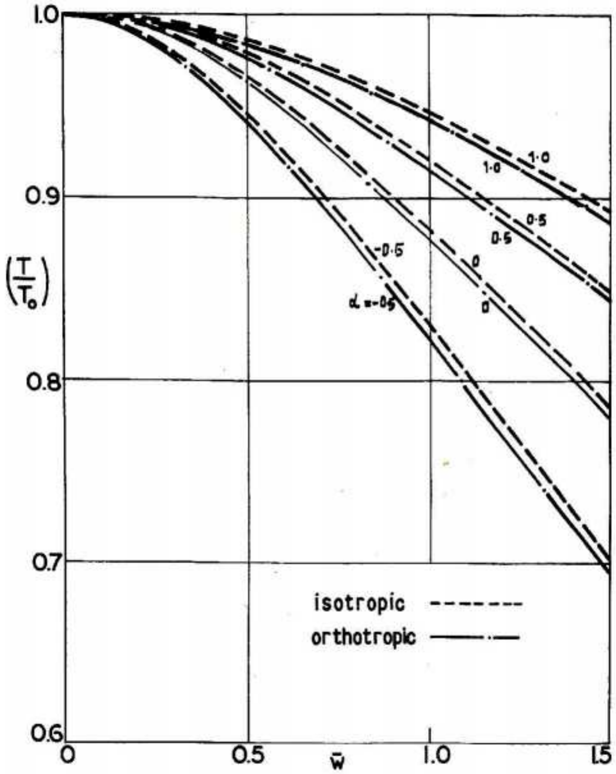

Amplitude vs period
θ = 0 , r = 0.5

FIG.3.

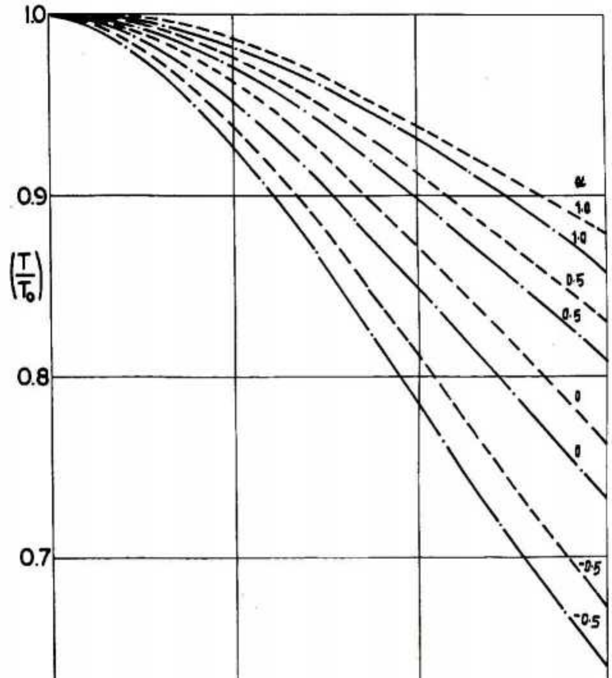

Amplitude vs period
θ = 0, r = 1.0

FIG.4

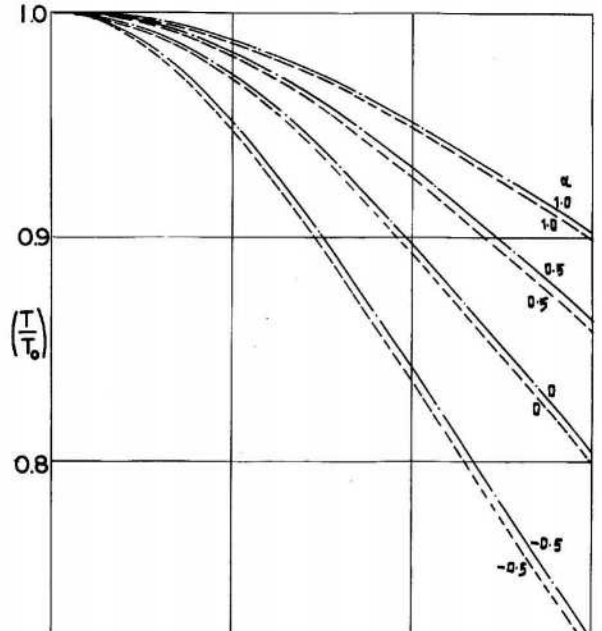

Amplitude vs period
θ=30°, r = 0.5

FIG. 5.

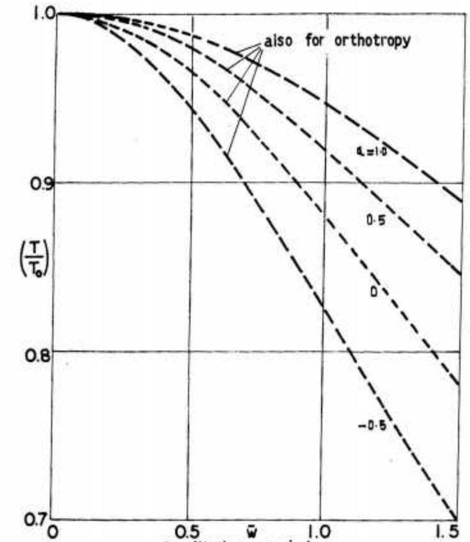

Amplitude vs period
θ = 30° r = 1.0
FIG.6.

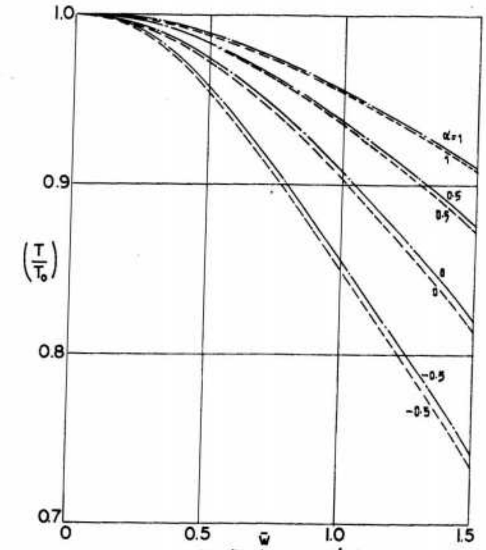

Amplitude vs period
θ=60° r=0.5
FIG.7

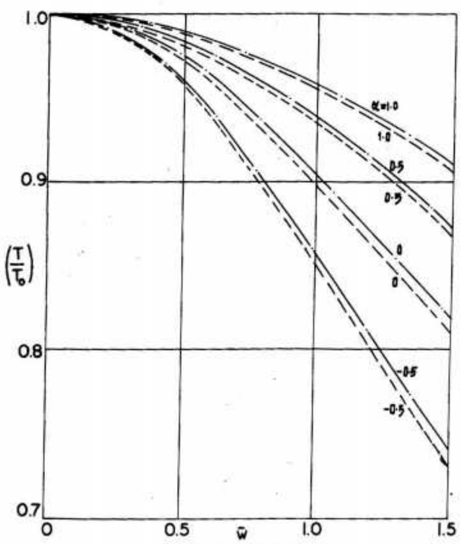

Amplitude vs period
θ = 60°, r = 1.0
FIG. 8.

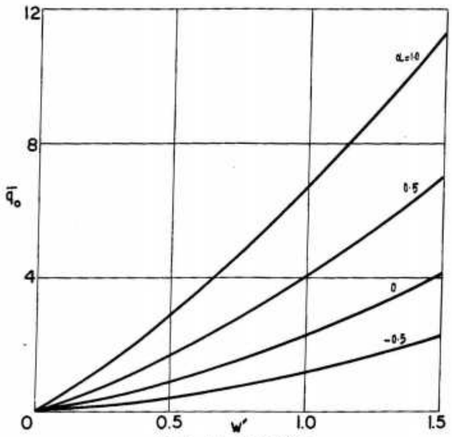

Load vs deflection
r = 0, all θ, isotropic & orthotropic
FIG. 9

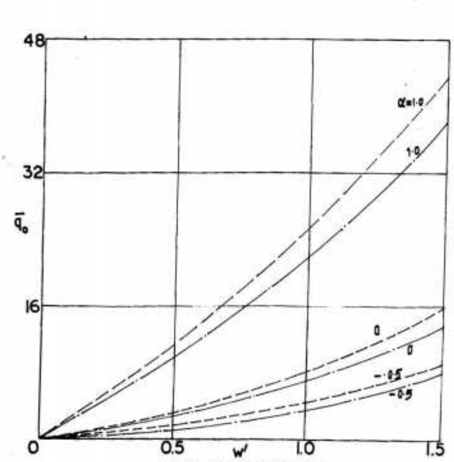

Load versus deflection
θ = 60°, r = 1
FIG.11

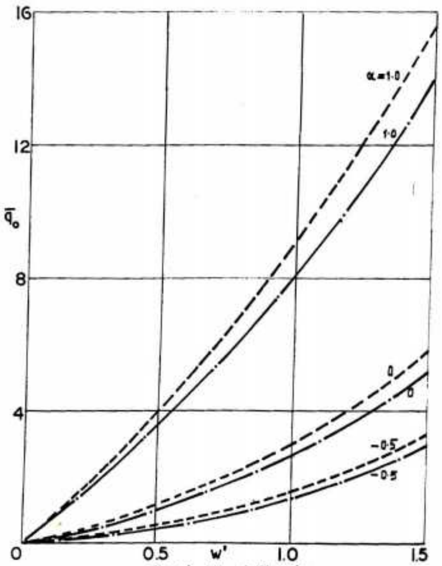

Load vs deflection
θ = 30°, r = 0.5
FIG. 10

TRANSVERSE VIBRATION OF ELLIPTIC PLATES WITH INPLANE FORCES

R. Jones
Department of Civil Engineering
Swinburne College of Technology
Hawthorn, Victoria

J. Mazumdar
Department of Applied Maths
University of Adelaide
Adelaide, S.A.

SUMMARY - The transverse vibration of thin elliptic plates with inplane forces is analyzed using a recently developed method. The method is based on the concept of contour lines of equal deflection on the surface of the plate. All details of the analysis are explained by graphs.

1. INTRODUCTION

The present study represents an extension of the method recently developed in four earlier publications [1,2,3,4] dealing with the bending, buckling, and vibration of thin elastic plates and shallow shells.

In the work which follows a brief resume of the method is first presented. This is then followed by a discussion of the transverse vibration of a thin elliptic plate with inplane forces, the edges of the plate being either clamped or simply supported.

2. THEORY

Consider a thin elastic, isotropic plate of thickness h loaded by compressive or tensile forces acting in the middle surface of the plate. Let the XOY plane coincide with the middle plane, and let the z axis be directed positively downward. When the plate vibrates in a normal mode the deflected form maintained by the plate at any instant τ may be described by a family of lines of equal deflection and it is possible to write

$$w(x,y,\tau) = W(x,y)\cos(\omega\tau + \varepsilon), \qquad (2.1)$$

where $\cos(\omega\tau + \varepsilon)$ is the normal coordinate, ω is the circular frequency, and W is the normal function determining the form of the deflected surface of the vibrating plate which is a suitable function of u, where $u(x,y) = \text{const.}$ is the equation of the lines of equal deflection.

Consider a portion of the plate bounded by a closed contour $u(x,y) = \text{const.}$ at any instant τ. The resultant tractions exerted upon this portion by the remainder will have components in the upward vertical direction given by $\oint V_n\, ds$ where

$$V_n = Q_n - \frac{\partial Mnt}{\partial s} - N_n \frac{\partial w}{\partial n}. \qquad (2.2)$$

The first term in (2.2) represents the shearing force, the second term is due to the distribution along the contour of the twisting moment, and the last term represents the component of the in-plane forces with act normal to the deflected middle surface of the plate. Consequently the application of D'Alembert's principle and the summing of the forces in the vertical direction yield the following dynamical equation.

$$\oint \left[Q_n - \frac{\partial Mnt}{\partial s} - N_n \frac{\partial w}{\partial n}\right] ds + \rho h \iint_{\Omega} \frac{\partial^2 w}{\partial \tau^2}\, dxdy = 0. \qquad (2.3)$$

The double integral in (2.3) is taken over the region bounded by the curve u = const. and represents the inertial force due to the vertical acceleration, ρ being the mass per unit area of the plate. If we now substite the well known expressions for Mn,Qn, and Mnt into (2.3) we finally obtain

$$\frac{d^3W}{du^3}\oint Rds + \frac{d^2W}{du^2}\oint Fds + \frac{dW}{du}\oint Gds + \frac{dW}{dn}\oint N_n\sqrt{t}\ .ds - \rho h\omega^2\iint_\Omega Wd\Omega = 0, \quad (2.4)$$

where the factor $\cos(\omega\tau + \varepsilon)$ has been cancelled. While deriving equation (2.4) use was made of the fact that W and its derivatives with respect to u are constant on the contour u = const. Here R,F,G etc are the following expressions involving u and its partial derivatives

$$R = -Dt^{3/2}$$

$$F = -D[3u_{xx}u_x^2 + 3u_{yy}u_y^2 + u_{xx}u_y^2 + u_{yy}u_x^2 + 4u_{xy}u_xu_y]\ /t^{1/2}$$

$$G = -D[u_{xxx}u_x^3 + u_{yyy}u_y^3 + (2-\mu)\ (u_{xxx}u_xu_y^2 + u_{yyy}u_x^2 + u_{xyy}u_x^3 + u_{xxy}u_y^3) + (2\mu - 1)\ (u_{xyy}u_xu_y^2$$

$$+ u_{xxy}u_x^2u_y) - 2(1-\mu)\ u_{xy}\ (u_xu_yu_{xx} - u_y^2\,u_{xy} - u_x^2u_{xy} + u_xu_yu_{yy}) + (1-\mu)\ (u_{xx} - u_{yy})(u_{xx}u_y^2$$

$$- u_x^2u_{yy})]\ /t^{3/2} + 2D(1-\mu)\ [u_{xy}\ (u_x^2 - u_y^2) - u_xu_y(u_{xx} - u_{yy})]^2\ /t^{5/2}$$

$$t = u_x^2 + u_y^2, \quad (2.5)$$

where μ is Poisson's ratio and D is the flexural rigidity of the plate.

3. VIBRATION OF ELLIPTIC PLATES

Let us now discuss the transverse vibration of a thin elliptic plate subject to uniform edge loading $N_x = N_y = N$, $N_{xy} = 0$. Let the semimajor and semiminor axes of the ellipse be a, and b respectively, then with the coordinates as shown in figure 1 the equation of the boundary is given by

$$1 - x^2/a^2 - y^2/b^2 = 0. \quad (3.1)$$

If attention is confined to symmetrical forms of vibration then from symmetry considerations one may assume that the lines of equal deflection form a family of similar and similarly situated ellipses starting from the outer boundary as one of these lines. Therefore the equation of the lines of equal deflection may be taken to be of the form

$$u(x,y) = 1 - x^2/a^2 - y^2/b^2. \quad (3.2)$$

It should be stressed that in the case of a circular plate this is no longer an assumption.

If the above expression for u is substituted into (2.4) and the necessary integration performed we finally obtain.

$$(1-u)^2\frac{d^3W}{du^3} - 2(1-u)\frac{d^2W}{du^2} - \frac{Na^2b^2(a^2+b^2)\ (1-u)}{D(3a^4+2a^2b^2+3b^4)}\frac{dW}{du} - \frac{\rho h\omega^2a^3b^3}{2\pi D(3a^4+2a^2b^2+3b^4)}\iint_\Omega Wd\,\Omega = 0, \quad (3.3)$$

which after differentiation reduces to

$$(((1-u)\frac{d^2}{du} - \frac{d}{du} + \alpha^2)\ ((1-u)\frac{d^2}{du^2} - \frac{d}{du} - \beta^2)W = 0, \quad (3.4)$$

where

$$\alpha^2\ \beta^2 = \rho h\omega^2a^4b^4/2D(3a^4+2a^2b^2+3b^4), \quad (3.5)$$

and

$$\alpha^2 - \beta^2 = Na^2b^2(a^2+b^2)/D(3a^4+2a^2b^2+3b^3). \quad (3.6)$$

The general solution to equation (3.4) is

$$W = A_1 J_0(2\alpha f) + A_2Y_0(2\alpha f) + A_3I_0(2\beta f) + A_4K_0(2\beta f), \quad (3.7)$$

where

$$f^2 = 1-u. \quad (3.8)$$

If α and β can be obtained the natural frequency of vibration can easily be calculated.

The boundary conditions at the edge f=1 and the condition at the centre, f=0, must now be imposed. Consider the following two cases.

3.1 CASE 1. THE EDGES OF THE PLATE ARE CLAMPED.

In this case the clamping condition ultimately reduces to, [1];

$$W\bigg|_{f=1} = \frac{dW}{df}\bigg|_{f=1} = 0. \quad (3.9)$$

In order to avoid infinite deflection at the centre it is necessary to omit the second and the fourth term in (3.7). Consequently, aside from the trivial solution $A_1 = A_3 = 0$, solutions with non vanishing constants are obtained if and only if

$$\begin{vmatrix} J_0(2\alpha) & I_0(2\beta) \\ 2\alpha J_0'(2\alpha) & 2\beta I_0'(2\beta) \end{vmatrix} = 0, \quad (3.10)$$

which reduces to

$$2\alpha J_1(2\alpha)/J_0(2\alpha) + 2\beta I_1(2\beta)/I_0(2\beta) = 0. \quad (3.11)$$

The natural frequency of the plate may now be determined from equations (3.6) and (3.11). Figure 2. shows the relationship between the fundamental frequency parameter $\lambda = \sqrt{\rho h/D}\,\omega a^2$ and the non dimensionalized buckling load

$$\phi = Na^2b^2(a^2+b^2)/3.67D(3a^4+2a^2b^2+3b^4), \quad (3.12)$$

where the value of $\phi = -1$ represents the critical buckling load of a hydrostatically compressed plate as determined in [2].

CASE 2. THE BOUNDARY OF THE PLATE IS SIMPLY SUPPORTED.

Suppose now that the plate is simply supported along its edges. The constants A_1, and A_3 must now be chosen so as to satisfy, [1];

$$\text{i)}\quad W\bigg|_{f=1} = 0$$

$$\text{ii)}\quad \frac{d^2W}{df^2} + \frac{\mu}{f}\frac{dW}{df}\bigg|_{f=1} = 0. \quad (3.13)$$

After detailed algebraic computation the resulting determinant can be reduced to the following frequency equation.

$$2\alpha J_1(2\alpha)/J_0(2\alpha) + 2\beta I_1(2\beta)/I_0(2\beta) = 4(\beta^2-\alpha^2)/1-\mu. \quad (3.14)$$

The natural frequency of the plate may now be determined from equations (3.6) and (3.14) for various values of N, and aspect ratio $\delta = a/b$. Figure 3 shows the relationship between the frequency parameter $\lambda=\sqrt{\rho h/D}\ \omega a^2$ and the nondimensionalized buckling load

$$\phi = Na^2b^2(a^2+b^2)/1.05\ (3a^4+2a^2b^2+3b^4)D, \qquad (3.14)$$

where $\phi = -1$ represents the critical buckling load for the hydrostatically compressed plate, [2].

4. REMARKS

The classical results for the vibration of a simply supported polygonal plate subject to hydrostatic edge loading were first proposed by Lurie [5] who stated that "for any thin plate of polygonal shape and uniform thickness which is simply supported all along its edges and subjected to a uniform thrust N per unit length, the frequency ω follows the relationship

$$(\omega/\omega^*)^2 = 1-N/Ncrt. \qquad (4.1)$$

However since when the boundary is curved Navier boundary conditions are no longer applicable" Lurie concluded that although the relationship is exact for a simply supported plate with an arbitrary number of sides it is not valid in the limit when the number of sides becomes infinite.

Here ω^* is the fundamental frequency and the Ncrt is the critical buckling load for the polygonal plate.

It is curious that the exact linear law appears to break down in the limit.

We are thus led to investigate whether such a relationship holds for either the simply supported, or the clamped elliptic plate. Suprisingly it holds for both, see figs 4 and 5.

In both cases when the aspect ratio $a/b \to 1$ the above results coincide exactly with those obtained by Wah [6] for a circular plate.

5. BIBLIOGRAPHY

[1] J.MAZUMDAR, A method for Solving Problems of Elastic Plates of Arbitrary Shape, Journal of Australian Mathematical Society XI, Part 1, 1970.

[2] J.MAZUMDAR, Buckling of Elastic Plates by the Method of Constant Deflection Lines, Journal of Australian Mathematicsl Society XII, part 1, 1971.

[3] J.MAZUMDAR, Transverse Vibrations of Elastic Plates by the Method of Constant Deflections Lines, J. Sound and Vibration, 18, 1971.

[4] R.JONES and J.MAZUMDAR, Transverse Vibrations of Shallow Shells by the Method of Constant Deflection Contours J. Acoust. Soc. Am. (to be published)

[5] H.LURIE, Lateral Vibrations as Related to Structural Stability, J. Appl. Mech. Vol 19, No.2, pp195-204, 1952.

[6] T.WAH, Vibration of Circular Plates, J. Acoust. Soc. Am., Vol 34, No.3, pp275-281, 1962.

STRUCTURE LIFE PREDICTION USING BROAD BAND ACOUSTIC FATIGUE THEORY

L. Yeh
G E C Power Engineering Ltd.
Leicester, U.K.

SUMMARY

Engineering structures are often required to be designed to perform a duty with a specific life. Generally speaking it is possible that many sources of excitation may occur simultaneously in the structure. Such as mechanical, aerodynamic, turbulence and acoustic noise excitation. The life prediction is thus becoming very difficult. This paper describes a technique developed in the Mechanical Engineering Laboratory of G.E.C. Power Engineering Company, so that the structure may be tested at design stage in an acoustic testing facility. The measured broad band stresses may be extrapolated to the anticipated excitation spectrum from site measurements. By the use of a broad band acoustic fatigue theory the life of the structure may be predicted. The technique is widely used in the nuclear engineering field where a structure life expectancy of 30 years is required.

1. Introduction

The designers are often confronted with a problem of design of structure to perform its function for a certain specified time, under an environmental conditions which may vary tremendously from very high vacuum up to 10^{-12} Torr and low temperature - 120°C for some spacecraft structures to 750 to 1000 lb/in^2 and 750°C for nuclear reactor structures.

The source of excitation may be mechanical, aerodynamic, turbulence, and acoustic noise.

The period for which the structure is required to stand the environment may be a few seconds, e.g. the spacecraft structure required to stand the launching noise, or may be 30 years for the structures in the nuclear reactors. (Because of the radiation hazard which prevents maintenance and repair to be carried out inside the reactor after the nuclear fuel is activated.) It becomes very important that a technique should be developed for life prediction at the structure development stage.

This paper describes a technique developed by the Mechanical Engineering Laboratory of the GEC/EE Co. at Whetstone, which only involves the fatigue life of the structure due to narrow and broad band vibrational stresses. These stresses may be induced by acoustic noise or turbulence in the fluid of a nuclear reactor.

A typical acoustical structural failure is shown in Fig. 1, which is a diffuser of the CO_2 circulator, 6 to 7 ft. dia., 12 ft long made of ¼ inch thick mild steel with fillet and butt welds. Failure took place after about 1000 hours testing run in one of the early design reactors.

Since then acoustic fatigue tests have been carried out on fillet welded plate specimens 12" x 12" x ¼" thick fillet weld to a heavy 2" x 2" frame as shown in Fig. 2a. The specimen hangs at the mouth of the high intensity horn, Fig. 3c. The fatigue specimens were tuned to its resonant frequency by the use of noise generated by an electro-pneumatic noise generator with pure tone excitation. The shortest time to cause failure was 90 seconds at 159 dB. All four sides of the welds failed simultaneously. The fatigue life curve plotted Vs. noise level is given in Fig. 2.

However, in service, the stresses experienced by the structures are often narrow band with Rayleigh distribution (see Fig. 4) or most likely broad band, with multi-modal vibration, a

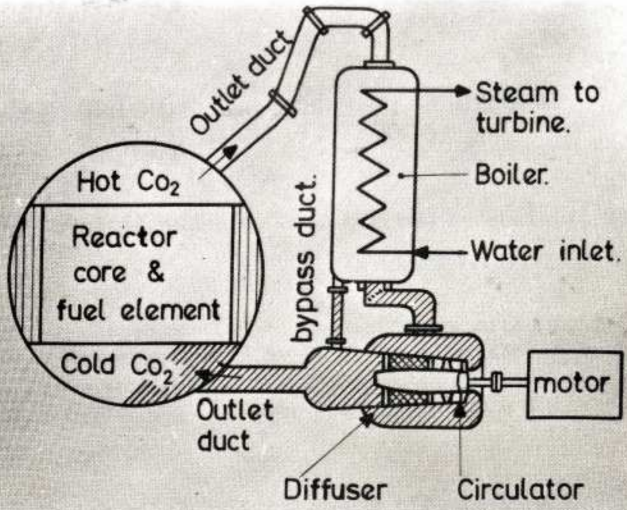

(a) A SIMPLIFIED SKETCH OF A NUCLEAR REACTOR. SHADED AREA SHOWS HIGH INTENSITY NOISE REGION.

(b) A TYPICAL SERVICE FAILURE DUE TO ACOUSTIC FATIGUE.

FIG 1.

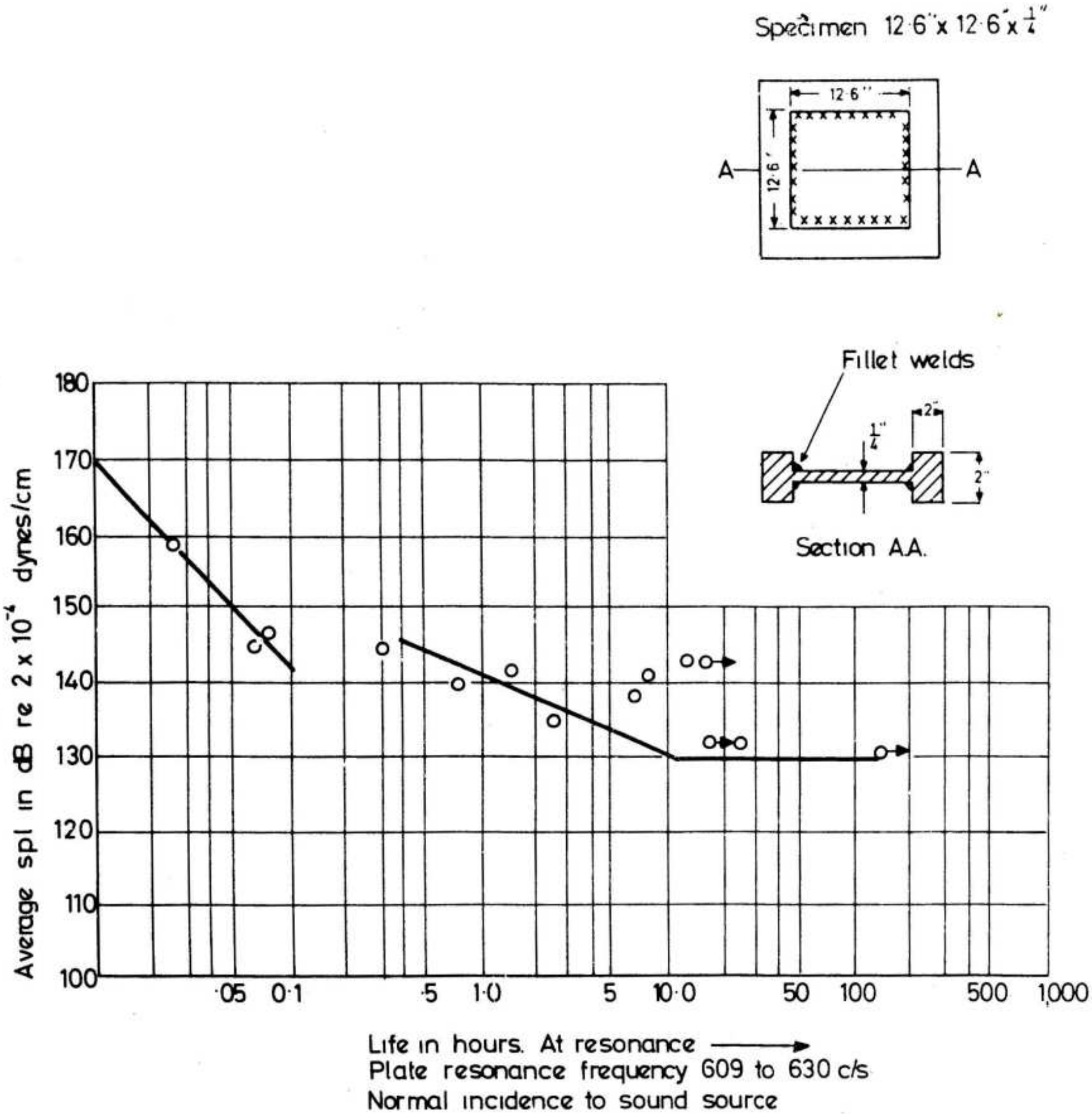

SOME ACOUSTIC FATIGUE RESULTS OF FILLET WELDS DUE TO PURE TONE EXCITATION

FIG. 2

typical structure response is shown in Fig. 5. The fatigue life prediction of these types of structures is the main concern of this paper.

2. Definition of acoustic stress or complex dynamic stress

2.1 Time average stresses

The conventional engineering stresses become inadequate in dealing with dynamic problems especially under random or acoustical excitation. The simple engineering stress expressed in lb/in^2 is useful for static (or D.C.) work, as the stress varies with time, for dynamic work, a time average stress or root mean square (r.m.s.) should be used. For sinusoid waveforms, the r.m.s. stress ($\sigma_{r.m.s.}$) is simply:-

$$\sigma_{r.m.s.(t)} = \frac{1}{\sqrt{2}} \quad \sigma_{0 \text{ to pk.}} \qquad \dots\dots\dots\dots \quad (1)$$

2.2 Spatial average stresses

The spatial average stress is an average stress covering an area of certain components and is defined as follows:

$$\sigma_{r.m.s.(t,\ s)} = \sqrt{\frac{1}{n}\left(\sigma_1^2 + \sigma_2^2 + \dots + \sigma_n^2\right)} \qquad \dots\dots\dots\dots \quad (2)$$

Experiments have been carried out on structures using from 6 to 250 strain gauges, the spatial average stress $\sigma_{r.m.s.(t,\ s)}$ evaluated, indicated a minimum of 12 randomly positioned strain gauges are required to get reasonable accurate spatial average stress results. (ref. 1).

2.3 Maximum/Spatial average stress ratio

The spatial average stress is useful as it simplifies the effect of the mode of vibration, and may be calculated easily by Statistical Energy Method (ref. 1). However, it is more important to determine the ratio of maximum stress/spatial average stress ratio. This ratio is found theoretically as 2.88 for simply supported plates (ref. 1), and 2.5 for beam type of structures (ref. 2). Experiments have shown that it never exceeds 3 for complex structures and 2.5 for beam type structures.

This maximum stress thus obtained is assumed to be applied at the weakest link of the structure and is used for the basis of fatigue life assessment.

2.4 Band stress and overall stress

Band stress are stresses induced on the structure by a band of frequency. The bandwidth could be changed from 1 or 2 Hz to say 20 k Hz.

With pure tone (single frequency) excitation at the resonance of structure a pure tone response may be obtained. (i.e. stress produced are of sine wave nature and of constant amplitude).

With narrow band excitation the stress response generally is of similar frequency but of varying amplitude (Fig. 4a top). As structures are mechanical filters, only allowing a narrow band of frequency to pass through it, the band width depends on its damping, generally about 20 - 30 Hz if the exciting frequency is within the band, narrow band response would be produced.

If the exciting bandwidth is wider then the structure bandwidth and a number of resonances may be excited at the same time the responded stress is called broad band stress. Fig. 4a bottom trace.

For acoustic work the noise measurement band pass filters are divided in ⅓ octave bands and octave bands. It is therefore convenient to use ⅓ octave band stress or octave band stress.

For acoustic excitation the noise level generally specified in S.P.L. (sound pressure level) in each ⅓ octave band or octave band, with an overall S.P.L. of:-

$$P_{overall} = \sqrt{P_1^2 + P_2^2 + P_3^2 + \dots} \qquad \dots\dots\dots\dots \quad (3)$$

where P_1, P_2 and P_3 are S.P.L. (lb/in^2) in each octave. S.I. Units (Kg/cm^2)

Similarly we may derive the overall stresses as follows:-

$$\langle\sigma^2\rangle_{overall} = \int_0^\infty S(\sigma)_{df} \qquad \dots\dots\dots\dots \quad (4) \quad \text{(ref. 4)}$$

where $\langle\sigma^2\rangle$ = time average mean square stress (lb/in^2)

$S(\sigma)$ = stress spectral density $(lb/in^2)/Hz$ S.I. Units $(Kg/cm^2)/Hz$

f = frequency in Hz

From (4) divided into smaller frequency bands we have

$$< \sigma^2 >_{overall} = \int_0^{f_1} S(\sigma_1) df + \int_0^{f_2} S(\sigma_2) df + \ldots..$$

$$= < \sigma_{0,1}^2 > + < \sigma_{1,2}^2 > + \ldots. \quad \ldots\ldots\ldots. \quad (5)$$

where $<\sigma_{0,1}^2>$, $<\sigma_{1,2}^2>$, $<\sigma_{2,3}^2>$ ..... are mean square stress levels in the frequency bands 0 to f_1, f_1 to f_2, f_2 to f_3 .... respectively; these bands may be $\frac{1}{3}$ octave or octave bands.

The overall stress is in fact the resultant of all the narrow band stresses in each octave band, i.e.

$$\sigma_{overall} = \sqrt{< \sigma_{0,1}^2 > + < \sigma_{1,2}^2 > + < \sigma_{2,3}^2 > + \ldots..} \quad . \quad \ldots\ldots\ldots. \quad (6)$$

3. Obtaining of service stress information for life prediction

Service stress may be obtained from existing structures in service, or they also may be obtained at design stage by testing in high intensity acoustic facility (see Fig. 3) as follows:-

The structures in question should first be divided into a number of sub-components, each sub-component consists of a simple geometrical system, a panel, a beam or a cylinder. At least 12 random strain gauges should be attached to each sub-component in order to obtain spatial average stress $< \sigma_{r.m.s.(t,s)} >$ Maximum stress can be obtained by the introduction of a factor of 3 for panel type structures and 2.5 for beam type of structures.

The structure should then be subjected to the service noise spectrum in the high intensity reverberation chamber. A typical one is shown in Fig. 6.

If the service noise level is beyond the capacity of high intensity noise facility an extrapolation technique may be used.

4. Extrapolation of stresses

Before any attempt to extrapolate the stress to any other levels of noise, the sub-component of the structure must be shown to be linear. This should be carried out experimentally by exciting the sub-component at three different noise levels for a certain band of frequency, say a $\frac{1}{3}$ octave band or octave band. Normally spatial average stresses should be determined at each level. The stress and noise level relationship should be linear. To save time a single gauge may be used as a preliminary test instead of using spatial average. A typical linearity curve is shown in Fig. 7.

The extrapolation is generally carried out for each $\frac{1}{3}$ octave band or octave band by extrapolating the stresses linearly with the S.P.L. i.e.

$$<\sigma>_{specified\ S.P.L.} = <\sigma>_{testing} \times \frac{S.P.L.\ specified}{S.P.L.\ testing}$$

5. General remarks on acoustic fatigue

As the acoustic wave impinges on the surfaces of a structure part of it reflects away and part of it is transmitted to the structure and generates bending waves in the structure, this in turn causes the structure to vibrate in various modes of vibration and produces stresses in the structure. The stress distribution will depend on the geometry and frequency of excitation. The high stresses produced by the acoustic noise at the resonances of the structure could cause metal fatigue of the structure.

The life prediction really involves the randomly varying stress, where "stress interaction" between the processes of damage at the different stress amplitude takes place, lowering or eliminating the endurance limit associated, with constant amplitude stress cycling, where no "stress interaction" will take place.

If the vibrational stress coincides with a position of stress concentration or is superimposed by other types of stresses such as local mean stress, residual stress, thermal stress or by fretting effects, premature fatigue failure may occur at nominal stresses far below the

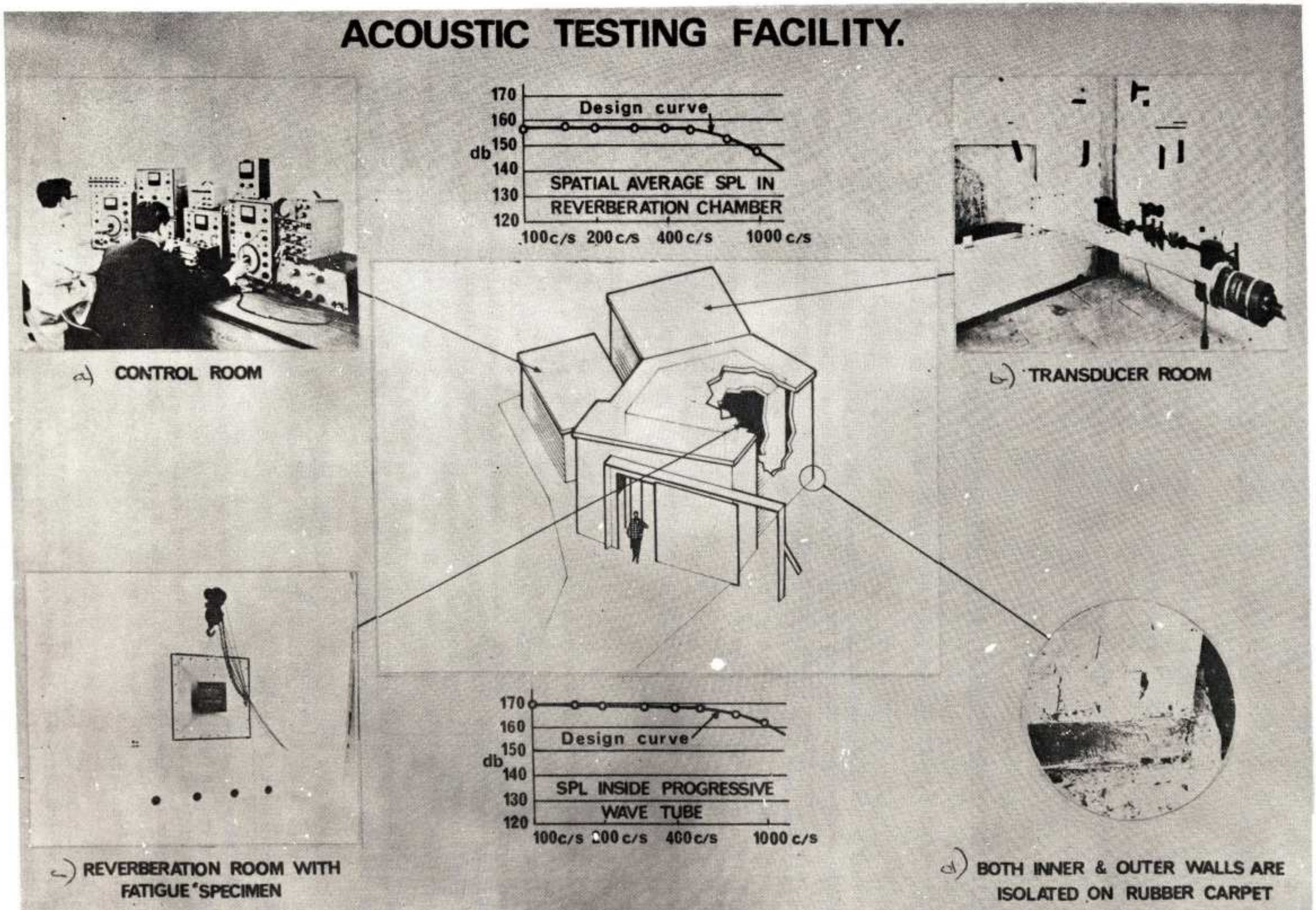

HIGH INTENSITY ACOUSTIC TESTING FACILITY AT

MECHANICAL ENGINEERING LABORATORY E.E. CO. WHETSTONE

FIG 3

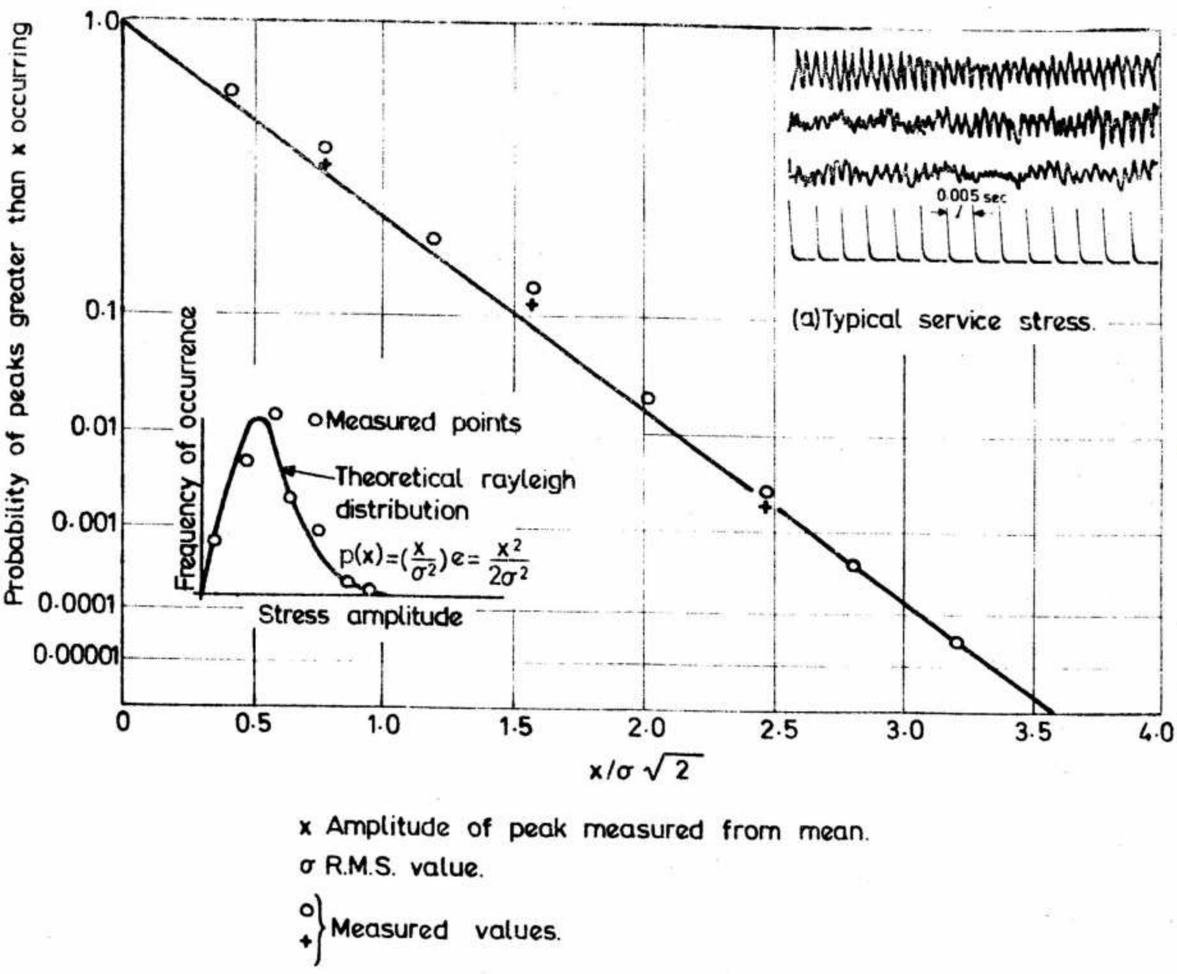

(b) DISTRIBUTION OF STRESS PEAKS OBTAINED FROM A NUCLEAR COMPONENT.

FIG 4

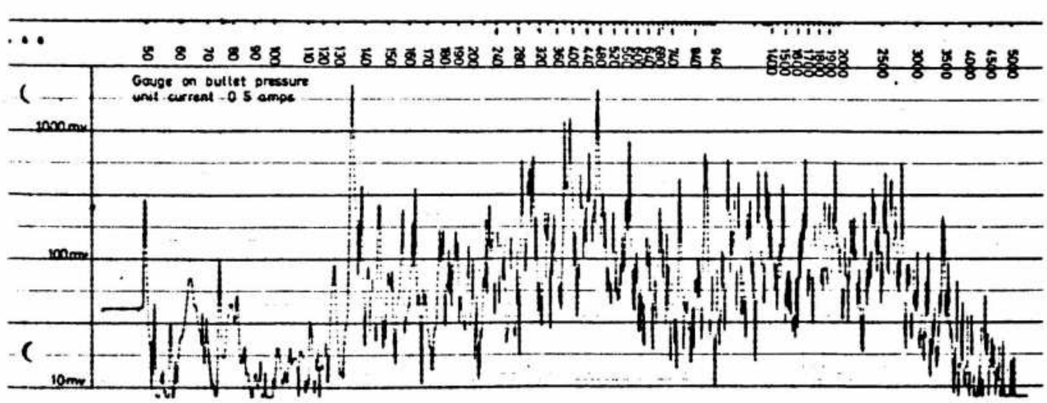

A TYPICAL STRUCTURE RESPONSE OF A NUCLEAR POWER STATION COMPONENT DUE TO ACOUSTIC EXCITATION.

FIG 5.

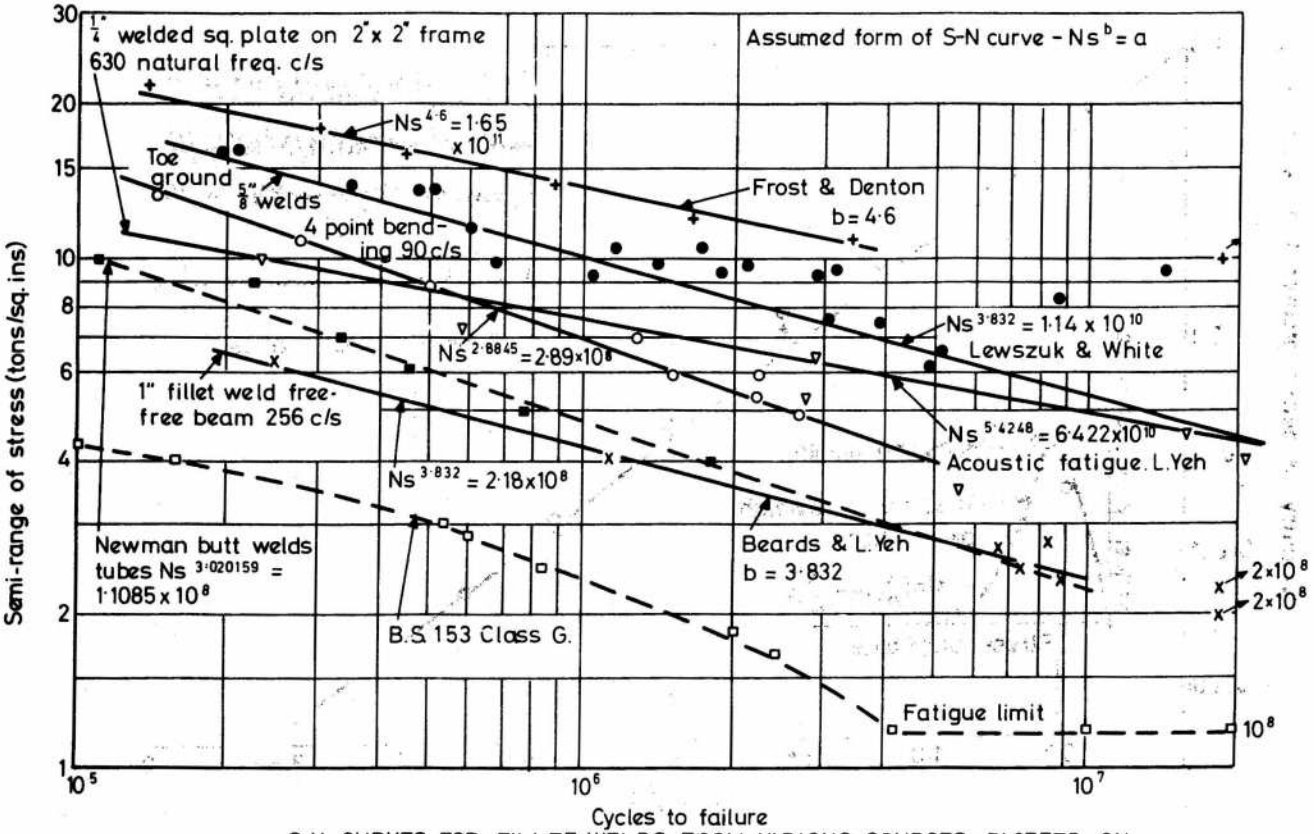

S-N CURVES FOR FILLET WELDS FROM VARIOUS SOURCES PLOTTED ON A LOG-LOG BASIS

FIG. 8

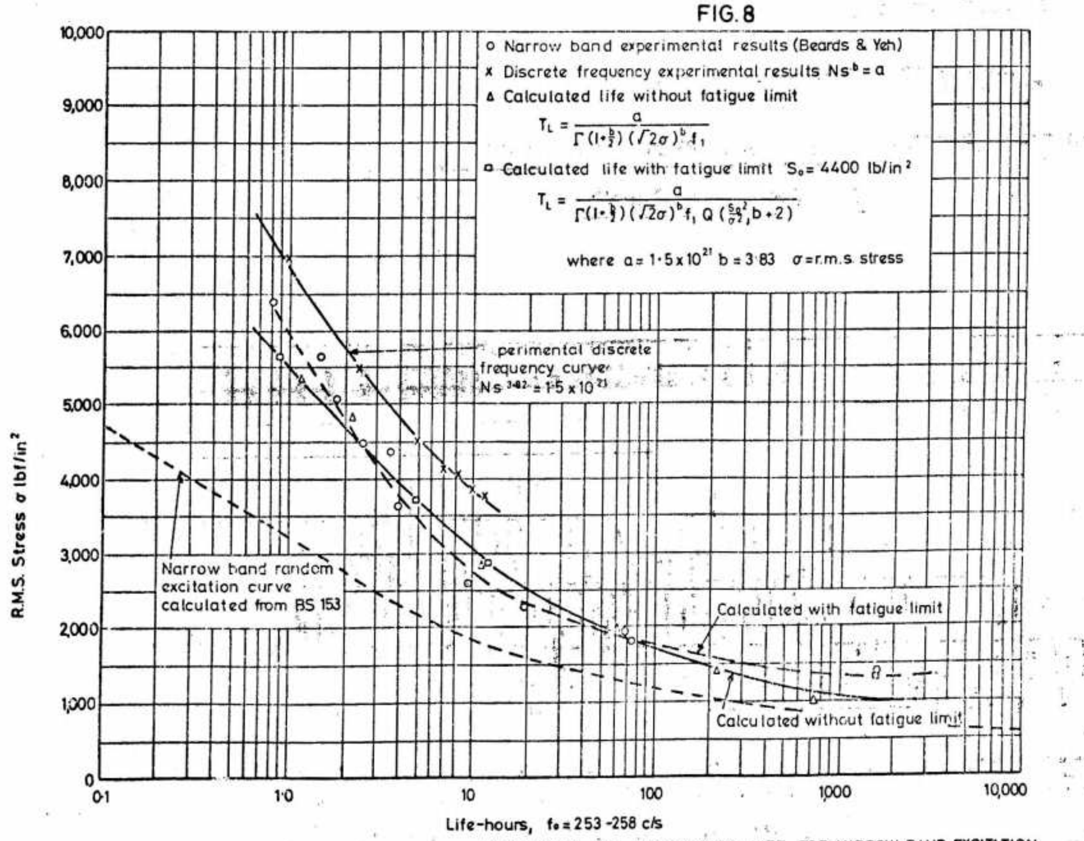

CALCULATED AND EXPERIMENTAL LIFE FOR NARROW BAND EXCITATION

FIG. 9

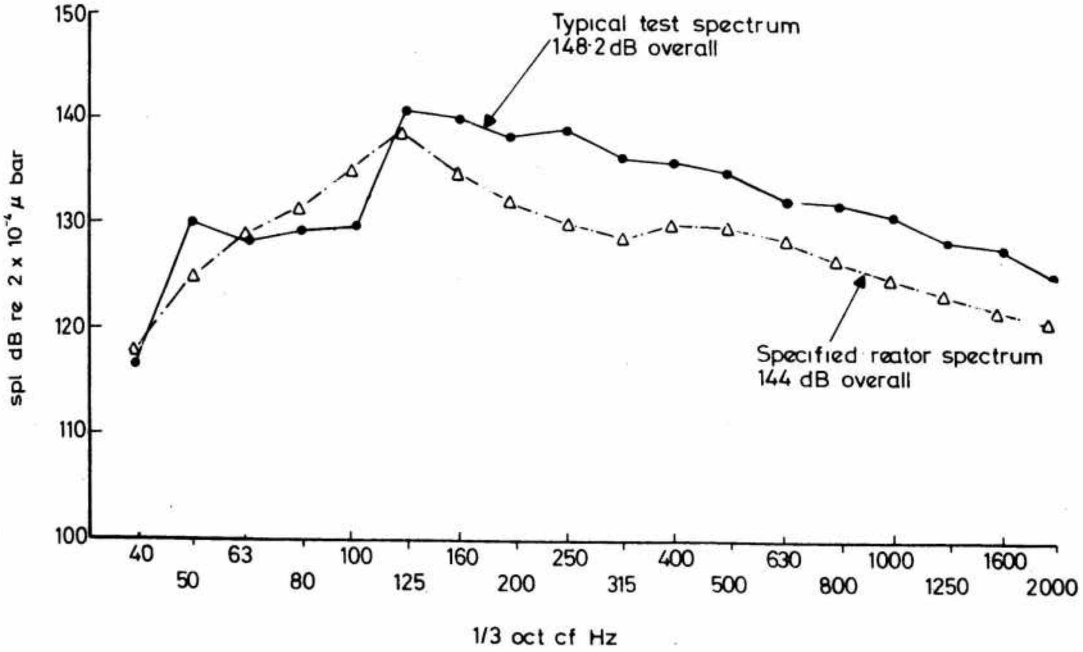

A TYPICAL SPECIFIED REACTOR SPECTRUM AND TYPICAL TEST SPECTRUM FOR STRUCTURAL COMPONENTS

FIG 6

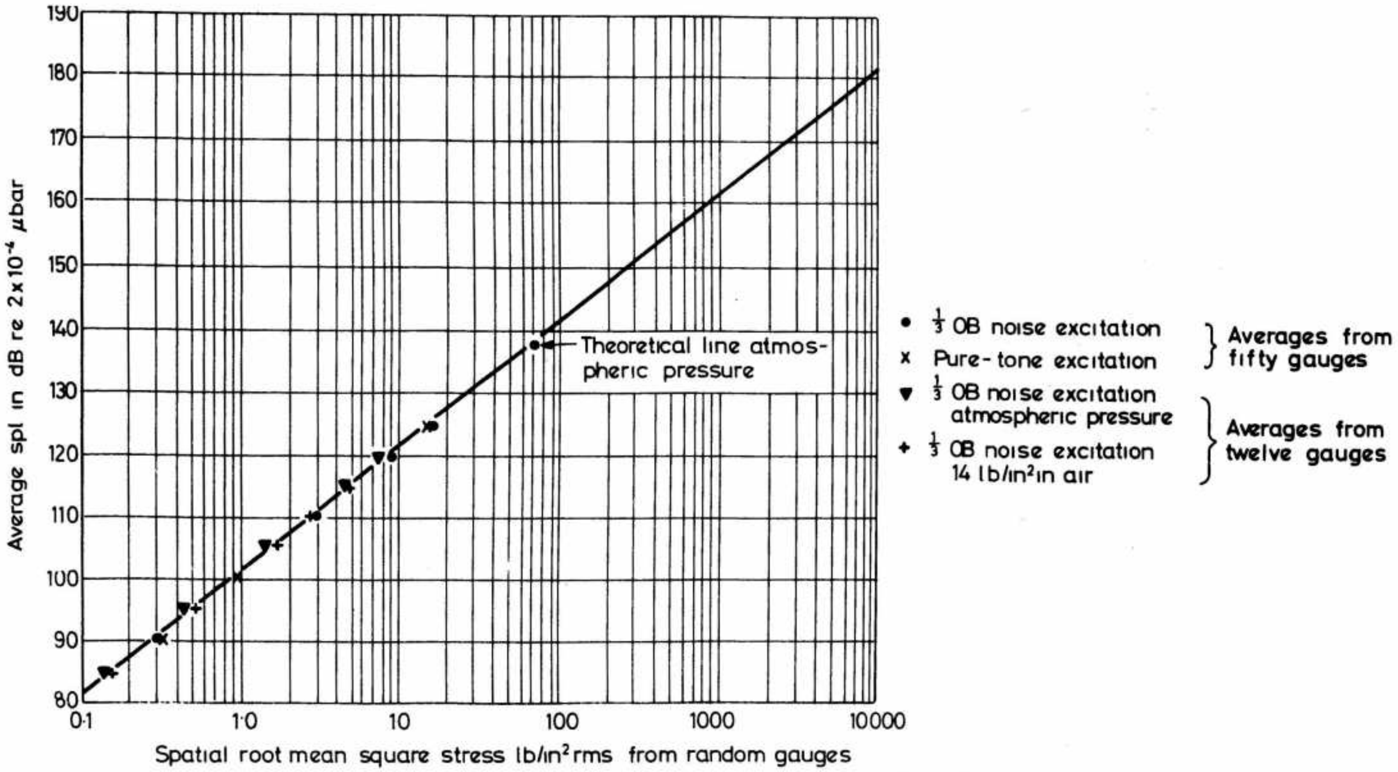

VARIATION OF SPATIAL RMS STRESS WITH SPL ON A TYPICAL STRUCTURE SHOWS THE LINEARITY OF STRESS vs SPL

FIG 7

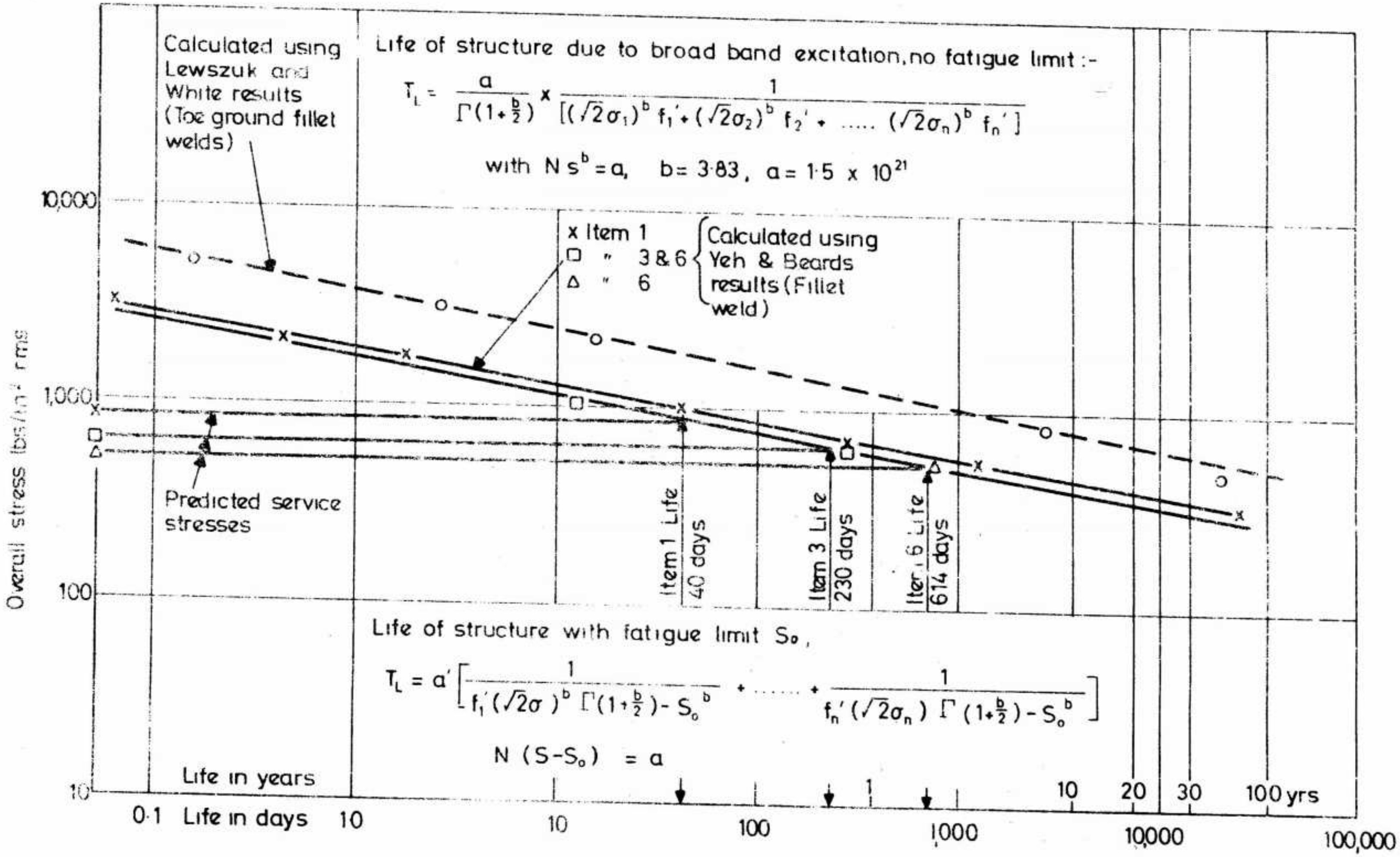

LIFE OF STRUCTURE DUE TO BROAD BAND EXCITATION ITEMS 1,3 & 6 FILLET WELDS

FIG. 10

fatigue limit of the parent material. These should be accounted for separately as described later.

The life prediction is generally aimed at the weakest link of structure, e.g. fillet welds, sharp edges, holes etc. where high stress concentration factors lie.

The technique described here requires the use of S-N curves on metals with constant amplitude and appropriate stress concentration factors. The latter means fatigue tests should be carried out on specimens with stress concentration, e.g. fatigue tests on fillet and butt welds.

6. Prediction of Fatigue life

If a certain material is subjected to a certain number of stress reversals, n_1, at a certain vibration level, and the total number of stress reversals to failure at this level is N_1, then the partial fatigue damage (ref. 7) according to Miner's cumulative damage law is:-

$$D_1 = \frac{n_1}{N_1} \qquad \text{..........} \quad (7)$$

If the vibration level is changed, a new 'partial' fatigue damage may be calculated for n_2 cycles at a failure life of N_2, where N_1 and N_2 may be found from the material S-N curve.

The totally accumulated fatigue damage after vibration at different levels is:

$$D_t = \frac{n_1}{N_1} + \frac{n_2}{N_2} + \ldots \qquad \text{..........} \quad (8)$$

Failure occurs when the damage is complete i.e.

$$D_t = 1 \qquad \text{..........} \quad (9)$$

(a) Narrow band fatigue

For narrow band fatigue, assuming stationary process, express the peak stresses in terms of probability density function with a centre frequency f_o. Then the total number of stress reversals in the time t_1 is $n_1 = f_o.t_1$, and the number of stress reversals around the stress value x, within a small stress interval dx is:-

$$n\ (x) = f_o.t.p(x)dx \qquad \text{..........} \quad (10)$$

where p(x) is the peak probability density function.

The partial fatigue damage caused by these stress reversals is, according to the Palmgren-Miner rule:-

$$D_x = \frac{n(x)}{N(x)} = f_o.t.\frac{p(x)dx}{N(x)} \qquad \text{.........} \quad (11)$$

where N(x) may be found from the S-N curve for the material being the failure cycles at stress level (x).

By summation of the partial fatigue damages for all values of 'x' we have:-

$$D = \Sigma_o^\infty\ D_x = \Sigma_o^\infty\ \frac{n(x)}{N(x)} = f_o.t.\int_o^\infty \frac{p(x)}{N(x)}\ dx \qquad \text{..........} \quad (12)$$

The life of the structure T_L (ref. 6 Crandall and Mark) i.e. the total average time to failure when D = 1 may be obtained by putting $t = T_L$, then:-

$$\text{Life} = T_L = \frac{1}{f_o \int_o^\infty \frac{p(x)}{N(x)}\ dx} \qquad \text{..........} \quad (13)$$

Substitute the peak probability density curve for the stresses: x and its r.m.s. value 'σ', then for Rayleigh distribution (see Fig. 4):-

$$p(x) = \left(\frac{x}{\sigma^2}\right) e^{\frac{-x^2}{2\sigma^2}} \qquad \text{..........} \quad (14)$$

and the number of stress reversals 'N' to failure at stress level may be obtained from:

$$Nx^b = a \qquad \text{.......} \quad (15)$$

where a and b are constants obtained from S/N curve, and the total damage is:-

$$D = f_1' \int_0^\infty \frac{px\,dx}{N(x)} = f_1' \int_0^\infty \frac{\left(\frac{x}{\sigma^2}\right) e^{\frac{-x^2}{2\sigma^2}}\,dx}{a/x^b}$$

$$= \frac{f_1'}{a} (\sqrt{2}\sigma)^b \ \Gamma\left(1 + \frac{b}{2}\right) \quad \text{when } \Gamma \text{ is gamma function} \quad \ldots\ldots (16)$$

$$= T_L = \frac{1}{\frac{f_1'}{a} (\sqrt{2}\sigma)^b \Gamma\left(1 + \frac{b}{2}\right)} \quad \text{See appendix I} \quad \ldots\ldots (17)$$

(b) Broad band fatigue

For broad band, first we divide it into a number of narrow bands, using octave or $\frac{1}{3}$ octave band, then integrate through the frequency range. The damage in a narrow band of centre frequency f_1 is:-

$$D_1' = \sum \left(\frac{n_1}{N_1}\right)_x = \sum \left(\frac{f_1\ t_1}{f_1\ T_1}\right)_x = \sum \left(\frac{t_1}{T_1}\right)_x$$

$$= \left[\left(\frac{t_1}{T_1}\right)_{x_1} + \left(\frac{t_2}{T_2}\right)_{x_2} + \left(\frac{t_3}{T_3}\right)_{x_3} + \ldots\right] \quad \ldots\ldots (18)$$

where f_1 is the centre frequency of each narrow band, t_1 is the time spent at stress level 'x'$_1$ and T_1 is the life of the structure material at x_1 and f_1.

The partial damage in this narrow band is:-

$$D_x' = \frac{n(x)}{N(x)} = f_1 T \int_0^\infty \frac{p(x)dx}{N(x)}$$

The total damage through the wide band from frequency f_o to f_n is:-

$$\sum_{f_o}^{f_n} D_x' = \sum_{f_o}^{f_n} \frac{n(x)}{N(x)} = \sum_{f_o}^{f_n} \left[tf \int_0^\infty \frac{p(x)dx}{N(x)} \right]$$

$$= \left[t_1 f_1' \int_0^\infty \frac{p(x)dx}{N(x)} \right]_{f_1}^{f_o} + \left[t_2 f_2' \int_0^\infty \frac{p(x)dx}{N(x)} \right]_{f_1}^{f_2}$$

$$+ \ldots \quad \ldots\ldots (19)$$

where f_1', f_2' are centre frequencies of the band f_1 to f_2 and f_2 to f_3 and t = time spent under broad band excitation.

Substitute the peak probability density curves for the stresses:-

$$p(x) = \left(\frac{x}{\sigma^2}\right) e^{\left(\frac{-x^2}{2\sigma^2}\right)}$$

and the number of stress reversals 'N' to failure at stress level x may be approximated as follows:-

$$Nx^b = a$$

where a and b are constants, b is the slop of S/N curve with constant amplitude fatigue tests. The damage due to fatigue, after substituting p(x) and N(x) is:-

$$D = \left[tf_1' \int_o^\infty \frac{p(x)dx}{N(x)} \right] = \left[tf_1' \int_o^\infty \frac{\left(\frac{x}{\sigma^2} e^{\left(\frac{-x}{2\sigma^2}\right)}\right) dx}{a/x^b} \right]$$

$$= \frac{f_1'}{a} \left[(\sqrt{2}\sigma)^b \; \Gamma\left(1 + \frac{b}{2}\right) \right] \text{ See Appendix I.}$$

The total damage for all the frequency bands in $\frac{1}{3}$ octave or octave band is:-

$$\sum_{f_o}^{f_n} D_x' = t \left[\frac{f_1'}{a} \left\{ (\sqrt{2}\sigma_1)^b \Gamma\left(1 + \frac{b}{2}\right) \right\} + \frac{f_2'}{a} \left\{ (\sqrt{2}\sigma_2)^b \Gamma\left(1 + \frac{b}{2}\right) \right\} + \ldots \right]$$

$$= \frac{1}{a} \Gamma\left(1 + \frac{b}{2}\right) \left[(\sqrt{2}\sigma_1)^b f_1' + (\sqrt{2}\sigma_2)^b f_2' + (\sqrt{2}\sigma_3)^b f_3' + \ldots \right] \quad \ldots.. (20)$$

where f_1', f_2' ... are centre frequency of each band, by putting $t = T_L$ then:-

$$\text{Life of structure } T_L = \frac{1}{\sum_{f_o}^{f_n} D_x'}$$

$$= \frac{a}{\Gamma\left(1 + \frac{b}{2}\right)} \times \frac{1}{\sqrt{2}^b \left[(\sqrt{\sigma_1})^b f_1' + (\sqrt{\sigma_2})^b f_2' + (\sqrt{\sigma_3})^b f_3' + \ldots \right]} \quad \ldots.. (21)$$

(c) Prediction of fatigue life with fatigue limit

For life predictions with lower stress levels, fatigue limit becomes important, however one must be aware that if the fatigue life is effected by random stress concentration, such as fillet welds, the measured stress may be low, but the actual stress causing damage due to stress concentration may be quite high. In addition, it may be argued that in fatigue under random loads the lower stress below the fatigue limit could continue to propagate a crack initiated at the higher stress levels. It is an author's opinion that the introduction of fatigue limit may give considerable longer predicted life than without fatigue limit, especially with fillet welds. Nevertheless in many cases such as mild steel without welds this is quite valid. Further research is required to clarify the effect of fatigue limit.

There are two ways of introducing fatigue limit in life prediction for narrow band, L. Yeh, I. Vesty and B.K. Foster (ref. 4), using incomplete gamma function (Report W/M(1C)p.1428. J. Lewszuk and D.J. White, Report W/M(1B)p.1611, (ref. 5) using $N(S - S_o)^b = a$. The latter may be solved to give a narrow band fatigue life of:-

$$T = \frac{a}{f_o\left\{(\sqrt{2}\sigma)^b\,\Gamma\left(1 + \frac{b}{2}\right)\right\} - S_o^b} \qquad \text{(see Appendix II)} \quad \ldots\ldots (22)$$

For broad band the total life of structure, by putting $t = T_L$ then:-

$$T_L = \frac{1}{\sum D_x^1}$$

$$= a\left[\frac{1}{f'_1\ (\sqrt{2}\sigma_1)^b\left\{(1 + \frac{b}{2}) - S_o^b\right\}} + \frac{1}{f'_2\ (\sqrt{2}\sigma_2)^b\left\{(1 + \frac{b}{2}) - S_o^b\right\}} + \ldots\right] \quad \ldots\ldots (23)$$

Using incomplete gamma function, (ref. 5), the narrow band total life of structure may be expressed as:-

$$T = \frac{a}{f_o\ (\sqrt{2}\sigma)^b\ \Gamma\left(1 + \frac{b}{2}\right)\ Q\left(\frac{S_o^2}{2}, b + 2\right)}$$

and for broad band:-

$$T_L = \frac{a}{\Gamma\left(1 + \frac{b}{2}\right)\left[(\sqrt{2}\sigma_1)^b\ f_1 Q\left(\frac{S_o^2}{\sigma_1^2}, b + 2\right) + (\sqrt{2}\sigma_2)^b\ f_2 Q\left(\frac{S_o^2}{\sigma^2}, b + 2\right) + \ldots\right]} \quad \ldots\ldots (24)$$

It should be noted that a and b for both expressions (23) and (24) are different, which depends on curve fitting of the experimental results.

The truncation of peaks is unimportant in acoustically induced stresses, therefore it is not discussed here.

7. Determination of the equation $N S^b = a$ for life prediction from fatigue results

(1) Fillet welds

The S/N curves for plain fillet welds from various sources are plotted on a log-log paper see Fig. 8. The equations are summarized as follows, 'a' is calculated for stresses in lb/in^2.

(1)	Frost and Denton	$S N^{4.6}$	=	4.41×10^{26}
(2)	Lewszuk and White	$S N^{3.832}$	=	7.19×10^{22}
(3)	Gurney	$S N^{2.8845}$	=	1.33×10^{18}
(4)	Acoustic fatigue L. Yeh	$S N^{3.832}$	=	9.832×10^{28}
(5)	C.F. Beards and L. Yeh	$S N^{3.832}$	=	1.5×10^{21}

also included is BS 153 Class G.

It is evident that the unexplainable difference of these results made the task of life prediction most difficult. The difference may be due to strength of welds, may be due to distribution of stress concentration or may be due to position of strain gauges, may be due to definition of nominal stress and life of failure, however it is thought that the safe life prediction is the best criterion in determining the structure life. Therefore the equation (5) is adopted. Fatigue limit may be introduced to increase the accuracy of life prediction at longer life. This was obtained by fitting narrow band experimental results up to 1750 hours test. Fatigue limit thus obtained is 4400 lb/in^2 onto peak stress. Figure 9 shows calculated results and experimental results for narrow band. The calculated results without fatigue limit are indicated by triangles and those with fatigue limit by squares. The experimental results are indicated by circles. The agreement may be seen to be good.

8. Example of life prediction

For a sub-component the maximum spatial average octave band stress as measured in acoustic testing facility under reactor S.P.L. and spectrum is listed as follows:-

Frequency c.f. in c/s	31.5 f'_1	63 f'_2	125 f'_3	250 f'_4	500 f'_5	1000 f'_6	2000 f'_7	4000 f'_8
S.P.L. in dB	137	145	143	142	141	145	139	130
Max. spatial average stress in lb/in^2 r.m.s.	201.29 σ_1	371.86 σ_2	258.41 σ_3	272.82 σ_4	453.39 σ_5	616.24 σ_6	209.42 σ_7	66.21 σ_8

Overall stress = 976 lb/in^2 r.m.s.

(i) Life prediction on Broad Band stress Without Fatigue limit

The discrete frequency fatigue tests, Fig. 8 gives fatigue failure and stress relationship without any fatigue limit as:-

$$N \cdot S^{3.83} = 1.5 \times 10^{21} \qquad \text{........ (25)}$$

where S = 0 to pk stress; $b = 3.83$ and $a = 1.5 \times 10^{21}$
N = cycles to failure at 0 to pk stress level 'S'

The life of structure without imposed fatigue limit is:-

$$T_L = \frac{a}{\Gamma\left(1 + \frac{b}{2}\right)} \times \frac{1}{(\sqrt{2}\sigma_1)^b\, f'_1 + (\sqrt{2}\sigma_2)^b\, f'_2 + \dots\ \sqrt{2}\sigma_8^b\, f'_8}$$

$$= \frac{1.5 \times 10^{21}}{\Gamma\left(1 + \frac{3.83}{2}\right)} \times \frac{1}{(\sqrt{2} \times 201.29)^{3.83} \times 315 + (\sqrt{2} \times 371.86)^{3.83} \times 63 +}$$

$$\times \frac{1}{(\sqrt{2} \times 258.41)^{3.83} \times 125 + (\sqrt{2} \times 272.82)^{3.83} \times 250 + (\sqrt{2} \times 453.39)^{3.83} \times 500}$$

$$\times \frac{1}{+ (\sqrt{2} \times 616.24)^{3.83} \times 1000 + (\sqrt{2} \times 209.42^{3.83} \times 2000 + (\sqrt{2} \times 66.21)^{3.83} \times 4000}$$

$$= 3.67074 \times 10^6 \text{ secs} = 1019.65 \text{ hrs} = 42.48 \text{ days} = 0.119 \text{ years.}$$

(ii) Life prediction of narrow band with fatigue limit (checked by fatigue experiments)

The narrow band experimental results of Fig. 9 were computed with the following equation with a fatigue limit 'S_o' of 4400 lb/in^2 (0 to pk) and the following equations:

$$N \cdot S^{3.83} = 1.5 \times 10^{21} \qquad \text{........ (26)}$$

$$\therefore\ T_L = \frac{a}{\left(1 + \frac{b}{2}\, Q\, \left(\frac{F^2}{\sigma^2} \cdot b + 2\right)\right) (\sqrt{2\sigma})^b\, f'} = 1560 \text{ hours} \qquad \text{... (27)}$$

The actual testing time to failure was 1680 hours, good agreement may be seen (see Fig. 9). Both calculated results for with and without fatigue limit are also plotted. It may be seen that those with fatigue limits agrees better with the experimental results.

(iii)For broad band with fatigue limit the Life is:-

$$T_L = \frac{a}{\Gamma(1 + \frac{b}{2})} \cdot \frac{1}{\sum_{f_o}^{f} Q(\frac{F^2}{\sigma^2} \cdot b + 2) \; (\sqrt{2}\sigma)^b f'} \quad \ldots\ldots\ (28)$$

with $F = 4400$ lb/in^2 Q may be found from BIOMETRIKA TABLES FOR STATISTICIANS by E.S. Pearson and H.O. Hartley, Volume 1, Table 7.

(b) Results of Life Prediction

(i) Fillet weld results

Assume stress in each band are linear to S.P.L. and the overall stress and spatial average narrow band stress relation are the same, then, an overall stress and T_L curve may be calculated for different levels of overall stress. The results of a typical structure are shown in Fig. 10 without considering any fatigue limit for safe prediction.

Items 1, 3 and 6 are sub-components with fillet welds the maximum spatial average stresses and estimated life are calculated. The calculated life curves are given in Fig. 10 as indicated. It can be seen the life curves of Items 1, 3 and 6 due to fillet welds are very close together. The estimated maximum stresses of item 1 is 976 lb/in^2 gives a life of 42 days. Item 3 at 649 lb/in^2 life of 230.7 days, Item 6 536 lb/in^2 life of 1.72 years.

The dotted line shows that if a toe ground fillet weld is used, the life could be improved considerably; for example, to about 25 years in the case of item 1.

9. Other factors effect the fatigue life

A number of factors could effect the fatigue life, care should be taken on these effects in obtaining the '$N S^b = a$' equation. These are: mean stress, residual stresses and stress concentration. Other effects such as stress changes due to temperature, fluid density, sound velocity, frequency and damping; allowance should also be made on creep, corrosion, fretting, etc.

10. Discussion on Life Prediction

The technique described so far is still at its infant stage, more research should be done to prove its validity, except on narrow band fatigue of fillet welds, which is well tested.

As a safe prediction of life it is better not to use the fatigue limit, even though this could give a better result, especially when long life prediction is required.

The work could apply to multi-modal vibration using each resonant frequency and its stress amplitude by analysing the service stress using 2 c/s bandwidth tracking filters. Using these frequencies and stress levels to calculate the failure life, should in theory prove to be better than those using $\frac{1}{3}$ octave band and octave band stresses.

N.B. Appendix I and II may be obtained from the author on request.

References

1. L. Yeh, E.M. Beaney and B. Smith.
   Acoustically induced stresses on Nuclear Power Station Structures.
   Paper 9 Symposium on high pressure gas as heat transfer medium.
   Inst. of Mech. Eng. December 1966.

2. L. Yeh, GEC MEL Report W/M(1C)u.9329.
   Maximum stress/spatial average stress ratios for beam type of structures.

3. Robson J.D. An introduction to random vibration.
   Edinburgh University Publication. Page 35 equation (2).

4. L. Yeh, I. Vesty and B.K. Foster. GEC MEL Report W/M(1C)p.1428.
   Fatigue test on integron finned boiler tubes.

5. J. Lewszuk and D.J. White. GEC MEL Report W/M(1B)p.1611. Also presented as a paper 4 during Welding Research Conference at Brighton 1970. Effect of mean stress and cumulative damage in bending fatigue of fillet welded mild steel plate subjected to narrow band random loading.

6. Crandall and Mark. Randóm Vibration in Mechanical Systems. Academic Press. New York, London. p.112.

7. Miner, M.A. Cumulative Damage in Fatigue. J. App. Mech. vol. 12, 1945.

ANTICIPATION OF ULTIMATE FAILURE IN CONRETE MASONRY STRUCTURES BY ACOUSTIC EMISSION

T. J. Stevens
Division of Building Research
Commonwealth Scientific and Industrial Research Organisation
Highett, Victoria

R. E. Lewis
Division of Building Research
Commonwealth Scientific and Industrial Research Organisation
Highett, Victoria

B. L. Schafer
Division of Building Research
Commonwealth Scientific and Industrial Research Organisation
Highett, Victoria

SUMMARY

Acoustic emission in the audio band has been used to anticipate the approach of ultimate failure in concrete masonry test specimens. The audio output from the specimen was fed to a loudspeaker and monitored by a human observer. The observer was easily able to interpret the load condition of the specimen for loads greater than 0.75 times the ultimate strength of the specimen and to give a clear warning when the ultimate failure was imminent.

INTRODUCTION

During the testing to destruction at the Division of Building Research, CSIRO, of large test panels of reinforced concrete masonry it became desirable to determine when the specimens were unsafe to approach. Failure of these specimens usually occurred suddenly and with an explosive force. Ultimate loads were greater than 2.6 MN and because of the way the load was applied a large amount of energy was released instantaneously. Flying debris during failure created a danger zone up to a 3 m radius from the specimen. It was necessary during most tests for a close visual examination to be made of the specimen, both to determine the extent and the nature of cracks that might have developed, and to take measurements of strain with a hand-held extensiometer. The prime objective of this work was therefore to guarantee the safety of persons entering the danger zone. In this paper a system detecting acoustic emission in the audio band is described which gives the required warning of the onset of failure in a concrete specimen and also gives other information about the load condition of test specimens which is useful in the management of tests.

DETECTION SYSTEM

A system detecting emission in the audio band was selected because of the simplification in design and operation this makes possible when compared with a system detecting ultrasonic emission. The emphasis in recently published work on acoustic emission (1,2,3,4,5) has been directed towards systems detecting ultrasonic emission with some ultrasonic systems being able to give information about the location and nature of micro-fractures within a specimen. In addition ultrasonic detection gives greater discrimination against unwanted noise from the specimen environment and is therefore necessary when the specimen material gives a very low level of emission. However, for an objective which is limited to interpretation at high load levels and prediction of ultimate failure in a material such as concrete, the sophisticated techniques used in detecting ultrasonic emission are not needed.

The intensity of audio-band emissions from concrete specimens allows a human observer to interpret directly and continuously the signals emitted as the specimen is being loaded. In the system described the observer listens to the amplified signals through a loudspeaker. The sound generated from within the specimen has an easily recognised character, different from externally generated signals which may reach the detector via the specimen. The sound is distinguishable even during periods of direct activity on the specimen. For example the use of hand-held extensiometers directly applied to the specimen produces output from the speaker, but the observer remains confident that he would still be able to recognise the approaching failure of the specimen. By comparison a system detecting ultrasonic emission cannot produce any direct human response and necessarily relies on complex instrumentation to achieve what the human observer does intuitively.

DETAILS OF SYSTEM

The system described used a piezoelectric accelerometer as the detector followed by a high-gain audio amplifier and speaker.

1. Accelerometer. The accelerometer used was a Columbia Model 302-5. The calculated sensitivity with a 2000 picofarad connecting cable is about 5 $mVm^{-1} s^2$. The specification of the accelerometer showed that its natural resonance was 16 kHz and that the response was uniform up to about 3 kHz. In addition our observations showed a broad peak in the response in the 6 kHz region and a falling response as the frequency was further increased until a sharp peak was reached at resonance.

2. Input Preamplifier. The input preamplifier was of standard design with high input impedance and low noise. It used a field effect transistor input stage and provided a fixed voltage gain of 400. The preamplifier must be placed close to the specimen in order to limit the cable capacitance load on the accelerometer. It was designed therefore to have low enough output impedance to operate into a cable about 30 m long linking it to the power amplifier.

3. Power Amplifier. The power output of the amplifier at clipping was 8 watts for a sine wave. Experience showed that adjustment of the voltage gain to a value of 20 was suitable. It is important that the amplifier be capable of operating in a continuously overloaded or clipped state without blocking, or it may stop operating in the presence of large input signals which occur as a specimen nears failure.

4. Speaker. The speaker was a 8 ohm 200 mm twin cone speaker of sensitivity 96 dB S.P.L. (average) per watt at 500 mm, and was operated in an 0.054 m^3 vented enclosure.

SENSITIVITY

The sensitivity of the system, and hence the output of the speaker was adjusted over a series of tests until the best listener response was achieved. An effort was therefore made to determine the sensitivity of the system and to develop tests so that the system could be set up with full confidence that it would operate efficiently when a test specimen was loaded.

A calculation of sensitivity for the system from the specifications of the component parts showed that an input acceleration of 0.25 $m\ s^{-2}$ at the accelerometer would produce 10 volts at the speaker terminals. In order to obtain an estimate of the sensitivity of the complete system an impulse force was applied to the structure with a pendulum. A small steel ball of mass 0.13 g was suspended on a 1.2 m length of fine cotton attached to a vertical face of the specimen. When the ball struck the specimen after swinging from an initial deflection of 25 mm an output of 20 volts peak was generated at the speaker terminals. The same test applied at various parts of the specimen resulted in output variations of less than 3 to 1. The energy input to the specimen by the impact must of necessity be less than the kinetic energy of the ball, 0.33 mJ. Although the pendulum test gives a quantitative estimate it is difficult to perform.

It is desirable to have a simple empirical test which can be used to prove the response of the system when it is applied to a specimen. For this purpose a reed relay (Hamlin Type MLC-2) on a metal mount of the same type that is used for the accelerometer was temporarily attached to the specimen in several locations. When the system was set up correctly electrical operations of the reed gave an output of about 3 volts peak at the speaker terminals from favourable positions and at least 1 volt from other parts of the specimen.

It has been our experience using concrete specimens with dimensions up to several metres that emission generated in any part of the specimen carried to the detector. We have not at any time had to relocate the accelerometer to optimise its sensitivity.

DESCRIPTION OF SPECIMENS AND LOADING

The structures loaded in the test described were sections of reinforced concrete masonry wall. The dimensions were 3 m in height, 1 m in width and 0.12 m thickness. The accelerometer was clamped onto the narrow edge of the wall with the sensitive direction along the 1 m horizontal dimension. This location gave minimum response to low frequency flexural modes in the specimen. A further advantage is that this location gave good mechanical protection to the accelerometer during the explosive failure of the specimen. The load was applied by a steel frame enclosing the test specimen and a pair of hydraulic flat jacks. The flat jacks were expanded with oil from a hand pump at pressures up to 13 MPa. The load was applied in 3 or 4 steps, the pauses being to allow for examination and strain measurements. The rate of load application during each step gave an approximate stress increase of 1.7 MPa/min to the specimen.

The specimens were generally loaded under axial compression and generated a typical concrete compression failure. A few specimens were loaded eccentrically and these developed a gradual bending failure leading to final collapse. There was no audible difference in the emission from the two types of failure.

In addition, the system has been connected to a variety of other concrete test specimens.

1. A large hollow-box structure of lightweight concrete which was loaded until considerable structural damage had occurred.

2. Several standard 150 mm x 300 mm cylinders of dense concrete which were loaded to failure in a testing machine.

3. Other small specimens of both dense and lightweight concrete which were loaded to failure in a testing machine.

In all cases the onset of ultimate failure was easily anticipated even when the specimen was of a type not previously tested. For those tests using the testing machines to load the specimens, noise from the machine motor was audible from the speaker. However, this background did not mask the emission from the specimen. It was found that noise from the motors was reduced by placing a piece of 5 mm plywood between the platens and the specimen. The rate of load application varied over wide limits but because of the high rate at which emission pulses are generated near failure the audible impression did not alter.

NATURE OF OUTPUT

The signal generated in the accelerometer by isolated emission pulses within the specimen was a single-frequency decaying wave train, in the frequency range 4 to 7 kHz. The frequency varied over this range for different specimens but in any given specimen it was constant for a given load. The single frequency increased about 5 per cent as the load was increased to failure. Figure 1 shows a single emission pulse and is typical of either external impact excitation or the early stages of loading when isolated pulses occur. A similar output was produced by the pendulum impacts described above.

In the initial work a transducer made from a cheap crystal gramophone pickup cartridge used in an inertial mount was compared to the accelerometer. After double differentiation to obtain a response proportional to acceleration the output from the crystal pickup was similar to that obtained from the accelerometer.

Although the emission detected was confined to a relatively narrow band of frequencies by the detection and reproduction system, the output closely resembled the sound one would expect instinctively. The output from the speaker is easily recognised by persons with no previous experience.

ACOUSTIC EMISSION DURING LOADING

The output generated when the specimen was loaded was similar to that described for single excitation. No significant output was obtained until the load exceeded 0.75 times the ultimate strength of the specimen; after that time an intermittent series of pulses occurred at a repetition rate of one or two per second. The output ceased if the load was held constant or allowed to fall slightly. At this time the sound from the speaker would be described as a soft ticking. As the load was increased to 0.9 times the ultimate strength, the pulses occurred at a repetition rate greater than 10 per second and increased in amplitude to the stage where the amplifier was clipping all pulses to a constant amplitude. The output no longer ceased if the load was held constant but it could be stopped if a load reduction greater than 3 per cent was allowed. When load was reapplied the emission immediately reappeared.

In the last few seconds before failure the pulse repetition rate increased greatly and the sound became a continuous roar. No listener, even one hearing the sound for the first time could mistake the warning.

While it is true that the amplification system could be prevented from clipping during the last stage of loading by the inclusion of an automatic gain control we found that the system operated satisfactorily without this added complexity.

USES OF SYSTEM

Apart from setting maximum strain limits based on knowledge of structural behaviour and material properties, the usual way of detecting the approach of ultimate failure of specimens is to look for non-linearity in the observed stress versus strain relationships. This method can give a very late warning or even no warning at all when applied to concrete specimens. In a test where a complex specimen is being loaded it is difficult and expensive to continuously monitor strain at the large number of points required to fully protect the structure against unexpected failure. Acoustic emission from the whole specimen can in most cases be monitored with a single transducer.

1. Safety. As acoustic emission is presented in the form of an audible signal it can be monitored by the operators of a test without distraction from their other duties. Thus all persons who may be endangered by a sudden ultimate failure of a test specimen can ensure their own safety.

2. Structural Model Protection. Often expensive structural models must be used in a series of tests where each test places the model at risk. With careful interpretation of the acoustic emission it is possible to stop loading before any damage is done to a model and yet still determine its ultimate strength with an accuracy of 5 per cent.

3. Photographic Recording of Failures. The technique has been used at the Division as an aid in the photographic recording of failures. Because of the short running time and high cost of photographic recording it is impractical to film a failure without a reliable indication of when to start the camera. With the aid of acoustic emission the photographer is able to start the camera just a few seconds before failure.

4. Failure Interpretation. Throughout the series of tests on masonry walls, all except two failures were successfully anticipated. Both of these failures were found to have been induced by malfunctions of the loading equipment causing sudden unbalance of loads and immediate failure of the specimen.

From a careful study of tape recordings of emissions made during the tests it was possible to determine the cause of the failure and estimate the true ultimate strength of each specimen thus recovering useful information from these tests despite the mishaps. These two cases illustrate that while the system described can be an important safety measure it cannot give a warning for shock-induced failures, and is no substitute for the care and attention that is necessary in all test loadings.

CONCLUSION

The system described is cheap and simple to set up and operate. It gives real time information about the specimen additional to that normally gathered in load tests without requiring extra staff or causing distraction from normal duties. While functioning mainly as a safety measure it can be used in many ways to improve test procedures. Listening to the acoustic emission makes it possible to follow and interpret the progress of a test instead of having to wait for the inevitable and possibly sudden failure without knowing when it is going to occur.

REFERENCES

1. Liptai, R.G., and Harris, D.O. - "Acoustic Emission - An Introduction Review", Materials Research & Standards, MTRSA, Vol.11, No.3, p.8

2. Tatro, C.A. - "Experimental Considerations for Acoustic Testing", Materials Research & Standards, MTRSA, Vol.11, No.3, p.17

3. Hutton, D.H., and Parry, D.L. - "Assessment of Structural Integrity by Acoustic Emission", Materials Research & Standards, MTRSA, Vol.11, No.3, p.25

4. Liptai, R.B. et al - "An Introduction into Acoustic Emission", ASTM Special Publication 505

5. Anon. - "Precast Concrete, June 1973", p.321.

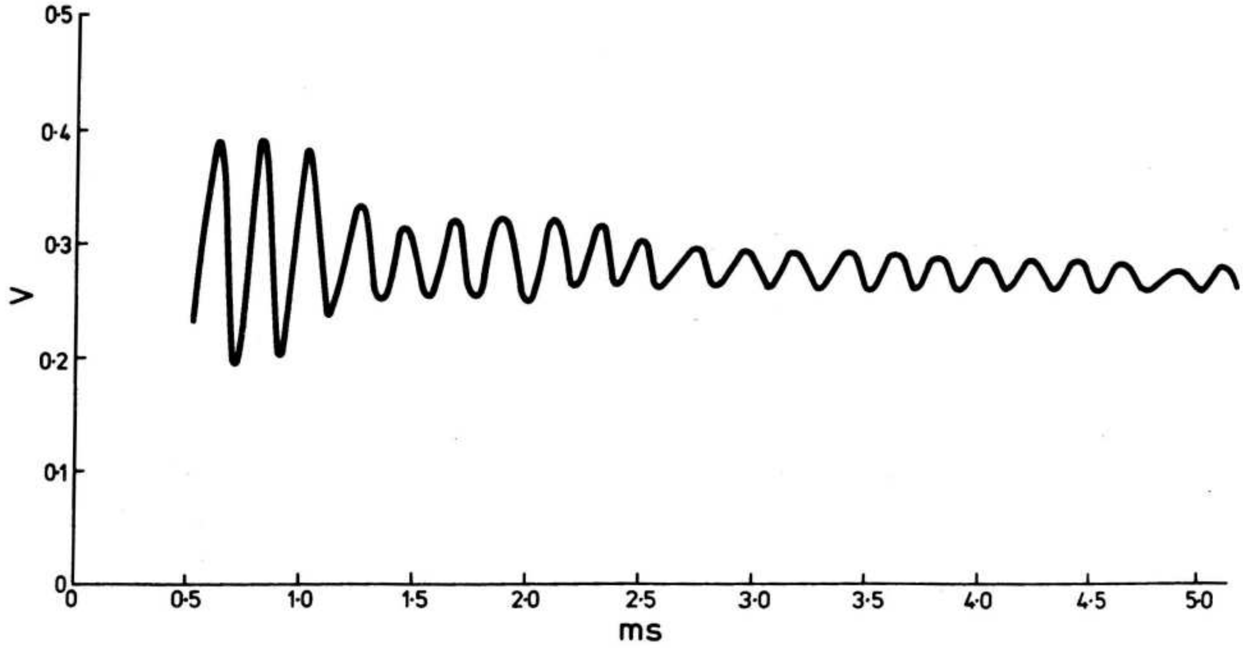

FIG. 1. FORM OF A SINGLE PULSE

DETERMINATION OF DYNAMIC CHARACTERISTICS OF VIBRATING STRUCTURES FROM ACOUSTIC RESPONSE STUDIES

M. G. Prasad
Department of Applied Mechanics
Indian Institute of Technology
Madras, India

J. Pattabiraman
Department of Applied Mechanics
Indian Institute of Technology
Madras, India

T. S. Shankara
Biomed. Eng. Division &
Department of Mathematics
Indian Institute of Technology
Madras, India

B. V. A. Rao
Department of Applied Mechanics
Indian Institute of Technology
Madras, India

SUMMARY - Vibration analysis of complex structures such as machine tools, aircrafts, etc. become extremely difficult owing to the presence of multitude of uncertainities. Most of such analyses requires a fast, high memory digital computer which may be uneconomical and time consuming. Actual vibration measurement at several points on the structure demands large number of transducers and accessories. In this paper although known but not completely explored technique by sound measurements on the vibrating structures is proposed to determine their dynamic responses.

Sound radiations from vibrating structures in the near field have been determined analytically using both monopole and dipole theories and compared well with experimental results. Further dynamic response for the same has been determined using well known vibration theories and compared well with experimental results. Subsequently the relation between the acoustic response and vibration responses have been established.

The comparison of these results reveal a good agreement among them for simple structures such as beams and plates. With the encouragement provided in this investigation, it is hoped that this method could be conveniently used to determine vibration responses of even complex structures from sound measurements.

GLOSSARY OF TERMS

ρ_o	density of air at rest (kgm^{-3})
c	velocity of sound (ms^{-1})
k	acoustic wave number (m^{-1})
r	radius vector (m)
p	acoustic pressure (Nm^{-2})
p_m, p_d	acoustic pressure due to monopole, dipole theories
h	vertical distance between surface and microphone
a	thickness of structure
m_n	generalised mass as defined in ref.[10]
$\phi_n(a), \phi_n(x)$	charecteristic functions of beam as defined in ref.[10]
j_o	spherical Bessel function
n_o	spherical Neumann function
p_o	reference acoustic pressure (=2x10^{-5}Nm^{-2})
ω	angular frequency (sec^{-1})
L	vibration displacement amplitude (m)
Y	real part of acoustic impedance ($=ka/(1+k^2a^2)$)
Z	imaginary part of acoustic impedance ($= 1/(1+k^2a^2)$)
SPL	sound pressure level (dB)
U	velocity amplitude (ωL)(ms^{-1})
R	radius of microphone
F	forcing amplitude (N)

1. INTRODUCTION

Theoretical determination of dynamic behaviour of complex structures such as space vehicles, ships, etc., is quite complicated and time consuming. Obtaining these through standard vibration tests involves simultaneous measurement of response at various points through use of several vibration pick ups. Evaluation of the same through sound measurements using a single microphone has been found quite advantageous. Exact estimation of the dynamic characteristics involves use of suitable acoustic theories. Many of the available analyses do not cover practical cases. Besides, the most of analyses and measurement confined to far field.

In this present paper an attempt is made to study both theoretically and experimentally the sound response of structures and compare with the results of vibration tests. While doing so, various effects such as near field, area of microphone, etc., are taken into account.

2. THEORETICAL APPROACH

The use of vibroacoustic data in the prediction of design and test criteria is well known [1]. Results are available for the evaluation of the distance of the receiver from the monopole and dipole acoustic sources by considering the sound energy at that location [2].

Any mathematical model involved in the vibroacoustic study comprises of elementary monopole and dipole sources, which are nothing but the first two terms in the series solution of acoustic wave equation [3,4,5]. The equation for pressure due to an elemental area radiating sound into a half space is given by [6,7].

$$dp = \frac{\rho_o ckU}{2\pi r} e^{jka} (Y+jZ)\, e^{j(\omega t-kr)} dS \qquad (1)$$

Since the microphone is made use of in the measurement of acoustic pressure, the above elemental pressure is integrated over the projected area of the microphone, on to the structure (which is a circle of the same radius). The microphone is placed along the direction of vibration and in the immediate vicinity of the structure. Since the dimension of this area over which integration is performed is very small compared to the rest of the area, one may assume an uniform velocity distribution U over that area (Fig.1.1) Eqn.(1) can be written as

$$dp = \frac{\rho_o ckU}{2\pi}(Y+jZ)(P+jQ)[j_o(kr) - jn_o(kr)]\ dS \qquad (2)$$

where $P = \cos(ka)$ and $Q = \sin(ka)$
substituting for the radius vector (Fig.1.2)

$r^2 = h^2 + \sigma^2, \qquad dS = 2\pi\sigma\, d\sigma$

After integration, Eq(2) becomes

$$p_m = \rho_o ckU \left\{[(YP-ZQ)^2+(ZP+YQ)^2].[(CI)^2+(SI)^2]\right\}^{\frac{1}{2}} \qquad (3)$$

where $CI = \frac{1}{k}[\sin(k\sqrt{(h^2+R^2)}) - \sin(kh)]$

$SI = \frac{1}{k}[\cos(kh) - \cos(k\sqrt{(h^2+R^2)})]$

Then sound level is evaluated from relation

$$SPL = 20 \log_{10}(p/p_o) \qquad (4)$$

The sound pressure levels are calculated for a given height of the microphone from Eqs.(3) and (4), in which the velocity amplitude can be evaluated from vibration displacement measurements.

As a next higher approximation, the vibrating structure is considered to be composed of dipole sources [8,9]. For this one has the following expressions (Fig.2.1 and 2.2).

$r_1^2 = r^2+L^2 - 2rL\cos\theta, \qquad r_2^2 = r^2 + L^2 + 2rL\cos\theta$

As the microphone centre is in line with the dipole axis, (Fig.2.3)

$r_1^2 = r^2 + L^2 - 2hL, \qquad r_2^2 = r^2 + L^2 + 2hL$

The Eqn.(1) gets modified for the case of dipole as

$$dp = \frac{\rho_o ckU}{2\pi} e^{jka} (Y+jZ)\left(\frac{e^{-jkr_1}}{r_1} - \frac{e^{-jkr_2}}{r_2}\right) dS \qquad (5)$$

Substituting the values of r_1 and r_2, in Eqn.(5) and integrating, then taking the modulus only

$$p_d = \rho_o ckU \left\{[(YP-ZQ)^2+(YQ+ZP)^2][(CD1-CD2)^2+(SD1-SD2)^2]\right\}^{\frac{1}{2}} \qquad (6)$$

where $\left.\begin{matrix} CD1 \\ CD2 \end{matrix}\right\} = \frac{1}{k}\left[\sin(k\sqrt{(h^2+R^2+\frac{Fu1}{Fu2})}) - \sin(k\sqrt{(h^2+\frac{Fu1}{Fu2})})\right]$

$\left.\begin{matrix} SI1 \\ SI2 \end{matrix}\right\} = \frac{1}{k}\left[\cos(k\sqrt{(h^2+\frac{Fu1}{Fu2})}) - \cos(k\sqrt{(h^2+R^2+\frac{Fu1}{Fu2})})\right]$

and $Fu1 = L^2 - 2hL, \qquad Fu2 = L^2 + 2hL$

The pressure component due to dipole assemblage is calculated using the already known velocity from Eqn.(5).

In addition to the measurements of amplitudes from tests, in case of cantilever structure, theoretical amplitudes were evaluated from vibration analysis for the first five modes. The response of a beam to a point harmonic excitation taking into account the damping is given by [10]

$$L = \sum_{n=1}^{\infty} \frac{\phi_n(a)\ \phi_n(x)\ F}{m_n \omega_n^2 \sqrt{[(1-\Omega^2/\omega_n^2)^2 + (\beta\Omega/\omega_n^2)^2]}} \qquad (7)$$

Since the microphone is placed in the immediate vicinity of the structure, the effect of its area is now taken into consideration and a fresh theoretical analysis is made. This shows some marked differences as compared to that of Eqs.(3 and 6). In this case the radius vector is given by (Fig.3)

$$r^2 = h^2 + \mu^2 + \sigma^2 - 2\mu\sigma\cos(\theta - \phi) \qquad (8)$$

Using this expression in Eqn.(3) and Eqn.(6) they get modified as

$$p_{ma} = \frac{\rho_o ckU}{2\pi R^2} \left\{[(YP-ZQ)^2 + (ZP-YQ)^2][(CIB)^2+(SIB)^2]\right\}^{\frac{1}{2}} \qquad (9)$$

where,

$CIB = 13.1595[(h^2+2R^2)^{3/2} - 2(h^2+R^2)^{3/2} + h^3] - 1.31595\ k^2[(h^2+2R^2)^{5/2} - 2(h^2+R^2)^{5/2} + h^5],$

and $SIB = 9.87\ k\ R^4\ [1-(k^2h^2/6) - (k^2R^2/6)]$

These expressions are to be used when the source is considered as monopole array.

However, in case of dipole array, they get modified as,

$$p_{da} = \frac{\rho_o ckU}{2\pi R^2} \left\{[(YP-ZQ)^2+(ZP-YQ)^2][(CID1-CID2)^2+(SID1-SID2)^2]\right\}^{\frac{1}{2}} \qquad (10)$$

where

$\left.\begin{matrix} CID1 \\ CID2 \end{matrix}\right\} = 13.1595\ [(h^2+2R^2+\frac{Fu1}{Fu2})^{3/2} - 2(h^2+R^2+\frac{Fu1}{Fu2})^{3/2} + (h^2+\frac{Fu1}{Fu2})^{3/2}]$

$\quad -1.31595 k^2[(h^2+2R^2+\frac{Fu1}{Fu2})^{5/2} - (h^2+R^2+\frac{Fu1}{Fu2})^{5/2} + (h^2+\frac{Fu1}{Fu2})^{5/2}]$

and

$\left.\begin{matrix} SID1 \\ SID2 \end{matrix}\right\} = 9.87\ k\ R^4 (1 - \frac{k^2h^2}{6} - \frac{k^2R^2}{6} - \frac{\frac{Fu1}{Fu2}k^2}{6})$.

and Fu1, Fu2 are same as before.

The numerical evaluation of the above expressions were carried out in the Computer IBM 370/155, using double precision arithmetic.

3. EXPERIMENTAL PROCEDURE

Cantilever beams and plates all edges clamped were tested for their resonant behaviour. The fixtures for these structures were mounted on effectively isolated foundation to eliminate outside disturbances. Sound tests were carried out mostly during late night hours to keep back ground noise level minimum.

For the vibration tests, electrodynamic exciter, contactless inductive pick up and other related equipment were used. By changing the position of the pick up, on each of the resonant frequencies mode shapes are obtained indicating the nodal positions.

For sound tests, a condenser microphone together with B and K Frequency Analyser unit was used. Frequency analyser was more effective than sound level meter as the former can filter the discrete frequencies. A special attachment (displacement apparatus) was used for traversing the microphone along the length of the structure. Care was exercised to maintain the constant air gap between the pick up and the structure, in addition the effect of using piezlelectric accelerometer was studied. The experimental set up could be seen from Fig. 8.

4. RESULTS AND CONCLUSIONS

The following conclusions may be drawn in these investigations:

a) In Figs.4 and 6 the results obtained for beam and plate are shown. 'A' refers to, the amplitude in dB estimated from sound measurement. Essentially the monopole theory has been used to evaluate the sound pressure level theoretically, from Eqn.(3). These are represented by 'B' and 'C', the measurements of vibration and acceleration amplitude being made through vibration pick up and an accelerometer respectively. The mass effect of accelerometer can be observed in above mentioned figures, particularly for thin structures at high frequencies (Tables 1 and 2).

b) In Figs.5.1 to 5.5 and 7.1 to 7.3, the mode shapes of both a beam and plate for their first five and three frequencies respectively are shown. It can be seen that monopole theory gives good qualitative results compared to dipole results. However dipole theory can be safely applied to lower frequencies.

c) The theoretical evaluation of SPL using Eqn.(9) which includes the effect of microphone area shows a consistent decrease of 3.5 dB to 4 dB. This could be clearly seen from Fig. 9.

d) It was observed in vibration tests, the measurement of amplitude using contactless inductive pick up becomes impossible at higher frequencies, and the use of piezo accelerometer also becomes ruled out due to large shift in the frequency of the system by which amplitudes get distorted. Specially at these high frequencies (i.e. audio range) the microphone as being contactless, effectively yields sharp nodal points (Figs.5.2 to 5.5 and Table 3).

e) Primarily, the monopole theory being suitable both at low and high frequencies, the addition of the monopole and dipole theory can be accepted as it corrects the monopole evaluation in favour of the required result(Fig.5.1).

f) It may be concluded, hence, that microphone can be effectively used as contactless sensing tool to evaluate mode shapes at low and high frequencies of oscillation. Further tests conducted in specially constructed anechoic chamber may give still better results.

ACKNOWLEDGEMENT

The authors wish to thank Mr.S.Swarnamani, Senior Technical Assistant, for his kind help while conducting the experiments.

REFERENCES

1. Development and application of vibroacoustical structural data banks in predicting vibration, design and test criteria for rocket vehicle structure NASA - TND 7159 - 1973

2. C.W. Horton and A.E. Sobey Jr., 'Studies on the near fields of monopole and dipole acoustic sources', JASA, (30), No.12, pp 1088, 1958

3. I. Malecki, 'Physical foundations of technical acoustics', PWN - Polish Scientific Publishers, Warzawa, 1969

4. E. Skudrzyk, 'Simple and complex vibratory systems', The Pennsylvania State University Press, 1968

5. B.V.A. Rao, B. Rama Bhat and R.V.R. Sastry, 'Determination of natural frequencies and modal patterns of vibrating structures by acoustic measurements', Proceedings of ISTAM - India, 1970

6. L.E. Kinsler and A.R. Frey, 'Fundamentals of acoustics', John Wiley and Sons, Inc., 1962

7. J.L. Hunter, 'Acoustics', Prentice-Hall Englewood Cliff - 1957

8. D.H. Towne, 'Wave phenomena', Addison Wesley Pub. Co., 1967

9. N. Curle, 'The influence of solid boundaries upon aerodynamic sound' Proc. of Royal Society, pp 505-514, 231, 1955

10. D. Young, 'Continuous systems' Chapter 61, Hand book of Engineering Mechanics ed.W. Flugge, McGraw Hill Book Co. Inc., 1962

Table 1

Comparison of theoretically evaluated natural frequencies with experimentally obtained by forced vibration tests with different pick ups for a cantilever beam

(37 x 5 x 0.5 cm)

Mode	Experimental Microphone Hz	Contactless Inductive pick up Hz	Accelerometer with magnetic base Hz	Theoretical Hz
1	25	25	21	29
2	158	159	141	181
3	438	440	411	508
4	900	897	770	997
5	1538	1540	1223	1648

Table 2

Comparison of theoretically evaluated natural frequencies with experimentally obtained by forced vibration tests with different pick ups for a plate all edges clamped (53 x 53 x 0.17 cm)

Mode	Experimental Microphone Hz	Contactless Inductive pick up Hz	Accelerometer with magnetic base Hz	Theoretical Hz
1	55.0	55.0	54.0	55.7
2	101.0	101.0	96.0	113.5
3	151.0	151.0	148.0	160.5

Table 3

Comparison of theoretically and experimentally obtained nodal positions (through sound measurements) for the above fixed free beam

Mode 2	Theoretical	0.783			
	Experimental	0.760			
Mode 3	Theoretical	0.504	0.868		
	Experimental	0.480	0.840		
Mode 4	Theoretical	0.358	0.646	0.906	
	Experimental	0.320	0.600	0.880	
Mode 5	Theoretical	0.278	0.500	0.723	0.927
	Experimental	0.240	0.480	0.720	0.920

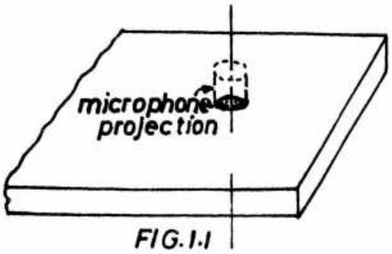

FIG.1.1

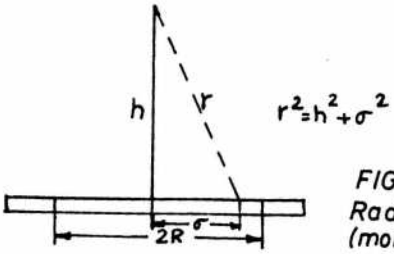

FIG.1.2 Radius vector (monopole)

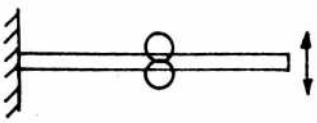

FIG.2.1a Dipole idealisation of the vibrating beam

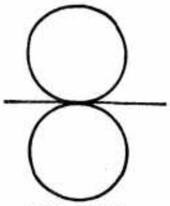

FIG.2.1b SPL distribution of an ideal dipole

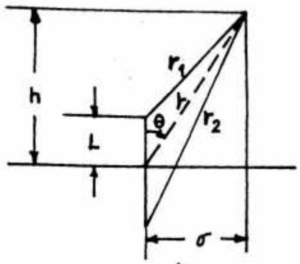

$$\cos\theta = \frac{h}{r}$$

$$r_1^2 = r^2 + L^2 - 2hL$$

$$r_2^2 = r^2 + L^2 + 2hL$$

FIG.2.2 Radius vectors (Dipole)

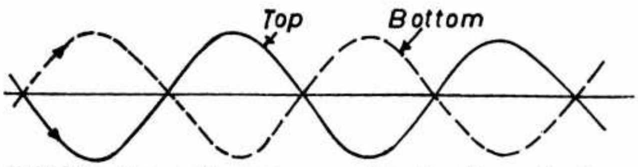

FIG.2.1c. Acoustic pressure fluctuations at the beam surface

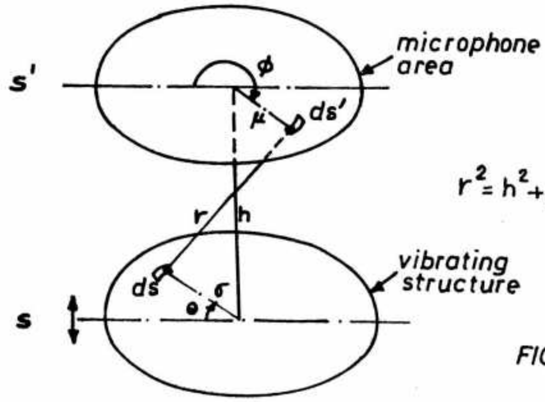

$$r^2 = h^2 + \mu^2 + \sigma^2 - 2\mu\sigma\cos(\theta - \phi)$$

FIG. 3 Inclusion of microphone area

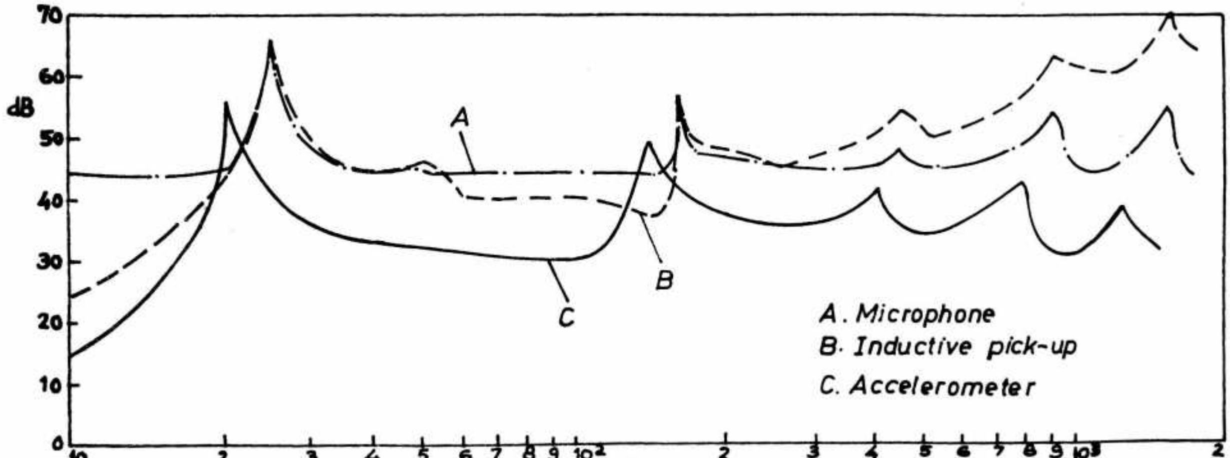

FIG.4 SPL Spectrum

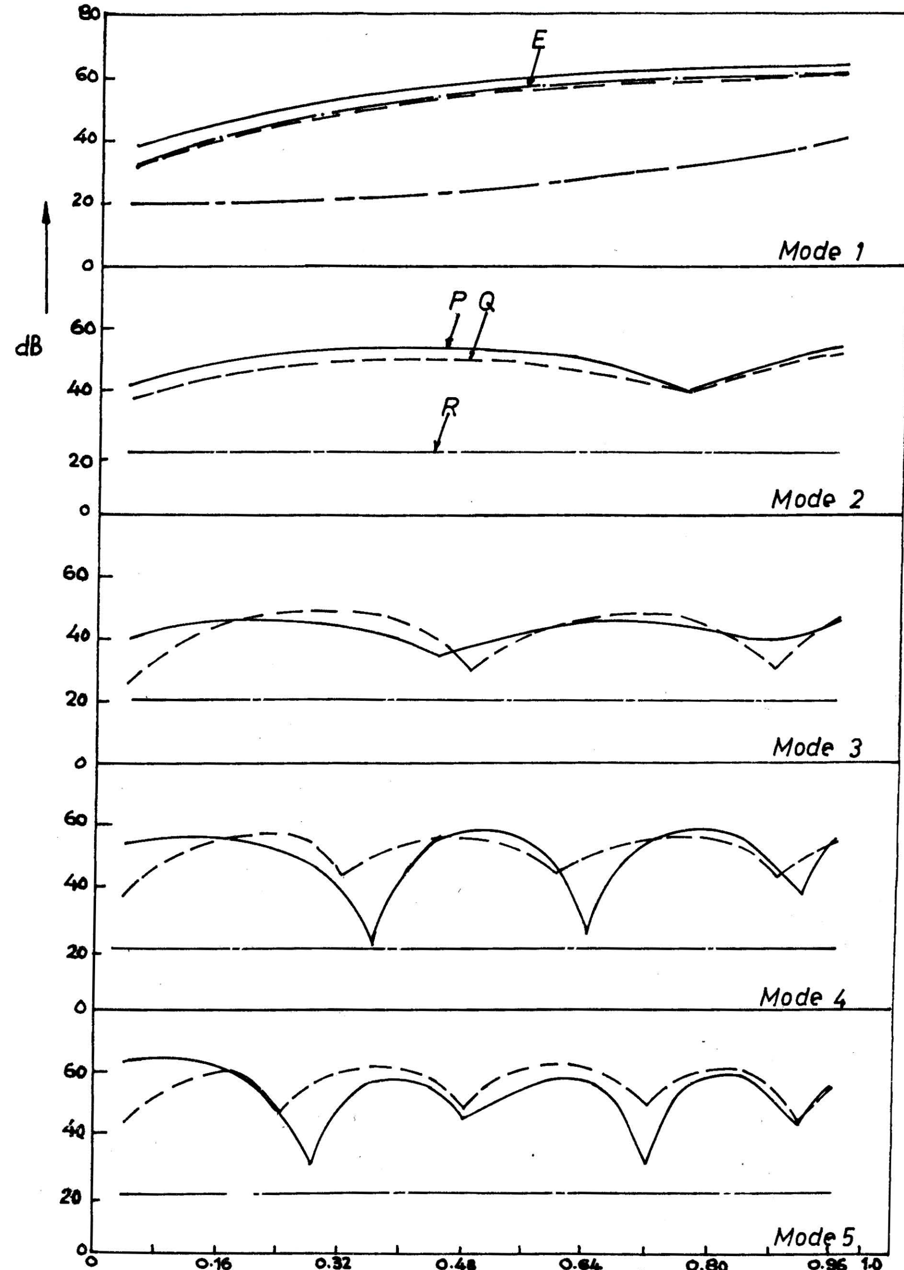

E. SPL from sum of eqns. 3 & 6

FIG. 5.1

FIG. 5.2

Mode shapes of fixed free beam.

FIG 5.3

P. Experimental

Q. Theoretical (From eqn. 3)

R. Theoretical (From eqn. 6)

FIG. 5.4

FIG 5.5

$\xi = \dfrac{X}{\text{Length of beam}}$

$\xi = 0$, fixed

$\xi = 1$, free

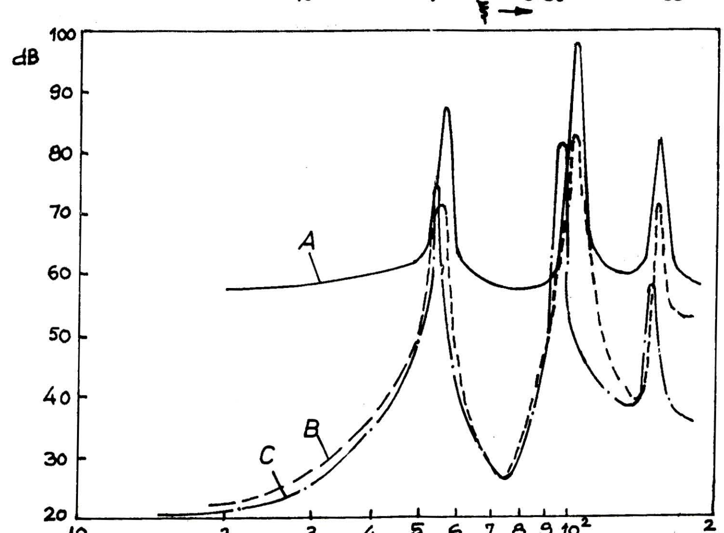

A. Microphone

B. Inductive pick-up

C. Accelerometer

FIG. 6. SPL Spectrum

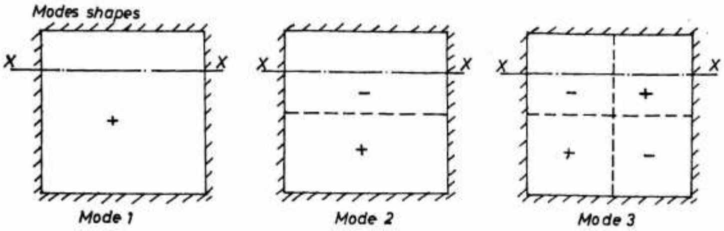

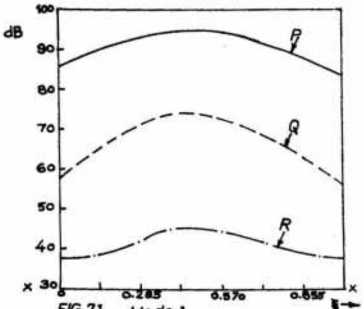

FIG. 7.1 Mode 1

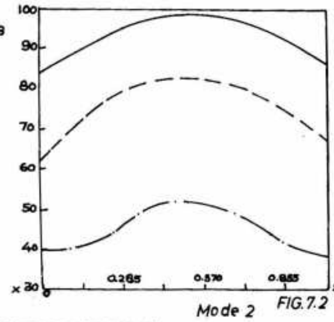

Mode 2 FIG. 7.2

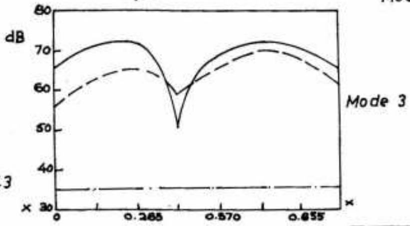

FIG. 7.3

P = Experimental
Q = Theoretical (From eqn. 3)
R = Theoretical (From eqn. 6)

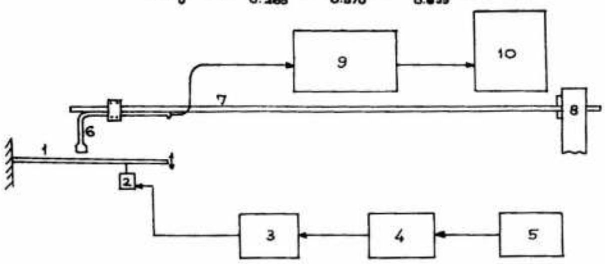

1. Specimen
2. Exciter
3. Multimeter
4. L.F. Oscillator
5. Digital Frequency counter
6. Condenser microphone
7. Holder for the pickup
8. Displacement apparatus
9. Audio spectrum analyser
10. Double beam oscilloscope

Fig. 8.1. Schematic diagram.

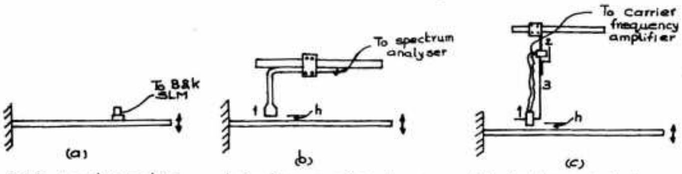

B&K Accelerometer with magnetic base

SLM – Sound Level meter

1. Condenser microphone

1. Contactless inductive pick up
2. Compensation pickup
3. Fixture

Fig. 8.2. Specimen-transducer arrangements.

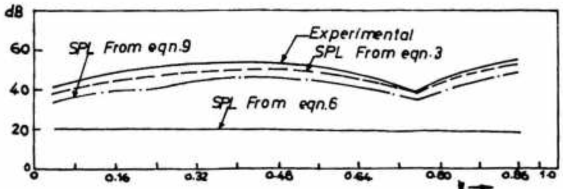

FIG. 9 . A typical plot showing the effect of including microphone area on SPL.

THE MEASUREMENT OF THE TRANSMISSION LOSS OF A LOW NOISE REDUCTION TEST ITEM

D. A. Bies
Department of Mechanical Engineering
University of Adelaide
Adelaide, S.A.

J. A. Pickles
Department of Mechanical Engineering
University of Adelaide
Adelaide, S.A.

Noise, Shock & Vibration Conference, 1974 — Monash University, Melbourne

SUMMARY -

The problem of the measurement of the transmission loss of a test item of low noise reduction is considered. The test item might be a low transmission loss panel, a small or even a large aperture. It is shown that energy feed back from the source room during measurement of the reverberant decay of the receiving room does not place a lower bound on the transmission loss that can be measured. It is shown that a reversal of the roles of the source and receiver rooms with each set of measurements is sufficient to unambiguously define the transmission loss of any test item even in the case of very low noise reduction.

GLOSSARY OF TERMS -
(The indices i and j may take the values of either 1 or 2)

- A constant of eq (21), joules/m^3
- A_i equivalent totally absorptive area for the walls of room i excluding the common partition and air propagation effects, m^2
- a a dimensionless quantity defined by eq (17)
- B constant of eq (22), joules/m^3
- B_i constant of eq (26)
- b dimensionless quantity defined by eqs (14) and (15)
- c speed of sound, m/sec
- D_{ir} reverberant field energy density in room i, joules/m^3
- H_i equivalent totally absorptive area for room i, m^2
- L_{io} steady state sound pressure level in the reverberant field of room i, dB/20μPA
- L_{it} instantaneous sound pressure level in the decaying reverberant field of room i, dB/20μPA
- M a dimensionless quantity defined by eq (18)
- M_i solutions to eq (23) given by eqs (24) and (25)
- m air absorption coefficient, m^{-1}
- $(NR)_{ij}$ noise reduction from room i to room j, decibels
- S area of the common partition, m^2
- S_i total surface area over all walls of room i, m^2
- (TL) transmission loss, decibels
- t time, sec
- V_i volume of room i, m^3
- $4V_i/S_i$ mean free path between reflections in room i, m
- W_{ij} power flow from the reverberant field of room i to room j through the common partition, watts
- W_{ir} power flow to the reverberant sound field of room i, watts
- α sound absorption coefficient of the common partition

α_i generalised absorption coefficient including not only wall absorption but propagation loss between reflections expressed as the fraction of incident acoustic energy absorbed averaged over all walls of room i

β_i fraction of incident acoustic energy absorbed averaged over all walls of room i

λ decay coefficient of eqs (21) and (22), sec^{-1}

λ_i decay coefficients of eq (26), sec^{-1}

σ_i fraction of transmitted energy delivered to the reverberant field in room i

τ fraction of incident sound energy transmitted through the partition

INTRODUCTION

The standard procedure for measuring the transmission loss of a test item requires a measurement of the noise reduction through the item and a measurement of the sound absorption of the receiving room.[1] The latter measurement is generally made by determining the reverberant decay of the receiving room with the test item in place on the assumption that the reverberant energy feed back from the source room is always quite negligible. Thomas Mariner[2] has analysed this situation and has shown that for some cases of interest the energy feed back may not be negligible and that in the case of low noise reduction through the test item the error experienced in neglecting energy feed back may be quite large. He further concludes that this situation imposes fundamental limits on the possible precision of measurement of transmission loss and that in the limiting case of little or no noise reduction the transmission loss cannot be measured with any predictable precision.

Mulholland and Parbrook[3] have considered the matter further, following Mariner's analysis, and have proposed an alternative procedure involving the use of a calibrated source and substitution panel. In their procedure first a thick panel is tested then the low noise reduction item is tested. Theygenerally agree with Mariner's conclusions but they do claim that low transmission loss test items can be measured using their substitution procedure. A search of the literature seems to show that the matter has rested there.

We have reconsidered Mariner's analysis and have found, contrary to the conclusions of the previous authors, that there is no fundamental limit to the precison of measurement implied. For example, we have found that the equations can readily be solved and the necessary analysis by which the transmission loss of a lossless aperture giving low noise reduction can be measured. The use of the procedure is then demonstrated for three cases: a large $9.7m^2$ opening, a $1.5m^2$ opening and a $1.5m^2$ mass law panel.

The matter of the power flow to the reverberant field of the receiving room is also considered. We argue that in spite of various attempts to define separately a direct and a reverberant field, the original assumption of Buckingham[4] that all of the transmitted acoustic power is delivered to the reverberant field of the receiving room is best on a purely pragmatic basis. We show, however that the calculated transmission loss is rather insensitive to the definitions of the reverberant field that have been proposed. The matter is only important to the conclusion that the transmission loss can be defined with precision in terms of measurable quantities.

EQUATIONS FOR TRANSMISSION LOSS MEASUREMENT

In this section we will consider the transmission of sound through a partition common to two reverberant rooms. We will follow the analysis generally outlined by Mariner[2] and considered further by Mulholland and Parbrook[3]. We will show that contrary to the conclusions of the authors cited, Mariner's equations for transmission loss are readily soluable in terms of measurable quantities . The transmission loss of a simple opening can be measured without resort to substitution methods and calibrated sound sources.

Alternative definition of the reverberant field

We assume that a sound source in room one establishes a reverberant field that is incident upon the common partition. As a consequence some acoustic energy flows through the partition into room two. Close to the partition in room two the sound field will be elevated and apparently dominated by sound radiating directly from the panel, however remote from the panel in a suitably live room the sound field will be sensibly constant and apparently dominated by multiply reflected sound. These observations may be described by defining a direct field and a reverberant field.[5] As detail about the direct field is seldom known or of importance it is commonly described as a spherically divergent field and consistent with the concept that the reverberant field describes the reflected sound it is defined as the field resulting after the direct field has been once reflected.

The suggested definitions of the reverberant and direct fields seem straightforward but as will be shown by reference to Mariner's formulation they lead to a conceptual difficulty. Mariner defines the power flow to the reverberant field of room two, W_{2r}, as follows.

$$W_{2r} = W_{12}(1 - \beta_2)\exp(-4V_2m/S_2) \tag{1}$$

Symbols are defined separately in the Glossary of Terms. In the above expression W_{12} is the acoustic power flow through the partition from room one to room two. The expression $(1-\beta_2)$ represents the fraction of acoustic power reflected at the walls of room two while the exponential term takes account of air propagation loss.

Since the quantities multiplying W_{12} in eq (1) are close to unity the equation may be readily linearized. Thus following Mariner we may write in place of eq (1)

$$W_{2r} = W_{12}\sigma_2 \tag{2}$$

where σ_2 is the fraction of transmitted energy which is delivered to the reverberant field. The quantity σ_2 is related to the generalised random incidence absorption coefficient α_2 as follows.

$$\sigma_2 = 1 - \alpha_2 \tag{3}$$

$$\alpha_2 = H_2/S_2 \tag{4}$$

$$H_2 = S_2\beta_2 + 4V_2m = A_2 + S\,(\alpha + \tau) + 4V_2m \tag{5}$$

As defined by eqs (4) and (5) the quantity α_2 takes account of sound absoprtion at all the walls in room two including transmission back to room one and dissipation at the common partition as well as air propagation loss.

The definition of the genrralised absorption coefficient α_2 is quite reasonable for multiply reflected sound. However, as Mariner concedes its use in eq (3) must lead to an under estimate of the power flow to the reverberant field. For example all the walls of room two cannot be equally effective in absorbing acoustic energy at the first reflection of the direct field. Further the direct field can hardly be described as randomly incident on any wall. Clearly the panel will never see the direct field; it will only see sound at least once reflected. Furthermore the air propagation loss of the direct field will depend upon the geometry of the room and it would be quite fortuitous if it could be estimated with any accuracy in terms of the mean free path, $4V_2/S_2$, between many reflections. The power flow as defined by eqs (2) and (3) must be considered as only approximate at best and thus a transmission loss using eq (3) cannot be defined with precision.

Donato[6] has considered the problem of the definition of the direct field and he concludes that it can be estimated with more precision than suggested by Mariner. He provides an analysis by which it can be described but the description requires more than a knowledge of the total wall area and volume of the receiving room. Donato does not, however, explain how the direct and reverberant fields are to be measured separately in the region where the reverberant field predominates, a requirement which must surely be met if the definitions are to be of use for the measurement of transmission loss.

When a measurement is made of the reverberant field it must always contain a contribution, however small, from the direct field. Thus a further difficulty with eq (3) is encountered; the reverberant field defined to exclude the direct field cannot be measured. Rather the sum of the direct and reverberant fields as defined above are always measured in the reverberant field. These considerations lead to the suggestion that the power flow to the reverberant field be set equal to the power transmitted through the panel in which case

$$\sigma_2 = 1 \tag{6}$$

The assumption expressed by eq (6) has the pragmatic advantage that the power flow to the reverberant field, as defined, can be measured. It is in agreement with the original assumption of Buckingham[4]. This definition of the reverberant field has the additonal advantages of providing an unambigious definition of transmission loss and an accurate description of a practical measurement situation.

Equation (6) is offered as an alternative to eq (3) which avoids the ambiguity which arises from the use of the former equation in defining the transmission loss. However, in any case,the generalised absoprtion coefficient α_2 is always small so that practically σ_2 is very little different from unity. The chief advantage then in the use of eq (6) is that a precise definition may be given for the transmission loss in terms of measurable quantities. The method for solution to be outlined below is equally effective if either eq (3) or eq (6) is used as will be shown.

The power flow in the reverberant field results in acoustic energy losses on propagating through the air and on reflecting at the walls. This fact may be expressed in terms of the reverberant field energy density as

$$W_{2r} = D_{2r}H_2c/4 \tag{7}$$

The power flow from the reverberant field of room one through the panel to room two on the other hand is

$$W_{12} = D_{1r}Sc\tau/4 \tag{8}$$

Substitution of eqs (7) and (8) into eq (2) gives the steady state relation between the reverberant fields of rooms one and two as

$$D_{1r}S\tau\sigma_2 = D_{2r}H_2 \tag{9}$$

Equation (9) provides the required relation between the reverberant sound field in room one and the resulting sound field in room two by which the transmission loss may be defined.

Transmission loss, noise reduction and some useful relations

The transmission loss of a partition may be defined in terms of the fraction of energy incident upon the partition which is transmitted. Thus by definition the transmission loss of a partition is

$$(TL) = -10 \log_{10}\tau \tag{10}$$

The noise reduction, on the other hand, may be defined as the difference in sound pressure levels in the reverberant fields of the two rooms. Thus according to eq (9) the noise reduction from room one to room two is

$$(NR)_{12} = -10 \log_{10}(S\tau\sigma_2/H_2) \tag{11}$$

while the noise reduction in the opposite direction, where the sound source is now placed in room two instead of roon one, is

$$(NR)_{21} = -10 \log_{10}(S\tau\sigma_1/H_1) \tag{12}$$

The transmission loss may be written in terms of the noise reduction from room one to room two using eqs (10) and (11) as

$$(TL) = (NR)_{12} + 10 \log_{10}(S/H_2) + 10 \log \sigma_2 \tag{13}$$

For later convenience we note the following relations. If we add the noise reductions measured in the opposite directions we obtain

$$(NR)_{12} + (NR)_{21} = 10 \log b \tag{14}$$

where

$$b = H_1H_2/S^2\tau^2\sigma_1\sigma_2 \tag{15}$$

On the other hand, if we subtract the noise reduction measured from room one to room two from the noise reduction measured in the opposite direction we obtain

$$(NR)_{21} - (NR)_{12} + 10 \log_{10}(V_2/V_1) - 10 \log_{10}M = 10 \log_{10}a \tag{16}$$

where

$$a = H_1V_2/H_2V_1 \tag{17}$$

and

$$M = \sigma_2/\sigma_1 \tag{18}$$

It will be shown that eqs (14) and (16) allow the determination of the transmission loss of a partition even when the transmission loss is zero and the noise reduction is very small.

Reverberant decay of two coupled rooms

Following Mariner we consider the decay of reverberant energy in room two where account is taken of energy flow back from room one. The decay of reverberant energy in room two is $V_2(dD_{2r}/dt)$ where the loss on reflection and propagation is $-D_{2r}H_2c/4$ and the energy supplied is given by eqs (2) and (8). Thus the energy balance for room two during decay may be written by modifying eq (9) to read as follows,

$$4V_2(dD_{2r}/dt) = -D_{2r}H_2c + D_{1r}S\tau\sigma_2c \tag{19}$$

Similarly we may write for room one

$$4V_1(dD_{1r}/dt) = -D_{1r}H_1c + D_{2r}S\tau\sigma_1c \tag{20}$$

Particular solutions for eqs (19) and (20) are

$$D_{1r} = A \exp(-\lambda t) \tag{21}$$

$$D_{2r} = B \exp(-\lambda t) \tag{22}$$

Substitution of eqs (21) and (22) into eqs (19) and (20) leads to the following expression which defines two particular values of λ.

$$\left.\begin{matrix} M_1 \\ M_2 \end{matrix}\right\} = 0.5[(a+1) \pm\sqrt{(a-1)^2 + ab}\ ] \tag{23}$$

where $$M_1 = 4V_2\lambda_1/H_2c \tag{24}$$

and $$M_2 = 4V_2\lambda_2/H_2c \tag{25}$$

In writing eq (23) use has been made of eqs (15) and (17). The quantities a and b are defined by eqs (14) and (16) in terms of readily measured quantities provided that in case M is not taken as unity and eq (3) is used that M can be estimated. It will be shown that in this case M may be determined by successive iteration. Thus in either case M_1 and M_2 may be determined from the two noise reduction measurements made in opposite directions.

The particular solutions given by eqs (21) and (22) may be generalised by making use of the solutions given by eqs (24) and (25). It will be sufficient to consider the case where the source is placed in room two and the reverberant decay in room two is subsequently measured when the source is abruptly shut off. In this case the reverberant energy density at time t subsequent to shutting off the source in room two is

$$D_{2r}(t) = D_{2r}(0)[B_1\exp(-\lambda_1 t) + B_2\exp(-\lambda_2 t)] \tag{26}$$

where initial conditions at time t equals zero require that

$$B_1 + B_2 = 1 \tag{27}$$

and $$D_{1r}(0) = D_{2r}(0)S\tau\sigma_1/H_1 \tag{28}$$

Substitution of eq (26) into eq (19) and the use of eq (28) leads to a linear equation in B_1 and B_2 which is independent of eq (27). Thus solutions for B_1 and B_2 may be determined using the latter equation and eq (27). The solutions are as follows,

$$B_1 = M_1(a-M_2)/a(M_1-M_2) \tag{29}$$

$$B_2 = M_2(M_1-a)/a(M_1-M_2) \tag{30}$$

The quantities B_1 and B_2 may thus be determined from the two noise reduction measurements described earlier using eqs (14), (16) and (23).

Equation (26) may be rewritten using eqs (24) and (25) as follows,

$$D_{2r}(t)/D_{2r}(0) = B_1[\exp(-M_1ct/4V_2)]^{H_2} + B_2[\exp(-M_2ct/4V_2)]^{H_2} \tag{31}$$

If we measure the change in sound pressure level in the reverberant field that takes place in time t then eq (31) may be used to determine H_2. For this measurement we use

$$L_{20} - L_{2t} = 10 \log_{10}(D_{2r}(0)/D_{2r}(t)) \tag{32}$$

We note in passing that a level change is measured, not the conventional decay rate, thus the decay rate need not be constant as suggested by eq (26).

The value of H_2 given by eq (31) allows the calculation of the transmission loss using eq (13) directly if σ_2 is set equal to unity. In case that the power flow to the reverberant field is defined, following Mariner, so that σ_2 is given by eq (3). Then an iteration procedure must be used. In this case reverberation decay measurements must be made in both rooms. One proceeds by initially assuming that M in eq (16) is unity. This is a fairly good assumption for most reverberant rooms. Then one proceeds to calculate values for H_1 and H_2 and, following the definition of eq (4) and its equivalent for room one, α_1 and α_2. These values of α_1 and α_2 are used to calculate a new value for M according to eq (18) which is entered into eq (16) and the whole process is repeated. It has been shown using a small computer programme that the process is convergent to at least three decimal place accuracy in M which is more than sufficient for the accuracy of measurement of sound pressure levels possible in most reverberation chambers.

TEST ARRANGEMENT

Test Rooms

Testing was done in the reverberation chambers of the Department of Mechanical Engineering at Adelaide University. This facility consists of two connected, rectangular chambers of volume $105.6m^3$ (6.09m x 5.18m x 3.36m) and $179.7m^3$ (6.84m x 5.57m x 4.72m). Construction is of 0.3m thick reinforced concrete faced internally with hard gypsum plaster. Isolation from ground vibration is accomplished by mounting each room independently on soft helical spring supports. The two rooms are connected by an opening of area $9.71m^2$ (3.04m x 3.20m). There is no mechanical connection between the two rooms, a 0.37m gap between them being bridged by a frame of 25mm thick chipboard supported from the external wall of the larger chamber. A small gap between the edge of this frame and the outer wall of the small chamber is sealed with nonhardening mastic.

The larger room contains a rotating vane diffuser of area $7.05m^2$ (2.90m x 2.43m). The diffuser was run at its maximum rate of rotation, 7 revolutions a minute, during all tests.

Removable Wall

The size of the aperture connecting the two rooms may be reduced by removing the chipboard frame and sliding a modular, double-leaf lead wall into place between the chambers. This wall consists of two independent wooden frames supporting free hanging lead sheets of surface density 39 kg/m^2. Each leaf of the wall is divided by the wooden frame into three panels running the full height (3.10m) of the aperture between the test rooms. The lead sheet in the two outer panels is permanently attached to the frame but that in the centre panel is hung on removable, modular wooden sub-frames so that a number of different aperture sizes may be easily obtained.

The walls are mounted independently, one being attached and sealed to the outer wall of the small test room and the other to the larger room. Rockwool blankets 90 mm thick are hung behind each lead sheet in the space between the two leaves of the wall as shown in figure 1.

When tested with the centre bay filled with three lead hung sub-frames the transmission loss of the composite wall was found to be 40 dB at 63 Hz rising to over 80 dB at frequencies greater than 500 Hz, as shown in figure 1.

For two of the tests reported in this paper one of the three subframes in the centre bay of the wall was removed and replaced by a metal frame. This frame was attached rigidly to one leaf of the double wall and a gap between it and the second leaf sealed with non hardening mastic. Test panels 1.5m x 1.0m were clamped in this metal frame.

Apparatus

Each room was acoustically excited by two 25 watt twin-cone loudspeakers located in opposite trihedral corners of the room. The speakers were powered by the one-third octave filtered output of a Bruel and Kjaer Random Noise Generator (Type 1402).

Bruel and Kjaer one-half inch microphones (Type 4134) were used in conjunction with a Bruel and Kjaer real-time analyser (Type 3347/4710) and graphic level recorder (Type 2305) to measure the sound pressure levels in each room. The real-time analyser contains one-third octave filters.

Time and space averaging of the acoustic field in the small room was effected by attaching the microphone to the end of a 1.0m long arm mounted on a continuously rotating Bruel and Kjaer turntable (Type 3921). To provide a signal suitable for transmission through the turntable sliprings the microphone signal was first passed through a Bruel and Kjaer precision sound level meter (Type 2203) mounted on the turntable. The period of rotation of the turntable was 80 seconds and the path length swept out by the microphone was 6.3m.

In the larger chamber the microphone traversed continuously along a wire stretched obliquely between two opposite faces of the chamber. The time taken to traverse the chamber in one direction was 66 sec over a length of path of 5m.

The same equipment was used for reverberation time measurements.

Measurement Procedure

Each measuring system was calibrated using a Bruel and Kjaer pistonphone (Type 4220).

The transmission characteristics of the opening or panel between the two rooms was measured first using the small room as the source room, and then in the reverse direction using the large room as the source room. Sound pressure levels in each of the rooms in each of the one-third octave bands between the 63 Hz and 8kHz centre-frequency bands were recorded on the graphic level recorder chart. Each record was sufficiently long to ensure one complete rotation of the microphone boom or one complete traverse of the larger room.

Reverberation measurements for each one-third octave band were made by abruptly stopping the output from the random noise generator after the establishment of a uniform reverberant sound field and recording the decaying reverberant sound field in the room on the graphic level recorder.

EXPERIMENTAL RESULTS

Three configurations were tested. In the first the two rooms were coupled by an open area of $9.71m^2$ (3.04m x 3.20m), that is the full transmission loss aperture. For the second test the double-leaf wall was mounted between the rooms and the centre sub-frame of the centre panel removed to give an open area of $1.5m^2$ (1.5m x 1.0m). Finally a sandwich panel with rubber core and steel sheet faces was mounted in the 1.5m x 1.0m aperture in the double-leaf wall. This panel has been designed to have a mass controlled response over a wide frequency range (coincidence frequency 129 kHz). It consisted of a 3.2mm thick sheet of 75 durometer hardness natural rubber bonded to 24 gauge cold-rolled steel facing sheets with Dunlop 5758 adhesive. The surface mass of this composite panel was 14.9 kg/m^2.

For each one-third octave band the average sound pressure level was estimated by eye from the graphic level recorder chart traces. At the lowest frequencies the spatial variation in reverberant level varied as much as ± 2.5 dB about the mean owing to the characteristics of the signal generator and the response of the room. Above 1000 Hz the level variation was ± 0.25 dB or less.

The sound pressure levels so obtained were used to calculate the aperture or panel transmission loss according to the usually accepted procedure[1], and also according to the modified procedure described above.

The transmission loss data so calculated are plotted in figure 2 for the $9.71m^2$ open area, in figure 3 for the $1.5m^2$ open area and in figure 4 for the $1.5m^2$ rubber cored panel. In these curves the mean trend is indicated by the straight lines. The vertical bar at each one-third octave band centre-frequency indicates the difference in estimated transmission loss between measurements made with transmission from the small to the large room and those made with transmission in the reverse direction.

DISCUSSION OF RESULTS AND CONCLUSIONS

The transmission loss of the full $9.7m^2$ opening of the Adelaide acoustic test facility was tested in order to provide strong coupling between the two rooms. It was expected that under such circumstances the effect of the omission or inclusion of energy feed back during reverberation measurements in the data analysis would have a strong effect on the results and indeed the data in fig. 2 confirm this expectation. On the other hand it must be admitted that the opening is so large as to clearly violate the requirement for diffuse reverberant fields in the two chambers unless the definition proposed in connection with eq (6) is accepted. Thus additional interest was provided by the exercise to see what answers would be obtained for clearly the transmission loss of the full opening must be zero over the entire frequency range shown in the figure. Above the 250 Hz one third octave band the error in measurement using the proposed procedure is less than 2.0 dB. The results using the standard procedure neglecting energy feed back are clearly inferior.

Tests were also run using the $1.5m^2$ opening. In this case the energy feed back between the two rooms would not be great but the reverberant fields in the two rooms should be more nearly diffuse. A second problem with the smaller opening is that the transmission loss is not necessarily zero over the entire frequency range of interest. However, we have estimated that the transmission loss should be only 1.5 dB in the 100 Hz band and that it should tend to zero at higher frequencies. Our estimate seems to be in general agreement with the predicitions for circular apertures.[7] Our estimate was carried out on the basis of a simple square piston type analysis.[8]

The data shown in fig. 3 generally lie within 1 dB of zero in the frequency range above the 200 Hz one third octave band. Again the results of the standard procedure, neglecting energy feed back, are clearly inferior. Our data using both the standard and modified procedures show an increase of transmission loss toward low frequencies generally not predicted by theory. The reason for this is not known but since similar behaviour was observed with the larger opening, it is thought that the problem lies with the finite size, especially of the smaller, of the reverberant rooms of the Adelaide University facility.

The data for the mass law panel shown in figure 4 are presented as a further comparison. In this case the panel was constructed to bend only in shear thus ensuring mass law response.[9] Thus the expected random incidence transmission loss could be calculated. We note thatthe modified procedure, which accounts for energy feed back, gives results identical to the standard procedure in this case where energy feed back is negligible.

We conclude that the modified procedure will give good results for measured transmission loss for at least three cases where the expected transmission loss can be predicted. These cases include even the case of zero transmission loss and very little noise reduction.

REFERENCES

1. ASTM Designation: E90-70

2. MARINER, Thomas. J.Acoust.Soc.Am. 33, 1131-1139 (Aug.1961)

3. MULHOLLAND, K.A. and PARBROOK, H.D., J.Sound Vib. 2 (4) 502-509 (1965)

4. BUCKINGHAM, Edgar, Sic.Papers Bur.Standards 20, 193 (1925)

5. BERANEK, L.L. Acoustics (McGraw-Hill Book Co.Inc., New York, 1954), p.321

6. DONATO, R.J., J.Acoust.Soc.Am. 40, 1-3 (Jan. 1966)

7. WILSON, G.P. and SOROKA, W.W., J.Acoust.Soc.Am. 37, 286-297 (Feb. 1965)

8. MALECKI, I., Physical Foundations of Technical Acoustics. English Translation by Bellert, Irene (Pergamon Press PWN - Polish Scientific Publishers) p.196. Alternatively, BURNETT, D.S. and SOROKA, W.W., J.Acoust.Soc.Am.51, 1618-1623 (Dec. 1969)

9. KURTZE, G. and WATTERS, B.G., J.Acoust.Soc.Am. 31, 739-748 (June 1959)

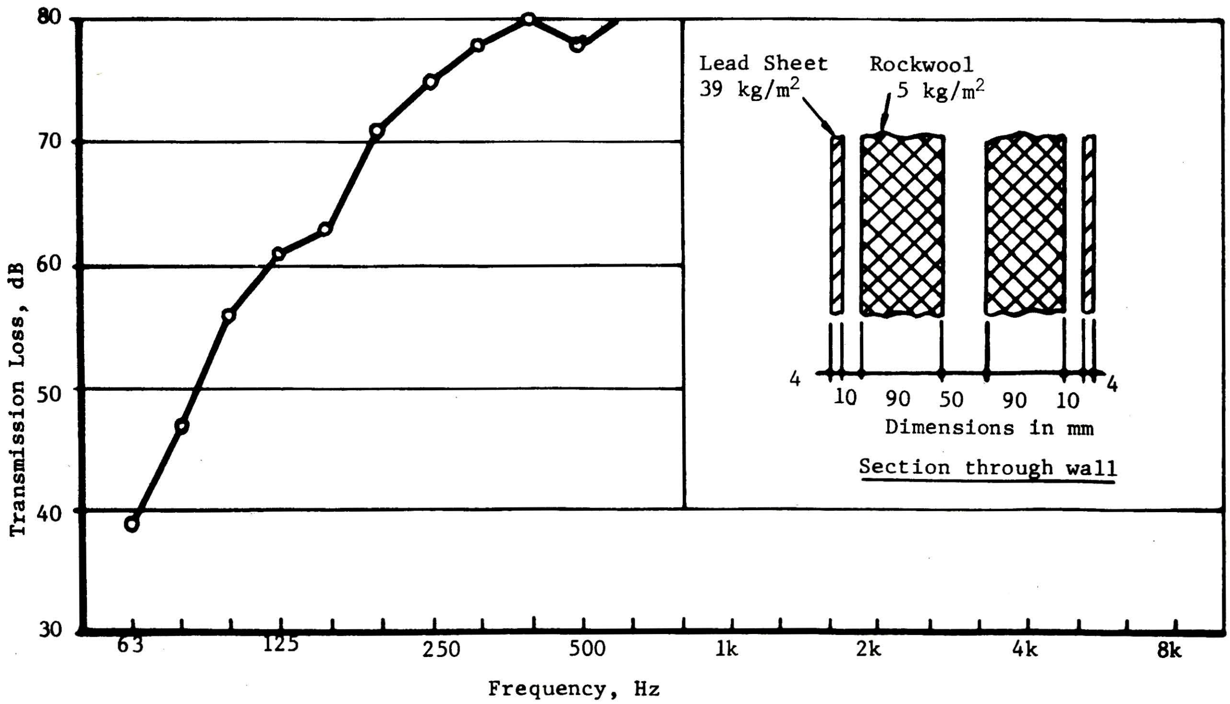

Fig. 1 Transmission Loss of Double Leaf Lead Wall

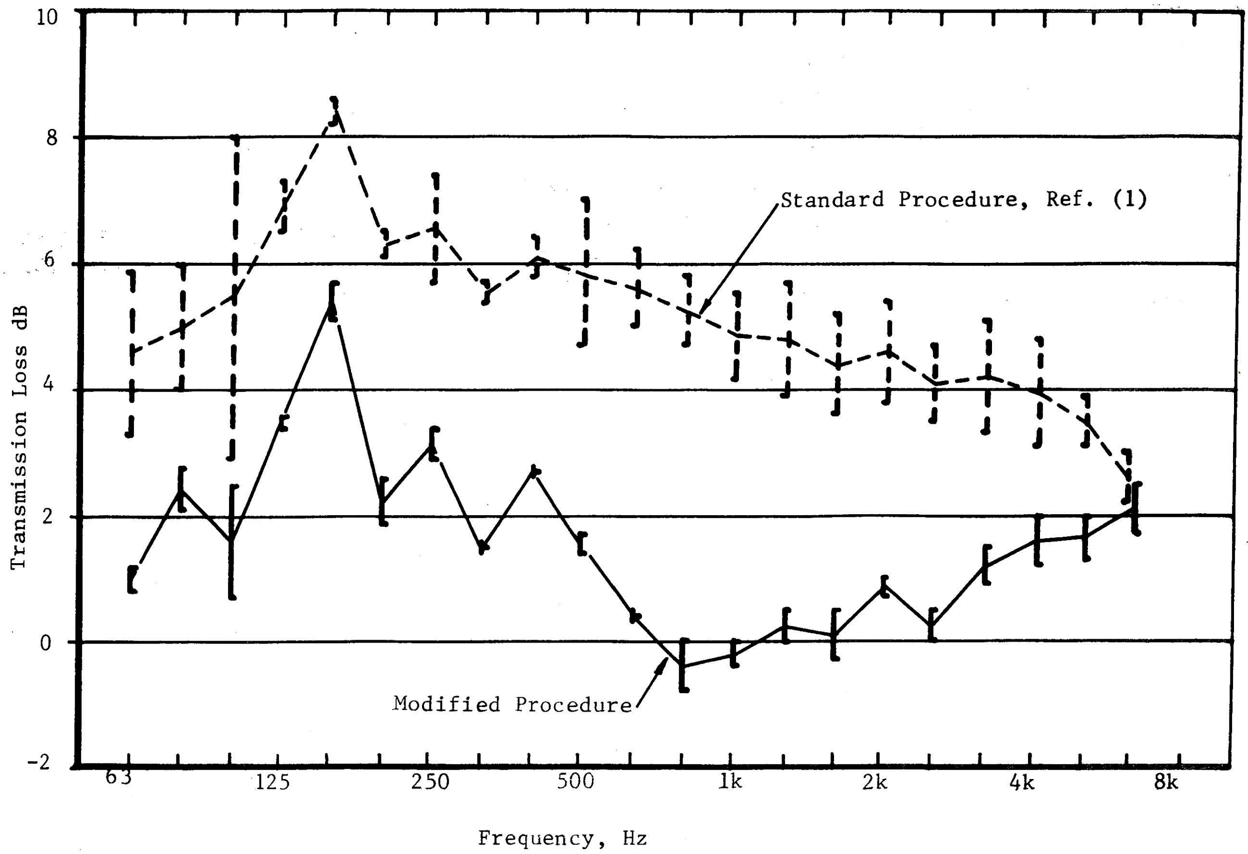

Fig. 2 Transmission Loss of 9.7m^2 Aperture

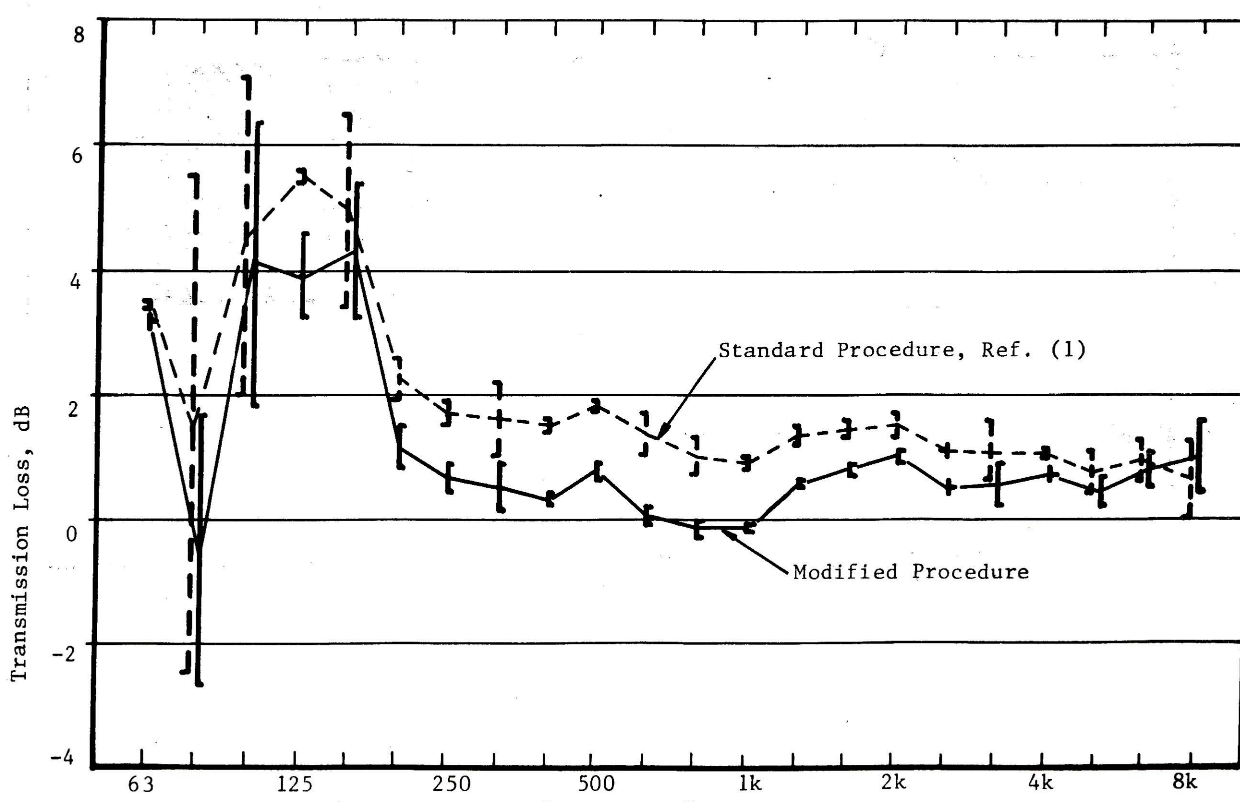

Fig. 3 Transmission Loss of 1.5m^2 Aperture

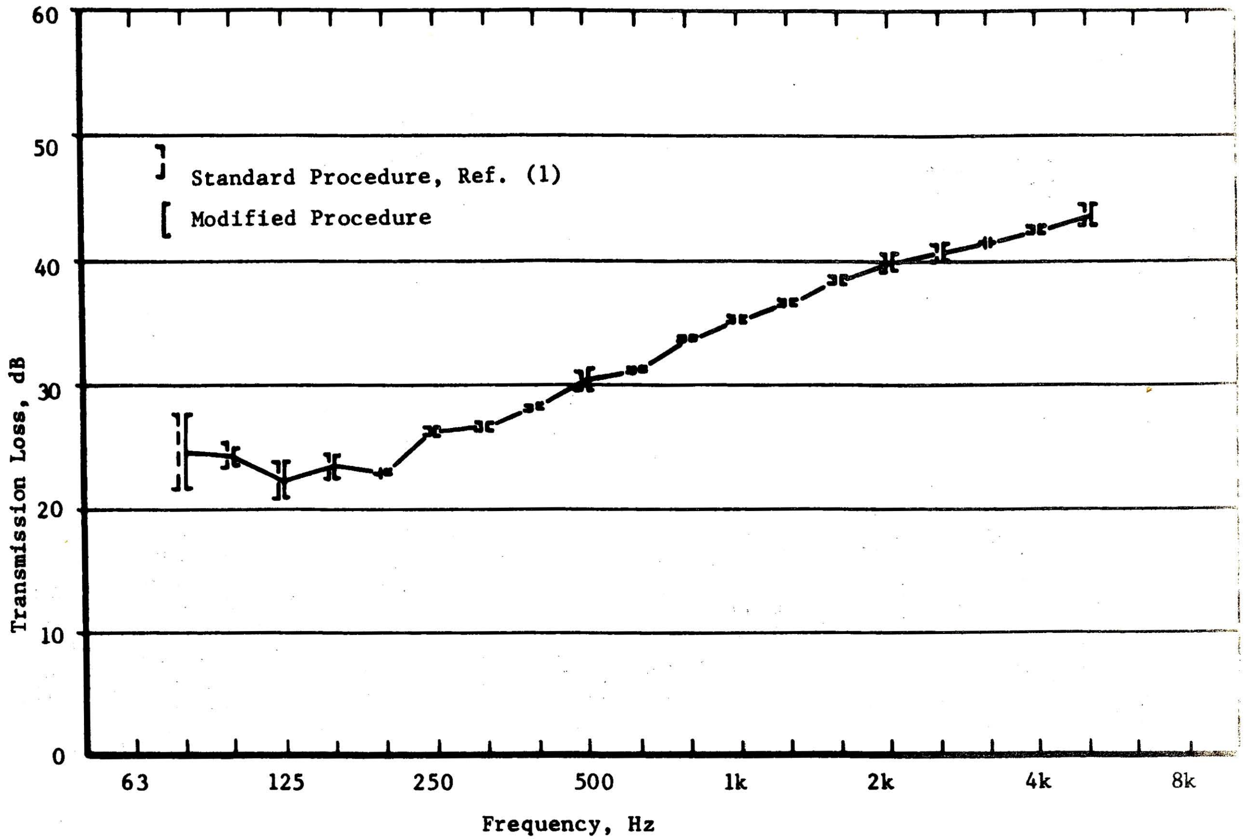

Fig. 4 Transmission Loss of 1.5m^2 Rubber-cored Panel

Noise, Shock & Vibration Conference, 1974 Monash University, Melbourne

MEASUREMENT OF ACOUSTIC ABSORPTION BY MEANS OF TWIN IMPEDANCE TUBES

B. G. Longstaff
School of Physics
The University of New South Wales
Sydney, N.S.W.

J. I. Dunlop
School of Physics
The University of New South Wales
Sydney, N.S.W.

Summary

An apparatus is described that can be used to measure the coefficient of absorption of acoustic materials. The apparatus consists of twin tubes or wave guides, one containing the sample and the other being used as a reference tube. Short bursts of sound are launched along the tubes and the coefficient of absorption calculated from measurements of the incident and reflected tubes. The apparatus offers two independent methods of determining the coefficient of absorption and compares well in accuracy with the conventional standing wave tube apparatus.

Introduction

The intrusion of higher noise levels into more and more aspects of our lives has meant that there is a growing awareness of the need to control our various acoustic environments. One such technique of control is to use acoustic absorptive materials. When used in circumstances where multiple reflections of sound occur, these materials are able to dissipate an appreciable amount of acoustic energy, and thus reduce noise levels.

To obtain the most effective use of these materials, accurate determination of their absorption and impedance characteristics is required. There are two conventional techniques used to measure the absorption characteristics of acoustic materials - the reverberation chamber and the impedance or standing wave tube. However there are often differences and discrepancies in the results obtained by these two methods casting doubts on the accuracy of either method. For example the reverberation chamber method may at times yield absorption coefficients in excess of 100%. Absorption measurements in the standing wave impedance tube are made by measuring the position and intensity of the standing wave minima. In order to do this it is necessary to move either the sample, the signal source or the microphones. Because of the resulting changes in the geometry of the system acoustic coupling or leakage is difficult to monitor or control. This may lead to an inaccurate measurement of the coefficient of absorption or the acoustic impedance.

This paper describes the development of an apparatus similar to that described by Powell & Van Houten[1] which can be used to determine the absorption coefficient of a material by the measurement of sinusoidal wave packets in a wave guide or tube. The use of twin tubes means that sample impedance measurements can also be made. In addition apparatus provides two independent methods of measuring absorption coefficients. This latter feature yields an indication of the accuracy of the technique as distinct from the precision with which the measurements can be made.

Wave Propagation in Air Filled Cylindrical Rigid Walled Tubes

As the twin tube system relies on the propagation of sinusoidal wave packets in a cylindrical tube the constraints of such a wave guide should be examined to evaluate the related limitations of the apparatus.

The tubes may be regarded as cylindrical wave guides with rigid walls. Generally propagation of waves along the axis of such tubes is attenuated by losses at the walls of the tube. These losses are caused by heat conduction but more significantly by viscous resistance offered to the fluid motion at the walls of the tube. This implies that (for loss free propagation) the radial boundary condition of zero velocity at the walls of the tube should exist. Pressure would therefore tend to be a maximum at this boundary.

The odd radial modes are rapidly attenuated with distance along the tube because their velocity tends to be high at the tube walls thus maximising this frictional dissipation of the energy. However the plane wave mode and the higher order even radial modes will propagate along the tube axis with negligible attenuation because they satisfy the condition of zero velocity at the boundaries

The almost uniform radial energy distribution of the plane wave mode makes it ideal for measurement with a probe microphone positioned somewhere along the axis of the tube. Signals propagated in the higher radial modes are not so suitable because of their varying energy distribution across the tube.

These considerations mean that the frequency of the acoustic waves used in the tube has to remain below the cut-off frequency of the first (1,0) radial mode.

The cut-off frequencies of the different modes that can propagate in the tubes may be calculated by solving the wave equations (in cylindrical co-ordinates) with suitable boundary conditions. The solutions generally involve Bessel and Newmann functions, the cut off frequency (f_{20}) of the second axial mode is given by (2)

$$f_{20} = \frac{3 \cdot 9 . C}{2\pi R}$$

where R is the tube radius,
C the velocity of sound
and λ the wavelength

At frequencies below the cut-off of this mode only plane waves in the axial direction are possible in the tube.

Obviously the frequency of the waves being propagated should be lower than the cut-off frequency. However other frequencies are involved because of the shape of the wave packet.

The wave packet signal may be described by the following function

$$F(t) = \sin \omega_o t \qquad 0 < t < nT$$
$$= 0 \qquad \text{elsewhere}$$

where
ω_o = angular frequency of the sinusoidal waveform
T^o = period of wave
n = number of cycles in wave packet

The frequency spectrum for this signal is given by

$$F = \frac{m\pi}{\omega_o} \left(\frac{\sin x}{x} - \frac{\sin y}{y}\right)$$

$$\text{where} \qquad x = \frac{m\pi}{\omega_o}(\omega_o - \omega) \quad y = \frac{m\pi}{\omega_o}(\omega_o + \omega)$$

This spectrum contains many harmonics of frequency above the required cut-off frequency. The magnitude of these harmonics can be reduced by changing the shape of the wave packet most simply by filtering. For example, after 1/3 octave band filtering the wave packet is no longer square but has the appearance shown in Figure 1 with considerably reduced higher harmonic content.

The advantages of filtering the wave packet are twofold. First, reducing the high frequency content of the signal reduces dispersion effects that might have occurred in the tube because of higher mode generation and differing propagation velocities. This would have resulted in distortion of the wave packet as it propagated along the tube. The second advantage of filtering is related to the response of the loudspeakers - these can accommodate more easily the filtered wave form because of the reduced frequency range.

Apparatus

The principle of the twin tube system involves launching sinusoidal wave packets of intensity 90-100 dB re 2×10^{-5} Nm^{-2} along rigid wall tubes. The sample being tested is placed either at the end of one tube with a rigid plate backing or at the centre of the tube. The other tube remains empty and is used as a reference tube for phase and intensity comparisons.

With the sample at the end of one tube the absorption coefficients of the material with a rigid backing are determined from measurements of the ratio (complex) of the intensity of the wave packet reflected from the sample to that reflected from the end of the empty tube. When placed at the centre of the tube the transmission and reflection coefficients of the sample may be found by using similar differential measurements. These latter measurements may then be used to calculate the value corresponding to the absorption coefficient of a sample with a rigid backing.

In Figure 2 is shown a sketch of the twin tube apparatus illustrating the manner in which the filtered sinusoidal tone burst is generated, amplified and propagated from speakers at the ends of the two tubes. The incident and reflected wave packets are detected by means of probe microphones located at corresponding positions in both tubes. The detected signals are amplified and then displayed on the screen of a dual trace storage C.R.O. from which all measurements are made.

The frequency response of the speaker or the cut off frequency for the higher modes will determine the upper frequency limit to be used. As the tubes used were 100 mm in diameter the upper cut off frequency was about 2 KHz. In order to produce the plane wave mode of the wave packet signal and restrict the generation of higher modes it is necessary for the cone diameter of the speakers to be approximately equal to the internal diameter of the tube. This introduces a lower frequency limit because of the restricted frequency range of small loud speakers.

The low frequency limit of the system is also related to the size of a suitable wave packet and the distances between the probe microphones and the ends of the tubes. That is, the length of wave packet has to be such that no overlap of reflected and incident parts of the packet will occur at the probe microphone. For the tubes used (20ft.long) this means that wave packets not greater than 30 ms in length can be used and as a minimum of 5 or 6 periods required in each packet the lower frequency limit is therefore about 200Hz.

Errors

All measurements made with the twin tube system are taken from a trace on a C.R.O. screen. Before any measurements are made the intensity and phase of the incident wave packets are calibrated by observing their coincidence on the C.R.O. screen. The C.R.O. traces in Figure 3 display the incident and reflected wave packets in both tubes. The upper trace is of the signal in the sample tube showing firstly the incident and then the attenuated reflected wave packet.

The errors involved in making intensity measurements are related to the ratio of the C.R.O. trace thickness to the screen height. For phase measurements the fractional error is the ratio of the trace thickness to the screen width.

The precision of the system in making intensity or phase measurements falls within 2-4%. The error in determining the absorption coefficient of a sample with rigid backing is therefore about 2-4%. However in calculating this absorption coefficient using values obtained from the transmission measurements the magnitude of the errors is usually much greater beacuse of extra computations and measurements required. These were conservatively estimated at between 5 and 10%.

The general accuracy of the measurements obtained may be estimated by comparing the results obtained using the twin tube apparatus with those obtained using the conventional standing wave tube.

Results

Thirty samples with widely varying absorption characteristics were tested using the twin tube apparatus. For each sample the absorption coefficient(with a rigid plate backing) was determined using the two methods outlined - with the sample positioned against the end plate and with the sample positioned in the middle of the tube. Each of the samples was also tested using the conventional standing wave impedance tube in two different laboratories.

The results of the testing showed that there was good agreement in the values obtained by all three methods at most frequencies. A major discrepancy was the values of absorption obtained between the twin tube results and the standing wave tube results at high frequencies for some samples. This is illustrated in Figure 4. No acceptable explanation for this phenomenon has yet been proposed but it may be related to acoustic coupling between speaker and microphone in the standing wave tube. Figure 4,5, illustrate some of the typical absorption results obtained.

Conclusion

Apart from the ease of operation and accuracy of the twin tube system there are the obvious drawbacks associated with the doubling of equipment and the difficulty in matching the speakers when a two tube system is used. On the other hand it seems possible that the system might be automated by using a swept frequency oscillator synchronised with a third octave band filter set. The changing frequency of the oscillator could be used to regulate the tone burst generator and thus to control the size of the wave packet. The detected signals could then be processed digitally or using analogue techniques to provide measurements of absorption coefficient over a frequency range.

The twin tube apparatus suffers the same restrictions on frequency range as does the standing wave tube mainly due to tube diameter. The frequency range could therefore be extended by the use of tubes of different diameters.

References

1. J.G.Powell and J.J.Van Houten: J.Acoustical Society of America 48 1299 (1970)

2. M. Redwood: "Mechanical Waveguides", Pergammon Press. Oxford 1960

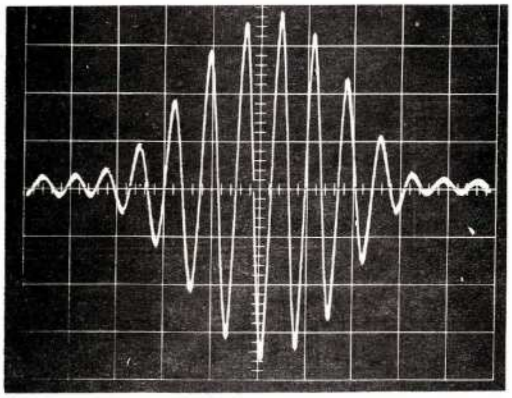

FIGURE 1. - Filtered Wave Packet

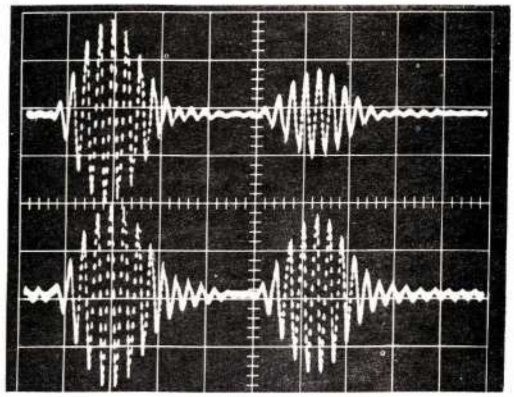

FIGURE 3. - Incident and Reflected Wave Packets - Upper Trace Refers to Sample Tube, Lower Trace to Reference Tube Measured.

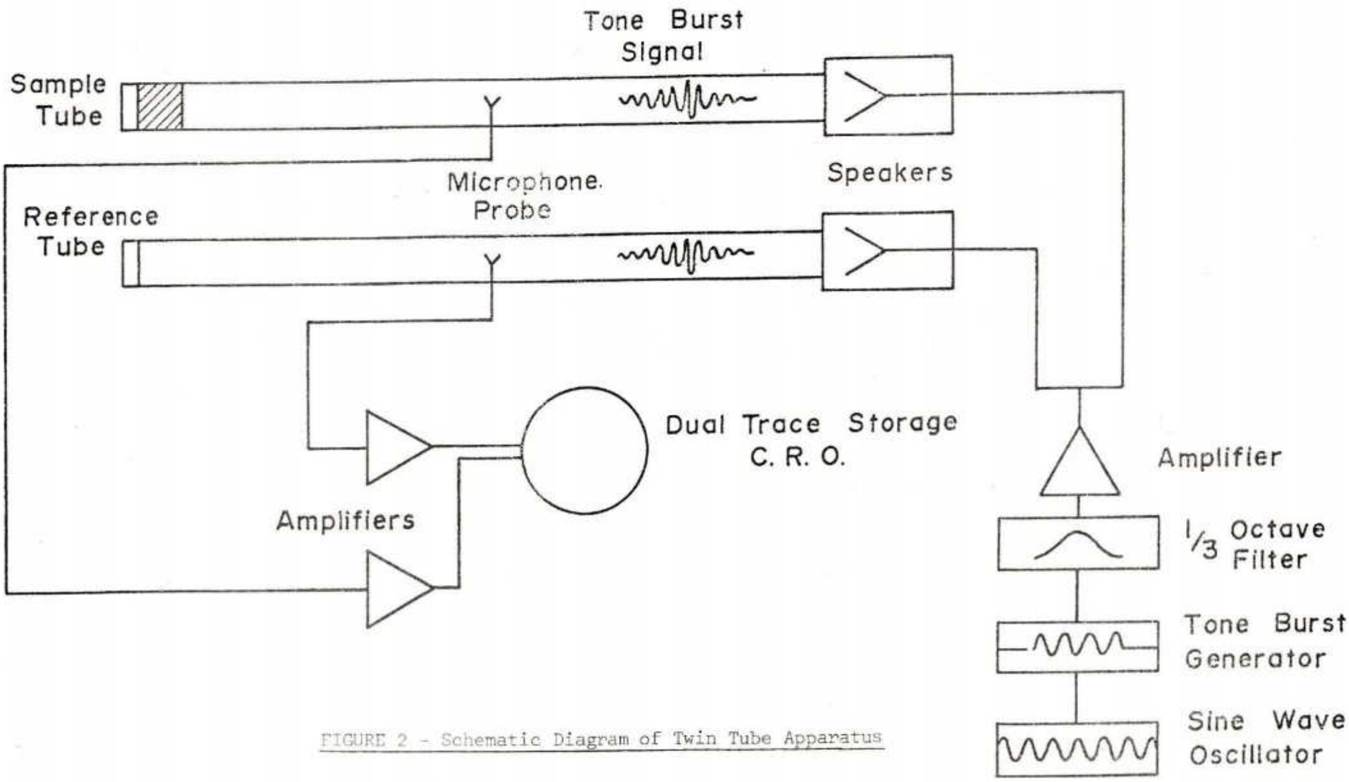

FIGURE 2 - Schematic Diagram of Twin Tube Apparatus

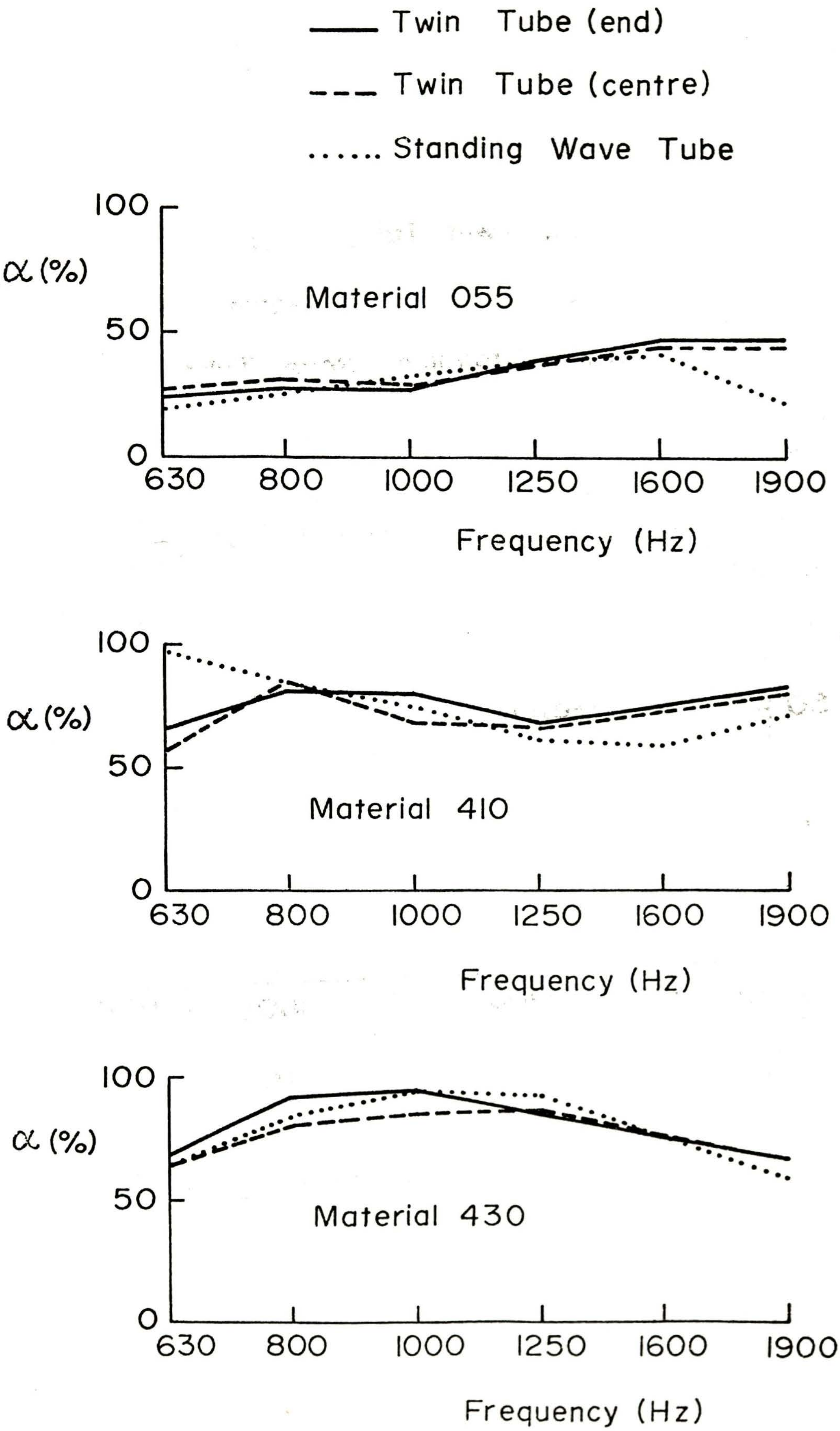

FIGURE 4. - Absorption Characteristics of Some Samples

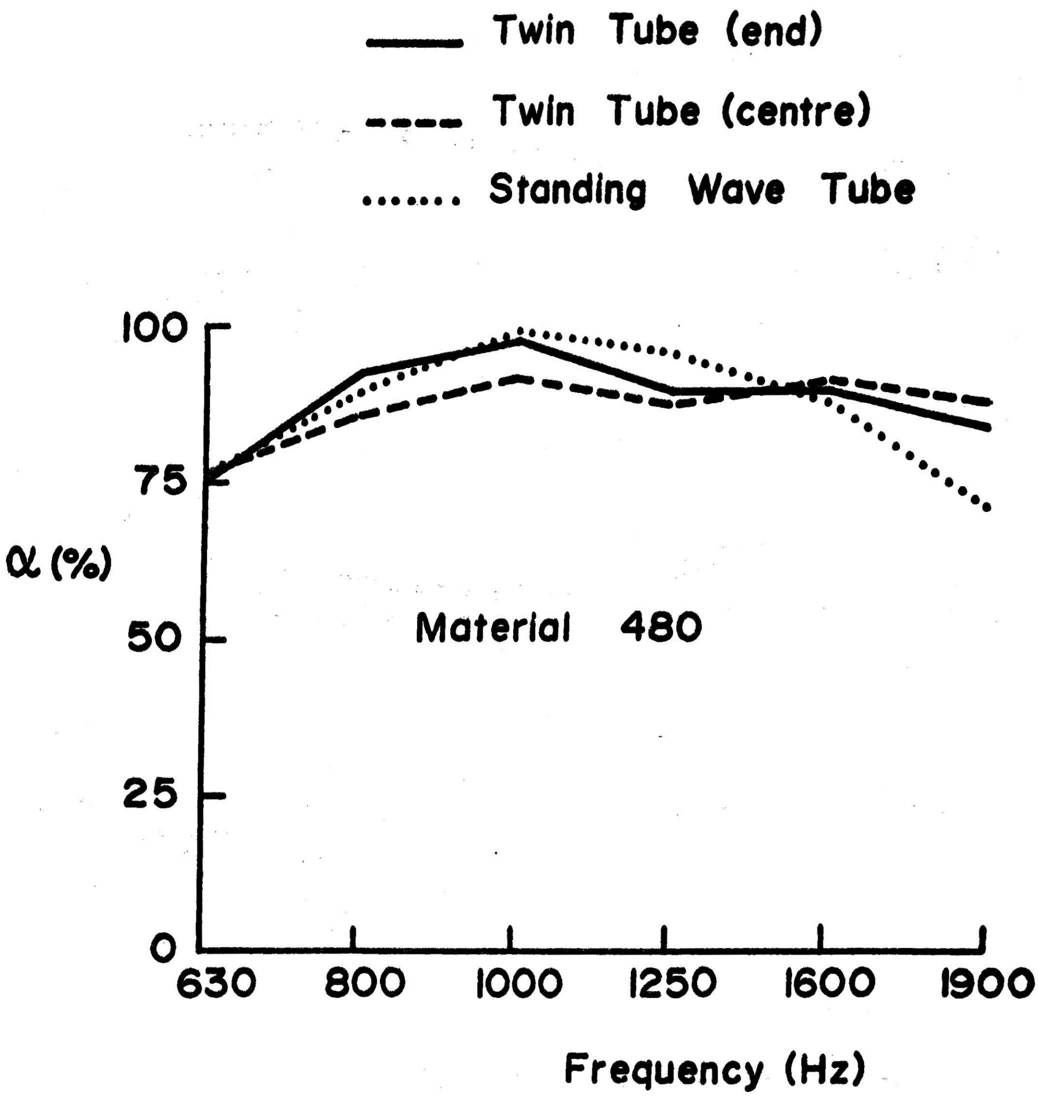

FIGURE 5. - Absorption Characteristics of a Sample

AN EXPONENTIAL HORN LOUDSPEAKER

P. L. Rossiter
Department of Materials Engineering
Monash University
Clayton, Victoria

The basic equations describing the behaviour of finite exponential horn loudspeakers are examined. From this study a compact 4-way horn system covering the frequency range 25Hz-20KHz has been designed around relatively inexpensive drivers in an attempt to optimize size, cost and performance requirements.

The low frequency horn is designed to radiate into the 'conical' area expansion of a trihedral room corner to provide a large final mouth area. This horn is decoupled from a smaller horn having a cutoff frequency of 120Hz by an acoustical low-pass filter. An electrical cross-over at 400Hz is then used to divide the drive signal between the bass unit and a smaller horn having a cutoff frequency of 270Hz. A commercial horn tweeter is used at frequencies above 7KHz.

The results of experimental steady-state and tone-burst tests are given and show that the design objectives have been satisfied.

GLOSSARY OF TERMS

ρ	density of air
c	velocity of sound
m	flare rate
S_T	throat area
S_M	mouth area
S_D	diaphragm area
Z_{AT}	complex acoustical throat impedance $= R_{AT} + jX_{AT}$
Z_{AM}	complex acoustical mouth impedance
z_{MT}	complex mechanical throat mobility $= \frac{1}{Z_{MT}}$
M_{MD}	mass of diaphragm and voice coil
M_{AB}	acoustic mass of air load on rear side of diaphragm due to box
u_T	particle velocity at throat
u_C	particle velocity at cone
C_{MS}	mechanical compliance of suspension
C_{MB}	mechanical compliance of air in box
C_{M1}	mechanical compliance of air space in front of driver
R_{AB}	acoustic resistance of box
r_{MS}	mechanical responsiveness of suspension
r_{MB}	mechanical responsiveness of air in box
r_{MT}	mechanical responsiveness of throat
f_T	force at throat
f_C	force at cone
U_T	volume velocity at throat
U_C	volume velocity at cone
U_B	volume velocity in box
C_{AB}	acoustical compliance of air in box

R_E	voice coil resistance	B	magnetic flux in voice coil air gap
R_g	resistance of signal generator	L	length of voice coil
L_V	voice coil inductance	ℓ	length of horn
e_g	voltage of signal generator	R	radius of mouth (or equivalent radius if mouth is not circular)

INTRODUCTION

There is currently a wide range of materials suitable for use as loudspeaker cones including polymer foams, dense polymers, metals and the more traditional doped paper. However the dynamic behaviour of these materials is determined by their mass, rigidity and damping and the acoustical output of the loudspeaker will generally deviate from the electrical input and could be quite different if such factors as cone breakup modes and resonances were not well controlled. In the case of a direct radiator loudspeaker there is a mis-match between the high impedance electro-mechanical circuit and the low impedance air mass of a room aggravating the problem of controlling the cone motion. Furthermore, because of the exacting nature of the hearing process, amplitude irregularities, harmonic and phase distortion are highly undesirable in a good quality system. Consequently despite a host of empirical and semi-quantitative rules for loudspeaker design, production of a good loudspeaker still demands an intensive program of testing and development and such units tend to be expensive.

An alternative approach to the problem of sound reproduction is the use of a light membrane driven uniformly over its surface by electrostatic or electromagnetic means. Such units are capable of very good free field amplitude and phase response but the problems of fragility and good acoustic accommodation have led to the continued pursuit of an "ideal cone".

The requirements of a cone driver are eased considerably if the abrupt impedance mismatch between the cone and air is avoided.

Correct acoustical coupling may be realised by loading the loudspeaker with some form of horn which effectively transforms the high particle velocities over a small area near the cone to low particle velocities over a larger area near the mouth of the horn, i.e. an acoustical transformer.

The impedance at low frequencies presented to a loudspeaker driver by a horn of fixed mouth and throat areas is governed by the rate of area increase (flare rate) and mathematical law governing the flare. A low flare rate near the throat of the horn as found in the hyperbolic horn for example is necessary for good low frequency performance. However, a sound wave in such a horn travels a relatively long distance before the pressure falls giving a higher value of non-linear distortion (resulting from the non-linear pressure-volume air characteristic) than a conical horn for example. An exponential area increase gives a reasonable compromise between these requirements. Comparisons between different horns are available in the literature (1-4) and this paper will now only consider the exponential horn.

THE EXPONENTIAL HORN

The area S at any point distance x from the throat of the horn is given by

$$S = S_T\, e^{mx} \qquad \text{...... (1)}$$

where S_T is the throat area and m the flare constant. The frequency dependence of the throat impedance of a range of horns is considered in the standard texts (1,2) and the results will only be summarized here.

If the horn is a number of wavelengths long and if the mouth circumference is larger than λ then the horn behaves as though it were infinitely long. The resistive and reactive components of the throat impedance then vary smoothly with frequency as shown in figure 1. Note that below a certain cutoff frequency f_c the resistive component R_{AT} is zero and no energy is transmitted. The cutoff frequency f_c is given by

$$f_c = \frac{mc}{4\pi} \qquad \text{...... (2)}$$

As the length and mouth area of the horn are reduced a series of peaks and troughs occur in R_{AT} and X_{AT} as shown for example in figures 8-10. As the dimensions are reduced further the horn finally acts as a cylindrical tube with resonances occurring at wavelengths which are half-integral multiples of the tube length.

For a finite exponential horn the acoustical throat impedance is given by

$$Z_{AT} = \frac{\rho c}{S_T} \left| \frac{S_M Z_{AM}[\cos (b\ell+\theta)] + j\rho c \sin b\ell}{j S_M Z_{AM} \sin b\ell + \rho c \cos (b\ell+\theta)} \right| \qquad \ldots\ldots (3)$$

where $\theta = \tan^{-1} \frac{a}{b}$ with $a = \frac{m}{2}$, $b = \frac{1}{2}\sqrt{4k^2 - m^2}$; $k = \frac{2\pi}{\lambda}$ and where Z_{AM} is the acoustical impedance seen by the mouth of the horn. The horn is usually assumed to be radiating into a free field and Z_{AM} is taken to be that seen by a flat diaphragm of area S_M mounted in an infinite baffle and is given by

$$Z_{AM} = \frac{\rho c}{\pi R^2} \left| 1 - \frac{J_1(2kR)}{kR} + \frac{j\omega\rho}{2\pi R^4 k^3} K_1 (2kR) \right| \qquad \ldots\ldots (4)$$

where R is the radius of the mouth and J_1 and K_1 are ordinary and modified Bessel functions of the first kind using the notation of Watson (5). In a small room Z_{AM} will probably differ from that given by equation 4 because of the effects of room eigentones but this expression is employed to keep the problem tractable. The resistive and reactive components of Z_{AM} may be calculated numerically from equations 3 and 4 or by using an analogue method (6) and the amplitude and phase response of the horn calculated. For high quality music reproduction the horn requirements may be summarized briefly as:

(i) mouth circumference large compared to λ so that the horn resonances are damped by R_{AT}.

(ii) length greater than $\frac{\lambda}{4}$ to minimize the effects of the impedance mismatch at the mouth.

(iii) f_c should be as high as possible in horns having a small throat area to avoid non-linear distortion.

It is usually inconvenient to build large horns with a circular cross-section and so rectangular cross-sections are usually employed. However, standing waves may be established between parallel or near-parallel walls if the lateral dimensions become comparable to the wavelength. These appear as absorption dips in the frequency response at wavelengths which are half integral multiples of the lateral dimensions and should be avoided. Another problem with bass horns is their great length (typically 6m for a 30Hz cutoff). Unless they are built into the listening area (7-9) they are usually folded for convenience. This has a negligible effect at frequencies where the diameter is a small fraction of the wavelength but at higher frequencies reflections may occur at bends if the inner and outer path lengths differ by an amount greater than $\lambda/2$. Consequently bends should take place near the throat where the diameter is small. If this is not possible then the horn may be divided into a number of parallel units to keep the cross-sections small as in the Klipsch design (10) for example.

Wavefront expansion at the mouth of an exponential horn may be restricted by a baffle or trihedral room corner. This is equivalent to extending the exponential horn into a conical horn but because a conical horn propagates spherical waves it does little towards effectively lengthening an exponential horn which propagates plane waves. The real advantage of this termination is that it restricts the solid angle into which the horn radiates permitting a reduction of the mouth area by a factor of four for a room corner as compared to an infinite baffle mounting. Most folded bass horns use a number of conical sections to approximate an exponential area increase and so operation will lie between that expected of pure conical and exponential horns. Another property of a horn which may be useful is its directionality. This will be determined by the phase and group velocities across various incremental areas and these depend upon the flare rate, the cross-sectional shape, the size of the mouth opening and the frequency. The mouth of a horn largely determines its directional characteristics when the wavelength exceeds the mouth diameter and at higher frequencies the flare rate becomes predominant. The directional property may be used to provide a uniform sound distribution over a chosen listening area.

THE HORN-DRIVER COMBINATION

The elements of a horn loudspeaker are shown in figure 2 and the corresponding equivalent circuit in the mobility representation shown in figure 3. All terms are defined in the glossary at the beginning of this paper.

To facilitate analysis of this circuit let us assume initially that $\frac{1}{z_{mT}}$ is purely resistive When the reactances of M_{MD} and C_{MS} in parallel with C_{MB} are equal and opposite a resonance occurs at the frequency ω_o given by

$$\omega_o = \frac{1}{\sqrt{M_{MD} \frac{C_{MS}\, C_{MB}}{C_{MD} + C_{MB}}}} \qquad \ldots\ldots (5)$$

This is just the free air fundamental cone resonance shifted by the additional compliance of the air space behind the driver. The resonance is damped by the parallel combination of r_{MS}, r_{MB} and the Q is given by

$$Q = r\,\omega_o\,M_{MD} = \frac{r}{\omega_o}\,\frac{C_{MS} + C_{MB}}{C_{MS}\quad C_{MB}} \qquad \ldots\ldots (6)$$

where r is the value of this parallel combination. The value of r is usually determined by r_{mT} and Q is usually quite low and hence the diaphragm resistance controlled.

At frequencies below ω_o the equivalent circuit reduces to that shown in figure 4. Consequently, if r_{MT} is constant and the value of Q is kept low (<1), the response of the loudspeaker will be uniform down to very low frequencies where it will fall off at a rate approaching 6db per octave, i.e. the loudspeaker will continue to operate well below the calculated cone resonance). In practice z_{mT} is a complex function of frequency near the horn cutoff and the operation of the loudspeaker in this frequency range will depend upon the horn characteristics. In fact the large reactive component of the throat impedance near f_c causes the response to fall sharply.

Beranek (2) shows that z_{mT} may be represented as a resistance in series with a negative mass reactance and so the effects of this reactance may be offset by the correct compliant loading of the driver and the conditions of resistive loading maintained at frequencies down to f_c.

Because of many conflicting requirements it is necessary to use more than one horn loudspeaker to cover the whole audio spectrum. However, because of the different horn lengths associated with different frequency ranges, unless the drivers are coplanar different propagation delays will be introduced. When using folded horns coplanar mounting of the drivers is not possible and it is so necessary to keep the difference in acoustic path lengths in horns covering adjacent frequency bands as small as possible. Indications (11) are that the minimum detectible time between acoustic events is $\sim$2.5 ms and so the path differences should be not greater than $\sim$0.8m.

THE LOUDSPEAKER DESIGN

In the loudspeaker system to be described here four horns are used with cross-over frequencies at 120 Hz, 400 Hz and 7 KHz and adjacent horns differ in acoustic path length by less than 1m avoiding any propagation delay effects. The loudspeaker system is shown in figure 5. Conventional cone drivers are used up to 7KHz because of their greater availability and lower cost than specialized pressure drivers. The throat areas of the horns have been kept approximately equal to the cone areas. While this results in a lower efficiency it was felt that cone flexibility might introduce non-linearities if any greater pressure loading was used and the efficiency of the system is still well above that associated with direct radiators. Furthermore, tone burst tests indicate that the damping provided by the horns under these conditions is quite sufficient. A commercial horn loaded tweeter is used for frequencies above 7KHz.

The crossover at 120Hz is performed acoustically by decoupling the low frequency horn from the rear of the bass driver with an acoustical low pass filter and loading the front of the driver with the higher frequency horn. This arrangement is shown schematically in figure 6. The equivalent acoustic circuit for this arrangement using the impedance analogy is shown in figure 7. Inspection of this diagram shows that at high frequencies the volume velocity of the rear throat U_T is much less than that of the cone U_C because of the shunting effect of the air compliance in the box. At these frequencies the throat impedance of the "front" horn is appreciable and so the sound energy is radiated from that horn. At low frequencies $U_T \sim U_C$ and the throat impedance of the front horn is low and so the sound energy is radiated from the "rear" horn. The crossover frequency is given approximately by

$$\omega_{CO} = \frac{c\,S_{TR}}{V} \qquad \text{......... (7)}$$

where V is the volume of the box and S_{TR} the throat area of the rear horn.

Because the low frequency horn is now restricted to frequencies below 120Hz there are no problems associated with folding this horn and the only folds in the front horn occur near the throat where the cross-sectional area is small. The compliances of the diaphragm suspension and cavity provide the reactance necessary to balance out the horn throat reactance as described in the previous section.

The 400Hz crossover is performed electrically and is low enough to prevent any standing waves occurring across the front bass horn. Because of the rise in impedance of the midrange horn in the vicinity of 400Hz the active crossover has the low-pass 3db point at 400Hz and the high-pass 3db point at 450Hz to maintain a uniform response. Third order Butterworth filters are used in an active crossover and separate power amplifiers drive the bass and midrange units. This is done to maintain good electrical damping in the crossover region (12). A passive third order Butterworth high-pass filter is used to drive the tweeter at frequencies above 7KHz. An attenuation network is necessary because of the high efficiency of the tweeter but this also provides good electrical damping. The natural rolloff in the mid-range response provides the necessary low-pass function and is probably due to cone break-up effectively reducing S_D and interference effects at the horn throat.

The design criteria for the system are as follows:

Rear bass horn:	cutoff frequency	35Hz
	mouth area	$0.56m^2$
	effective mouth area	$2.2m^2$
	throat area	$2.3x10^{-2}m^2$

The calculated fundamental cone resonance (equation 5) of the bass driver mounted in the box is 70Hz with a Q (equation 6) of 1.0.

Front bass horn:	cutoff frequency	120Hz
	mouth area	$0.35m^2$
	throat area	$4.5x10^{-2}m^2$
Acoustical Crossover:	cutoff frequency	120Hz
	air volume	$4.7x10^{-2}m^3$

Bass Driver:	Effective cone mass	1.5×10^{-2} Kg
	Free air cone resonance	50Hz
	Diameter	0.3m (12")
	Type used	Plessey-Rola 12UX
Midrange horn:	Cutoff frequency	270Hz
	Mouth area	$6.0 \times 10^{-2} m^2$
	Throat area	$6.0 \times 10^{-3} m^2$
	$f >> f_c$ (Approx. vertical dispersion angle 30°	
	(Approx. horizontal dispersion angle 90°	

These criteria produce a horn essentially the same as that described by Greenbank (13)

Midrange Driver:	Effective cone mass	1.8×10^{-3} Kg
	Free air cone resonance	80Hz
	Diameter	0.1m (4")
	Type used	Foster FE103
Tweeter:	Type used	Foster FHT6

The calculated throat impedances for the horns constructed are shown in figures 8-10. The impedance fluctuations give a calculated variation in the acoustic output not exceeding ±3db. The sinewave response of the individual horns and the composite curve for the complete system are shown in figure 11. At the time of writing there was no reverberant chamber available for measurement of the overall frequency response. The response of the rear bass horn was taken as the pressure at its mouth in an attempt to avoid the effects of standing waves in the measuring room. That of the front bass horn was taken outdoors with the microphone 1m on axis. These tests were performed using a home-built capacitor microphone and preamplifier and IEC 53A function generator. Point by point measurements were taken with all major peaks and troughs recorded. The midrange horn and tweeter were tested in the anechoic chamber, Department of Mechanical Engineering, Monash University. These tests used a B&K 4133 ½" microphone, 2604 microphone preamplifier and RMS rectifier, 1022 B.F.O. and 2305 level recorder.

The frequency responses of the bass horns are as expected. The dip occurring at 500Hz in the mid-range horn is due to reflections down the axis of the horn resulting from the impedance mismatch at the horn mouth and that around 1500Hz is due to standing waves between the nearly parallel top and bottom of the horn. The effects of these resonances were investigated using tonebursts generated by the function generator and two worst-case results are shown in figure 12. The rapid rise and decay of the tonebursts indicates the good transient response at these frequencies and highlights the good damping provided by horn loading (14).

The maximum sound pressure level obtained with a stereo pair of units just before the onset of appreciable distortion was 115 db measured at 3m on axis in a well damped 5mx7mx3m room. This level produced a reading of 125db at 0.3m for the midrange horn mouth. All measurements were taken with a B&K S.P.L. meter on the linear scale using recorded orchestral music as the source.

The midrange horn and an electrostatic loudspeaker array have been compared on a direct A-B basis using the same bass horn. Consistent identification of the sound source operating has proved very difficult using a wide variety of music indicating subjectively the good transient response and low distortion obtained by horn loading (15).

ACKNOWLEDGEMENTS

I would like to acknowledge the assistance of Dr. L. Koss and Dr. R. Alfredson (Monash) in taking some measurements, and of the long-suffering people who have endured many hours of loudspeaker assessment.

REFERENCES

1. H.F. Olson, "Acoustical Engineering", Van Nostrand, 1957.
2. L.L. Beranek, "Acoustics", McGraw-Hill, 1954.
3. H.J.F. Crabbe, "Horn-type Speakers", Hi-Fi News, November 61-June 62.
4. R.N. Baldock, "Horn Acoustics", Hi-Fi News, April 1967.
5. G.N. Watson, "Theory of Bessel Functions", Cambridge Press, London, 1922.
6. B.N. Locanthi, J.Audio.Eng.Soc. 19, 778, 1971.
7. R.N. Baldock, "Acoustic Compensation", Hi-Fi News, Nov. 1964.
8. J. Crabbe, "A Concrete Horn Loudspeaker System Mk II", Hi-Fi News, Oct.-Nov. 1967, (see also 3)
9. C. Walker, "Hiding a Pair of Monsters", Hi-Fi News, Sept. 1967.
10. P.W. Klipsch, J.Acoust.Soc.Amer., 13, 137, 1941, ibid 14, 181, 1943, ibid 17, 254, 1946 [Construction plans for the Klipsch bass radiator are given in: H. Souther, "The Georgian" Radio & Television News, April 1955]
11. E. Roerbaek Madsen, J.Audio Eng.Soc., 18, 490, 1970.
12. A.P. Smith, J.Audio.Eng.Soc., 19, 674, 1971.
13. J. Greenbank, Wireless World, 76, 202, 1970. Revised in Wireless World 78, 14, 1972.
14. V.J. Kaminsky, J.Audio Eng.Soc., 13, 119, 1965. See also references 1,2.
15. P.W. Klipsch, J.Audio Eng.Soc., 17, 194, 1969, ibid 18, 29, 1970

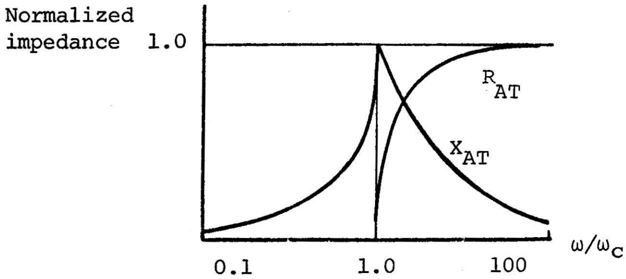

Fig. 1. Normalized Resiatance and Reactive Components of the Acoustic Throat Impedance

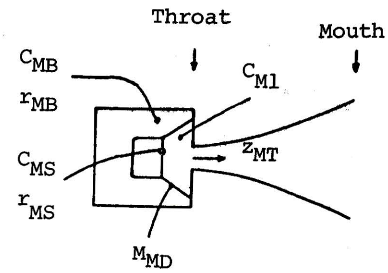

Fig. 2 Basic Horn Loudspeaker

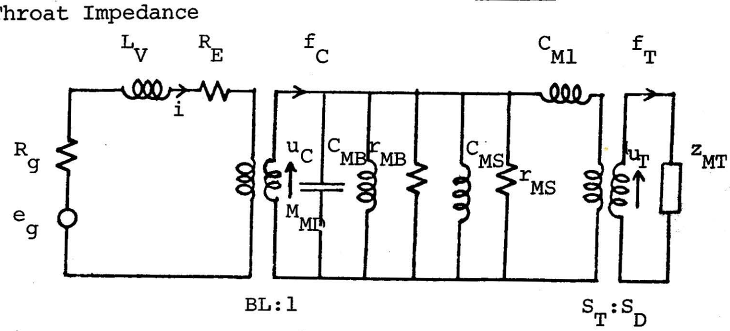

Fig. 3 Mobility Equivalent Circuit of Horn Loudspeaker shown in Figure 1.

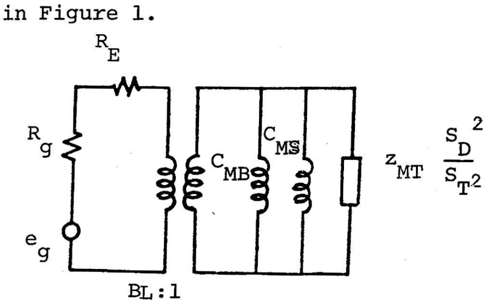

Fig. 4 Mobility equivalent circuit of Horn Loudspeaker at Low Frequencies

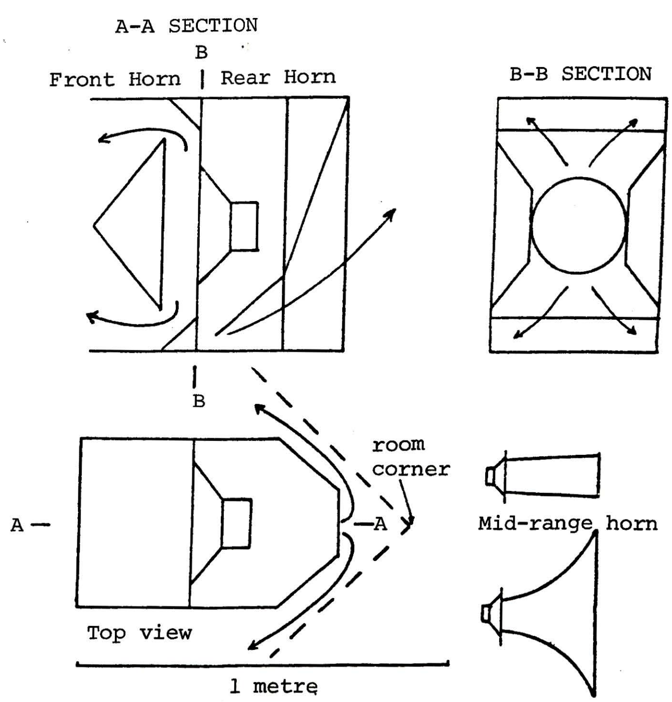

Fig. 5 Horn Loudspeaker

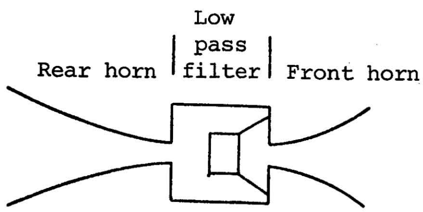

Fig. 6 Dual Horn Loudspeaker

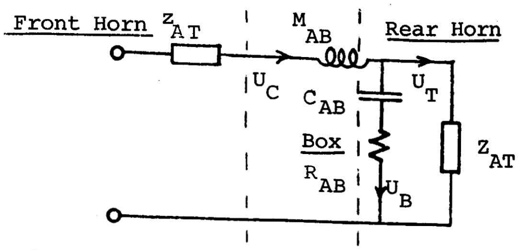

Fig. 7 Acoustic Circuit in Impedance representation of horn loudspeaker

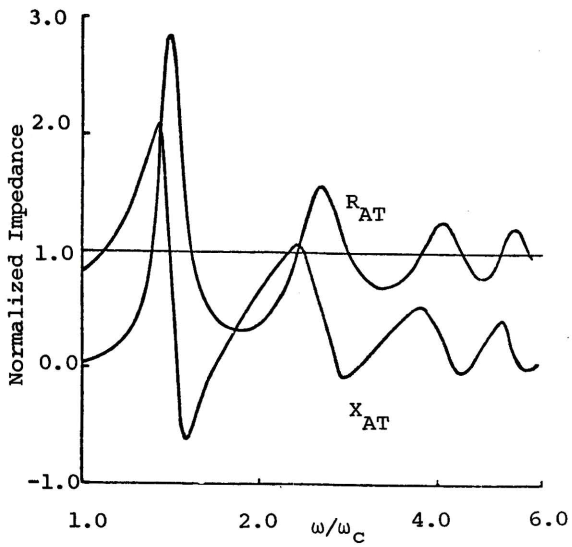

Fig. 8 Acoustic Resistance and Reactance at Throat of Rear Horn

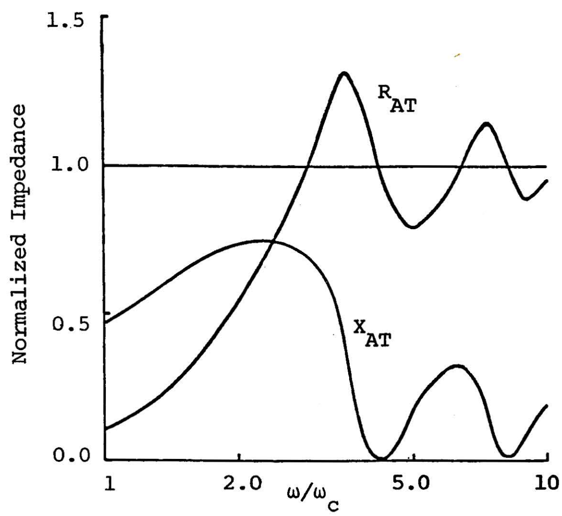

Fig. 9 Acoustic Resistance amd Reactance at Throat of Front Horn

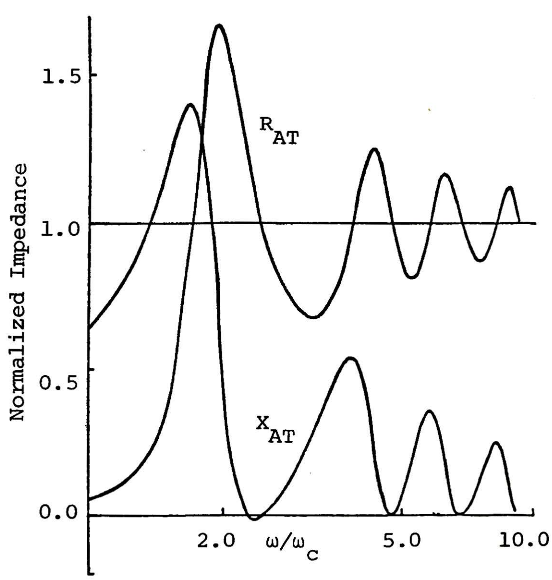

Fig. 10 Acoustic Resistance and Reactance at Throat of Mid-Range Horn

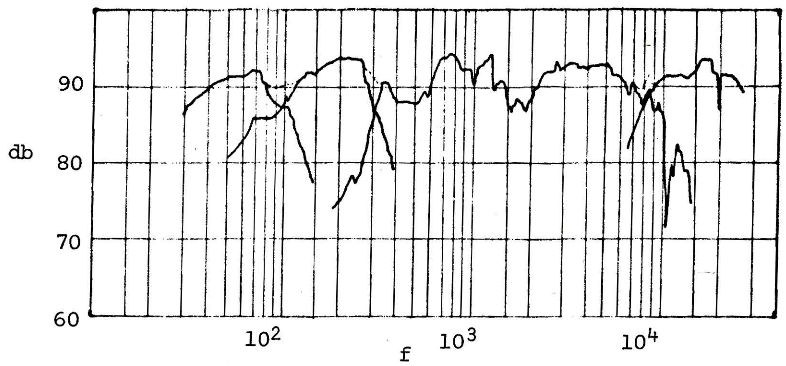

Fig. 11 Frequency Response of Loudspeaker
The conditions of test are given in the text.

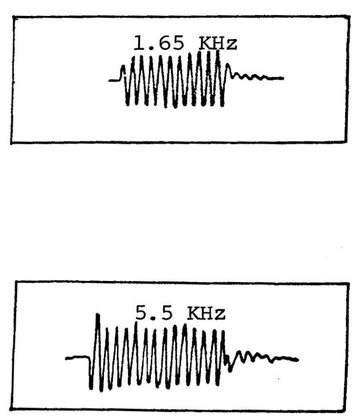

Fig. 12 Tone Burst Tests at 1.65 KHz and 5.5 KHz indicating good damping.

Noise, Shock & Vibration Conference, 1974 Monash University, Melbourne

A REFINED THEORY OF TORTIONAL VIBRATION OF BARS

J. S. Rao
Department of Mechanical Engineering
Indian Institute of Technology
Kharagpur, India

Noise, Shock & Vibration Conference, 1974 Monash University, Melbourne

SUMMARY - Using classical elasticity equations and Hamilton's principle, the existing theories of torsional vibrations of bars viz., the elementary theory, St. Venant's theory, Love's theory, Timoshenko and Gere's theory, Reissner and Lo-Goulard's theory and Barr's theory are briefly reviewed and a refined theory taking into account the Poisson displacements is constructed. This theory removes the discrepancies in the strain-displacement relations of the existing theories and gives rise to a sixth order differential equation with corresponding boundary conditions. The paper proposes a method of solving the differential equation for a given boundary condition.

1. Introduction

Coulomb (1) developed the elementary theory of torsion of bars with circular cross-section, under the assumption that the cross-sections remain plane and rotate without any distortion during twist. Navier (1) applied this elementary theory to bars with non-circular cross-sections and arrived at erroneous results with respect to angle of twist and maximum shearing stress. St. Venant (1) used a semi-inverse method and obtained correct solutions of the problem of torsion for prismatical bars with non-circular cross-section. Poisson (2) is reported to be the first to have applied the elementary theory of Coulomb to determine the torsional vibration characteristics of bars with circular cross-section. For bars with non-circular cross-section, the torsional stiffness term can be modified according to St. Venant's theory to obtain better results, e.g., see the work of Rao, Belgaumkar and Carnegie (3).

Love (2) considered the effect of longitudinal inertia in the torsional vibration of bars with non-circular cross-section. Timoshenko (4) considered the effect of normal strain in the torsion problem which was later extended by Gere (5) for dynamic problems.

Reissner (6) extended the torsion problem to include nonuniform twist and Lo and Goulard (7) generalized this to vibration problems. Barr (8) included the effect of longitudinal inertia in Lo and Goulard's work.

In this paper, we propose a new theory considering the Poisson strains for uniform twist.

2. Nomenclature

A	=	area of cross-section of the bar
b	=	breadth of the bar
B_2	=	$C_1 G$
B_4	=	$EI_{\phi\phi} + \gamma^2 G C_4 + 2\gamma G C_3$
B_6	=	$\gamma^2 G C_2$
C	=	$C_1 = G_A\int [(\phi,_y - z)^2 + (\phi,_z + y)^2]dA$
C_2	=	$_A\int [(\int\phi dy)^2 + (\int\phi dz)^2]dA$
C_3	=	$_A\int [(\phi,_y - z)\int\phi dy + (\phi,_z + y)\int\phi dz]dA$

$C_4 \;=\; {}_A\int[(\int\phi dy)_{,z} + (\int\phi dz)_{,y}]^2 dA$

$C_5 \;=\; {}_A\int[z\int\phi dy - y\int\phi dz]dA$

$d \;=\; {}_o\int^l E\theta^2_{,xx}dx \;;\; d_R = {}_o\int^L E\alpha^2_{,x}dx$

$D_o \;=\; \zeta I_p$

$D_2 \;=\; \zeta I\phi\phi - 2\zeta C_5\nu$

$D_4 \;=\; C_2\zeta\nu^2$

E = modulus of elasticity

$g \;=\; {}_o\int^l G\theta^2_{,x}dx \;;\; g_R = {}_o\int^L G\alpha^2 dx$

G = modulus of rigidity of the material

I_p = polar moment of inertia of cross-section

$I_{\phi\phi} \;=\; {}_A\int\phi^2 dA$

l = length of the rod ; $L = \int(y\phi_{,z} + z\phi_{,y})dA$, $K = \int(\phi^2_{,y} + \phi^2_{,z})dA$

M = amplitude of θ

p = frequency

$r \;=\; {}_o\int^l \zeta\theta^2_{,xt}dx$

t = time

T = kinetic energy

u_x, u_y, u_z = displacements along x,y and z directions

U = strain energy

x = axial coordinate

y,z = cross-sectional coordinates

θ = angle of twist

ϕ = warping function

ε_{ij} = components of strain tensor

τ_{ij} = components of stress tensor

ζ = mass density

ν = Poisson ratio

α = unit twist

subscripts x,y and t after a comma denote partial derivatives.

3. Revision of Existing Theories

The theories mentioned earlier in the Introduction are given in Table 1. Starting from an appropriate state, the strain energy and kinetic energy are calculated and variational principle is used in deriving the differential equation of motion and the corresponding boundary conditions for the bar. This table shows the derivation of equations in an unified manner and also reveals that the assumed state in Timoshenko-Gere's theory does not satisfy the strain-displacement relations according to Poisson equations.

4. Refined Theory for Torsional Vibrations

To remove the discrepancy in the theories which is mentioned in section 3, the following state is assumed for the bar.

$$u_x = \phi\theta_{,x}$$
$$u_y = -z\theta - \nu\theta_{,xx}\int\phi dy$$
$$u_z = y\theta - \nu\theta_{,xx}\int\phi dz \qquad (1)$$

The corresponding velocities are

$$u_{x,t} = \phi\theta_{,xt}$$
$$u_{y,t} = -(z\theta_{,t} + \nu\theta_{,xxt}\int\phi dy)$$
$$u_{z,t} = y\theta_{,t} - \nu\theta_{,xxt}\int\phi dz \qquad (2)$$

The components of strain for the state given in equation (1) are

$$\varepsilon_{xx} = \phi\theta,_{xx} \qquad \varepsilon_{xy} = 1/2[(\phi,_y - z)\theta,_x - \nu\theta,_{xxx}\int\phi dy]$$
$$\varepsilon_{yy} = -\nu\phi\theta,_{xx} \qquad \varepsilon_{yz} = -\nu(\theta,_{xx})/2[(\int\phi dy),_z + (\int\phi dz),_y]$$
$$\varepsilon_{zz} = -\nu\phi\theta,_{xx} \qquad \varepsilon_{zx} = 1/2[(\phi,_z + y)\theta,_x - \nu\theta,_{xxx}\int\phi dz] \tag{3}$$

The corresponding stresses are

$$\tau_{xx} = E\phi\theta,_{xx} \qquad \tau_{xy} = G[(\phi,_y - z)\theta,_x - \nu\theta,_{xxx}\int\phi dy]$$
$$\tau_{yy} = 0 \qquad \tau_{yz} = -\nu\theta,_{xx}G[(\int\phi dy),_z + (\int\phi dz),_y]$$
$$\tau_{zz} = 0 \qquad \tau_{zx} = G[(\phi,_z + y)\theta,_x - \nu\theta,_{xxx}\int\phi dz] \tag{4}$$

The strain energy and kinetic energy of the system are then obtained as

$$2U = {}_o\int^L EI_{\phi\phi}\theta^2,_{xx}dx + {}_o\int^L C_1G\theta^2,_x dx + {}_o\int^L \nu^2GC_2\theta^2,_{xxx}dx$$
$$- {}_o\int^L 2\nu GC_3\theta,_x\theta,_{xxx}dx + {}_o\int^L \nu^2GC_4\theta^2,_{xx}dx$$
$$2T = {}_o\int^L \zeta I_p\theta^2,_t dx + {}_o\int^L C_2\zeta\nu^2\theta^2,_{xxt}dx + {}_o\int^L 2\zeta\nu C_5\theta,_{xxt}\theta,_t dx$$
$$+ {}_o\int^L \zeta I_{\phi\phi}\theta^2,_{xt}dx \tag{5}$$

Applying Hamilton's principle, viz., ${}_{t1}\int^{t2}(U-T)dt$ is stationary for a conservative dynamical system taken between two arbitrary intervals of times, and taking the variations, we arrive at the following differential equation and the corresponding boundary conditions:

$$\nu^2GC_2\theta,_{xxxxxx} - (EI_{\phi\phi} + \nu^2GC_4 + 2\nu GC_3)\theta,_{xxxx} - C_2\zeta\nu^2\theta,_{xxxxtt}$$
$$+ C_1G\theta,_{xx} + (\zeta I_{\phi\phi} - 2\zeta\nu C_5)\theta,_{xxtt} - \zeta I_p\theta,_{tt} = 0$$
$$\{[- (EI_{\phi\phi} + \nu^2GC_4)\theta,_{xxx} + C_1G\theta,_x + \nu^2GC_2\theta,_{xxxxx} - 2\nu GC_3\theta,_{xxx}$$
$$- C_2\zeta\nu^2\theta,_{xxxtt} - \zeta\nu C_5\theta,_{xtt} + \zeta I_{\phi\phi}\theta,_{xtt}]\delta\theta\}_o^1$$
$$+ \{[EI_{\phi\phi} + \nu^2GC_4)\theta,_{xx} - \nu^2GC_2\theta,_{xxxx} + \nu GC_3\theta,_{xx} + C_2\zeta\nu^2\theta,_{xxtt}$$
$$+ \zeta\nu C_5\theta,_{tt}]\delta\theta,_x\}_o^1 + \{[\nu^2GC_2\theta,_{xxx} - \nu GC_3\theta,_x]\delta\theta,_{xx}\}_o^1 = 0 \tag{6}$$

with $\nu = 0$, the above equations (6) agree with Timoshenko-Gere's theory given in Table 1.

5. Solution for Free Torsional Vibrations

For free vibrations, θ is assumed as

$$\theta = \Theta\sin pt \tag{7}$$

Then the differential euqation (6) becomes

$$\nu^2GC_2\Theta,_{xxxxxx} - (EI_{\phi\phi} + \nu^2GC_4 + 2\nu GC_3 - C_2\zeta\nu^2p^2)\Theta,_{xxxx}$$
$$+ (C_1G - \zeta I_{\phi\phi}p^2 + 2\zeta\nu C_5p^2)\Theta,_{xx} + \zeta I_{pp}{}^2\Theta = 0 \tag{8}$$

Equation (8) can be written also as

$$B_6\Theta,_{xxxxxx} - (B_4 - D_4p^2)\Theta,_{xxxx} + (B_2 - D_2p^2)\Theta,_{xx} + D_op^2\Theta = 0 \tag{8a}$$

Solution of equation (8a) can be written as $\Theta = Me^{bx}$ and hence

$$B_6b^6 - (B_4 - D_4p^2)b^4 + (B_2 - D_2p^2)b^2 + D_op^2 = 0 \tag{9}$$

Equation (9), is cubic in b^2 and let the three roots be $b^2{}_1$, $b^2{}_2$, $b^2{}_3$. These three roots in turn will give six roots of b, viz. b_{11}, b_{12}, b_{21}, b_{22}, b_{31}, b_{32}. These roots may be real or complex and are functions of p^2. The complete solution of equation (8a) then becomes

$$\Theta = M_{11}e^{b_{11}x} + M_{12}e^{b_{12}x} + M_{21}e^{b_{21}x} + M_{22}e^{b_{22}x} + M_{31}e^{b_{31}x} + M_{32}e^{b_{32}x} \tag{10}$$

For the case of fixed-fixed boundary conditions, $\Theta = \Theta,_x = \Theta,_{xx} = 0$ at $x = 0$ and 1 and hence we get

$$\begin{bmatrix} 1 & 1 & 1 & 1 & 1 & 1 \\ b_{11} & b_{12} & b_{21} & b_{22} & b_{31} & b_{32} \\ b_1^2 & b_1^2 & b_2^2 & b_2^2 & b_3^2 & b_3^2 \\ e^{b_{11}l} & e^{b_{12}l} & e^{b_{21}l} & e^{b_{22}l} & e^{b_{31}l} & e^{b_{32}l} \\ b_{11}e^{b_{11}l} & b_{12}e^{b_{12}l} & b_{21}e^{b_{21}l} & b_{22}e^{b_{22}l} & b_{31}e^{b_{31}l} & b_{32}e^{b_{32}l} \\ b_1^2 e^{b_{11}l} & b_1^2 e^{b_{12}l} & b_2^2 e^{b_{21}l} & b_2^2 e^{b_{22}l} & b_3^2 e^{b_{31}l} & b_3^2 e^{b_{32}l} \end{bmatrix} = 0$$

Equation (11) can be reduced to a 5 x 5 determinant whose elements are functions of p^2. If p is one of the natural frequencies equation (11) will be identically satisfied. But since the natural frequency is not known, to start with, an approximate value of p^2 can be assumed and the determinant of equation (11) can be evaluated. An interpolation procedure can be adopted by increasing the values of p^2 at regular intervals until the determinant changes its sign and the appropriate root is found then by the Regula falsi method. Similar to equation (11), the corresponding determinant equations can be set up for other boundary conditions as well.

6. Conclusions

Based on a unified approach, with the help of classical elasticity equations and Hamilton's principle, the existing theories for torsional vibrations of bars are reviewed. A refined theory taking into account the Poisson displacements is constructed and a procedure for the solution is proposed. The actual numerical calculations are under progress and will be reported subsequently.

7. References

1. Timoshenko, S., and Goodier, J.N., 'Theory of Elasticity', McGraw-Hill Book Company, 1951.

2. Love, A.E.H., 'A Treatise on Mathematical Theory of Elasticity', Dover Publications, 1944.

3. Rao, J.S., Belgaumkar, B.M., and Carnegie, W., 'Torsional Vibration Characteristics of a Cantilever beam of Rectangular Cross-section with Uniform Taper,' Bull. Mech. Engng. Educ., Vol. 9, 1970, pp. 61-67.

4. Timoshenko, S., 'Theory of Bending, Torsion and Buckling of Thin-Walled Members of Open Cross-section', Journal of Franklin Inst., Vol. 239, 1945, p. 201, 249, 343.

5. Gere, J.M., 'Torsional Vibrations of Beams of Thin-walled Open Section', J. of Applied Mech., Vol. 21, No. 3, 1954, p. 381.

6. Reissner, E., 'On nonuniform Torsion of Cylindrical Rods', J. of Math. Phys., Vol. 31, 1952, p. 214.

7. Lo, H., and Goulard, M., 'Torsion with warping restraint from Hamilton's Principle', Proc. of 2nd Midwestern Conf. on Solid Mech., 1955, p. 68.

8. Barr, A.D.S., 'Torsional waves in Uniform rods of non-circular section', J. Mech. Engg. Sci., Vol. 4, No. 2, 1962, p. 127.

Table 1. Various Theories of Torsional Vibrations of Bars

No.	Author	State Assumptions	Resulting differential equations	Resulting boundary conditions	Differential equn. of warping function
1	Elementary Theory for circular rods	$u_x = 0$ $u_y = -z\theta$ $u_z = y\theta$	$\zeta I_p\ddot{\theta} - GI_p\theta_{,xx} = 0$	$[GI_p\theta_{,x}\delta\theta]_o^L = 0$	no warping
2	St. Venant's Theory	$u_x = \phi\theta_{,x}$ $u_y = -z\theta$ $u_z = y\theta$	$\zeta I_p\ddot{\theta} - C_1\theta_{,xx} = 0$ (longitudinal inertia is ignored)	$[C_1\theta_{,x}\delta\theta]_o^L = 0$	$\nabla^2\phi = 0$
3	Love's theory	$u_x = \phi\theta_{,x}$ $u_y = -z\theta$ $u_z = y\theta$	$(\zeta I_p - \zeta I_{\phi\phi}\partial_x^2)\ddot{\theta} - C_1\theta_{,xx} = 0$	$[(\zeta I_{\phi\phi}\ddot{\theta}_{,x} + C_1\theta_{,x})\delta\theta]_o^L = 0$	$g\nabla^2\phi - r\phi = 0$
4	Timoshenko and Gere's Theory	$u_x = \phi\theta_{,x}$ $u_y = -z\theta$ $u_z = y\theta$ $\varepsilon_{xx} = \phi\theta_{,xx}$ $\varepsilon_{yy} = -\nu\varepsilon_{xx}$ $\varepsilon_{zz} = -\nu\varepsilon_{xx}$	$\zeta I_p\ddot{\theta} + (-C_1\partial_x^2 + EI_{\phi\phi}\partial_x^4)\theta = 0$	$[EI_{\phi\phi}\partial_x^2\theta\delta\theta_{,x}]_o^L = 0$ $[(C_1\partial_x - EI_{\phi\phi}\partial_x^3)\theta\delta\theta]_o^L = 0$	$-g\nabla^2\phi + d\phi = 0$
5	Reissner and Lo/Goulard's Theory	$u_x = \phi\alpha$ $u_y = -z\theta$ $u_z = y\theta$ $\varepsilon_{xx} = \phi\alpha_{,x}$ $\varepsilon_{yy} = -\nu\varepsilon_{xx}$ $\varepsilon_{zz} = -\nu\varepsilon_{xx}$	$\begin{bmatrix} \zeta I_p & 0 \\ 0 & 0 \end{bmatrix}\begin{bmatrix} \ddot{\theta} \\ \ddot{\alpha} \end{bmatrix} + \begin{bmatrix} -GI_p\partial_x^2 & -GL\partial_x \\ GL\partial_x & (GK - EI_{\phi\phi}\partial_x^2) \end{bmatrix}\begin{bmatrix} \theta \\ \alpha \end{bmatrix} = \begin{bmatrix} 0 \\ 0 \end{bmatrix}$ (longitudinal inertia is ignored)	$[(GI_p\theta_{,x} + GL\alpha)\delta\theta]_o^L = 0$ $[-EI_{\phi\phi}\alpha_{,x}\delta\alpha]_o^L = 0$	$-g_R\nabla^2\phi + d_R\phi = 0$
6	Barr's Theory	, ,	$\begin{bmatrix} \zeta I_p & 0 \\ 0 & \zeta I_{\phi\phi} \end{bmatrix}\begin{bmatrix} \ddot{\theta} \\ \ddot{\alpha} \end{bmatrix} + \begin{bmatrix} -GI_p\partial_x^2 & -GL\partial_x \\ GL\partial_x & (GK - EI_{\phi\phi}\partial_x^2) \end{bmatrix}\begin{bmatrix} \theta \\ \alpha \end{bmatrix} = \begin{bmatrix} 0 \\ 0 \end{bmatrix}$	, ,	, ,

TRANSIENT NONLINEAR RESPONSE OF BEAM COLUMNS

K. S. Raghavan
Department of Mechanical Engineering
Indian Institute of Technology
Kanpur, India

V. Sundararajan
Department of Mechanical Engineering
Indian Institute of Technology
Kanpur, India

Noise, Shock & Vibration Conference, 1974

Monash University, Melbourne

SUMMARY - Transient nonlinear response of beam columns has been studied analytically in this paper. Such a study enables us to understand the response of load bearing columns to blast loads. The present work deals with the transient response taking into account the effects of axial force due to the mid-plane stretching and the applied compressive force. Galerkin's technique has been employed to solve the equation of motion choosing the normal modes of linear vibration of beam columns as comparison functions. A fourth order Runge-Kutta method is employed to solve the coupled ordinary non-linear differential equations in time-dependent generalised coordinates.

Results are obtained for beam columns with simply supported and built-in end conditions. The load on the beam is uniformly distributed and the pulse is assumed to be of rectangular shape. Response is obtained for various ratios of axial force to critical buckling load and for differential magnitudes of pressures. Non-linear responses are compared with the corresponding linear solutions. The effect of nonlinearity plotted as a function of linear deflection/thickness ratio for various axial force ratio reveals that the effect of nonlinearity is strongly dependent on the end conditions and also on the magnitude of compressive force for a given deflection to thickness ratio. In general the effect of mid-plane stretching on lateral deflection increases as flexural rigidity decreases. The nonlinearity is of hardening type. Convergence characteristics of Galerkin's method and stability of numerical integration procedure are also established.

1. Introduction

One often comes across beam columns which undergo large transient lateral displacements (as for example, load-beaming columns subjected to blast loads). The present work deals with transient response of such elements, taking into account the effects of axial force due to mid-plane stretching and the applied compressive force.

Earlier works in this field are restricted to linear, small amplitude vibrations of beam columns (1). Effects of midplane stretching due to large amplitudes have been studied only for simple beams undergoing free and steady vibrations (2,3).

In the present work, response is obtained by Galerkin's method followed by numerical integration. Normal modes of linear vibration of beam columns are chosen as comparison functions. A fourth-order Runge-Kutta method is applied to solve the equations in time-dependent generalised coordinates. Comparisons are made with the response obtained disregarding the effect of midplane stretching to establish the 'nonlinearity effect' as a function of amplitude ratio. Beams with simply supported and fixed ends are studied.

2. Equations of Motion and Method of Solution

The equation of motion for the lateral vibration of a beam column, including the effect of midplane stretching, but neglecting the effect of shear deformations and rotary inertia, can be written as

$$El \frac{\partial^4 y}{\partial x^4} + P \frac{\partial^2 y}{\partial x^2} - \frac{EA}{L} \left\{ \int_0^L (\frac{\partial y}{\partial x})^2 \, dx \right\} \frac{\partial^2 y}{\partial x^2} + m \frac{\partial^2 y}{\partial t^2} = F\ (x,t) \qquad (1)$$

where E is Young's modulus, I - moment of inertia, P is the constant axial force, A is area of cross section, L the length and F is the transverse external load. The third term on the left hand side of Eq. 1 is due to the effect of midplane stretching. Of course Eq. 1 is to be supplemented by proper boundary and initial conditions.

Closed form analytical solution is possible when the beam is simply supported, with no axial force (P = 0) and F(x,t) is sinusoidal in t. For this case solution can be obtained through elliptic functions (4). Otherwise one has to resort to approximate analytical or numerical procedure.

To solve Eq. 1, Galerkin's method is applied in the present work. For this purpose eigen functions of free linear vibrations are chosen as comparison functions.

The equation for free linear vibrations can be written as,

$$EI \frac{\partial^4 y}{\partial x^4} + P \frac{\partial^2 y}{\partial x^2} + m \frac{\partial^2 y}{\partial t^2} = 0 \qquad \ldots(2a)$$

which can be written in non-dimensional form as

$$\frac{\partial^4 \eta}{\partial \xi^4} + c.r. \frac{\partial^2 \eta}{\partial \xi^2} + \frac{\partial^2 \eta}{\partial \theta^2} = 0 \qquad \ldots(2b)$$

with $\eta = \frac{y}{L}$; $\xi = \frac{x}{L}$; $\theta = t\sqrt{\frac{EI}{mL^4}}$

$r = P/P_{cr}$, P_{cr} being the buckling load; m = beam mass per unit axial length,
and $c = \pi^2$ for simply supported beam
$c = 4\pi^2$ for built-in beam.
Solution of Eq. 2b is of the form

$$\eta(\xi,\theta) = Y\ (\xi)\ T\ (\theta) \qquad \ldots(3)$$

For a simply supported beam Eq. 3 takes the form

$$\eta(\xi,\theta) = Sin(\eta\pi\xi)\ .\ sin(\omega\theta) \qquad \ldots(4)$$
$$\eta = 1,2, \text{---}\ .$$

From Eqs. (4) and 2b, we get

$$\omega^2{}_\eta = \eta^4\pi^4 - c.r.\eta^2\pi^2. \qquad \ldots(5)$$

For the case of a built-in-beam, writing Eq. 3 as

$$\eta(\xi,\theta) = Y(\xi)sin(\omega\theta) \qquad \ldots(6)$$

the following results can be obtained (1)

$$Y_n(\xi) = Cosh\ p_n\xi - Cos\ q_n\xi - Q_n(Sinh\ p_n\xi - p_n/q_n\ Sin\ q_n\xi)$$
$$Q_n = \frac{Cosh\ p_n - cos\ q_n}{Sinh\ p_n - p_n/q_n\ Sin\ q_n}$$

where p_n and q_n are related to ω_n as

$$s^2{}_n = c^2r^2/4 + \omega_n^2$$
$$p^2{}_n = s_n - c.r/2$$
$$q^2{}_n = s_n + c.r/2$$

and satisfy the transcendental equation

$$Cosh\ p_n\ Cos\ q_n + 0.5 \frac{(q^2{}_n - p^2{}_n)}{p_n \cdot q_n}\ sin\ q_n\ sinh\ p_n = 1.$$

The response of the beam column is assumed to be of the form

$$y(x,t) = \sum_{n=1}^{N} Y_n(x) T_n(t)$$

where Y_n's are linear normal modes previously discussed and T_n's are to be determined. As usual Eq. 6 is substituted in Eq. 1 and the resulting error is orthogonalised with respect to each of the comparison functions Y. As a result we obtain ordinary non linear coupled differential equations in T_n's. For N = 2, the two equations in T_1 and T_2 are obtained as

$$\ddot{T}_1 + \left(\frac{EI}{mL^4}\omega_1^2\right) T_1 - \frac{EA}{mL^4}\{B_{11}(A_{11}T_1^3 + A_{22}T_1T_2^2 + 2A_{12}T_1^2T_2) + B_{21}(A_{11}T_1^2T_2 + A_{22}T_2^3 + 2A_{12}T_1T_2^2)\} = G_1 * Q(t) \quad \ldots(8)$$

$$\ddot{T}_2 + \left(\frac{EI}{mL^4}\omega_2^2\right) T_2 - \frac{EA}{mL^4}\{B_{12}(A_{11}T_1^3 + A_{22}T_1T_2^2 + 2A_{12}T_1^2T_2) + B_{22}(A_{11}T_1^2T_2 + A_{22}T_2^3 + 2A_{12}T_1T_2^2)\} = G_2 * Q(t). \quad \ldots(9)$$

In Eqs. 8 and 9 the following notations are used:

$$A_{ij} = \int_0^L Y_i'(x)Y_j'(x)dx$$

$$B_{ij} = \int_0^L Y_i''(x)Y_j(x)dx$$

$$G_i = \int_0^L P(x)Y_i(x)dx$$

where $F(x,t) = P(x) * Q(t)$

$$(\cdot) = \frac{d}{dt}\,;\ (\ )' = \frac{d}{dx}\,.$$

Also orthogonality properties of normal modes are made use of in obtaining Eqs. 8 and 9 that is

$$\int_0^L Y_i(x)Y_j(x)dx = \delta_{ij}$$

$$\int_0^L Y_i(x) * L\,[Y_j(x)]\,dx = \omega_i^2\delta_{ij}$$

where L is the differential operator of Eq. 2a. For this reason, note that the linear terms are not coupled in T_1 and T_2. For N = 3, resulting equations are given in the Appendix.

3. Results and Discussions

A computer programme was written to generate comparison functions and to obtain non-linear transient response. Eqs. 8 and 9 were numerically integrated by Gill's extension of fourth order Runge-Kutta method for the purpose of comparison of linear response was also computed in the same program by Duhamel's integral.

Results are obtained for a steel beam ($E = 30 \times 10^6$ psi, $\rho = 0.289$ lbs/in^3) of length 14.5 inches and cross-section 1 in. width and 0.25 inch depth. Loading on the beam is uniformly distributed over the whole length and the pressure pulse is rectangular of sufficient duration to give maximum dynamic amplification (equal to 2.00) in linear vibration. Ratio of axial force P to critical buckling load and the magnitude of pressure are the parameters.

In figures 1 and 2, effect of nonlinearily (percentage reduction in maximum dynamic deflection based on linear response) is shown as function of linear deflection/thickness ratio and axial force ratio r. From these it is seen that the nonlinearity effect is strongly dependent on the axial force, and increases as the axial force increases. From figure 2 it can be seen that non-linearity effect is much higher for simply supported beam than for clamped beam. This is consistent with earlier results obtained for free vibration and frequency response (2,6). From the nature of dependence on axial force and end conditions, it may be inferred that the smaller the bending rigidity, the higher the effect of nonlinearity. These observations are more clearly seen in Fig. 3, where 'dynamic beam stiffness' is plotted for linear and nonlinear cases.

It is of interest to note from Fig. 3, that the nonlinear stiffness curves for non-zero compressive force intersect the linear stiffness curve for the simple beam (r = o). At such points, compressive and tensile forces may be said to nullify one another.

Results were obtained employing first two and first three symmetric modes. The results are seen to be in very good agreement (see Table 1). Excellent convergence is thereby indicated, even for large amplitudes.

Figures 4 and 5 show the response in first cycle, with pressure intensities as parameter. The responses are typical of hardening type nonlinearity. For higher intensities of loading, and thus for larger amplitudes, response time and deflection to load ratio are smaller. The numerical integration procedure was tested for stability by varying the step size. No appreciable difference was found in results over a wide range of step sizes.

4. Concluding Remarks

As has been discussed, the effect of axial tension on transverse vibration is a function of bending rigidity of the beam. In the study of beam columns, linear theory over-estimates the response by a larger margin as compared to a beam having the same order of deflection. The errors are of still greater consequence if one studies dynamic yielding, where one is likely to use a wrong yield function by disregarding the axial force.

The study of nonlinear response of beam columns also helps one to estimate the magnitudes of tensile force developed for a simple beam as a function of amplitude.

Apart from its central purpose, this paper has also demonstrated the utility and power of Galerkin's method. Excellent convergence with two modes has been achieved even for cases which cannot be classified as "weakly nonlinear".

References

1. Rondiak, R and M.H. Cobble, "Displacement of a Vibrating Beam with Arbitrary Axial Load and Arbitrary Axial Compression", Jnl. Sound and Vibration, Vol. 12, No. 4, 1970, pp. 411-420.

2. Evensen, D.A., "Nonlinear Vibration of Beams with Various Boundary Conditions", AIAAJ, Vo. 6, 1968, pp. 370-372.

3. Srinivasan, A.B., "Large Amplitude Free Vibrations of Beams and Plates", AIAAJ, Vol. 3, 1965, pp. 1951-1953.

4. Woinowsky Kreiger S., "Effects of Axial Force on Vibration of Hinged Bars", J. App. Mech., Vol. 17, 1950, pp.35-36.

5. Gill S., "A Process for Step-by-Step Integration of Differential Equations in an Automatic Digital Computing Machine", Proc. Cambridge Phil. Soc., Vol. 47, 1951, pp. 96-108.

6. Aravamudan, K.S., "Vibration of Beams with Time-Dependent Boundary Conditions", M.Tech. Thesis Dept. of Aero. Engg., Indian Institute of Technology, Kanpur, 1971.

Appendix

For 3-mode approximation the equations in time-dependent generalized coordinates are

$$\begin{aligned}\ddot{T}_1 &+ \left(\frac{EI}{mL^4}\,\omega^2{}_1\right) T_1 - \frac{EA}{mL^4}\,\{ A_{11}B_{11}T^3{}_1 + A_{22}B_{21}T^3{}_2 + A_{33}B_{31}T^3{}_3 + (A_{11}B_{21} + 2A_{12}B_{11}) \\ &T^2{}_1T_2 + (A_{11}B_{31} + 2A_{23}B_{21})\, T^2{}_1T_3 + (A_{22}B_{31} + 2A_{23}B_{21})\, T^2{}_2T_3 \\ &+ (A_{22}B_{11} + 2A_{12}B_{21})\, T^2{}_2T_1 + (A_{33}B_{11} + 2A_{13}B_{31})\, T^2{}_3 \\ &+ 2(A_{12}B_{31} + A_{23}B_{11} + A_{13}B_{21})\, T_1T_2T_3 \} = G^*_1Q(t) \end{aligned} \tag{A}$$

$$\begin{aligned}\ddot{T}_2 &+ \left(\frac{EI\omega^2{}_2}{mL^4}\right) T_2 - \frac{EA}{mL^4}\,\{ A_{11}B_{12}T^3{}_1 + A_{22}B_{22}T^3{}_2 + A_{33}B_{32}T^3{}_3 \\ &+ (A_{11}B_{22} + 2A_{12}B_{12})\, T^2{}_1T_2 + (A_{11}B_{32} + 2A_{13}B_{12})\, T^2{}_1T_3 \\ &+ (A_{22}B_{32} + 2A_{23}B_{22})\, T^2{}_2T_3 + (A_{22}B_{12} + 2A_{12}B_{22})\, T^2{}_2T_1 \\ &+ (A_{33}B_{12} + 2A_{13}B_{32})\, T^2{}_3T_1 + (A_{33}B_{22} + 2A_{23}B_{32})\, T^2{}_3T_2 \\ &+ 2(A_{12}B_{32} + A_{23}B_{12} + A_{13}B_{22})\, T_1T_2T_3 \} = G^*_2Q(t) \end{aligned} \tag{B}$$

$$\begin{aligned}\ddot{T}_3 &+ \left(\frac{EI}{mL^4}\,\omega^2{}_3\right) T_3 - \frac{EA}{mL^4}\,\{ A_{11}B_{13}T^3{}_1 + A_{22}B_{23}T^3{}_2 + A_{33}B_{33}T^3{}_3 \\ &+ (A_{11}B_{23} + 2A_{12}B_{13})\, T^2{}_1T_2 + (A_{11}B_{33} + 2A_{13}B_{13})\, T^2{}_1T_3 \\ &+ (A_{22}B_{33} + 2A_{23}B_{23})\, T^2{}_2T_3 + (A_{22}B_{13} + 2A_{12}B_{23})\, T^2{}_2T_1 \\ &+ (A_{33}B_{13} + 2A_{13}B_{33})\, T^2{}_3T_1 + (A_{33}B_{23} + 2A_{23}B_{33})\, T^2{}_3T_2 \\ &+ 2(A_{12}B_{33} + A_{23}B_{13} + A_{13}B_{23})\, T_1T_2T_3 \} = G_3 * Q(t). \end{aligned} \tag{C}$$

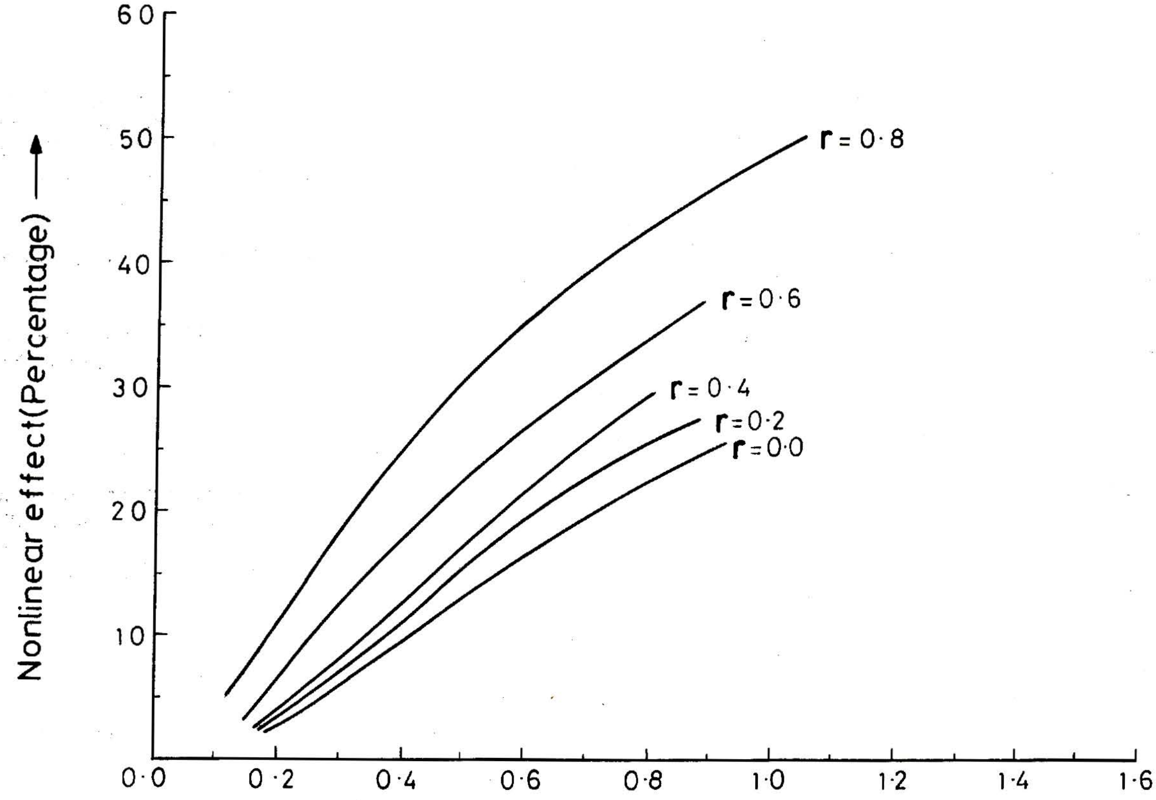

Fig 1 Effect of axial force(clamped beam)

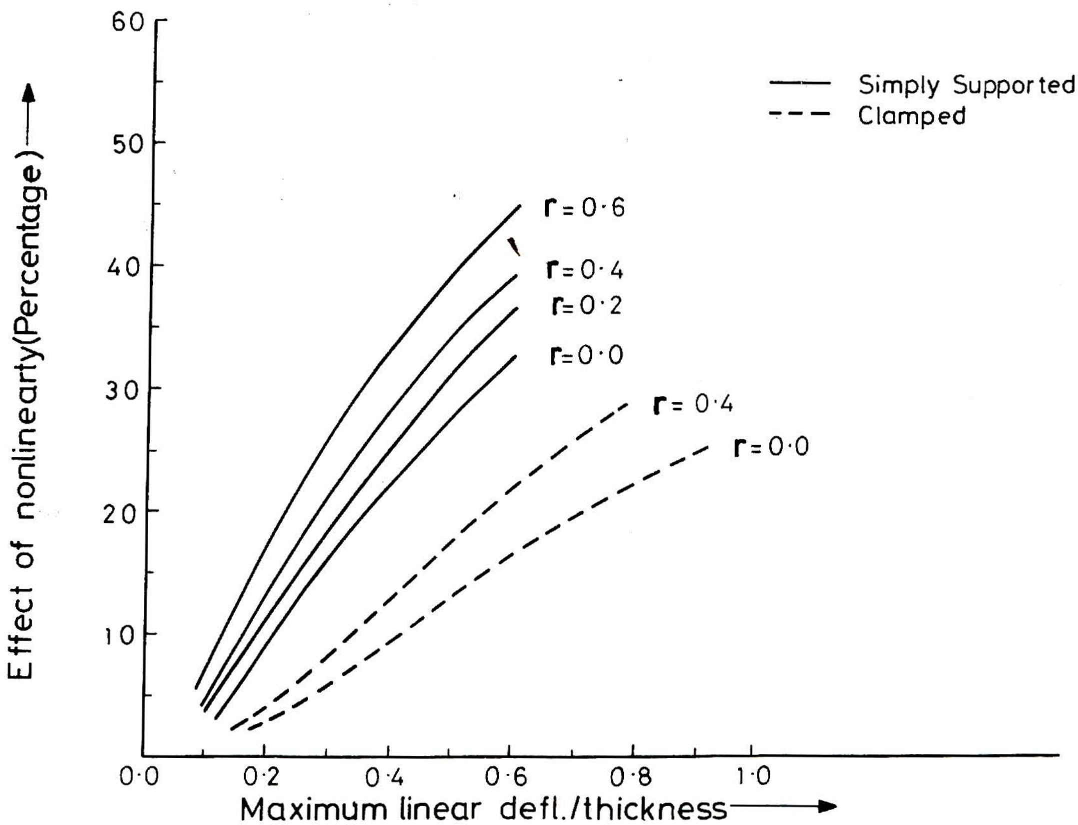

Fig 2 Effect of axial force and end conditions

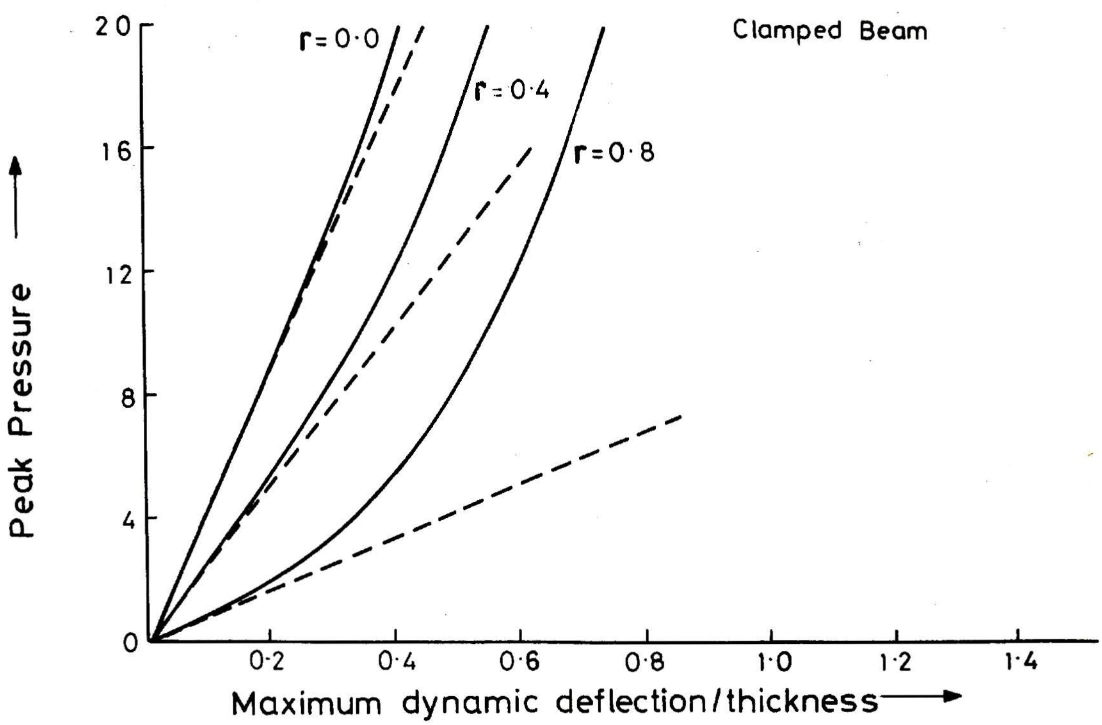

Fig.3. Nonlinear dynamic characteristics

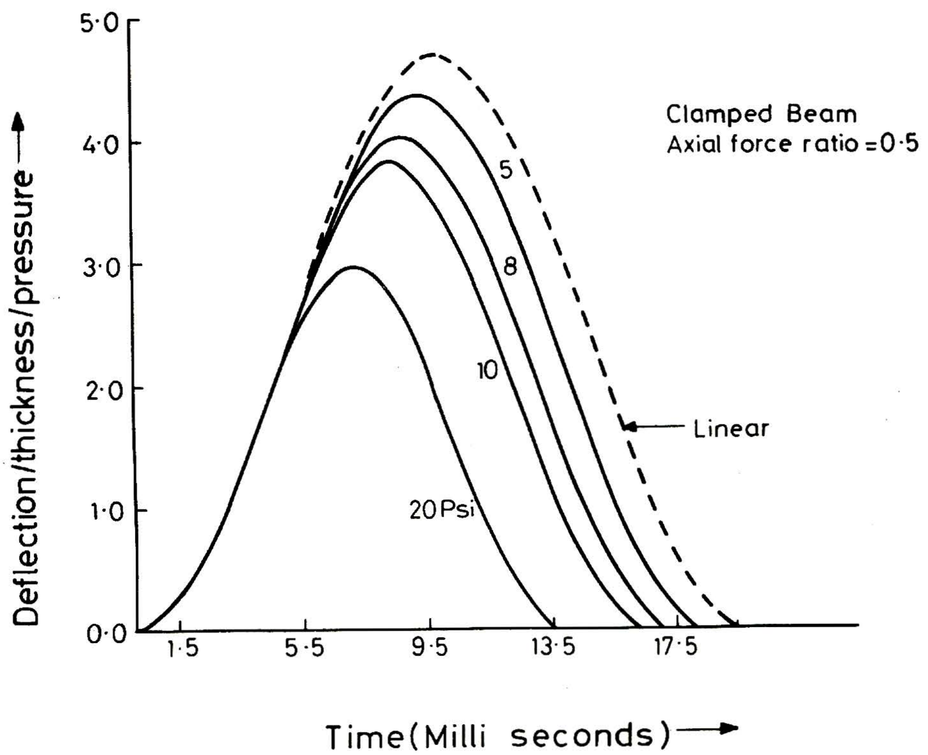

Fig. 4. Response due to various pressures

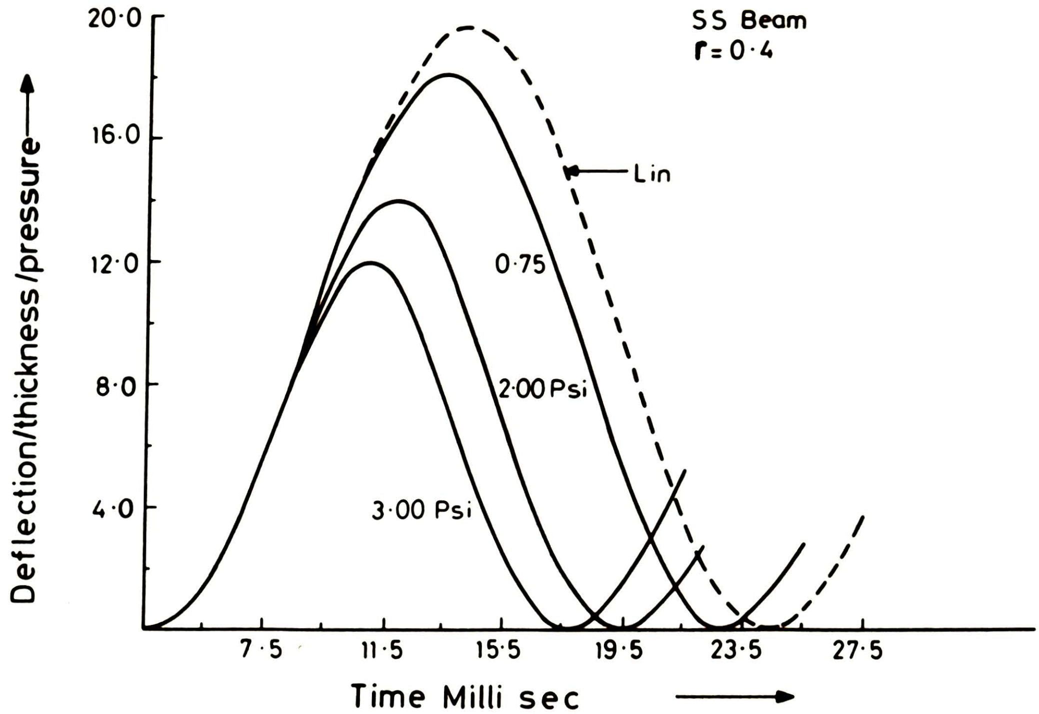

Fig 5 Response of S.S. beam

TABLE 1-a

Simply Supported r = 0.6

Pressure	Defl./thickness Lin.	NL	Max. NL Response (Inches) 2 Modes	3 Modes
0.50	0.15	0.131	0.032 736	0.032739
1.00	0.30	0.218	0.054396	0.054401
1.50	0.45	0.279	0.069787	0.069795
2.00	0.60	0.327	0.081655	0.081665

Table 1-b

Built-in Beam r = 0.80

5.00	0.584	0.379	0.094695	0.94690
8.00	0.934	0.488	0.12206	0.12215
10.00	1.17	0.544	0.13597	0.13606
15.00	1.751	0.655	0.16382	0.16349

Noise, Shock & Vibration Conference, 1974

Monash University, Melbourne

EFFECTS OF TRANSVERSE SHEAR AND ROTATORY INERTIA ON THE NATURAL FREQUENCY OF A CANTILEVER BEAM WITH A TIP MASS

N. G. R. Iyengar
Department of Aeronautical Engineering
Indian Institute of Technology
Kanpur, India

SUMMARY

An account is given of a study of the effects of shear deformation and rotatory inertia on the natural frequency of a uniform cantilever beam with a tip mass and moment of inertia at the tip. Exact frequency equation has been derived. Numerical results for the first three modes have been obtained for several combinations of mass and mass moment of inertia of the tip mass and rotatory inertia of the beam. The results are presented in the form of graphs which indicate the effects are substantial for higher modes.

INTRODUCTION :

The problem of free vibration of uniform cantilever beams with a concentrated mass at the tip has been studied extensively by several authors. The notable ones are due to Pipes [1], Prescot [2] and Temple and Bickley [3]. Durvasula [4] analysed the above problem by including the effect of mass moment of inertia of the tip mass. These problems may be considered as a simplified version of a large aspect ratio wing carrying a heavy tip mass or fan blades of a turbofan jet engine or a wind tunnel sting carrying a missile model. The analysis carried out by the above authors does not take into account the effect of shear deformation and rotatory inertia of the beam. It is well known that the classical, Euler-Bernoulli theory is inadequate for the study of higher modes of tbe beams, as well as for the modes of beams for which the cross-sectional dimensions are not small when compared to their length between the modal section. Rayleigh [5] introduced the effect of rotatory inertia and Timoshenko [6] modified the theory to include the effect of transverse shear deformation. Since, then it has been studied extensively by Searle [7], Kruszewski [8] and Huang [9,10] by approximate methods. Caligo and Calabrase [11] used the method of initial constraints to derive equation for frequency in a closed form for uniform beams with clamped or free ends. Carr [12] employing the characteristic functions and energy approach obtained the natural frequency for beams. Carnegie and Thomas [13] used a finite difference method to obtain the response of the system. All these studies, however, have been made for a uniform beam without a tip mass. In the investigation described here, the influence of transvesse shear and rotatory inertia on the natural frequency of a uniform cantilever beam with a tip mass and inertia are presented. The exact frequency equation is derived in a closed form. Numerical results have been obtained in terms of parameters for shear deformation, rotatory inertia, tip mass and mass moment of inertia of the tip mass and are presented in a graphical and tabular forms.

Analysis for the vibrations of a finite beam on elastic foundation is in progress.

FORMULATION OF THE PROBLEM :

The differential equation that govern the total deflection $W(x,t)$ and the bending slope $\psi(x,t)$

of a beam vibrating freely are

$$K\,G\,A\left(\frac{\partial^2 W}{\partial x^2} - \frac{\partial \psi}{\partial x}\right) = A\,\rho\,\frac{\partial^2 W}{\partial t^2} \tag{1}$$

and

$$E\,I\,\frac{\partial^2 \psi}{\partial x^2} + K\,G\,A\left(\frac{\partial W}{\partial x} - \psi\right) = I\,\rho\,\frac{\partial^2 \psi}{\partial t^2} \tag{2}$$

where EI is the bending rigidity of the beam, K is shear coefficient, A is area of cross section and ρ is the mass density of the beam.

Shear Slope; $\phi(x,t) = \frac{\partial W}{\partial x} - \psi$ (3)

Bending moment; $M(x,t) = -EI\,\frac{\partial \psi}{\partial x}$ (4)

Shear force; $Q(x,t) = K\,G\,A\left(\frac{\partial W}{\partial x} - \psi\right)$ (5)

Eliminating W or ψ from equations (1) and (2), one obtains the following two uncoupled equations in W and ψ

$$E\,I\,\frac{\partial^4 W}{\partial x^4} + \rho\,A\,\frac{\partial^2 W}{\partial t^2} - \left(\rho\,I + \frac{E\,I}{G\,K}\,\rho\right)\frac{\partial^4 W}{\partial x^2\,\partial t^2} + \frac{I\,\rho^2}{K\,G}\,\frac{\partial^4 W}{\partial t^4} = 0 \tag{6}$$

$$E\,I\,\frac{\partial^4 \psi}{\partial x^4} + \rho\,A\,\frac{\partial^2 \psi}{\partial t^2} - \left(\rho\,I + \frac{E\,I}{G\,K}\,\rho\right)\frac{\partial^4 \psi}{\partial x^2\,\partial t^2} + \frac{I\,\rho^2}{K\,G}\,\frac{\partial^4 \psi}{\partial t^4} = 0 \tag{7}$$

When the nondimensional parameter ξ is introduced, defined by

$$\xi = x/L, \quad d\xi = (1/L)\,dx \tag{8}$$

equations (6) and (7) can be rewritten as

$$\frac{E\,I}{L^4}\,\frac{\partial^4 W}{\partial \xi^4} + \rho\,A\,\frac{\partial^2 W}{\partial t^2} - \frac{\rho\,I}{L^2}\left(1 + \frac{E}{G\,K}\right)\frac{\partial^4 W}{\partial \xi^2\,\partial t^2} + \frac{I\,\rho^2}{K\,G}\,\frac{\partial^4 W}{\partial t^4} = 0 \tag{9}$$

$$\frac{E\,I}{L^4}\,\frac{\partial^4 \psi}{\partial \xi^4} + \rho\,A\,\frac{\partial^2 \psi}{\partial t^2} - \frac{\rho\,I}{L^2}\left(1 + \frac{E}{G\,K}\right)\frac{\partial^4 \psi}{\partial \xi^2\,\partial t^2} + \frac{I\,\rho^2}{K\,G}\,\frac{\partial^4 \psi}{\partial t^4} = 0 \tag{10}$$

Assuming the motion to simple harmonic, $W(\xi,t)$ and $\psi(\xi,t)$ can be written in the form

$$\begin{aligned} W(\xi,t) &= W(\xi)\,\exp\,(ipt) \\ \psi(\xi,t) &= \psi(\xi)\,\exp\,(ipt) \end{aligned} \tag{11}$$

Substitution of equation (11) in equations (1), (2), (6) and (7) leads to

$$s^2\,\frac{d^2\psi}{d\xi^2} - (1 - b^2\,r^2\,s^2)\,\psi + \frac{1}{L}\,\frac{dW}{d\xi} = 0 \tag{12}$$

$$\frac{d^2 W}{d\xi^2} + b^2\,s^2\,W - L\,\frac{d\psi}{d\xi} = 0 \tag{13}$$

$$\frac{d^4 W}{d\xi^4} + b^2\,9(r^2 + s^2)\,\frac{d^2 W}{d\xi^2} - b^2(1 - b^2\,r^2\,s^2)\,W = 0 \tag{14}$$

$$\frac{d^4\psi}{d\xi^4} + b^2 (r^2 + s^2) \frac{d^2\psi}{d\xi^2} - b^2 (1 - b^2 r^2 s^2) \psi = 0 \tag{15}$$

where

$$b^2 = \frac{\rho A L^4}{E I} p^2 \tag{16}$$

$$r^2 = I/A L^2 \tag{17}$$

$$s^2 = E I/K G A L^2 \tag{18}$$

The dimensionless parameter b is directly related to the frequency of vibration p. The dimensionless parameters r and s are measures of the effects of rotatory inertia and shear deformation. Solutions of equations (14) and (15) are

$$W(\xi) = C_1 \cosh \alpha\xi + C_2 \sinh \alpha\xi + C_3 \cos \beta\xi + C_4 \sin \beta\xi \tag{19}$$

$$\psi(\xi) = C_1' \sinh \alpha\xi + C_2' \cosh \alpha\xi + C_3' \sin \beta\xi + C_4' \cos \beta\xi \tag{20}$$

where

$$\alpha = \frac{1}{\sqrt{2}} [\{[b^2(r^2 - s^2)]^2 + 4b^2\}^{1/2} - b^2(r^2 + s^2)]^{1/2}$$

$$\beta = \frac{1}{\sqrt{2}} [\{[b^2(r^2 - s^2)]^2 + 4b^2\}^{1/2} + b^2(r^2 + s^2)]^{1/2} \tag{21}$$

The constants in equations (19) and (20) are not independent, but related by the equation (12) or (13) as follows,

$$C_1' = \frac{\alpha^2 + b^2 s^2}{L \alpha} C_2 , \quad C_2' = \frac{\alpha^2 + b^2 s^2}{L \alpha} C_1 \tag{22a}$$

$$C_3' = \frac{\beta^2 - b^2 s^2}{L \beta} C_4 , \quad C_4' = \frac{s^2 b^2 - \beta^2}{L \beta} C_3 \tag{22b}$$

It should be noted that the solutions in equations (19) and (20) are valid only under the conditions

$$[b^2 (r^2 - s^2)]^2 + 4b^2 > 0 \tag{23a}$$

and

$$\{[b^2(r^2 - s^2)]^2 + 4b^2\}^{1/2} \pm b^2(r^2 + s^2) > 0 \tag{23b}$$

The boundary conditions are

$$W(0) = 0 \quad ; \quad \phi(0) = 0 , \tag{24a}$$

$$\frac{dW}{d\xi} - L \phi = b^2 s^2 \frac{M}{m} W(\xi) \tag{24b}$$

and

$$\frac{d\phi}{d\xi} = \frac{B L}{E I} p^2 \phi \tag{24c}$$

Making use of the boundary conditions, the frequency equation can be written as

$$- 2 + \frac{(\beta^2 - \alpha^2)}{\alpha\beta} \sinh \alpha \sin \beta + (\frac{\alpha\eta}{\beta\zeta} + \frac{\zeta\beta}{\alpha\eta}) \cosh \alpha \cos \beta$$

$$+ \frac{1}{\alpha\zeta\eta(\eta-\alpha)} [b^2 s^2 \delta(\alpha^2 + \beta^2) \{-\zeta \sinh \alpha \cos \beta - \eta \cosh \alpha \sin \beta\}$$

$$+ \theta b^2 (\alpha\zeta + \eta\beta) \{\zeta \cosh \alpha \sin \beta - \eta \sinh \alpha \cos \beta\}$$

$$+ \theta b^4 s^2 \delta \{-2\eta\zeta + 2\eta\zeta \cosh \alpha \cos \beta - \sinh \alpha \sin \beta$$

$$(\zeta^2 - \eta^2)\}] = 0 \tag{25}$$

where

$$\theta = B/mL^2 \quad , \delta = \frac{M}{A\rho L}$$

$$\eta = \frac{\alpha^2 + s^2 b^2}{\alpha} \quad \text{and } \zeta = \frac{s^2 b^2 - \beta^2}{\beta} \tag{26}$$

NUMERICAL EXAMPLE :

Frequencies have been completed for the first three modes from the frequency equation (25). A ratio of $E/G = 8/3$ and a shape factor $K = 2/3$ have been assumed. Under these assumptions, $s = 2r$ and the variables α, β , η and ζ become function of the parameter r.

α and β can now be written as

$$\alpha = \frac{1}{\sqrt{2}} \{(9r^4 b^4 + 4b^2)^{1/2} - 5b^2 r^2\}^{1/2}$$

$$\beta = \frac{1}{\sqrt{2}} \{(9r^4 b^4 + 4b^2)^{1/2} + 5b^2 r^2\}^{1/2} \tag{27}$$

Equation (25) is solved to obtain the first three roots for all combinations of the values of δ, θ, and r listed below :

r = 0.02, 0.04, 0.06, 0.08, 1.0

δ = 0.25, 0.5 , 1.0 , 2.0 , 3.0, 5.0

and θ = 0.004,0.008,0.01, 0.012,0.04

Method of Regula-Falsi is used to obtain the results on the IBM 7044 digital computer. The results are presented in the form of graphs (Figs. 1 to 3) for the first three modes. Whereever, the curves get close to each other, they are omitted for the sake of clarity.

DISCUSSION AND CONCLUSION :

From the graphs it can be seen that the roots decrease with increasing values of θ and δ. This is to be expected, as an increase in δ means that the external mass is more while an increase in θ means an increase in the inertia properties and hence the frequencies should indicate a decreasing trend. Further, the graphs show the effect of increase in the value of r. It is seen that the first mode values are not very much affected (curve is almost flat). However, for higher modes the frequencies decrease very rapidly with increase in r (see Figs. 2 and 3). At higher values of δ, the curves tend to coalase with an increase in θ, which corresponds to the case of a fixed-fixed beam.

Tables 1 and 2 show the variation of frequency with δ fpr a given value of θ and r. It is seen that for a given value of θ and r, the frequencies decrease very rapidly in the lower range of δ and do not change much in the higher ranges thus exhibiting a symptotic behaviour. This effect is pronounced for higher modes.

REFERENCES :

[1] Pipes, L.A., Applied Mathematics for Engineers and Physicists, McGraw-Hill Book Co.p.263.
[2] Prescot, J., Applied Elasticity, Dover Pub. 1946, p. 213.
[3] Temple, G. and Bickley, W.G., Rayleigh's Principle, Dover Pub. 1956, p. 111.
[4] Durvasula, S., "Vibrations of a Uniform Cantilever Beam Carrying a Concentrated Mass of Moment of Inertia at the Tip", J. Ae. Soc. Ind. Vol. 18, 1966, p. 18.
[5] Rayleigh, Lord, Theory of Sound, Macmillan Co. N.Y. p. 293.
[6] Timoshenko, S.P., "On the Correction for Shear of the Differential Equation for Transverse Vibration of Prismatic Bars", Phil. Mag. Vol. 41, 1921, p. 744.
[7] Searle, J.H.C., "The Effectso of Rotatory Inertia on the Vibration of Bars", Phil. Mag. Vol. 14, 1907, p. 35.
[8] Kruszewski, E.T., "Effects of Transverse Shear and Rotatory Inertia on the National Frequencies of a Uniform Beam", NACA TN. 1909, 1949.
[9] Huang, J.C., "The Effect of Rotatory Inertia and Shear on the Vibration of Beams Treated by the Approximate Methods of Ritz and Galerkin", Proc. 3rd U.S. Nat. Cong. Appl. Mech. ASME 1950, p. 189.
[10] Huang, J.C., "The Effect of Rotatory Inertia and of Shear Deformation on the Frequency and Normal Mode Equations of Uniform Beams with Simple End Conditions", J. Appl. Mech. Vol. 28, 1961, p. 578.
[11] Caligo, D. and Calabrese, G., "Effect of Transverse Shear and of Rotational Inertia on the Vibration of Elastic Beam", Rendiconti di Mathematica Serie, Vol. 6, 1970, p. 481.
[12] Carr, J.B., "The Effect of Shear Flexibility and Rotatory Inertia on the Natural Frequency of Uniform Beams", Aeroneutical Quart. Vol. 21, 1970, p. 79.
[13] Carnegie, W. and Thomas, J., "The Effect of Shear Deformations and Rotatory Inertia on the Lateral Frequencies of Cantilever Beams in Bending", J. Engg. for Industry, Vol. 94, 1972, p. 267.

Table 1. VARIATION OF FREQUENCY $(b)^{\frac{1}{2}}$ WITH δ

δ	FIRST MODE θ = .004, r = .02	SECOND MODE θ = .004, r = 0.02	THIRD MODE θ =.004, r = 0.02
0.50	1.41377	3.88095	6.18374
1.0	1.24403	3.82945	6.18362
2.0	1.07374	3.79732	6.18355
3.0	0.97908	3.78541	6.18352
5.0	0.86857	3.77538	6.18350

Table 2. VARIATION OF FREQUENCY $(b)^{\frac{1}{2}}$ WITH δ

δ	FIRST MODE θ = 0.04, r = 0.02	SECOND MODE θ = 0.04, r = 0.02	THIRD MODE θ = 0.04, r = 0.02
0.5	1.37848	2.96757	5.08621
1.0	1.22487	2.96577	5.00551
2.0	1.06439	2.96451	4.95132
3.0	0.97335	2.96401	4.93042
5.0	0.86529	2.96358	4.91248

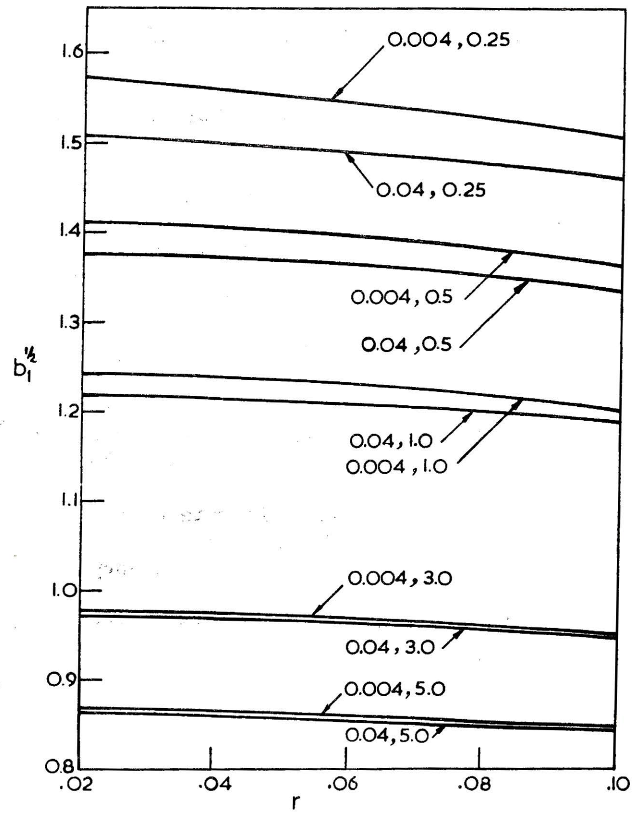

FIG.1_VARIATION OF FIRST NATURAL FREQUENCY.

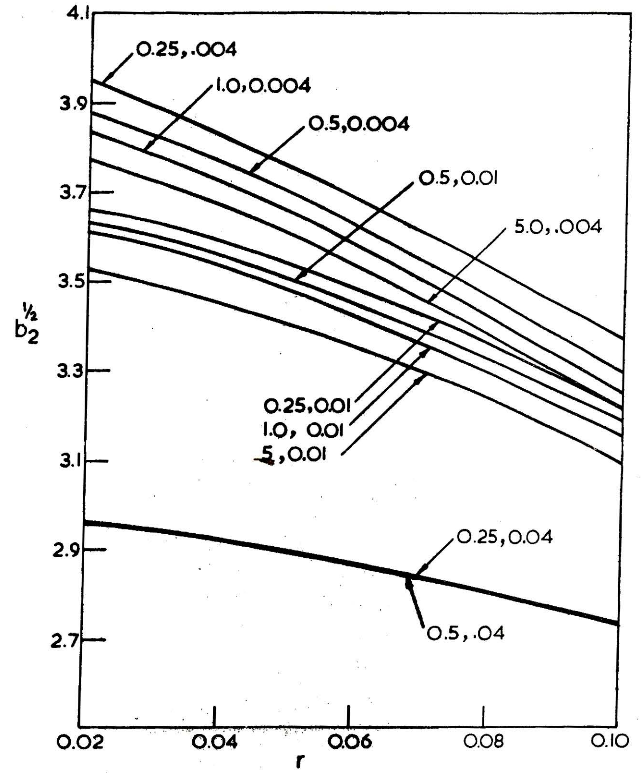

FIG.2 VARIATION OF SECOND NATURAL FREQUENCY

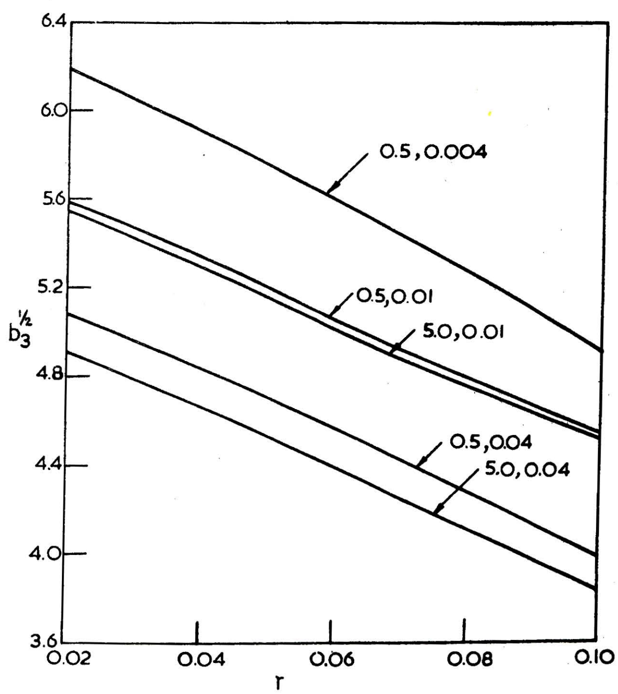

FIG.3 VARIATION OF THIRD NATURAL FREQUENCY

Noise, Shock & Vibration Conference, 1974

Monash University, Melbourne

IDENTIFICATION OF STATIC PROPERTIES OF BUILDING STRUCTURES FROM SMALL AMPLITUDE RESONANCE TESTING

Y. J. Sokal
Civil Engineering Department
University of Queensland
St. Lucia, Queensland

SUMMARY -

Most of the modern building structures have to be analysed for horizontal dynamic loads like earthquakes and wind. The analysis of these structures can be done by different approaches which can be generally classified as purely analytical and experimental-analytical.

In the pure analytical method assumptions are being made as to the mechanical characteristics of the element from which the structural resisting system is composed. These assumptions are used to build a mathematical model (i.e. spring-mass system with defined degrees of freedom) which is used for the determination of the static stiffness properties of the overall structure. Stiffness properties are then used for the calculation of static deflections and stresses and also for the calculation of natural frequencies and the corresponding mode shapes which are required for the calculation of deflections and stresses resulting from dynamic loads.

In the experimental-analytical model the results of the theoretical analysis are checked against experimental results made on a simplified laboratory size model.

It is the author's opinion that the main disadvantages of the two above methods are as follows:-

- in the purely analytical method the success of solution depends largely on the assumptions made at the start and any wrong assumption cannot be improved whatever the refined techniques of calculations used later.
- in the experimental-analytical method the simplified laboratory model, generally made from a homogeneous material different from the one used in the real building, cannot give reliable results.

The small amplitude resonance testing method consists in inducing small amplitude vibrations to a real structure from which the true resonant frequencies and mode shapes are determined. These are later used in calculation of static stiffness properties of a mathematical model of the structure in which the definition of the degrees of freedom and the distribution of masses only are required. The computation of the latter model therefore is much simpler than the one mentioned above.

The main contribution of the small amplitude resonance testing is therefore in providing tool for checking the validity of assumptions for the mechanical characteristics of structural elements. The author does not know about any other available method in which such a check can be made on the whole structural system.

The paper reviews the techniques of the small amplitude resonance testing, together with the main equipment required. The formation of a suitable analytical model for symmetric structures is discussed and numerical methods for the solution for stiffness properties are presented.

The method is then applied to two laboratory size structures which are experimentally tested both for resonant frequencies and static stiffness.

1. Introduction

The use of resonance testing to determine static characteristics has been applied in the past decade to a variety of structures.

It consists mainly in processing the data from resonance testing using theory derived from the modal analysis. To make the understanding of the paper more efficient, basic principles of the modal analysis are concisely explained.

There are several methods of processing the data from resonance testing and general classification of them with particular emphasis on the use in aircraft has been given by Young and On (3)**

Nielsen(1) used resonance testing to identify a five-storey symmetric reinforced concrete building and his method of "processing" is applied in the present paper. The author used Nielsen's method in the past in investigation of reinforced concrete walls(4). Another method of "processing" resonance data has been described by Berman and Flannelly(2) and their method is also used in the present paper.

In what follows, the structure is assumed to be elastic and linear within the range of investigated deformations. These assumptions allow the use of small deflection theory. The experimental work has indeed proved that maximum deformations of the structures during resonance testing were indeed very small. They were much smaller than the deformations required for static testing.

The investigated structures are analysed for horizontal loads only.

Notations are explained where they first appear.

2. Resonance Testing of Structures

There are several methods through which a structural system with constraints (subsequently defined as system) can be brought into a vibratory motion. These methods can be classified as forced and ambient.

In the forced method, vibrations of a vibration generator (subsequently defined as shaker) are transmitted to the system. If the vibrations of the shaker are periodic and of constant amplitude, then the resulting vibrations of the system are of the steady-state type, with the same period of vibration, but with different amplitudes. In the resonance testing the vibrations are in addition harmonic so that slow sweep over a range of frequencies allows detection of resonances which occur at modal (natural) frequencies of the system. This method is usually defined as forced-steady-state.

There are other forced methods such as deceleration of a shaker brought to a high frequency - the run-down test, and the impulse method. It is the author's opinion that these are much less suitable for the purpose, and therefore are not investigated here.

In the ambient method, wind induced vibrations of the system are recorded and decomposed by means of Fourier Transform technique into harmonic vibrations. The resonances are detected by comparing the relative amplitudes of particular harmonics.

In the present investigations the forced steady-state method has been used. The equipment consisted of a shaker and accelerometer transducers, the description of which is given below.

** Raised numbers in brackets in the text refer to literature references.

Shaker: Electromagnetic with a permanent magnet field. The unit produces unidirectional motion and has been tailored to develop up to 50 lbs. force in the frequency range from 0-400 Hz. Maximum amplitude of movement is ½ inch peak to peak, but it has never been fully used. The vibrations of the shaker were generated by a harmonic frequency generator controlled by a frequency counter with five digits reading capacity. The output from the generator was magnified by a D.C. amplifier.

Accelerometer: four-arm Wheatstone bridge consisting of semi-conductor strain gauges attached to a cantilever arm. Resonant frequency maximum 450 Hz and range in some: -10 to + 10g and in the others: -50g to +50g.

During tests, the shaker was suspended by means of thin steel wire from a rigid surface so that it formed a low frequency, low stiffness independent system and was attached to the tested system by an articulated, long and thin arm, capable of transmitting unidirectional motion only.

3. Theoretical fundamentals of the use of resonance testing results for the computation of static properties of the system

3.1 Modal Analysis

As mentioned earlier, modal analysis forms the theoretical fundamentals of the method.

For the purpose of performing modal analysis the following assumption is added to that previously stated: the system is constrained and it possesses a finite number of degrees of freedom. Unfortunately there is no systematical approach in the mathematical sense as to the determination of the number and of the location of these degrees of freedom, apart from the requirement that these degrees of freedom should fairly represent the motion of the system under the considered system of forces (in the present case - horizontal forces).

These assumptions can be used to construct two representative matrices of the system. These are the stiffness (or flexibility) matrices and the mass matrix. All matrices are square of the order n x n, where n - the number of degrees of freedom.

The stiffness matrix $\{K\}$ is symmetrical and in general case full, while in particular cases it may be a band matrix. The meaning of a coefficient, k_{ij}, in the matrix (where i and j specify respectively number of the row and number of the column) is the force at the degree of freedom i and in the direction of that degree of freedom due to unit displacement at and in the direction of degree of freedom j while all other degrees of freedom, including i, are restrained against motion.

The flexibility matrix $\{F\}$ is simply the inverse of the stiffness matrix and the meaning of the coefficient, f_{ij}, is the displacement at and in the direction of the degree of freedom i due to a unit force at and in the direction of the degree of freedom j.

The mass matrix $\{M\}$ is a diagonal matrix of order n x n and the meaning of coefficient m_{ii} is the lumped mass at degree of freedom i. The lumping of the masses is done using simple geometrical consideration of the distribution of masses around the particular degree of freedom.

If now (x) denotes vector of order n x 1, representing the displacements of the system, the conservative equation of motion becomes:

$$\{M\}(\ddot{x}) + \{K\}(x) = (0) \tag{1}$$

where (0) is a zero vector and $(\ddot{x})$ is the vector of accelerations, i.e. second derivative with respect to time of displacement vector.

Equation (1) is transformed into a system of homogeneous equations with respect to w^2 by the following substitution:

$$(x) = (A)e^{-jwt} \tag{2}$$

where (A) is n x 1 vector of amplitudes, j - imaginary number ($j^2 = -1$), w - circular frequency and t - time, e - the base of natural logarithm.

That substitution yields:

$$(-w^2\{M\} + \{K\})(A) = (0) \tag{3}$$

The solution of equation (3) gives the modal matrix {D} of order n x n where each column, i, is a natural vector (d_i) of order n x 1 corresponding to mode i of vibration and a diagonal matrix w^2 of order n x n; where w_i^2 is the square of circular frequency of mode i.

The relationship between the {K} and {M} matrices and the modal solution can be written as a modal equation of equilibrium:

$$\{K\}\{D\} = \{M\}\{D\}\{w^2\} \tag{4}$$

The following orthogonality properties of the modes will be used subsequently:

$$\{D^T\}\{M\}\{D\} = \{GMS\} \tag{5}$$

where the top suffix T denotes transposition and {GMS} is a diagonal matrix of generalized masses.

$$GMS_{ii} = (d_i^T \{M\}(d_i) \tag{6}$$

The off-diagonal elements of {GMS} are zero because of the orthogonality property of modal vectors corresponding to different modes:

$$(d_j^T)\ \{M\}\ (d_i) = 0 \text{ for any } i \neq j$$

In mathematical sense, modal analysis is the solution of the characteristic value problem for a conservative system.

3.2 Direct Solution for Stiffness and Flexibility

In the so-called direct solution equation (4) can be solved for {K}(2) to yield:

$$\{K\} = \{M\}\{D\}\{w^2\}(\{GMS\})^{-1}\{D^T\}\{M\} \tag{7}$$

where $(\{\ \})^{-1}$ denotes the inverse of a square symmetric matrix.

If equation (7) is premultiplied by $(\{K\})^{-1} = \{F\}$ then the new equation can be solved for {F} .

$$\{F\} = \{D\}(\{w^2\})^{-1}(\{GMS\})^{-1}\{D^T\} \tag{8}$$

We notice that both equations (7) and (8) require inversion of diagonal matrices only. Inversion of such matrices does not require the use of special algorithms; in the inverse of a diagonal matrix the diagonality is fully preserved and it is sufficient to rewrite the matrix by filling the diagonal with reciprocals of the elements.

3.3 Properties of Equations (7) and (8)

- both equations can be solved for any number of modes, i.e. when {D} is a rectangular matrix of order n x m, where n - as before, number of degrees of freedom, and m - number of available modal vectors. Matrices $\{w^2\}$ and {GMS} are in this case of the order m x m.

- in general case, equation (8) cannot be obtained by inversion of equation (7) and vice-versa, the particular case when it is possible being when all n modes are available and matrix {D} has been normalised with respect to {M} so that {GMS}= {1} (a unit matrix).

- for m < n equation (7) and (8) will yield different results. The question which of the equations is more reliable when the data from the resonance testing is used, is investigated in the present paper.

- also, for m < n the calculated {K} and {F} are singular, so that they cannot be inverted.

3.4 Nielsen's Approach[1]

The modal equation of equilibrium (4) for the case where {D} is of the order n x 1 can be written as:

$$\{A_i\}(k) = w_i^2\{M\}(d_i) \tag{9}$$

where matrix $\{A_i\}$ is constructed from components of modal vector (d_i) and is of the order n x p[4] where p - number of unknown coefficients in {K} and (k) is vector of these p unknown coefficients. The choice of number of coefficients in (k) and the construction of $\{A_i\}$ must be done with special care. To do this the structure must be represented as a spring-mass system with number of masses equal to the number of degrees of freedom and the number of springs varies according to the model of the structure, i.e. "close coupled", "far-coupled", etc. In the present paper three of such models are investigated for structure No. 2.

Equation (1) cannot be solved directly as matrix $\{A_i\}$ is not a square matrix.

There are two different approaches to the solution of equation (9) and both lead to the same final equation.

Nielsen[1] used a statistical approach which consisted of rewriting equation (1) in terms of an error vector (V).

$$\{A_i\}(k) - w^2\{M\}(d_i) = (V) \tag{10}$$

squaring both sides of equation (10) and differentiating with respect to (k), leads to equation (11):

$$\{A_i^T\}\{A_i\}(k) = w^2\{A_i^T\}\{M\}(d_i) \tag{11}$$

where $\{A_i^T\}\{A_i\}$ is a square matrix but not necessarily non-singular, the inverse of which, if possible, will yield results for (k).

Equation (11) can also be obtained if the concept of pseudoinverse matrix is used[6]. In publication (6), pseudoinverse of a rectangular matrix {B} with real coefficients is defined as $(\{B^T\}\{B\})^{-1}$.

We notice that equation (11) can be obtained from equation (10) by premultiplying both sides of the last one by $\{A^T\}$. Using now the concept of pseudoinverse, the solution for (k) is given by equation (12).

$$(k) = (\{A_i^T\}\{A\})^{-1} w_i^2\{A_i^T\}\{M_i\}(d_i) \tag{12}$$

In the present paper this method is applied to Structure No. 2.

If several modes of the structure are available, equation (10) can be rewritten:

$$\begin{Bmatrix} \{A_1\} \\ \{A_2\} \\ \{A_i\} \end{Bmatrix} (k) = \begin{pmatrix} w_1^2\{M_1\}(d_1) \\ w_2^2\{M_2\}(d_2) \\ w_i^2\{M_i\}(d_i) \end{pmatrix} \tag{13}$$

which again can be rewritten as:

$$\{AA\}(k) = (Z) \tag{14}$$

where {AA} is a rectangular matrix of the order (n x m) x p and vector (Z) is of the order (n x m) x 1, where m - number of available modes of vibration.

Equation (14) is again solved using equation (12).

The influence of the number of modes upon the solution is also investigated in the present paper.

4. The Investigated Structures

Structure No. 1 is shown on Figure 1. It is a two-storey symmetric space frame with square concrete rigid floors and I-steel columns. The columns were bolted to the floors through anchor steel plates. At the base column were fixed through heavy beams to the testing floor (5' thick reinforced concrete).

Two degrees of freedom were assumed for the horizontal motion of the structure. Theoretical stiffness matrix has been calculated assuming full restraint (no rotation) at column joints. Experimental flexibility matrix has been determined statically by applying horizontal loads at the floor levels. The inverted theoretical stiffness and the experimental flexibility matrices are presented below: units are in/lbs for flexibility and lbs/in for stiffnesses.

Theoretical (Inverted)

$$\{F\} = 10^{-5}\begin{bmatrix} 0.658 & 0.658 \\ 0.658 & 1.316 \end{bmatrix}$$

Experimental

$$\{F\} = 10^{-5}\begin{bmatrix} 1.66 & 1.89 \\ 2.07 & 3.60 \end{bmatrix}$$

Theoretical Stiffness

$$\{K\} = \begin{bmatrix} 303951.4 & -151975.7 \\ -151975.7 & 151975.7 \end{bmatrix}$$

Two translational modes of vibration were determined experimentally in one direction only.

Structure No. 2 is shown on Figure 2. It is a three-storey symmetric space steel frame. Columns are continuous I-beam sections, while floors are made from interconnected channel steel beams. At the bottom, columns were cast into a rigid reinforced concrete base, which was then fixed to the testing floor. Three degrees of freedom were assumed for the horizontal motion of the structure. Theoretical stiffness matrix has been calculated by taking into consideration the actual floor stiffnesses and experimental flexibility matrix has been determined through static experiments.

Three translational modes of vibration have been determined experimentally in one direction only.

The inverted theoretical stiffness matrix and the experimental flexibility matrices are presented below:

Theoretical (Inverted)

$$\{F\} = 10^{-5}\begin{bmatrix} 0.719923 & & \text{symmetric} \\ 0.887895 & 1.867783 & \\ 0.903488 & 2.059768 & 3.089737 \end{bmatrix}$$

Experimental

$$\{F\} = 10^{-5}\begin{bmatrix} .864 & 1.16 & 1.26 \\ 1.10 & 2.49 & 2.92 \\ 1.20 & 2.78 & 4.31 \end{bmatrix}$$

Theoretical Stiffness

$$\{K\} = \begin{bmatrix} 343797 & & \text{symmetric} \\ -198494 & 316759 & \\ 31794 & -153127 & 125150 \end{bmatrix}$$

5. Presentation of the results

Experimentally determined and theoretically computed stiffness and flexibility matrices follow the descriptions of the tested structures. In Figure 3 a comparison is made between flexibilities obtained by using different methods of processing the data from the resonance testing. Since comparison between coefficients of several flexibility matrices is difficult an imaginary horizontal unit load vector is applied to the structure and deflections at each degree of freedom are calculated subsequently. This leads in fact to summations of rows in flexibility matrices and these are then compared.

For the sake of completeness of representation, full matrices are given in Table I.

6. Conclusions:

Structure 1 - assuming that the static experimental flexibility matrix is the most reliable, the direct solution for flexibilities gives rowwise results which differ by no more than 6.2%. If averages are considered, then that difference reduces to 1.4%. There is no consistency in these variations, i.e. some are towards increase in stiffness (smaller flexibility coefficients) and others towards decrease in stiffness. On the other hand comparison of data in Figure 3 and Table I shows that direct solution for stiffnesses compares well with theoretical solution only if all three modes of vibration are used. But the theoretical stiffness matrix when inverted has the average flexibility reduced by 25.5%, and so must be the solution for stiffness. If three different spring-mass models are considered, then the best results are obtained through model No. 3, but only if the number of used modes of vibration is equal to the number of degrees of freedom.

If model No. 2 is compared with model No. 1 then the two give results which deviate in opposite directions. While model No. 1 gives much stiffer structure, model No. 2 is more flexible. The increase in stiffness in the case of model No. 1 becomes evident if the type of the structure which the model can represent is taken into account: it is the so-called shear structure with infinitely rigid floors.

For Structure No. 1 only direct solution is available using one mode and two modes. In both cases the average results differ by 11.5% from the static experimental value, the direction of the variation being uniform towards increase in stiffness. That increase in stiffness can be perhaps explained by the fact that in resonance testing the amplitudes of the structure were much smaller than in static experimental testing.

In general it can be concluded that the direct method of solution for flexibilities is the most successful one. The author has not at present an explanation why the direct solution for stiffness is less successful than the direct solution for flexibilities. But this is an advantage for structural solution, where in most cases analysts are interested in deformations of the structure for a given set of forces. Now the deformations are obtained by multiplication of the flexibility matrices by force vector.

For more complex structures analytical models are extremely difficult to build, a fact which favours again the use of the direct method.

7. Acknowledgements

The author is indebted to colleagues, Mr. R.D. Nilsson, Senior Lecturer in Civil Engineering, who devoted hours in introducing the author into the use of the Department's terminal of the PDP-10 Computer and Mr. B. Hooker, Senior Lecturer in Mechanical Engineering, for his advice in the purchase and use of testing equipment.

Thanks are given to the Structures Laboratory staff for their help in experimental work and especially to Mr. B. Joyce.

The experimental work has been carried out by students Mr. Nuss and Mr. Durack within the framework of their fourth year thesis.

8. References

(1) Nielsen, N. Norby - "Dynamic Response of Multistorey Buildings", Earthquake Engineering Research Laboratory, California Institute of Technology, Pasadena, California (June 1964).

(2) Berman, Alex and Flannelly, William - "Theory of Incomplete Models of Dynamic Structures", AIAA Journal, Vol. 9, No. 8, August 1971.

(3) Young, P. Joseph and On, Frank J. - "Mathematical Modeling Via Direct Use of Vibration Data", Preprint 690615, Oct. 1969, National Aeronautics and Space Engineering and Manufacturing Meeting, Society of Automotive Engineers, Los Angeles, Calif.

(4) Sokal, Yehuda J. - "Dynamic Response of Composite Reinforced Masonry Walls", Thesis for the Degree of Doctor of Science in Technology, Technion, Israel Institute of Technology, Haifa, July, 1970.

(5) Trifunac, Mihails D. - "Wind and Microtremor Induced Vibrations of a Twenty-two Storey Steel Frame Building", Earthquake Engineering Research Laboratory, California Institute of Technology, Pasadena, California, 1970.

(6) Greville, T.N.E. - "The Pseudoinverse of a Rectangular or Singular Matrix and Its Application to the Solution of Systems of Linear Equations", SIAM Review, Vol. 1, No. 1, January, 1959.

(7) D'Allessandro, D. - "Identification of Structural Systems Through Near-Resonance Testing", Bachelor of Engineering Thesis, University of Queensland, 1972.

(8) Durack, James M. - "An Experimental Investigation of the Validity of Some Static & Dynamic Analyses of Complete Structures", Bachelor of Engineering Thesis, University of Queensland, 1973.

(9) Nuss, M. - "The Dynamic Behaviour of Structures in Resonance", Bachelor of Engineering Thesis, University of Queensland, 1973.

TABLE I

VALUES OF STIFFNESS AND FLEXIBILITY MATRICES FOR STRUCTURES NO. 1 AND NO. 2

Units are lb/in for stiffness matrices and in/lb for flexibility matrices: 1 in/lb = 5.71 N/mm.
1 lb/in = 0.175 mm/N.

STRUCTURE NO. 1

Direct Solution

1. Two Modes

$$K=\begin{bmatrix} 176279.4 & -90294.8 \\ -82805.3 & 71654.9 \end{bmatrix} \quad F=10^{-5}\begin{bmatrix} 1.390169 & 1.751799 \\ 1.606495 & 3.419976 \end{bmatrix}$$

2. One Mode

$$K=\begin{bmatrix} 6900.67 & 10547.16 \\ 10547.16 & 16120.54 \end{bmatrix} \quad F=10^{-5}\begin{bmatrix} 1.141777 & 1.918185 \\ 1.918185 & 3.222551 \end{bmatrix}$$

STRUCTURE NO. 2

Direct Solution

1. Three Modes

$$K=\begin{bmatrix} 335336.4 & -219910.6 & 50335.6 \\ -220603.9 & 330250.8 & -155299.2 \\ 59989.3 & -171054.0 & 119390.6 \end{bmatrix} \quad F=10^{-5}\begin{bmatrix} 0.873458 & 1.198071 & 1.190156 \\ 1.155743 & 2.513342 & 2.782004 \\ 1.216983 & 2.998946 & 4.225429 \end{bmatrix}$$

2. Two Modes

$$K=\begin{bmatrix} 97005.05 & 48845.24 & -65415.39 \\ 47598.31 & 27854.02 & -25260.94 \\ -67608.84 & -27206.28 & 57618.83 \end{bmatrix} \quad F=10^{-5}\begin{bmatrix} 0.834311 & 1.241940 & 1.166892 \\ 1.281925 & 2.370474 & 2.867580 \\ 1.259605 & 2.949806 & 4.260041 \end{bmatrix}$$

STRUCTURE NO. 2 (Cont.)

First Model
(Flexibility matrices obtained by inversion of the stiffness matrix)

1. Three Modes

$$K=\begin{bmatrix} 388380 & & \\ -242576 & 363018 & \\ 0 & -120442 & 120442 \end{bmatrix} \quad F=10^{-5}\begin{bmatrix} 0.685852 & & \\ 0.685852 & 1.098094 & \\ 0.685852 & 1.098094 & 1.928369 \end{bmatrix}$$

2. Two Modes

$$K=\begin{bmatrix} 248379.9 & & \\ -116098.2 & 170937.1 & \\ 0 & -54838.9 & 54839 \end{bmatrix} \quad F=10^{-5}\begin{bmatrix} 0.755961 & & \\ 0.755961 & 1.617299 & \\ 0.755961 & 1.617299 & 3.440822 \end{bmatrix}$$

3. One Mode

$$K=\begin{bmatrix} 359196.0 & & \\ -164119.4 & 215325.5 & \\ 0 & -51206.1 & 51206.1 \end{bmatrix} \quad F=10^{-5}\begin{bmatrix} 0.512619 & & \\ 0.512619 & 1.121931 & \\ 0.512619 & 1.121931 & 3.074824 \end{bmatrix}$$

Second Model
(Flexibility matrices obtained by inversion of the stiffness matrix)

1. Three Modes

$$K=\begin{bmatrix} 335599.7 & & \\ -218038.3 & 336087.5 & \\ 48979.1 & -163661.3 & 114682.2 \end{bmatrix} \quad F=10^{-5}\begin{bmatrix} 0.993671 & & \\ 1.435726 & 3.049775 & \\ 1.624522 & 3.739112 & 5.514197 \end{bmatrix}$$

2. Two Modes

$$K=\begin{bmatrix} 302398.2 & & \\ -182157.7 & 288723.6 & \\ 33490.1 & -138204.2 & 104714.1 \end{bmatrix} \quad F=10^{-5}\begin{bmatrix} 0.887077 & & \\ 1.150641 & 2.432668 & \\ 1.234616 & 2.841959 & 4.309898 \end{bmatrix}$$

Third Model
(Flexibility matrices obtained by inversion of the stiffness matrix)

1. Three Modes

$$K=\begin{bmatrix} 329026.6 & & \\ -219303.8 & 336394.9 & \\ 54060.1 & -162740.5 & 116943.6 \end{bmatrix} \quad F=10^{-5}\begin{bmatrix} 0.868031 & & \\ 1.137706 & 2.400893 & \\ 1.181980 & 2.815186 & 4.226364 \end{bmatrix}$$

2. Two Modes

$$K=\begin{bmatrix} 483962.0 & & \\ -400840.0 & 546831.0 & \\ 132415.0 & -252730.0 & 154541.0 \end{bmatrix}$$

FOR DETAILS OF MODELS SEE FIGURE NO. 3.

FIGURE 3

For each Matrix the first column includes the Value of the Row and the second column the Percentage with respect to Static Experimental Matrix

Sum of Rows in Flexibility Matrices of Structure No. 1

	STATIC EXPERIMENTAL MULT. BY 10^{-5}		DIRECT SOLUTION Two Modes MULT. BY 10^{-5}		DIRECT SOLUTION One Mode MULT. BY 10^{-5}	
ROW 1	3.55	100	3.141968	88.5	3.060962	86.2
ROW 2	5.67	100	5.026471	88.7	5.140736	90.7
AVERAGE %		100		88.6		88.5

Units are:
for flexibility in/lb. 1 in/lb = 5.71 N/mm.
for stiffness lb/in. 1 lb/in = 0.175 mm/N.

Sum of Rows in Flexibility Matrices of Structure No. 2

	STATIC EXPERIMENTAL MULT. BY 10^{-5}		DIRECT SOLUTION Three Modes MULT. BY 10^{-5}		DIRECT SOLUTION Two Modes MULT. BY 10^{-5}		DIRECT SOLUTION One Mode MULT. BY 10^{-5}		FIRST MODEL Three Modes MULT. BY 10^{-5}		FIRST MODEL Two Modes MULT. BY 10^{-5}		FIRST MODEL One Mode MULT. BY 10^{-5}		SECOND MODEL Three Modes MULT. BY 10^{-5}	
ROW 1	3.284	100.0	3.261	99.3	3.243	98.8	3.081	93.8	2.0576	62.7	2.267883	69.1	1.53786	46.8	4.053919	123.4
ROW 2	6.51	100.0	6.451	99.1	6.520	100.2	6.424	98.7	2.88204	44.3	3.9906	61.3	2.75648	42.3	8.300895	127.5
ROW 3	8.29	100.0	8.441	101.8	8.47	102.2	8.581	103.2	3.712315	44.8	5.814082	70.1	4.709374	56.8	10.877837	131.2
AVERAGE %		100.0		99.7		100.4		98.6		50.6		66.8		48.6		127.4

THIRD MODEL Three Modes MULT. BY 10^{-5}		THEORETICAL FROM INVERTED CALCULATED STIFFNESS	
3.187717	97.1	2.511183	76.5
6.353785	97.6	4.815432	74.0
8.223535	99.2	6.052993	73.0
	98.0		74.5

Models for Structure No. 2

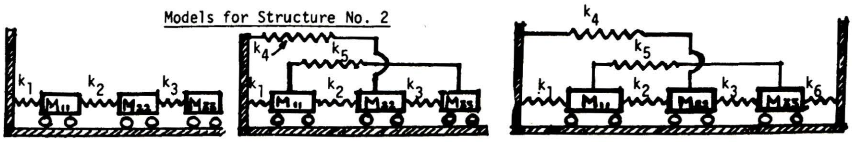

First Model — Second Model — Third Model

General Stiffness Matrix:

$$K=\begin{bmatrix} k_1+k_2 & & \text{symmetric} \\ -k_2 & k_2+k_3 & \\ 0 & -k_3 & k_3 \end{bmatrix}$$

General Stiffness Matrix:

$$K=\begin{bmatrix} k_1+k_2+k_5 & & \text{symmetric} \\ -k_2 & k_2+k_3+k_4 & \\ -k_5 & -k_3 & k_3+k_5 \end{bmatrix}$$

General Stiffness Matrix:

$$K=\begin{bmatrix} k_1+k_2+k_5 & & \text{symmetric} \\ -k_2 & k_2+k_3+k_4 & \\ -k_3 & -k_3 & k_3+k_6+k_5 \end{bmatrix}$$

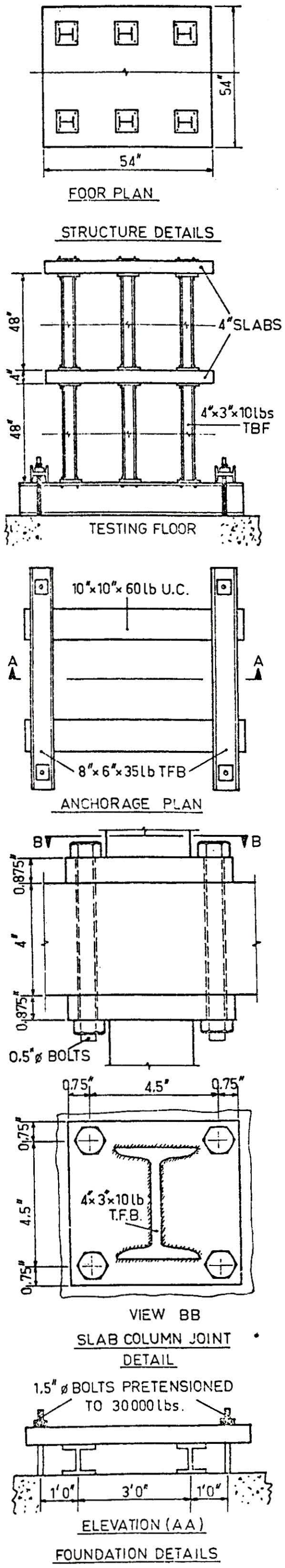

STRUCTURE NO.1

FIG.1

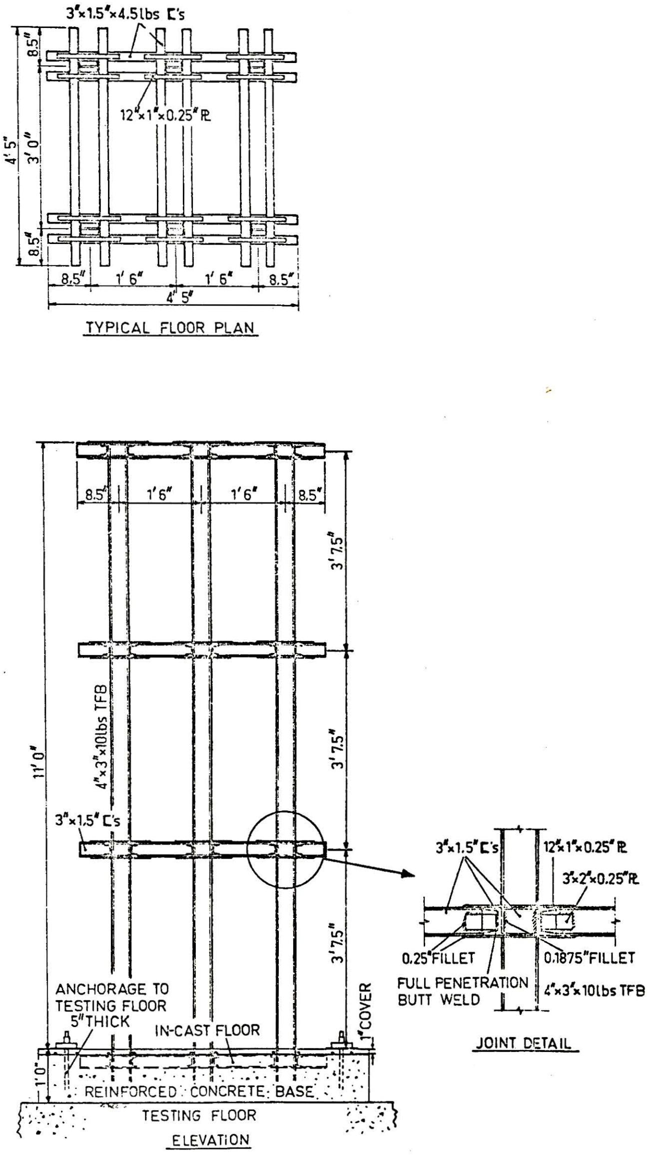

STRUCTURE NO.2

FIG.2

Noise, Shock & Vibration Conference, 1974 Monash University, Melbourne

OFFICE FLOOR VIBRATIONS – DESIGN CRITERIA AND TESTS

M. M. Mc Cormick
BHP Melbourne Research Laboratories
Clayton, Victoria

D. Mason
John Connell & Associates
Melbourne, Victoria

SUMMARY - The paper reviews available criteria for assessment of human perceptibility to occupant-induced vibrations in office building floors. The characteristics of typical vibrations and methods for their calculation are investigated and verified by several tests which are described. Design recommendations are presented.

1. BACKGROUND AND SCOPE

In early 1972, John Connell and Associates (JCA), structural designers of the Collins Place Development in Melbourne, sought advice from officers of BHP's Melbourne Research Laboratories (MRL) on some aspects of the design of composite steel beam-concrete slab floor systems with particular reference to vertical vibration induced by normal conditions of office occupancy and potential annoyance to the occupants.

BHP's Head Office building employs a similar floor system to that projected for Collins Place, and MRL had become involved in conjunction with designers Irwin, Johnston and Partners (IJP) in solving a similar design problem some four years earlier.

Both buildings are similar in that the designers sought to provide large column-free work areas in which flexible furnishing and partitioning arrangements are possible. This approach to building planning is relatively new in Australia, and means that many sources of vibration damping present in buildings constructed in the past may not necessarily be present in these buildings.

Further, in order to achieve this objective, longer span floor beams (12 to 13 m) are used than has been common in the past (6 to 8 m). Finally, economic considerations require that the floor system be as shallow and as light as possible which led in each building to the selection of lightweight concrete floor slabs acting compositely with high strength steel beams.

As a result of these largely non-structural factors, the floor systems are longer, shallower, lighter, more flexible and potentially less well damped than floors within the designers' previous experiences, for which reason the designers in each case saw fit to consider in more than the usual detail the possibility of floor vibrations and their likely effects upon occupants.

This paper describes the criteria which were considered in the designs, several tests which were undertaken to verify a number of design assumptions, the solutions which were derived, and subsequent performance of the floors in BHP House. In the light of this experience, a design method is recommended.

Only transient vertical vibrations caused by normal occupancy and usage are considered. Steady state vibration caused by plant operation is usually isolated at its source and is not considered here. Lateral vibration caused by wind forces was also considered by the designers in each case but a discussion of that subject is outside the scope of this paper.

2. THE DESIGN PROBLEM

There are two aspects to the design problem, namely:

(i) the prediction of relevant characteristics of vibration likely to be induced, and
(ii) determination of an acceptable level of vibration.

With regard to the first, there are numerous methods available for calculating structural response to a given disturbance. These include some fairly comprehensive computer programs which are available commercially. However, a design office seeks simple, economical and reliable checks to ascertain whether or not a problem is likely to exist before considering recourse to such programs. Further, reliable computer analyses tend to find at least three significant degrees of freedom in a typical building floor, and the response patterns obtained are difficult to relate to available human sensitivity criteria. Finally, the damping characteristic of the floor is of fundamental importance, and this is difficult to predict analytically. Therefore, primary attention has been directed to simple methods which can be related to available sensitivity criteria. However, several computer analyses were made and are referred to later.

With regard to the second aspect, there is a paucity of useable information available, despite the fact that mechanisms of human response to vibration are now being researched (e.g. 5) and various measures of human response to steady state vibration have been available for some years (6, 9). Reference 9 in particular gives a good review of the state of knowledge in this area up to 1965. A brief review of the little information on human response to transient vibration that is available is given below.

Reference 1 - Lenzen

Lenzen is believed to have been the first to attempt a solution to this problem. His solution has been directed specifically towards a particular type of floor system which utilizes a light weight concrete slab (of the order of 70 mm thick) supported compositely by closely spaced (approximately 1 to 1½ m) light steel trusses with spans up to about 8 m. The total depth of the floors is such that most satisfy the span/depth ratio recommendations of the U.S. Specification for steel building design (15). The SAA Steel Structures Code (14) contains no such provision. The floors of interest in this paper use heavier slabs (100 to 140 mm thick) compositely supported by heavier rolled steel beams at typical 3 to 4 m spacings over spans of 12 to 13 m. Total floor system depth is about the same as for Lenzen's trussed floors, but approach the limits recommended in Reference 15 for span/depth ratio.

Lenzen studied a number of both in-situ and full scale model floors, and the response of occupants to various types of disturbance creating transient vertical vibration. He found that

(i) damping was themost significant factor influencing human response.
(ii) when damping exceeded about 5%*, the occupant felt only an initial impact.
(iii) when damping was less than about 3%, the occupant responded as though to a steady state vibration.
(iv) when damping was between 3% and 5%, human response was reasonably well described by reference to a vibration perceptibility chart.
(v) the usual formula $f = (\pi/2L^2)\sqrt{(EI/m)}$ gave reasonable estimates of the natural frequency f hz with which the floors responded. In this formula, L is the span, EI the flexural rigidity and m the mass/unit length of a single simply supported beam.

Lenzen's vibration perceptibility chart derived on the basis of his observations simply modifies an earlier chart by Reiher and Meister (see Ref. 9) by multiplying the amplitude scale by a factor of 10. This is shown in Figure 1, and requires that damping be between 3% and 5% approximately.

He also found that a typical vibration amplitude could be approximately ascertained as the equivalent of the static deflection under a 1.35 kN point load. This load was to be modified to $(0.015L^2/D)$ kN for longer span floors without partitions, where L and D are the span (m) and depth (m) respectively. The closely spaced truss and slab floor shows significant two-way action, and Lenzen's earlier work suggested that no more than 10 trusses be assumed to act together when calculating the deflection. Later work (7) gives a more rigorous method of calculating stiffness. It was initially believed that the 10-truss assumption was the basis for the 10-fold amplification of the amplitude scale referred to earlier, but this belief has subsequently (7) been found to be incorrect.

Thus the second aspect of the design problem has been almost inseparably keyed to the first in Lenzen's approach because of its inherent empiricism.

---

*Throughout this paper, all figures for damping are quoted as % of critical damping.

Lenzen's approach has been critically reviewed by Chang (8, 10), who suggests that its validity for other types of floor system is doubtful. Nevertheless, it has been adapted by Khan (2) and applied to a wide variety of floors, using deflection under a 1.35 kN point load as an estimate of likely vibration amplitude. It is claimed thatuse of this procedure has not resulted in any unsatisfactory floors in the U.S., and the range of floor characteristics considered by Khan are shown in Figure 1.

Finally, it is worth noting that Lenzen shrewdly made no recommendation for limiting amplitude and frequency. It has been left entirely to the designer to ascertain an acceptable limit. Lenzen's approach only gives the designer a description of the type of vibrations likely to be encountered. A further review of the problem is given by Lenzen in Reference 11.

Reference 12 - Soretz and Holzbein

The authors of Reference 12 quote a further reference which claims that disturbing vibration is avoided when a floor deflects no more than 0.7 mm under a 1 kN point load. (Approximately 1 mm under 1.35 kN as used by Lenzen and Khan.) They also point out the need for further research. The 1 mm limit is plotted on Figure 1 for comparison with other criteria.

Reference 4 - I.S.O.

The recommendations ofthis document are intended to apply to all types of vibration although the present authors feel they are more directly applicable to continued steady state vibration. The document recommends maximum values of r.m.s. acceleration continued for various periods to give several levels of occupant comfort and work efficiency. The stated threshhold levels for reduced comfort with exposure times of 1 minute and 1 hour are shown in Figure 1. Although it is difficult to relate these exposure timesto typical building floor vibrations of interest here (they may be accumulated times of a series of individual events), it is seen that a reasonable comparison may be drawn with Lenzen's criteria, without the need to make any assumption as to the source and magnitude of the disturbance.

Reference 9 - Steffens - Authors' modifications

Lenzen's approach and its reasonable comparison with the ISO recommendation prompted the present authors to apply a similar approach to Dieckmann's criteria for steady state vibration. Steffens (12) summarized Dieckmann's criteria and part of a German standard DIN 4025. The author's adaption amounts to increasing Dieckmann's value of K by a factor of 10. It is shown in Figure 1, and it is suggested that for transient vibration K = 1 corresponds to a threshold level, K = 1 to 3 to just perceptible, K = 3 to 10 to clearly perceptible, K = 10 to 30 to strongly perceptible, but not annoying, work unlikely to be affected. Again, a rough but not unreasonable comparison can be drawn with the other criteria plotted in Figure 1.

Summary

The four sets of criteria which have been reviewed are all approximately comparable on a qualitative basis. A rigorous quantitative comparison is not possible because of the subjective nature of the descriptions of zones of perceptibility and the individual interpretations which can be placed upon these descriptions. The apparent accord between these criteria does not, however, necessarily vouchsafe their successful application. IJP, JCA and the authors were aware of a number of problems which were again reported by Lay (13) on his return from a visit to the U.S. He observed that information relating to in situ performance could not be obtained and stated that "Clearly, some of the proposals (being developed for perceptibility criteria and methods of performance assessment) would be highly controversial and potentially discreditable to some (floor) systems".

There are three possible explanations for the circumstances surrounding Lay's observation:

(i) Lack of damping in some floors. According to Lenzen's observations, if damping is less than about 3%, the original Reiher/Meister sensitivity scale would be applicable and such floors, if plotting near the upper edge of the shaded area in Figure 1, would then be classified as having annoying or disturbing vibration characteristics.

(ii) use of over-optimistic estimatesof stiffness to calculate approximate vibration amplitudes, possibly due to misapplication of Lenzen's recommendations outside their range of validity. This is the basis of Chang's (8, 10) criticism of Lenzen's approach. It is discussed further here in a later section.

(iii) use of incorrect equivalent static load for estimation of typical vibration amplitudes, or a similar problem with other (unknown) developments.

These and other matters are probed in the work described in the following sections.

3. THE MODELS

In each case, full scalemodels of sections of the floor had been built. Each model consisted of a pair of beams supporting a compositely attached concrete slab which overhung the beams on each side.

The BHP model used 530UB82 Universal Beams in mild steel castellated to a depth of 730 mm. Beam spacing was 3.05 m and span was 12.6 m. The slab used a Grade 20 lightweight concrete with 65 mm depth over permanent steel formwork with 55 mm deep ribs. The slab overhung the edges of the beams by 850 mm. No attempt was made to simulate end fixity conditions.

The Collins Place model used 530UB82 Universal Beams in mild steel with 430 mm circular web openings for carrying mechanical services. Beam spacing was 4.3 m and spans were 11.7 m and 13.1 m - a feature which, in retrospect, caused unnecessary complication when interpreting test results. The slab was 125 mm thick in lightweight Grade 20 concrete, and overhung the edges of the beams by 1.83 m. Although mild steel beams were used in the model, high strength steel beams are to be used in the structure. This model attempted to simulate end fixity conditions.

4. THE BHP MODEL TESTS

The calculated stiffness and natural frequency of the model were verified by static and dynamic tests. All tests have been reported elsewhere by Foden (17). Typical results are plotted in Figure 1. Unfortunately, the instrumentation was fairly crude, using a slow response pen recorder which severely attenuated amplitude signals, with the result that natural frequency was the only dynamic parameter reliably measured.

In addition to static load and mass dropping tests, vibrations were also created by people walking, running and "heel dropping" (sudden transfer of body weight from toes to heels) and the subjective response of anumber of observers obtained. Light pedestrian traffic produced slightly perceptible vibrations, although strongly perceptible vibration could be created by a number of people running in step. Although difficult to judge because of the absence of reliable amplitude signals, the results tended to support Lenzen's observation that (with damping estimated at about 1%) the Reiher Meister steady state vibration criteria would be applicable. Nevertheless, the Figure 1 plot indicated that the response of the floor was typical of that in the U.S. The designers IJP adopted the design without modification on the basis that it was known from design logic and from their overseas experience and data that the in-situ floors would be stiffer and better damped than was the model. Therefore, the Figure 1 plot should not become worse and the presence of more damping should render it valid. The desirability of undertaking future in-situ tests was noted.

5. COLLINS PLACE MODEL TESTS

The tests initially undertaken here were very similar to those on the BHP model some four years earlier. However, instrumentation was much improved and gave satisfactory measurements of amplitude, frequency and damping. Typical results are plotted in Figure 1. Subjective observations of vibration due to various types of pedestrian traffic were similar to those obtained from the BHP model tests. Interpretation of results was made difficult due to a "beating" effect between the two unequal span beams with similar but non-identical frequencies.

An attempt was then made to simulate better the in-service conditions. The free edges of the slab were propped to approximate in-situ connections to adjacent panels of floor, and the model was furnished to some extent with underfelt and office furniture. No partitions were used, and the extent and type of furnishing was generally far lighter than would be achieved finally. The furnishing together with occupants standing/sitting on the furniture reduced subjective human sensitivity a little but had no significant measurable effect. The effect of then propping the slab was measurably beneficial, andtypical results are plotted in Figure 1. Subjectively, vibrations due to pedestrian traffic were still perceptible to all observers. Some further similar tests were also conducted using a mechanical impactor/vibrator built at MRL. The objective of using this machine was to create distrubances which could be reproduced exactly on other floors, and later on Collins Place floors at various stages of construction.

In general, the results of all tests were then not sufficiently conclusive to enable a firm design decision to be made. The designers JCA withheld their final decision to proceed with the design until after assessment of test results from BHP House which had recently been completed. In this respect JCA were more fortunate than IJP had been four years earlier in that local experience was now available. In the absence of data from BHP House, JCA would have adopted reasoning similar to that used by IJP.

6. TESTS IN BHP HOUSE

BHP House had recently been completed and was awaiting occupation. Floors were carpeted, office partitions were in place, and some furniture had been installed.

At a subjective level, the response offloors to walking, running, jumping and heel dropping was judged to be acceptable, similar to that typically experienced in the home but marginally more perceptible than is common in office buildings.

Tests were also conducted using the mechanical impactor and typical results are plotted in Figure 1. A steady state vibration was also induced with resonance being established at two frequencies, about 6 hz and 10 hz. Single impact free response was at a frequency of 10 hz which was considered to be the relevant (natural) frequency of the floor. The lower frequency is believed to be due to vibration of the slab between the beams. The increase in frequency from model (6 hz) to in situ (10 hz) conditions is attributed to increased stiffness. All tests indicated quite acceptable performance and supported the designers' reasoning in arriving at their decision as described earlier.

At the time this paper was written, BHP House had been occupied for about one year and while some occupants say that vibration under normal office use is perceptible, no complaints have yet been received in regard to this type of vibration.

In regard to the assessment of the Collins Place floors, the performance of floors in BHP House, particularly theimprovement in damping characteristics, satisfied JCA that their design would be similarly adequate.

7. OTHER DATA

In an endeavour to ascertain the extent to which the performance of the two floor systems may be typical of Australian practice, information from public construction authorities was sought with little success. The S.A. Public Buildings Department kindly provided some data (3) and calculated characteristics of two composite steel beam-concrete slab floors from a school and a hospital are shown in Figure 1. The extent of damping in each floor is unknown, although both are considered to perform satisfactorily. It is seen that the predicted response of these floors is more perceptible than that of most others plotted.

8. GENERAL OBSERVATIONS AND ANALYSES OF TEST RESULTS

(i) In all tests which were undertaken, it was found that impact from a 23 kg mass dropped through 300 mm created vibrations which were reasonably typical of those produced by moderately heavy pedestrian use. The use of a 138 kg mass (1.35 kN force, after Lenzen) applied statically produced results which were lower than but comparable with the 23 kg impact, although there was considerable variation which is attributed to variations in the dynamic magnification factor applied to the 23 kg impact.

(ii) When amplitudes are predicted using Lenzen's $0.015L^2/D$ kN in place of 1.35 kN point load and plotted on Figure 1, the results bear little correlation with observations. It is considered that this empirical adjustment is not applicable to beam-slab floors of the type considered here, and should not be used.

(iii) Performance of model floors can be predicted analytically with a reasonable degree of accuracy, as described in the next section. Although exact details of the response, (as typified by the beating effect observed on the Collins Place model) were predicted by a finite element computer analysis, a simple slide-rule analysis gave results from which much the same conclusions could be drawn. The extent of damping could not be predicted analytically. The simple analysis on which all results plotted in Figure 1 (except points 11 and 12) are based, used the formula for frequency given earlier, and ignored any two-way action in the floor system. That is, all calculations were made for a single, simply supported beam. There was good correlation between predicted and observed performance. The results from the impact type loading tend to give a better subjective measure of vibration performance than do results for the 1.35 kN point load. Thus, on Figure 1, points 6 and 8 are considered to be most relevant, (points 2 and 4 have doubtful validity because of the low damping in these cases and vibration was far more perceptible than is indicated by Figure 1 for these two).

(iv) Subjectively, vibrations created by identical disturbances in BHP House are less perceptible than those on the Collins Place propped-edge model, yet Figure 1 indicates the converse. This difference is attributed to differences in the damping in each floor, BHP House having 10% or more, Collins Place model with propped edges having between 2% and 4%. It is expected that damping will be further increased in the full in-situ condition in Collins Place.

(v) There is no apparent correlation between vibration performance and span/depth ratio limitation as recommended in Reference 15. The traditional recommended live load deflection limitations (14, 15) appear to beequally irrelevant to this problem. In the next section it is shown that the ratio of span to beam spacing can have a significant influence.

9. DESIGN RECOMMENDATIONS

The following recommendations are made on the basis of the authors' observations and results.

(i) Natural frequency:

Calculate natural frequency for a single beam from

$$f = \frac{\pi}{2L^2}\sqrt{\frac{EI}{m}}$$

where the terms and the equation are as given earlier. Include all possible sources of stiffness in the calculation, and make most realistic estimate possible for m in order to increase estimate of f.

(ii) Vibration amplitude (simply supported beams):

Calculate amplitude from

$$A = \frac{M}{N} \cdot \frac{PL^3}{48EI}$$

where $P = 0.2$ kN

M = dynamic magnification factor

$= (1 + \frac{\pi}{2}f)$ with a minimum value of 2.0

N = no. of effective beams contributing to stiffness

$= \frac{L}{S}\frac{\pi^3}{48}\sqrt{2(1+\alpha)}\;(\frac{St^3}{12nI})^{\frac{1}{4}}$

S = beam spacing

t = slab thickness

n = modular ratio

α = ratio of arithmetic mean of torsional stiffnesses per unit width to geometric mean of bending stiffnesses per unit width taken parallel andtransverse to the beam axis

EI = bending stiffness as used in frequency calculation.

The dynamic magnification factor is an upper bound estimate of the exact formulation given by

$$M = \left[(1 - \cos 2\pi f t_0)^2 + (2\pi f t_o - \sin 2\pi f t_o)^2\right]^{\frac{1}{2}}$$

where t_o is the time during which the 20 kg mass drops through 300 mm, i.e. $t_o = 0.25$ sec. For most practical floors, the value of M is between 6 and 15.

The effective number, N, of beams contributing to the stiffness has been determined from the theory of orthotropic plates (16) assuming an infinitely long plate transverse to the beam axis, simply supported at the span ends. The question of end fixity effects on amplitude has not been investigated by the authors. The significance of the beam span to spacing ratio is clear. Values of the ratio α are commonly less than 0.1, and may be assumed to be zero for all practical purposes except in the case of unusually thick slabs. Values of N are typically 1.0 to 1.5 for the widely spaced beam and slab floors used in BHP House and Collins Place, but may be as high as about 8 for closely spaced truss and slab systems common in the U.S. - the L/S ratio effect.

It seems reasonable tosuggest that this disparity, or lack of appreciation of it, could be the source of trouble that has resulted in some criticism of Lenzen's work when it is applied to other floor systems.

(iii) Perceptibility:

Floors in which damping exceeds about 3% should prove acceptable when Af is less than 2mm/sec, (line E in Figure 1) although vibration caused by normal use may be perceptible to the occupants. For damping considerably in excess of 3% (say about 10% as in BHP House) a higher limit than 2 mm/sec should be possible, but in the absence of data on unsatisfactory floor performance, such a limit cannot be established.

Floors in which damping is less than about 3% are likely to have potentially objectionable vibrations, even when Af < 2 mm/sec, and consideration should then be given to supplementing the naturally available damping, preferably to a minimum of 5%. Lenzen (1) gives guidance on selection of damping devices.

Floors as conventionally constructed with the usual degree of furnishing and partitioning tend to provide sufficient natural damping. BHP House is relatively lightly furnished and partitioned and provided adequate damping.

(iv) Application:

Application of this design criterion to the floors of BHP House and Collins Place result in the points numbered 11 and 12 respectively in Figure 1. Note that in each case, the calculated frequencies of 6 hz and 4.5 hz respectively are used.

10. CONCLUSIONS

The paper has reviewed available information on human perceptibility to transient floor vibration, and methods of assessing likely levels of vibration. The design recommendations are similar to those advanced by Lenzen and the authors found nothing which would refute his work except as qualified herein. In particular it is essential when applying it outside the range of its original validity, to make a proper assessment of likely vibration amplitudes.

The development of more positive design recommendations seems to await data on unacceptable floors, and more qualitative data on damping sources and effects on people. Future tests at various stages of construction in Collins Place are aimed at providing the latter. The authors support Lenzen's observation that damping is probably the most relevant parameter.

It is expected that floors in Collins Place will give satisfactory performance.

11. ACKNOWLEDGEMENTS

The authors thank the JCA, IJP and BHP organizations for permission to present this paper, the Principal Engineer, Public Buildings Department, S.A. for the data which was provided, and Mr. J. Fowler of IJP for reviewing the paper and for his valuable comments. Finally, acknowledgement is due to the efforts of all previous researchers in this field, particularly those of Professor Lenzen. Without such effort, this paper could not have been presented.

12. REFERENCES

1. Lenzen, K.H.,
Vibration of Steel Joist - Concrete Slab Floors,
AISC Engineering Journal 3(3), July 1966, pp133-136.

2. Khan, F.R.,
Study for John Hancock Centre - Report on Vibration of Floors,
Personal Communications, 1971.

3. The Principal Engineer, Public Buildings Department, South Australia,
Data on Typical Steel Beam-Concrete Slab Composite Floor Systems,
Personal Communication, 1972.

4. ISO/DIS 2631,
Guide For the Evaluation of Human Exposure to Whole Body Vibration,
ISO, 1972.

5. Guignard, J.C.,
Human Sensitivity to Vibration,
Journ. Sound and Vibration, 15(1), 1971, pp11-16.

6. Vibration in Buildings, Parts 1 and 2,
Building Research Station (UK) Digests 117 and 118, 1970.

7. Galambos, T.V.,
Vibration of Steel Joist - Concrete Slab Floors,
Personal Communications, 1972. (Paper to be published).

8. Chang, F.K.,
Human Response to Motions in Tall Buildings,
Proc. ASCE Jour. Struct. Divn. 99(ST6), June 1973, pp1259-1272.

9. Steffens, R.J.,
Some Aspects of Structural Vibration,
From "Vibration in Civil Engineering", B.O. Skipp (Ed.), Butterworths London, 1966, pp1-30,
(Symposium proceedings Imperial College, April 65).

10. Chang, F.K.,
Psychophysiological Aspects of Man - Structure Interaction,
Proc. ASCE-IABSE Conference Planning and Design of Tall Buildings, 1972, Vol. 1, pp173-189.

11. Lenzen, K.H.,
Vibration of Floor Systems of Tall Buildings,
Ibid, Vol. 17, pp39-45.

12. Soretz, S., Holzenbein, H.,
Stiffness Requirements in Terms of Human Comfort,
Ibid., Vol. 24, pp63-65.

13. Lay, M.G.,
The Lehigh Tall Buildings Conference,
BHP Melb. Res. Lab. Report 17/21, Oct. 1972.

14. Standards Association of Australia,
SAA Steel Structures Code,
AS 1250-1972.

15. American Institute of Steel Construction,
Specification for the Design, Fabrication and Erection of Structural Steel for Buildings
(Including Commentary),
AISC Manual of Steel Construction, 7th Edition, 1970, pp5.5 to 5.166.

16. Rowe, R.E.,
Concrete Bridge Design,
John Wiley and Sons Inc., 1962.

17. Foden, P.J.,
Prototype Floor Test for New BHP Building,
BHP Melb. Res. Lab. Report 16/1, Sept. 69.

13. POSTSCRIPT

Since this paper was written, two further references have been found. These are:

18. Yokel, F.Y., Somes, N.F.,
Structural Performance Evaluation of Innovative Building Systems,
U.S. Dept. Commerce Nat. Bur. Stds., NBS Tech. Note 706, Aug. 72.

19. Commonwealth Experimental Building Station (Australia),
Human Sensitivity to Vibration in Buildings,
CEBS Researches and Facilities, RF No. 12, May 66.

Reference 18 describes a proposed standard test method which consists of dropping a leather bag containing sand and lead shot and having a mass of 11.34 kg through a distance of 914 mm. It also suggests a standard method of instrumentation very similar to that finally adopted in the work described here, using a linear variable differential transformer mounted from a fixed reference, whose output is displayed on a recording oscilloscope. The proposed standard excitation is also similar to a method used in the earliest tests by the authors which was discontinued when it was found to produce vibrations less typical of in-service conditions than did the method finally adopted. However, in terms of the present authors' recommended formula for amplitude calculations, the two different impacts result in essentially identical calculated amplitudes for floors with natural frequencies in the 6 to 10 hz range.

Reference 19 is of particular interest in that it is the earliest published reference of direct relevance to the present problem which has so far been found by the authors. The prime conclusions were (i) that the original Reiher-Meister sensitivity scale is far too severe to describe human reaction to transient floor vibration and (ii) floors with higher levels of damping of transient vibrations were less likely to be prone to unsatisfactory performance than were floors with lower levels of damping. The present authors' work supports both of these conclusions. Reference 19 also states that the person who causes the vibration by walking is likely to feel more uncomfortable (than a bystander) on a lightly damped floor than on a heavily damped floor, because of an absence of comparable transience. In retrospect, the present authors cannot support this statement from within the limits of their experiences and a number of researchers believe that the reverse situation usually prevails. However, this statement together with differences in methods of producing impacts between Reference 18 and this report leads to the hypothesis that apparent inconsistencies could be explained in terms of the floor coverings which exist between the source of vibration, the floor, and the perceivor of the vibration. That is, the comparatively "hard" impact used by the authors on a "soft" floor covering could produce a similar response to the Reference 18 "soft" impact on a "hard" floor covering. In a similar vein, the Reference 19 final statement could be explained by having the person walking on a hard floor while bystanders are comparatively better cushioned, e.g. seated on well padded chairs.

Finally, Reference 19 showed a plot of "vibrations that have elicited no comment from unsuspecting subjects during repeated exposure". This was given in the 10 to 50 hz frequency range and when extrapolated to the 1 to 10 hz range, closely follows line D2 in Figure 1 herein. This line could then be regarded as the lower limit to human perception of the vibrations of interest here, although the extent of damping in the CEBS tests is not given in Reference 19. It is possible that further tests may show that the authors' recommended limit (Fig. 1, line E) could be liberalized slightly to follow line D3 or perhaps C1. However, the liberalization would affect only the comparatively unusual floors with natural frequencies below about 5 hz.

FIG. 1. VIBRATION PERCEPTIBILITY CHART.

A LENZEN (REF. 1)

BELOW A1	NOT PERCEPTIBLE
A1 - A2	SLIGHTLY PERCEPTIBLE
A2 - A3	DISTINCTLY PERCEPTIBLE
ABOVE A3	STRONGLY PERCEPTIBLE

B SORETZ AND HOLZEBEIN (REF. 12)

C I.S.O. (REF. 4) REDUCED COMFORT THRESHOLDS.
C1 :- 1 HOUR EXPOSURE C2 :- 1 MINUTE EXPOSURE.

D AUTHORS MODIFIED DIECKMANN CURVES : D1 : K = 1 D2 : K = 3 D3 : K = 10 D4 : K = 30

E AUTHORS DESIGN RECOMMENDATION , Af = 2mm sec^{-1}

SHADED AREA - KHAN (REF. 2)

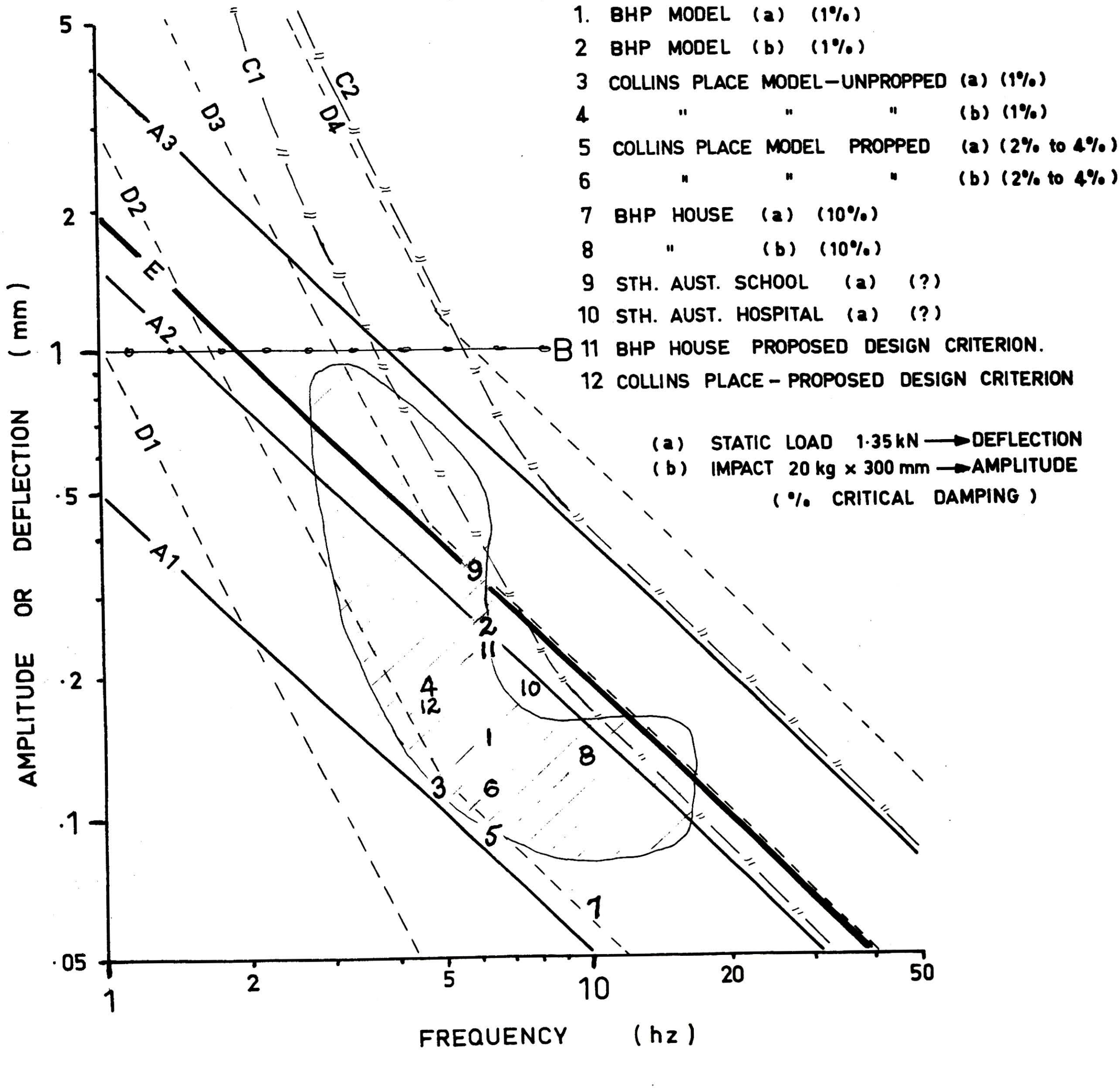

DYNAMICAL RESPONSES OF FLOATING BRIDGES UNDER MOVING LOADS

Chau-Shioung Yeh
Civil Engineering Department
University of Singapore
Singapore

Si Him Chan
Housing & Development Board
Singapore

SUMMARY

In the present investigation, the response of a floating bridge under moving loads is studied. The floating bridge is modelled as a continuous beam with concentrated masses supported by elastic supports. The effects due to both damping and the added mass of supports are neglected.

A dimensionless overall transfer matrix is first constructed. Then the relation between the conditions at two exterior ends of the bridge can now be described by an equation using this over-all transfer matrix. By substituting the prescribed boundary conditions into this equation, one obtains a frequency equation, the roots of which can be found numerically. The results for several cases are presented. It is found that the natural frequencies are affected by three parameters, namely α, the ratio of buoyancy resistance to the stiffness of beam; β, the ratio of the mass of the supports to that of the beam and n, the number of spans.

The method is extended to analyse forced vibration of floating bridges. Two cases are studied in detail. One is the response of a floating bridge under a constant force with uniform velocity and the other is that under a pulsating force with uniform velocity. The method of modal analysis is employed to obtain the DLF (dynamical load factor) for each case. In the first case, the maximum DLF is generally found to be decreasing when α is increased with β and the velocity of load kept constant. Also, the maximum DLF is found to be increasing when the velocity becomes slower. In the second case, the maximum DLF is computed. It is found to be increasing when n is decreased and decreasing when the velocity is increased. Under certain conditions, the maximum DLF can reach the value as high as 8.7.

INTRODUCTION

A floating bridge is most commonly used for military purpose. In the design of a floating bridge, the dynamical considerations such as the most dangerous vehicle speed and the range of dynamic responses under the moving vehicle are essential.

Timoshenko[(1)] solved the problem of a beam under a pulsating force moving with uniform velocity. Sir Inglis[(2)] investigated the vibration of railway bridges subjected to a transversing force with non-uniform velocity. Both investigations were limited to the simply supported structure. With regard to continuous beams, Ayre, Ford and Jacobsen[(3),(4)] studied a problem of transverse vibration of a multiple-spans beam under the action of a moving constant uniform force. They derived the exact solution for bending stresses and deflections of continuous beam. Experiments were performed to verify the theoratical results.

In this paper, a floating bridge is modelled as a continuous beam with concentrated masses supported by elastic supports in which the elastic coefficients k are the buoyant resistance of masses. Both the effects of damping, shear deformation, and rotatory inertia and the effect of added mass due to water are assumed to be negligible. The method of transfer matrix is adopted to calculate the natural frequencies and the method of modal analysis is applied to calculate its response to moving loads.

A n-span floating bridge supported by n+1 floating pontoons is shown in Fig. 1. In order to determine the natural frequencies of the bridge, a transfer matrix is firstly developed. On the assumption that the effects of damping, shearing deformation and rotatory inertia of the bridge can be neglected, a dimensionless equation of free vibration may be written as

$$\frac{\partial^4 y}{\partial x^4} + \frac{\gamma a}{ei}\frac{\partial^2 y}{\partial t^2} = 0 \qquad (1)$$

with

$$\begin{aligned} y(x) &= Y/L, & x &= X/L \\ \gamma &= \rho/\rho_0, & a &= A/A_0 \\ e &= E/E_0 & i &= I/I_0 \\ t &= \tau/T, & T &= (\rho_0 A_0 L^4/E_0 I_0)^{\frac{1}{2}} \end{aligned} \qquad (2)$$

where τ is the time, X is coordinate along the beam, Y is the delfection and ρ_0, A_0, E_0, I_0 are the density, cross-sectional area, Young's modulus and second moment of area of a reference span, respectively. We note that γ, a, e and i are constants for each span.

The solution of equation (1) may be written as

$$y_r(x,t) = f_r(t)\phi_r(x) \qquad (3)$$

with

$$f_r(t) = B_{r1}\sin\omega_r t + B_{r2}\cos\omega_r t \qquad (4)$$

and

$$\phi_r(x) = A_{r1}\sin\lambda_r x + A_{r2}\cos\lambda_r x + A_{r3}\sin\lambda_r x + A_{r4}\cosh\lambda_r x \qquad (5)$$

where ω_r is the dimensionless natural circular frequency of the r^{th} mode and is related to the natural circular frequency, $\bar{\omega}_r$, $\omega_r = \bar{\omega}_r T$, and the frequency constant λ_r is defined as

$$\lambda r = (\gamma a \bar{\omega}_r^2/ei)^{\frac{1}{4}} \qquad (6)$$

$\phi_r(x)$ describes the r^{th} mode shape. The constants A_{r1}, A_{r2}, A_{r3} and A_{r4} are determined by boundary conditions. $f_r(t)$ indicates that the time function is harmonic with natural frequency ω_r. The constants B_{r1} and B_{r2} are determined by initial condition. The relations between dimensionless forces and deformations may be written as

$$m = -ei\frac{\partial^2 y}{\partial x^2}$$

$$q = -ei\frac{\partial^3 y}{\partial x^3} \qquad (7)$$

with $m = M/M_0$, $q = Q/Q_0$, $M_0=E_0I_0/L$, $Q_0=E_0I_0/L^2$. M and Q are the bending moment and shear force, respectively.

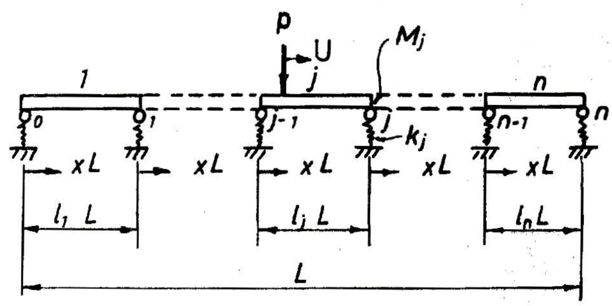

FIG. 1 Schematic Diagram of a Floating Bridge under a Moving Load.

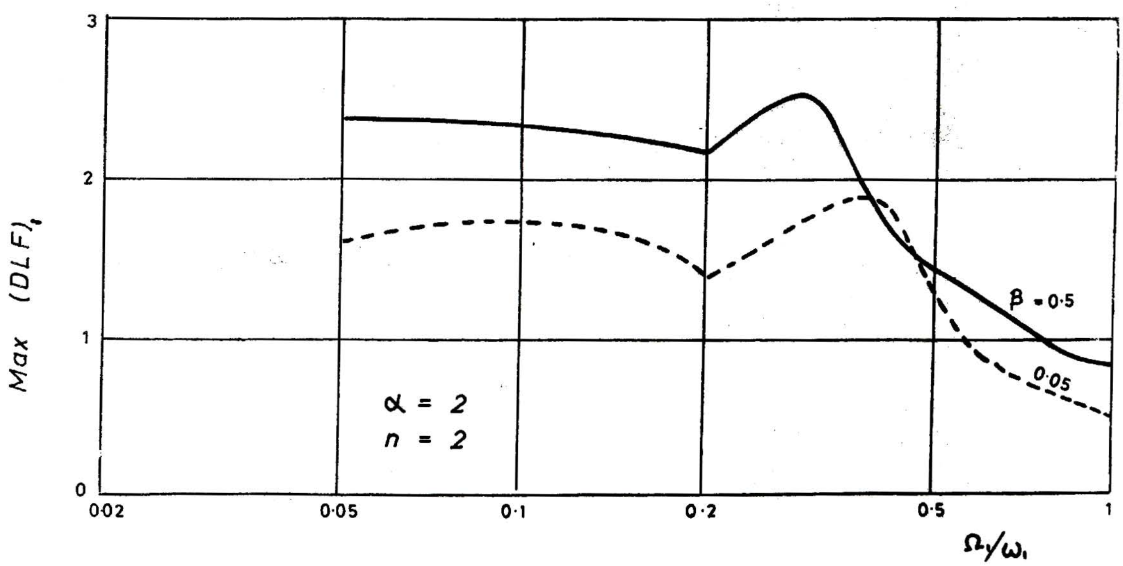

FIG. 2 Max. (DLF)$_1$ of two-span bridge under constant load with uniform velocity.

Consider the j^{th} span of beam, a dimensionless field matrix $[F]_j$ may be developed by following the procedure described in ref (5). It relates the displacement y, slope ψ $(=-\partial y/\partial x)$, moment m and shear force q at the right end R of $(j-1)^{th}$ support to those at the left end L of j^{th} support with the equation

$$\{Z\}^L_j = [F]_j \{Z\}^R_{j-1} \tag{8}$$

where $\{Z\}$ denotes the column matrix with four elements $Z_1 = -y$, $Z_2 = \psi$, $Z_3 = m$, $Z_4 = q$, and

$$[F]_j = \begin{bmatrix} C_1 & C_4/\lambda & C_3/(\lambda^2 ei) & C_2/(\lambda^3 ei) \\ \lambda C_2 & C_1 & C_4/(\lambda ei) & C_3/(\lambda^2 ei) \\ \lambda^2 eiC_3 & \lambda eiC_2 & C_1 & C_4/\lambda \\ \lambda^3 eiC_4 & \lambda^2 eiC_3 & C_2\lambda & C_1 \end{bmatrix}_j \tag{9}$$

with

$$\begin{aligned} C_1 &= \tfrac{1}{2}(\cos\lambda l + \cosh\lambda l) \\ C_2 &= \tfrac{1}{2}(-\sin\lambda l + \sinh\lambda l) \\ C_3 &= \tfrac{1}{2}(-\cos\lambda l + \cosh\lambda l) \\ C_4 &= \tfrac{1}{2}(\sin\lambda l + \sinh\lambda l) \\ l &= \text{length of span}/L \ . \end{aligned} \tag{10}$$

Consider the balance of forces at j^{th} floating support with mass M_j which is assumed constant. A dimensionless point matrix $[P]_j$ which relates $\{Z\}^R_j$ to $\{Z\}^L_j$ maybe written as

$$[P]_j = \begin{bmatrix} 1 & 0 & 0 & 0 \\ 0 & 1 & 0 & 0 \\ 0 & 0 & 1 & 0 \\ ei\beta\lambda^4 - \alpha & 0 & 0 & 1 \end{bmatrix}_j \tag{11}$$

where $\alpha = KL^3/E_oI_o$ and β is the ratio of M_j to the mass of beam.

Defining

$$[T]_j = [F]_j [P]_{j-1} \tag{12}$$

we may write

$$\{Z\}^R_n = [U]\{Z\}^L_o \tag{13}$$

where $[U] = [P]_n [T]_n [T]_{n-1} \ldots [T]_1$ relates the deflection, slope, moment and shear force at the first support to those at the last support. We note that the elements in U are function of ω.

Determination of Natural Frequencies

The natural frequencies can be determined by applying the boundary conditions to Eq. (13). For a floating bridge, the moment and shear force at both ends are zero, i.e.

$$m^L_o = q^L_o = m^R_n = q^R_n = o \tag{14}$$

Substituting the boundary conditions (14) into Eq. (13), we have

$$U_{31}(-y)^L_o + U_{32}\psi^L_o = o \tag{15}$$

$$U_{41}(-y)_o^L + U_{42}\psi_o^L = o$$

The condition that a non-trival solution exists gives the determinant

$$\begin{vmatrix} U_{31} & U_{32} \\ U_{41} & U_{42} \end{vmatrix} = 0 \qquad (16)$$

which is called frequency equation. The roots of Eq. (16) can be obtained by the method of trial and error for each specific value of α and β. Corresponding to each root of Eq. (16), ψ_o^L can be expressed in terms of y_o^L by applying Eq. (15). Then the deflection, slope, moment and shear force at any section of any span (say j^{th} span) can be calculated by the following equation

$$\{Z\}_j = [B]_j\,[T]_{j-1}\;\cdots\;[T]_1\,\{Z\}_o^L \qquad (17)$$

where

$$\{Z\}_o^L = \begin{Bmatrix} -y \\ -U_{31}(-y)/U_{32} \\ o \\ o \end{Bmatrix}_o^L$$

and

$$[B]_j = \begin{bmatrix} \frac{D_1}{\lambda^3 ei} & -\frac{D_2}{\lambda^3 ei} & \frac{D_3}{\lambda^3 ei} & \frac{D_4}{\lambda^3 ei} \\ -\frac{D_2}{\lambda^2 ei} & -\frac{D_1}{\lambda^2 ei} & \frac{D_4}{\lambda^2 ei} & \frac{D_3}{\lambda^2 ei} \\ -\frac{D_1}{\lambda} & \frac{D_2}{\lambda} & \frac{D_3}{\lambda} & \frac{D_4}{\lambda} \\ D_2 & D_1 & D_4 & D_3 \end{bmatrix}_j$$

with $D_1 = \cos\lambda x$, $D_2 = \sin\lambda x$, $D_3 = \cosh\lambda x$ and $D_4 = \sinh\lambda x$.

Since the lower modes are more important in engineering applications, we have calculated the first three frequency constants from Eq. (16) for various values of α and β. The results for two-equal-span bridge and three-equal-span bridge are shown in Table 1 and Table 2, respectively. To study the effect of number of spans, n, on the natural frequencies we have also calculated λ_1^2 for $\alpha = 10$ with various β. The results are listed in Table 3. We find that the natural frequencies decrease as n increases.

Response of Floating Bridges to Moving Loads

In this section, the responses of floating bridges to moving loads are investigated. The moving loads are classified into two types: (a) constant concentrated load; (b) pulsating force. The method of modal analysis is used in our analysis. The dynamic load factors $(DLF)_r$ for any r^{th} mode are derived and the numerical results for max $(DLF)_1$, are calculated in detail.

For convenience of analysis, consider a dimensionless force F(t) moving across the span of the floating bridge at a dimensionless uniform velocity c as shown in Fig. 4, where $F(t) = F'(\tau)L^2/E_oI_o = F_of(t)$ and $c = UT/L$. The modal equation of motion may be written as (6):

Table 1:

The Frequency Constants, λ_r, for a Two-span Floating Bridge

β	order of mode r^{th}	α = 0.0	50.0	100.0	150.0	200.0
0.0	1	4.730	5.602	6.182	6.615	6.960
	2	7.853	8.063	8.275	8.483	8.682
	3	10.996	11.090	11.186	11.282	11.378
0.01	1	4.625	5.445	6.045	6.475	6.813
	2	7.710	7.916	8.093	8.353	8.495
	3	10.749	10.832	10.917	11.002	11.088
0.05	1	4.303	5.074	5.609	6.020	6.355
	2	7.329	7.456	7.592	7.786	7.967
	3	10.121	10.176	10.231	10.288	10.345
0.1	1	4.031	4.729	5.226	5.613	5.931
	2	7.068	7.151	7.242	7.341	7.446
	3	9.691	9.729	9.767	9.807	9.847
0.5	1	3.162	3.642	3,996	4.281	4.521
	2	6.547	6.559	6.572	6.587	6.602
	3	8.667	8.677	8.686	8.696	8.706
1.0	1	2.761	3.162	3.457	3.695	3.921
	2	6.427	6.431	6.435	6.440	6.444
	3	8.344	8.349	8.352	8.357	8.361
5.0	1	1.923	2.195	2.392	2.550	2.684
	2	6.314	6.315	6.315	6.315	6.315
	3	7.970	7.970	7.961	7.970	7.972
10.0	1	1.627	1.857	2.023	2.157	2.269
	2	6.299	6.299	6.300	6.299	6.300
	3	7.916	7.915	7.916	7.916	7.915
50.0	1	1.094	1.248	1.360	1.449	1.525
	2	6.287	6.287	6.287	6.288	6.289
	3	7.867	7.872	7.867	7.867	7.862
100.0	1	0.921	1.050	1.144	1.219	1.283
	2	6.286	6.286	6.287	6.287	6.286
	3	7.826	7.855	7.856	7.863	7.858

Table 2:

The Frequency Constants, λ_r, for a Three-span Floating Bridge.

β	order of mode r^{th}	α = 0.0	50.0	100.0	150.0	200.0
0.0	1	4.730	5.565	6.119	6.528	6.849
	2	7.853	8.138	8.405	8.653	8.884
	3	10.995	11.074	11.156	11.240	11.321
0.1	1	4.040	4.729	5.215	5.593	5.904
	2	6.627	6.811	6.988	7.157	7.320
	3	10.059	10.078	10.098	10.118	10.139
0.5	1	3.144	3.642	3.999	4.284	4.522
	2	5.245	5.367	5.481	5.589	5.692
	3	9.611	9.613	9.615	9.617	9.619
1.0	1	2.728	3.152	3.455	3.696	3.898
	2	4.585	4.689	4.786	4.878	4.965
	3	9.523	9.524	9.525	9.526	9.526
5.0	1	1.881	2.170	2.376	2.539	2.675
	2	3.188	3.259	3.326	3.389	3.449
	3	9.446	9.445	9.446	9.446	9.446
10.0	1	1.588	1.833	2.006	2.143	2.259
	2	2.695	2.755	2.812	2.866	2.916
	3	9.436	9.436	9.436	9.435	9.435
50.0	1	1.066	1.229	1.346	1.438	1.516
	2	1.811	1.851	1.889	1.925	1.959
	3	9.438	9.422	9.400	9.438	9.419
100.0	1	0.897	1.035	1.133	1.210	1.275
	2	1.524	1.558	1.590	1.620	1.648
	3	9.508	9.370	9.387	9.520	9.348

Table 3: λ_1^2 for α = 10

n \ β	0.05	0.10	0.50	1.00	10.00
2	18.8466	17.6703	10.7160	8.1481	2,8261
3	18.9263	17.5948	10.6416	8.0013	2,7107
4	18.7916	17.4534	10.3839	7.7269	2.5942
5	18.5991	17.3121	10.0948	7.4925	2.4898
6	18.3854	17.0881	9.8123	7.2504	2.3962
7	18.1651	16.9163	9.5480	7.0393	2.3179
8	17.9452	16.6445	9.3045	6,8292	2.2399

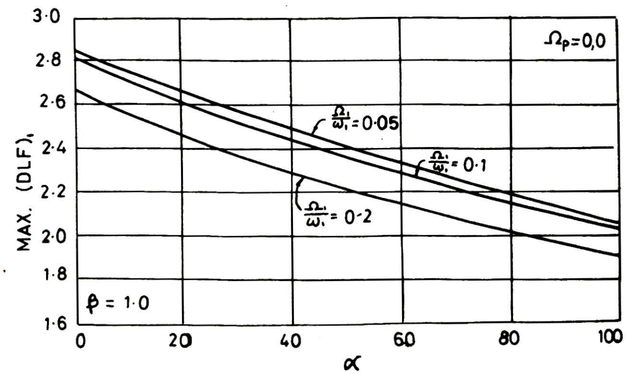

FIG. 5. MAX. (DLF), OF A SINGLE SPAN BRIDGE UNDER A CONSTANT VELOCITY WITH UNIFORM VELOCITY.

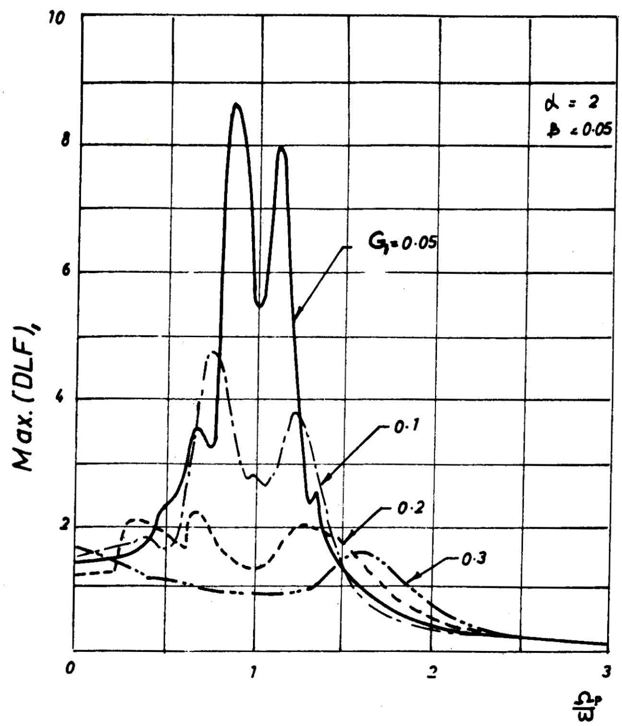

FIG. 3 Max. (DLF)$_1$ of a two-span bridge under a pulsating force moving with uniform velocity.

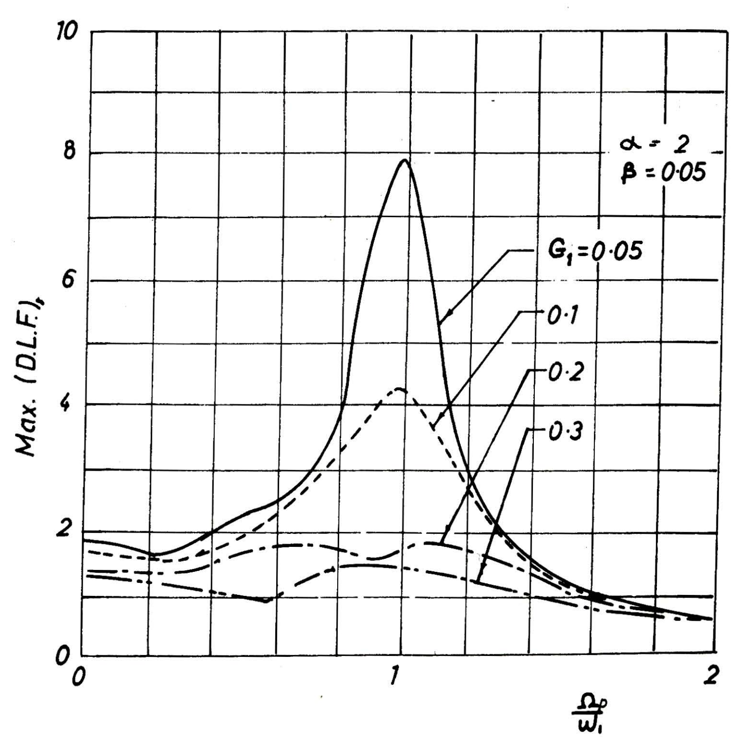

FIG. 4 Max. (DLF)$_1$ of a three - span bridge under a pulsating force moving with uniform velocity.

$$\ddot{A}_r + \omega_r^2 A_r = F_o f(t)\phi_{rj}(ct)/\left[\sum_{j=1}^{n}\int_o^{l_j} \gamma_j(\phi_{rj}(x))^2 dx\right] \tag{18}$$

where $A_r(t)$ is the modal amplitude and $\cdot$ indicates d/dt.
The modal-shape function, ϕ_{rj}, may be expressed as

$$\phi_{rj}(x)=H_{1j}\cos\lambda_r x + H_{2j}\sin\lambda_r x + H_{3j}\cosh\lambda_r x + H_{4j}\sinh\lambda_r x \tag{19}$$

with

$$H_{1j}=\tfrac{1}{2}(-y)^L_{j-1}-\frac{1}{2\lambda_r^2(ei)_j}(n)^L_{j-1}$$

$$H_{2j}=\frac{(ei\beta\lambda_r^4-\alpha)_{j-1}}{2\lambda_r^3(ei)_j}(-y)^L_{j-1}+\frac{1}{2\lambda_r}(\psi)^L_{j-1}-\frac{1}{2\lambda_r^3(ei)_j}(q)^L_{j-1} \tag{20}$$

$$H_{3j}=\tfrac{1}{2}(-y)^L_{j-1}+\frac{1}{2\lambda_r^2(ei)_j}(m)^L_{j-1}$$

$$H_{4j}=\frac{(ei\beta\lambda_r^4-\alpha)_{j-1}(-y)^L_{j-1}}{2\lambda_r^3(ei)_j}+\frac{1}{2\lambda_r}(\psi)^L_{j-1}-\frac{1}{2\lambda_r^3(ei)_j}(q)^L_{j-1}$$

As each span of the bridge is uniform,

$$I_{rj}=\int_o^{l_j}\gamma_j\phi_{rj}^2(x)dx$$

$$=\frac{\gamma_j}{4\lambda_r}(W_{1j}+W_{2j}+W_{3j}+W_{4j}+W_{5j}+W_{6j}+W_{7j}+W_{8j}+W_{9j}+W_{10j}) \tag{21}$$

with

$W_{1j} = H_{1j}^2(V_1+2\lambda_r l_j)$, $\quad W_{2j} = H_{2j}^2(2\lambda_r l_j - V_1)$

$W_{3j} = H_{3j}^2(V_3+2\lambda_r l_j)$, $\quad W_{4j} = H_{4j}^2(2\lambda_r l_j - V_3)$

$W_{5j} = 2H_{1j}H_{2j}(V_2-1)$, $\quad W_{6j} = 2H_{3j}H_{4j}(V_4-1)$

$W_{7j} = 4H_{2j}H_{3j}(V_5V_7-V_6V_8+1)$

$W_{8j} = 4H_{1j}H_{4j}(V_6V_8+V_5V_7-1)$

$W_{9j} = 4H_{1j}H_{3j}(V_6V_7+V_5V_8)$

$W_{10j}= 4H_{2j}H_{4j}(V_5V_8-V_6V_7)$

where $V_1=\sin 2\lambda_r l_j$, $V_2=\cos 2\lambda_r l_j$, $V_3=\sinh 2\lambda_r l_j$, $V_4=\cosh 2\lambda_r l_j$

$V_5=\sin\lambda_r l_j$, $V_6=\cos\lambda_r l_j$, $V_7=\sinh\lambda_r l_j$, $V_8=\cosh\lambda_r l_j$

The modal solution of Eq. (18) may be written as

$$A_r(t) = A_{rst}(DLF)_r \tag{21}$$

where A_{rst} is the deflection under the static load F_o and maybe expressed as

$$A_{rst} = F_o/\omega_r^2\left(\sum_{j=1}^{n} I_{rj}\right) \tag{22}$$

and $(DLF)_r$ is the dynamic load factor of the r^{th} mode. $(DLF)_r$ can be calculated by the integral,

$$(DLF)_r = \omega_r \int_0^t f(t')\phi_{rj}(ct')\sin\omega_r(t-t')dt'$$
$$\text{or } = \tfrac{1}{2}(R_{1r}+R_{2r}+R_{3r}+R_{4r}) \tag{23}$$

where R_{1r}, R_{2r}, R_{3r} and R_{4r} for two cases are derived and listed as follows:
Case (a), constant load described with $f(t)=1$:

$$\begin{aligned}
R_{1r} &= \frac{2H_{1r}}{1-G_r^2}(\cos\Omega_r t - \cos\omega_r t)\\
R_{2r} &= \frac{2H_{2r}}{1-G_r^2}(\sin\Omega_r t - G_r\sin\omega_r t)\\
R_{3r} &= \frac{2H_{3r}}{1+G_r^2}(\cosh\Omega_r t - \cos\omega_r t)\\
R_{4r} &= \frac{2H_{4r}}{1+G_r^2}(\sinh\Omega_r t - G_r\sin\omega_r t)
\end{aligned} \tag{24}$$

with $G_r = \Omega_r/\omega_r$ and $\Omega_r = \lambda_r c$

Case (b), pulsating load described with $f(t) = \cos\Omega_p t$:

$$\begin{aligned}
R_{1r} &= H_{1r}\ \frac{1}{1-K_r^2}(\cos K_r\omega_r t - \cos\omega_r t) + \frac{1}{1-N_r^2}(\cos N_r\omega_r t - \cos\omega_r t)\\
R_{2r} &= H_{3r}\ \frac{1}{1-K_r^2}(\sin K_r\omega_r t - K_r\sin\omega_r t) + \frac{1}{1-N_r^2}(\sin N_r\omega_r t - N_r\sin\omega_r t)\\
R_{3r} &= H_{3r}\ \frac{1}{1+P_r^2}(\cosh P_r\omega_r t) + \frac{1}{1+Q_r^2}(\cosh Q_r\omega_r t - \cos\omega_r t)\\
R_{4r} &= H_{4r}\ \frac{1}{1+P_r^2}(\sinh P_r\omega_r t - P_r\sin\omega_r t) - \frac{1}{1+Q_r^2}(\sinh Q_r\omega_r t - Q_r\sin\omega_r t)
\end{aligned} \tag{25}$$

with $K_r = (\Omega_p/\omega_r) + G_r$, $N_r = (\Omega_p/\omega_r) - G_r$,

$P_r = \sqrt{-1}\,(\Omega_p/\omega_r) + G_r$, $Q_r = \sqrt{-1}\,(\Omega_p/\omega_r) - G_r$

Thus the deflection at any span for any case can be written as:

$$y_j(x,t) = \sum_{r=1}^{n} \frac{F_o}{\omega_r^2 \sum_{j=1}^{n} I_{rj}} (DLF)_r \phi_{rj}(x) \tag{26}$$

For the engineering applications, the $\max(DLF)_1$ is the most important. The time t_{rmax} when the $\max(DLF)_r$ occurs can be obtained by the equation

$$\frac{d}{dt}(DLF)_r = 0 \tag{27}$$

Then the $\max(DLF)_r$ is given by

$$\max(DLF)_r = g(G_r, \Omega_p/\omega_r, t_{rmax}) \tag{28}$$

The results for some cases are shown in Fig. (2)~(5).

Conclusion

The natural frequencies of floating bridge are affected by three parameters α, β, and n. When a constant force moves with uniform velocity the max $(DLF)_1$ is found to be generally decreasing as α increase when β and the velocity of load are kept constant. Also, the max$(DLF)_1$ is found to be increasing when the velocity becomes slower. When a pulsating force moves with uniform velocity, the max$(DLF)_1$ is found to be increasing when n is decreased and decreasing when the velocity is increased. For the case, $\alpha = 2$, $\beta = 0.05$, $\Omega_1/\omega_1 = 0.05$, $\Omega p/\omega_1 = 0.875$, the max$(DLF)_1$ reaches up to 8.7.

We believe that our approach can be applied to analyse the responses of a floating bridge with any number of spans to dynamic loads.

Perhaps the effect of damping of bridge and the effect of added masses and rotatory inertias of floating supports also play important roles. The analysis including these effects should be performed in further investigation.

BIBLIOGRAPHY

1. S.P. Timoshenko, "On the Forced Vibration of Bridges" Phil. Magazine, vol. 43(1922), p. 1018.
2. Sir C.E. Inglis, "A Mathematical Treatise on Vibrations in Railway Bridges", Camb. Univ. Press, (1934).
3. R.S. Ayre, G. Ford & L.S. Jacobson, "Transverse Vibration of a Two-span Beam Under Action of a Moving constant Force", J. Appl. Mech., vol. 27 (1950), p.1.
4. R.S. Ayre & L.S. Jacobson, "Transverse Vibration of a Two-span Beam under the Action of a Moving Alternating Force", J. Appl. Mech. vol. 27 (1950), p. 283.
5. E.G. Pestel & F.A. Leckie, "Matrix Method in Elastomechanics" McGraw-Hill Book Comp., N.Y. (1963).
6. J.M. Biggs, "Introduction to Structural Dynamics, "McGraw Hill Book Comp. N.Y. (1964).

EXPERIMENTAL STUDY OF NOISE FROM A PULSED JET

R. J. Hooker
Department of Mechanical Engineering
University of Queensland
St. Lucia, Queensland

R. H. Rumble
Department of Mechanical Engineering
University of Queensland
St. Lucia, Queensland

M. H. Andrews
Department of Mechanical Engineering
University of Queensland
St. Lucia, Queensland

SUMMARY - Many gas-powered devices operate in such a way that the exhaust is a non-steady jet. This operation has been simulated by a simple pulse jet generator in which a rotating valve interrupts a flow of air. The valve porting was chosen to produce an exhaust cycle similar to that of the pneumatic impact drill and the noise produced by the generator is similar to that of a drill exhaust.

The noise field around the pulsed jet has been measured in free field conditions. Results are presented showing sound levels, spectra, and directivity patterns for a range of supply pressures.

INTRODUCTION

In many gas-powered devices the working fluid is released periodically producing an intermittent or pulsed exhaust. Internal combustion engines are an obvious example but the situation applies to a wide range of equipment, e.g. air motors, pneumatic impact tools and control valves in automated production machines. In most cases the gas is released suddenly from a pressure well above ambient and excessive noise is produced. Although extensive theoretical and experimental studies have been made of the noise from steady jets it appears that little attention has been given to pulsed jets other than through engine exhaust investigations. An understanding of the nature of noise production in a pulsed jet or at least a knowledge of the effect of important parameters is desirable as a basis for design of exhaust silencing schemes.

The work reported here formed part of a project concerned with reduction of pneumatic rock drill noise. Initial test results agreed with the findings of Beiers (1) that the exhaust is the major noise contributor in these machines - suppressing the exhaust noise by fitting a long exhaust hose produces a 10 dB reduction in sound pressure level (Figure 1). Nevertheless, detailed analysis of exhaust noise on an actual drill is subject to interference from other noise sources such as piston impact and control valve operation. These and all other periodic processes in the drill occur at either the same frequency as the exhaust pulses or at a harmonic or sub-harmonic of that frequency. Changing the drill operating conditions to vary exhaust parameters also varies the contribution of the other "background" sources, thus making interpretation of experimental results uncertain. To simplify the study of exhaust noise an exhaust simulator free of extraneous noise sources was built.

EXHAUST SIMULATOR

The simulated exhaust is produced by periodically releasing high pressure air through a rotary valve (Figure 2). The cylindrical valve spindle is belt-driven from a variable speed motor giving a pulse frequency range of 0 to 120 Hz. The inlet and outlet ports are circular, 19 mm dia., and the transfer passage through the spindle is 19 mm square in cross-section. Air is supplied from a 600 kPa line via a 25 mm industrial pressure regulator and 5 m of 19 mm bore flexible nylon-reinforced P.V.C. tubing. A strain gauge type pressure transducer is fitted in an adaptor immediately upstream of the valve. Care was taken in the design and manufacture of adaptor and fittings to ensure smooth flow to the valve.

The opening phase of the simulator cycle is similar to the exhaust process in a drill; air is suddenly released and the pressure upstream of the valve falls (Figure 3a). However, in its closing phase the simulator action differs from the drill exhaust. In the drill, the exhaust port remains open and the air supply is cut off. In the simulator, the valve closes and the air

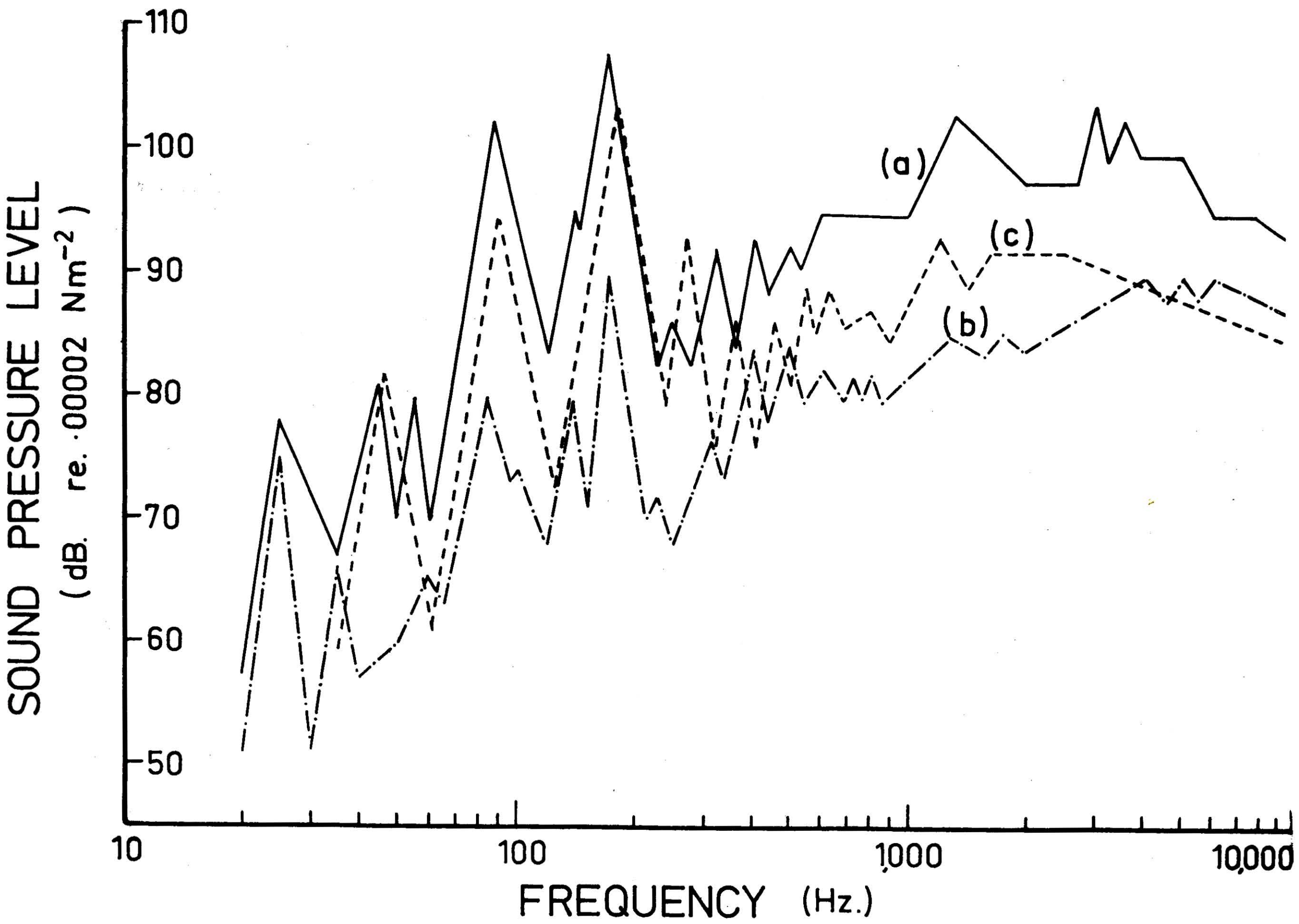

Figure 1. Comparison of Spectra

(a) Unsilenced rock drill.
(b) Rock drill fitted with exhaust hose.
(c) Simulator.

supply is maintained. It is possible to reproduce the drill pressure changes more closely by using two valve in series but this was considered unnecessary in a first investigation.

In operation the simulator sounds like a rock drill running without impact. This subjective assessment is supported by comparison of spectra (Figure 1). It is also apparent subjectively that sound level is dependent on air supply pressure and detailed examination of this dependence was made.

EXPERIMENTAL INVESTIGATION

Overall sound pressure levels, narrow band (6%) spectra and directivity patterns were determined at pulse frequency 100 Hz for 12 supply pressures in the range 35 to 500 kPa. The measurements were made in an anechoic chamber with working enclosure 3.2 m x 2.2 m x 2.4 m and lower limiting ("cut-off") frequency 135 Hz. To obtain directivity patterns, 77 microphone positions were used, all in the horizontal plane containing the jet axis. Simulator and microphone were mounted on vibration isolators.

In order to assess possible interference by upstream noise generation, e.g. from the regulator, provision was made for fitting a silencer before the valve. The silencer used was an absorption lined expansion chamber, details of which are shown in Figure 2. The silencer could be replaced by an equal length of 19 mm bore straight pipe.

The air pressure values quoted in the results are the values measured at the supply point to the 5 m flexible hose. During the "closed" portion of the valve cycle the pressure at valve entry recovered to supply pressure, except possibly for the lowest pressure (35 kPa). The values given can therefore be taken as the pressure immediately upstream of the valve at the point of

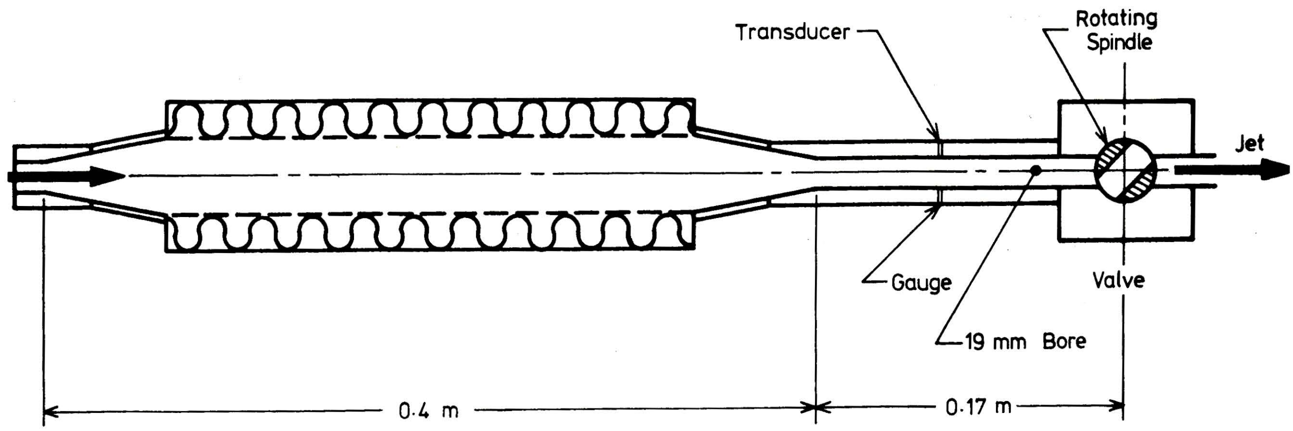

Figure 2. Diagrammatic Arrangement

valve opening. Mass flow is approximately linear with pressure and is 0.011 kg sec^{-1} per 100 kPa.

General Character of Pulsed Jet Noise

Typical spectra for the pulsed jet are shown in Figure 4 and a spectrum for a steady jet (simulator not rotating) is included also. The noise produced by the pulsed jet shows two distinctive characteristics. At low frequencies the noise is composed of discrete tones at the pulse frequency and its harmonics, up to about the tenth. At high frequencies (2000 to 20000 Hz) there is broad-band noise similar to that of a steady jet. The low frequency components (fundamental and second order) and the high frequency noise have approximately equal sound pressure levels but on A scale weighting the high frequency noise is more significant.

The upstream pipe configuration (silencer or straight pipe) had almost no effect on overall, 100 Hz, 200 Hz and high frequency level (Table I and Figure 4). The pressure waveform at valve inlet, however, was changed markedly due to reflections of the pulses caused by valve opening and closing. With the silencer fitted, pressure oscillations in the frequency range 300 - 800 Hz occurred (Figure 3(b)) and sound levels in this range were affected. There is some evidence of correlation between pressure waveform components and SPL components.

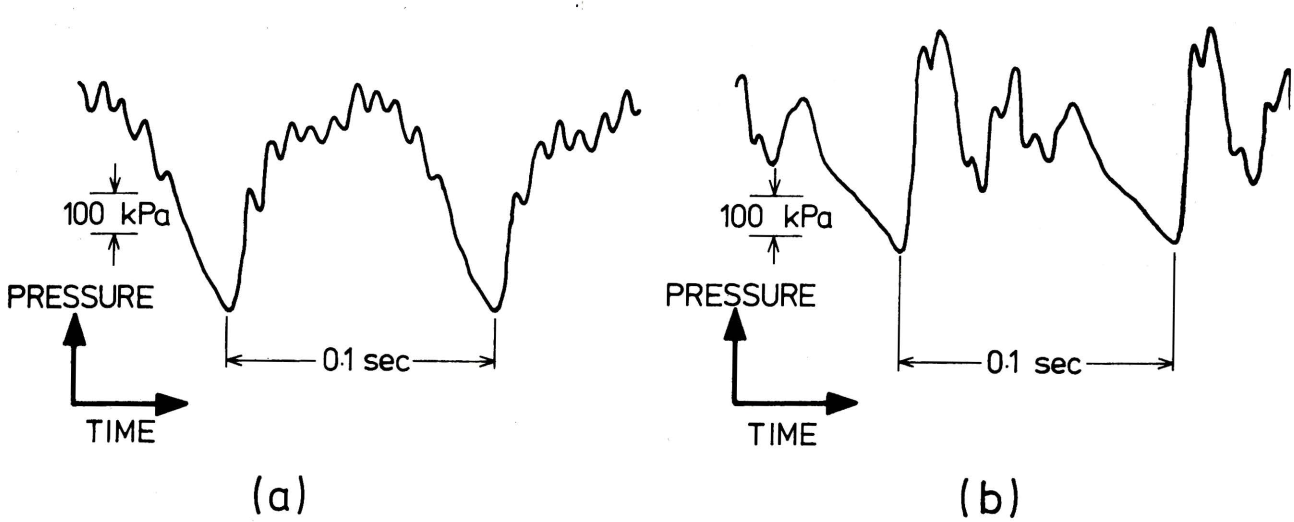

Figure 3. Pressure Traces. (410 kPa)

(a) Without silencer.
(b) With silencer.

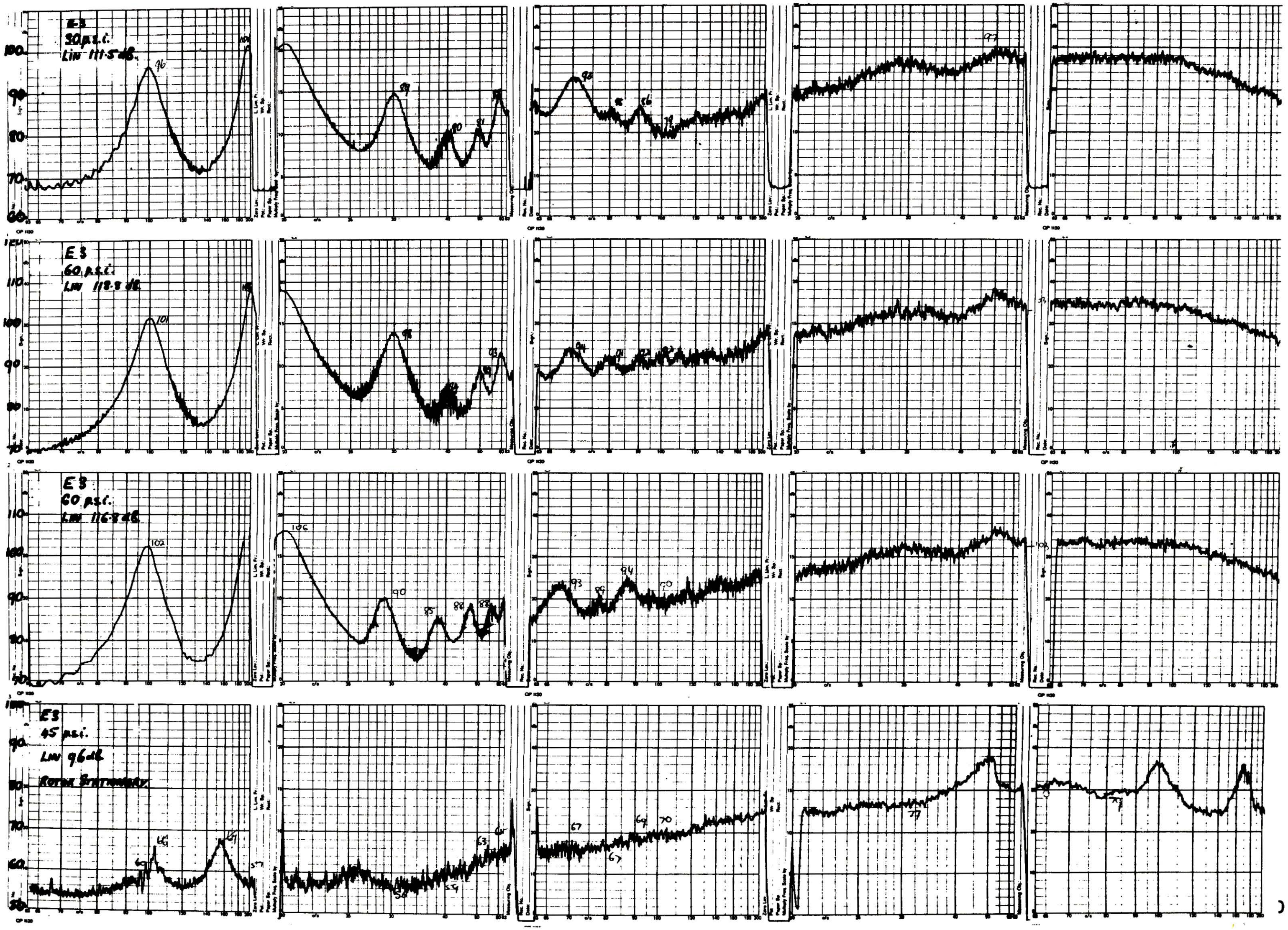

Figure 4. <u>Typical Spectra</u>

(a) upstream silencer fitted, supply pressure 210 kPa
(b) upstream silencer fitted, supply pressure 420 kPa
(c) straight pipe fitted, supply pressure 420 kPa
(d) steady jet (rotar stationery) supply pressure 315 kPa.

TABLE I : MEASURED SOUND PRESSURE LEVELS

In dB re 20 μN m^{-2}
Measuring position E3, Figure 6. 1.6 m from exit, 28° to jet axis
Background 55 dB Linear (valve running, no air flow)

(a) With silencer upstream
(b) Without silencer (equal length of straight pipe)

Air Supply Pressure kPa	SPL							
	Linear		Narrow Band Only (6%)					
			100 Hz		200 Hz		300 Hz	
	(a)	(b)	(a)	(b)	(a)	(b)	(a)	(b)
35	95	91	80	79	86	82	79	69
69	100	98	84	83	92	88	84	70
104	104	101	88	87	95	92	87	72
138	107	104	90	89	97	94	89	73
172	109	106	92	91	100	97	90	75
207	111	108	94	93	101	98	92	77
242	112	110	95	94	102	100	93	81
276	112	112	97	95	103	101	95	83
310	115	114	98	97	105	103	96	87
345	116	115	99	98	105	104	97	88
380	117	116	100	100	106	105	99	90
414	118	117	101	102	108	106	100	90

Effect of Supply Pressure

Variation in SPL with air supply pressure is shown in Figure 5. The overall level falls with decreasing pressure, following a straight line relation down to about 125 kPa. This pressure corresponds to a pressure ration ambient/supply of 0.45, which is approaching the critical pressure ratio. Figure 5 also shows the variation of low frequency components (100, 200 and 300 Hz) with pressure. Again an approximate straight line relation exists down to 125 kPa but the behaviour becomes more irregular with the higher harmonics. The broad-band noise shows much the same spectral shape for all supply pressures and a "representative" level was assessed by eye for the range 3000 to 10000 kHz. The variation with pressure (Figure 5) was similar to that of the low frequency components. Hence all significant noise components show a trend of 3 dB reduction for 75 kPa reduction in supply pressure down to 125 kPa.

Directivity Patterns

The distribution of overall SPL around the jet was determined for the 12 supply pressures. For one supply pressure (310 kPa) spectra were taken at all measuring positions and the distribution determined for all frequency components.

The overall SPL directivity patterns for the various supply pressures are shown in Figure 6. At low pressures radiation is essentially spherical, a monopole source characteristic. As supply pressure is increased there is a gradual change to a lobed pattern typical of steady jet noise. Directivity patterns for the various frequency components at supply pressure 310 kPa are given in Figure 7. At low frequencies radiation is spherical gradually changing to the lobed shape as frequency is increased. Thus, at low supply pressures and low frequencies the pulsed jet acts as a simple source. At high supply pressures and high frequencies the directivity behaviour is similar to that of steady jet noise.

CONCLUSION

The noise produced by a pulsed jet is composed of high frequency broad-band noise and low frequency discrete tones at the pulse frequency and its harmonics. Measured sound pressure levels of the broad-band noise and the low harmonics are approximately equal. The high frequency is therefore more significant on an A-scale weighted basis.

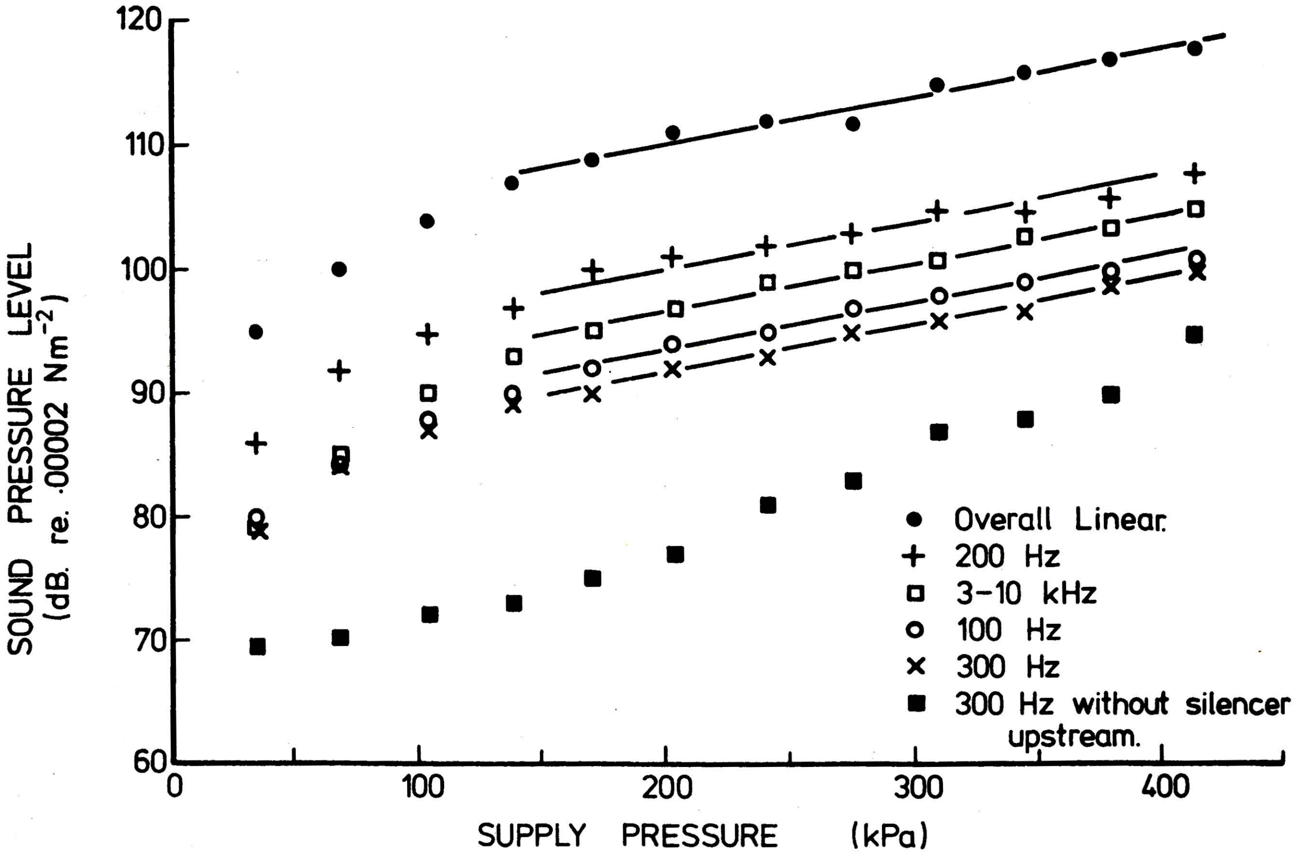

Figure 5. Effect of Air Supply Pressure.
With silencer upstream except as shown.
Full lines are at 3 dB per 75 kPa.

All sound levels - overall, low frequency and high frequency - are dependent on supply pressure. Over the pressure range 125 to 400 kPa, sound level decreases about 3 dB for a 75 kPa reduction of supply pressure. Directivity patterns show point source behaviour for low frequency tones and low supply pressures, gradually changing to a lobed pattern at high frequencies and pressures.

To minimise noise production from a pulsed jet the lowest possible pressure at point of exhaust is required. Further reduction would require attenuation of high frequencies first and then the fundamental and low order pulse frequencies.

ACKNOWLEDGEMENT

This project was carried out in part under the sponsorship of the Australian Mineral Industries Research Association, Incorporated, and grateful acknowledgement is extended to the Association for its support and for permission to publish this paper.

REFERENCE

1. BEIERS, J.L. A Study of Noise Sources in Pneumatic Rock Drills. *Jour. Sound and Vibration,* Vol. 3, 1966, pp. 166-94.

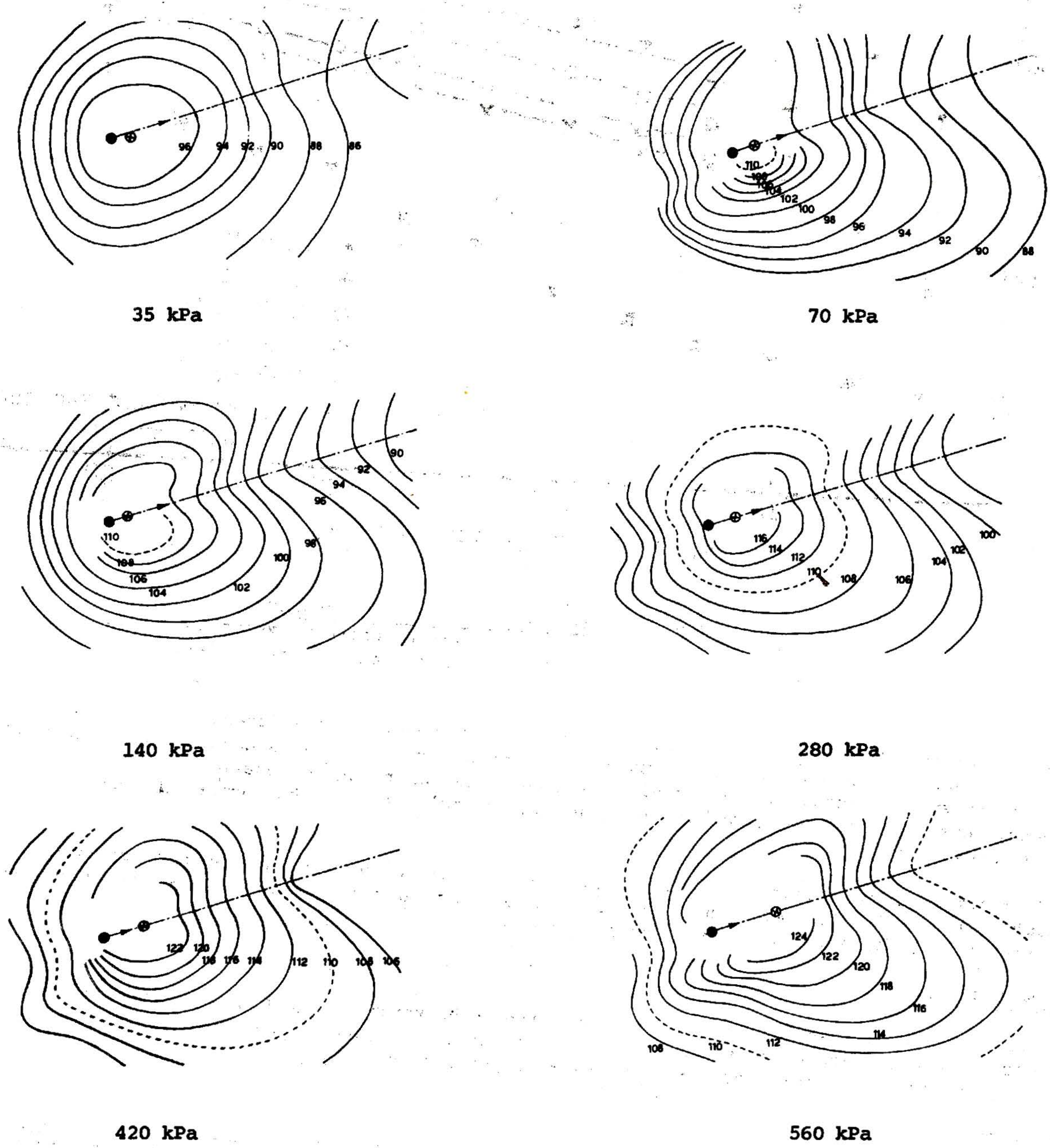

Figure 6. <u>Directivity Patterns for Various Supply Pressures</u>

Sound Pressure levels marked on contours (dB lin.)

●→ position of actual source

⊗ position of virtual source.

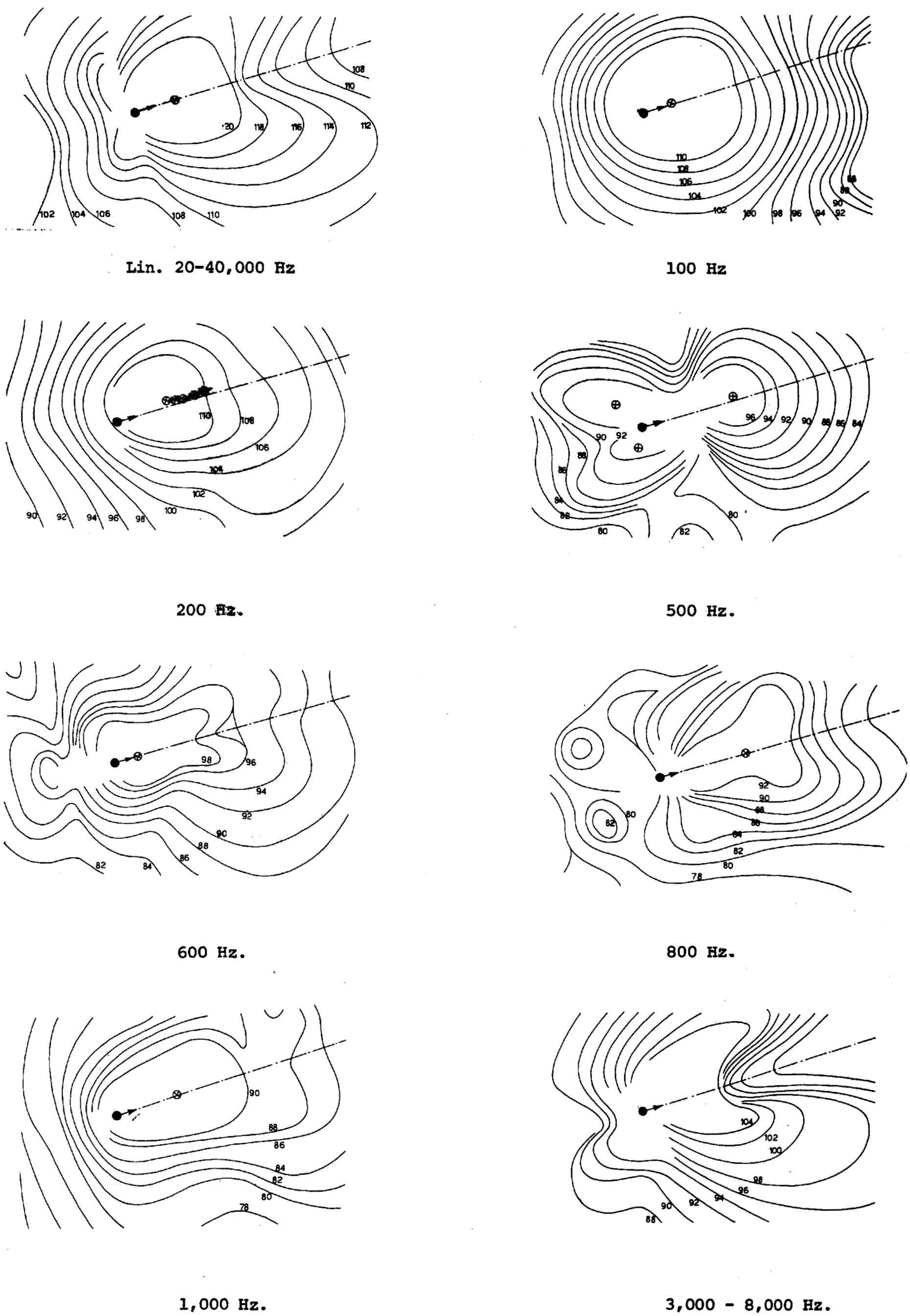

Figure 7. <u>Narrow-Band Directivity Patterns at Supply Pressure 310 kPa</u>

ON THE CORRELATION TECHNIQUE IN THE SUBSONIC JET

N. W. M. Ko
Department of Mechanical Engineering
University of Hong Kong
Hong Kong

SUMMARY

Using the technique of digital cross-spectral analysis and the fast Fourier transform, measurements of both the covariance and correlation coefficient inside circular subsonic jets have been obtained. Detailed comparison shows the effect of varying turbulence intensity and the interference of the upstream hot wire wake on the correlation coefficient. Thus, it indicates the advantage in obtaining the covariance.

The highly correlated field indicated by the covariance measurements substantiates the work reported by the author and other workers. The field bore some relationship to the noise sources within the noise producing region of the jet.

INTRODUCTION

In understanding the statistical properties of the velocity of pressure fluctuations of subsonic jet, correlation technique is important. The velocity correlation coefficient measurements in the mixing region (1, 2, 3) and in the potential cone (4, 5) were aiming at this goal. The longitudinal cross correlation coefficients obtained inside the mixing region (2, 3) establish the non-frozen pattern of turbulence in the mixing region. These measurements further yield the fact that the eddies inside the high turbulent region are convecting downstream. This velocity of convection of the eddies varies with positions and not necessarily be the same as the local mean velocity. The above authors also observed that different frequency components convect downstream at different velocities. The radial and longitudinal cross correlation measurements inside the potential cone (4, 5) indicate a highly correlated field inside the cone. This field is found to be related to the noise source in the mixing region. Further indication from the correlation measurements suggests that the noise sources may be due to vortices which are situated in the mixing region. The exact location of the vortices has not been determined.

Nearly all the correlation measurements presented by different workers were correlation coefficients. In the mixing region, the turbulence intensity level was nearly constant with spatial distance in the axial position. In this respect, the longitudinal correlation coefficient was almost equivalent to the covariance or the actual relationship between the signals investigated. However, for the radial correlation coefficient, the equivalence was not true because of the large radial variation in the turbulence intensity.

In the potential cone, though the mean velocity is uniform, the fluctuating components vary with the axial and radial positions. By the same argument equivalence between the coefficient and covariance is also not necessarily true. Thus, it is highly desirable to consider the covariance for exact information.

The other factor which may affect the interpretation of the coefficient is the effect of upstream hot wire wake on the downstream wire (6). The higher turbulence intensity sensed by the downstream wire can even/be recorded at 9 x 10^3 wire diameter downstream. Using a wire diameter of 5 μm, the distance involved can be as high as 4.5 cm. This effect is more severe when the local turbulence intensity is low in compared with the wake intensity, such as in the potential cone. In the mixing region the local intensity is high, the wake effect may not be noticeable. In this respect the consideration of covariance may eliminate the uncertainty due to this effect.

With the above limitations in mind, attempts were made by the author in obtaining the covariance inside the potential cone (7). Unfortunately, the available analogue correlators, using analog stores, were not suitable in determining accurately a small correlated signal within a large masking or uncorrelated signal. It is due to the fact that the correlator has a maximum limit in its input and the small correlated output signal, was in the range of the electronic noise and the drift of the correlator. Accurate results could not be obtained.

With the advent of the fast and efficient digital computer calculation of two-point correlations (8, 9) the present study of the correlation covariance technique is feasible. The study was undertaken to determine the correlation covariance or function inside the jet. Direct comparison between the covariance and coefficient was attempted to establish the importance of the covariance measurements. From the covariance measurements, establishment of a regular field inside the potential cone and the mixing region was attempted.

DEFINITION

The cross covariance involves the correlation of signals from two spatially separated positions. One signal is delayed by a time τ. If $u_1(r,t)$ denotes the signal received at one position at time t and $u_2(r + \Delta r,t + \tau)$ denotes the signal received at another position distance Δr from the first and at time $t + \tau$, their cross covariance, $C_{r\tau}$, may be defined as

$$C_{r\tau} = \lim_{T\to\infty} \frac{1}{T} \int_0^T u_1(r;t)\, u_2(r + \Delta r;t + \tau)dt. \tag{1}$$

The cross correlation coefficient is the normalised covariance and may be defined as

$$R_{r\tau} = \lim_{T\to\infty} \frac{1}{T} \int_0^T \frac{u_1(r;t)\, u_2(r + \Delta r;t + \tau)}{(\overline{u_1^2(r;t)})^{\frac{1}{2}}\ (\overline{u_2^2(r + \Delta r;t + \tau)})^{\frac{1}{2}}}\, dt\ , \tag{2}$$

where the over-bar indicates averaging over a period of time sufficiently long to obtain stationary values.

For the axial components of the signals of two hot wires separated in the axial direction, that is, $u_x(o,o,o;t)$ and $u_x(\Delta x,o,o;t + \tau)$, $C_{x\tau}$ and $R_{x\tau}$ represent the longitudinal cross covariance and coefficient respectively. For the axial components separated in the radial direction, that is, $u_x(o,o,o;t)$ and $u_x(o, \Delta y,o;t + \tau)$, $C_{y\tau}$ and $R_{y\tau}$ represent the radial cross covariance and coefficient respectively. It has to be remembered that the coefficient is obtained by dividing the covariance by the two r.m.s. values of the two hot wire signals.

From the definition, although a cross correlation coefficient of unity is usually taken to mean perfect correlation between the two signals considered, and zero is usually taken to mean imperfect correlation, the coefficient does not necessarily given a true picture of the degree of correlation between the signals. By referring to the definition of the coefficient, if the two signals give a constant covariance for different separations, the normalised value of the coefficient does not necessarily yield a constant value for the covariance, because it depends upon the value of $(\overline{u_x^2(r;t)})^{\frac{1}{2}}$ and $(\overline{u_x^2(r + \Delta r;t + \tau)})^{\frac{1}{2}}$. The value of $(\overline{u_x^2(r;t)})^{\frac{1}{2}}$ is fixed as the reference value at a particular position, but the value of $(\overline{u_x^2(r + \Delta r;t + \tau)})^{\frac{1}{2}}$ may vary, depending on the position of the moving wire. If $(\overline{u_x^2(r + \Delta r;t + \tau)})^{\frac{1}{2}}$ increases, even with constant covariance, the coefficient will not have a constant value for different separations. This effect definitely shows up when there is a small correlating signal in a large masking signal. Thus, interpretation of the correlation measurements can be difficult.

COMPUTATION METHOD

With the development of the fast Fourier transform it is more efficient to estimate the cross spectra and then fast Fourier retransform to give the correlation functions. Since the estimation of the cross spectra and the correlation function are standard programmes in the Institute of Sound and Vibration Research, Southampton, a brief outline of the equations envolved is described. Briefly, the discrete Fourier transforms of two discrete time series with unit time spacing and of K sets, $x_k(j)$, $y_k(j)$ are $X_k(f)$ and $Y_k(f)$ respectively, i.e.,

$$X_k(f) = \frac{1}{N} \sum_{j=0}^{N-1} x_k(j) \exp\left(\frac{-i2\pi fj}{N}\right) ,$$

$$Y_k(f) = \frac{1}{N} \sum_{j=0}^{N-1} y_k(j) \exp\left(\frac{-i2\pi fj}{N}\right) ,$$

where $j=0, 1, 2 \ldots, N-1$ and $k = 0, 1, 2 \ldots K-1$. Both equations are for the frequencies $f = 0, 1, 2 \ldots, N-1$. As $X_k(f)$ and $Y_k(f)$ are complex, they can be written in the form

$$X_k(f) = X_{kr}(f) + i\, X_{ki}(f)$$

$$Y_k(f) = Y_{kr}(f) + i\, Y_{ki}(f) .$$

Then the estimate of cross-power spectrum is

$$G_{xy}(f) = \frac{N}{K} \sum_{k=0}^{K-1} X_k(f)\, Y_k{}^*(f).$$

.where the * denotes the complex conjugate.

The retransform into the correlation function is based on the following (9) :

$$R_{xy}(\tau) = \frac{1}{2} \int_0^\infty [G_{xy}(f) + G_{yx}(f)] \cos 2\pi f\tau df + \frac{i}{2} \int_0^\infty [G_{xy}(f) - G_{yx}(f)] \sin 2\pi f\tau df.$$

EXPERIMENTAL ARRANGEMENT

The experiments were carried out within a 5 cm diameter jet. The nozzle which generated the jet, has an area contraction ratio of 9:1. There was a Burgess type silencer after the gate valve and the settling chamber was the core of silencer. The Reynolds number was above a value of 10^5. The mean exit velocity was 70 m/s.

The hot wire anemometer used was a constant temperature type with linearised output (7). The wire itself, having an operating resistance of 15 ohms, had a diameter of 5×10^{-6} m and a length of 2 mm. At the end of the wire were the copper plated portions, which had a diameter of 0.025 mm. The distance between the two supports of the wire was 4 mm.

The analysis of the data was carried out on the I.S.V.R. myriad computer in Southampton. A total of 20,000 samples from each of the two hot wires were acquired simultaneously by an analogue-digital converters at a rate of 20,000 samples/second/channel. After passing through identical high-pass and low-pass filters set to 20 Hz and 10 KHz, they were recorded on-line on the magnetic discs for later processing. This on-line recording into the computer eliminated the inherent error of the magnetic tape recorder. Before the transformation the two signals were deliberately multiplied by a factor of 10 such that the correlated parts of the signals were well above the noise of the computer. The two digitised files were divided into segments, Fourier analysed and ensemble averaged to give the two power spectra and the cross spectra. The spectra were smoothed using a Barlett filter. The frequency resolution was of 78.125 Hz and approximately 620 statistical degrees of freedom. The spectra were then fast Fourier transform to give the cross correlation covariance. The actual time for the analysis and plotting took about 10 min.

RESULTS

The boundaries of the potential cone, the mixing region and the entrainment region are shown in Fig. 1. The inner boundary with the cone, where the uniform nozzle exit mean velocity, $\bar{U}_o$, exists, is defined by the mean velocity ratio $\bar{U}/\bar{U}_o = 0.999$.

The turbulence intensity inside the jet is shown in Fig. 2. It is plotted with the non-dimensional radial distance, $\eta = \frac{y - D/2}{x}$, where D is the diameter of the nozzle. Within the potential cone the intensity varies with both the axial and radial direction, but less than 3% of the mean exit velocity. The variation in intensity is fairly gentle. In the mixing region the turbulence is higher, with a maximum of about 14%. However, at the radial position of maximum intensity y/D = 0.5 the level is more or less constant with axial position. Instead of constant level the radial variation of intensity is very high, from 3% to 14%.

Effect of the variation of turbulence level on the maximum longitudinal cross correlation coefficients, $(R_{x\tau})_{max}$, is shown on Fig. 3. The fixed wire was situated at x/D = 2, y/D = 0.2. The definition of coefficient used here is the quotient of the maximum cross covariance and the standard deviations of the two signals. Depending on the non-zero mean value of the fluctuating components, it is not necessarily equal to the usual definition of coefficient shown in Section 2 (10). The longitudinal cross correlation coefficient curve shown on Fig. 3 decreases as the increase in the turbulence intensity level. This coefficient curve gives quite a different picture from the curve of the maximum cross correlation covariance, $(C_{x\tau})_{max}$, which is also shown. Instead of constant decrease from $\Delta x/D = 0.1$ the maximum cross covariance $(C_{x\tau})_{max}$, increases with axial separation of the two wires. It reaches the highest value at a separation of $\Delta x/D = 1$ and then decreases only slightly. According to the coefficients, the peak is definitely not shown. Even up to the separation of $\Delta x/D = 2.7$, that is, the downstream wire was at x/D = 4.7, and y/D = 0.2, the maximum cross covariance is only marginally lower than the values at smaller separations. This indicates the unreliability of the coefficient measurements and suggests near perfect correlation even at such a large separation.

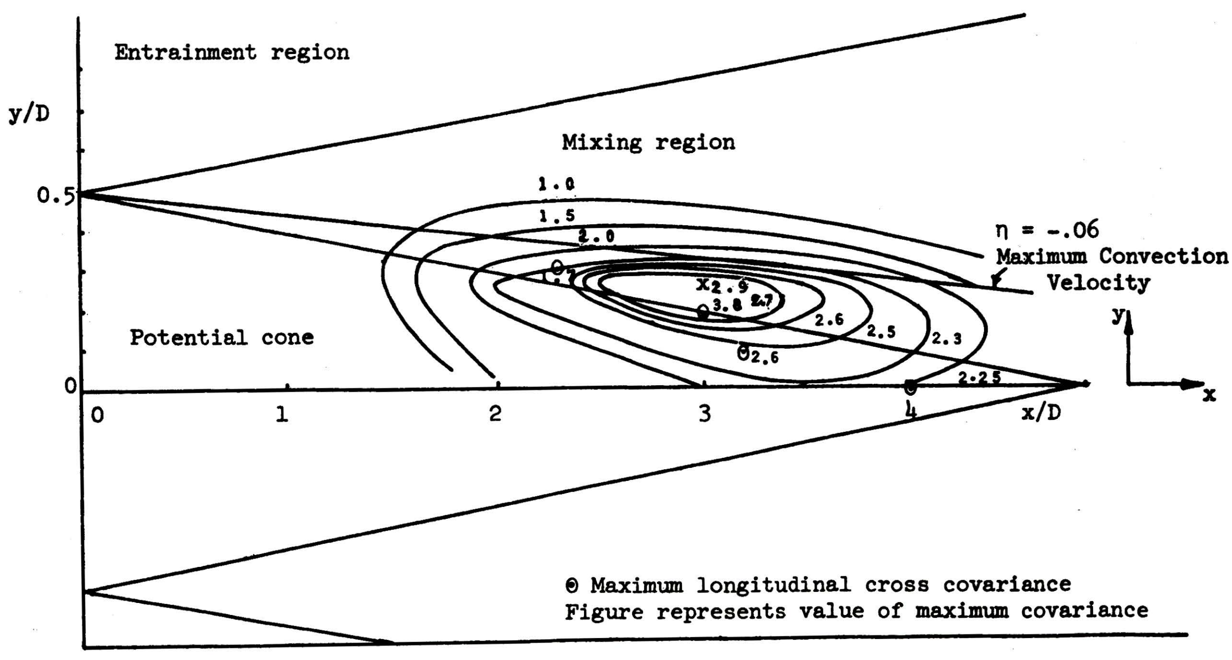

Fig. 1 Profile of Subsonic Circular Jet

Effect of the upstream hot wire wake on the longitudinal cross correlation coefficient can also be seen on Fig. 3. Depending on the position of the downstream wire with respect to the upstream wire, the intensity measured by the former can vary. This effect of the wake is clearly shown at the axial separation of $x/D = 0.1$. Because of this, the correlation coefficient has a very low value of 0.66, while the covariance is only very marginally lower than the values at other separations.

Better example in showing the effect of spatial variation in intensity level on the coefficient can be found in the radial cross correlation measurements of the axial velocity components (Fig. 4). Because of the larger variation in the radial direction, the extent on the coefficient is much more severe. From the maximum radial cross covariance curve, extremely good correlation exists even when the separation is $\Delta y/D = 0.35$. From the coefficient results the degree of correlation is negligible at the same separation.

Similar to the longitudinal cross correlation coefficient measurements, the coefficient results shown on Fig. 4 do not indicate clearly the peak at the separation $\Delta y/D = 0.25$. The significance of this peak will be discussed later.

The above evidence clearly indicates the difficulty in interpretating the coefficient results and emphasise the fact that covariance is the necessary information for correct interpretation. Without this precaution a completely different picture may be obtained.

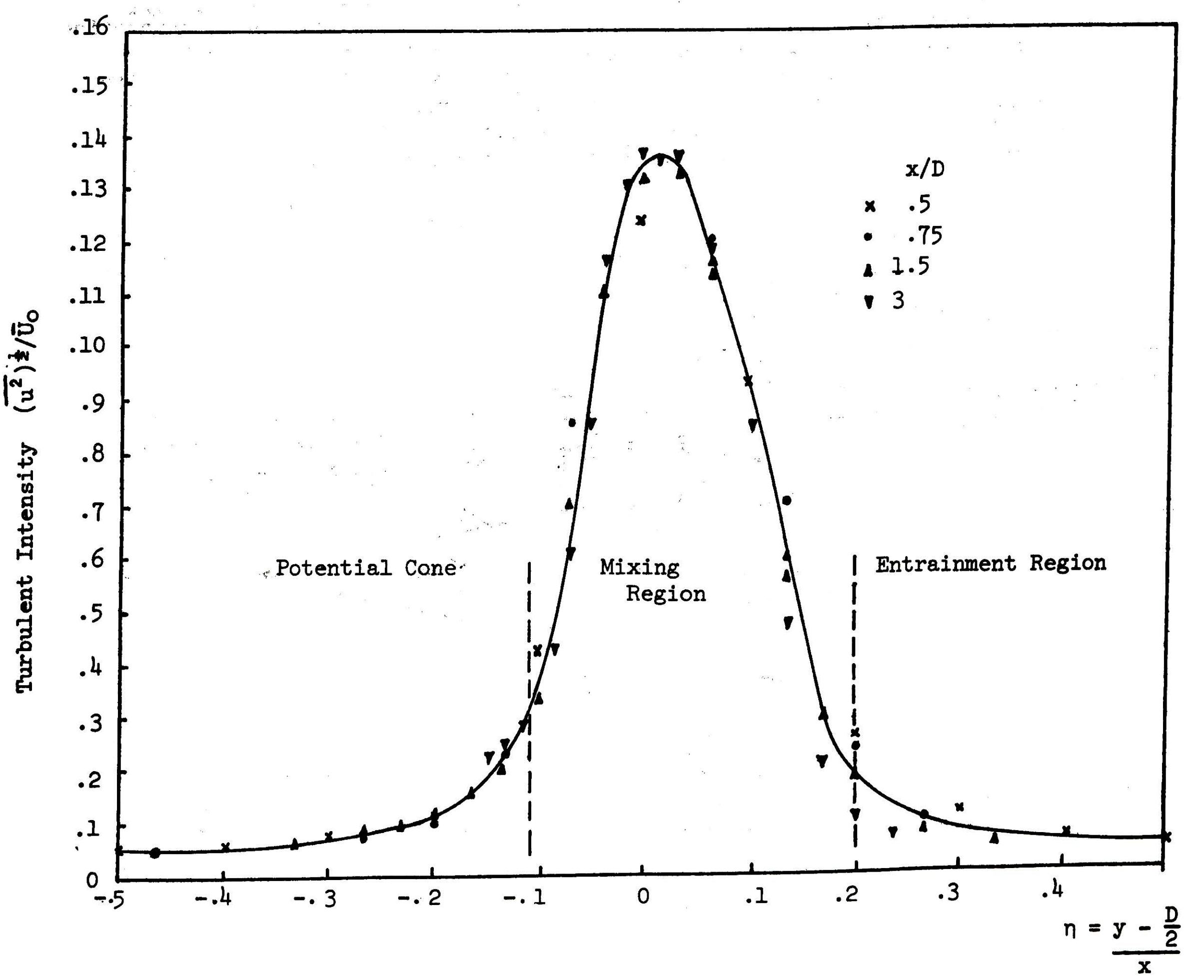

Fig. 2 Radial Distribution of Turbulent Intensity

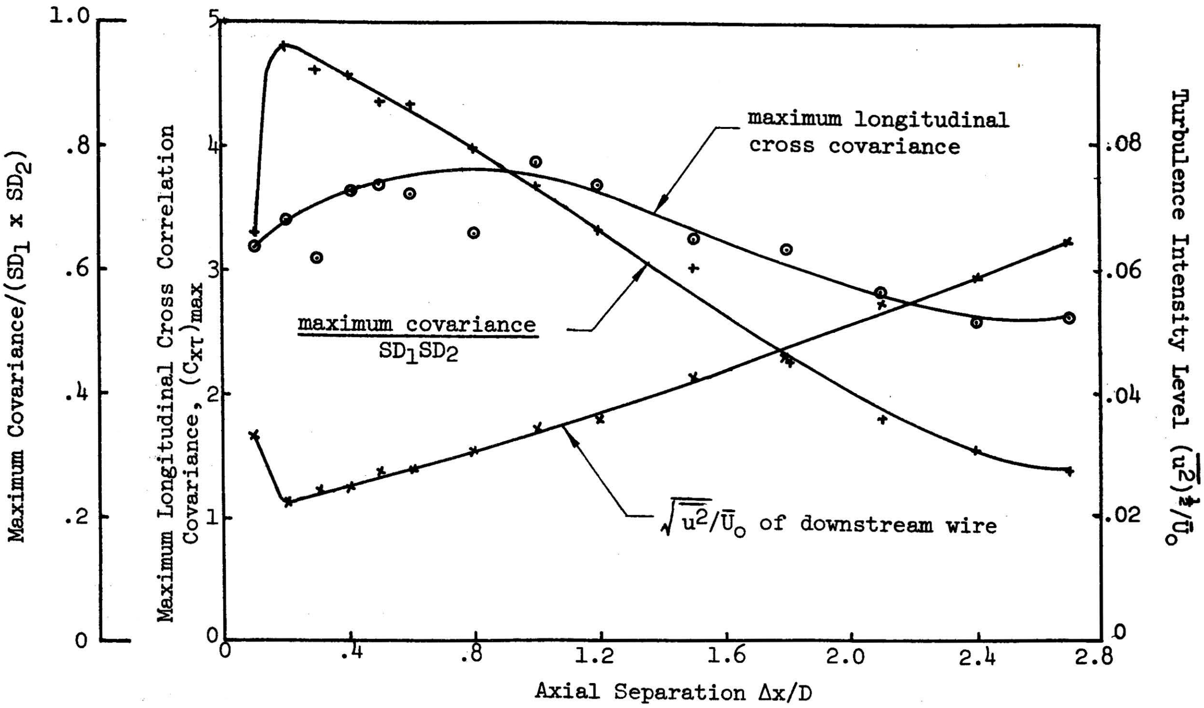

Fig. 3 Variation of Maximum Longitudinal Cross Covariance, Coefficient and Turbulence Intensity Level with Axial Separation.

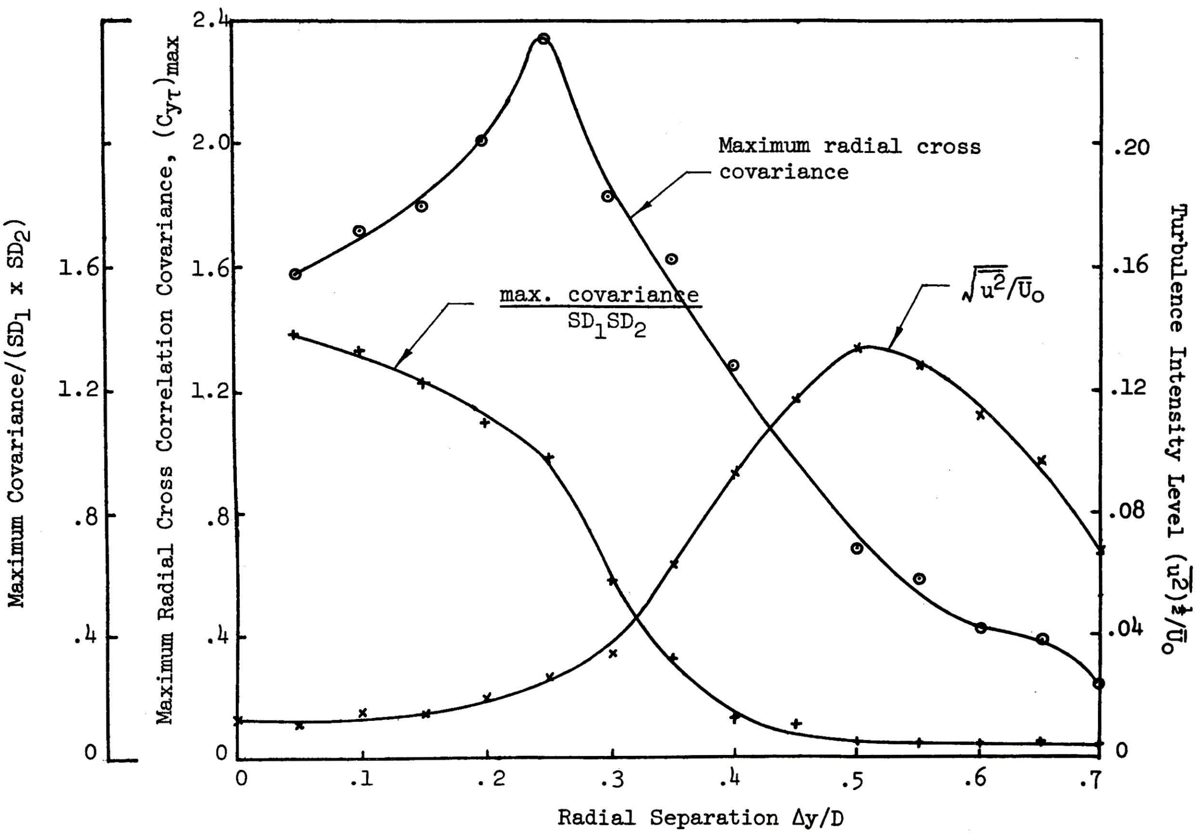

Fig. 4 Variation of Maximum Radial Cross Covariance, Coefficient and Turbulence Intensity Level with Radial Separation.

LONGITUDINAL CROSS CORRELATION COVARIANCE

The maximum longitudinal correlation covariances, $(C_{x\tau})_{max}$, obtained inside the potential cone and mixing region are shown in Fig. 5. The fixed wire was situated at x/D = 2 and different y/D and the moving wire was situated with a radial separation of Δy/D = 0 and different axial separations Δx/D. Fig. 5 is presented in logarithmic form because of the large covariance obtained over small separations inside the mixing region. From the results the covariance can be separated into two distinct regions. The first region is the ones obtained inside or very near the potential cone (y/D ⩽ 0.3) and the second is the ones obtained within the mixing region (0.4 ⩽ y/D ⩽ 0.7). Over the whole potential cone, constant maximum covariance is more or less achieved. In addition, the highest maximum covariance occurs when the wires were at the radial position of y/D = 0.2.

In the first region, y/D ⩽ 0.3, more or less constant maximum covariance is achieved. This constancy occurs not only when the moving wire was in the potential cone, also when it was in the mixing region. This means that a highly correlated field exists in the potential cone and part of the mixing region which is adjacent to it.

Closer look at the three covariance curves within and at the boundary of the boundary cone show peaks on the curves. For y/D = 0, the peak is roughly at Δx/D = 2.0; y/D = 0.1, at Δx/D = 1.2; y/D = 0.2, at Δx/D = 0.8; and y/D = 0.3, at Δx/D = 0.3. The significance of the peaks will be discussed later.

In the second region, 0.4 ⩽ y/D ⩽ 0.7, in the mixing region, the maximum cross covariance decreases very rapidly with axial separation. However, the high correlation at small separations is due to the characteristics of eddies (11, 12). At larger separation, where the correlation of the velocity fluctuations of the eddies is not dominant, the levels of the maximum cross correlation covariance, $(C_{x\tau})_{max}$, are of the same value as the ones observed inside the potential cone. The separation at which this occurs is at Δx/D = 1.2. This means that the same field is responsible for the good correlation inside the jet, except at y/D ⩽ 0.7.

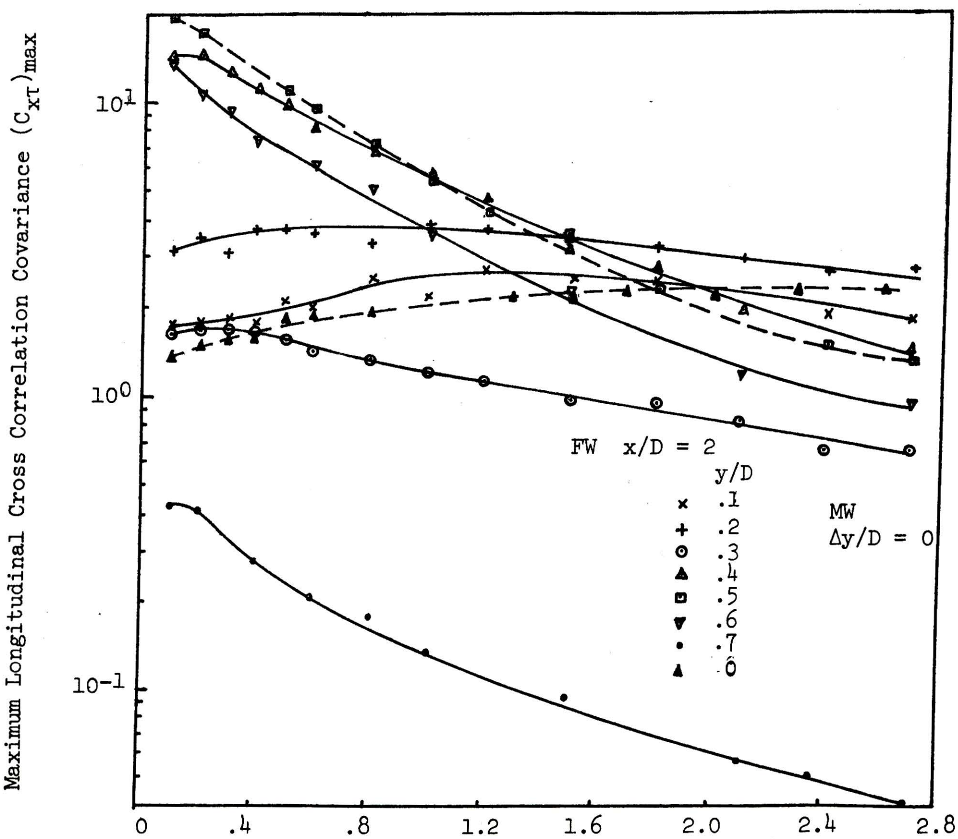

Fig. 5 Maximum Longitudinal Cross Correlation Covariance with Axial Separation

RADIAL CROSS CORRELATION COVARIANCE

The maximum radial cross correlation covariance, $(C_{y\tau})_{max}$, of two single wires are shown on Fig. 6. The fixed wire was situated at x/D = 2, y/D = 0 and the moving wire was at different axial and radial positions. There are peaks on the covariance curves when the wire was at different axial separations. The best correlation occurs when the moving wire was at x/D = 3, y/D = 0.25, then at x/D = 3.5, y/D = 0.2 and x/D = 2.5, y/D ≈ 0.25. The correlation at x/D = 2 is not as good as the last three positions which are further downstream. Generally, Fig. 6 shows good correlation inside the potential cone and the part of mixing region which is near the cone (y/D ⩽ 0.5) and not much correlation for y/D ⩾ 0.5.

By replotting the curves on Fig. 6, the contours of the maximum radial cross correlation covariance are shown on Fig. 1. It has to be remembered that the fixed wire was situated at x/D = 2, y/D = 0 and Fig. 1 shows the correlation of the fluctuations at different positions with respect to this fixed wire. The picture shown on Fig. 1 is extremely interesting. The shapes of the equi-contour lines look like an ellipse and the highest level of covariance occurs between 2.5 ⩽ x/D ⩽ 3.5. The major axis of the ellipse is roughly along the constant η line instead of along constant y/D line.

The peaks of the longitudinal cross correlation covariance curves from Fig. 5 are also shown on Fig. 1. Although the peak covariance levels do not exactly agree with the levels obtained by the radial covariance measurements, they roughly fall into the contours shown. The reason for the difference in levels and positions may be due to the difference in the correlation method. As has been pointed out, the longitudinal measurements were obtained with the fixed wire at x/D = 2 and different y/D, while the radial ones with the fixed wire at one particular position, x/D = 2, y/D = 0.

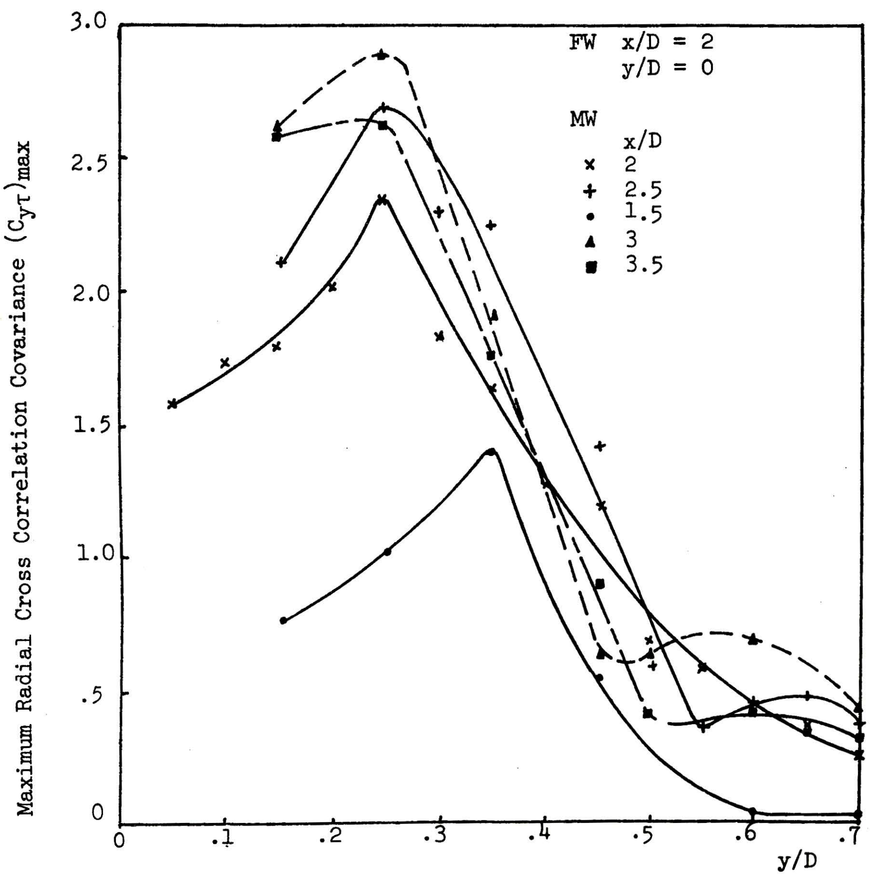

Fig. 6 Maximum Radial Cross Correlation Covariance with Radial Separation

The region of highest degree of correlation occurs between the axial positions, $2.5 \leqslant x/D \leqslant 3.5$ and it is nearer to the boundary of the cone than to the highest turbulence region, $\eta = 0$. This suggests that as far as the axial velocity fluctuations is concerned, the field imposed in the potential cone is due to sources in the mixing region. These sources may not be at the highest turbulent region nor the highest shear region, $\eta = 0$ (12), but near the inner boundary, around $\eta = -0.087$. Further, they tend to convect downstream along the constant η line or along the line of constant mean velocity.

From the convection velocity measurements (4, 7), the convection velocity at $\eta = -0.087$ is 0.77 of the nozzle exit velocity. At the axis, the convection velocity obtained is only 0.64 of the exit velocity. This means that the sources travel at a faster velocity than the field induced in the potential cone. It may be due to this higher convection velocity at the sources that the peak of the maximum covariances is situated at the axial position of $2.5 \leqslant x/D \leqslant 3.5$ while the fixed wire was at $x/D = 2$.

The reason for this higher convection velocity of the sources is not known. As far as the mean velocity is concerned, the local mean velocity at the radial position $\eta = -0.087$ is very nearly the same as the nozzle exit velocity, $\bar{U}_0$. It thus seems that the mean velocity is not responsible for the difference in the convection velocity.

The further complication is the method in obtaining the convection velocity. Usually, the convection velocities were obtained along constant y/D lines but not along constant η lines. In this respect, the velocity thus obtained may not represent the true convection velocity of the vortice which seems to convect along the constant η lines.

The above contours yield the approximate position of the sources. It is because the effects of the local mean velocity on the convection velocity of the sources, and on the propagation of the field into the cone are not yet known. With the understanding of the above effects and coupled with more contour maps with the fixed wire at different positions, the exact location of the sources may be found. However, the usefulness of the above mapping of the covariance in the determination of sources can never be doubted.

CONCLUSION

In this paper the correlation technique in subsonic jet has been discussed in details. Due to the variation of intensity with spatial separation the coefficient is not the desirable factor in the understanding of the field. Further, the effect of hot wire wake may also affect the values of coefficient obtained. Detailed comparison between the coefficient and covariance has shown the misleading information the coefficient may supply in these fields of varying intensity.

The covariance measurements, obtained by the digital technique, have shown the significance of the covariance in the proper interpretation of the field inside the jet. It has found that the highly correlated field inside the potential cone has its origin in the mixing region. The estimation of the position of the sources is in the part of the mixing region which is nearer to the potential cone, but not at the highest turbulent region and shear region. Though more information is required before the exact location can be found, the above technique offers an useful tool in this respect.

ACKNOWLEDGEMENT

The work was done during the author's stay in the I.S.V.R., Southampton, under a Senior Research Fellowship granted by S.R.C., Great Britain. Thanks are due to Prof. P.O.A.L. Davies for his helpful discussion and encouragement.

REFERENCES

(1) Corrsin, S.
"Investigation of flow in an axially symmetrical heated jet of air",
NACA, A.C.Rep. 3L23, 1943.

(2) Fisher, M.J. & Davies, P.O.A.L.
"Correlation measurements in a non-frozen pattern of turbulence",
J. Fluid Mech., Vol. 18, 1964.

(3) Wills, J.A.B.
"On convection velocities in turbulent shear flow",
J. Fluid Mech., Vol. 20, 1964.

(4) Ko, N.W.M. & Davies, P.O.A.L.
"The near field within the potential cone of subsonic cold jets",
J. Fluid Mech., Vol. 50, 1971.

(5) Lau, J.C., Fisher, M.J. & Fuchs, H.V.
"The intrinsic structure of turbulent jets",
J.S.V., Vol. 22, 1972.

(6) Ko, N.W.M. & Davies, P.O.A.L.
"Interference effect of hot wires",
I.E.E.E. Trans. Instrumentation and Measurements, Vol. IM-20, 1971.

(7) Ko, N.W.M.
"The near field structure of subsonic cold jets",
Ph.D. thesis, University of Southampton, 1969.

(8) Van Atta, C.W. & Chen, W.Y.
"Correlation measurements in grid turbulence using digital harmonic analysis",
J. Fluid Mech., Vol. 34, 1968.

(9) Davies, P.O.A.L. & Mercer, C.A.
"Phase velocity measurements using the cross power spectrum".

(10) Bendat, J.S. & Piersol, A.G.
"Measurements and analysis of random data",
John Wiley & Sons, New York, 1965.

(11) Davies, P.O.A.L., Fisher, M.J. & Barratt, M.J.
"The characteristics of the turbulence in the mixing region of a round jet",
J. Fluid Mech., Vol. 15, 1963.

(12) Bradshaw, P., Ferriss, D.H. & Johnson, R.F.
"Turbulence in the noise-producing region of a circular jet",
J. Fluid Mech., Vol. 19, 1964.

Noise, Shock & Vibration Conference, 1974 Monash University, Melbourne

NOISE IN HYDRAULIC CONTROL SYSTEMS

P. Dransfield
Department of Mechanical Engineering
Monash University
Clayton, Victoria

J. S. Stecki
Department of Mechanical Engineering
Monash University
Clayton, Victoria

P. Wilkins
Department of Mechanical Engineering
Monash University
Clayton, Victoria

SUMMARY - Noise levels in working hydraulic control systems are often high enough to be uncomfortable, and, in the future, possibly illegal. The reasons for noise development, the sources of noise, and the remedial actions taken to reduce noise, are reviewed and presented in a consolidated form derived from many listed references.

Suppression of high noise levels in a 1000 ton double acting hydraulic drawing press is described. The problem was quite severe, involving a commissioned 250 HP 3000 psi hydraulic system, whose main pressure generator is a seven piston axial pump. The main noise generation sources were located. Several designs of acoustic filter were developed and tried before one was selected for installation in the reservoir of the press hydraulic system, which was integral with the press structure. Noise levels in the working press were reduced to acceptable levels.

1. INTRODUCTION

Hydraulic control systems operating in the pressure range 1000 - 5000 psi are increasingly being utilized in powered control situations. Aircraft controls, machine tool drives, industrial presses, and an ever increasing range of mobile lifting, digging, and materials handling equipment are major fields of application. Modern hydraulic control system development has been led by aircraft requirements in which maximization of power to weight and power to volume ratios has been a critical influence. The result has been continuing trends towards increased working pressure, increased pump drive speed, and increased oil flow velocity.

Each of these trends increases the potential for increased noise generation by the working hydraulic system. In addition, the noise generated is likely to be increasingly offensive due to increasing frequencies. Many working hydraulic systems generate noise levels beyond what is today acceptable and even legal. Probably the intermittent nature of the use of hydraulic systems has kept such systems marginally acceptable. On the other hand, high-pressure high-speed hydraulic systems can be designed and operated with acceptable noise emission. This may involve component design, system design, and inclusion in the system of muffling devices.

In the present paper, the origins of noise generation in hydraulic control systems is reviewed and presented in a consolidated form. In addition, a successful control of noise emission from a hydraulic press drive is outlined and discussed.

2. NOISE GENERATION

A hydraulic control system consists basically of :

1. A positive displacement pump driven by a prime mover (electric motor, I.C. engine, aircraft engine, etc.), which converts primary power to hydraulic power (pressure x flowrate of oil). The pump is normally driven at constant speed, but may be of variable stroke and hence displacement.

2. Valving to control pressure, flowrate, and flow direction.

3. An actuator (linear power cylinder, or rotary hydraulic motor) which receives oil and provides linear or rotary motion to the load being controlled.

4. The plumbing to interconnect these primary components. This includes piping and reservoir.

5. Auxiliary devices such as filters (which are essential) and accumulators (which may be advisable) to optimize systems performance and life.

Fig. 1 (modified from Ref. 1) shows a basic hydraulic control system with recognized zones of noise generation and transmission, with their relative ratings. Noise can be transmitted from a source in three basic ways :

1. Airborne noise direct from the source;

2. Structure borne transmission of vibration from the source to excite another source. Such transmission can be along any solid or liquid path.

3. Fluid borne transmission due to pressure pulsations, turbulent flows, cavitation, etc.

Table 1 shows detailed analyses of sources, causes, transmission paths, and common remedies of noise in hydraulic control systems. The Table is a consolidation of information available in the references noted, and is an attempt to categorize the noise problem.

The pump is potentially the main noise generator. Whether it be gear, vane, or multiple-piston type, the pump accepts oil at low pressure and injects it in discrete overlapping quanta at high frequency into a high pressure environment of restricted volume. The low compressibility of oil ensures that this operation induces a high frequency pressure fluctuation at the pump discharge. A degree of cavitation is to be expected in the suction side of the pumping chamber as the viscous oil charge is drawn in in a very short period of time. Both of these pressure change effects are accompanied by noise which is transmitted directly, and also by the fluid, the supporting structure, and the plumbing, to other system components.

3. NOISE REDUCTION

It is readily appreciated from Table 1 and its references, and from consideration of phenomena associated with the high-frequency large pressure drop fluctuating flows in working hydraulic systems, that noise generation in these systems is interactive and complex. However, reduction of local noise generation can be expected to reduce system noise emission. Designers of modern pumps minimize flow restrictions into the suction side to minimize cavitation; reservoirs are designed to allow de-aeration of the return oil before it is re-admitted to pump suction; reservoirs are placed so that positive head is applied to pump suction; some pumps are supercharged by auxiliary pumps; pump discharge porting is designed to minimize pressure shock by rounding off the sharp-edged cusp-like pump pressure ripple. Frequency of pressure fluctuations at the pump can be reduced by using lower pump drive speeds. For many applications, the increase in system bulk resulting from a decision to run the pump at lower speed is of no practical consequence. There is also the possibility of utilizing the directional characteristic of noise emission, to ensure that generated noise is directed away from personell in the vicinity of the working system.

Noise transmission of amplification sources.

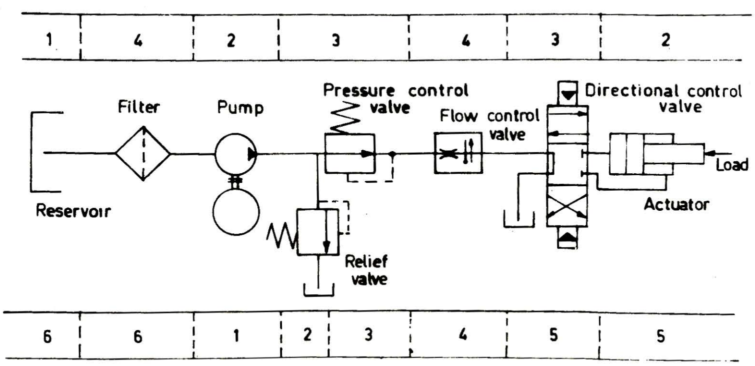

Noise generating sources.

Fig.1 Sources of Hydraulic Control System Noise.

TABLE 1 (continued over page)

PHENOMENON	CAUSE	DESCRIPTION	POSSIBLE REMEDY	REFERENCE
1. PUMP & MOTORS				
1.1. Turbulence (Broadband noise)	1.1.1. Aeration caused by air being leaked into system.	Fluid in the reservoir "milky" or "frothy", however level in the reservoir is correct.	Repair sources of leaks. Bleed the air from hydraulic system. Potential noise reduction of 2 - 4 db.	1,10
	1.1.2. Aeration caused by hydraulic fluid leaking out of the system (air leaking in).	Fluid in the reservoir "milky" or "frothy". Level of fluid in the reservoir is down.	As above. Fill up reservoir to the correct level. Potential noise reduction 1 - 3 db.	1,10,14
	1.1.3. High air contents in the hydraulic fluid.	As above.	Maintain care when filling the system. Use hydraulic fluid with anti-foam additives. Potential noise reduction of 2 - 4 db.	1,10,14
	1.1.4. Aeration in a hydraulic system equipped with cooling system.	Leaking cooling coils causing water to leak into hydraulic system. The fluid will have "milky" or "frothy" appearance. Clear fluid in the reservoir after period of rest will indicate air leak (1.1.1., 1.1.2., 1.1.3.). Persisting milky appearance indicates water in hydraulic fluid.	Repair the leak. Drain the system and refill with new fluid. Bleed the lines. Potential noise reduction 2 - 4 db.	1,14
	1.1.5. High flow velocity through the passages.	The flow passages too small.	Manufacturer's responsibility. Flow velocity in delivery lines < 4.5 m/sec.	6,10,15
	1.1.6. Flow disturbance.	Internal geometry of the pump. Flow irregularity caused by shape of passages and sudden changes of flow direction.	Manufacturer's responsibility.	7,10,13,15
1.2. Cavitation (High frequency noise of up to 20000 hz).	1.2.1. Low viscosity of hydraulic fluid.	Rattling or clanking noise which disappears shortly after start-up. "Frothy" appearance of fluid in the reservoir indicates system cavitation.	Provide heating to bring fluid to proper working temp. ($50^{o}C$) or run the system under no-load until above temperature is reached. Potential reduction of noise 10 - 15 db.	1,2,3,6,10,14,15
	1.2.2. Restriction in the system.	Rattling or clanking noise which appears during system operation. Cavitation caused by restriction in system immediately ahead of pump, manifested by erratic operation of actuators.	Check fluid level. Check hydraulic lines for foreign objects (rags, tools etc.). Potential noise reduction 10 - 15 db.	1,6,14
	1.2.3. Low fluid level in the reservoir.	Rattling or clanking noise.	Clean the fluid, refill reservoir. Bleed the system before start-up. Potential noise reduction 10 - 15 db.	1,14,16
	1.2.4. Collapsing single air bubbles.	1. Single loud clank noise repeating at irregular intervals. Caused by faulty design of suction line or leaking suction line. Hydraulic oil contains up to 8% of air under normal conditions, which can be released as single bubbles.	Tighten all connections on suction side. Fill up reservoir. Check position of suction line (must be below fluid level at all times). Clean oil filter, bleed oil lines. Avoid air-boosted reservoirs. Potential noise reduction 4 - 8 db (peaks).	1,5,6,10
		2. Pump rotated backwards after stopping, causing release of air from the oil on pressure side.	Install check valve on pump suction side.	10
	1.2.5. Entrained air.	High frequency noise generated by hydraulic pump operating under cavitation conditions.	– Return and suction lines to enter reservoir below lowest level of fluid in the reservoir. – The flow path from return to suction lines should be as long as possible to facilitate dissipation of air bubbles. – Buffers should be installed between return and suction lines. – Proper design of suction line (bell-mouth) and return line (diffuser) entries. – Install bubble separator. – Size of suction line to be maximum possible. – Provide positive head on pump suction. – Use adequate air breather opening.	4,5,6,11,14,15,16
	1.2.6. System operating conditions.	Flow velocity, local static pressure fluid temperature, geometric configuration of the system, hydraulic oil specification.	– Avoid sudden changes in passage size. – Avoid sharp flow direction changes (use bends instead of 90^{o} elbows). – Flow velocity in suction lines < 1.5 m/sec. – Flow velocity in return lines < 2.5 m/sec. – Check direction of pump rotation.	6,14
1.3. Hydraulic shock.	1.3.1. High energy reversal.	Sharp rise in system pressure caused by sudden reversal of load.	Equip actuators with cushioning devices. Use decelerating valves or shock absorbers.	6
	1.3.2. Pumping action (piston pumps).	Sudden pressure rise when pumping chamber open to discharge line.	Change of pump valve plate timing (manufacturer's responsibility).	2,16
	1.3.3. Fluid hammer effect.	Caused by rapid closing or opening valve or other flow-controlling component. The occurence of fluid hammer will depend on fluid properties, aeration, and system operating characteristics.	– Modify the valve or flow-controlling component to have smooth action within allowable time. – Add capacitance to the system. – Use dashpots. – Use cam timed valves or pilot operated valves. – Match dynamically components. – Use cushioned actuators or decelerating valves.	1,3,4,5,6,10
	1.3.4. Sticking component.	The hydraulic shock occurs when sticking part suddenly overcomes constricting force.	– Clean the filter and offending component. – Check the hydraulic fluid type (viscosity, density). – Flush system thoroughly. Possible noise reduction 10 - 20 db (peaks).	1
1.4. Flow/pressure ripple (fluidborne sound)	1.4.1. Turbulence.	See 1.1.	– Insert flexible hose in sharp bend areas and at the pump. Possible noise reduction 2 - 3 db.	1
	1.4.2. Discontinuity of pumping action.	Caused by discreet character of pumping action which is inherent in positive displacement pumps. The flow ripple is result of: – High rate of pressure change. – Unsatisfactory flow passages. – Timing of valve plate (piston pumps). – Speed of rotation. – Operating pressure. – Pumping mechanism geometry. – Compressibility of fluid (air contents). – Hydraulic fluid temperature and viscosity. – Back flow from discharge port into pumping chamber (see 1.3.2.). – Fill-up of pumping chambers during suction.	– Use odd number of pumping elements. – Use damping materials in pump construction. – Select carefully system components. – Operate pump at recommended rotational speed (lower if practicable). Possible noise reduction of 7 - 12 db. – Do not exceed recommended pump pressure. – Use acoustic mufflers or desurgers. – Use proper viscosity fluid. – Bleed the system before start-up.	1,2,3,6,7,10,11,12,13,14,16,17

	1.4.3. System impedance.	Pressure fluctuations caused by circuit resistance to unsteady flow (flow ripple). The pressure fluctuations will depend on dynamic characteristics of the load circuit	– Reduce resistance to flow by proper design of flow passages. – Analyse circuit components downstream from the pump. possible noise reduction 5 - 8 db.	2,10,15,16
	1.4.4. Standing waves.	Caused by local restrictions, reflecting pulsating flow. Capacitance (filter, accumulator, enlarged passage etc.) may increase pulsations if situated close to pumps.	– Determine lengths of tubing such that no standing wave can set at whole range of the pump frequencies.	10,12,15, 16
1.5.Vibration (airborne sound)	1.5.1. Mechanical.	Possible causes of mechanical vibrations are: – Misalignment. – Dynamic unbalance of el. motor and pump. – Type and condition of bearings. – Transmission of vibrations from pump-el. motor assembly – Mechanical vibrations due to moving parts (rotation, sliding etc.). – Fluctuating shaft RPM. – Type of pump mounting. – Type of coupling. – Resonance of internal components. – Vibration of external components (shafts, body covers etc.). – Worn or damaged parts. – Faulty pump assembly (loose bolts etc.). – Excessive clearances and low component stiffness (narrow band noise).	– Use shaft couplings with rubber or plastic interfacing – Balance el. motor and pump (manufacturer's responsibility). – Check bearings. Possible reduction of 1 - 2 db. – Use rigid mounting plate and isolate from the rest of the system. – Replace or repair worn or damaged components. – Reduce clearances. – Stiffen the components. – Improve quality of finish. – Use material with damping properties in pump construction.	1,2,3,6,7, 8,10,11,13, 14,15,16
	1.5.2. Hydraulically induced vibrations.	Possible causes of hydraulically induced vibrations are: – Exchange of energy between fluid and its container. – Transmission of fluid pulsations to receivers (reservoir, filter, accumulator etc.) carried along delivery lines. – Vibration of pumping elements (swash plate, gears, venes) due to fluctuating load. – Distortion of pump case (airborne sound). – Shaft torqne fluctuating due to internal loading.	– Use resilient mounting. – Isolate pump using flexible hoses. – Use damping material in pump construction. – Diminish structural response to noise energy. – Use pressure desurger or acoustic mufflers. – Use bigger capacity pump operating at lower rotational speed.	2,3,6,8,10, 11,13,14,16
1.6.Other.		Pump noise level will depend also on maximum horse-power transmitted, and rotational speed. Increased horse-power: SPL db = 17 log (hp ratio) Increased rotational speed: SPL db = 20 : 50 log (speed ratio)		18
2. VALVES				
2.1.Turbulence (broadband noise)	2.1.1. Aeration.	See 1.1.1. - 1.1.4.		1,5,6,10, 14
	2.1.2. High flow velocity through the passages.	See 1.1.5. liquid eddies and turbulent flow through valves passages causing valve chatter. High velocity of flow through valve passages may cause local cavitation (see 2.2.). Sound pressure level proportional to 7 - 8 power of the flow velocity through the valve.	– Replace orifices with check valves. – Proper design of flow passages. – Avoid sharp changes of shape, direction or size of fluid passages. – Avoid using undamped direct acting valves (inherently unstable). – Slow down operation of the valve to avoid fluid hammer effect (chokes). – Prevent unstable operation of valve by careful selection of circuit components. – Reduce valve clearances.	1,3,5,6, 10,15,16, 19
	2.1.3. Flow disturbance.	See 1.1.6. Transient noise caused by sudden switching.	– Control valve response time.	6
2.2.Cavitation (high frequency noise of up to 20000 hz)	2.2.1. Low viscosity of hydraulic fluid.	See 1.2.1. Rattling or clanking noise disappearing after start-up.	– Keep hydraulic fluid at correct temperature (50°C).	1,6,10
	2.2.2. Restriction in the system.	See 1.2.2. Rattling or clanking noise which appears during system operation.	– Clean the system. – Clean the hydraulic filter. – Check the system for foreign objects.	1,6,10
	2.2.3. Pressure drop across valve seat.	Pressure drop across valve seat causes local cavitation The air bubbles can cause severe vibration of the moving part.	– Avoid using undamped direct acting valves. – Reduce velocity of flow through the valve. – Avoid sudden changes in the shape, direction or size of flow passages.	3,5,16,19
2.3.Hydraulic shock	2.3.1. Valve sticking.	See 1.3.4. Hydraulic shock caused when sticking part suddenly overcomes constricting force (possible SPL peaks of 10 - 20 db).	– Clean the hydraulic filter and components. – Check the hydraulic fluid type. – Flush the system thoroughly.	1
	2.3.2. Fluid hammer effect.	See 1.3.1. Caused by rapid closing or opening valve or other flow-controlling component. The occurance of fluid hammer will depend on fluid properties, aeration, and system operating characteristics.	– Slow down operation of valves by choking, or using spools with throttling grooves. – Add capacitance to the system to absorb the shock (or use desurgers, accumulators). – Time valve operation using cams or pilot operation. – Use nested springs.	3,4,5,6,16
	2.3.3. Standing waves.	See 1.4.4.	– Avoid lengths of tubing which will facilitate setting of standing waves in the system.	10,12,15, 16
2.4.Vibrations	2.4.1. Mechanical.	Mechanical vibration may be caused by: – Resonance of internal components. – Excessive wear. – Excessive clearances. – Low stiffness of the components. – Transmission of vibration from other sources (pump, motor, reservoir etc.).	– Stiffen valve components. – Isolate the valve from other components (flexible tubing). – Reduce clearances. – Provide dashpot or other form of internal damping. – Use manifold mounted valves.	1,15
	2.4.2. Hydraulically induced vibrations.	See 1.5.2. Possible causes of hydraulically induced vibrations are: 1. Transmission of fluid pulsations from the pump. 2. Distortion of valve bodies under pressure (airborne sound). 3. Turbulent flow through valve body. 4. Jet action. 5. Cavitation (causing valve chatter). 6. Resonance. 7. Hydrodynamic oscillatory behaviour.	1. Use desurger or acoustic mufflers in pump delivery lines. 2. Stiffen valve components. 3. Avoid sudden changes in the shape, direction or size of fluid passages. 4. Select correct size components. 5. Avoid using undamped direct acting valves. 6. Slow down operation of valves. 7. Place the pressure controlling valves next to the pump. 8. Reduce valve clearances. 9. Change the angle of flow in the valve opening. 10. Reduce mass of the moving part.	1,3,4,5,6, 9,10,15,16

3. ACTUATORS				
3.1.Turbulence	See 1.1.1. - 1.1.4.			
3.2.Cavitation	See 1.2.1. - 1.2.6.			
3.3.Hydraulic shock	3.3.1. High energy reversal.	See 1.3.1.	– Use cushioning. – Use mechanical shock absorbers or dashpots. – Bleed the actuators before start-up.	4,6
3.4.Vibrations		– Caused by aeration of hydraulic fluid (erratic action of the piston). – Side loading on the piston rod. – Chatter of sealing elements. – Transmission of mechanical vibrations from other system components.	– Use floating seals. – Use cushioning. – Avoid side loading on piston rod. – Bleed air from the circuit. – Use deceleration valves. – Do not operate actuator above rated capacity.	6
4. DELIVERY LINES				
4.1.Turbulence	See 1.1.1. - 1.1.4.	Turbulence caused by high velocity of fluid in hydraulic lines.	Select line sizes to limit maximum flow velocity to following values: suction lines < 4.5 m/sec return lines < 1.5 m/sec delivery lines < 2.5 m/sec	1,10,14,18
4.2.Cavitation	See 1.2.1. - 1.2.6.	Presence of restriction in the line. Flow noise SPL = 60 log V_2/V_1 (no cavitation) and SPL = 120 log V_2/V_1 (cavitation). V_1, V_2 - velocity of fluid before and through restriction.		1,10,18
4.3.Hydraulic shock	See 1.3.3. Fluid hammer effect.	Caused by rapid opening or closing valve.	– Use desurger. – Use flexible hoses. – Slow down valve operation.	1,4,5,6,10, 15
4.4.Vibrations	4.4.1. Mechanical vibrations transmitted from other conponents.	– Vibration transmitted from pump structure. – Vibration transmitted to reservoir. – Resonance. – Tubing hitting floor, panels etc.	– Use flexible tubing. – Isolate hydraulic lines from other components using resilient mountings.	1,2,3,15
	4.4.2. Hydraulically induced vibrations.	– Standing waves in delivery lines. – Flow/pressure pulsations transmitted from pump. – Sharp changes in flow direction. – High pressure drop (diameter of tubing too small). – Resonance caused by presence of restrictions reflecting pulsating flow.	– Avoid length of tubing which could cause standing waves (wave length = 22000/f). – Alter transmission path. – Detune the receiver (reservoir, tank etc.). – Isolate using flexible tubing. – Use desurgers, mufflers etc. – Use formed tube bends instead of 90° elbows (bent radii > 5 times tube diameter).	1,2,3,6,10, 15,16
4.5.Fluid borne noise	4.5.1. Fluid borne noise transmission.	Noticable increase in overall noise caused by thin, hot hydraulic fluid.	– Check hydraulic fluid temperature (50°C). – Increase reservoir capacity. – Add cooling unit.	1
5.SUCTION LINES				
5.1.Cavitation	See 1.2.1. - 1.2.6.	Loud knocking noise caused by: – Large air bubbles in the suction line. – Pump motored backwards after being stopped.	– Install check valve in suction line. – Use large diameter suction line (fluid velocity < 1.5 m/sec). – Use flexible tubing. – Return lines exits should be placed below lowest level of fluid in the reservoir. – Use large bell mouth entry to suction line. – Use bubble separator in reservoir. – Check fluid level in the reservoir. – Maintain correct fluid temperature. – Check pump rotation. – Check for vacuum leaks in suction line.	1,3,6,10, 14,15,16, 18
5.2.Vibration	See 4.4.			
6. RESERVOIR				
6.1.Cavitation	See 1.2. Caused by incorrect design of reservoir.			1,4,5,6,10 14
6.2.Vibrations	6.2.1. Amplification of noise.	Loud "thrumbing" noise caused by amplification of noise transmitted from other parts of the system. Large surface areas serve as noise emitters.	– Isolate pump/el. motor assembly, pipes etc. from reservoir. Possible reduction of noise 2 - 4 db. – Eliminate unused areas while maintaining adequate strength. – Use non-metalic parts at impact points.	1,3,8
	6.2.2. Transmission of vibrations.	Loud mechanical noise caused by excessive transmission of vibration throughout the system.	– Install heavier base plate for pump/el. motor assembly – Use quiet couplings and flexible hoses. Possible noise reduction 6 - 9 db.	1,3,6,10, 15

Noise emanating from steady fluid flow can be reduced simply by reducing flow velocities. The main difficulty here is in the high speed flow over control valve orifices. Mechanical chatter in pressure relief valves can be controlled by designing adequate damping in the valve mechanism.

Avoidance of pipe lengths and system structural characteristics which result in exitation of local resonances is another area of system design which can lead to noise level control. Substitution of a hose for a rigid pipe can sometimes suitably isolate a component from an excitation source.

Another approach to noise control is the location of an acoustic muffler in the pump discharge line. This is a common suggestion, but there are few reported successful applications of it. The following Section 4 describes a successful muffler application to an industrial hydraulic system.

4. NOISE SUPPRESSION IN A HYDRAULIC PRESS

The authors were associated in an attempt to reduce the noise levels of the 1000 ton double-acting hydraulic press shown in Fig. 2. The press can operate in three modes :

1. Pressing with the main ram, with the cushion inoperative.
2. Drawing with the main ram and cushion.
3. Reverse drawing.

Fig. 3 shows a simplification of the hydraulic circuit, illustrating how the press works. In fact, the hydraulic pumps are situated with the reservoir in the crown of the press. Fig. 3 includes details of the system power units and their main parameters. The only divergence from normal practice is the relatively high speed of the main pump (about 50% higher than recommended for this pump in normal practice, but still just inside the allowed maximum speed).

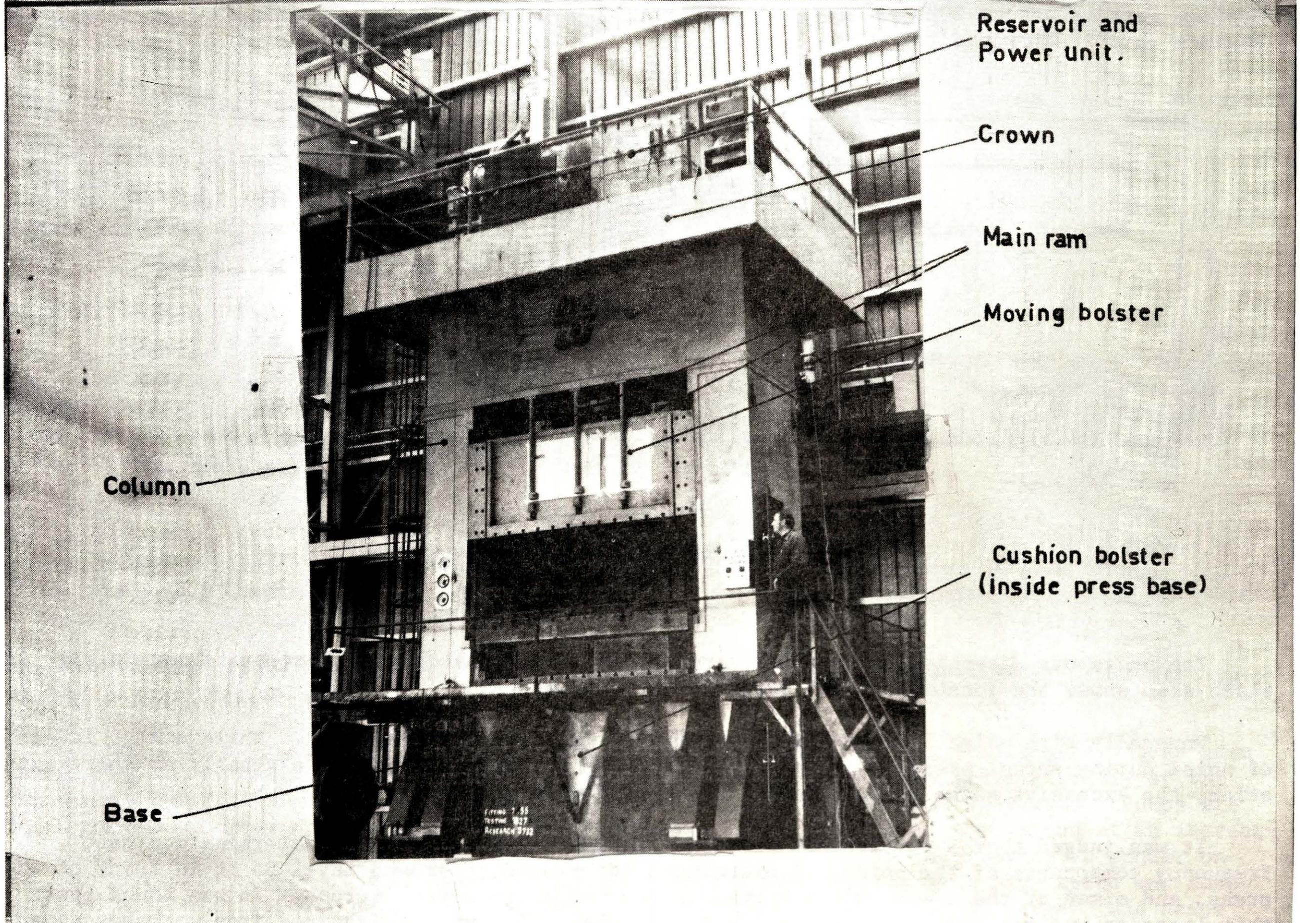

Fig. 2 1000 Ton Double Acting Hydraulic Press

1. Main Drive. BRUNINGHAUS PISTON PUMP, 740 CV-3000 -R3341, 7 pistons, variable displacement.
Theoretical max. displacement 29.35 in^3/rev.
Rotational speed: Nominal - 970 RPM
Maximum - 1500 RPM
Delivery at max. RPM - 159 IGPM.
Max. delivery with self suction - 103 IGPM
Min. charge pressure - 45 $lb.in^{-2}$
Max. pressure at max. flow - 3000 $lb.in^2$
BROOK ELECTRIC MOTOR, 250 HP, 1440 RPM.
2. Cushion Drive. HYDRECO GEAR PUMP, 1711C2A1A(L)
Theoretical displacement 2.175 in^3/rev.
Max. operating pressure 3000 $lb.in^{-2}$
Delivery at 2940 RPM and
Max. pressure - 23.5 IGPM
Max. rotational speed - 4000 RPM
POPE ELECTRIC MOTOR, 50 HP, 2940 RPM.
3. Servo Drive. IMO SCREW PUMP, ACG6-70-2-N2F
Theoretical displacement - 18 in^3/rev
Max. pressure - 224 $lb.in^{-2}$
Delivery at 2940 RPM
and no pressure - 195 IGPM
Max. rotational speed - 3000 RPM
4. Auxiliary Drive. VICKERS PISTON PUMP, PVB5-LSY-11-C-10.
Pressure compensated.
Max. rated delivery 3.3 IGPM at 1440 RPM.
Max. pressure - 3000 $lb.in^{-2}$
Max. rotational speed - 3600 RPM.
POPE ELECTRIC MOTOR, 20 HP, 1440 RPM.
5. Main Pump Control. DOUBLE VANE PUMP, V2230-9-2-10C-20-S214.
9 IGPM - at 1440 RPM (large cartridge).
2 IGPM - at 1440 RPM (small cartridge).
Maximum rated pressure 2000 $lb.in^2$.
Maximum rotational speed 1800 RPM.

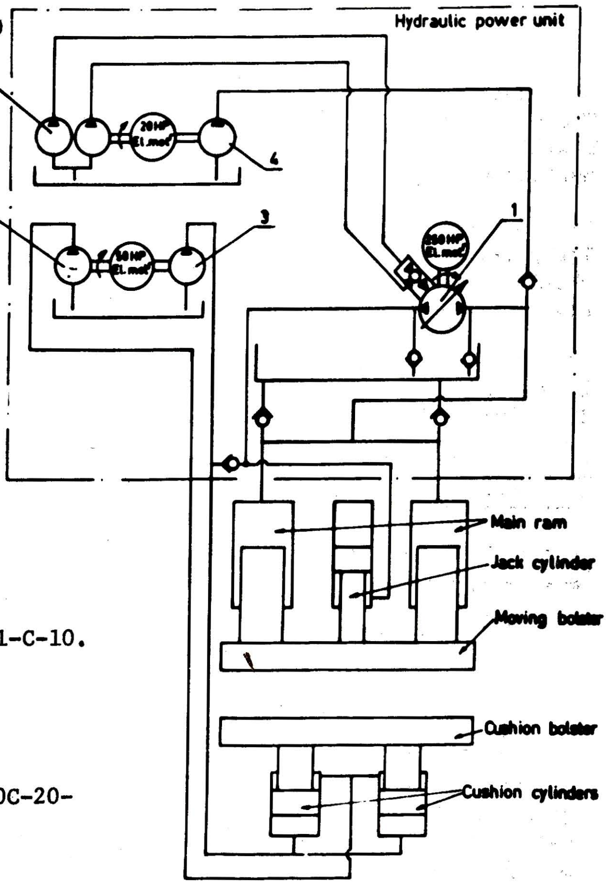

Fig.3 Simplified hydraulic circuit of Press.

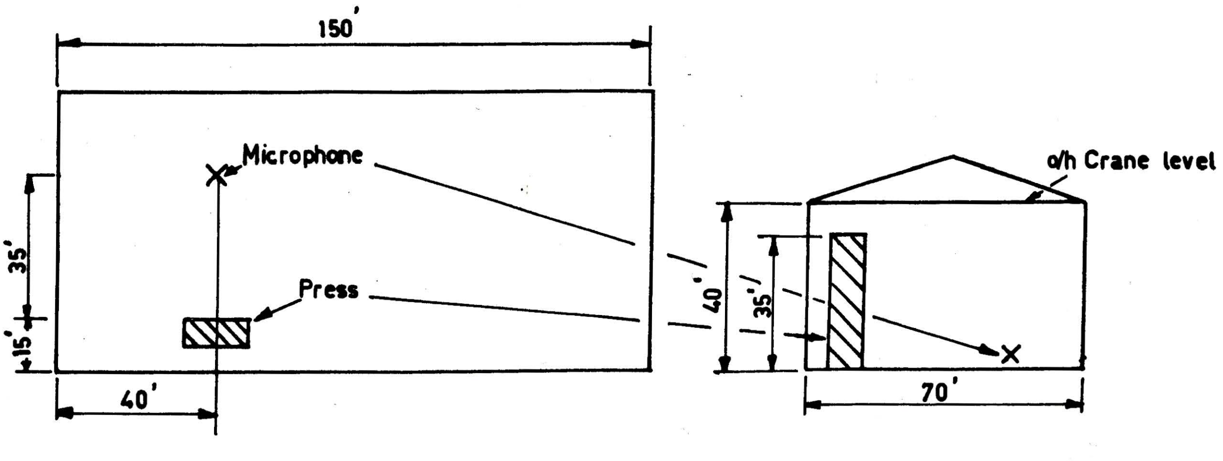

Fig.4 Location of Press in workshop.

The press was assembled for pre-delivery trials in a workshop of dimensions shown in Fig. 4, which also shows the location of the press in the shop.

Unusually high noise levels were apparent when the press was operated. While a high level of noise during actual pressing is largely acceptable to operators as it is usually of short duration, the excessive noise during drawing was regarded as unacceptable.

It was judged that a narrow band frequency analysis was required to determine dominant frequency components of the noise. A microphone was placed at ground level 35 ft in front of the press, and aimed at the crown, which contained the hydraulic power sources. It was found that this location was not critical, as the large and relatively empty galvanized iron workshop acted as a reverberation chamber. Measurements were made during lulls in surrounding activity, and background noise levels for this state were established to allow estimation of noise levels due solely to the press.

Measurements were made with the ram pressing against the cushion. Ram pressing speeds of 40, 46, and 52 in/min were investigated. Strokes were such that noise measurements could be made over time intervals of 50 - 75 seconds.

Fig. 5 shows typical narrow band frequency characteristics. The most noticeable feature is the presence of sound level peaks near 180 hz. Thus, the main pump was isolated as the main contributor to noise emission during ram manoeuvring. A lower but consistent peak occurred at 50 hz, and is attributable to the drive speed of the servo pump.

The obvious cure to the problem was to replace the main pump with a larger, lower speed unit of similar power. A danger in increasing pump speed for economic reasons lies exposed. Because of expense and delivery delays, pump replacement was not viable. Inability to eliminate the main source of noise left only the option to suppress it by acoustic filtering, using a reactive filter (muffler).

Using established principles, four types of mufflers were designed, built, and tested in the hydraulic system. They were located in the pump discharge line, adjacent to the pump. The effect of inserting the mufflers is shown on Fig. 5 and Table 2. The stand pipe unit required tuning of the pipe lengths by ear. As shown in Table 2, the press was noisier with this muffler. A narrow band analysis confirmed that main pump frequency noise was substantially reduced. However, the stand pipes themselves were vibrating and acting as noise sources. This could probably be eliminated by using heavier pipes, possibly with bracing.

The single chamber unit was the most successful. It reduced SPL by between 3 and 8 db, depending on ram speed, and resulted in the press operating at an acceptable level of noise.

The double chamber unit was less successful than the single chamber unit. It was felt that interaction of the two chambers was not adequately involved in the simple theory used for the design.

The perforated tube unit gave contradictory results. The SPL readings show it to be the most effective. However it failed to eliminate a particularly offensive noise apparently due to one of the multiples of pump frequency.

Fig. 6 shows approximate attenuation curves for the four mufflers. It confirms the general effectiveness of the single chamber unit, and, with its negative peaks, probably explains the contradiction in the effectiveness of the perforated tube unit.

The physical chamber size of the muffler used was approximately 10 in internal dia. x 22 in long. Physical dimensions of all of the mufflers were limited by the size of the system reservoir, into which they, along with the pump, had to fit.

5. DISCUSSION

The muffler approach was certainly successful, in that it reduced operating noise levels of the press from an unacceptable to an acceptable value. However each muffler design was a one-shot affair. It is not claimed that the muffler adopted was an optimum of the single chamber form; nor that the effectiveness of each of the other three forms could not have been improved, perhaps dramatically, if time and experience could be utilized.

The noise levels measured and given apply only to approximately 0.8 of maximum loading of the press. They jump higher when full load pressing is being performed. Under these conditions a maximum SPL reading of 102 db was obtained when no muffler was used, and 96 db when the single chamber unit was installed. The actual full load pressing time in the press cycle is small, and it appears that operators are conditioned to accept these short periods of excessive noise.

The results given in the paper are representative of a much more substantial investigation carried out by Wilkins (Ref. 20).

In the case discussed, noise became a severe problem because of the choice of a higher than normal pump drive speed for the particular pump used. The pump operates satisfactorily at the increased speed. However, its effectiveness as a noise generator is also increased. Pumps are usually the most expensive item in a hydraulic system. If a particular pump is run at an increased speed, it delivers similarly increased flow rate and power. It is interesting to ponder on the economic possibility of a smaller (and hence cheaper) pump running atwa high speed and complemented with a relatively cheap muffler compared with adoption of a slower, larger (and hence more expensive) pump operating without a muffler.

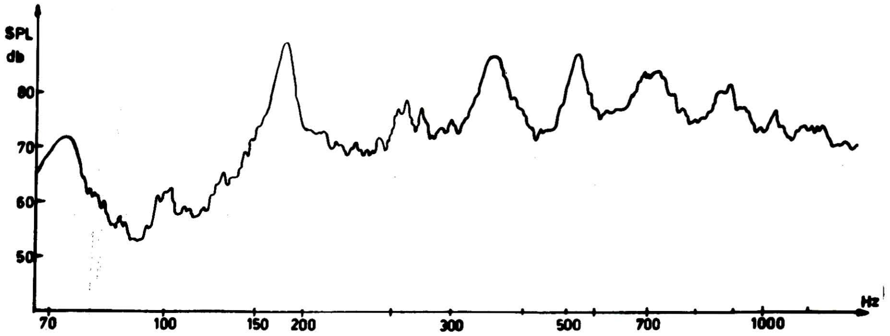

No muffler, Ram speed 52 in/min.

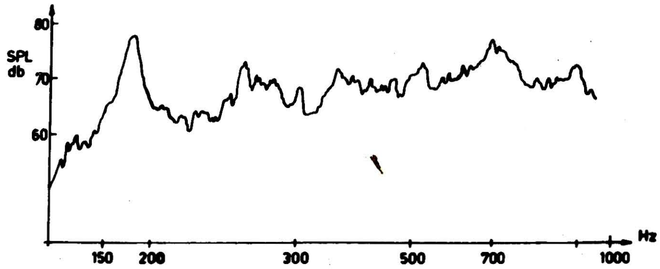

Perforated Pipe, Ram speed 52 in/min.

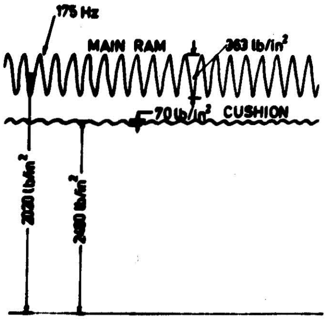

No muffler, pressure recording.

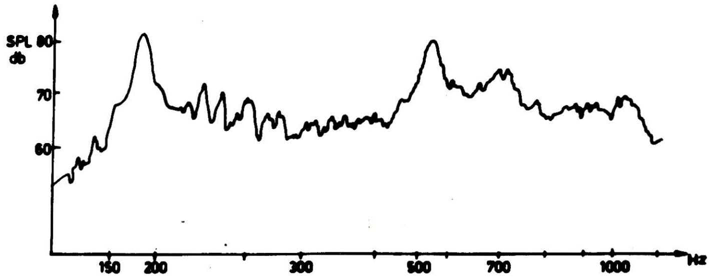

Single Chamber, Ram speed 52 in/min.

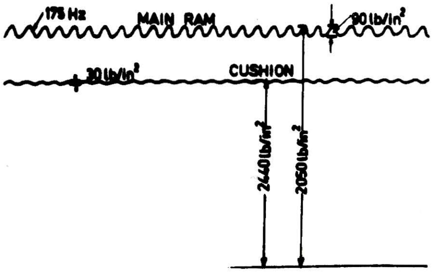

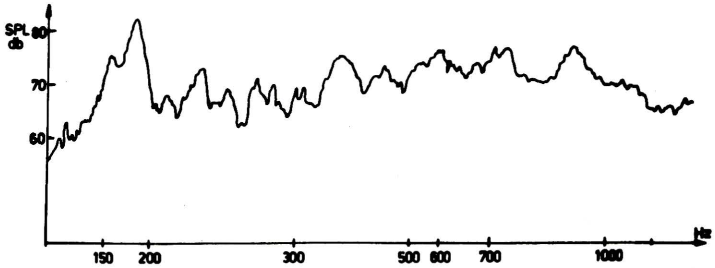

Double Chamber, Ram speed 52 in/min.

Single chamber, pressure recording.

Fig 5 Typical Noise and Pressure results. Ram pressing against Cushion to simulate loading.

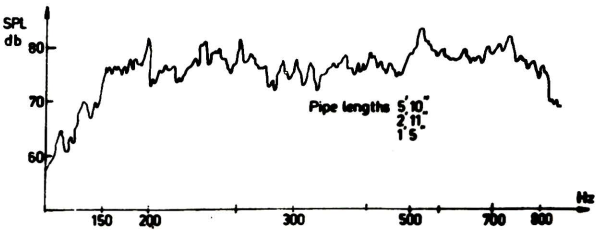

Stand Pipe, Ram speed 52 in/min

TYPE	SHAPE	EXPECTED ATTENUATION CHARACTERISTIC	EFFECT on SYSTEM, db — RAM SPEED, in/min: 40		46		52	
			SPL	IL	SPL	IL	SPL	IL
No Muffler	–	–	86	–	88	–	94	–
Stand Pipe	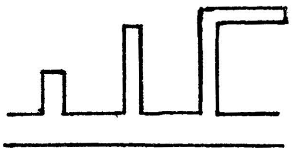	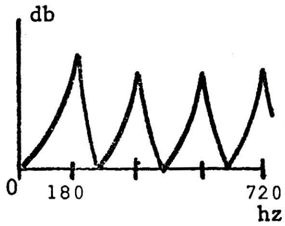	87	-1	90	-2	93	1
Single Chamber		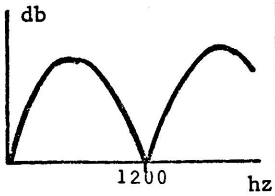	83	3	85	3	86	8
Double Chamber	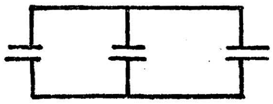	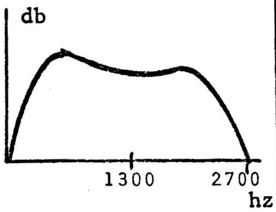	87	-2	89	-1	88	6
Perforated Tube	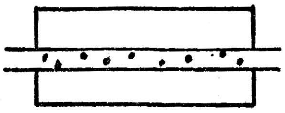	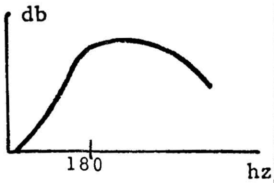	82	4	86	2	87	7

TABLE 2
Mufflers and their Effects
SPL - Sound Pressure Level, db
IL - Insertion Loss, db

The various means of reducing noise emission from hydraulic control systems are well documented. However, successful (or unsuccessful) applications of these techniques are not well documented, and so confirmed experience is not widely available. The case studied in the present paper, while by no means optimized in its suppression of noise, shows that noise reduction by muffling is both practical and effective.

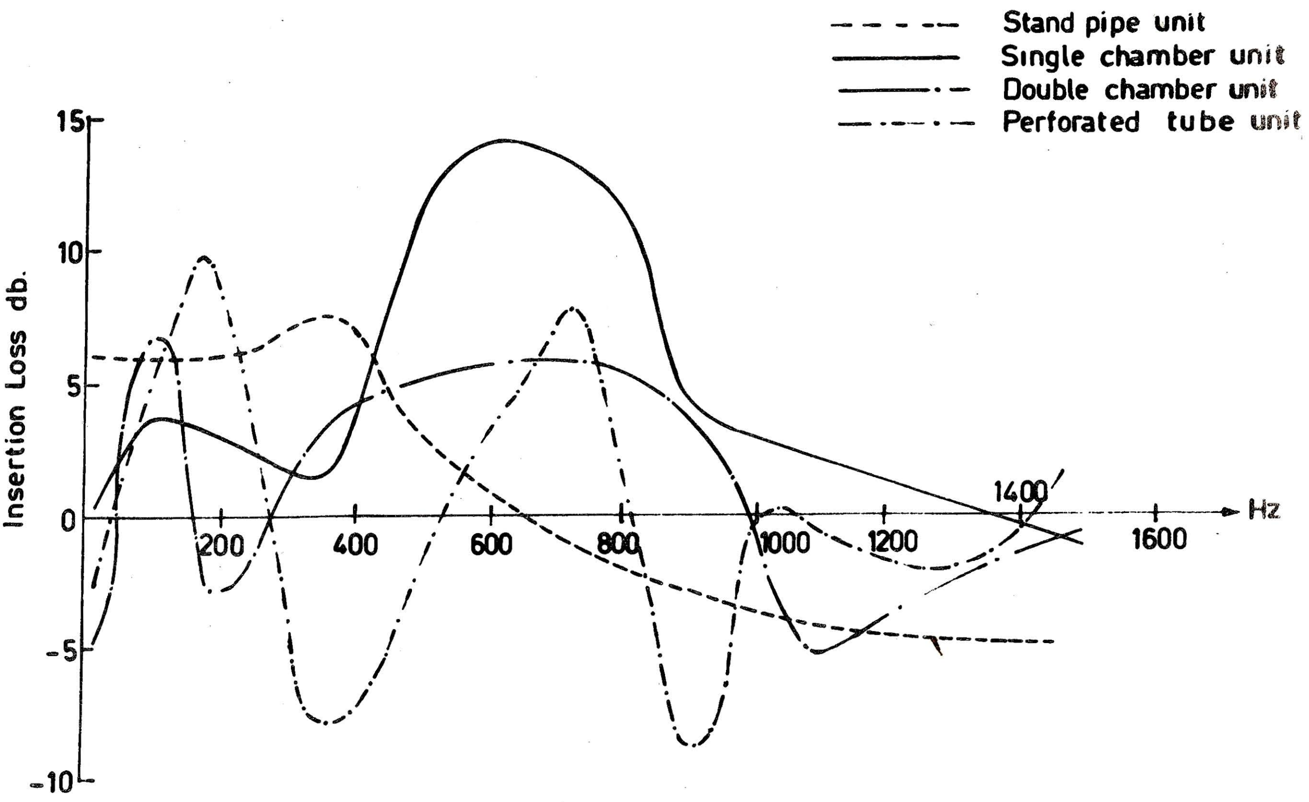

Fig. 6 Approx. Attenuation Effects of Mufflers.

6. REFERENCES

1. ANON. - Reducing the Operating Noise of Industrial Hydraulic Systems. Parker Hannifin Publication, Oct. 1962.
2. SKAISTIS, S.J., KENNAMER, D.E., and WALRAD, J.F. - Quieting of High-Performance Hydraulic Systems. Proc. 20th National Conference on Fluid Power, Oct. 22, 1964.
3. VAN HOENE, H.L., and PIETERSON, G.H. - Hydraulic System Noise. Machine Design, Feb.1, 1962.
4. YEAPLE, F.D. (editor) - Hydraulic and Pneumatic Power and Control. McGraw - Hill, 1966.
5. GREEN, W.L. - Cavitation in Hydraulic Components. Fluid Power International, July, 1967.
6. SULLIVAN, J.W. - Design for Quiet Hydraulic Systems. Machine Design, Sept. 14, 1967.
7. NOSS, J.S. - Can You Hear the Hydraulic System? Machine Design, Sept. 17, 1960.
8. RIFFENBURG, R.E. - Design for Quiet Mechanical Systems. Machine Design, Sept. 17, 1967.
9. GELMAN, A.S., and FURMAN, F.A. - Valve Oscillations in Hydrostatic Transmissions. Russian Engineering Journal, Vol 51, No. 6.
10. KANE, F., RICHMOND, T.D., and ROBB, D.N. - Noise in Hydrostatic Systems and Its Suppression. Hydraulic Pneumatic Power, Part 1, Jan. 1967, pp.26-40. Part 11, Feb. 1967, pp. 77-83.
11. BEYER, R. - Noise Reduction in Gear Pumps. Proc. Fluid Power International Conf., Lond, 1964
12. ZAHID, A. - Controlling Hydraulic System Pulsations. Automation, March 1973.
13. CHARSON, G.L. - Will You Reduce Noise on Your Designs for the 1970's? Hydraulic and Pneumatics, Nov. 1969.
14. ANON. - Fluid Power Design Engineers Handbook. Parker - Hannifin (Australia) Pty Ltd.
15. CURRIE, J.A. - The Design of Low Noise Hydraulic Circuits and Components. NEL Report.
16. BASHTA, T.M. - Noise in Machine Hydraulic Systems. Russian Engineering Journal, V51N6.
17. ZAICHENKO, I.Z., and BOLTYANSKII, A.D. - Reducing Noise Level of Axial-Piston Pumps. Russian Engineering Journal, Vol. 49, No. 4.
18. DIEHL, G.M. - Think Quiet. Compressed Air publication, 1971.
19. ANON.- Roaring Valves, Screaming Jets, Whining Compressors Challenged. Product Engineering, Dec. 15, 1968.
20. WILKINS, P. - Noise in Hydraulic Systems. Final Year Project Monash University, 1970.

Noise, Shock & Vibration Conference, 1974 Monash University, Melbourne

ON THE CORRELATION OF THE ACOUSTIC PRESSURE AND VELOCITY FIELD OF AN UNHEATED, PULSATING AIR JET

K. Bremhorst
Department of Mechanical Engineering
University of Queensland
St. Lucia, Queensland

W. H. Harch
Department of Mechanical Engineering
University of Queensland
St. Lucia, Queensland

SUMMARY

Broad-band cross-correlations between the acoustic pressure at a field point and the square of the instantaneous velocity at a point in the flow field of an unheated, pulsed jet were used in an attempt to locate regions of significant noise production. Results were found to be relatively insensitive to changes of position in the flow field. Spectral correlations were also measured. These reflect distinct features of the flow and are quite sensitive to changes of position in the flow field. The spectral results show the existence of a contribution to the total noise at the pulsating frequency and some higher harmonics, as well as a significant broad-band contribution at higher frequencies. This is in agreement with observed sound pressure level readings near the jet but when carried further than in the present work, will yield the location of the source within the flow of the various frequency components.

INTRODUCTION

The noise emitted by pulsating sources such as exhausts from reciprocating or impact type air tools is being investigated in the Department of Mechanical Engineering at the University of Queensland. One method of investigation already described by Hooker et al (2) gives information concerning the spatial distribution of sound pressure level. The situation investigated consisted of a rotating valve which simulated exhausts from pneumatic tools such as rock drills. Results indicate that, although the exhaust is strongly pulsating, the noise perceived by the human ear is not predominantly a pulsating one but, instead, it sounds like a steady jet with a small pulsating contribution.

Since sound emitted from the exhaust and the velocity field of the exhaust jet are intimately linked, a separate line of investigation was commenced. The objectives of this were to obtain information about the velocity field and the contribution to the acoustic pressure at a field point made by different regions of the jet using cross-correlations between the acoustic pressure at a field point and the velocity components in the jet - a method pioneered by Lee (3) in a steady jet.

THEORETICAL CONSIDERATIONS

For an unheated, turbulent air jet in which the viscous stresses are negligible compared with inertial stresses and in which molecular heat conduction is negligible, an approximate form of the instantaneous momentum equation which describes the acoustic pressure fluctuations generated by the flow can be written as

$$\frac{1}{c_0{}^2}\frac{\partial^2 p(\underline{x},t)}{\partial t^2} - \frac{\partial^2 p(\underline{x},t)}{\partial x_i{}^2} = \rho_0 \frac{\partial^2 (u_i u_j)}{\partial x_i \partial x_j} \tag{1}$$

where c_0 is the time average of the speed of sound, ρ_0 the ambient air density, and a repeated index implies summation. This equation follows from Lighthill (4). It is the classical wave equation of the acoustic pressure, $p(\underline{x},t)$, with a source distribution represented by the right hand side of Eq.(1), the source strength per unit volume being $\rho_0\ \partial^2(u_i u_j)/\partial x_i \partial x_j$.

The solution of Eq.(1) in an unbounded medium is given by the Kirchhoff retarded potential solution,

$$p(\underline{x},t) = \frac{\rho_0}{4\pi}\int_\infty \left|\frac{\partial^2 u_i u_j(\underline{y},t)}{\partial y_i \partial y_j}\right|_{\tau_0} \frac{d^3\underline{y}}{|\underline{x}-\underline{y}|} \tag{2}$$

where $|\ \ |_{\tau_0}$ denotes evaluation at the retarded time given by $(\tau-\tau_0)$, τ_0 being $|\underline{x}-\underline{y}|/c_0$. If the surface integral of $u_i u_j$ vanishes at infinity, $|\underline{x}-\underline{y}|$ is much longer than a typical wavelength and $|x|>>|\underline{x}-\underline{y}|$ then Eq.(2) may be rewritten in the form due to Proudman (5),

$$p(\underline{x},t) = \frac{\rho_0}{4\pi\ c_0{}^2|\underline{x}|}\int_\infty \left|\frac{\partial^2 u_x{}^2}{\partial t^2}\right|_{\tau_0} d^3\underline{y} \tag{3}$$

where u_x is the component of the instantaneous velocity in the $\underline{x}$ direction, $\underline{x}$ being the position vector from the origin of the co-ordinate system to the point $\underline{x}$, where $p(\underline{x},t)$ is measured (refer Fig. 1).

If $p(\underline{x},\underline{y},t)$ denotes the acoustic pressure at $\underline{x}$ contributed by unit volume at $\underline{y}$ then from Eq.(3) it follows that,

$$p(\underline{x},\underline{y},t) = \frac{\rho_0}{4\pi\ c_0{}^2|\underline{x}|}\left|\frac{\partial^2\ u_x{}^2}{\partial t^2}\right|_{\tau_0} \tag{4}$$

Using this result the contribution to the acoustic pressure at $\underline{x}$ from any unit volume at $\underline{y}$ in the jet can be found by cross-correlating the acoustic pressure at $\underline{x}$, $p(\underline{x},t)$, as measured by a microphone, with the quantity on the right hand side of Eq.(4) for which u_x can be obtained with hot wire anemometers at $\underline{y}$. Such correlations can also be performed on a spectral basis which would then yield the spectral contributions to the acoustic pressure made by different parts of the jet.

Letting $p^1(\underline{x},t)$ denote the acoustic pressure measured at $\underline{x}$ with a microphone then, as shown by Lee (1971), $C_{p^1p}(\underline{x},\underline{y},\tau_0)$ defined by Eq.(5) below is $\rho_0 c_0$ times the acoustic intensity at $\underline{x}$ due to unit volume at $\underline{y}$ and if $C_{p^1p}(\underline{x},\underline{y},\tau_0,f)$, defined by Eq.(6), is the spectral contribution then its relation to $C_{p^1p}(\underline{x},\underline{y},\tau_0)$ is given by Eq.(7).

$$C_{p^1p}(\underline{x},\underline{y},\tau_0) = \overline{p^1(\underline{x},t)\ p(\underline{x},\underline{y},t)} = \frac{\rho_0}{4\pi\ c_0{}^2|\underline{x}|}\ \overline{p^1(\underline{x},t)\left|\frac{\partial^2 u_x{}^2}{\partial t^2}\right|_{\tau_0}} \tag{5}$$

where $\overline{\qquad}$ denotes time averaging.

$$C_{p^1p}(\underline{x},\underline{y},\tau_0,f) = \overline{p^1(\underline{x},t,f)\ p(\underline{x},\underline{y},t,f)} = \frac{\rho_0}{4\pi\ c_0{}^2|\underline{x}|}\ \overline{p^1(\underline{x},t,f)\left|\frac{\partial^2 u_x{}^2}{\partial t^2}(f)\right|_{\tau_0}} \tag{6}$$

$$C_{p^1p}(\underline{x},\underline{y},\tau_0) = \int_0^\infty C_{p^1p}(\underline{x},\underline{y},\tau_0,f)df \tag{7}$$

The results of Eq.(5) could be applied directly but the double time differentiation of the instantaneous velocity signal would make such an approach doubtful from the practical viewpoint because of the very large noise-to-signal ratio which would result. It should be noted, however, that if the noise resulting from the double differentiation is uncorrelated with the turbulence and pressure signals, - a generally reasonable assumption - then the cross-correlations would be unaffected although correlation coefficients (cross-correlations normalized on the r.m.s. values of p and p^1) would be affected.

The need to double differentiate the velocity signal can be avoided if the signals are statistically stationary. For this latter case,

$$\overline{p^1(\underline{x},t) \left| \frac{\partial^2 u_x{}^2}{\partial t^2} \right|_{\tau_0}} = \frac{\partial^2}{\partial \tau^2} \overline{p^1(\underline{x},t)|u_x{}^2|_{\tau_0}} = \frac{\partial^2}{\partial \tau^2} C_{p^1 u_x{}^2}(\underline{x},\underline{y},\tau_0) \qquad (8)$$

which can be substituted in Eq.(5) to yield,

$$\text{Intensity at } \underline{x} \text{ due to unit volume at } \underline{y} = \frac{1}{4\pi\, c_0{}^3 |\underline{x}|} \frac{\partial^2}{\partial \tau^2} C_{p^1 u_x{}^2}(\underline{x},\underline{y},\tau_0) \qquad (9)$$

To find the contribution to acoustic intensity made by different parts of the jet then only requires cross-correlation of $p^1(\underline{x},t)$ and $u_x{}^2$ and evaluation of the curvature of the resultant correlation curve at τ_0. For qualitative results as desired in the present work, it is, therefore, sufficient to plot the correlation curves $C_{p^1 u_x{}^2}(x,y,\tau)$ against τ at various points in the flow and by inspection compare the curvatures at the various points in the flow at τ_0. This provides a very quick evaluation of the relative importance of different parts of the flow in the production of noise.

Similarly, the practical aspects of obtaining spectral results can be improved significantly through use of the Fourier transform of Eq.(9). The result is shown by Eq.(10) and the formal details are contained in Lee (3).

$$\text{Intensity at } \underline{x} \text{ due to unit volume at } \underline{y} \text{ associated with frequency } f = \frac{-\pi}{c_0{}^3 |\underline{x}|} f^2 C_{p^1 u_x{}^2}(\underline{x},\underline{y},\tau_0,f) \qquad (10)$$

where $C_{p^1 u_x{}^2}(\underline{x},\underline{y},\tau_0,f) = \overline{p^1(\underline{x},t,f)|u_x{}^2(f)|_{\tau_0}}$

Using the result of Eq.(6) would require double differentiation followed by narrow-band filtering which is quite feasible, but the result of Eq.(10) avoids the need for such a procedure and requires the correlation of filtered pressure and velocity squared signals only, followed by a simple multiplication by frequency squared.

The present investigation applied aspects of the above results to an unheated, pulsed jet.

EXPERIMENTAL APPARATUS

The Department did not have an anechoic chamber at the time of the present investigations, thus requiring all tests to be carried out in a laboratory. However, since time delayed cross-correlations were used the effect of reflection on the end results is small. The pulsed jet was produced by a rotating ball valve which discharged to atmosphere through a 0.75 in (1.91 cm) dia throat. The acoustic pressure was measured using a B&K type 4145 one inch diameter condenser microphone, placed at $|\underline{x}| = 6$ ft (183 cm) and 40^0 horizontally from the jet axis, valve rotation being in the vertical plane. The assumptions used to arrive at Eq.(3) are, therefore, not entirely valid at frequencies below approx. 200 Hz but in view of the significant simplification permitted by the result, no attempt was made to introduce appropriate corrections.

Velocity measurements were made with a linearized, constant temperature hot wire anemometer. A single wire 5μm dia x 0.75 mm long of tungsten was placed normal to the flow direction, thus responding to the instantaneous velocity in the mean flow direction and was taken to be proportional to u_x.

Practical details such as hot wire calibration, mass flow measurement, hot wire preparation and mounting, and hot wire probe design to minimize vibration are documented fully in Harch (1). Silencing of the air supply to the rotating valve was not used. The effect on the cross-correlations of noise generated by valves and fittings should, however, be negligible, provided that the flow is not affected by such acoustic disturbances.

Signal processing equipment consisted of special purpose wide-band amplifiers, a wide-band multiplier to form u_x^2, a 14 channel Hewlett-Packard FM tape recorder operated at 60 in/sec for record and playback, a Hewlett-Packard Model 3721A correlator, and two B&K type 2107 narrow-band analysers.

EXPERIMENTAL RESULTS

In view of the vast amount of time consuming signal processing required to obtain results outlined in the theoretical section, correlation measurements were limited to one $\underline{x}$ station and vertical diametral velocity traverses at 3, 5, 7 and 9 exit diameters from the valve outlet.

Mean velocity measurements are shown in Fig. 2 which like the steady jet velocity profiles have the typical bell shape. The maxima of these are replotted in Fig. 3 and compared with the decay law for a steady jet. For the range of measurements the pulsed jet and steady jet trends are identical.

Typical broad-band correlations are shown in Fig. 4 where $C_{p^1 u_x^2}(\underline{x},\underline{y},\tau)$ has been normalized using the r.m.s. value of u_x^2 at the centre line of the jet for the particular x_1/D position and the r.m.s. of the acoustic pressure signal. Thus, the relative contribution to the acoustic intensity from different radial positions at a given x_1/D can still be obtained by inspection.

Correlograms are shown for time delays up to 28 msec although only the shape at $\tau=\tau_0 \approx 5.25$ msec is required. Unfortunately, the curvature at $\tau=\tau_0$ does not vary significantly with radial position and, therefore, indicates that broad-band correlations are insufficiently sensitive for firm conclusions to be drawn. A trend towards greater curvature as the edge of the jet is approached can, however, be seen for all x_1/D. It is also noteworthy that quite high correlation coefficients exist at large τ, but at the required retarded time of τ_0, values are in the range 0 to ±0.2. The fact that correlation curves at diametrically opposed points are not identical is an indication of the lack of axisymmetry in the jet - a result to be expected with the type of valve used, but not readily detectable from the velocity results of Fig. 2. The very high correlation coefficients at $\tau>\tau_0$ are attributed to reflections from surrounding equipment, walls ceiling and floor of the laboratory.

A typical plot of $C_{p^1 u_x^2}(x,y,\tau,f)$ is shown in Fig. 5 and as expected, the value of τ at the peak of the cross-correlation curve corresponds closely with the time taken for an acoustic signal to be propagated at sonic velocity from $\underline{y}$ to $\underline{x}$. A plot such as Fig. 5 is required for each frequency of interest, at every radial position in the flow thus making it an extremely time consuming measurement. These data can then be combined as in Fig. 6 where the ordinate is $f^2 C_{p^1 u_x^2}(\underline{x},\underline{y},\tau_0,f)$ which from Eq.(10) is directly proportional to the acoustic intensity at $\underline{x}$ due to turbulence in unit volume at $\underline{y}$ at frequency f.

Some uncertainty exists with these results because of the large spectral peaks at the pulsating frequency and the first few harmonics which could not be analysed accurately with the available analysis equipment.

It is expected, however, that such components give rise to narrow spectral peaks as indicated by the dashed lines in Fig. 6 where the points between the discrete frequencies are actually measured values.

The results of Fig. 6 show quite clearly that even close to the jet exit a significant contribution to the intensity is made by the high frequency components which are spread over a broad band compared with the low frequency components which approach a pure tone. Although results were obtained only at $x_1/D = 3$, it is reasonable to expect that the contribution of the high frequency, broad-band type of noise to the total noise will increase with x_1/D. This is then in agreement with the qualitative observations outlined in the beginning of the paper.

CONCLUSIONS

The feasibility of measuring the contribution to jet noise made by different parts of the flow has been established. Broad-band measurements were found to lack sensitivity to changes of position in the flow but spectral measurements overcame this problem. The latter showed that even close to the jet exit, a significant high frequency, broad-band contribution to total noise exists. Application of the measurement technique to other flow situations is now possible.

REFERENCES

1. HARCH, W.H. (1974): "On the Correlation of the Acoustic Pressure and Velocity Field of an Unheated Pulsating Air Jet". M.Eng.Sc. Thesis, Department of Mechanical Engineering, University of Queensland.

2. HOOKER, R.J., RUMBLE, R.H. and ANDREWS, M.H. (1974): "Experimental Study of Noise from a Pulsed Jet". N.S.V. Conference, Monash University.

3. LEE, H.K. (1971): "Correlation of Noise and Flow of a Jet". UTIAS Report No. 168, Institute for Aerospace Studies, University of Toronto.

4. LIGHTHILL, M.J. (1952): "On Sound Generated Aerodynamically I - General Theory". Proc.Roy.Soc. A. 211, 564-587.

5. PROUDMAN, I. (1952): "The Generation of Noise by Isotropic Turbulence". Proc.Roy.Soc. A. 214, 119-132.

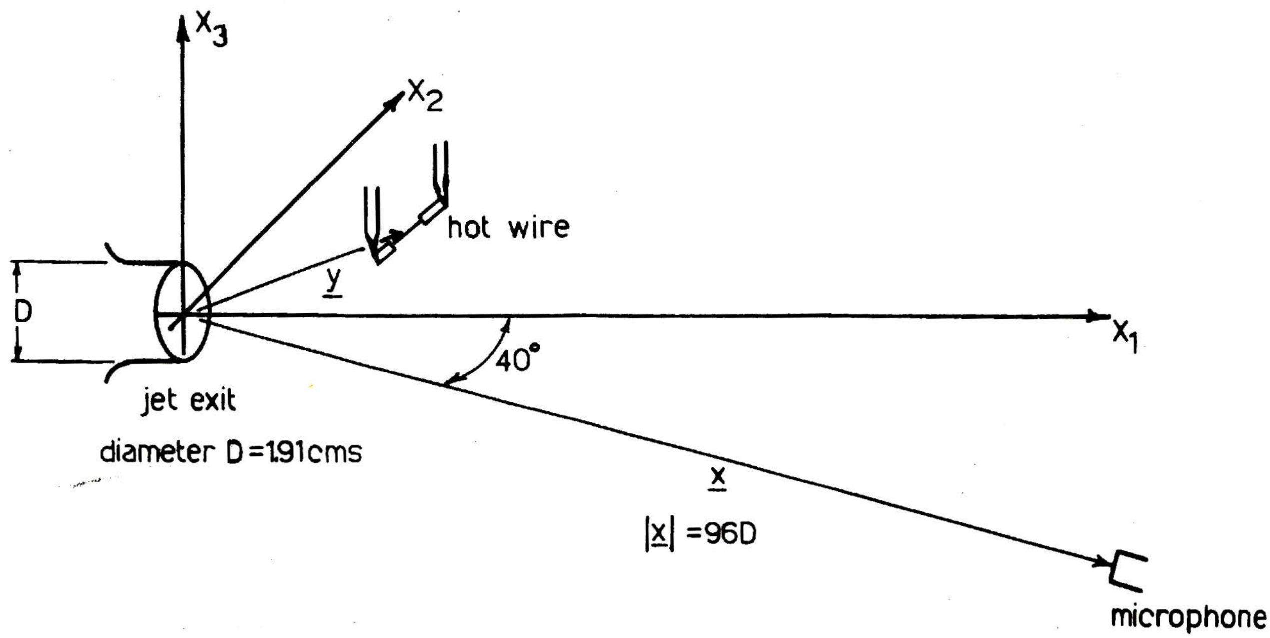

CO-ORDINATE SYSTEM

FIG 1

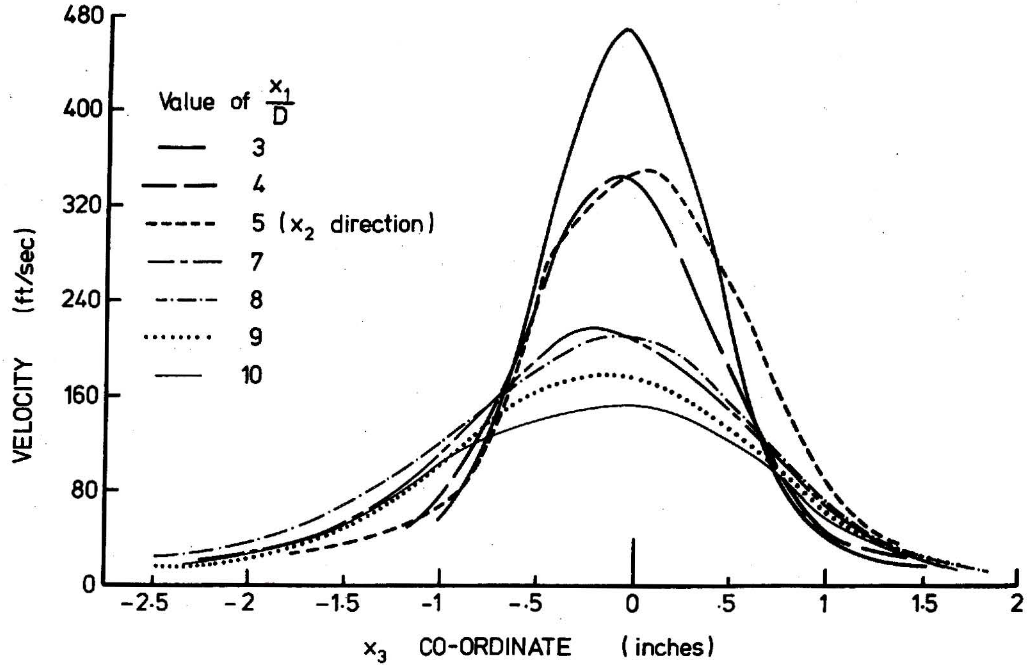

FIGURE 2. Average Velocity Distributions.

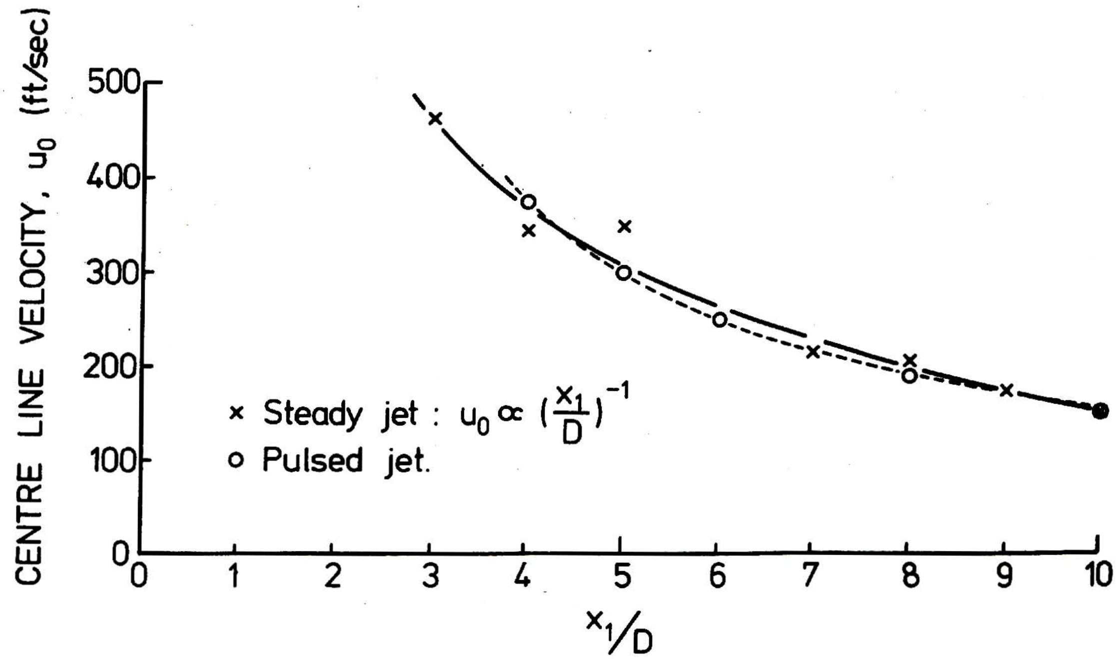

FIGURE 3. Comparison of Average Centre Line Velocity of Steady and Pulsed Jets.

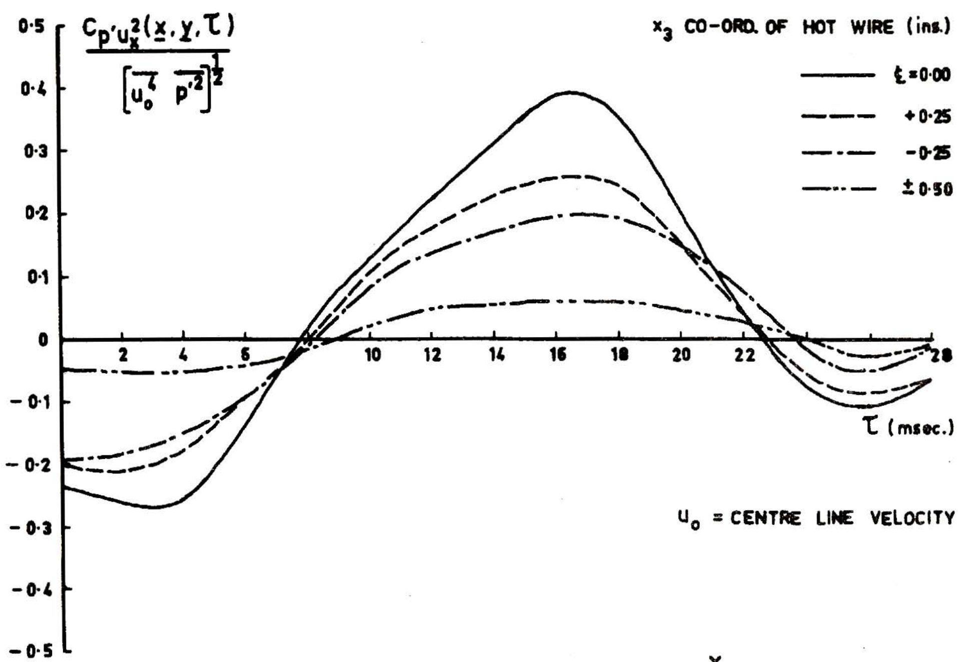

BROAD-BAND CORRELATION CURVES. $\dfrac{x_1}{D} = 3$

FIG. 4

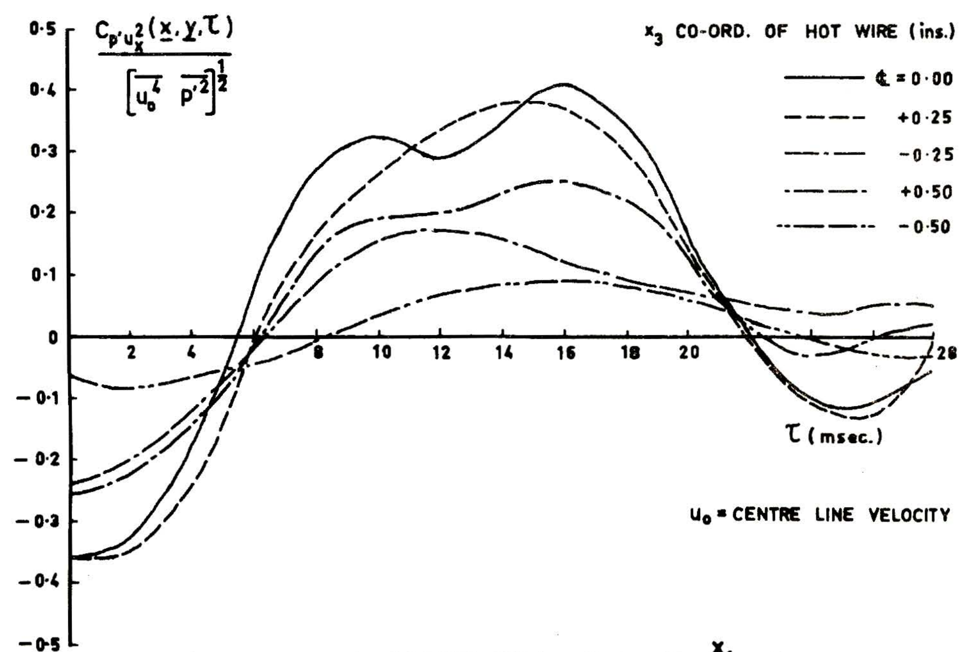

BROAD-BAND CORRELATION CURVES. $\dfrac{x_1}{D} = 5$

FIG. 4 cont.

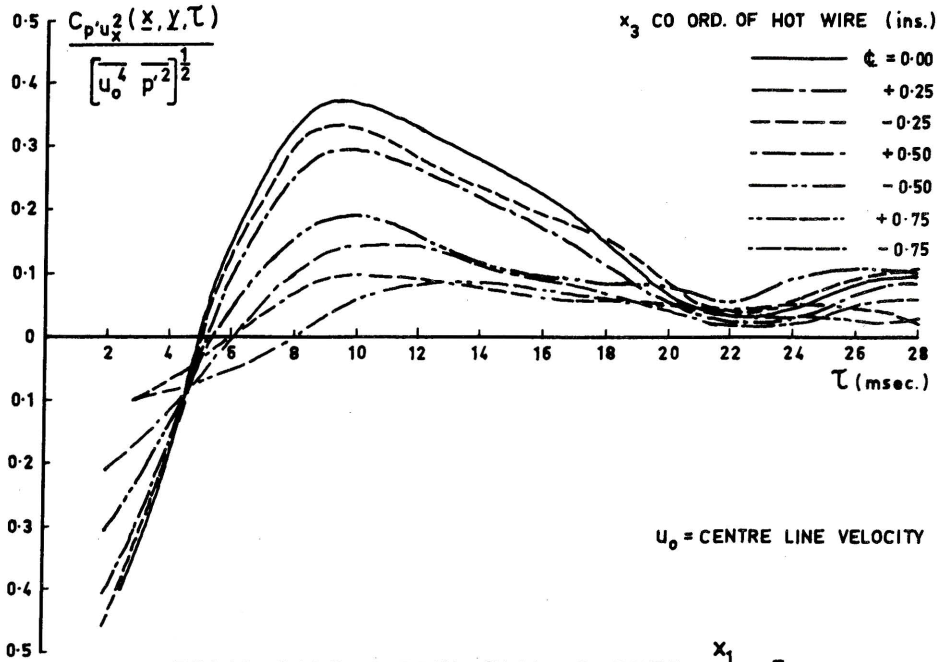

BROAD-BAND CORRELATION CURVES. $\frac{x_1}{D} = 7$

FIG. 4 cont.

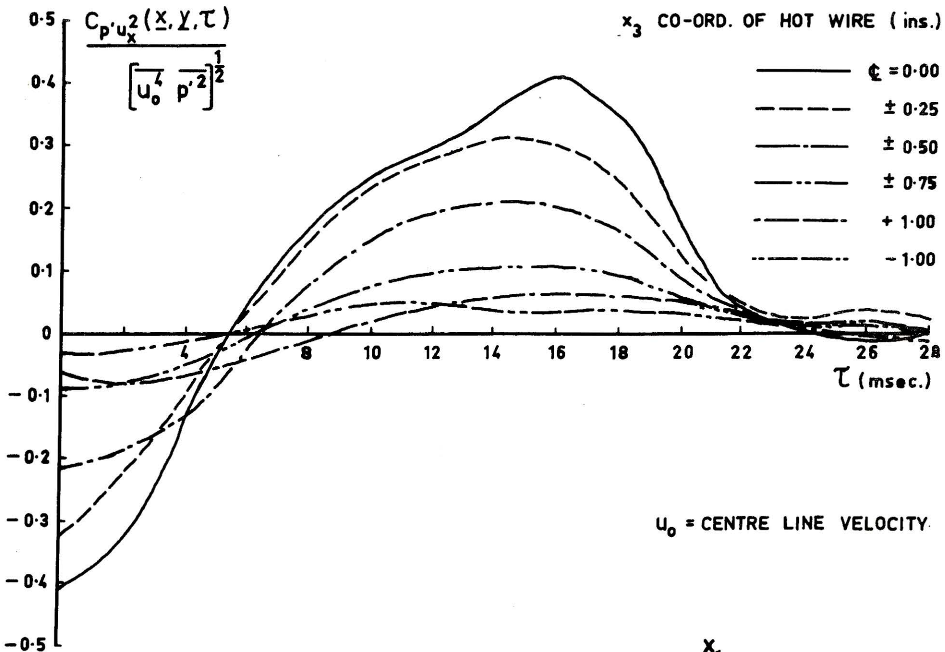

BROAD-BAND CORRELATION CURVES. $\frac{x_1}{D} = 9$

FIG. 4 concluded

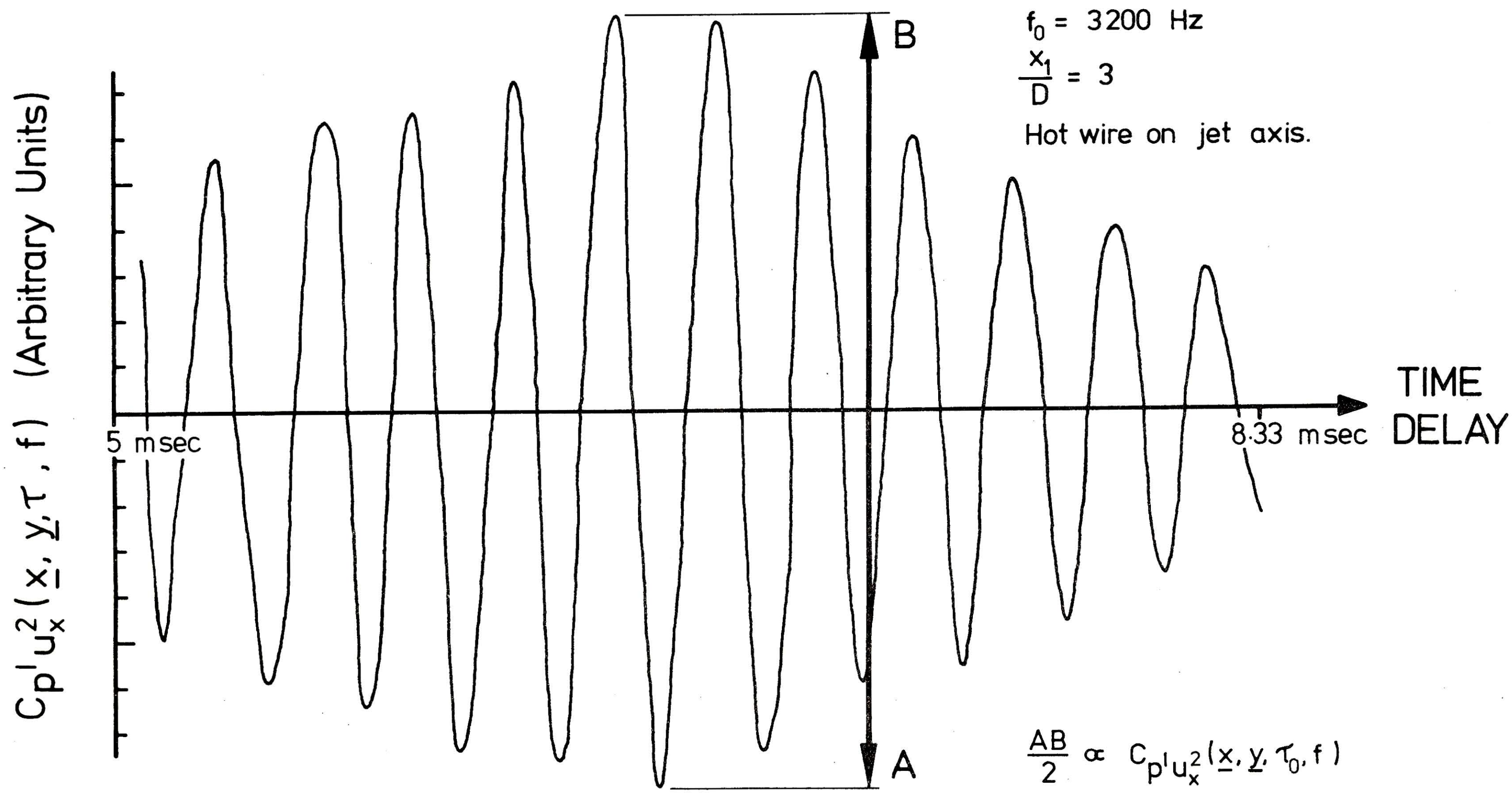

FIGURE 5. Typical Narrow-Band Cross Correlation.

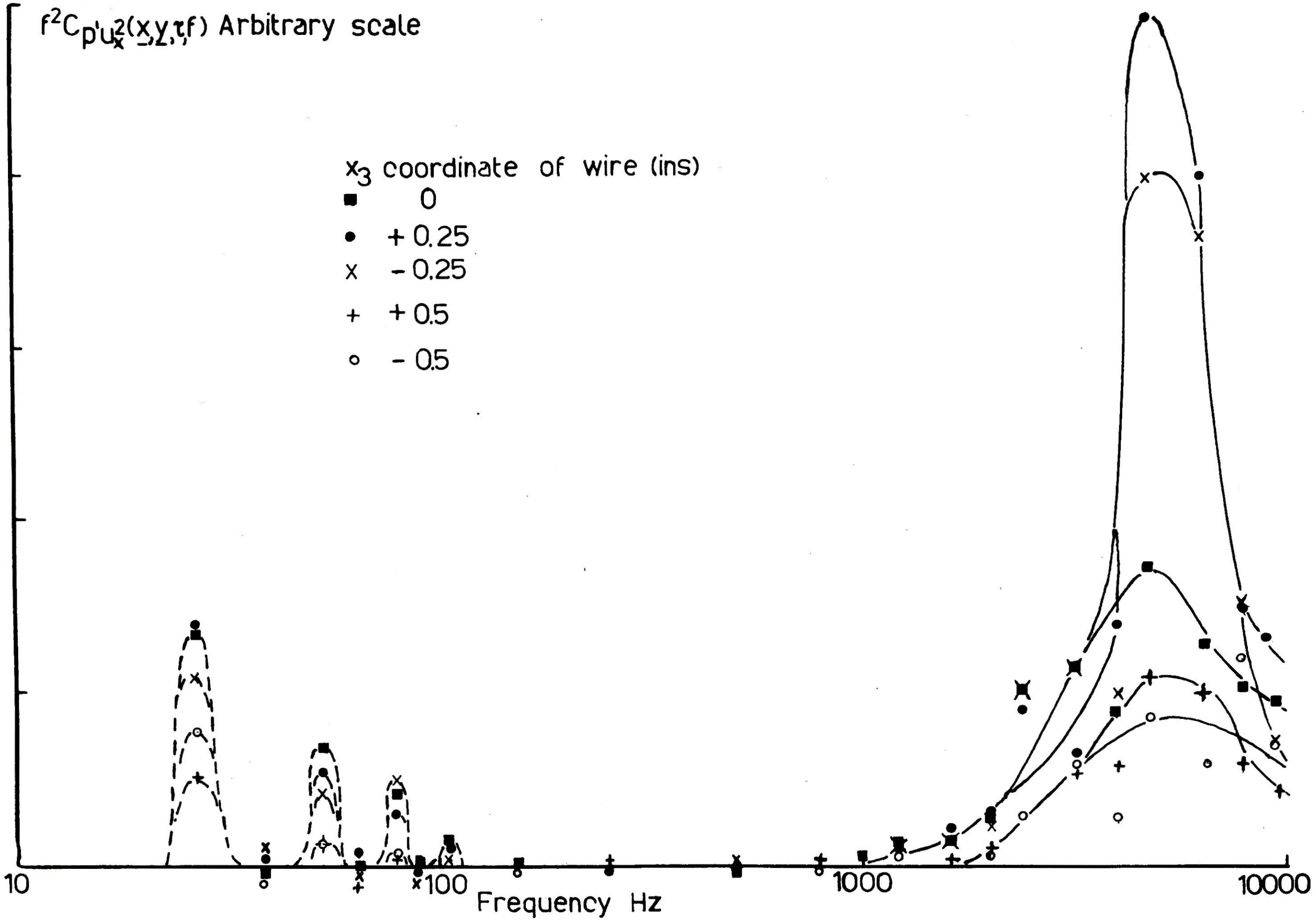

SPECTRAL CORRELATIONS OF u_x^2 AND p'

FIG.6

Noise, Shock & Vibration Conference, 1974 Monash University, Melbourne

A NEW CONCEPT FOR THE USE OF VISCO-ELASTIC MATERIALS IN THE DAMPING OF STRUCTURES

Y. G. Jullien
Centre de Recherches Physiques
Marseilles, France

SUMMARY -

Theoretical and experimental investigations have been performed on the damping of structures by viscoelastic layers. Total loss factor and the effect of the parameters in the constitutive law of the material have been determined. This paper investigates the optimum distribution of the viscoelastic material placed on the structure and yielding maximum structural damping. The transverse motion of a heterogeneous beam (with and without damping) is given by the solution of the unidimensional problem formulation. The eigen values in the solution are given by a determinant $\Delta(\eta,x)$ of 8th order, in accordance with the conditions at the boundary and junctions. The damped part x of the beam which produces maximum damping is given by $\Delta_x'(\eta,x)=0$, solved on the computer. Theoretical and experimental results are compared.

1. INTRODUCTION

We know that vibrations of structures used in mechanical and civil engineering can reach amplitudes which generate noise and which become annoying to humans. By changing the geometry of the structure it is possible sometimes to reduce the vibration but in most cases this reduction is insufficient. For this reason the use of viscoelastic material layers in structures has assumed an important role during the last years. The methods used for the determination of the total loss factor of structures with viscoelastic layers are still uncertain, and the selection and optimal placement within the structure of viscoelastic layers is a process which has been the subject of argument. For the case of simple viscoelastic layers, results have been given for bending mode vibrations by Lienard [1] and Oberst [2]. Oberst gave further optimized results specifically for amorphous high polymers [3]. These experimental results were found to be in good agreement with the previous theoretical work of Ruzicka [4]. Later, more accurate theoretical investigations have been reported, dealing with the problem of unsymmetrical three layer beams in transverse vibration: position of the neutral axis with constrained viscoelastic layers, distribution of shear stresses and vibration characteristics were studied for the purpose of maximizing damping. We shall mention here only the works of Kerwin [5] [6] and Di Taranto [7] [8] which represent fine contributions to the beam problem, and the study of Yu [9] [10] in the case of plates. By giving consideration to the boundary conditions, Mead and Markus [11] showed how the above results can be applied to practical cases. In a different context, Jullien [12] investigated the influence of a non linear constitutive law of viscoelastic material on the well known results of bending vibrations of composite beams.

A survey of these studies shows that analytical spatial optimization has not been considered, however, empirical solutions to this important problem are given. For instance, we know that different waves in solid bodies are influenced differently by damping layers and if we are able to identify these waves, we can arrange, according to the method of Heckl [13], viscoelastic materials so that the radiation of sound can efficiently be reduced. Using the same idea, it is possible to cover only a part of the structure by viscoelastic material when we want to reduce the bending vibrations of a girder which has a particular cross section; it is known that viscoelastic damping materials are necessary on the base and on the flange but not on the web of the girder. We see that, by intuitive arguments, we are able to solve some particular problems of distribution of the damping material on the structure. But we do not have the solution to the following general problem of optimal distribution: given a vibrating structure, which domain is to be covered by viscoelastic material for maximum damping? Expressed mathematically, it is required to find a unique solution to a boundary value problem which is defined by different partial differential operators. These operators are determined by the characteristics of the domain under consideration. In other words, the boundary and joint conditions must be compatible, whatever the form of the differential operators. Expressed in this general form, the problem is very difficult. For simplicity, therefore, only the bending mode vibrations of a one dimensional beam system will be studied.

2. STATEMENT OF THE PROBLEM

Let us consider a beam (figure 1) simply supported at the ends, damped on a length (b-a) by a viscoelastic constrained layer. The variables of such a damped sandwich beam are:

E_1 Young's modulus, h_1 thickness, I_1 transverse moment of inertia of the elastic constraint layer.

G complex shear modulus, h_2 thickness of the medial viscoelastic damping material.

E_3 Young's modulus, h_3 thickness, I_3 transverse moment of inertia, 1 total length of the elastic layer of the beam, when $0< x <a$ and $b< x <1$.

We know that the transverse motion W of the beam when the steady state is reached, is given by a differential equation:

$$L(W) - m\omega^2 W = 0 \tag{1}$$

in which m is the mass per unit length and $\omega = 2\Pi f$ angular velocity of the natural frequency f. L is a real fourth order differential operator when $0< x <a$ and $b< x <1$, but a complex sixth order linear differential operator when $a< x <b$. For reasons of compatibility of the real solutions that we have to get finally to solve the physical problem, the eigen value equation for the damped part (b - a) of the beam becomes a numerical fourth order equation. This result has been given by Mead and Markus [14], who showed that it is in good agreement with Di Taranto [7], for beam ends simply supported. Then the general solution of the vibrating composite system contains eight independent constants of integration, which derive from the two fourth order eigen value equations corresponding to the damped and undamped parts of the beam. Eight joint and boundary conditions are necessary to get the general eigen value equation, which is expressed as an eighth order determinant. The coefficients of this determinant are expressed in terms of the characteristics of the three layer (two elastic and one viscoelastic) beam, and of the natural frequency. Let us write:

$$F(\eta,a,b) = 0 \tag{2}$$

for the eigen value equation. The physical optimization problem becomes a variational problem, solved by:

$$F'_\eta\, d\eta + F'_b\, db + F'_a\, da = 0 \tag{3}$$

In the case where a = 0, the problem becomes easier, because η is maximum for $F'_b = 0$, indeed if a is fixed,

$$\frac{d\eta}{db} = -\frac{F'_b}{F'_\eta} \tag{4}$$

is maximum for $F'_b = 0$. It follows that solutions are to be found for b and η of equation (4). We see that the mathematical model, which we have chosen, leads without major difficulties to a variational equation giving the response to the following optimization problem: which are the abscissas a and b giving the maximum loss factor of a beam partially damped over a length (b-a)? The algebraic development will show that we get complicated expression for the function F; however there is no problem in getting numerical solutions to this function by computer.

3. THEORETICAL DEVELOPMENT

According to the figure 1, W_1, W_2, W_3, are respectively the general transverse motion for $0< x <a$, $a< x <b$, $b< x <1$.

3.1. Computation of W_1: $0< x <a$.

In this case, we know that the differential operator is a fourth order linear one, namely:

$$L \equiv \frac{\partial^4}{\partial x^4} - \lambda_1^4$$

in which

$$\lambda_1^4 = \frac{m\omega^2}{E_3 I_3}$$

The two boundary conditions $W_1(0) \equiv W_1''(0)=0$ for a simply supported beam must be satisfied. Thus the solution W_1 for $0< x <a$ depends only on two constants A and B of integration:

$$W_1 = A \operatorname{sh} \lambda_1 x + B \sin \lambda_1 x \tag{6}$$

3.2. Computation of W_2 = $a< x <b$.

In this case, we must consider the damped sandwich beam with three layers. Details of computation are given in the references [11] and [14], and we recall here only the principle of the method. If u_1 and u_3 are respectively the longitudinal displacements of the mid-planes of the upper and lower elastic layers, and if u is the longitudinal displacement component of any point in the medial viscoelastic layer, geometrical considerations lead to a simple relation between h_1, h_2, h_3, u, u_1, u_3 so that consistent with the assumption of zero longitudinal direct stress in the viscoelastic layer (which implies constant shear stress τ across the thickness), we get:

$$\tau = G\left[\left(1 + \frac{h_1 + h_3}{2h_2}\right) \frac{\partial \overline{W}_2}{\partial x} + \frac{u_1 - u_3}{h_2}\right] \tag{7}$$

The total shear force S on the cross-section of the composite beam is composed of the shear forces of the top and bottom elastic face-plates and the shear force in the viscoelastic layer acting uniformly between the mid-planes of the face-plates. Considering the equilibrium of the longitudinal forces, we find an additional relationship between u_1 and u_2 and the general equation of equilibrium is:

$$\frac{\partial S}{\partial x} = [D_1 + D_3] \left\{ \frac{\partial^4 \overline{W}_2}{\partial x^4} - \frac{G d^2}{h_2(D_1 + D_3)} \frac{\partial^3 \overline{W}_2}{\partial x^2} + \frac{Gd(E_1h_1 + E_3h_3)}{E_1h_1(D_1 + D_3)} \frac{\partial u_3}{\partial x} \right\} \tag{8}$$

where D_1 and D_3 are the flexural elastic rigidities of the face-plates and

$$d = h_2 + \frac{h_1 + h_3}{2}$$

is the distance between the mid-planes of the face-plates. Combining equation (8) and the relation for longitudinal force

$$E_3 h_3 \frac{\partial^2 u_3}{\partial x^2} = - \tau$$

and using equation (7), we obtain the general equation of transverse motion W_2:

$$\frac{\partial^6 \overline{W}_2}{\partial x^6} - M \frac{\partial^4 \overline{W}_2}{\partial x^4} = \frac{1}{D_1 + D_3}\left[\frac{\partial^3 S}{\partial x^3} - N \frac{\partial S}{\partial x}\right]$$

where

$$M = \frac{G}{h_2} \frac{(E_1h_1 + E_3h_3)}{E_1E_3h_1h_3} \left[1 + \frac{d^2}{D_1 + D_3} \cdot \frac{E_1E_3h_1h_3}{E_1h_1 + E_3h_3}\right] \tag{9}$$

and

$$N = \frac{G}{h_2} \frac{E_1h_1 + E_3h_3}{E_1E_3h_1h_3}$$

With harmonic excitation

$$\frac{\partial S}{\partial x} = - m \frac{\partial^2 \overline{W}_2}{\partial t^2} + F e^{i\omega t}$$

we can take for $\overline{W}_2$ (x,t) a separable form in x and t ($\overline{W}_2(x,t) = W_2(x)T(t)$). We get one differential equation of second order in T, and, assuming that an identity exists between the problem coefficients and those of the classical forced vibrations with global damping η, we may write:

$$\ddot{T} + \omega^2(1 + i\eta) = D\, e^{i\omega t}$$

we get finally for W_2 :

$$\frac{\partial^6 W_2}{\partial x^6} - M \frac{\partial^4 W_2}{\partial x^4} - \omega^2(1 + i\eta)\frac{m}{D_1 + D_3}\left[\frac{\partial^2 W_2}{\partial x^2} - NW_2\right] = 0 \tag{10}$$

In the case of the vibrating beam, we must get a real solution for W_2. If we separate real and imaginary parts of equation (10), we obtain two differential equations for W_2, one of sixth order, and the other of fourth order, Putting

$$W_2 = \sum_n \lambda_2^n\, e^{\lambda_2^n x}$$

We derive two algebraic characteristic equations of different order. The compatibility conditions show that only the equation of lower order can apply, so that we retain:

$$- N'\beta \lambda_2^4 - \omega^2 \frac{m}{D_1 + D_3}\left[\eta \lambda_2^2 - N'(\eta + \beta)\right] = 0 \tag{11}$$

Where

$$N' = \frac{G'}{h_2}\,\frac{E_1 h_1 + E_3 h_3}{E_1 E_3 h_1 h_3}$$

and the complex modulus G of the viscoelastic material having damping coefficient β is given by $G = G'(1 + i\beta)$. Equation (11) gives two solutions:

$$\begin{matrix}(\lambda_2)^2 \\ (\lambda_2')^2\end{matrix} = \frac{m\omega^2\eta}{(D_1 + D_3)\beta N'} \pm \sqrt{\left[\frac{m\omega^2\eta}{(D_1 + D_3)\beta N'}\right]^2 + \frac{4m\omega^2}{\beta(D_1 + D_3)}(\eta + \beta)} \tag{12}$$

and the general solution W_2 is, according to the linear differential equation of fourth order derived from equation (10):

$$W_2 = C_1 \cos\lambda_2 x + C_2 \sin\lambda_2 x + D_1\,\mathrm{ch}\,\lambda_2' x + D_2\,\mathrm{sh}\,\lambda_2' x \tag{13}$$

3.3. Computation of W_3: $b< x <1$.

The boundary conditions for this part of the beam are $W_3(1) \equiv W_3''(1) = 0$, so that the general solution depends only on two constants of integration, E and F:

$$W_3 = E\left[\mathrm{sh}\,\lambda_1 x - \frac{\mathrm{sh}\,\lambda_1 1}{\mathrm{ch}\,\lambda_1 1}\,\mathrm{ch}\,\lambda_1 x\right] + F\left[\sin\lambda_1 x - \frac{\sin\lambda 1}{\cos\lambda 1}\cos\lambda_1 x\right] \tag{14}$$

3.4. Boundary and Joint Conditions:

Before considering general conditions, let us examine the particular case a = b, which gives $W_2 = 0$. The additional four boundary conditions are: $W_1(1) \equiv W_1''(1) \equiv W_3(0) \equiv W_3''(0) = 0$. We will find without difficulty that this means $A \equiv E = 0$ and $\mathrm{sh}\,\lambda_1 = 0$ according to the well known eigen value equation of a simply supported bending beam. Writing the joint condition $W_1(a) = W_3(a) \rightarrow B\sin\lambda_1 a = F \sin\lambda_1 a$, we get B = F. This argument shows that we can simplify the above results by taking E = A and F = B in the expression for W_3, which gives six integrating constants A, B, C_1, C_2, D_1, D_2.

The continuity equations may be written by inspection: transverse motion, bending moment and shear force must be the same on both sides of sections x = a and x = b. Thus:

$$\begin{gathered} W_1(a) = W_2(a)\ ;\ M_{F_{W_1}}(a) = M_{F_{W_2}}(a)\ ;\ S_{W_1}(a) = S_{W_2}(a) \\ W_2(b) = W_3(b)\ ;\ M_{F_{W_2}}(b) = M_{F_{W_3}}(b)\ ;\ S_{W_2}(b) = S_{W_3}(b) \end{gathered} \tag{15}$$

The expressions of bending moment M_F and shear force are different for $0< x <a$, $b< x < \ell$ and $a< x <b$, and are given by:

$$M_{F_{W_1}}(x) = EI\,W_1''(x) \; ; \; S_{W_1}(x) = -\,EI\,W_1'''(x) \tag{16}$$

$$M_{F_{W_2}}(x) = -\frac{D_1 + D_3}{N}\left[\frac{\partial^4 W_2}{\partial x^4} - M\,\frac{\partial^2 W_2}{\partial x^2} - \frac{m\omega^2}{D_1 + D_3}(1 + i\eta)\,W_2\right] \tag{17}$$

$$S_{W_2}(x) = -\frac{D_1 + D_3}{N}\left[\frac{\partial^5 W_2}{\partial x^5} - M\,\frac{\partial^3 W_2}{dx^3} - \frac{m\omega^2}{D_1 + D_3}(1 + i\eta)\,\frac{\partial W_2}{dx}\right] \tag{18}$$

$$M_{F_{W_3}}(x) = EI\,W_3''(x) \; ; \; S_{W_3}(x) = -\,EI\,W_3'''(x) \tag{19}$$

Equations (17) and (19) for the uncovered beam are the classical formulas derived from the basic laws of strength of materials. Equation (18) is obtained by application of the relation

$$S = \frac{\partial M_F}{\partial x}$$

to equation (17). Equation (17) may be obtained in two different ways: either by integrating twice equation (9) and taking account of the relationship between $\bar{W}_2$ and W_2, or by using the definition of the total bending moment, which is the sum of the bending moments

$$D_1\,\frac{\partial^2 W_2}{\partial x^2}, \qquad D_3\,\frac{\partial^2 W_2}{\partial x^2}$$

of the face-plates and the bending moment in the medial viscoelastic layer $M_2 = -\int \tau d.dx$. This can easily be shown from equation (7) and the relation

$$\frac{\partial^2 u_3}{\partial x^2} - N u_3 = -\,\frac{Gd}{h_2 E_3 h_3}\cdot\frac{\partial W_2}{\partial x}\ .$$

We will get the same result by integrating (9). Equations (17) and (18) are not simple but they are linear in terms of the constants A,B,C_1,C_2,D_1,D_2. If we write the six equations (15) using (16)(17)(18) and (19), we get six linear equations in terms of the six constants for which the term of order zero is null. We know that the solution is indefinite only if the determinant of the coefficients of the constants is equal to zero which is in agreement with the basic theory of vibrations of elastic systems [15]. Writing the determinant for the six equations, we get the expression of the general eigen value equation of the system.

3.5. Eigen Values.

The determinant described above is: F = 0, i.e.

$$\begin{vmatrix}
-\,\mathrm{sh}\,\lambda_1 a & -\sin\lambda_1 a & \cos\lambda_2 a & \sin\lambda_2 a & \mathrm{ch}\,\lambda_2' a & \mathrm{sh}\,\lambda_2' a \\
-\,\mathrm{sh}\,\lambda_1 b + p\,\mathrm{ch}\,\lambda_1 b & -\sin\lambda_1 b + q\cos\lambda_1 b & \cos\lambda_2 b & \sin\lambda_2 b & \mathrm{ch}\,\lambda_2' b & \mathrm{sh}\,\lambda_2' b \\
-\,\mathrm{sh}\,\lambda_1 a & \sin\lambda_1 a & X\cos\lambda_2 a & X\sin\lambda_2 a & Y\,\mathrm{ch}\,\lambda_2' a & Y\,\mathrm{sh}\,\lambda_2' a \\
-\,\mathrm{sh}\,\lambda_1 b + p\,\mathrm{ch}\,\lambda_1 b & \sin\lambda_1 b - q\cos\lambda_1 b & X\cos\lambda_2 b & X\sin\lambda_2 b & Y\,\mathrm{ch}\,\lambda_2' b & Y\,\mathrm{sh}\,\lambda_2' b \\
-\,\mathrm{ch}\,\lambda_1 & +\cos\lambda_1 a & -X\sin\lambda_2 a & X\cos\lambda_2 a & Y\,\mathrm{sh}\,\lambda_2' a & Y\,\mathrm{ch}\,\lambda_2' a \\
-\,\mathrm{ch}\,\lambda_1 b + p\,\mathrm{sh}\,\lambda_1 b & \cos\lambda_1 b + q\sin\lambda_1 b & -X\sin\lambda_2 b & X\cos\lambda_2 b & Y\,\mathrm{sh}\,\lambda_2' b & Y\,\mathrm{ch}\,\lambda_2' b
\end{vmatrix} = 0$$

where $p = \mathrm{sh}\,\lambda_1\, 1/\mathrm{ch}\,\lambda_1 1$

$q = \sin\lambda_1\, 1/\cos\lambda_1 1$

and λ_1 is given by equation (5). Also

$$X = -\frac{D_1 + D_3}{NE_3 I_3} - \frac{D_1 + D_3}{E_3 I_3}\,\frac{M}{N} + \frac{m\,\omega^2}{NE_3 I_3}(1 + i\eta)$$

$$Y = X + 2\,\frac{D_1 + D_3}{NE_3 I_3}\,M$$

According to equation (12), λ_2 and λ_2' are functions of m, ω, η, E_1, E_3, h_1, h_3, h_2, G', so that $\Delta = 0$ is a certain function

$$F(m, E_1, E_3, h_1, h_3, h_2, G', \beta, \eta, a, b, \omega) = 0 \tag{20}$$

This function is too complicated to allow an analytical expression to be derived for F and we must resort to numerical solution by computer.

It is interesting to note that we can get the exact natural frequency of a partially damped beam. This implies that when we want to use a damping material, we must know its damping coefficient β at the natural frequency of the composite system, and not at the natural frequency of the undamped system. The characteristic curve $\beta(\omega)$ of a viscoelastic material shows that for some narrow frequency bands β can change and this can be one reason why we may not get the expected damping.

3.6. Variational Problem.

We return now to the optimization problem: what should be the relationship between a and b to maximize the total loss factor η of the composite beam? Equation (3) gives the answer to this question. The derivative of a n^{th} order determinant Δ is the sum of n determinants of n^{th} order, composed like Δ but in which a row is replaced by the derivative of the row. For example

$$\begin{vmatrix} a & b \\ c & d \end{vmatrix}' = \begin{vmatrix} a' & b' \\ c & d \end{vmatrix} + \begin{vmatrix} a & b \\ c' & d' \end{vmatrix} \quad \text{for a second order determinant.}$$

We see that the transcription of equation (3), using the expression for the determinant, is very complicated. However, in the particular case where a is fixed, equation (4) can be solved numerically by computer and it is possible to find the value of b which yields the maximum η. It is important to check if the theoretical solution is correct. For that, we will try to get solutions, without numerical computation, for the particular case a = 0, i.e. for

$$\Delta = \begin{vmatrix} 1 & 0 & 1 & 0 & 0 & 0 \\ \cos\lambda_2 b & \sin\lambda_2 b & \mathrm{ch}\,\lambda_2' b & \mathrm{sh}\,\lambda_2' b & -\mathrm{sh}\,\lambda_1 b + p\,\mathrm{ch}\,\lambda_1 b & -\sin\lambda_1 b + q\cos\lambda_1 b \\ X & 0 & Y & 0 & 0 & 0 \\ X\cos\lambda_2 b & X\sin\lambda_2 b & Y\,\mathrm{ch}\,\lambda_2' b & Y\,\mathrm{sh}\,\lambda_2' b & -\mathrm{sh}\,\lambda_1 b + p\,\mathrm{ch}\,\lambda_1 b & \sin\lambda_1 b - q\cos\lambda_1 b \\ 0 & X & 0 & Y & -1 & -1 \\ -X\sin\lambda_2 b & X\cos\lambda_2 b & Y\,\mathrm{sh}\,\lambda_2' b & Y\,\mathrm{ch}\,\lambda_2' b & -\mathrm{ch}\,\lambda_1 b + p\,\mathrm{sh}\,\lambda_1 b & \cos\lambda_1 b + q\sin\lambda_1 b \end{vmatrix}$$

We must find

$$\frac{d\Delta}{db} = \sum_{n=1}^{6} \Delta_n$$

where Δ_n is the determinant Δ, in which the n^{th} row is replaced by the derivative with respect to b. It is obvious that $\Delta_1 = \Delta_3 = \Delta_5 = 0$ because the first and fifth rows are independent of b. Moreover $\Delta_4 = 0$, because rows four and six become identical. We therefore obtain

$$\frac{d\Delta}{db} = \Delta_2 + \Delta_6$$

Verification.

Suppose we take b = 1, then a = 0. We expect to find that b is a solution, because we are sure to get the maximum loss factor η if the beam is fully covered; that means $\Delta_2 + \Delta_6 = 0$ for b = 0. We will find easily that $\Delta_6 = 0$ for b = 0, because the two last columns are composed of zeros except for the coefficient. We have only $\Delta_2(b = 0)$ to be determined. We don't give here the computation in detail, but it is relatively easy to find $\Delta_2 = 0$, and the corresponding maximum loss factor η which is given in a simple form in terms of D_1, D_3, m, ω.

We thus see that in adopting the above mathematical fomulation the problem turns out to be well conditioned. In the case a = 0, the problem reduces to that of finding the solution to $\Delta_2 + \Delta_6 = 0$, that means to a solution for b, given D_1, D_3, h_1, h_2, h_3, β, G, ω. In the asymptotic cases, we have shown that algebraic formulation is convenient:

1) When a = b, we obtain the well-known eigen value equation of the transverse motion of a simply supported beam.

ii) When $a = 0$, the maximum loss factor is obtained when $b = 1$, that means the beam is fully covered. We can prove also that η is maximum when the bending moments are maximum.

4. EXPERIMENTAL INVESTIGATION

We have undertaken a series of experiments to check the accuracy of the numerical solutions. The first problem was to find the parameters β and G of the viscoelastic material. We know that β is dependent on the temperature and on the frequency. The frequency range we have investigated corresponds to the usual frequencies of metal sheets used in mechanical engineering applications, i.e. relatively low frequencies. For experimental investigation we have chosen the impulse method in preference to the phase or progressive wave methods. Blanc [16] describes this method in detail, which is convenient for soft materials such as polymers. Figure 2 shows schematically the principle of measurement. In this the end of a rod of viscoelastic material is subjected to a shock which generates a velocity graph $v(x,t)$ on signal recording equipment. The method is suitable for a range of frequencies from 50 to 10,000 Hz, and for a range of temperatures from -40^oC to 100^oC. An example of the results obtained for the real and imaginary parts of E at 20^oC is shown in figure 3. Moreover, the accuracy of this method is sufficiently high to reveal second order characteristics of the materials used for damping metal sheets. The verification of the theory itself of damped structures is not completed.

A further investigation was undertaken to experimentally study the beam system shown in Figure 1. Figure 4 shows the apparatus used for this purpose. For simplicity, the experiment was begun on a free-free beam even though the above theory relates to a simply supported beam. The difference in support conditions has led to slight quantitative departures of experimental results from those obtained theoretically, however, qualitatively the agreement between both has been preserved. We have used the classical resonance method, incorporating in this also the effects due to the dissipation mechanism, so that the loss factor is not given exactly by a simple difference of two frequencies. We have found it necessary to perform a series of experiments on one two-layer beam (one metal sheet, covered by an unconstrained viscoelastic layer). This first investigation has given information on preferred values for the arbitrary variables h_1, h_2 and ℓ. It also has enabled us to compare such values with the corresponding dimensions used in practice. To this date we have many empirical results on beams and plates, but not enough results on three-layer beams to allow us to fully assess the agreement between experiment and theory.

5. CONCLUSIONS

The theory presented in this paper contributes to the interpretation of the phenomenon of damping by the use of viscoelastic materials. For reasons of economy, vibrating structures in practice may be covered only in part by the damping material. Empirical results have shown that in some cases this does not change the effectiveness of damping, whereas in other cases it has happened that this partial damping is not sufficient or otherwise ineffective. Although developed for the case of a beam structure, the present theory answers some of the general questions on the difficult problem of optimal distribution of viscoelastic damping material on vibrating structures.

6. ACKNOWLEDGEMENT

We take the opportunity to thank here Mlle Cassien, MM. Blanc, Delfosse and Romieu of the "Laboratoire de Mécanique et d'Acoustique (ex Centre de Recherches Physiques), C.N.R.S. de Marseille for the help in writing this paper.

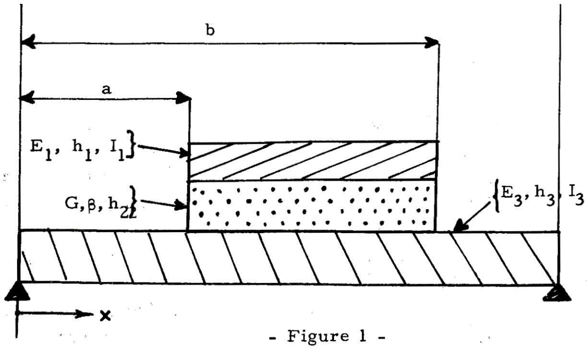

- Figure 1 -

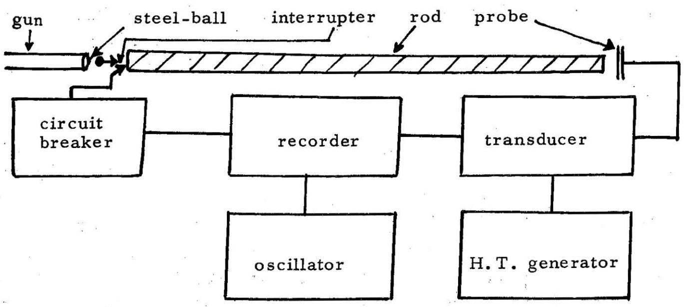

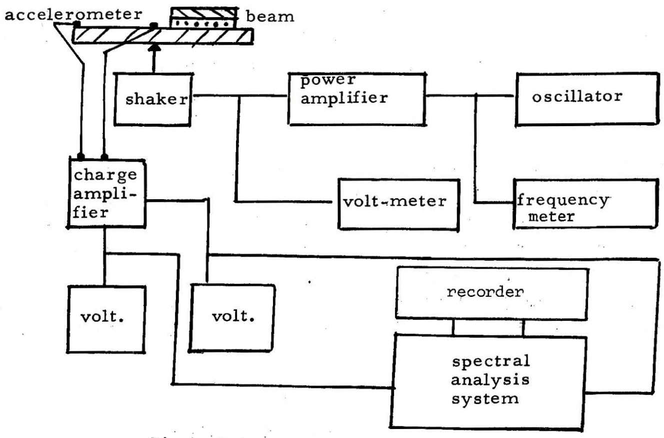

- Figure 2 -

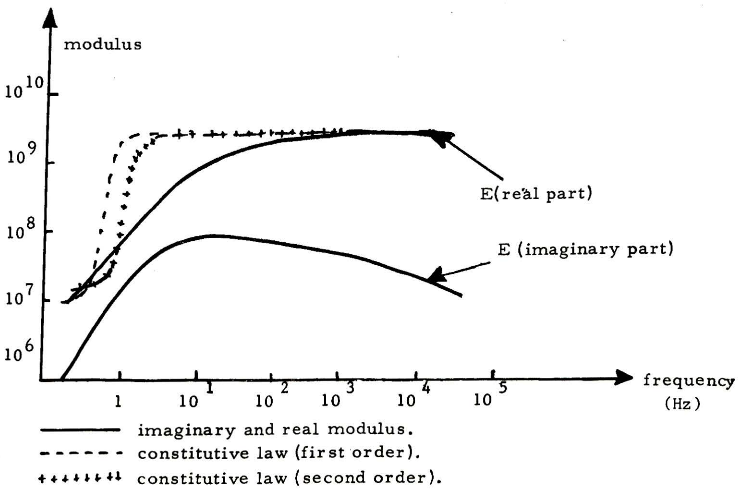

- Figure 3 -

REFERENCES.

[1] P.LIENARD.
"Etude d'une méthode de mesure du frottement intérieur de revêtements plastiques travaillant en flexion".
La Recherche Aéronautique, n°20, 1951, p.11-22.

[2] H.OBERST.
"Uber die Dämpfung der Bregeschwingungen dunner Bleche durch fest haftende beläge"
Acustica, vol.2, n°4, 1952, p.181-94.

[3] H.OBERST.
"Vibration damping of metal structures".
Symposium international sur "l'amortissement des vibrations de tôles par revêtement".
Louvain, 14-16 septembre 1967.

[4] J.E. ed RUZICKA.
"Structural damping".
The American Society of Mechanical Engineers. New-York, 1959.

[5] E.M.KERWIN - E.E.UNGAR.
"Plate damping due to the thickness deformations in attached visco-elastic layers".
J.A.S.A., 1964, p.386.

[6] E.M.KERWIN.
"Damping of flexural waves by a constrained visco-elastic layers".
J.A.S.A., vol.31, n°7, p.952 (1959).

[7] R.A.Di TARANTO.
"Theorie of vibratory bending for elastic and visco-elastic layered finite lenght beams".
J.A.Mec, vol.32, 2E n°4, p.881, (1955).

[8] R.A.Di TARANTO and R.BLASINGAME.
"Composite loss factors of selected laminated beams".
J.A.S.A., vol.40, p.187 (1966).

[9] Y.Y.YU.
"Simple thickness shear modes of vibration of infinite sandwich plates".
J.A.S.A., vol.29, p.790 (1959).

[10] Y.Y.YU.
"Damping of flexural vibration of sandwich plates".
J. Aerosp. Sci., Vol.29, p.790, (1962).

[11] D.J.MEAD and S.MARKUS.
"Forced vibration of a three-layer, damped sandwich beam with arbitrary boundary conditions".
J. Sound Vib. (1969) 10 (2), 163-175.

[12] Y.JULLIEN.
"Recherche d'un matériau de revêtement à équation d'état généralisée conduisant à une loi de frottement non linéaire optimale".
Symposium international sur "l'amortissement des vibrations de tôles par revêtement".
Louvain 14-16 septembre 1967.

[13] M.A.HECKL.
"The effect of damping layers on waves of different types".
Symposium international sur "l'amortissement des vibrations de tôles par revêtement".
Louvain 14-16 septembre 1967.

[14] D.J.MEAD and S.MARKUS.
"Loss factors and resonant frequencies of encastre damped sandwich beams".
J. Sound Vib. (1970) 12 (1), 99-112.

[15] Y.JULLIEN.
"Vibration des systèmes élastiques".
NEB, Paris, 1971.

[16] R.BLANC.
"Détermination de l'équation de comportement des corps visco-élastiques par une méthode d'impulsion".
Problèmes de la rhéologie. Varsovie 1973. p.65-85.

Mr. Dable. (Knitting needles)

Noise, Shock & Vibration Conference, 1974

Monash University, Melbourne

HIGH DAMPING STRUCTURAL MATERIALS

B. A. Parker
Department of Materials Engineering
Monash University
Clayton, Victoria

SUMMARY

Many materials are used for damping acoustic and mechanical vibrations in engineering structures. A characteristic of a majority of these materials is a non-crystalline structure with a relatively low elastic modulus. Such materials are frequently difficult to incorporate into structures because of their high deflections under load and their poor resistance to service conditions such as elevated temperatures. In this paper materials combining a high elastic modulus together with excellent damping properties are considered. The mechanisms by which these materials achieve their properties are outlined and examples given of their present and potential use in Engineering applications.

INTRODUCTION

The need for the damping of mechanical and acoustic vibration in engineering structures is becoming increasingly important, both to reduce the sound and vibration radiation from the structure and to avoid problems such as metal fatigue. Damping may be present or incorporated into structures in several ways. The most common is to utilise joints at which energy is dissipated by the relative motion of the components at the joint interfaces; these joints may occur as a result of functional design or be deliberately inserted for damping purposes; they may further incorporate low modulus materials in order to increase the energy loss. Another solution to a vibration problem is to redesign the structure and alter the vibration characteristics by changes in stiffness or mass, such a redesign is often difficult and expensive. In certain circumstances, the use of a material having an inherently high damping capacity* may be beneficial in reducing the response of a structure and the concern of this paper is with these materials and their utilisation.

A pre-requisite is that the damping of the structure itself be at least an order of magnitude below that of the material. If a system has an inherent level of damping of 50%, then the raising of the damping capacity of the material in its components from 0.1 to 1% would have a negligible effect. It should, however, be recognized that the prediction of a level of system damping is difficult at the design stage of a structure and consequently the selection of a high damping material may provide an additional insurance against excessive noise and vibration. The use of high damping materials in such a belt and braces situation presumes availability of the materials at an appropriately low cost.

The selection of high damping materials is complicated by the fact that the damping levels are, in most cases, stress sensitive; materials having excellent damping properties at high stress levels ($\sim 0.5\ \sigma_y$) may be less satisfactory at low stress levels. The state of stress, for example the variation of a cyclic stress about a mean value considerably different from zero, may also have an effect in certain materials.

*The specific damping capacity of the material is used in this paper as a measure of damping and is the ratio of the energy loss per cycle to the maximum strain energy reached in the cycle. This measure is common in literature on material damping properties. Relationships between the specific damping campacity, loss coefficient and logarithmic decrement may be found in standard texts. (1)

If it appears advantageous to use a high damping material in a particular situation then the choice is limited if the retention of a high strength, modulus and elevated temperature performance is required. Such properties are generally only displayed by metallic or ceramic crystalline materials and some composites and only a few of these materials have high damping properties. Typical materials in this category are the familiar cast irons and the recently available manganese-copper alloys. There are a few other metals and alloys exhibiting high levels of damping but these are generally of exotic compositions and unsuitable for general engineering application. A few, more common, alloys may be modified to improve their damping properties, and although high values are not achieved, useful improvements may be obtained.

The mechanisms of damping in existing materials will now be considered with a view to establishing criteria for further development.

MECHANISMS OF DAMPING

A wide range of mechanisms has been described (1, 2). Many of these, however, refer to damping peaks at very low stress levels or of insignificant magnitude. These mechanisms provide valuable information regarding the structure of the materials concerned but have little relevance to their application in engineering structures. The discussion here will be restricted to those mechanisms leading to significant damping at useful stress levels. These may be divided into four categories : (i) Plastic strain damping, (ii) Magneto-elastic damping (iii) Damping at internal interfaces and (iv) Damping in composites. In Fig. 1 a variety of materials is compared in the form of graphs of damping capacity vs. surface shear stress. Of those materials displaying a high damping capacity nickel and Armco iron utilise magneto elastic damping, the manganese copper alloy internal interface damping, and the cast irons appear to combine these two and possibly other mechanisms.

(i) Plastic strain damping

This occurs at high stress levels and is associated with irreversible dislocation movement, such deformation gives rise to cumulative damage in the material eventually resulting in failure by the process of metal fatigue. Such an energy dissipation mechanism must therefore be disregarded as being suitable for engineering components in other than structures designed to meet shock conditions where the plastic strain developed may damp the effects of the shock conditions on pre-existing cracks in the components.

The high levels of damping in lead are due largely to dislocation movement with some contribution from mobile grain boundaries. The temperature at which lead recrystallizes is below room temperature and hence deformed lead can recover and recrystallize in order to eliminate the accumulated plastic deformation. The mechanical properties of lead are very poor and the use of traditional alloying methods to increase the strength results in a lowering of the damping properties. The development of composites based on lead may lead to self supporting high damping structural components but at the present time lead is only utilised as a cladding material.

(ii) Magneto-elastic damping

In this mechanism damping is dependent on the coupling of the elastic and magnetic properties of materials and is necessarily dependent on the presence of a ferromagnetic structure. The bulk of engineering materials, i.e. steel, is ferromagnetic and would therefore be expected to exhibit some level of magneto-elastic damping.

Ferromagnetic materials contain domains which have a recognizable magnetization vector, in unmagnetized material these vectors are randomly oriented but become parallel to the magnetic field as the field strength is increased. If the field is removed, some small relaxation of the domain orientation may occur but a residual preferred orientation remains. The application of a strain field may cause the reorientation of some of these vectors since energy may be minimised if the strain and magnetic fields are parallel. The result of applying a cyclic stress to a partially ferromagnetic material is to cause cyclic reorientation of the magnetic domains giving rise to an energy absorbtion. The effect is not observed in fully magnetized material since insufficient energy is supplied to rotate the domain vectors in the presence of the high internal magnetic field. In unmagnetized material only a small effect occurs since few domains are reoriented by the strain field.

The energy dissipated increases with the third power of the stress up to a limiting value (the magneto-mechanical coercive force) (3) beyond which level it declines. Typical stress levels are 35 MPa m^{-2} for Armco iron and 105 MPa m^{-2} for an En 3b steel in a quenched and tempered condition. This damping mechanism is independent of frequency over a wide range (up to 100 kHZ). The effects of stress and state of magnetization on a stress relieved En 3b steel are shown in Fig. 2. The application of a static mean stress may have a similar

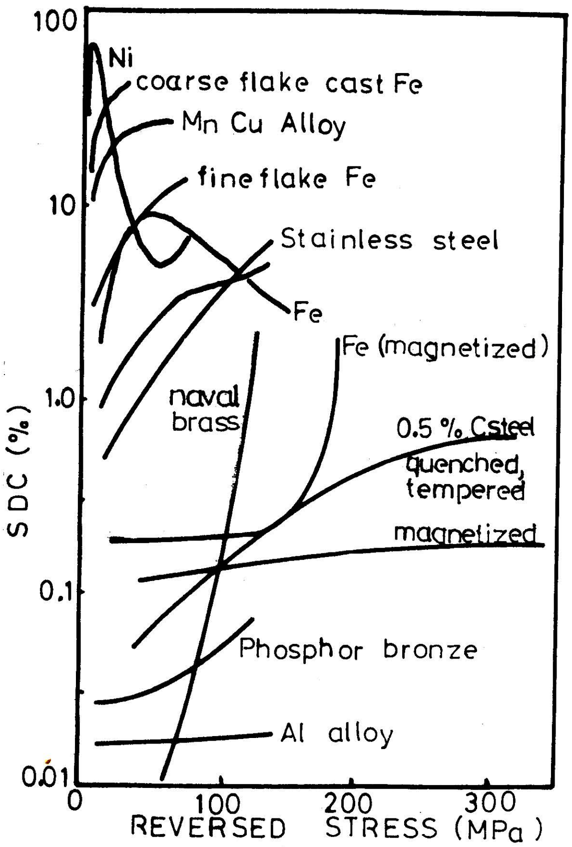

FIG.1 Specific damping capacity vs. reversed stress for various metals measured in the free/free longitudinal mode. (6).

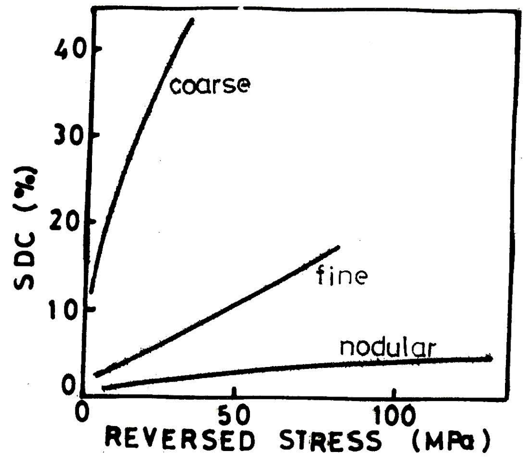

FIG.3 Damping vs. stress for three cast iron samples having coarse flake, fine flake and nodular graphite microstructures.

FIG.4. Transmission electron micrograph of a commercial Mn-Cu alloy x 50,000.

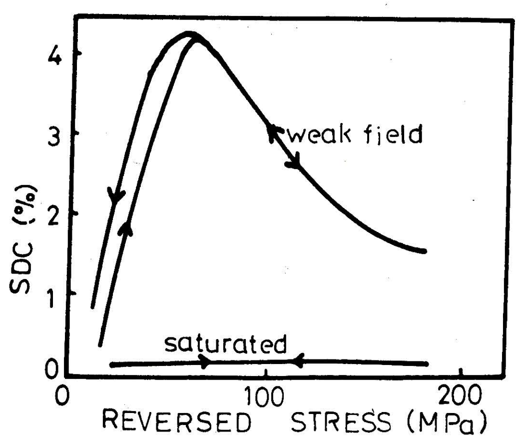

FIG.2. Damping vs. stress for a stress relieved 0.12% C steel showing the effect of increasing and decreasing stress. (6).

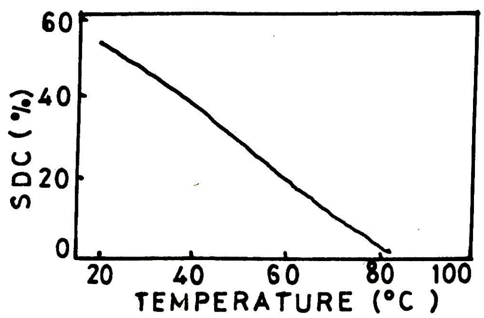

FIG.5. Damping vs. temperature for a commerical Mn-Cu alloy (12).

effect to a high magnetic field, i.e. the domains are pre-oriented by static stress and little further energy is expended by the alternating stress. The permissible static stress level is determined by the magneto-mechanical coercive force.

Magneto-elastic damping materials have been used for turbine blades. However, the selection of material is further limited at elevated temperatures since magneto-elastic damping decreases sharply as the Curie point is approached.

(iii) Damping at internal interfaces

Since damping in structures most commonly arises from the presence of interfaces, it should not be surprising that the more useful high damping alloys incorporate internal interfaces at which energy may be dissipated. The interfaces involved may be on a microscopic scale, like the graphite/iron interface in cast iron, or on an even smaller scale like the "microtwin" boundaries in manganese-copper alloys which are only visible in the electron microscope.

Mechanical energy may be lost at internal interfaces either by movement of the interface cyclically over a local energy barrier or by a discontinuity in stress transfer across the interface. The damping in cast iron is typical of the latter and that in manganese-copper of the former and these two materials will now be considered in more detail.

Cast iron

Cast iron containing free carbon in the form of graphite has traditionally been regarded as a high damping engineering material. However, it has not been until the recent work of Adams (4, 5 and 6) that the damping behaviour has been related to the microstructure. An early model (7) for the damping of cast iron supposed plastic strain damping at stress concentrations around the graphite inclusions. However, Adams showed that a sample with a fine flake graphite size exhibited lower damping properties than the coarse graphite samples although a larger number of stress conetrating centres were present. Some of the results of this work are shown in Fig. 3. where the damping/stress behaviour of three cast irons of differing graphite morphology is displayed.

The conclusions from this work were (i) that damping was highest in the coarse flake graphite samples and lowest in irons containing nodular or spheroidal graphite.

(ii) Microscopical observation suggested that energy losses occurred by the movement of micro-cracks within the graphite and also by plastic slip on the basal planes of the graphite crystals.

(iii) Cast irons having relatively low damping properties showed a component of magneto-elastic damping under appropriate conditions. Cast irons are sensitive to stress history and permanent damage to the graphite by overstressing results in a reduction of damping.

The principle problem with the utilisation of cast irons of high damping capacity is that the structure exhibiting the best damping properties is that which has the least satisfactory mechanical properties, i.e. low toughness and strength. Some compromise must therefore be made in the selection of the appropriate properties for a given application.

Manganese-copper alloys

Considerable effort went into the study and development of these alloys in the mid-sixties since they appeared to combine excellent damping properties with adequate mechanical properties and environmental resistance (8). The alloys consist of 50-80% manganese with a balance of copper and minor additions of other elements. Structures suitably heat treated to produce high damping contain large numbers of small twin-like domains when viewed in the electron microscope. These domain boundaries move readily under thermal stresses induced by the electron beam whereas dislocations in the same structures do not move. The damping in these alloys has therefore been attributed to motion of the domain boundaries. Fig. 4 is a transmission electron micrograph showing these domains, they move readily under the weak thermal stress induced by the beam in the electron microscope.

The matrix structure in the high damping condition is tetragonal, the change in c/a ratio resulting from an antiferromagnetic ordering of the manganese atoms. The domains represent regions in which the C-axis alignment is constant but it varies from domain to domain. The application of stress causes a reorientation of some of the domains such that the C-axis is parallel to the stress; energy losses occur as the domain walls move to accommodate the C-axis changes. The relaxation mechanism is therefore similar to that of the magneto-elastic materials except that antiferromagnetic rather than ferromagnetic ordering is the prime cause (9, 10).

Antiferromagnetic ordering has a characteristic order disorder temperature, the Neél temperature, similar to the ferromagnetic Curie point. This temperature is in the vicinity of 100°C for manganese-copper alloys and damping properties fall away rapidly as this temperature is approached. (Fig. 5.) The usefulness of these alloys for other than room-temperature applications is therefore restricted although it is believed that recent development of modified alloys has increased the temperature range considerably.

The damping in these alloys increases with increasing stress reaching a maximum value which might be an equivalent of the magneto-mechanical coercive force. This latter value is sensitive to microstructure in a similar way to the coercive force. The performance of these alloys under multiaxial stress situations and under situations with a non-zero mean stress is not well documented. It is to be expected that if the non-mean stress exceeds the stress at which damping saturates then a reduction in damping capacity would result.

(iv) Composites

Composite materials (e.g. fibreglass and carbon fibre reinforced resin) consist of fibres of high modulus material in a low modulus matrix. Considerable heat is generated in these materials under vibrating conditions indicating a high energy loss (11). Since a majority of composites are poor thermal conductors the heat generation is likely to be deleterious particularly in view of the degradation in mechanical properties of resins as the temperature rises. Composites containing large volume fractions of Carbon fibres (e.g. prototype Rolls-Royce RB211 compressor blades) will conduct heat as will composites having a metal matrix. These latter composite types are of relatively recent development and their damping characteristics are not well known. The high cost of manufacture is also a limitation on the use of these more sophisticated composites.

APPLICATIONS OF HIGH-DAMPING ALLOYS

Various alloys have been produced and a number have been tested in engineering situations, these include:

(i) Marine propellors to damp out the 'ringing' of the blades and subsequent blade loss by fatigue. This together with related, classified, defence applications would seem to be the only commercially successful applications to date (12).

(ii) Shanks for road drills: slabs of manganese-copper alloy have been shown to reduce the higher frequency components of noise from road drills, however whilst these higher frequencies are irritating the noise level reduction is insufficient to justify the expense of these alloys in consumable parts.

(iii) Gear noise. Noise and vibration from gearboxes, transmissions and other components of machinery may be signifcantly reduced by incorporating components of high damping alloy although similar results can be obtained by improved bearing design and the location of rubber dampers. Manganese-copper alloys are likely to find increasing application in this area if the Neél temperatures of the alloys can be increased.

(iv) Cladding. A number of experiments have been conducted using attachments of high damping alloy to traditional e.g. steel components such as large flat panels. A reduction in the 'drumming' of these panels is achieved but normally a redesign of the panel or the incorporation of rubber dampers is a more effective and economic solution. The results of cladding an experimental steel structural member (I-beam) with Mn-Cu alloy are compared in Fig. 6 with the damping behaviour of a Mn-Cu alloy beam and with an unclad steel beam. The damping of the beam was only marginally improved by the alloy cladding, however, considerable improvement was observed when the cladding was constrained by another steel layer on its outer surface. Since the Mn-Cu alloy has a lower modulus than steel lower stresses are induced in the cladding; the additional steel layer induces higher shear stresses in the cladding and consequently higher levels of damping (14).

Whilst the more exciting applications and experiments have in recent years been conducted on alloys of the manganese-copper type, the applications of cast irons should not be forgotten. Cast iron beds have been used for machines for a long time now, successfully reducing the transmission of vibrations from different parts of the machine. The development of higher-performing cast irons, with some attention paid to achieving high damping properties, may result in a cheaper alternative to the manganese-copper alloys.

There have been few systematic attempts to combine sound mechanical design with the use of high damping structural materials to ensure their most effective use. Most of the examples cited above are the result of the direct substitution of traditional materials with the high damping materials. Some preliminary measurements have been made (13, 14) on simple systems and the results show that damping depends on structural geometry and the nature of the excitation. An interesting conclusion was that, in certain circumstances, a material of high damping capacity but low fatigue strength may often be preferable to a low damping, fatigue resistant alloy.

The use of high damping alloys has been suggested for many noise and vibration problems. However, the result of such a suggestion has frequently been that the problem has, for the first time been examined by a vibration expert and a solution to the problem has been achieved without the use of high damping alloys. Further progress in the use of these alloys requires co-operation between the materials experts and design engineers - it is however some ten years since such a sentiment was first voiced by Birchon (8) and these materials have yet to find wide application. Noise and vibration problems are still with us and one can only hope that the next decade results in better co-operation between those developing alloys and those using them.

References:

1. B.J. Lazan, Damping of Materials & Members in Structural Mechanics, Pergamon, Oxford, 1968.
2. C. Zener, Elasticity and Anelasticity of Metals, Univ. of Chicago Press, 1948.
3. H.G. van Bueren, Imperfections in Crystals, North-Holland, Amsterdam, 1961.
4. R.D. Adams and M.A.O. Fox, J.I.S.I., 1973, 211, 37.
5. R.D. Adams and M.A.O. Fox, J.Mech.Eng.Sci., 1973, 15, 53.
6. R.D. Adams, J.Sound Vib., 1972, 23, 199.
7. H.T. Angus, Physical and Engineering Properties of Cast Iron, BCIRA, 1960.
8. D. Birchon, Eng.Materials and Design, 1964, 7, p 606 and p 692.
9. D. Birchon, D.E. Bromley and D. Healey, Met.Sci.J., 1968, 2, 41.
10. J.A. Hedley, Met.Sci.J., 1968, 2, 129.
11. M.J. Owen, "Glass Reinforced Plastics", Ed. B. Parkin, Iliffe, 1970, p.254.
12. J.M. Langham, Foundry Trade Journal, 1968, 989.
13. R.D. Adams and D.J. Mead, I.S.A.V. Rept., 158, 1966.
14. J.F. Nachman, J.C. Napier and A.N. Hammer, I.N.C.R.A. Rept., 152, 1970.

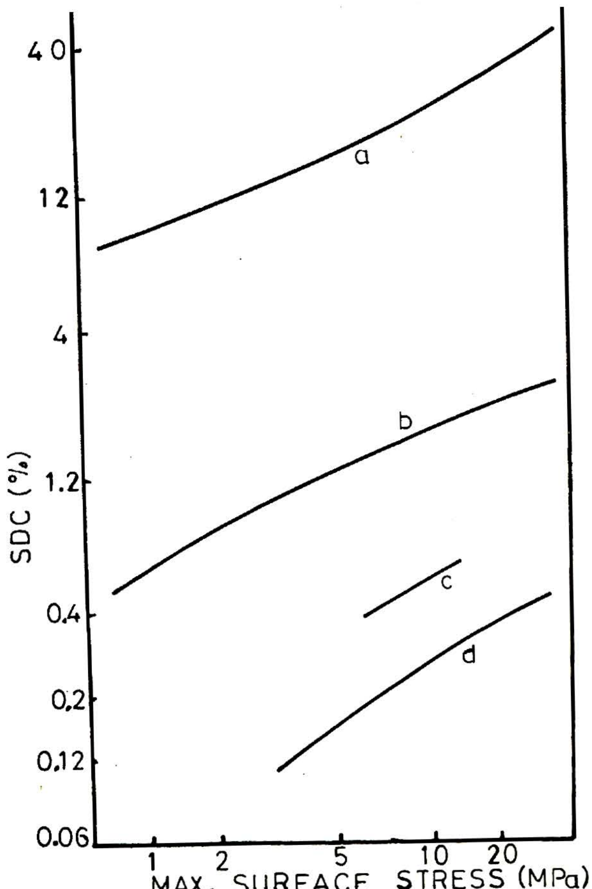

Figure 6. Damping behaviour of a series of I beams. (a) Manganese-Copper alloy (b) Steel Beam with constrained cladding of Mn-Cu alloy (c) Steel beam with unconstrained cladding and (d) Steel beam. (14)

THE RADIAL DYNAMIC PROPERTIES OF PNEUMATIC TYRES

R. J. Hooker
Department of Mechanical Engineering
University of Queensland
St. Lucia, Queensland

K. W. Gambling
Department of Mechanical Engineering (formerly)
University of Queensland
St. Lucia, Queensland

SUMMARY - Radial dynamic properties of pneumatic tyres have been determined using a drum-type testing machine. The tyre is mounted as normally on a conventional wheel which is free to move along the wheel-drum line of centres. Wheel displacement is controlled by a position-feedback electro-hydraulic servo system. Thus, for example, sinusoidal wheel vibration can be obtained with independent control of mean position, displacement amplitude and frequency. The drum is driven by a variable-speed D.C. motor giving separate control of "road" speed. The force applied to the drum by the wheel is measured and hence the force-deflection relationship for the tyre is determined.

Results are presented for a typical passenger-car cross-ply tyre, from an extensive series of tests covering ranges of vibration amplitude and frequency, road speed and tyre pressure. For sinusoidal motion of the wheel the wheel-to-drum force is essentially sinusoidal and a linear representation is adopted. The radial dynamic stiffness with wheel rotating is substantially less than that with wheel stationary, but the stiffness when rotating is relatively independent of road speed. The variation with amplitude and frequency is shown, and the contributions to stiffness of pneumatic and casing effects are separated.

Damping in the tyre is small and could not be measured with any certainty due to the effects of tyre non-uniformities.

The tyre properties are modelled by a series-parallel spring-damper assembly which fits the observed behaviour.

INTRODUCTION

The pneumatic tyre is required to perform both traction and suspension functions. In order to predict the behaviour of a pneumatic-tyred vehicle it is desirable that the dynamic characteristics of tyres be known as fully as possible. This paper deals with the radial, i.e. "vertical", flexibility of a tyre and is thus principally concerned with the suspension function. Additionally, however, knowledge of the radial dynamic force-deflection behaviour is necessary for a complete analysis of longitudinal and lateral tractive behaviour of a vehicle.

The material presented is based on an experimental investigation. In experimental work on vertical response characteristics of tyres, considerable difficulty is met because of the several parameters involved and the difficulty of achieving independent control of them. Problems in control of test conditions lead to laboratory tests using some kind of artificial "road" rather than on-the-road testing. A flat, moving, artificial road cannot be provided easily and either a flat, stationary surface or a moving curved surface is used. Overton et al (1) made studies using flat, stationary surfaces, i.e. with a non-rolling tyre, whilst appreciating that there is a substantial difference between the rolling and non-rolling characteristics and that non-rolling tests have limited significance. Laboratory rolling tests at other than very low speed use drum-type machines. Vibration excitation can be achieved by modifications to the drum surface. Barson and Dodd (2) used bolted on obstacles and for lower frequency excitation Grigg set the drum eccentric (3). With excitation by drum surface, however, it is not possible to control road speed and excitation frequency independently nor is it possible to control readily the displacement amplitude of the tyre and wheel system.

Chiesa and Tangorra (4) used concentric drums of various diameters and determined natural frequencies of the tyre-wheel-supporting arm assembly. By changing the inertia of the assembly some variation in frequency could be obtained, but direct measurement of force and control of amplitude and frequency were not obtained.

In the comprehensive investigation carried out by Mills and Dunn (5) a smooth concentric drum was used and tyre motion generated by an electromagnetic vibrator operating on the wheel/tyre assembly. This arrangement provides independent control of road speed and excitation frequency. The lowest frequency attained was 10 Hz and it appears that no account was taken of possible variation of characteristics with amplitude of motion. Since tyre behaviour might be expected to be non-linear because of rubber characteristics and tyre geometry it is desirable that experimental work include study of the effect of amplitude. Also, Mills and Dunn took force measurements in the actuating shaft between vibrator and wheel assembly. The measurement therefore includes forces associated with wheel assembly inertia as well as tyre forces.

The experiments reported in this paper were carried out on a smooth concentric drum and include non-rolling and rolling tests. The wheel/tyre motion was obtained by an electro-hydraulic servo system. The arrangement provided independent control of road speed, excitation frequency, mean deflection (and therefore static load) and vibration amplitude. Tyre-to-drum force was measured directly.

APPARATUS

The arrangement of the testing machine is shown in Figure 1. The drum is driven by V-belts from a Ward Leonard controlled D.C. motor. "Road" speeds of over 100 km h^{-1} can be obtained. The wheel is mounted on a stub axle fixed to a loading beam. This beam is carried in bearings in the main frame of the testing machine and the dimensions are so chosen that beam motion results in radial deflection of the tyre. Strictly the beam motion is rotation but the non-straightline movement is neglected since the arc of motion is less than ± 10 mm at a radius of 725 mm.

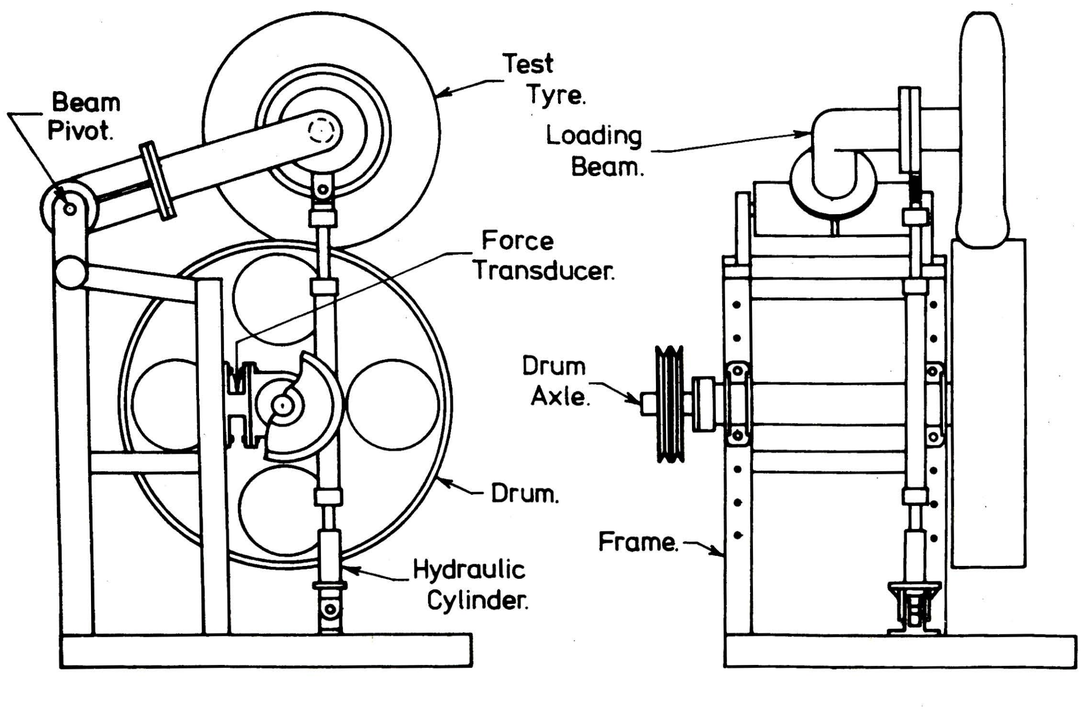

FIGURE 1 Tyre Testing Machine

A chosen motion (e.g. sinusoidal) is applied to the wheel and the force exerted on the drum is measured. Wheel motion is produced by a double-acting ram controlled by an electro-hydraulic servo valve. A displacement transducer mounted on the ram provides a signal for tyre position feedback and for chart or other recording and processing. In the feedback circuit a set-point control is included and this enables the mean deflection to be controlled independently.

The effect of changing the relative positions (i.e., radii on the loading beam) of wheel and actuating rod was examined. A large radius for actuating rod attachment appears to enable larger forces to be obtained at the wheel due to the lever ratio. The gain is offset, however, by the increased inertia of the longer loading beam and by adverse flow rate and pressure drop effects in the servo valve. For this particular application (constrained by existing machine frame and hydraulic power supply) a 1:1 ratio gave maximum performance capability. The arrangement chosen can apply force within the range ± 13 kN over a total travel of 50 mm. In dynamic tests, the combined effect of inertia loading and hydraulic characteristics restricts the range available and a typical operating limit is 5 mm peak-peak displacement at 10 Hz.

The force transducers are short strain-gauged cantilevers which carry the drum axle housing. Thus a direct measurement of tyre-road force is obtained except for the effect of drum assembly inertia forces. The design of the cantilever members requires a compromise between minimizing drum assembly vibration and obtaining a sufficiently large strain gauge output signal. An error of 1% arises due to drum assembly inertia and this has been neglected. Strain gauge wiring was arranged so that the force measuring elements were responsive only to vertical forces and it was subsequently verified experimentally that the effect of the horizontal Vee belt tensions was negligible. The drum was dynamically balanced to eliminate unbalance force generation.

The testing machine suffers the disadvantage of all drum-type machines, viz. the tyre is run on a curved rather than a flat surface. Drum diameter was 0.85 m. A second (smaller) drum is available to assist in extrapolation back to zero curvature. This was done by Chiesa and Tangorra (4) but has not been attempted with these results. An interesting possibility is the application of trends determined on flat and curved surfaces with a non-rolling tyre to the case of the rolling tyre.

EXPERIMENTAL RESULTS

The experiments covered a range of combinations of inflation pressure, road speed, excitation frequency and displacement amplitude for both rolling and non-rolling cases. Results are presented for a 6.95 L14 4 Ply Tubeless Rayon Cross-ply Tyre mounted on a 14 x 5J rim. In all tests the static load was adjusted to give a static deflection of 20% of section height (viz. 25 mm). Sinusoidal excitation was used. The ranges covered were:-

Road speed	0 to 32 km h^{-1} (Limited number of tests to 64 km h^{-1})	(0-20 m.p.h.)
Inflation pressure	140 to 240 kPa	(20-35 p.s.i.)
Vibration, sinusoidal		
Amplitude (peak-peak)	4 to 9 mm	(0.15-0.35 inch)
Frequency	1 to 7.5 Hz	

For each individual test the apparatus was run until the desired steady state conditions were achieved - principally this required adjustment of inflation pressure because of temperature changes. A pen recording of tyre deflection and force signals was then taken. From the recording amplitude and phase relations were obtained. A sample recording is shown in Figure 2. The tests were grouped into sets, each set comprising a range of vibration amplitudes with all other conditions constant. For each set a dynamic force v. deflection plot was drawn as in Figure 3.

Figure 2 shows that the applied wheel motion was sinusoidal as intended and the force signal was approximately sinusoidal in shape and at a small phase angle to wheel displacement. There was, however, considerable scatter of force amplitude and phase angle values. The percentage variation in force amplitude, determined by averaging the maximum percentage variations from all rolling tests, was ± 6.5%. The variation was less than ± 15% for 95% of the tests and there was one isolated case of ± 20%. The scatter was very much less in the non-rolling tests (average ± 2,8%, worst case ± 5.5%). It was also noted that in rolling tests with wheel not vibrating a force output signal was present, ranging from about 120 N in a severe case to almost zero in others. This is to be compared with force values from 500 to 2000 N in the normal test range. These effects were attributed to tyre non-uniformities, which arise from inevitable manufacturing inaccuracies (radial run-out, ply joints, tread joints, non-uniform material distribution).

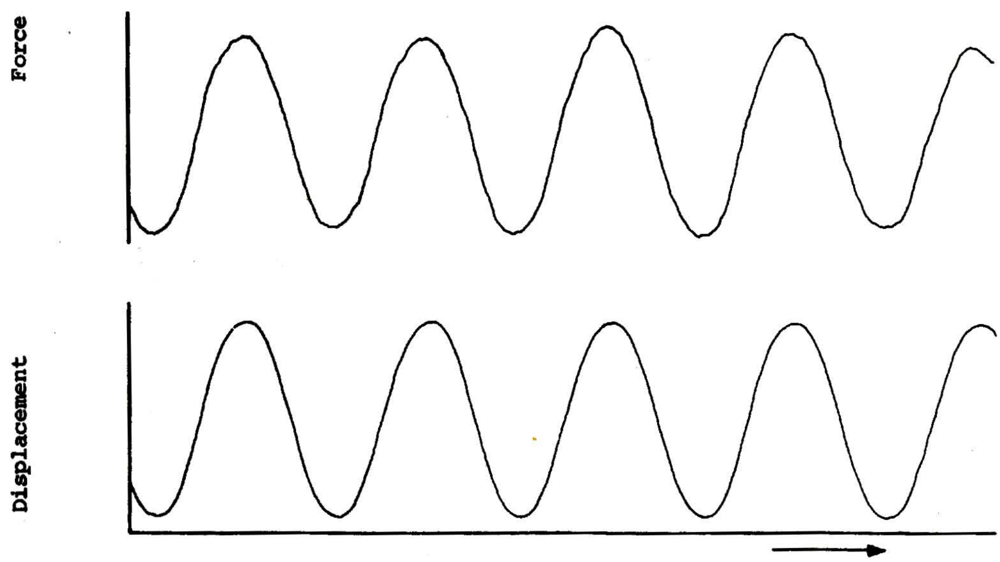

<u>FIGURE 2</u> Force and Displacement Record
16 km h^{-1}, 140 kPa, 2.5 Hz

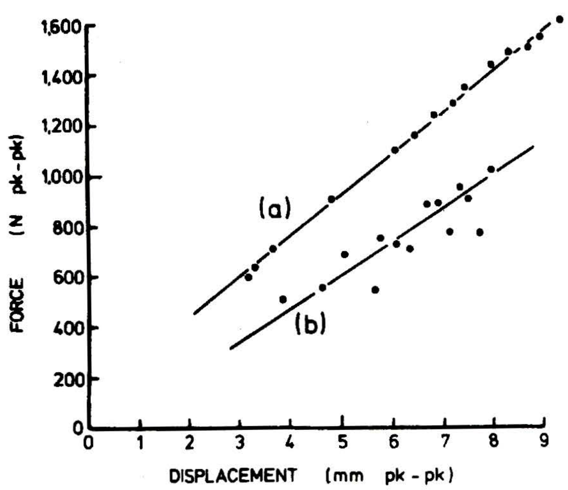

<u>FIGURE 3</u> Force Amplitude v. Displacement Amplitude
(a) 32 km h^{-1}, 172 kPa, 1 Hz
(b) 32 km h^{-1}, 140 kPa, 7.5 Hz

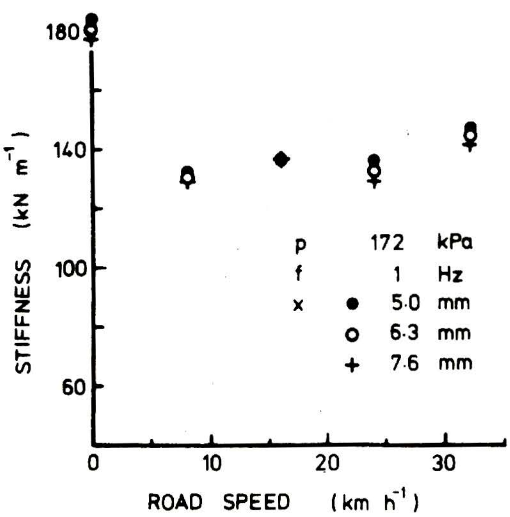

<u>FIGURE 4</u> Effect of Road Speed

Because of the scatter, "averaging" of results was necessary. The general trend of the force-deflection plots showed a straight line relationship (see Figure 3, especially the low-scatter test set, curve a). A least squares error straight line was fitted to the force v. deflection plot and all subsequent examination of results based on that line. Curve b of Figure 3 shows a high-scatter test set, this particular one representing the worst of the results accepted.

The static force-deflection curve for a cross-ply tyre is non-linear, showing a stiffening characteristic at small deflections and changing to softening at large deflection (1). In this study, dynamic behaviour is determined by imposing oscillations about a mean deflected position. Behaviour might or might not be linear and probably will not follow the static deflection characteristic. Hence the fitted line might intersect the force axis at, or above, or below the origin. It was found that for all test conditions the force axis intercept was small (average 75 N, 90% less than 180 N, 90% positive). Since also the force signal shape was reasonably close to sinusoidal it was assumed that for any individual test the behaviour could be analysed as that of a combination of linear elements (springs and dampers). The radial dynamic stiffness k is taken as (force amplitude)/(displacement amplitude), i.e., the modulus of a complex stiffness, and will change from one set of conditions to the next.

In all tests the phase angle was small, ranging up to mean values of 6° for rolling and 8° for non-rolling tests. The elastic component of k can then be taken as numerically equal to the modulus, and using the phase angle an equivalent viscous damping coefficient can be calculated for each test. The coefficient was generally less than 1.75 kN m^{-1} s but because of scatter the results are unreliable. All that can be concluded is that damping is small and its effect is of the same order as the influence of tyre non-uniformities.

Effect of Road Speed

Tests were conducted with the tyre stationary and at speeds up to 32 km h^{-1}. The dynamic stiffness of the rolling tyre, although in all cases 20% to 30% lower than the non-rolling value, was substantially independent of road speed. Figure 4 shows typical results. A few tests at higher speeds, up to 64 km h^{-1}, also showed stiffness independent of speed.

At higher vibration frequency the stiffness change with speed was less than that shown for 1 Hz on Figure 4, and for some conditions decreased slightly with increasing road speed. The small variation of stiffness with displacement amplitude is also apparent in the Figure.

Effect of Inflation Pressure

All stiffness values at frequency 1 Hz, i.e. results for all road speeds and displacement amplitudes from 5 to 7.5 mm peak-peak, are included in Figure 5(a). Similarly all stiffness values at 7.5 Hz are included in Figure 5(b). Noting the suppressed zeroes, a straight line relation between stiffness and inflation pressure seems reasonable for the rolling tyre. The least squares error straight line is shown for each frequency. These lines have a positive intercept on the stiffness axis and hence the overall radial dynamic stiffness k for the rolling tyre can be expressed as

$$k = k_c + k_p = k_c + ps_p$$

where k_c is a casing stiffness, k_p a pneumatic stiffness, p the inflation pressure and s_p a pneumatic stiffness coefficient. This is the representation discussed by Cooper (6) for static force-deflection behaviour.

Results for the non-rolling tests are too few to justify a fitted curve. For the two frequencies, the trends are similar and suggest departure from a straight line relationship.

Effect of Vibration Frequency

The behaviour of rubber is frequency dependent and a variation of stiffness with frequency can be expected. Figure 6 shows the observed variation. Stiffness increases with increasing frequency, but the extent of the increase is relatively small for the rolling tyre. The effect is much more marked for the non-rolling tyre.

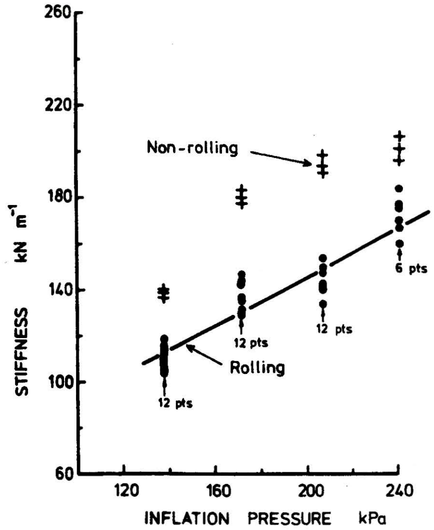

(a) Frequency 1 Hz.

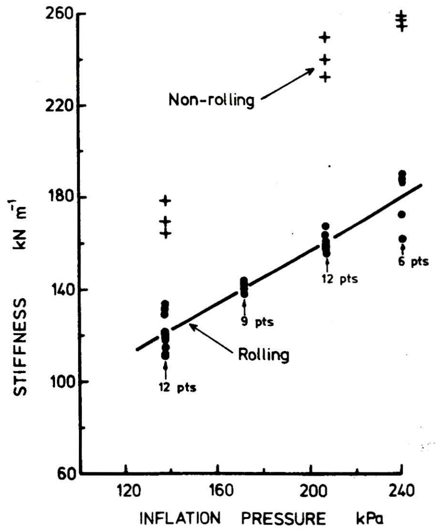

(b) Frequency 7.5 Hz.

FIGURE 5 Effect of Inflation Pressure

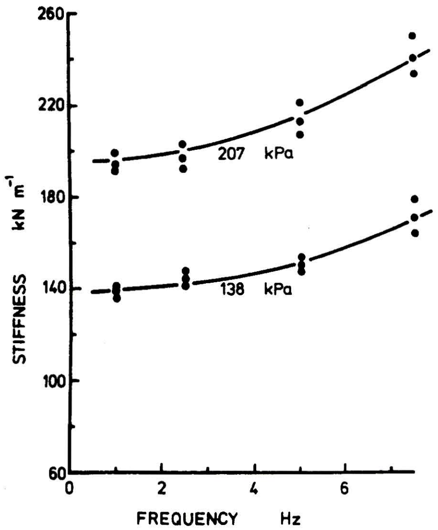

(a) Non-rolling.

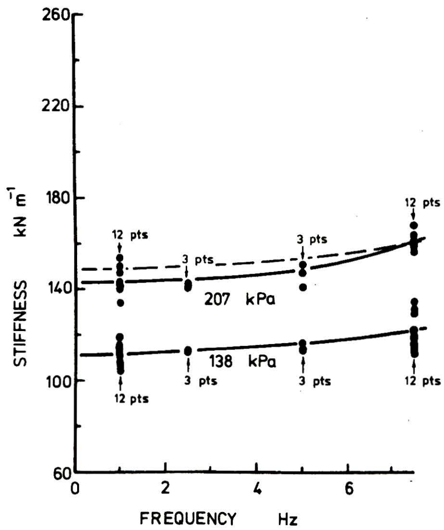

(b) Rolling.

FIGURE 6 Effect of Frequency

REPRESENTATION OF TYRE BEHAVIOUR

From the data collected it is possible to propose a physical model which approximately fits the observed behaviour of a rolling tyre. It was noted above that behaviour for an individual test was reasonably close to that expected from linear elements and that stiffness showed a straight line relationship with inflation pressure. Figure 6(b) shows that there is a frequency dependence but that the difference between the curves for the two inflation pressures is roughly constant, i.e. the frequency effect is independent of change of inflation pressure and can be considered a casing effect.

An arrangement which exhibits such behaviour is drawn in Figure 7. The pneumatic stiffness is k_p and the combined group k_1, k_2 and c represents casing stiffness. The stiffness of this model is

$$\hat{k} = k_p + k_1 + \frac{k_2 c^2 \omega^2}{k_2^2 + c^2\omega^2} + i \frac{k_2^2 c\omega}{k_2^2 + c^2\omega^2}$$

Parameter values can be determined from the experimental results. Pneumatic stiffness coefficient s_p is taken as the mean of the slopes of the fitted lines in Figure 5. (Fitted values 0.524 and 0.576 m.) Redrawing these lines through the mid-range point gives approximate stiffness v. pressure lines which are produced to intercepts on the stiffness axis. These intercepts represent stiffness at zero pressure i.e. casing stiffness, at 1 and 7.5 Hz. This extrapolation is not necessarily physically significant and is performed only to determine parameters for the normal operating ranges.

The intercept at 1 Hz is taken as k_1, since change of stiffness with frequency is small in this region (see Figure 6(b)). From the corresponding intercept at 7.5 Hz and the mean phase angle 6° at 7.5 Hz the remaining constants can be determined. The parameters calculated are

s_p	0.55 m (kN m^{-1}/kPa)
k_1	35 kN m^{-1}
k_2	34 kN m^{-1}
c	0.5 kN m^{-1} s

These values produce stiffness characteristics virtually indistinguishable from the lines on Figure 5 and the 138 kPa curve on Figure 6(b). The model characteristic at 207 kPa is shown as the dashed curve on Figure 6(b).

Corresponding values for the non-rolling tyre have not been calculated. For the non-rolling tyre, the few results, uncertain trends and incomplete examination of tyre non-uniformities result in an inadequate basis for parameter calculation.

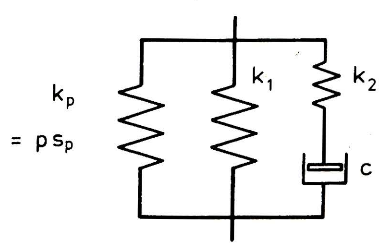

FIGURE 7 Tyre Model

CONCLUSION

The dynamic radial stiffness of a pneumatic tyre has been determined for rolling and non-rolling conditions and for ranges of road speed, inflation pressure, vibration amplitude and frequency. The stiffness with wheel rotating is substantially less than with wheel stationary, but the stiffness when rotating is relatively independent of road speed. There is a rather irregular variation with amplitude but behaviour is approximately linear for sinusoidal vibratio in the range 4 to 9 mm peak-peak. A consistent but not large frequency dependence exists, the stiffness increasing with increasing frequency.

The contribution to stiffness of pneumatic and casing effects can be separated for the rolling tyre. Pneumatic stiffness is linear with inflation pressure but independent of road spe and vibration frequency. Casing stiffness includes a frequency dependent component. A set of parameters has been determined for a physical model which represents the rolling tyre. It must noted, however, that the determination of parameters involves averaging and approximation.

The non-rolling tyre results show a stiffness behaviour somewhat different from that of the rolling tyre. No further explanation can be offered for an apparent non-linear dependence on inflation pressure although possible factors are tyre non-uniformities and varying geometry in the contact area.

Within the range of test conditions the radial damping is small and its effects are masked by interference arising from tyre non-uniformities.

ACKNOWLEDGEMENT

The assistance of the Olympic Tyre and Rubber Co. Pty. Ltd. is gratefully acknowledged.

REFERENCES

1. OVERTON, J.A., MILLS, B. and ASHLEY, C. The vertical response characteristics of the non-rolling tyre. *Proc. Instn Mech. Engrs*, Vol.184, Part 2A, 1969-70, pp.25-40.

2. BARSON, C.W. and DODD, A.M. Vibrational characteristics of tyres. *Symp. Vibration and Noise in Motor Vehicles, Instn Mech. Engrs*, 1972, pp.1-12.

3. GRIGG, F.W. The radial stiffness and damping properties of pneumatic tyres. *Trans. Instn Engrs Aust.*, Vol.MC3, 1967, pp.239-248.

4. CHIESA, A. and TANGORRA, G. The dynamic stiffness of tyres. *Revue Générale du Caoutchouc*, Vol.36, 1959, pp.1321-1329.

5. MILLS, B. and DUNN, J.W. The mechanical mobility of rolling tyres. *Symp. Vibration and Noise in Motor Vehicles, Instn Mech. Engrs*, 1972, pp.90-101.

6. COOPER, D.H. Radial stiffness of the pneumatic tyre. *Trans. Instn Rubber Industry*, Vol.40, 1964, pp.T58-T70.

DYNAMIC RESPONSE OF ACCELERATING VEHICLES TO GROUND ROUGHNESS

N. C. Nigam
Indian Institute of Technology
Kanpur, India

D. Yadav
Indian Institute of Technology
Kanpur, India

SUMMARY

A vehicle moving on the ground with a variable velocity is subjected to nonstationary base excitation due to surface uneveness. By transforming the governing equations of motion from time domain to space domain, the response of the vehicle to such excitation is determined using the Evolutionary Spectra Approach. Mean square acceleration and first passage probability of tyre bottoming is determined for a simple model of an aircraft during take-off run.

INTRODUCTION

All vehicles moving in contact with the ground are subjected to random base excitations due to surface uneveness. The vibration of vehicle systems due to such excitations may cause passenger discomfort, loss of control effectiveness and structural damage. The uneveness of prepared surfaces such as runways, highways, railway tracks etc. may be treated as a homogeneous random process and described to second order statistics by its power spectral density (P.S.D.)[1,2]. If a vehicle moves on such a surface with constant velocity, the base excitation is stationary and the dynamic response statistics of the vehicle can be obtained using the time or frequency domain random vibration analysis [3,4]. If the vehicle moves with a variable velocity, as during take-off and landing of aircraft, the base excitation becomes nonstationary. The difficulties associated with the nonstationary analysis (time domain or generalized P.S.D. analysis) can be circumvented by transforming the governing differential equations from time to space domain. The transformed equations are differential equations with variable coefficients and contain surface uneveness as a homogeneous random process. In this form the second order statistics of the response can be determined using the evolutionary spectra approach [5] in the frequency domain. The second order statistics can be used to determine fatigue life [6] and first passage failure [7] behaviour of the response. In this paper a simple model of the aircraft is used to determine the second order statistics of the response during take-off. The response characteristics are used to compute the first passage probability of tyre bottoming.

EQUATION OF MOTION

For the system model shown in Fig. 1, the governing equations of motion in terms of absolute displacement about the mean position are

$$\begin{bmatrix} m_1 & 0 \\ 0 & m_2 \end{bmatrix} \begin{Bmatrix} \ddot{z}_1 \\ \ddot{z}_2 \end{Bmatrix} + \begin{bmatrix} c_1 & -c_1 \\ -c_1 & c_1 \end{bmatrix} \begin{Bmatrix} \dot{z}_1 \\ \dot{z}_2 \end{Bmatrix} + \begin{bmatrix} k_1 & -k_1 \\ -k_1 & k_1+k_2 \end{bmatrix} \begin{Bmatrix} z_1 \\ z_2 \end{Bmatrix} = \begin{Bmatrix} 0 \\ k_2\, y(t) \end{Bmatrix}$$

$$\text{or } [m]\{\ddot{z}\} + [c]\{\dot{z}\} + [k]\{z\} = \{f(t)\} \tag{1}$$

Here ($\dot{}$) denotes differentiation w.r.t. time t and $y(t)$ is the random base excitation due to track uneveness.
Define the generalised coordinates x_n, n = 1,...,4 with

$$z_i = \sum_{n=1}^{4} u_{in}\, x_n, \quad \dot{z}_i = \sum_{n=1}^{4} \alpha_n\, u_{in}\, x_n \qquad i = 1,2 \tag{2}$$

where α_n are the eigen values and u_{in} are the elements of the modal column matrix

$$[U] = \begin{bmatrix} [\alpha u] \\ \hline [u] \end{bmatrix}$$

of the 4×4 system dynamical matrix

$$[D] = \begin{bmatrix} [0] & [I] \\ -[k]^{-1}[m] & -[k]^{-1}[c] \end{bmatrix}$$

In generalized coordinates the decoupled equations are [8]

$$\dot{x}_i - \alpha_i\, x_i = \frac{u_{2i}\, k_2\, y(t)}{2\alpha_i(m_1 u_{1i}^2 + m_2 u_{2i}^2) + c_1(u_{1i} - u_{2i})^2} \qquad i = 1,\dots,4 \tag{3}$$

Let the vehicle position along the runway at any time t be given by

$$s = a\, t^b$$

so that $\dot{s} = a\, b\, t^{b-1} = a_2\, s^{(b-1)/b}$ and $\ddot{s} = a\, b(b-1)\, t^{b-2}$

where a and b are constants and $a_2 = a^{1/b} \cdot b$ (4)

Using Eq. (4),Eq. (3) can be transformed from time to space domain

$$a_2\, s^{(b-1)/b}\, x_i' - \alpha_i\, x_i = \frac{u_{2i}\, k_2\, Y(s)}{2\alpha_i(m_1 u_{1i}^2 + m_2 u_{2i}^2) + c_1(u_{1i} - u_{2i})^2} \tag{5}$$

where (') denotes differentiation w.r.t. s and Y(s) is the random process representing the track uneveness.
General solution of Eq. (5) is

$$x_i = B_i \exp\left(\frac{b}{a_2}\,\alpha_i\, s^{1/b}\right) + \int_{-\infty}^{\infty} H_i(\Omega,s) \exp(j\Omega s)\, dF(\Omega) \qquad i = 1,\dots,4 \tag{6}$$

with

$$H_i(\Omega,s) = \frac{u_{2i}\, k_2}{[2\alpha_i(m_1 u_{1i}^2 + m_2 u_{2i}^2) + c_1(u_{1i} - u_{2i})^2]\,[j\Omega a_2 s^{(b-1)/b} - \alpha_i]}$$

$$Y(s) = \int_{-\infty}^{\infty} \exp(j\Omega s)\, dF(\Omega) \tag{7}$$

B_i are constants of integration, Ω is spatial frequency, $j = \sqrt{-1}$ and $\Phi_{YY}(\Omega)\, d\Omega = E[|dF(\Omega)|^2]$

If the initial conditions are

at $s = 0$: $z_i = d_i$ and $\dot{z}_i = v_i$ $\qquad i = 1,2$

the constants of integration are given by $\{B\} = [U]^{-1}\, [v_1\; v_2\; d_1\; d_2]^T$ (8)

From Eqs. (6) and (2) for i = 1,2

$$z_i = \sum_{n=1}^{4} u_{in}\, B_n \exp\left(\frac{b}{a_2}\,\alpha_n\, s^{1/b}\right) + \sum_{n=1}^{4} u_{in} \int_{-\infty}^{\infty} H_n(\Omega,s) \exp(j\Omega s)\, dF(\Omega) \tag{9}$$

$$\dot{z}_i = \sum_{n=1}^{4} \alpha_n u_{in} B_n \exp\left(\frac{b}{a_2}\alpha_n s^{1/b}\right) + \sum_{n=1}^{4} \alpha_n u_{in} \int_{-\infty}^{\infty} H_n(\Omega,s)\exp(j\Omega s)\, dF(\Omega) \tag{10}$$

Differentiating Eq. (10) w.r.t. t

$$\ddot{z}_i = \sum_{n=1}^{4} \alpha_n^2 u_{in} B_n \exp\left(\frac{b}{a_2}\alpha_n s^{1/b}\right) + a_2 s^{(b-1)/b} \sum_{n=1}^{4} \alpha_n u_{in} \int_{-\infty}^{\infty} \exp(j\Omega s)\{j\Omega H_n(\Omega,s) + H_n'(\Omega,s)\}dF(\Omega) \tag{11}$$

$$\text{with } H_n'(\Omega,s) = \frac{j\Omega(b-1)\, a_2 u_{2n} k_2}{b\, s^{1/b}[2\alpha_n(m_1u_{1n}^2+m_2u_{2n}^2)+c_1(u_{1n}-u_{2n})^2][j\Omega a_2 s^{(b-1)/b} - \alpha_n]^2} \tag{12}$$

SECOND ORDER STATISTICS OF RESPONSE

The runway uneveness Y(s) is assumed to be a homogeneous random process with zero mean and P.S.D. $\Phi_{YY}(\Omega) = \sigma^2\gamma/[2\pi(\Omega^2+\gamma^2)]$ where σ is the r.m.s. value of profile and γ is a small constant [9]. Hence

$$\mu_{z_i} = E[z_i] = \sum_{n=1}^{4} u_{in} B_n \exp\left(\frac{b}{a_2}\alpha_n s^{1/b}\right)$$

$$\mu_{\dot{z}_i} = \sum_{n=1}^{4} \alpha_n u_{in} B_n \exp\left(\frac{b}{a_2}\alpha_n s^{1/b}\right) \tag{13}$$

$$\mu_{\ddot{z}_i} = \sum_{n=1}^{4} \alpha_n^2 u_{in} B_n \exp\left(\frac{b}{a_2}\alpha_n s^{1/b}\right) \qquad i = 1,2$$

Spectral density and covarience function are given by the following relations [5]

$$\Phi_{z_i z_\ell}(\Omega,s) = \Phi_{YY}(\Omega) \sum_{p=1}^{4}\sum_{n=1}^{4} u_{ip} u_{\ell n} H_p(\Omega,s) H_n(-\Omega,s)$$

$$\Phi_{\dot{z}_i \dot{z}_\ell}(\Omega,s) = \Phi_{YY}(\Omega) \sum_{p=1}^{4}\sum_{n=1}^{4} \alpha_p \alpha_n u_{ip} u_{\ell n} H_p(\Omega,s) H_n(-\Omega,s) \tag{14}$$

$$\Phi_{\ddot{z}_i \ddot{z}_\ell}(\Omega,s) = a_2^2 s^{\frac{2(b-1)}{b}} \Phi_{YY}(\Omega) \sum_{p=1}^{4}\sum_{n=1}^{4} \alpha_p\alpha_n u_{ip} u_{\ell n}[j\Omega H_p(\Omega,s)+H_p'(\Omega,s)][-j\Omega H_n(-\Omega,s) + H_n'(-\Omega,s)]$$

and

$$\kappa_{z_i z_\ell}(s_1,s_2) = \sum_{p=1}^{4}\sum_{n=1}^{4} \int_{-\infty}^{\infty} \Phi_{YY}(\Omega)\, u_{ip} u_{\ell n} H_p(\Omega,s_1) H_n(-\Omega,s_2)\exp\{j\Omega(s_1-s_2)\}\, d\Omega$$

$$= 2\pi j C k_2^2 \sum_{p=1}^{4}\sum_{n=1}^{4} \frac{u_{ip} u_{\ell n} u_{2p} u_{2n}(R_1+R_2)}{[2\alpha_p(m_1u_{1p}^2+m_2u_{2p}^2)+c_1(u_{1p}-u_{2p})^2][2\alpha_n(m_1u_{1n}^2+m_2u_{2n}^2)+c_1(u_{1n}-u_{2n})^2]} \tag{15}$$

$$\kappa_{\dot{z}_i\dot{z}_\ell}(s_1,s_2) = 2\pi j C k_2^2 \sum_{p=1}^{4}\sum_{n=1}^{4} \frac{\alpha_p \alpha_n u_{ip} u_{\ell n} u_{2p} u_{2n}(R_1+R_2)}{[2\alpha_p(m_1u_{1p}^2+m_2u_{2p}^2)+c_1(u_{1p}-u_{2p})^2][2\alpha_n(m_1u_{1n}^2+m_2u_{2n}^2)+c_1(u_{1n}-u_{2n})^2]} \tag{16}$$

$$\kappa_{\ddot{z}_i \ddot{z}_\ell}(s_1,s_2)=2\pi j C k_2^2 a_2^2 (s_1 s_2)^{\frac{b-1}{b}} \sum_{p=1}^{4}\sum_{n=1}^{4} \frac{\alpha_p\, \alpha_n\, u_{ip}\, u_{\ell n}\, u_{2p}\, u_{2n}\, \partial^2(R_1+R_2)/\partial s_1 \partial s_2}{[2\alpha_p(m_1u_{1p}^2+m_2u_{2p}^2)+c_1(u_{1p}-u_{2p})^2]\,[2\alpha_n(m_1u_{1n}^2+m_2u_{2n}^2)+c_1(u_{1n}-u_{2n})^2]} \tag{17}$$

with

$$R_1 = \frac{j\, \exp\{-\gamma(s_1-s_2)\}}{\gamma(a_2\gamma s_1^{(b-1)/b}+\alpha_p)(a_2\gamma s_2^{(b-1)/b}-\alpha_n)}\; ; \; R_2 = \frac{j\, a_2 s_1^{\frac{2(b-1)}{b}} \exp\{\alpha_p(s_1-s_2)/(a_2 s_1^{\frac{b-1}{b}})\}}{(a_2^2\gamma^2 s_1^{\frac{2(b-1)}{b}}-\alpha_p^2)(s_1^{\frac{b-1}{b}}\alpha_n+s_2^{\frac{b-1}{b}}\alpha_p)} \tag{18}$$

$$C = \frac{\sigma^2\gamma}{2\pi}$$

For $i, \ell = 1,2$ and $s_1 \geq s_2$.

Equation (17) is obtained by differentiating Eq. (16) w.r.t. t_1 and t_2.

FIRST PASSAGE PROBABILITY OF TYRE BOTTOMING

The first passage probability beyond a barrier level S in the duration (0,s) is [7]

$$P(z>S|s) = \int_0^s \frac{\sigma_{z'}(p)}{2\pi\sigma_z(p)} \exp\{-\frac{S^2}{2\sigma_z^2(p)}\}\, dp \tag{19}$$

where $\sigma_z(p)$ is the standard deviation of the process at p.

The downward motion of the lower mass beyond a certain limit relative to the ground represents tyre bottoming. In considering the tyre bottoming in an aircraft, the effect of lift force on the dynamic response of the aircraft should also be included. The lift provides a time-varying deterministic force giving a time-varying deterministic bias to the response mean position. Incorporating the lift force into the equation of motion, the displacement from free position relative to the ground is

$$z_i = \sum_{n=1}^{4} u_{in} B_n \exp(\frac{b}{a_2}\alpha_n s^{1/b}) + g\sum_{n=1}^{4}\frac{u_{in}\,\alpha_n(m_1 u_{1n}+m_2u_{2n})}{2\alpha_n(m_1u_{1n}^2+m_2u_{2n}^2)+c_1(u_{1n}-u_{2n})^2}$$

$$-a_2^2 C_\ell \sum_{n=1}^{4} \frac{u_{in}\, u_{1n}[s^{2(b-1)/b}+\frac{2a_2(b-1)}{\alpha_n b} s^{(2b-3)/b}+\frac{2a_2^2(b-1)(2b-3)}{\alpha_n^2 b^2} s^{(2b-4)/b}+\dots+\dots]}{\alpha_n[2\alpha_n(m_1u_{1n}^2+m_2u_{2n}^2)+c_1(u_{1n}-u_{2n})^2]}$$

$$+\sum_{n=1}^{4} u_{in}\int_{-\infty}^{\infty} H_n(\Omega,s)\exp(j\Omega s)\, dF(\Omega) - \int_{-\infty}^{\infty}\exp(j\Omega s)\, dF(\Omega) \tag{20}$$

where lift $L = C_\ell\, \dot{s}^2$ (21)

and C_ℓ is assumed to be a constant.

For the lower mass and b = 2

$$\sigma_{z_2}^2(s) = \kappa_{z_2 z_2}(s,s) = \frac{C}{\gamma} - 4\pi C k_2 \sum_{n=1}^{4} \frac{u_{2n}\,\alpha_n\,(1/\gamma + \frac{a_2 s^{\frac{b-1}{b}}}{2\alpha_n})}{[2\alpha_n(m_1u_{1n}^2+m_2u_{2n}^2)+c_1(u_{1n}-u_{2n})^2]\,[a_2^2\gamma^2 s^{2(b-1)/b}-\alpha_n^2]}$$

$$-2\pi C\, k_2^2 \sum_{p=1}^{4} \sum_{n=1}^{4} \frac{u_{2p}^2\, u_{2n}^2 \left[\frac{1}{\gamma(a_2\gamma s^{(b-1)/b} - \alpha_n)} + \frac{a_2 s^{(b-1)/b}}{(\alpha_p+\alpha_n)(a_2\gamma s^{(b-1)/b} - \alpha_p)}\right]}{[2\alpha_p(m_1u_{1p}^2+m_2u_{2p}^2)+c_1(u_{1p}-u_{2p})^2]\,[2\alpha_n(m_1u_{1n}^2+m_2u_{2n}^2)+c_1(u_{1n}-u_{2n})^2(a_2\gamma s^{(b-1)/b}+\alpha_p)} \tag{22}$$

and $$\sigma_{z_2'}(s) = \kappa_{z_2'z_2'}(s,s) = \frac{\partial^2}{\partial s^2}\kappa_{z_2z_2}(s,s) \tag{23}$$

$\sigma_{z_2}(s)$ and $\sigma_{z_2'}(s)$ from Eqs. (22) and (23) can be used to determine the first passage probability of tyre bottoming.

RESULTS AND DISCUSSIONS

The system parameters of Boeing 707 aircraft are used to illustrate the application of above formulation. Following values of system parameters are used [3,4]

m_1 = 10,060 lb sec^2/ft (14,970 kg sec^2/m); m_2 = 155 lb sec^2/ft (230.2 kg sec^2/m);

c_1 = 116,460 lb sec/ft (173,400 kg sec/m); $k_1 = 2.03\times10^6$ lb/ft (30.2×10^6 kg/m);

$k_2 = .162\times10^6$ lb/ft ($.2402\times10^6$ kg/m)

a = 1.2205125 ; b = 2

γ = .001791 ; C = .00001

The damping coefficient has been taken equal to the equivalent damping coefficient at 100 ft/sec velocity from Ref. [4]. The values of a and b are chosen to give constant acceleration with take-off at 140 mph over a 8600 ft run. The runway roughness constant represents an average runway. The value of γ is taken from Ref. [9] where the roughness is described by its correlation function. Value of C_ℓ is determined by taking the lift force equal to total weight of aircraft at take-off.

The r.m.s. value of the upper mass acceleration is plotted against the distance along the runway in Fig. 2. At take-off the r.m.s. value of the acceleration is .1731 g.

First passage probability of tyre bottoming for a barrier level of 3.5 in is $.11\times10^{-8}$.

The r.m.s. value of the acceleration at the aircraft C.G. increases nonlinearly during the take-off run. The maximum value occures at take-off and is less than the r.m.s. values of acceleration during taxi (.185 g at 40 mph [4]). Probability of tyre bottoming is very small, as expected since landing impact is a more critical condition for tyre bottoming. The paper illustrates the application of Evolutionary Spectra Approach to a problem where the underlying process is homogeneous.

REFERENCE

1. Bogdanoff, J.L., Cote, L.J. and Kozin, F., "Introduction to a Statistical Theory of Land Locomotion-II, Ground Roughness", Journal of Terramechanics, Vol. 2, No. 3, 1965, pp.17-27.
2. Milwitzky, B., "Study of Taxiing Problem Associated with Runway Roughness", NASA MEMO.2-21-59L, March 1959, Pages 12.
3. Tung, C.C., Penzien, J. and Horonjeff, R., "The effect of Runway Uneveness on the Dynamic response of Supersonic Transports", NASA CR-119, 1964, pages 109.
4. Kirk, C.L. and Perry, P.J., "Analysis of Taxiing Induced Vibration in Aircraft by the Power Spectral Density Method", Aeronautical Journal, Vol. 75, No. 723, March 1971, pp.182-194.
5. Pristley, M.B., "Time Dependent Spectral Analysis and its Application in Prediction and Control", Journal of Sound and Vibration, Vol. 17, No. 4, 1971, pp. 361-364.
6. Yang, J.N. and Heer, E., "Reliability of Randomly Excited Structures", AIAA Journal, Vol.9, No. 7, July 1971, pp. 1262-1268.

7. Bolotin, V.V., "Statistical Methods in Structural Mechanics", Holden-Day. Inc., 1969.
8. Foss, K., "Coordinates which Uncouple the Equation of Motion of Damped Linear Systems", Journal of Applied Mechanics, Vol. 25, No. 3, 1958, pp. 361-364.
9. Tung, C.C., "The Effect of Runway Roughness on the Dynamic Response of Airplanes", Journal of Sound and Vibration, Vol. 5, No. 1, 1967, pp. 164-172.

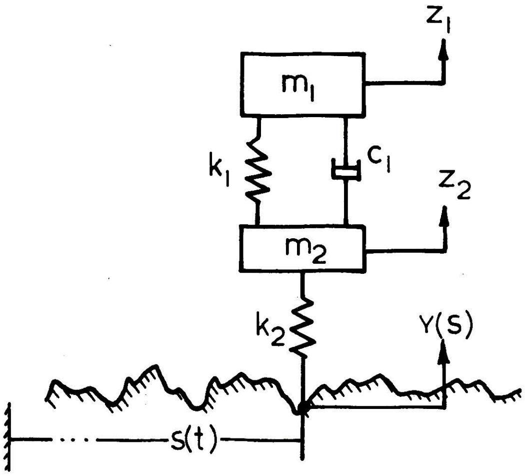

FIG.1_SYSTEM MODEL

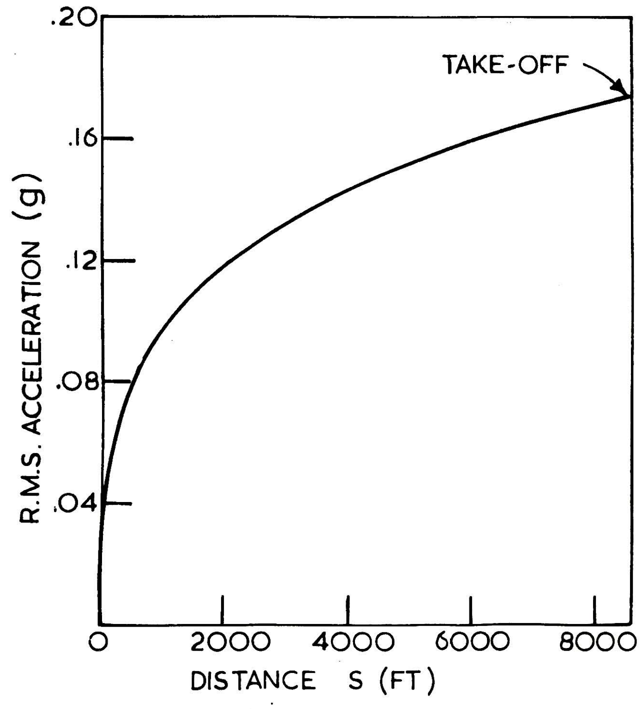

FIG.2_UPPER MASS R.M.S. ACCELERATION AGAINST DISTANCE

Noise, Shock & Vibration Conference, 1974 Monash University, Melbourne

FINITE ELEMENT SOLUTIONS OF THE WAVE EQUATION

G. J. Mc Rae
Department Mechanical Engineering
Monash University
Clayton, Victoria

Summary - This paper illustrates the application of the finite element technique to the solution of acoustic field problems in one, two and three dimensional coordinate systems.The method is compared with the traditional analytic and finite difference solutions to the space part of the wave equation,(the scalar Helmholtz equation) in particular for non-regular boundary geometries. A brief discussion of convergence of the numerical solution is included together with the steps involved in the derivation of high order elements. It is demonstrated that under certain conditions the finite element method is equivalent to the finite difference technique. The power and ease with which the method can be applied is illustrated by example of a sound field inside a car. A digitial computer program and the procedure for computation is presented. Rules for continuum discretization are developed from experience of the technique in solid mechanics.

1. Introduction

Finite element methods have been used with considerable success for obtaining approximate solutions to complex problems in structural and solid mechanics (13). The technique has gained general acceptance because a wide variety of problems with diverse geometrical configurations can be studied with a single computer program. Oden (12) and Zienkiewicz (20) have demonstrated that the variational principles utilized in structural mechanics can be applied to solve a wide variety of field problems whose solutions consist of continuous functions defined in spaces of finite dimension. As a result, considerable interest has been shown in extending the technique to such other domains as heat flow, fluid seepage in porous media, hydrodynamics, viscoelasticity and applied electrophysics (7). The purpose of this paper is to present the basic concepts of the finite element method and its application to acoustic field problems.

2. Solution of the Wave Equation

Propagation of sound in a homogenous, isotropic medium is described by the undamped wave equation (3).

$$\nabla^2\Psi = \frac{1}{c^2}\frac{\partial^2\Psi}{\partial t^2} \qquad - 1$$

The time and space parts of equation 1 can be seperated to give the scalar Helmholtz equation. (p' -is the excess pressure variation and k-the wave number)

$$\nabla^2 p' + k^2 p' = 0 \qquad - 2$$

In a more general sense equation 2 can be used to solve many boundary value problems in electromagnetics and electroacoustics (16); it contains Laplace's equation as a special case. Analytic solutions of 2 to determine the normal modes and frequencies of bounded acoustic fields have employed the method of seperation of variables, Green functions and collocation (10). Most of these methods are restricted to problems with relatively simple boundary conditions. Seperation of variables, for example, can only be applied to three co-ordinate systems in twodimensional space(9). In some cases conformal transformations can be used to map complex boundary geometries into simple shapes for solution by elliptic differential operators. Theoretical solutions to known shapes have been purturbed for other problems (4) however in general it is impossible to obtain analytic solutions to many practical problems.

Finite difference methods have been employed by a number of investigators to obtain numerical solutions in situations such as acoustic fields in ducts (1), rooms (5), and cars(14). There are a number of basic limitations associated with replacing 2 by a set of difference equations:

(a) The field is undefined except at discrete mesh points.
(b) Singular and source points are difficult to handle.
(c) Awkward boundary shapes often require special difference operators which necessitates a unique computer program for each new problem.

It was in an effort to improve on these limitations that attention has been directed to the use of the finite element method.

3. The Finite Element Method.

The basic concept of the finite element method is the representation of a continuum by an assemblage of subdivisions or finite elements connected on their boundaries at a discrete number of nodal points (figure 1). A distinction between a spatial and material subdivision of the continuum must be made for acoustic field problems. With air, the finite element defines the space through which the fluid flows - in solid mechanics, distortion of the material is described by a spatial change in the finite element mesh. It is convenient, in acoustics, to formulate the unknowns in terms of nodal pressures; and since pressure is a scalar quantity it is only necessary to use one unknown per node (5). The acoustic field over the entire domain is approximated by a set of continuous algebraic functions defined over individual elements. Within a particular element the pressure is assumed to be represented by a polynomial function of the field variables at the individual nodes.

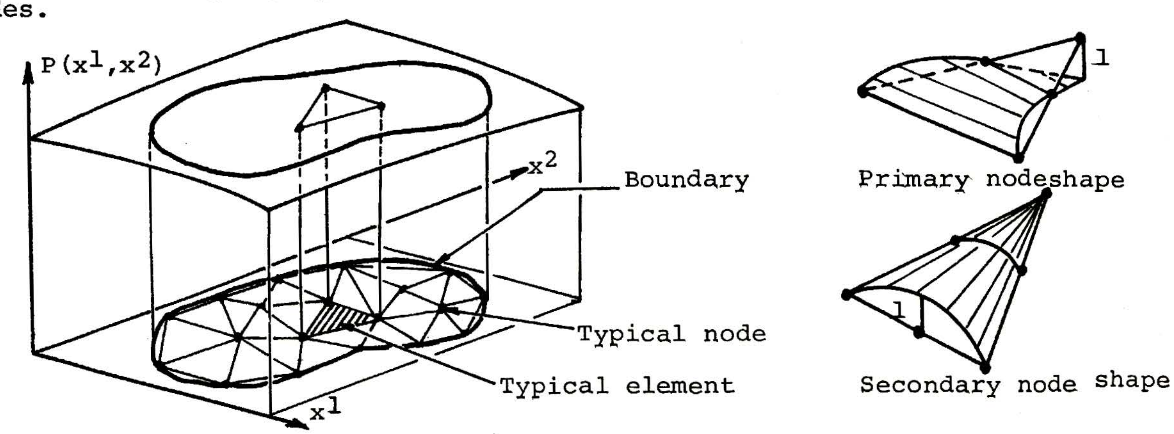

Figure 1 :- Finite element representation of a continuum and two typical polynomial shape functions for the field variation over element.

The derivation of the set of equations for the continuum may be achieved by direct, residual or by variational methods. In this paper minimization of a functional expression is carried out with respect to the field variables at each of the nodes. Complementary formulations may require a maximization, however both are usually subsumed under the more general stationarity requirement (19). In elasticity the formulation of the equations is achieved by minimizing a functional describing the total potential energy of the system. Zienkiewicz(20) has shown the generality of the variational approaches in field problems where stationarity of a functional, subject to the boundary conditions, gives the exact solution. Craggs (5) and Shuku (14) have formulated frequency dependent functionals for the acoustic wave equation, which after setting the first variation to zero results in the Helmholtz equation and the boundary condition 3 at the surface of the acoustic space.

$$\text{grad } p' = -i\rho\omega A p' \qquad - 3$$

In this paper hard boundary conditons are assumed so that the specific acoustic impedance A = 0 and grad p = 0, there is in principal no difficulty associated with using either homogenous Neumann or Dirichlet boundary conditions.

4. Natural Co-ordinate Systems.

The formulation of the variational expressions and calculation of the element properties can be simplified by the use of natural cordinates. A local system is one that is defined for a particular element, not necessarily for the entire space, the system for the complete continuum is called the global co-ordinate system. A natural co-ordinate system is a local one which permits specification of a point within an element by a set of dimensionless numbers whose magnitudes never exceed unity. In a d-dimensional co-ordinate system $x^1, x^2, \ldots, x^d$ the finite element is a simplex with at least d+1 vertices (figure 2), whose size is given by $S=D/d!$. D is defined by the determinant 4, note that for example the size of a line is its length, triangle its area, etc.

$$D = \begin{vmatrix} 1 & x_1^1 & x_1^2 & \cdots & x_1^d \\ 1 & x_2^1 & x_2^2 & \cdots & x_2^d \\ \vdots & \vdots & \vdots & & \vdots \\ 1 & x_{d+1}^1 & x_{d+1}^2 & \cdots & x_{d+1}^d \end{vmatrix} \qquad -4$$

If P is a point within the element and S_m the size of the simplex defined by P and all other vertices except m then it is obvious that the set of equations 5 define uniquely any interior point.

$$L_i = \frac{S_m}{S} \qquad -5$$

A further result from linear dependence is given by 6

$$\sum_{i=1}^{d+1} L_i = 1 \qquad -6$$

Geometrically the L_i co-ordinates measure normalized distances towards the m-th vertex orthogonally from the d-1 -dimensional simplex defined by all vertices of the element except m (17). If necessary the L_i co-ordinate system can be defined in terms of the Cartesian x^i system by the use of 7.

$$L_i = \frac{1}{D}\left(a_i^0 + a_i^1 x^1 + \ldots + a_i^d x^d \right) \qquad -7$$

Where a_i^r are the minors of the r-th row of D. A natural co-ordinate system simplifies problem formulation, preserves symmetry and facilitates the integration over the element. For example, using polynomial expansion and integration by parts a cartesian surface integral can be expressed simply as:

$$I_{pq} = \iint L_1^p L_2^q \, ds = 2D \int_0^1 \int_0^{1-L_2} L_1^p L_2^q \, dL_1 \, dL_2 = 2D \frac{p!\,q!}{(p+q+2)!} \qquad -8$$

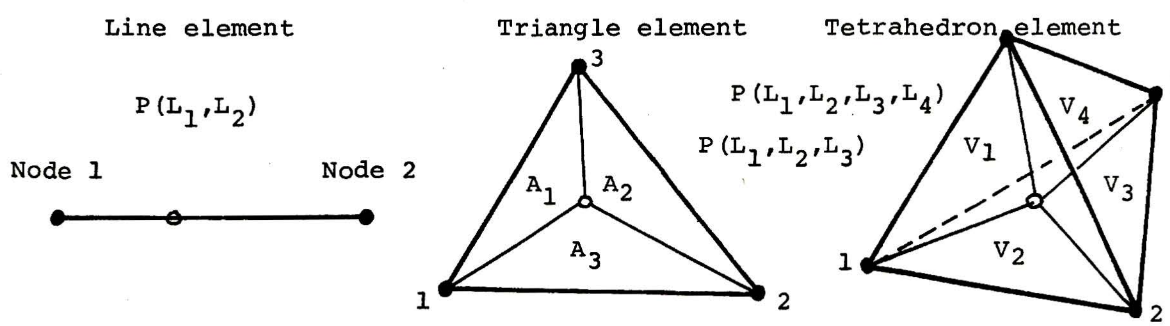

$L_i = \frac{L_i}{L}$ $\qquad A_i = \frac{A_I}{A}$ $\qquad V_i = \frac{V_i}{V}$

L = element length $\qquad$ A = element area $\qquad$ V = element volume

Figure 2 :- Examples of natural co-ordinate systems.

5. Pressure Variation over an Element.

The solution of 2, subject to the associated boundary conditions, is equivalent to minimizing the functional 9 over the element volume (19).

$$F(p) = \frac{1}{2} \int_V (|\text{grad } p|^2 - k^2 p)\, dv \qquad - 9$$

F(p) is stationary if, and only if, p equals the true solution for p'; so the basic problem of the finite element method is to construct a solution for p over each element so as to obtain the best approximation for p' over the complete solution space. A common approach is to assume that within an individual element the pressure p can be represented by a polynomial function of the nodal coordinate system (2,6,15,18,20). In order to guarantee solution isotropv or geometric invariance the polynomial expression applicable to each element must be complete. If n is the order of the polynomial there must be at least $N=(n+d)!/(n!d!)$ terms to satisfy this condition. Geometrically this implies that the pressure distribution is permitted an equal complexity of curvature in any direction. A further condition is that within an individual element a 'pressure rigid body mode' is allowed; this corresponds to a uniform pressure rise. The polynomial must in addition satisfy the conditions of pressure continuity within an individual element and for the assemblage as a whole. The continuity of p is essential to the valid use of 9. At the boundaries between elements the normal derivit ive is not continuous, this however does not introduce any errors as the net integrated value of these discontuities is zero.

Modifying Silvester's notation (15) the pressure variation within an element can be defined in the form

$$p^e = \sum_{m=1}^{N} p_m^e \, \alpha_m (L_1, L_2, \ldots, L_{d+1}) \qquad - 10$$

$$= \sum_{m=1}^{N} p_m^e \, \alpha_m \qquad - 11$$

Where α_m are the interpolation polynomials of degree N on the element and p_m^e is the value of p at the interpolation node m The coefficients of α_m, for equispaced nodes are of the closed Newton-Cotes type defined by equations 13 and 14.

$$\alpha_m (L_1, L_2, \ldots, L_{d+1}) = \sum_{k=1}^{d+1} P_{j_k}(L_k) \qquad - 13$$

Where

$$P_m(z) = \frac{1}{m!} \prod_{k=0}^{m-1} (Nz-k) \quad ; \quad m>0 \qquad - 14$$

$$P_m(z) = 1 \quad ; \quad m=0 \qquad - 15$$

Each node has associated with it d+1 integers $j_1, j_2, \ldots, j_{d+1}$ which sum to n and vary cyclically through the mesh (6,17). The polynomials 13 satisfy all the previous conditions and, at the interpolation nodes, satisfy 10 and 11 identically.

6. Solution of the Variational Expression

The minimization of F(p) over the assembled elements is equivalent to the minimization of $F(p^e)$ over an individual element. Within any element the conditions to be satisfied are:

$$\frac{\partial F(p^e)}{\partial p_m^e} = 0 \quad ; \quad m=1,2, \ldots, N \qquad - 16$$

i.e. substituting into equation 9

$$\frac{1}{2} \int_V \frac{\partial}{\partial p_m^e} |\text{grad } p^e|^2 \, dv = \frac{k^2}{2} \int_V \frac{\partial}{\partial p_m^e} p^{e2} \, dv \qquad - 17$$

Equation 11 is used to calculate $|\text{grad } p^e|^2$ and p^{e2}, these results are then sudstituted into 17 and after some manipulation, result in the set of linear algebraic eigen value equations 18.

$$S_{mq}\, p_q = k^2\, T_{mq}\, p_q \qquad - 18$$

Where the matrices S_{mq} and T_{mq} are given by:

$$S_{mq} = \frac{1}{D^2} \sum_{k=1}^{d} \sum_{i=1}^{d+1} \sum_{j=1}^{d+1} a_i^k\, a_j^k \int_V \frac{\partial \alpha_m}{\partial L_i} \frac{\partial \alpha_q}{\partial L_j}\, dv \qquad - 19$$

$$T_{mq} = \int_V \alpha_m\, \alpha_q\, dv \qquad - 20$$

The matrices S and T for each element can be assembled into two global matrices A and B by a simple mapping operation to form the eigen value problem for the complete model.

$$A\, p = \lambda B\, p \qquad - 21$$

The mapping is based on nodal connectivities, for example in figure 3 the pressure at node 2 is common to elements 2,3 and 4. The contribution from each element to form A and B is simply the sum of the individual contributions from S and T. The associated Boolean connectivity matrix is shown in figure 3b, this matrix is not needed explicitly and is usually coded directly into the computer program.

Finite element Model

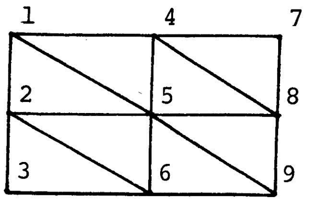

2 - element number
3 - node number

(b)

Nodal Connectivity Matrix

$$\begin{array}{c} \\ 1\\2\\3\\4\\5\\6\\7\\8\\9 \end{array} \begin{array}{c} \begin{array}{ccccccccc} 1&2&3&4&5&6&7&8&9 \end{array} \\ \left[\begin{array}{ccccccccc} 1&1&0&1&1&&&& \\ 1&1&1&0&1&1&&& \\ 0&1&1&0&0&1&0&& \\ 1&0&0&1&1&0&1&1& \\ 1&1&0&1&1&1&0&1&1 \\ &1&1&0&1&1&0&0&1 \\ &&0&1&0&0&1&1&0 \\ &&&1&1&0&1&1&1 \\ &&&&1&1&0&1&1 \end{array}\right] \end{array}$$

Semi band width = 3

(a)

Figure 3:- Typical finite element model and connectivity matrix

7. Properties of Matrices S,T,A and B

The properties of A and B depend on the structure of the submatrices S and T. It can be seen by inspection of 19 and 20 that S and T are symmetric. A and B are formed from the matrix sum of the symmetric submatrices and as a result are symmetric, sparse and banded.

(a) T is always positive definite and diagonally dominant.
(b) The diagonal elements of S are positive with the row and column sums equal to zero. The matrix S is singular and positive definite.

The positive definite nature of S and T ensures that A and B are also positive definite, this property ensures the convergence of iterative solutions to the eigen value problem (8). Simple computational checks can be based on (a) and (b); a useful fact is that the sum of the elements of T is equal to the element size (D/d!).

8. Calculation of the Components of the Matrices S and T

Silvester (15) has shown that the total number of operations required to evaluate the element matrices S and T varies as n^6. Manual evaluation of the components is restricted in most cases to low order elements and so for higher orders the process must be automated. The symbol manipulation capabilities of PLI and FORMAC were used to perform the basic polynomial operations required to evaluate 19 and 20. Symmetry properties and the generalised form of 8 can be exploited to reduce the computational burden. The approach can be illustrated by evaluating 19 and 20 for a tetrahedron. Tetrahedrons are a very useful three dimenensional elements as they can be used to form triangular prisms, pyramids and hexahedrons. The formation of S requires a summation over 48 terms, of these only 18 are independent by using 8 and 21.

$$\sum_{i=1}^{4} a_i^j = 0 \qquad ; \quad j=1,2,3 \qquad - 21$$

$$S_{mq} = - \frac{1}{6V} \sum_{k=1}^{3} \sum_{i=1}^{3} \sum_{j=i+1}^{4} a_i^k a_j^k \int_v \frac{\partial \alpha_m}{\partial L_i} \frac{\partial \alpha_q}{\partial L_j} dv \qquad - 22$$

Similarly for matrix T

$$T_{mq} = 6V \int_v \alpha_m \alpha_q \, dL_i \, dL_j \, dL_k \qquad - 23$$

The matrices S and T for a number of standard elements are shown in figure 4. In accord with convention and because of symmetry only the upper half for T and the lower triangle for S are recorded. In the case of the triangle element the matrix S is formed using 24 (15).

$$S = \sum_{i=1}^{3} Q_i \cot \theta_i \qquad - 24$$

The matrices Q_i are simply row and column permutations of each other and can be formed from Q_1.

7. Convergence of the Finite Element Solution

For any numerical solution involving approximation it is important to consider the requirements for convergence to an exact solution. The accuracy can be improved by two methods, mesh refinement or by selection of higher order polynomial models. Thereis no simple answer to whichis the best method as an acceptable balance between accuracy and computer time to achieve the results must be established. Zienkiewicz (20) has shown that the finite element method provides an upper bound to the true solution. As the finite element mesh is successively refined the approximate solution will converge to an exact result from above. The physical conditions to ensure convergence with mesh refinement are:-

(a) All previous meshes should be contained within the refined mesh.
(b) The same polynomial models should be retained for the refinement.
(c) Any point in the domain can be included in the refined mesh.

A result of this is that a single problem solution is not sufficient to prove convergence and a check should be made by repeating the process with a refined mesh. In regions of abrupt changes it is often necessary to construct a fine mesh in these cases elements with small vertex angles should be avoided. There is no clear cut approach to the selection of the finite element model and the following guidelines are based on experience. Simple low order elements can give good results for low order modes. For a given level of accuracy the use of higher order models reduces the computer time for solution. The time to calculate the result varies as the number of nodes and is practictically independent of the order of individual elements. Daly (6) has shown that by considering the individual rows of A and B, for symmetric elements, equations can be developed which are equivalent to the finite diffreence forms. As an example consider a string composed of elements for which n=1. Using the elements of S and T from figure 4 the eigen value equations for a typical pressure node p_n is given by 25.

$$-1\, P_{n-1} + 2\, P_n - 1\, P_{n+1} = \frac{(kh)^2}{6} (P_{n-1} + 4\, P_n + P_{n+1}) \qquad - 25$$

If all the right hand side weighting is placed on the central node 25 is the standard finite difference form of 2 (1).

Line element n=1

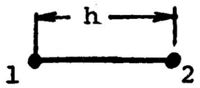

$S = \frac{1}{H}(\ )$

$T = \frac{h}{6}(\ )$

$$\begin{bmatrix} & 2 & 1 \\ 1 & & 2 \\ -1 & 1 & \end{bmatrix}$$

Line element n=2

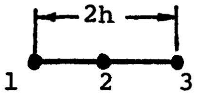

$S = \frac{1}{6h}(\ )$

$T = \frac{h}{15}(\ )$

$$\begin{bmatrix} & 4 & 2 & -1 \\ 7 & & 16 & 2 \\ -8 & 16 & & 4 \\ 1 & -8 & 7 & \end{bmatrix}$$

Triangular element n=1

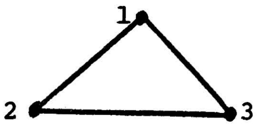

$Q_1 = \frac{1}{2}(\ )$

$T = \frac{A}{12}(\ )$

$$\begin{bmatrix} & 2 & 1 & 1 \\ 0 & & 2 & 1 \\ 0 & 1 & & 2 \\ 0 & -1 & 1 & \end{bmatrix}$$

Triangular element n=2

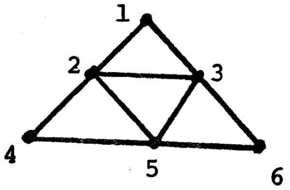

$Q_1 = \frac{1}{6}(\ )$

$T = \frac{A}{180}(\ )$

$$\begin{bmatrix} & 6 & 0 & 0 & -1 & -4 & -1 \\ 0 & & 32 & 16 & 0 & 16 & -4 \\ 0 & 8 & & 32 & -4 & 16 & 0 \\ 0 & -8 & 8 & & 6 & 0 & -1 \\ 0 & 0 & 0 & 3 & & 32 & 0 \\ 0 & 0 & 0 & -4 & 8 & & 6 \\ 0 & 0 & 0 & 1 & -4 & 3 & \end{bmatrix}$$

Regular tetrahedron n=1

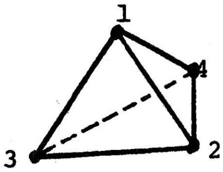

$S = \frac{h}{12}(\ )$

$T = \frac{h^3}{60}(\ )$

$$\begin{bmatrix} & 2 & 1 & 1 & 1 \\ 3 & & 2 & 1 & 1 \\ -1 & 3 & & 2 & 1 \\ -1 & -1 & 3 & & 2 \\ -1 & -1 & -1 & 3 & \end{bmatrix}$$

Right tetrahedron n=1

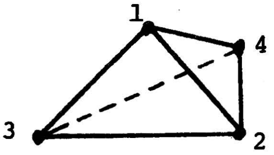

$S = \frac{h}{6}(\ )$

$T = \frac{h^3}{120}(\ )$

$$\begin{bmatrix} & 2 & 1 & 1 & 1 \\ 3 & & 2 & 1 & 1 \\ -1 & 1 & & 2 & 1 \\ -1 & 0 & 1 & & 2 \\ -1 & 0 & 0 & 1 & \end{bmatrix}$$

Cube element n=1(Composed of tetrahedrons)

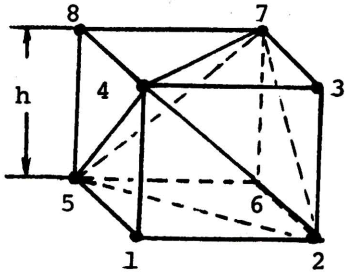

$S = \frac{h}{12}(\ )$

$T = \frac{h^3}{120}(\ )$

$$\begin{bmatrix} & 2 & 1 & 0 & 1 & 1 & 0 & 0 & 0 \\ 6 & & 10 & 1 & 4 & 4 & 1 & 4 & 0 \\ -2 & 9 & & 2 & 1 & 0 & 0 & 1 & 0 \\ 0 & -2 & 6 & & 10 & 4 & 0 & 4 & 1 \\ -2 & -1 & -2 & 9 & & 10 & 1 & 4 & 1 \\ -2 & -1 & 0 & -1 & 9 & & 2 & 1 & 0 \\ 0 & -2 & 0 & 0 & -2 & 6 & & 10 & 1 \\ 0 & -1 & -2 & -1 & -1 & -2 & 9 & & 2 \\ 0 & 0 & 0 & -2 & -2 & 0 & -2 & 6 & \end{bmatrix}$$

Figure 4 :- Some examples of acoustic finite elements

It can be shown for line, rectangular and cuboidal enclosures that the finite element solution converges to the exact solution as $h \to 0$; the eigenvalues are given by equation 26.

$$k^2 = | 1 + O(h^{2n}) | \sum_{i=1}^{d} \left(\frac{m_j \Pi}{c_i} \right)^2 \quad ; j=1,2,.. \qquad - 26$$

Where m_j are the mode numbers and c_i the characteristic dimensions in the x^i directions. Note that as the mode number increases so does the error; this is also apparent in the eigen vectors as they are discrete samples of the exact solutions.

8. Computer Solution Process

Each element is defined by its type, node co-ordinates, node numbers, polynomial order, and the associated material property. This information together with the prestored matrices S and T for each element type is used to assemble the base matrices A and B. Element edges are identified by the numbers assigned to the nodes they join together. The inter-element continuity requirements enables the assembly of A and B in their correct sequence to form the eigen value problem 21. Computational efficiency can be improved by minimising the maximum difference between connected node numbers. In order to be able to solve 21 economically it is essential to fully exploit matrix sparcity and the positive definite nature of the constituent matrices. Most eigen value algorithms are based on either transformation or iterative methods. In transform methods the relevant matrix is formed into a diagonal, tridiagonal or upper Hessenberg type by a similarity transform. In most cases the transform matrix destroys the sparcity and for large problems standard programs are not economical with respect to either storage or solution time. The usual iterative procedures on the other hand, operate on either one or a pair of matrices extracting the roots one at a time. The algorithm used for this paper was based on the combined Sturm sequence - inverse iteration method developed by Gupta (10). With this approach the Sturm sequence property is used to isolate the root and then a decomposition of $A - \lambda B$ extracts the eigenvalue and its vector simultaneously. This method has a number of advantages, in addition to computing speed, over conventional approaches:-

(a) The routine is capable of calculating roots lying between specified lower and upper bounds of λ. This is very useful in situations where a uniform pressure rise can occur.
(b) The program exploits matrix sparsity.
(c) The routine is numerically stable and convergence is assured.

Computer times for problems with up to 200 degrees of freedom and 15 eigenvalues are typically less than five minutes on a Burroughs B6700.

9. Sample Problem

The operation of the program and convergence of the elements were checked using problems with known analytic solutions - vibrating strings, rooms and plates. A practical application of the method, that can be confirmed by experimental results is the determination of the sound field inside a car (5,6). The results for the first two modes are shown in figure 5 together with the finite element model of a vertical section through a uniform car. With a more refined model it would be possible to include the effects of the seats. Such an approach would enable the designer to avoid resonant modes near the drivers head. Table 1 is a comparison of the finite element solutions for three polynomial orders with the finite difference and experimental solutions of Shuku (6).

Table 1:- Comparison of the Normal mode frequencies of a car interior using finite element, finite differences and experimental results.

Mode	Polynomial Order of Model			Finite Difference	Experimental
	1	2	3		
1	86.9 Hz	86.9 Hz	86.8 Hz	88.0 Hz	87.5 Hz
2	142.7 Hz	141.0 Hz	138.8 Hz	137.7 Hz	138.5 Hz

The finite element results are very close to the experimental values and any difference is probably due to the assumption of hard boundary conditions in the finite element case. The convergence of the frequencies with increasing element order confirms the results of equation 26 and that the finite element method convergesto the true solution form above. Similarly it is well known that the finite difference method converges to the exact solution from below this is confirmed for the second mode. Solution times for the finite element method were less than two minutes

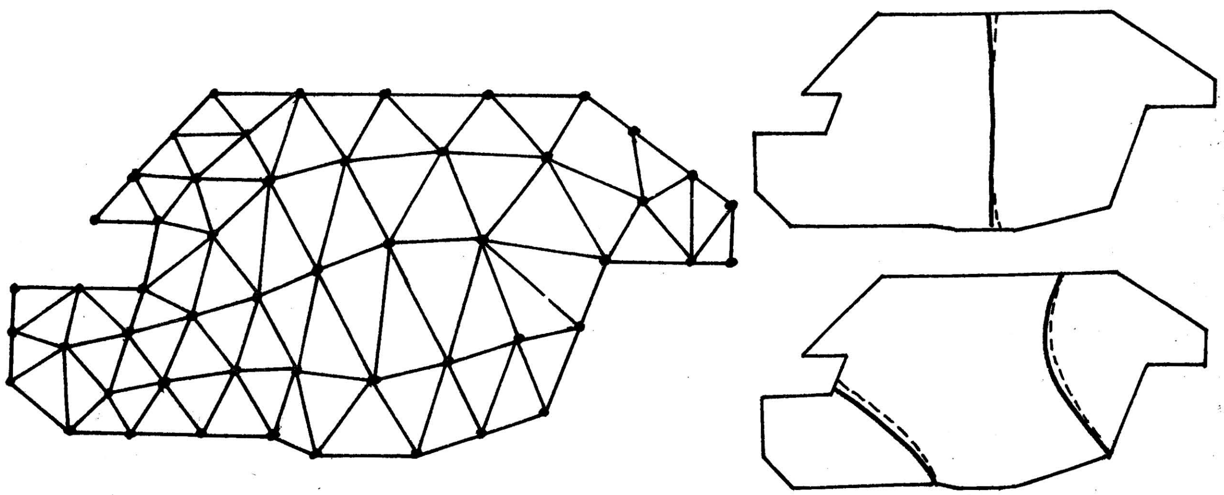

Figure 5 :- Finite element model and mode shapes for the first two modes of a nonvented car enclosure (hard boundary conditions).

Conclusion

The finite element method is rapidly gaining acceptance as a technique in practical engineering analysis and has a potential for future application in acoustics. Like all numerical approximations the technique is based on the concept of discretization. Despite this fact the formulation of the pressure models in terms of nodal variables allows a solution to be obtained over the complete continuum. The variational formulation of the pressures results in an eigen value problem whose solution represents an upper bound to the exact result. The accuracy and convergence of the method has been satisfactorily confirmed against known analytic, finite difference and experimental solutions. Under certain conditions the finite element and finite difference solutions are identical. Further work is being conducted to include complex boundary conditions and solutions to transient field problems. Finally, as for any numerical method, the results of a finite element analysis must be interpreted with care and tempered with engineering judgement - the purpose of computing is to gain insight not numbers.

Acknowledgements

The author is indebted to Dr. K.K. Gupta of the Jet Propulsion Laboratory for his valuable assistance with the development of the computer algorithm to solve the algebraic eigenvalue problem.

References

1. Alfredson, R.J., 'A Note on the Use of the Finite Difference Method for Predicting Steady State Sound Fields' , ACUSTICA, Vol. 28, p296-301, 1973.

2. Ahmed, S. and Daly, P., 'Waveguide Solutions by the Finite Element Method', The Radio and Electronic Engineer, Vol. 38, No. 4, p217-223, Oct. 1969.

3. Beranel, L.L., "Acoustics', McGraw-Hill, New York, 1954.

4. Bolt, R.H., Feshbach, H. and Clogston, R.M., 'Perturbation of Sound Waves in Irregular Rooms', J. Acoustical Society of America, Vol. 13, p65-73, 1942.

5. Craggs, A., 'The use of Simple Three-dimensional Acoustic Finite Elements for Determining the Natural Modes and Frequencies of Complex Shaped Enclosures'; J. of Sound and Vibration, Vol. 23, p331-339, 1972.

6. Daly, P. and Helps, J.D., 'Exact Finite Element Solution to the Helmholtz Equation', Int. J. for Numerical Methods in Engineering, Vol. 6, p529-542,1973.

7. Desai, C.S. and Abel, J.F.,'Introduction to the Finite Element Method', Van Nostrand Reinhold Company, New York, 1972.

8. Gupta, K.K.,'Eigenproblem Solution by a combined Sturm Sequence and Inverse Iteration Technique', Int. J. for Numerical Methods in Engineering, Vol. 7. p.17-42, 1973.

9. Moon, P. and Spencer, D.E. 'Partial Differential Equations' , D.C. Heath and Company, Massachusetts, 1969.

10. Morse, P.M. and Feshbach, H., 'Methods of Theoretical Physics', McGraw-Hill, New York, 1953.

11. Motz, H., 'Calculation of the Electron Field Frequency and Circuit Parameters of high Frequency Resonant Cavities', J. IEE (London), Vol. 9 Pt 3. p335-343 1946.

12. Oden, J.T., 'A General Theory of Finite Elements: Part 1 Topological Considerations' Int. J. for Numerical Methods in Engineering, Vol. 1 No.2,1969.

13. Przemiencki, J.S., 'Theory of Matrix Structural Analysis', McGraw-Hill, New York 1968.

14. Shuku, T. and Ishihara, K., 'The Analysis of the Acoustic Field in Irregularly Shaped Rooms by the Finite Element Method', J. of Sound and Vibration, Vol. 29, No. 1, p 67-76 1973.

15. Silvester, P., 'High-order Polynomial Triangular Finite Elements for Potential Problems,', Int. J. of Engineering Science, Vol. 17, 849-861, 1969.

16. Silvester, P., 'A General High-Order Finite Element Waveguide Analysis Program', IEEE Transactions on Microwave Theory and Techniques, Vol. MTT-17, No.4 1969.

17. Silvester, P.,'Symmetric Quadrature Formulae for Simplexes', Mathematics of Computation, Vol. 24 No. 109, p.95 - 100, January 1970.

18. Silvester, P. and Konrad, A., 'Axisymmetric Triangular Finite Elements for the Scalar Helmholtz Equation', Int. J. for Numerical Methods in Engineering, Vol. 5, p. 481-497, 1973.

19. Stakgold, I.,'Boundary Value Problems of Mathematical Physics', Macmillian, New York, 1968.

20. Zienkiewicz, O.C., and Cheung Y.K.,"The Finite Element Method in Structural and Continuum Mechanics', McGraw-Hill, London, 1967.

Noise, Shock & Vibration Conference, 1974 Monash University, Melbourne

UTILIZATION OF VIBRATORY DISPLAYS IN MANUAL SITUATIONS

T. J. Triggs
Department of Psychology
Monash University
Clayton, Victoria

SUMMARY -

This paper reports on a study of tactual flight control displays including the initial development of the displays and their evaluation using formal experiments. The need for transmitting information to pilots in other than the visual modality has been recognized increasingly over the last decade. Tactual displays have significant potential for situations where task demands do not allow the human operator to fixate a visual tracking display continuously. Vibro-tactile and electrocutaneous stimulation techniques were investigated in both psychophysical judgment and manual control experiments, using several basic display geometries. Although electrocutaneous stimulation could be made tolerable by adjustment for some subjects, vibratory stimulation was judged to be more satisfactory. Continuous manual tracking was carried out using both vibratory and visual displays using one display geometry. In addition, combined tracking and visual monitoring tasks were used to provide relative comparisons of tactual and visual tracking displays in situations imposing a high visual scanning workload. Although the tactual displays yielded generally inferior performance to the visual displays, inter-task interference effects were substantially less with the tactual display in the high visual demand situation.

INTRODUCTION -

When "vibration" and "human performance" are spoken of together, a degradation in performance is usually what is assumed. It has been generally shown that vibration of the human or the environment in which he is working degrades his performance, and this phenomenon has been subjected to systematic study (e.g. Grether) (1). However, there is another side to all this. Vibration, or indeed a range of various stimulation techniques, applied selectively to a human's skin holds the promise of expanding the available ways of displaying information. While the visual modality is truly dominant in the area of information

*This research was supported by the Advanced Research Projects Agency, Department of Defense, was monitored by the Office of Naval Research under Contract No. N00014-73-C-0031: John J. O'Hare, Scientific Officer, Engineering Psychology Programs, and was performed when the author was at Bolt, Beranek and Newman, Cambridge, Massachusetts.

displays, recent work in the cutaneous area shows that it represents a viable alternative. Possibly the best examples of a current commercial tactual display system is the "Optacon" (optical to tactile converter) currently being marketed in the United States which afford blind people direct access to printed material of a wide range of font types. This portable reading device relieves blind people from dependence on Braille, and early evaluations have judged it to be very successful, although as yet reading speeds do not match that of Braille.

This paper reports on the evaluation of tactual displays for the control of flight. In current aircraft, nearly all flight parameter information available to the pilot is transmitted to him visually, whether under visual contact or instrument flying conditions. It has long been recognized that during instrument flying conditions the task of scanning just the essential instruments is a taxing, fatiguing one (2).

Investigation has shown that the minimum time required to accommodate from outside the cockpit to the instrument panel, read an instrument, and then return to viewing the external scene is approximately 2.5 sec (3). Such large time measures indicate that this transitioning constitutes a significant loss in the time available to the pilot for actually processing visual information.

Midair collisions frequently can be attributed to the fact that pilots were not maintaining sufficient viewing of the outside scene. Zeller and Burke (4) found that 80% of one class of midair collisions occurred in daylight under contact conditions. Thus, poor visibility and increasing air speeds are not the only major contributing causes of midair collisions (5); it seems fair to say that lack of external viewing is also a significant factor. Pilots tend to use extra-cockpit visual information only a small proportion of the time available (6).

Displays to sense modalities other than vision have the advantage of presenting continuous information to the pilot independently of his head position and eye orientation, but probably would not suffer any of the disadvantages described for helmet-mounted displays. Not only can display of information to other modalities free the eyes substantially from tasks inside the cockpit, but it is reasonable to expect that such displays could alleviate the demands of the visual scanning task within the cockpit as well. The nonvisual display provides a close coupling between the stimulus and the operator.

Auditory flight displays have received some research attention, and one system referred to as flying by auditory reference (FLYBAR) was developed to supply to the pilot all the necessary information for him to maintain a required flight path (7, 8). At least one of the display systems developed yielded performance in a Link Trainer comparable with that obtained from the standard visual instrument panel. However operational systems did not emerge from these early studies.

Tactual displays, on the other hand, may offer two possible advantages over auditory displays for presentation of basic flight control data. First, tactual displays should not interfere in any real way with speech communication. Second, tactual presentation is not as limited in its ability to present information in a spatial pattern. This should be important in the flight control situation where the required information has a strong spatial component, e.g. vehicle orientation, attitude and location in space. There has been some previous work in tactual flight control displays. However, the displays developed were either relatively simple (9), or were considered to be supplements to the visual displays (10).

In comparison of tactual and visual tracking, several studies have found that, when compared with a similarly quantized visual display, tactual displays yielded very similar performance (11, 12). Hill (13) found that a "ripple" tactual display yielded superior performance to a standard, continuous CRT visual display.

Most studies in this modality have used mechanical vibration after the pioneering work of Geldard (14). However, electrotactors have also been explored. The greatest difficulty in the latter form of stimulation is to obtain inputs well above threshold but yet entirely acceptable and comfortable (15).

In this research study, an initial comparison of electrocutaneous and mechanical means of tactual stimulation was carried out using stimulation forming an array on the torso (i.e. chest and abdomen). Several display configurations in some preliminary experiments. On the basis of these, a single display configuration was subjected to detailed study, both with and without an additional visual search task.

EVALUATION OF ELECTROCUTANEOUS DISPLAY -

Much of the prior experimentation with electrocutaneous displays employed a single conductor electrode with a large return plane at a remote location on the body. This type results in through-body conduction, which was considered in this study to be objectionable for an array using a large number of tactors. Guided by the work of Saunders and Collins (16), a number of different silver coaxial electrodes were explored in this program. It was found that a smaller diameter inner electrode produced a lower threshold, but in general the sensation was subjectively more sharp. Insulation width (the annulus) did not appear to have a noticeable effect on the sensation, while the overall size of the electrodes did not appear to improve comfort. As the size was increased, the current required for an equivalent intensity of sensation was found to increase.

The final tactor geometry selected was a 5 mm. diameter inner electrode, an insulating annulus of width 1 mm., and an outer electrode diameter of 11 mm. Initial experiments on acceptability with stimulators applied to the region of the chest and stomach led to the adoption of a pulse repetition frequency of 250 Hz. However, these early experiments showed that the necessary intensity levels of stimulation for adequate display of information caused significant discomfort in some of the subjects. A "bimorph" mechanical stimulator was adopted for the formal tracking experiments. This form of stimulator is a piezoelectric vibrator, after the work of Holmlund and Collins (17). The optimal driving of the bimorph was found to be in 6 cycle bursts of 170 Hz, 150 V (rms). Beyond 170 Hz, the operation of the bimorph degrades too much for good stimulation levels.

TRACKING EXPERIMENTS -

Preliminary psychophysical and step-input tracking experiments were carried out to evaluate several different display configurations. On the basis of these it was found that generally increased spacing of stimulators in the display array gave improved performance. The performance obtained was relatively insensitive to changes in the inter-stimulator time interval. These earlier results also showed essentially no difference in the performance obtained with the equivalent electrocutaneous and vibrotactile displays.

The basic objectives of the formal tracking studies were to evaluate the tactual display parameters in a situation relevant to flight control and to characterize the pilot-display interactions in quantitative terms.

An X-Y two-axis display array was selected for these experiments. The array consisted of stimulators arranged in a vertical and a horizontal line crossing on a common tactor. Tracking error was indicated both by the number of stimulators excited in a sequence and by the rate at which successive stimulators were excited. Two types of basic coding of the display were studied: Polarized and Nonpolarized. For the polarized display, the mode of data presentation involved sequential activation of the stimulators (7 on each axis), beginning in each sweep with the centre stimulator and sweeping outwards. The two axes were activated alternately. In the non-polarized mode, the signal commences at the first stimulator in a line, and sweeps across to the last stimulator (4 stimulators per axis).

Some comparative tracking data were also obtained on a visual display geometrically "equivalent" to the tactual display, and a standard visual flight display.

A pitch-and-roll aircraft control task was simulated, using a two-axis hand control for independent control of each axis. The control was primarily a force-sensitive device. Disturbance inputs were constructed by summing together a number of sinusoids, with independent application to each axis. The experiments used two subjects(D. E. and N. G.) who were both instrument-rated aircraft pilots. They were given considerable initial practice on the control task.

Several independent variables were investigated: Display size (spacing between the stimulators), polarized vs nonpolarized, display coding (high threshold for the stroking of all stimulators vs low threshold), and time-sharing with an added visual search task vs tracking alone.

In the first tracking experiment, the effects of form of polarization, display size and coding on performance were determined. The effects of display polarization are shown in Table 1. An analysis of variance shows that polarization is significantly superior to the nonpolarized configuration ($F(1,21) = 19.62$, $p < .001$). Table 2 shows the effects of different display codings and display size on tracking performance. The data were not sensitive to varying the display coding, but display size had a statistically significant effect ($F(1,14) = 5.77$, $p < .05$), with the larger display yielding the better performance.

Table 1
Effect of Display Polarization in Tracking Performance*

	Display	
S	Polarized	Nonpolarized
D. E.	4.4	6.4
N. G.	3.7	4.6
Mean	4.1	5.5

*Mean squared error score average of eight replications; arbitrary units

Table 2
Effect of Display Coding and Size on Tracking Performance with the Polarized Display*

S	Large Display		Small Display	
	High Threshold	Low Threshold	High Threshold	Low Threshold
D. E.	3.4	3.9	3.6	4.1
N. G.	3.0	3.5	4.4	3.8
Mean	3.2	3.7	4.0	3.9

*Mean squared error score average of three replications; arbitrary units

The data also showed that, with the tactual displays, the subjects used a control strategy of "pulsing" the stick rather than showing a continuous control strategy that was found in the situation with a normal visual display. Subjects also demonstrated pulsing when quantized equivalent visual display was used. Thus, this control strategy is apparently a function of the quantization and the sequential displaying coding for the two dimensions, although the pulsing was not as marked in the case of the visual quantized display.

The performance obtained with the quantized visual display was essentially the same as that gained with the tactual displays, where as the conventional visual display yielded markedly better performance.

On the basis of these results, the remaining experimental data were taken using the larger format polarized display.

A comparison of one-axis and two-axis tracking showed that no significant inter-axis interference effects occurred with the visual display as the 1-axis and 2-axis error on both the pitch and roll scores were virtually identical. However, these interference effects with the tactual display were statistically significant. Two-axis tracking error scores were about 35% greater for both pitch and roll.

Using techniques discussed by Kleinman, Baron and Levison (18), the tracking data were subjected to model analysis. In general, error and control scores were matched to within 10 percent, and pilot describing functions and control spectra were matched within 2 or 3 db.

An acceptable match to single-axis pitch performance was obtained with a time delay of 0.65 sec., a motor time constant of about 0.11 sec., an observation noise/signal ratio of approximately -21.5 db, and a motor noise/signal ratio of about -14.5 db. The experimental frequency-domain measures for one-dimensional tactual tracking are shown in Figure 1.

The condition where a visual monitoring task was combined with the single-axis tracking task was studied in order to determine the potential effectiveness of tactual displays in multi-task situations that impose a high visual scanning workload. The subjects were trained on the following five tasks: (a) monitoring only, (b) tracking-only with the continuous visual display, (c) tracking-only with the tactual display, (d) combined monitoring and tracking with the visual display and (e) combined monitoring and tracking with the tactual display. Tracking and monitoring scores are shown in Figure 2 for the single- and combined-task situations. Tracking scores are given in terms of mean-squared error (arbitrary units); monitoring scores are in terms of fraction-of-time of incorrect response (i.e. whether the pointer was inside or outside a target zone on the monitoring display), normalized to make these scores numerically comparable to the tracking score.

Although visual tracking error scores were consistently lower than corresponding tactual tracking scores, the interference of the monitoring task with tracking performance was considerably less when the tactual display was used. Single-task and combined-task tactual tracking scores differed on the average by about 12%, which an analysis of variance showed was statistically insignificant. On the other hand, the combined-task visual tracking score was over three times as great as the single-task score (significant at the 0.001 level).

Performance on the monitoring task was significantly degraded by the presence of the tracking task. The increase in the monitoring incorrect-response-time was approximately 35% (significant at the 0.01 level) and was the same whether the tactual or the visual display was used in the concurrent tracking task.

CONCLUSIONS -

The experimental results lead to the following conclusions:

a. Tracking performance was superior with larger, polarized tactual displays.

b. Interference between a tracking task and a visual monitoring task is considerably reduced when the tactual tracking display replaces a continuous visual tracking display.

c. Tracking errors obtained with the tactual display used in this study were greater than errors obtained with the continuous visual display in a similar flight-control situation. Differences between 1-axis and 2-axis tracking performance are also greater for the tactual display.

d. Performance degradation of the tactual display is due primarily to the display code adopted in this study - not to the use of the tactual sensory mode itself.

e. In order to obtain minimum MSE, tracking errors were corrected by intermittent pulse-like control inputs when the tactual display is used, apparently because of the wide band disturbance function and the large effective time lag imposed by the display code.

Preliminary results suggest that the tactile display used in this study has fulfilled the original expectations. At the cost of degraded single-task tracking performance, a tactile display has been designed which appears to allow relatively little interference between tracking and visual monitoring tasks.

Redesign of the tactual coding scheme should allow the presentation of error in one axis to be more nearly independent of the error on the orthogonal axis than is currently the case. Perhaps the most important source of inter-axis effects is the sequential presentation of errors on the two axes. With this display algorithm, the time between successive presentation of error on a given axis is increased about 20 percent on the average. This increased display time causes a performance degradation beyond that normally associated with the requirement of the pilot to share attention between two tasks.

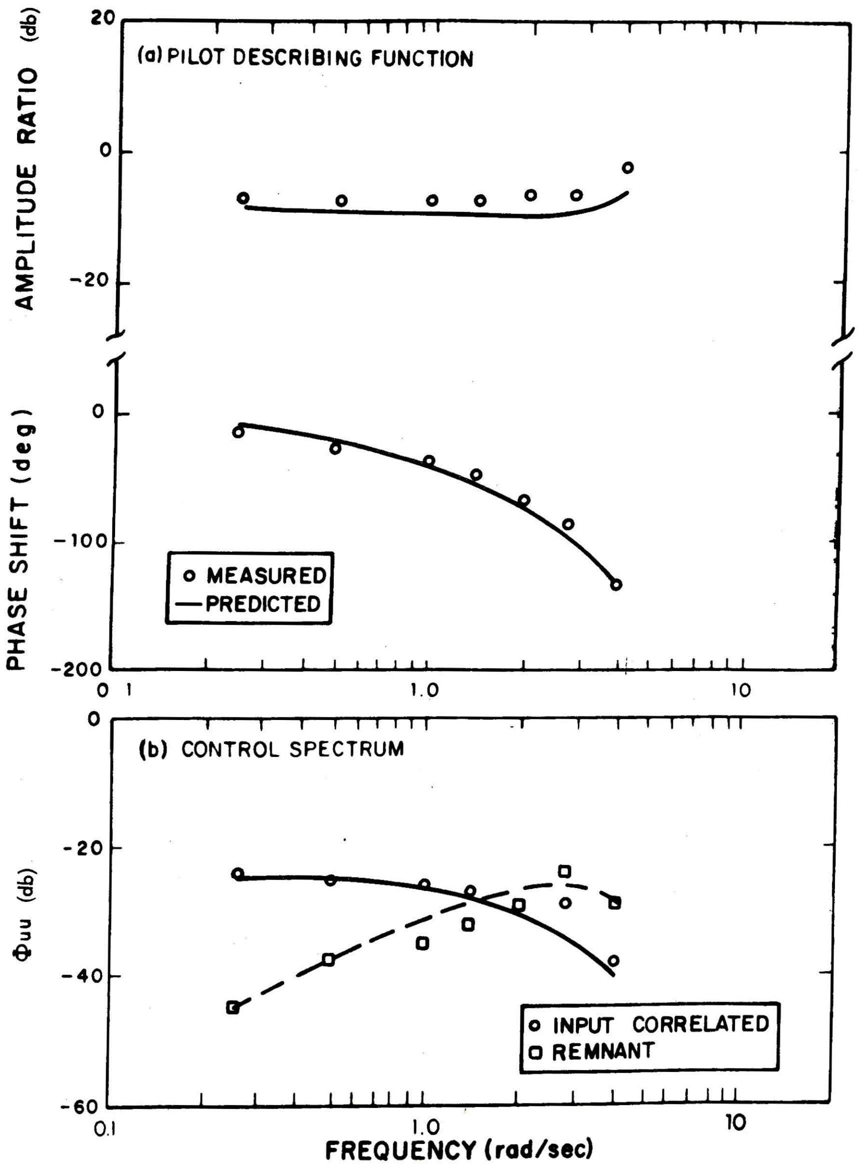

Figure 1   Frequency-Domain Measures for Tactual, 1-axis Pitch

There is also a tendency to attend primarily to the larger of the two errors when the errors in the two axes are not equal. If the error imbalance is appreciable, the smaller error may be ignored altogether until the larger error can be reduced. Although a short-term unbalance of attention would be expected with any display, one would expect less of an adverse effect if the effective display period were to be reduced. That is, if the display can be made to respond faster, the period of unattentiveness to any one axis should be reduced on the average.

Improved display coding will not eliminate interaxis effects altogether. There will always be a certain amount of task interference because of the pilot's inability to share attention between two or more tasks without some loss of effectiveness in each task.

There are several approaches that might be followed in developing a refinement of the coding scheme to reduce the effective time delay: allowing independent operation of each axis, elimination of the sample-hold feature, reduction of the interaxis interval, and reduction of the stimulus period.

REFERENCES -

1. Grether, W. F. Vibration and human performance. Human Factors, 1971, 13, 203-216.

2. Chapanis, A., Garner, W. R., and Morgan, C. T. Applied experimental psychology: Human factors in engineering design. New York: Wiley, 1949, p. 251.

3. Gabriel, R. F., and Burrows, A. A. Improving time-sharing performance of pilots through training. Human Factors, 1968, 10, 33-40.

4. Zeller, A. F., and Burke, J. M. USAF mid-air collisons. Directorate of Flight Safety Research, Norton Air Force Base, California, November, 1968.

5. Tibbs, A. M. Summary of collision and near collision statistics. Potential of airborne collision prevention devices. Washington, D. C.: FAA, 1962.

6. Lybrand, W. A., Heron, M. D., Gartner, W. B., Searr, H. A. and Hackman, R. C. Simulation of extra-cockpit visual aids in contact flight transition trainers. USAF: AFPTRC, TR 58-111, February, 1958.

7. Forbes, T. W., Garner, W. R., and Howard, J. G. Flying by auditory reference ("Flybar"). Psycho-Acoustic Laboratory, Harvard University, OSRD Report No. 5123, 1945.

8. Flynn, J. P., Goffard, S. J., Truscott, I. P., and Forbes, T. W. Auditory factors in the discrimination of radio range signals: Collected informal reports. Psycho-Acoustic Laboratory, Harvard University, OSRD Report No. 6292, 1945.

9. Ballard, J. W., and Hessinger, R. W. Human-engineered electromechanical tactual sensory control system. Electrical Manufacturing, 1954, 54, 118-121.

10. Hirsch, J., and Kadushin, I. Experiments in tactile control of flying vehicles. 6th Annual Conference of Aviation and Astronautics, 1968, 64-68.

11. Howell, W. C. and Briggs, G. E. An initial evaluation of a vibrotactile display in complex control tasks. Ohio State University Technical Reports (813)-5, AD - 320472, October, 1959.

12. Seeley, H. F., and Bliss, J. C. Compensatory tracking with visual and tactile displays. IEEE Transactions on Human Factors in Electronics, 1966, 7, 84-90.

13. Hill, J. W. A describing function analysis of tracking performance using two tactile displays. IEEE Transactions on Man-Machine Systems, 1970, MMS-11, 92-101.

14. Geldard, F. A. Cutaneous channels of communication. In W. A. Rosenblith (Ed.) Sensory communication. Cambridge, Mass: M.I.T. Press, 1961, Pp. 73-87.

15. Gibson, R. H. Electrical stimulation of pain and touch. In D. R. Kenshalo (Ed.) The skin senses. Springfield, Ill: Thomas, 1968.

16. Saunders, F. S., and Collins, C. C. Electrical stimulation of the sense of touch. Journal of Biomedical Systems, 1971, 2, 27-37.

17. Holmlund, G. W., and Collins, C. C. An electromagnetic tactile stimulator. Journal of Biomedical Systems, 1970, 1, 25-40.

18. Kleinman, D. L., Baron, S., and Levison, W. H. A control theoretic approach to manned-vehicle systems analysis. IEEE Transactions on Automatic Control, AC-16, No. 6, 1971.

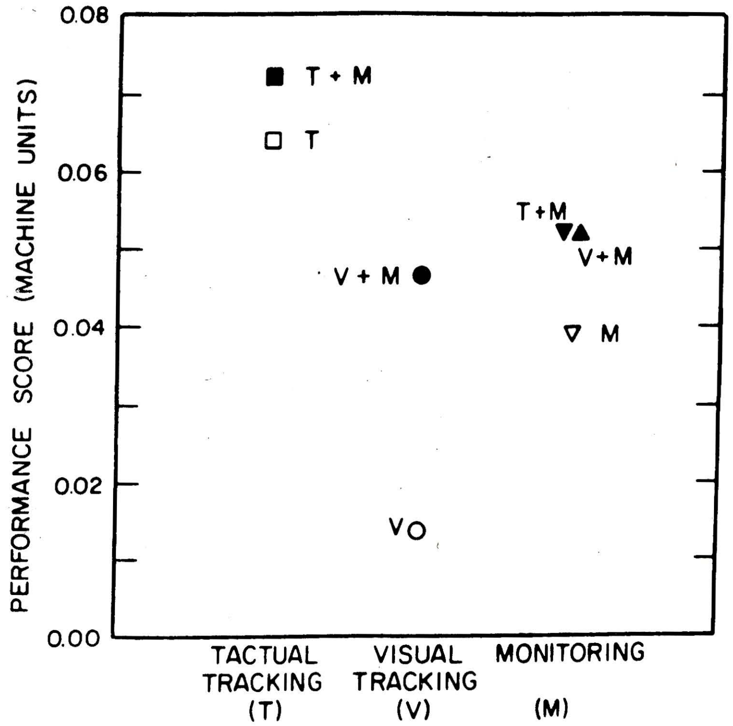

Figure 2 Comparison of Single and Combined-Task Tracking and Monitoring Performance Scores

Noise, Shock & Vibration Conference, 1974 Monash University, Melbourne

MICROSECOND AND NANOSECOND SPARKS FOR PHOTOGRAPHIC TECHNIQUES

H. G. Patzke
IMPULSPHYSIK GmbH
Hamburg, West Germany

F. Früngel
IMPULSPHYSIK GmbH
Hamburg, West Germany

Summary

The paper gives a review on spark flash equipment for micro- and nano-second flashes, discusses design parameters and describes practical applications in high-speed photography. Operational techniques with various camera types and accessories such as Kerr cells (STROBOKERR-Method) and X-ray flash adapters are explained. Examples are given for various photographic techniques from simple front- and backlighting set-ups to schlieren- and interference photography, shadowgraphy, micro-graphy and spark tracing of air flows.

In order to yield satisfactory results any type of photography and high-speed-photography in particular must meet five basic requirements, namely :

1. Single frame exposure must be short enough in order to avoid any object motion blur.
2. Sufficiently intensive object illumination must be provided to achieve adequate blackening of the photographic emulsion.
3. High film transport speed in order to accommodate the large number of single frames in a certain time unit, for instance 10 000 frames per second.
4. Perfect synchronisation of the transient with the moment of exposure.
5. Good optical resolution of details so that the results have sufficient information value.

As can be seen requirements are more or less extreme in all points and as often in technology these requirements seem to contradict each other at first sight. Already the first two requirements seem to exclude each other : exposure time and light intensity. If one value is increased one has also to increase the other. Sooner or later one reaches the practical limit be it the efficiency of the shutters, be it that the object to be photographed can only stand a certain heat radiation. Also the third point of our requirements, the transport speed of the film, has its limit which is given by the tensile strength of the commercially available film, whilst for our fourth requirement perfect synchronisation possibilities between event and moment of photography our modern electronics offer a great number of solutions. It is the fifth requirement which of course is of paramount importance and decisive, since it concerns the total result of the efforts : negative size, optical resolution, contrast, definition, taking rate, total number of frames, and analysability or projectability are essential prerequisites for the suitability of the photographic technique employed. It is obvious that not all requirements can be met in equally excellent manner so that one has to search for the most favourable compromise in relation to the photographic problem on hand, i.e. for example high taking rates in order to obtain sufficient single phases of the movement, or shortest possible exposure time in order to stop motion blur.

Since we are concerned with flash photography of transients we should try to establish some point of reference which we can find in nature's spark discharge, viz. the thunder flash or lightning. Potential : several million volts, current flow : up to 150 000 Ampères, flash duration between a few microseconds up to several milliseconds.

Starting with the invention of the Leyden jar and Toepler's first experiments on photographing shock waves, the electric spark is perhaps the oldest tool in the history of high-speed photography. The electric spark is used in high-speed motion analysis in broadly four ways :

a) The spark light is used to illuminate the surface of non-radiating objects in micro or nanosecond time and at high repetition rates. Each spark produces one image and has to deliver a certain number of lumenseconds (Früngel 1965).

b) The spark is focused with a mirror system the entire surface of which radiates at the spark's brightness. With a spark serving as practically a point source of light, this arrangement is used in techniques of schlieren interferometry or shadowgraphy to examine shock waves and transparent media such as gases. The spark must have a very high luminosity in candles per square centimeter, the total amount in lumenseconds being unimportant.

c) The spark serves as an electric switch only and feeds pulses at high repetition rates into X-ray flash systems, Kerr cells for lasers and the spark resistance must be low to obtain a switch-like operation and quenching must be very rapid (Früngel 1962 and 1965).

d) The spark now long and thin with low energy but still with a high repetition rate is used as a massless indicator for motion analysis of three-dimensional gas flows, boundary layers at a very wide range of pressures and speeds and also in other circumstances where lack of transparency makes it impossible to employ method b). The voltage must rise very rapidly to give blur-free sparkovers.

As in the ordinary electronic flash which is generally known, the electric energy which on discharge into a gas atmosphere is partly transformed into radiation energy (light) is stored in a capacitor. In order to keep the discharge time considerably shorter than in case of the ordinary electronic flash (approximately 1 millisecond) one uses the following possibilities : First one employs higher charging voltages (around 10 kV), higher gas pressure in order to proceed from the arc-like gas discharge to a proper sparkover which is the fastest possible energy transduction, which in turn requires extremely low induction discharge paths, reduction of the discharge energy, and by dimensioning all factors which have an influence on the discharge (capacitance, inductivity, resistance) in such a way that the so called aperiodic damping condition is reached, i. e. a suppression of oscillations in the discharge circuit. By all these measures one achieves a flash duration in the microsecond range, i. e. 1000 times shorter than the electronic flash but with comparable energy per flash. If one can reduce the flash energy further, then one can also make light sources with a flash duration in the nanosecond range. A nanosecond is a billionth of a second and the shortness of this time span surpasses our imagination. Yet the photographic process is still operative. Even our eye can still see objects which are illuminated by such short light flashes. However, it is more difficult to measure such extremely short time intervals. Here one uses multipliers in combination with high-speed oscilloscopes.

It is obvious that the practical realisation of such high-speed light sources is not quite easy. Let us sum up some requirements : first flash duration within the microsecond range, secondly a flash energy of several wattseconds is required and if possible a very high repetition rate of the flashes at time intervals of milli- respectively even microseconds. If we compare the known data of the ordinary electronic flash : here we have a flash duration of approximately 1 millisecond, a flash energy of between 20 and 100 wattseconds, and a repetition rate of 5 to 10 seconds. By which measures the flashes can be shortened has already been mentioned. In order to increase the flash repetition rate or flash frequency one has to realize two things :

1. The energy supply (recharging of the lamp capacitor) must be increased and accelerated, and

2. the discharge gap (flash lamp) must be so dimensioned that physically and thermically it can stand a great number of discharges at high repetition rates.

Both Harald E. Edgerton and Früngel have realized these requirements into commercially available high-speed stroboscopic instrumentation. Früngel with his STROBOKIN has developed a universal flash unit which is being built for more than a decade and is known the world over. With its accessories it constitutes an instrumentation program which is suitable for the solution of many high-speed problems. The technical data of this ultra rapid flasher unit STROBOKIN are as follows : energy per flash maximum 10 watt-seconds, flash duration 1 microsecond, flashing rate variable between 16 and 100 000 flashes per second and single flash. Total energy of a flash burst is 50 kilowatt-seconds. The only limitation seems to be the thermal capacity of the flash lamp. Anyhow a flash burst at medium frequency, let us say 10 kHz, would permit to expose several thousands frames. A 125 ft. 16 mm film, having around 4 000 frames, can easily be exposed from beginning to end.

The power pack is operated by 3phase current. Control of flashing rate and burst duration is effected by a heavy duty control unit. The most essential part, however, is in the flash lamp, the so called Quenchotron. It would be beyond the scope of the present paper to explain in detail the complicated principles of operation and construction. Be it sufficient to say that it operates as a high frequency switch for quick deionisation of the gas particles in the light emitting spark chamber. Whilst the highest possible repetition rate without quenchotron would be 500 flashes per second, this component permits to increase the flashing rate up to 100 000 flashes per second. The inductivity of the discharge circuit is reduced to the lowest possible limit so that despite a comparatively high flash energy a flash duration of 1 microsecond could be achieved.

We should now consider how such flash bursts are used in practical high-speed photography. Often the event itself provides the required frame separation. In this case one superposes several flash photographs on a stillstanding plate. Here, one uses the normal photographic technique whereby for instance the flash synchronisation contact of the camera shutter can trigger the flash burst. The number of flashes is either limited by the camera's shutter opening time whereby the number of flashes fired during the opening of the shutter can be preselected in such a way that sufficient phases of the event are covered. Or one can also preset the number of flashes to be fired at the control unit of the flasher. An example of this type of photographic technique is the flying bullet. The image is always projected onto new unexposed parts of the film and the final photograph shows - at known flashing rate - velocity, spin and aerodynamic behaviour of the bullet as well as the effects on impact. In this way one has all parameters for analysis on one picture.

Proper frame separation is already provided in high-speed cinematography by for instance rotating prism cameras which take separated single frames. Here, an intensive spark light source with high repetition rates can advantageously be used for the following reasons :

a) In some cases it is very difficult or even impossible to obtain, with continuous illumination, the intensity required for the very short exposure times of such a camera. In such cases spark light flashes supply the required intensive illumination of the object.

b) When using flash illumination, the single frame exposure time of the rotating prism camera, which is normally between 20 to 500 microseconds, depending upon camera type and taking rate, can be reduced to less than 1 microsecond. This is important for all photographic problems, where a taking rate of say 10 000 frames per second would be sufficient for analysis but the exposure time of the camera itself would cause blur owing to the object speed, particularly with small but rapid moving objects, e. g. droplets from an injection nozzle (Früngel 1959).

c) Heat sensitive objects like insects cannot stand the warm illumination of a continuously burning lamp. Spark light however, generates cold blue-white light flashes which do not cause trouble.

By combining a heavy duty spark light flash system with a rotating prism camera films for motion picture projection up to 400 ft. in length can be taken. The spark light flashes must always be tripped exactly at the moment when the rotating prism camera shutter is open. For this reason the electronic system has to be synchronized with the camera by an appropriate triggering system, e. g. an optical pick-up installed in the camera.

The taking rate of a rotating prism camera, however, is limited to at present 10 000 frames per second full frame and 20 000 frames half frame or double eight.

If higher taking rates are essential, one has to resort to a drum type camera. Though one no longer obtains ready for projection films, the drum camera is the most suitable kind of photographic equipment for motion analysis with spark light illumination. For an exposure the drum camera is focused on the object and rotated at a speed corresponding to the desired taking rate. Shortly before the exposure, the camera shutter is opened and the flash series is triggered at the desired phase of the event. As the film in the camera is running past the lens with a speed corresponding to the preset rate of revolution, a single picture, separated from the preceding one, is exposed by each flash. Even though the film is moving while the flash is taking place there will be no blur since the travelling speed of the film, even at the maximum rate of revolution of the camera, is slow in relation to the very short flash duration.

To avoid double exposures, the camera shutter should be open for only one revolution of the drum. Because of the extreme intensity of the illumination flashes, photographs can be taken in subdued daylight. If the photographs are taken in a darkened room, the camera may be open before the exposure is made. In this case the selected duration of the flash series will correspond to the time required for one revolution of the drum.

For spontaneous and automatic closing, special shutters are available. In both cases the operation of the shutter and the triggering of the flash series are started by the event itself via the control unit. The camera shutter can also be operated manually in which case the event and the flash series are both triggered by the shutter contact.

A typical drum camera is the STROBODRUM which loads a normal 36 exposure cartridge 35 mm film, the circumference of the drum is approximately 5 ft., the camera achieves at maximum 3600 revolutions per minute which would correspond to a travelling speed of the film of 300 ft. /sec. With increasing flashing rate the frame height has of course to decrease, because even at maximum speed an ever decreasing length of film can be transported during the flash intervals. For instance at 3500 flashes per second a standard 35 mm cine frame can be transported between flashes. At 12 500 flashes per second, the frame height has already decreased to 7. 5 mm which corresponds to a 16 mm film and at 50 000 flashes per second only 2 mm of film can be moved between flashes. The frame height is thus dependent on two parameters, a) RPMs of the drum and b) flashing rate and the correct setting of the variable slot masks can be read from a corresponding table.

For analysis of very fast events -such as explosions, detonations, shock waves, dynamic optical stress etc. - the taking rates of rotating prism or drum cameras will no longer suffice. As with these cameras the strength limits of the film are already reached with regard to tensile stress or centrifugal force, a new principle of frame separation has to be employed. : one again uses a stillstanding plate and frame separation is achieved by beam separation. It is the so called Cranz-Schardin method, a multiple spark gap. Here, not only one and the same spark gap is used for a flash series, but a number between 8 up to 24 separate spark gaps are fired and a like number of taking lenses is used on the camera. By using a spherical mirror every taking lens only receives the light from one spark which is attached to this particular lens. The object to be photographed is at such a point of the beam that it is illuminated by the light of every spark and also seen from every taking lens. This principle is limited to backlighting and therefore suitable for schlieren-, shadow- and interferometer photography, it is, however, not suitable for front lighting. The mentioned photographic techniques do not only show object movement, but permit also analysis of the atmosphere surrounding the moving object, in particular pressure - air flow - air density and temperature conditions. In combination with image separation according to the Cranz-Schardin principle they constitute a very successful method of high-speed-photography and analysis of extremely fast events. It offers no particular difficulties to fire these separate sparks in very rapid succession for instance at time intervals of 1 microsecond with a resulting taking rate of 1 million frames per second.

A camera designed on this principle is the CHRONOLITE, which provides eight sparks at only 9 mm spacing and the eight images are obtained on a standard 4 x 5 inch plate or Polaroid film. An external trigger pulse starts the impulse generator which supplies spark impulses of 40 nanoseconds halfwidth. Simultaneously the first flipflop in the shift register of an 8-section circuit is triggered. This in turn opens a gate amplifier through which the first pulse from the impulse generator triggers the first thyratron. In addition to the trigger pulse for the thyratron the amplifier sends another starting impulse to the following flipflop. Consequently the trigger sequence is repeated at equal intervals in accordance with the preset time schedule. The thyratrons, via impulse transformers trigger the corresponding spark gaps. After the eight circuits have been triggered, a final pulse stops the impulse generator. Also, the eight flipflops are pulsed back to the reset condition immediately after the switching action. Following each series, the equipment is ready to start again as soon as the spark gap capacitors are recharged. Using the polarized adapter a series of eight pictures can be shot every ten seconds. With an object distance of 3 to 5 m the vertical parallax is hardly noticeable, because of the small spark separation, while there is no horizontal parallax at all. The small spark dimensions of 2 x 0. 5 mm make a pin hole mask unnecessary. An auxiliary continuous light source with eight miniature lamps can be plugged in for alignment and focusing. The entire spark gap assembly is placed in a rare gas environment, which gives greater emission of light than is obtained in air.

The head of the corresponding camera comprises : a rotating shutter, a common reflecting prism for all eight pictures, eight knife edges located in the spark image plane and adjustable simultaneously, eight adjustable reflecting prisms for image separation, and an achromatic lens as photographic objective. The rotating slit shutter with synchronisation contact for event triggering permits operation in moderately illuminated rooms. The utilisation of a common objective lens for all eight pictures provides for simple focusing to any object distance by sliding the back of the camera towards or away from the lens. Optimum utilisation of the 4 x 5 inch film area is achieved with the aid of the eight adjustable prisms.

The equipment is therefore a combination of the electronics, spark head and camera system. The diameter of the spherical mirror, which is not part of the Chronolite equipment, depends on the size of the phenomenon. The minimum size is 25 cm but often mirrors of 60 cm in diameter are used. The eight frames' sequence, taken at 50 000 frames per second of a pallet striking the edge of a sheet of safety glass is an excellent illustration of the spreading of the breakage front which progresses with considerably higher velocity than the faintly visible air shock wave. The shattering into small phragments is a characteristic of the behaviour of safety glass. The other sequence, taken at 100 000 flashes per sec.shows a rifle bullet (V_0 = 1200 m/s = 3950 f/s) striking a metal strip. Both, the bullet as well as the small particles coming out of the rifle barrel or from the metal strip are seen to have shock waves.

If the small parallax of the Chronolite spark is still disturbing, the so called spark cascade can be used (Patzke, 1967). As shown, cascading spark flashes appear as a single point source of light through a series of consecutive focusing lenses. As many as six spark gaps can be used without noticeable deterioration of light intensity. Miniature capacitors supply energy to air gap spark electrodes. Trigger electrodes are fired by an electronic pulse source up to 10^6 per second, and, if desired, with different times between the sparks.

A very difficult photographic problem is encountered when the event has a self luminous phase which disguises the actu l research phenomenon, as for instance the transport of material from the electrode in arc welding. Here the solution is offered by the so called STROBOKERR method. This is a combination of the flash with a Kerr cell shutter which is mounted in front of the camera lens, whereas the flash is used as backlighting. The Kerr cell is operated by the flasher unit in such a way that it opens during the moment of the spark's peak light emission for an appreciater shorter interval than the duration of the spark, say 80 nanoseconds in case of a 1 microsecond spark. What now happens is the following : 50% of the light emitted by the event are lost at the Kerr cell's first polariser, another 30% are lost in the nitrobenzene and the remaining 20% can get through for only 80 nanoseconds - this is entirely insufficient to expose the film. The spark, however, has at its peak a brightness of approximately 10^8 stilb and is therefore several hundred times brighter than the light from the event and, though it suffers the same Kerr cell loss, is still powerful enough to expose the film and give a shadowgraph-like picture. The companying photograph shows the transfer of liquid metal drops from the welding electrode to the weld in a 200 A DC welding arc, with the luminosity of the welding arc having been completely suppressed by this Strobokerr-method.

An example where the spark is used primarily to switch capacitor discharges into a pulse transformer is the X-ray cinematographic method. The STROBO-X-Pack used for high-speed X-ray cinematography, consists of a complete high energy, high repetition rate spark generator and an impulse transformer. The pulses which normally serve to produce the light flashes are now tapped off at the flash lamp in the form of megawatt electric pulses which are stepped up by a differential transformer and then utilized for feeding the X-ray tube. The control functions with regard to the flash burst are exactly the same as when operation is with the spark light flashes, except that the maximum flashing rate is limited to approximately 40 000 X-ray flashes per second.

An image converter displays the X-ray pictures, in the original size, as pictures on the fluorescent screen. These are then photographed by a rotating prism camera. The equipment is capable of giving 3000 X-ray flashes per second, each delivering 50 milli-Roentgen at 50 cm distance and of providing adequate exposure using the image converter, through as much as 10 mm of steel or 30 mm of aluminium. Some applications are studies of encapsulated low and high power switches and relays, mechanical gears, sodium flow in steel tubes in nuclear power plants for detecting the appearance of bubbles, arc welding in underpowder welding conditions where the arc itself is covered by the powder. Even medical and biological problems such as body research inside animals especially mice or insects for example can be investigated by high-speed X-ray photography. The equipment, however, cannot be employed for human medicine because here special precautions necessary for human safety are required which this equipment as a special techni cal research tool does not have.

With a new type of anode it is possible to dissipate the heat generated by 10 000 Joule bursts. It is permissible to drive the anode up to yellow heat for some time, thus taking advantage of the power available. The fairly slow decay time of recently available X-ray image converters reduces tne operational range to a maximum of about 6 000 frames per second. At higher frequencies a ghost information must be accepted due to overwriting effects. Above these frequencies therefore a drum camera should be used without the image converter. This however, limits the object to a size dictated by the drum camera frame height which as already mentioned, depends on drum speed and flashing rate.

Mainly the high-speed X-ray flash method has been employed in the following fields of research : flow of material in underpowder arc welding, formation of cavitation bubbles in sodium heat exchangers used in atomic reactors, switching action in encapsulated switches and relays, explosion and magnetic shaping of work pieces, insulation breakdown in opaque dielectrics, and shock waves in liquids.

SPARK TRACING. In studying gas flow the physical motion of the medium is normally made visible by blowing in smoke or light weight particles. These methods are limited to the observation of more complicated phenomena like turbulence, boundary layer flow or three-dimensional flow. The well known interference method does not show the flow but only the pressure pattern. The schlieren- and shadowgraph methods show density variations over cross section, but both are limited in application to thin cross sections because of the impossibility of taking high-speed stereo pictures with these techniques.

Here the spark tracing technique is the method of choice (Beumelburg, 1955, Herzog and Weske 1957, Weske 1958, and Beumelburg et al. 1959). The main applications are three-dimensional flows, boundary layer flow and all other aerodynamic studies up to Mach No. 20 and down as low as 10 m per second. The method can be applied up to pressures of 50 atmospheres and, under proper conditions, down to 10 Torr.

In spark tracing the luminous ionized plasm channel of an electric spark discharge is the indicator which offers the particular advantage that it is comparatively massfree because the luminous ions of gas discharge consist of the material of the flowing medium. This method offers special advantages with three dimensional or non-stationary flows (Früngel 1961 and 1963).

The principle may be described as follows : the first discharge generates a spark path between two points of wires. If high voltage pulses are now fed to the same electrodes at such high repetition rates that during the interval between the two pulses the plasm of the spark path has not yet completely deionized, then every subsequent voltage pulse will trace the path of the first spark, which, however, in the meantime has been moved away by the air current.

The plasm channel can thus be made to light up periodically at the preset pulsing rate during a preset burst time (Früngel 1960). Since the pulse power system (STROBOKIN) provides an electric pulsing rate generated with extreme accuracy - e. g. by quartz control of the oscillator - it is possible to obtain with the same accuracy, velocity or acceleration vectors or isochrons in a representative section of air flow by photographic methods. A simple camera with open shutter is the only optical instrument required. Often, for three dimensional flow patterns, three-dimensional photographs are necessary, calling for two cameras or a stereoscopic camera (Früngel 1962 and 1963).

One essential component for this technique is a spark triggered heavy duty pulse transformer fed by a Strobokin and operating as a differential transformer. This design is particularly suitable where rather long sparkover distances must be achieved. The triggering spark gap is a three electrodes spark gap system which can be controlled up to 100 000 flashes per second.

Within the flow channel guide wires are required and as material for these guide wires any bare metal wire can be used. Manganin wire is particularly suitable because of its low electronic work function (Ullmann, 1968). The first sparkover occurs at the point where the gap is smallest, and can be made linear by an electric arrangement which destroys the homogenity of electric fields, e. g. by inserting insulated needles into the first spark path.

Japanese quantitative measurements and considerations regarding accuracy of spark tracing show that at air speeds above 2 to 4 m/sec. the disturbance of the flow by the spark energy can be neglected (Nagao et al., 1967 and Nakayima et al., 1968).

The spark tracing method appears to be suitable for investigating the flow conditions on high-speed turbines. It yields a qualitative picture of the air current flow and also permits quantitative analysis. Since the sparkover always starts at the narrowest part of the electrode gap, the method is particularly suitable for air flow investigations in tunnels with divergent walls which at the same time serve as electrode supports, i. e. for decelerating flow patterns, which occur also in such equipment as radial compressors (Koenig and Ullmann, 1969).

The spark technique, has been found, especially in Japan, to be very useful for internal combustion engine research. A single cylinder engine with an experimental combustion chamber model, which has a transparent window, was used. High frequency high voltage electric pulses generated by the Strobokin apparatus were applied to the spark gap installed in the chamber. The swirl of air was analysed photographically by utilizing the spark plasma as the light source. The fact that intensity and characteristic of the swirl depends on design configuration of the chamber, as well as of the inlet duct, was experimentally confirmed. The influence of swirl intensity on the injected fuel and engine performance was also investigated Various types of swirl chamber were used and relations between shape of chamber, engine revolutions, swirl motion and engine performance were examined. It was found that engine performance is improved by rather weaker swirl motions than had previously been considered.

To obtain the ordinate correlation of the flow one may blow in different gases in order to colour the plasm columns, since the colour of the spark path varies with different gases - for instance blue-white in air, white in argon, red in neon etc. (Früngel, 1961 and Patzke et al. 1960). The auxiliary gas can be introduced by means of a nozzle without any disturbance of the flow itself. The movements of the different gases and also of their mixture can be traced in space and time either by taking colour photographs or by visual observation. Then the sparks make the particular position of the vapour volume element spectral coloured, but even the spark paths as such show different colours in air and sodium vapour (Früngel, 1965). With the continuous advance of science and technology the need for still shorter than microsecond light sources became apparent. The development of coaxial capacitorscircuits with minimum inductivity (below 10^{-9} Henri) made it possible to reduce the light pulse duration of flash lamps to a few nanoseconds and at the same time to increase luminous density and light output considerably. Such ultra-short flash lamps have been designed by Prof. Dr. H. Fischer and are commercially available under the name of NANOLITE. The operating data are as follows : capacitance : 3,4 x 10^{-9} F, spark length : 1,2 mm, breakthrough voltage : 4,5 kV, inductivity : 1 x 10^{-9} Henri, maximum light density : 18 x 10^{6} stilb, maximum light output : 10^{5} cd, diameter of the spark channel : 0,3 mm, maximum pulsing rate : 10^{3} per second, life expectancy at single pulse or low frequency operation : several million flashes. These NANOLITES can be operated as air gaps or, with a screw-on pressure head, also in rare gas atmospheres such as argon, krypton and xenon. Rare gas operation increases the light output up to 10-fold, however, flash duration is, of course, increased by about 50%. For single flash and low frequency operation a driver is available from 1 - 30 Hz. For higher flashing rates the NANOLITE can be driven from the STROBOKIN Control Unit up to 10 kHz for the 18 nanosecond lamp, 15 kHz for the 11 nanosecond lamp and 20 kHz for the 8 nanosecond lamp. At these high frequencies a burst is, of course, limited to about 300 flashes.

The main fields of application for such short flashes are in supersonic wind tunnels, optical stress photography, ballistic shadowgraphs, schlieren photographs, micrography and droplet research.

At first sight the application of such ultra-short nanosecond flashes in micro- and macrography seems to be a paradoxon, because one starts from the assumption that in small dimensions also small movements only can take place and that therefore no high object velocities can occur. This is not so because : angular velocities are independent from spacial dimensions and in order to make small particles visible respectively make them accessible for photography, one has to depict them on the negative several times their original size. The velocity of the object image, however, increases linearly with the magnification scale. Practical experience proves, that for instance in droplet research - where there occur very small and often also very fast particles - mostly exposure times in the nanosecond range are necessary. Because in order to achieve sharp definition, the object to be photographed must only move by a friction of its own size during exposure otherwise blur would result. A practical example may illustrate this : when investigating fuel injection nozzles average droplet size is approximately 30 nanometer and average droplet velocity is 300 m/sec. If one permits a movement blur of 1/5 of the droplet size (i.e. 6 nm), then there results a permissible exposure time of 20 nanoseconds. It therefore is not only desirable, but imperative to employ nanosecond flashes for analysis of fast droplets. Besides droplet size, the statistical distribution of droplets as well as the velocity of the different particles are of great interest. Here a double shot will yield the desired results and for this purpose the double flash unit NANO TWIN has been developped , which takes two phases out of a moving event at predetermined time intervals, thus supplying a trajectory diagram of the event. As flash lamps one uses the just described Fischer Nanolite lamps with pressure caps filled with rare gas. The flashing interval is preset by the RETARDER from the STROBOKIN program, permitting time intervals between shots from 1 microsecond to 1 second. The exposure time of a pressurized Nanolite is in the range of 30 nanoseconds.

By an imaging system according to the Cranz-Schardin principle one obtains two separate images which have already threefold magnification on the negative. The field of illumination is approximately 2 sq. in. The two separate images are taken on a 4 x 5 inch plate, sheet film or Polaroid can also be used. The light intensity is sufficiently high to allow the use of slow, fine grain emulsions for colour film. The double exposure can be triggered by the event. The accompanying photographs show the optical principle, the optical arrangement and the complete NANO TWIN instrumentation. As photographic examples there may serve one schlieren photograph showing schlieren formation in a thin layer of liquid and marginal atomisation into small droplets. The other photograph shows the collision of two droplets and the subsequent change of shape.

Considering the fact that now flash lamps are under development with only 2 nanoseconds halfwidth value there arises the question where are the limits of photographic analysis and of high-speed photography ? Perhaps one should discern here between the limits of the technically achievable and the limits imposed by a rational application of the technical possibilities. One requires for instance no shorter exposure time than necessitated by the event. It would also not be advisable to drive time expansion to such extremes that we no longer can correlate movements. The majority of the phenomenon in nature and technique takes place in time intervals which can be frozen in or slowed down sufficiently by the just described methods. Extremely fast events as they occur in supersonic wind tunnels, in shock wave tubes, injection nozzles and detonation phenomena pose requirements which come very near to the limits of the technically realisable photographic methods. For the phenomena occuring in plasm and nuclear physics new photographic possibilities will have to be developped. Here also essential pioneer work has been performed. At the bubble chamber in CERN a flash lamp system has been installed consisting of three synchronous flash lamps with 2 kWs flash energy each and the installation operates continuously at 3 sec. intervals around the clock in order to photograph nuclear and subnuclear particle traces. There seem to be no limits to what science and technique can achieve. New problems result in the development of new methods for investigation. New investigation possibilities to solve problems, invite new questions. This dynamical process is inherent in science and research and the techniques of high-speed photography are an essential part of it.

Recommended reading : A. S. Dubovik, Institute of Physics of the Earth, Moscow : Photographic Recording of High-Speed Processes. Pergamon Press Oxford Headington Hill Hall, 4 &5 Fitzroy Square, London W. 1. Harold E. Edgerton, Massachusetts Institute of Techn. Cambridge, Mass., USA, McGrawhill Book Company, New York. : Electronic Flash Strobe. Frank Früngel, Impulsphysics Ass., Hamburg, W. Germany : High-Speed-Pulse Technology. Vol. I, Academic Press, New York - London. William G. Hyzer, New York - USA : Engineering and Scientific High-Speed Photography. The MacMillan Company, New York.

References : Beumelburg, H. J. (1955) : A method for the measurement of the flow of air by means of series of electric sparks. University of Maryland. Inst. Fluid Dyn. Appl. Math. TN BN-68. Beumelburg, H. J., Herzog, J. and Weske, J. R. (1959). The electric spark method for quantitative measurements in flowing gases, Flugwissenschaft 7H 11 322-329. Ebeling, D. (1968) Improved X-ray flash technique broadens field of application. Proceedings 8th Int. Congress on High-Speed Photogr., Stockholm : Almquist & Wiksell, 245-248. Fischer, H. (1961), Millimicrosecond light source with increased brightness. J. Opt. Soc. Am. 51 (5), 543-547. Fischer, H., Gallagher, C. C. and Tandy, P. (1962) : Improved nanosecond light sources. Proc. 6th Int. Congr. High-Speed Photogr., The Hague, 152-157. Fister, W. (1963). Versuche zur Erfassung der Strömungsverhältnisse an Radiallaufrädern. Forschungsbericht der Aerodynamischen Versuchsanstalt Göttingen, Nr. 63-01, 106-129. Fister, W. (1966). Sichtbarmachung der Strömungen in Radialverdichterstufen, besonders der Relativströmung in rotierenden Laufrädern durch Funkenblitze. Brennstoff-Wärme-Kraft (BWK) Bd. 18. No. 9, 425-429. Früngel, F. (1958) : High-Speed slow motion pictures by means of spark flashes, Explosivstoffe 10, 295-246. Früngel, F. (1959) High frequency spark device. U. S. Patent 2, 906-924. Früngel, F. (1960) : Bewegungsaufnahmen rascher Luftströmungen und Stosswellen durch hochfrequente Hochspannungsfunken. Jahrbuch der WGL 2, 175-182. Früngel, F. (1961a) Methoden der photog. Erfassung schneller Bewegungsvorgänge in Strahl-, Strömungs- und Werkstofforschung. Motortechn. Z. 22 H 5, 155-159. Früngel, F. (1961b) : Apparatus for high-speed photography of gas flow phenomena. Canad. patent No. 667-115. Früngel, F. (1962) : Proc. of the 5th Int. Congr. High-Speed Photogr. SMPTE, 138-140 and 170-172. Früngel, F. (1963) : Stereoskopische Funkenblitzserien, dreidimensionale Bewegungsaufnahmen instationärer Strömungen durch hochfrequente Hochspannungsfunken. Proc. 6th Int. Congr. High-Speed Photogr., The Hague, 622-623. Früngel, F. (1965) High-Speed Pulse Technology Vol. II, pp. 162-182., New York Acad. Press. Herzog, J. and Weske, J. R. (1957) : Characteristic of the technique of aerodynamic investigation by means of series of electric sparks., University of Maryland, Inst. Fluid Dyn. App. Math. König, G. and Ullmann, W. (1969) : Gesichtspunkte bei der Sichtbar - machung von Strömungen in kleinen Bauelementen mit der Funkenblitzmethode.

2. Konf. Pneumatische Strahlelemente, 24, 2-1.3. Dresden, Patzke, H. G. (1967) Confocal lens eliminates Spark Flash Parallax, Hamburg-Impulsphysik. Nagao, K. Kakoto Ikegami et al. (1967) : Air motion and combustion in a swirl chamber typ. diesel engine. Bulletin of JSME 10 Nr. 4, 833-845. Nakajima, K., Kajiya, S. and Nagao, F. (1968) An exp. investig. of the air swirl motion and combustion in the swirl chamber of diesel engines XII Congr. Int. FISTA, Barcelona, Spain. Patzke, H. G., Früngel, F. and Thorwart, W. (1960) : High-sp. photogr. of rapid currents and shock waves by means of high frequency high voltage sparks. Proc. 5th Int. Congr. High-Speed Photogr. Washington, 498-502. Thorwart, W. (1958) : Dyn. Spannungsoptik und aerodyn. Strömungsbilder mit Funkenblitzen, Kino-Technik 9, 254-258. Thorwart, W., Suarez, F. and Patzke, H. G. (1968) : Chronolite 8 a versatile multiple high-speed spark camera. Explosivstoffe Nr. 3 FFK 685 (I), 691 (3), 775 (I) 49-57. Ullmann, W. (1968) : Auswertbarkeit und Anwendungsgrenzen der Funkenblitz-Methode bei der Untersuchung von Wandstrahlelementen. Diplomarbeit Inst. f. Steuerungs- u. Regelungs-Technik TU Dresden. Weske, J. R. (1958) : Ein Beitrag zur Untersuchung stetiger und unstetiger dreidimensionaler Strömungsfelder in Trubomaschinen, Z. angew. Math. Phys. 9B, 721-724.

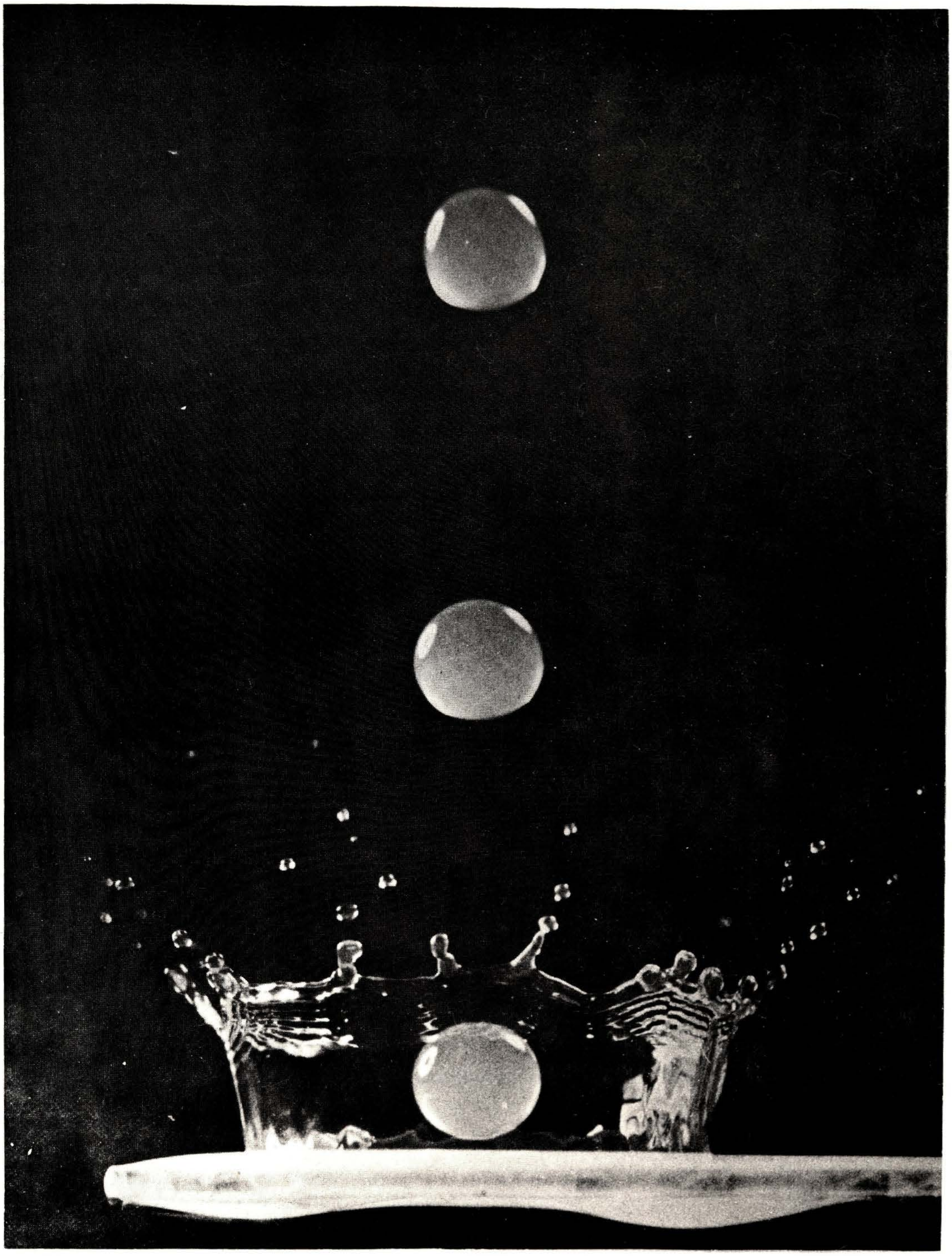

Coronet formed by falling droplet. Four STROBOKIN microsecond flashes superposed on one plate.

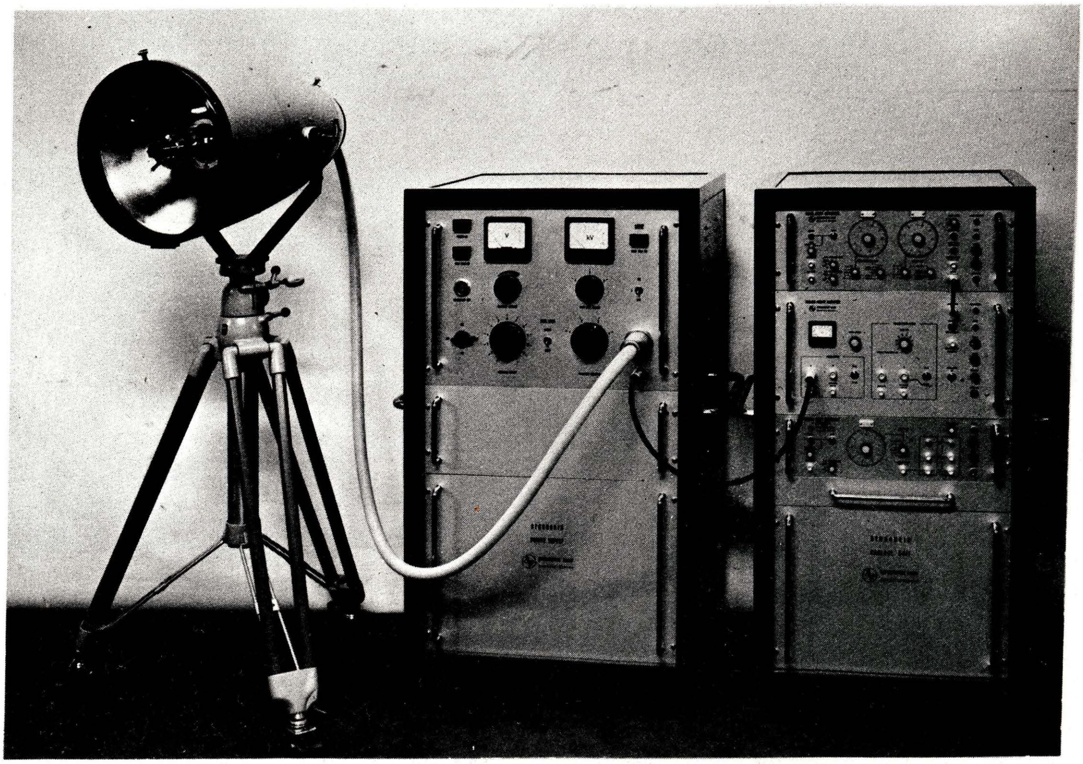

Basic combination STROBOKIN

Standard outfit for drum camera and rotating prism camera operation.

Strobokin flash lamp, either with Cu or CuWoDur Quenchotron, built-in capacitor bank, parabolic and ellipsoidal reflector and tripod.
Strobokin power pack for full load operation up to 400 ft. of film = 14 400 flashes, 3-phase 100 kVA short burst operation (approx. 2 sec.)
Additional capacitive energy storage for approximately 100 flashes up to the maximum flashing rate of 100 kHz.
Strobokin control unit with trigger pulse amplifier, power supply and pulse burst generator for presetting burst durations .
External trigger input, e. g. for pick-up triggering from a high-speed camera.
Universal Retarder for delay times from 1 microsecond to 1 second.

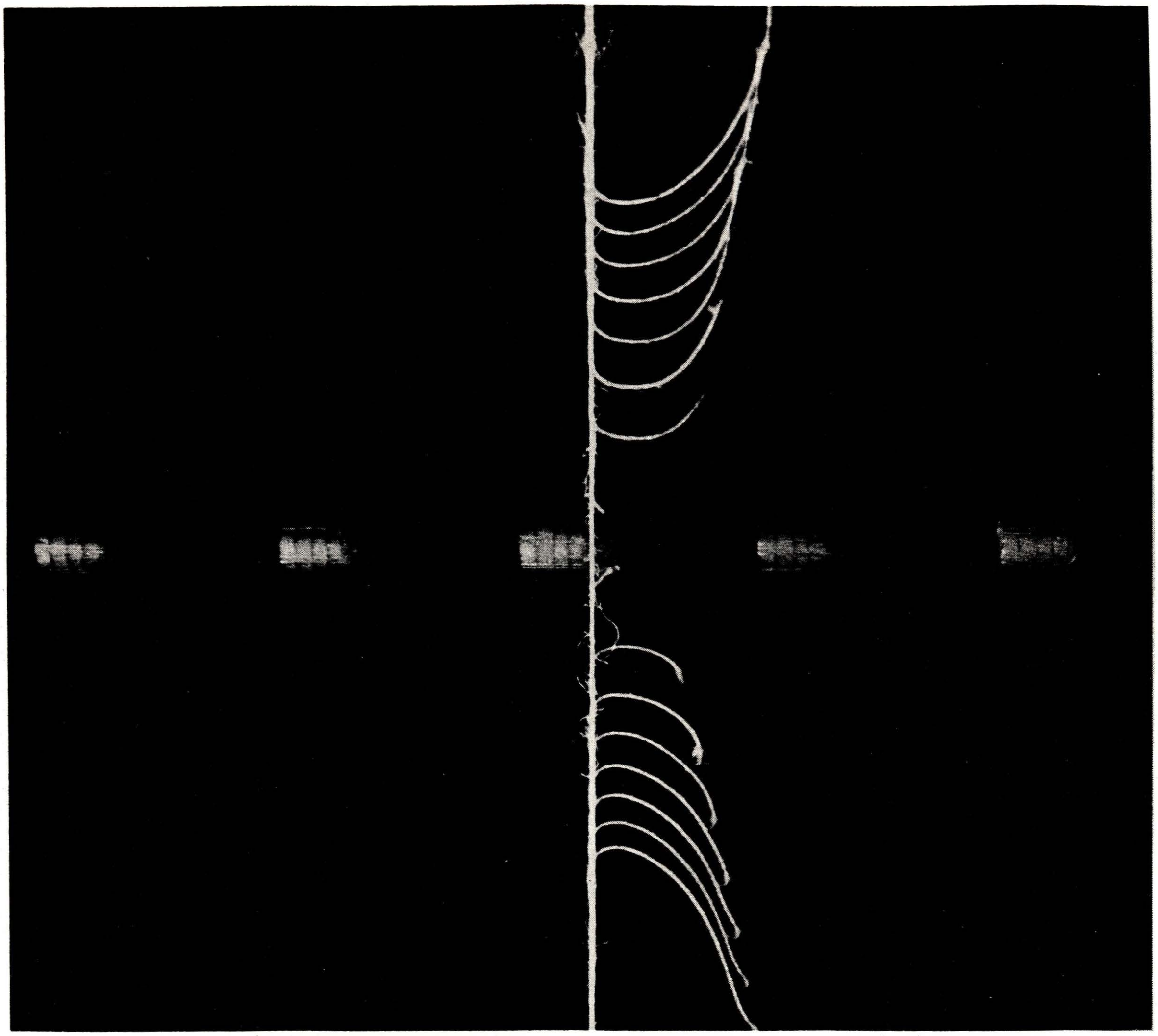

Bullet, V_0 = 330 m/sec., snapping a thread.
Twelve STROBOKIN microsecond flashes superposed.

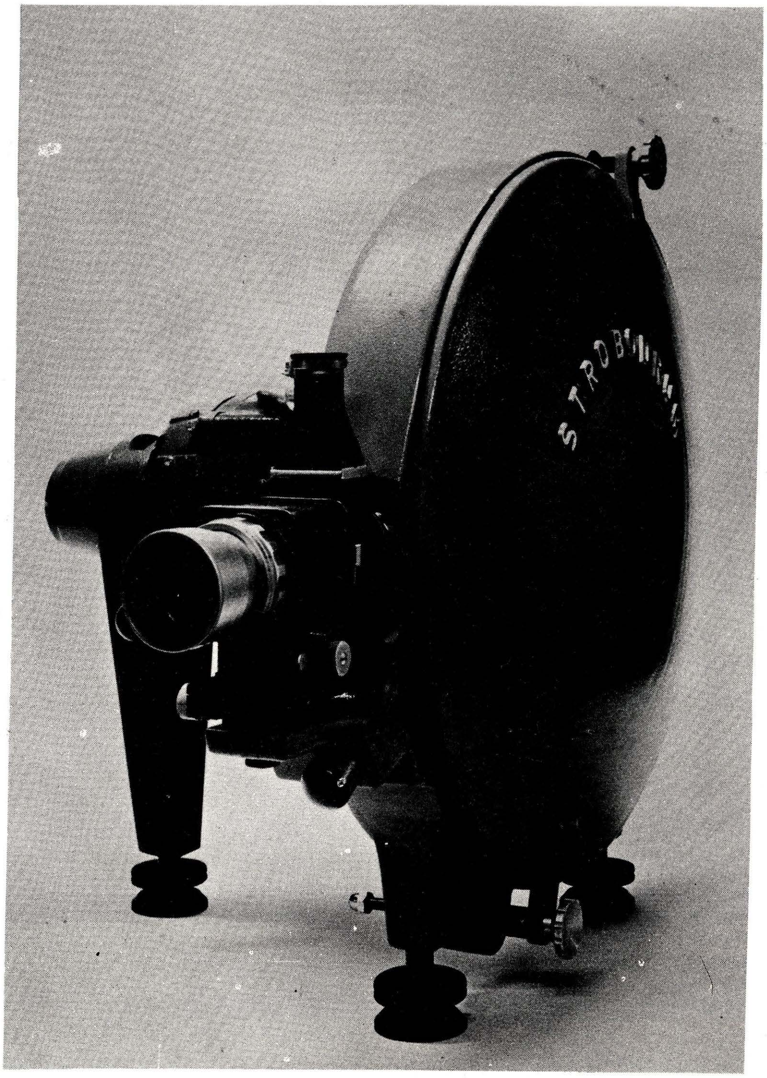

STROBODRUM Camera with Leitz bellows extension, Visoflex reflex focusing device and Leitz SUMMICRON lens 90 mm f/2.

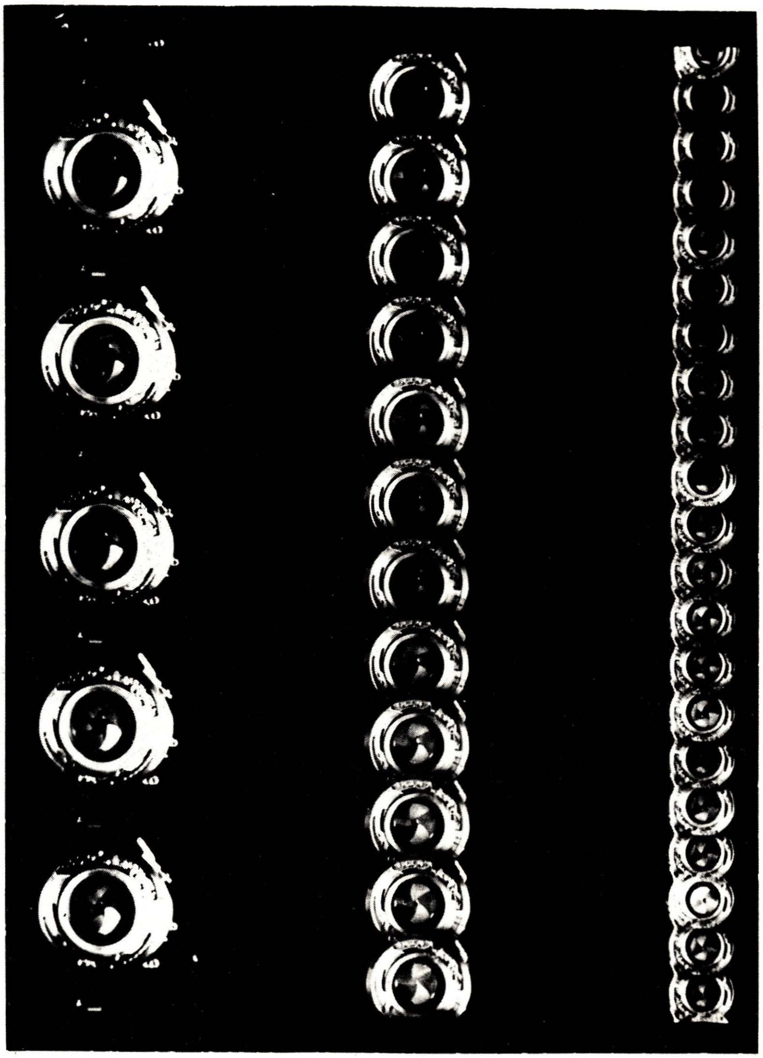

Closing action of a central shutter.
Three drum camera shots taken at 3000, 6000 and 9000 frames per second, showing decreasing frame height with increasing flashing rate.

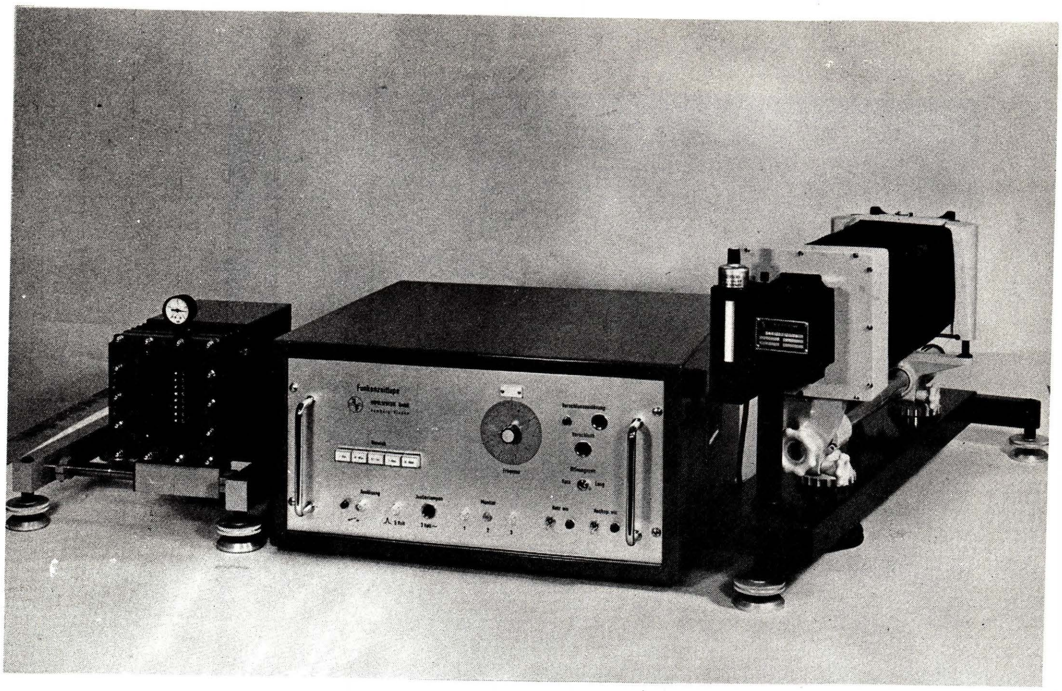

CHRONOLITE 8

from left to right : pressurized spark head, power supply and control unit, optical bench mounted taking camera with rotating magnet shutter.

Below : optical principle of the CHRONOLITE 8

MULTIPLE SPARK CAMERA

III PERSPECTIVE ILLUSTRATION OF FUNCTIONAL OPERATION (OBLIQUE FROM TOP)

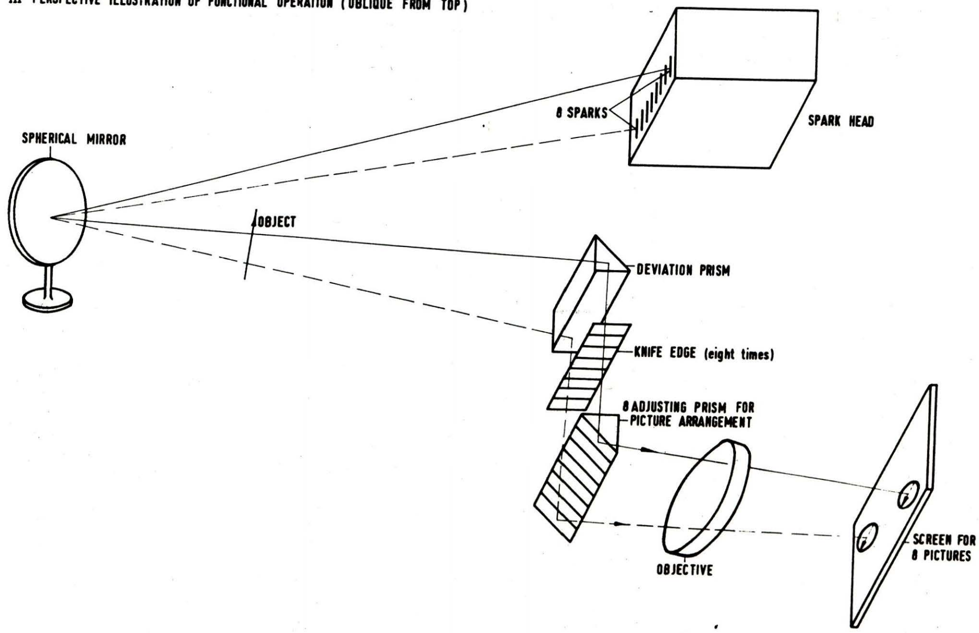

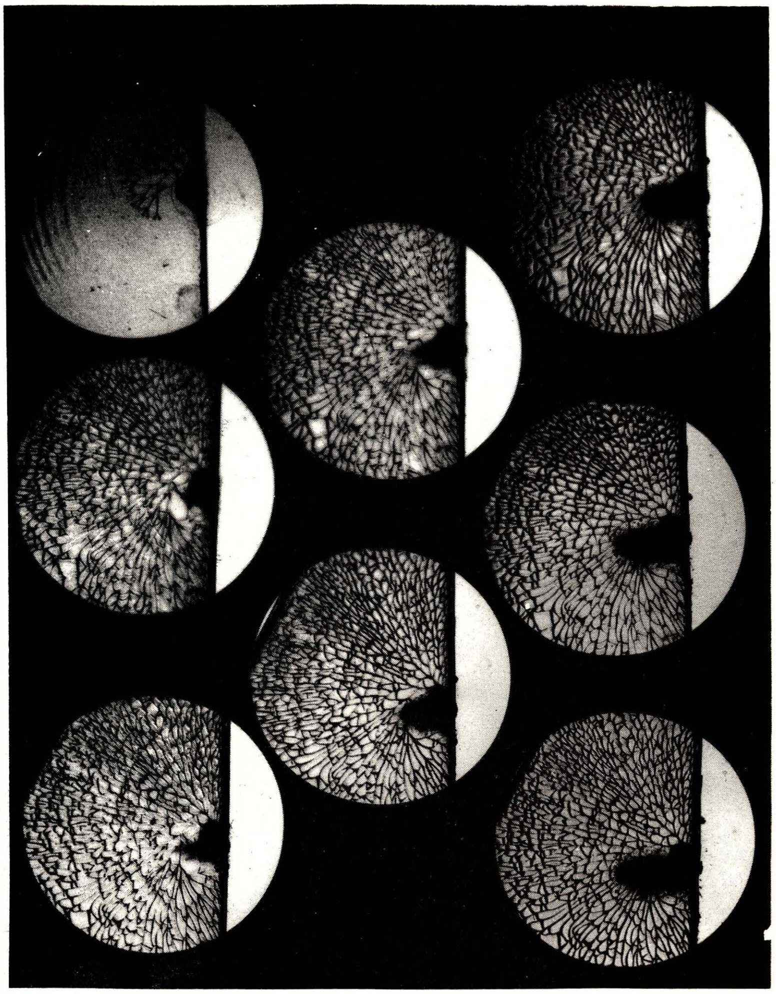

CHRONOLITE 8 sequence showing shot against edge of safety glass. 50 000 frames per second.

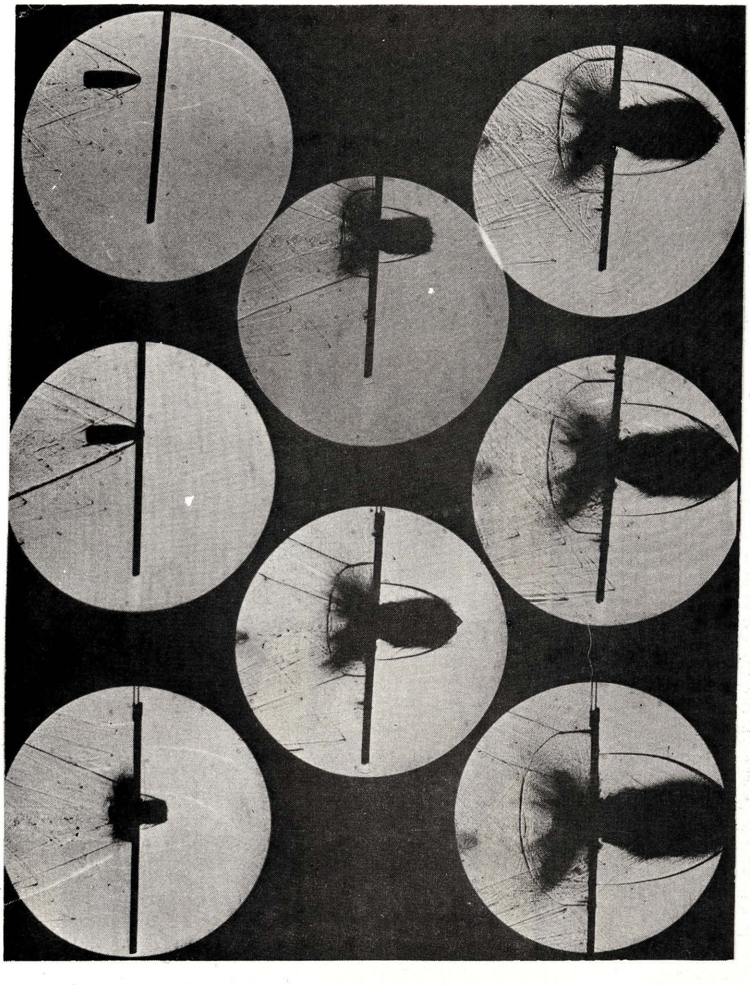

CHRONOLITE 8 sequence taken at 100 000 frames per second showing supersonic rifle bullet (V_0 = 1200 m/sec.) penetrating a metal strip.

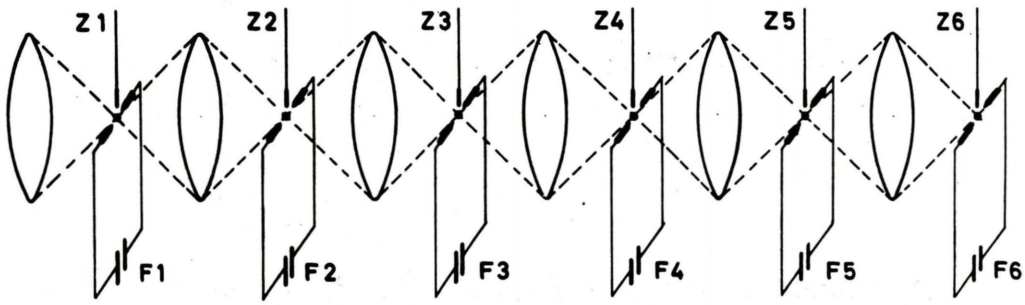

Operating principle of the CHRONOLITE confocal spark cascade according to Patzke.

The individual spark gaps Z 1 - Z 6 with their capacitors F 1 - F 6 are on a common optical axis. The light from each spark gap is projected by a lens into the point of the next gap. The spark gaps are fired in the order from Z 6 to Z 1. Thus, all sparks appear to emanate from Z 1, from where they are focused and directed onto the object to be illuminated by a projection lens.
Practical experience has shown that in most cases 2 to 3 spark gaps arranged in this fashion will suffice, as, because of the high flashing rates, superpositions will have to be made. More than three images on one plate, however. may in many cases be detrimental to the clarity of information.

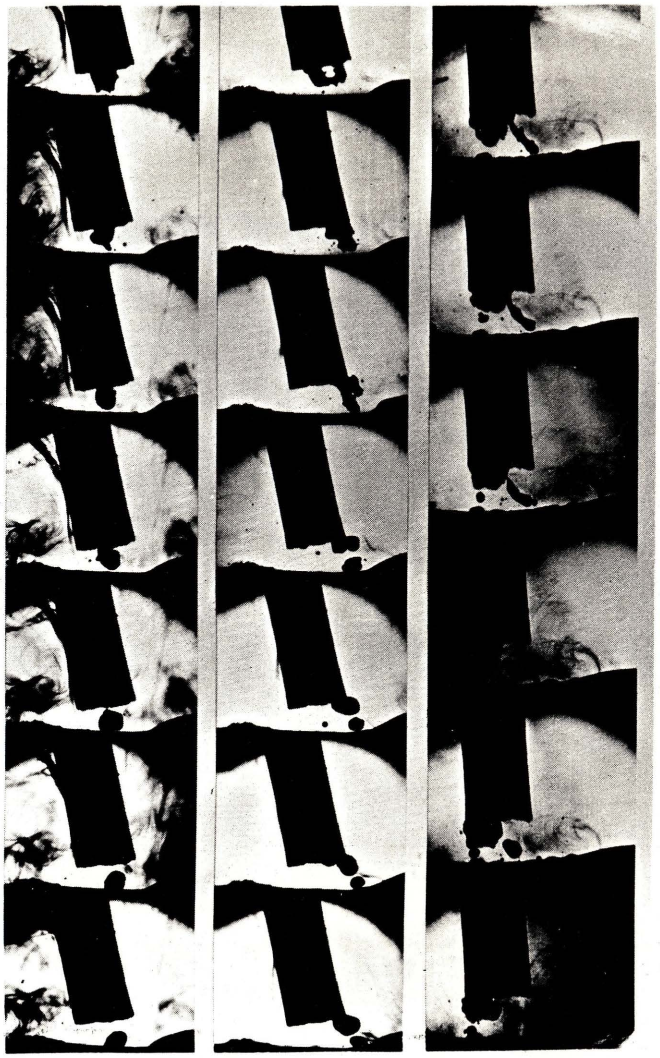

STROBOKERR Method

Drop transfer from a welding electrode to the weld.
A Kerr cell in front of the rotating prism camera lens, pulsed in synchronisation with the flash frequency, reduces the light intensity of the welding arc plasm by several magnitudes more than the light from the flash. This makes the luminous welding plasma virtually invisible and the film shows only the phenomena taking place in the plasma. (DC welding arc, approx. 200 amps.).

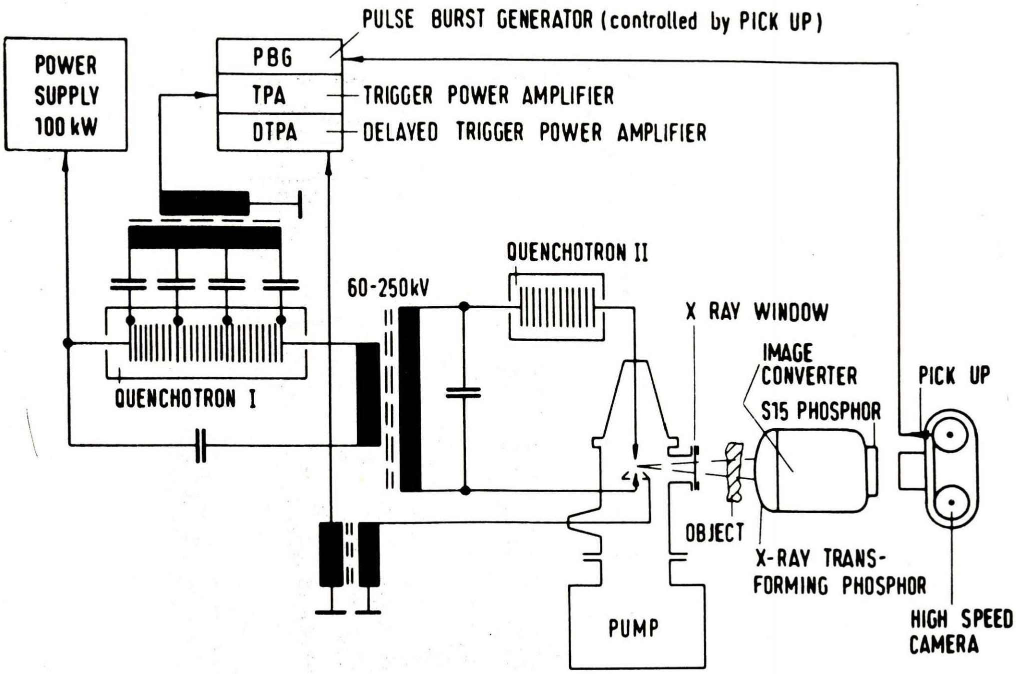

Operating principle of the STROBOKIN X-PACK.

The pulses, which normally serve to produce the light flashes, are tapped off at the flash lamp, stepped up by a differential transformer and are then fed into the X-ray flash tube.
The image on the anode of the X-ray image converter is filmed by a rotating prism camera. The optical pick-up of the camera controls the X-ray flashing rate.
Because of the comparatively slow decay time of the phosphor screen 5000 to 6000 frames per second are the maximum taking rates, otherwise "ghosting" may occur.

Scene from a STROBOKIN X-ray flash film, showing the action of an encapsulated relay. Taking rate : 5000 frames per second.

above :

X-ray flash photographs of an exploding wire. Drum camera film, 10 kHz without image converter.

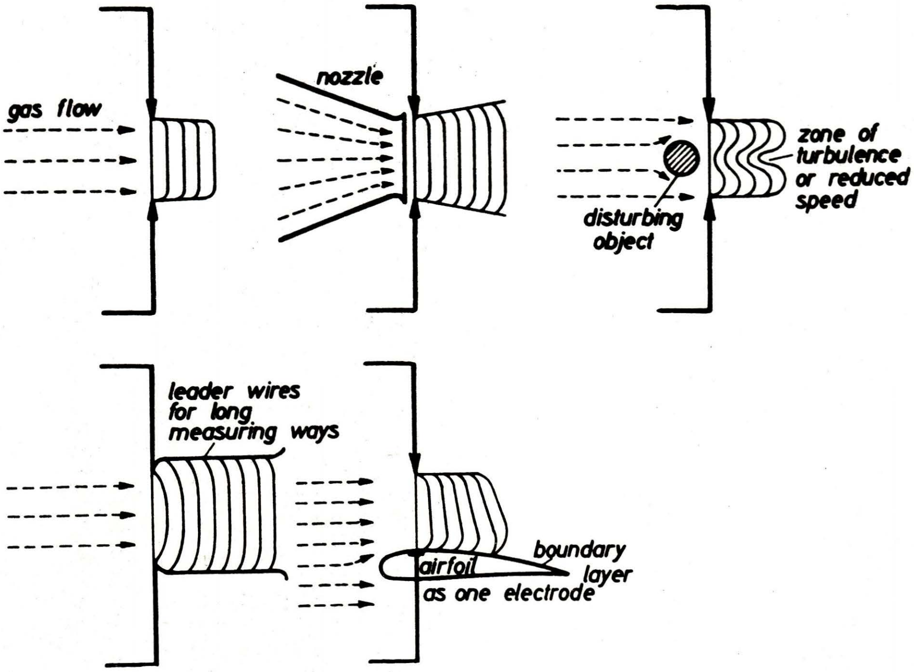

Principle of Spark Tracing

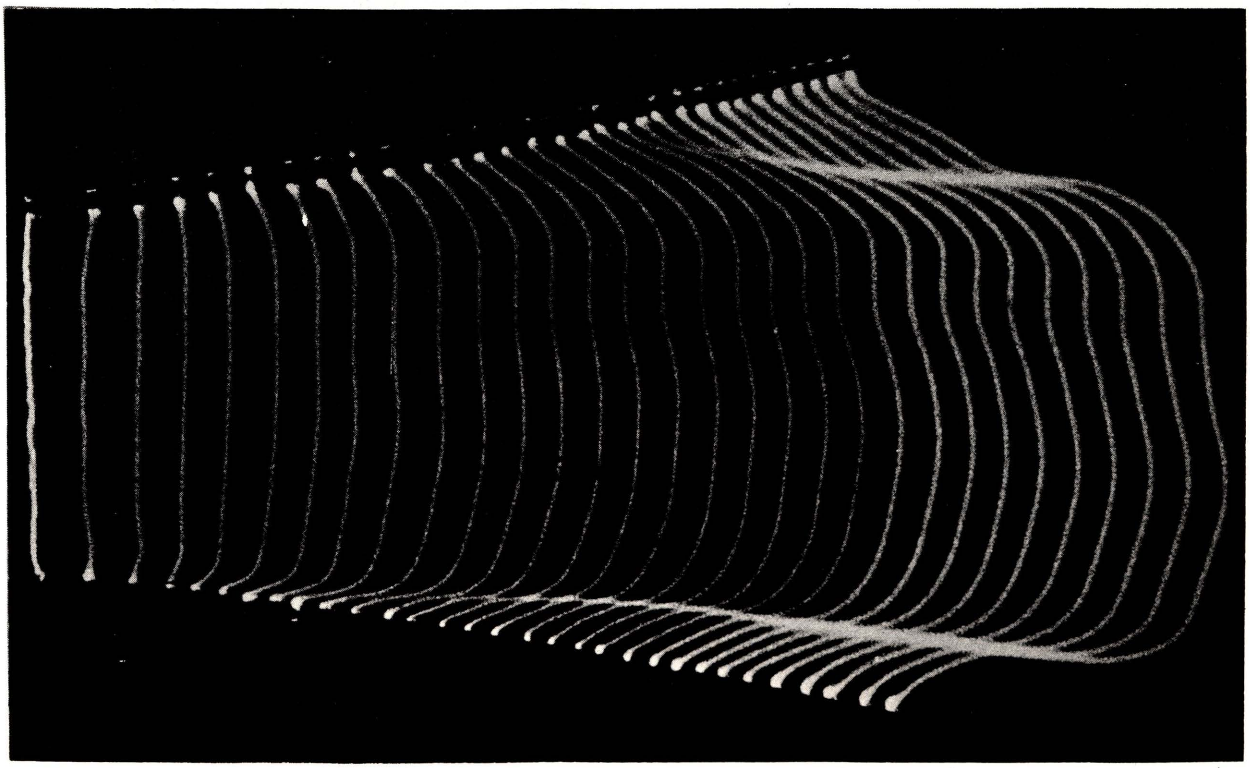

Spark trace of an air flow

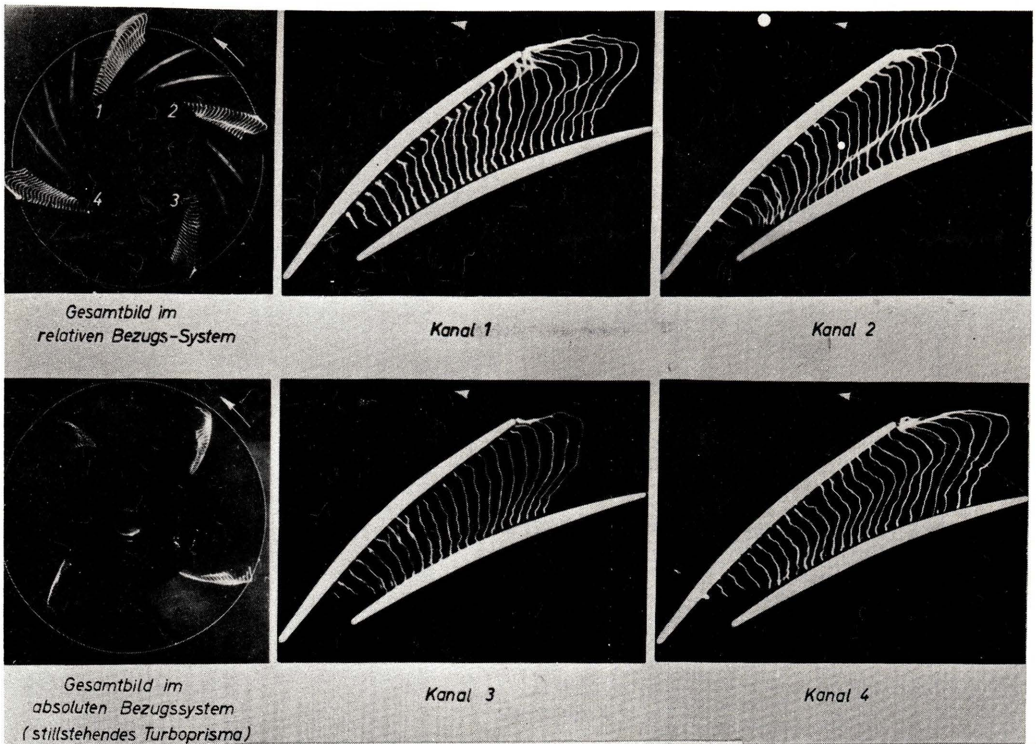

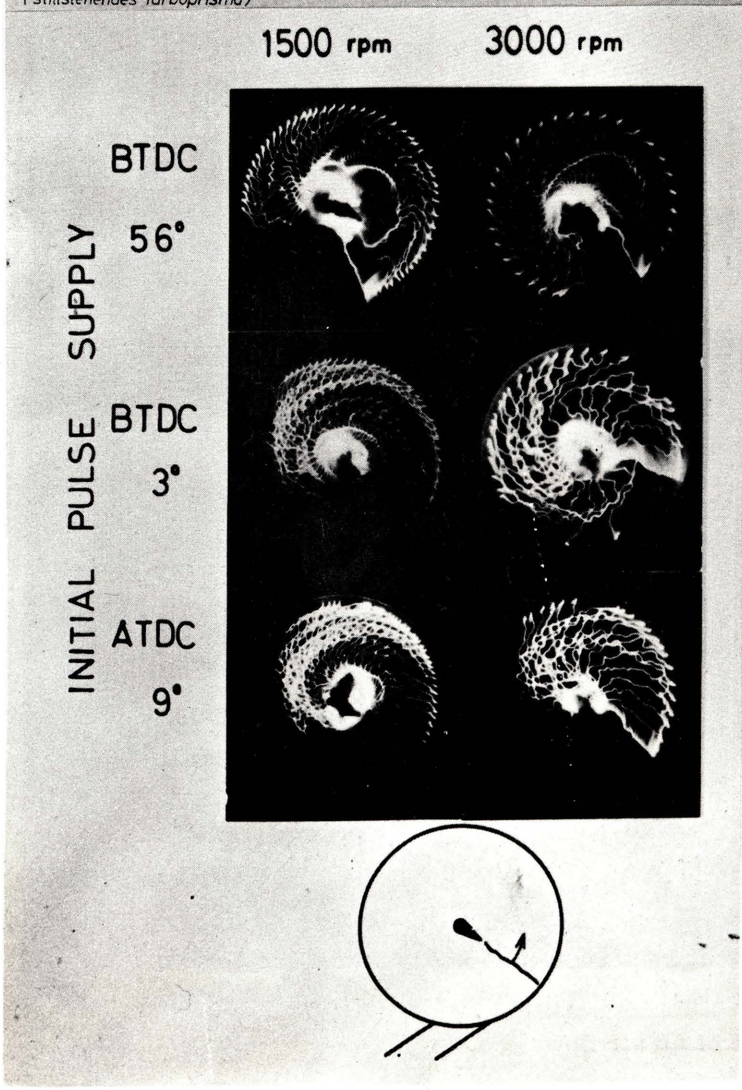

Top :

Spark traces between the turbine blades of a radial compressor.

Left :

Spark traces in the swirl chamber of a 1 cylinder diesel engine

Components of a Fischer NANOLITE lamp.
Top from left to right : pressure cylinder with filling vent, circular beam head, sleeve, high voltage connector.
Bottom row : achromatic condensor, pressure chamber with filling vent, front beam head, line capacitor.

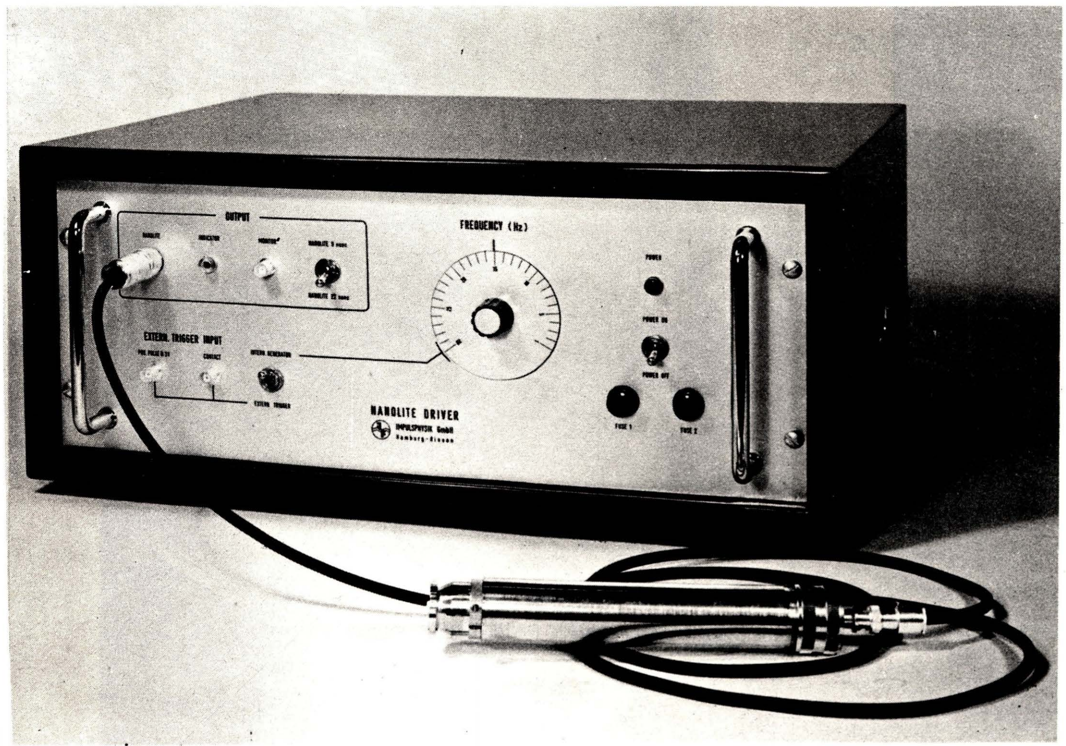

NANOLITE drive 1 - 30 Hz with 18 nanosecond NANOLITE flash lamp connected.

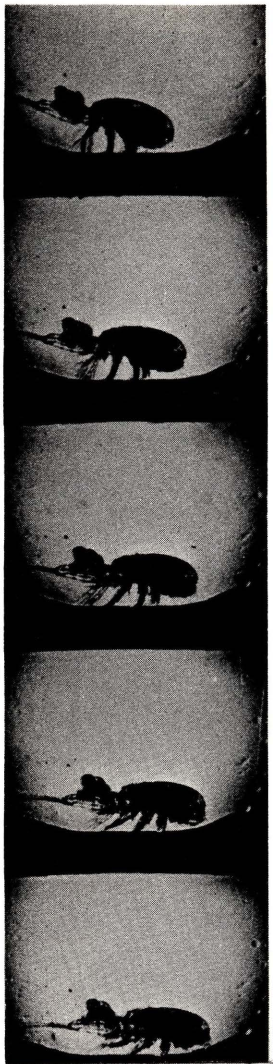

left : micrograph scene from a 16 mm high-speed film showing a codepoda in a brackwater droplet.
50 times microscopic magnification, 1000 frames per sec.
illumination with synchronized Fischer NANOLITE.

bottom : shadowgraph of a bullet taken directly on photographic film without any lens, using the NANOLITE.
(Laboratoire de Ballistique Ecole Royale Militaire, Bruxelles).

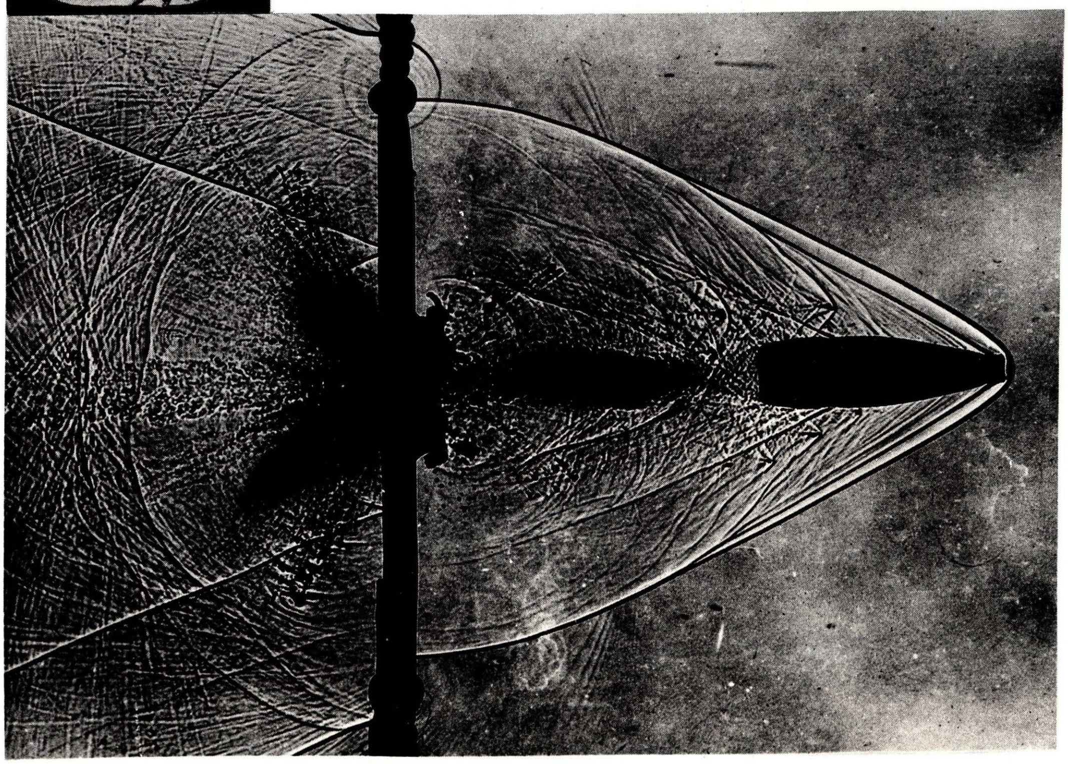

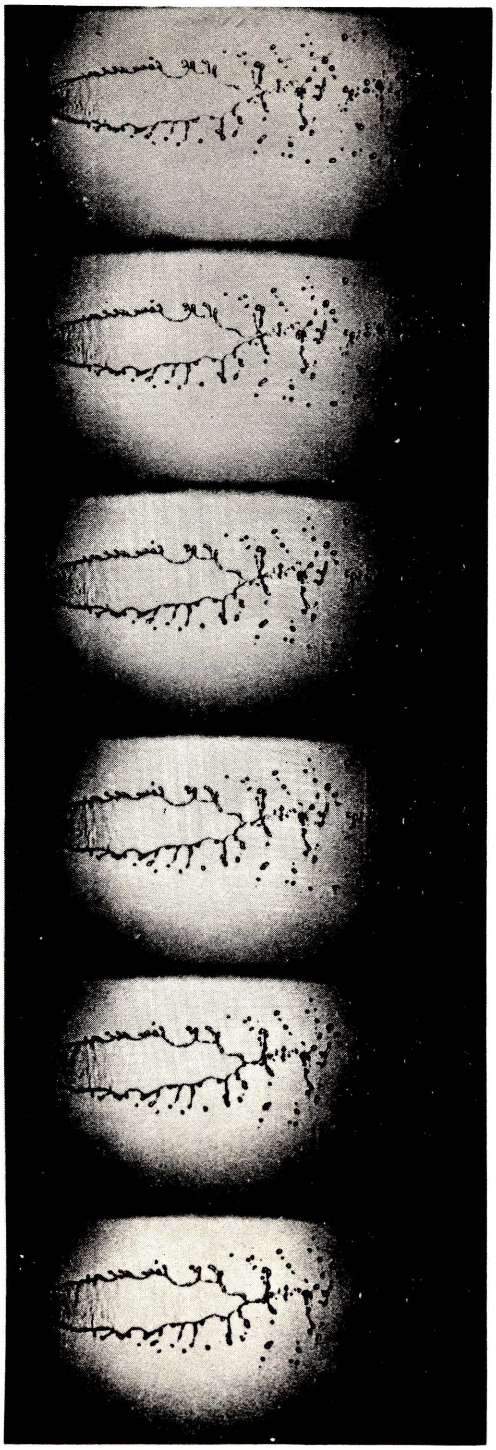

Jet from a high pressure nozzle. NANOLITE driven at 10 kHz from the STROBOKIN control unit. Taking camera : STROBODRUM, backligthing, single frame exposure 18 nanosecs.

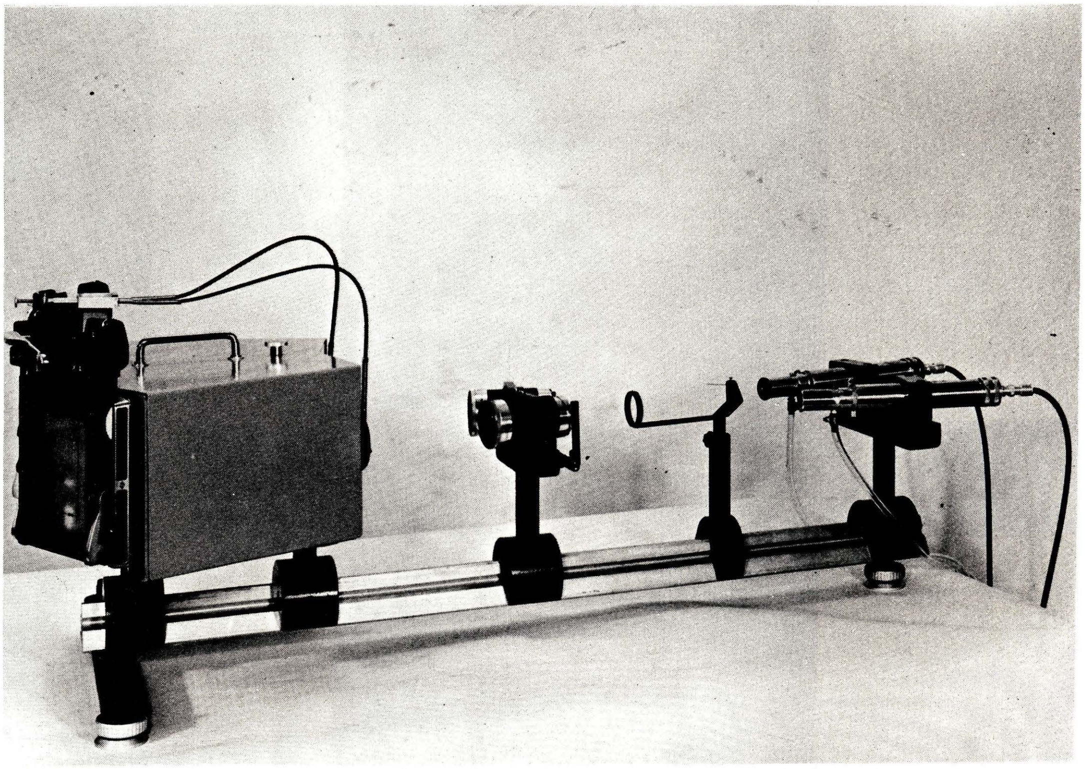

NANO TWIN instrumentation on optical bench.
From left to right : Double body camera with shutters and cable releases, taking lenses, field of view frame and marker, two Nanolites 18 KL-L with front beam heads, pressure chambers and optical condensor lenses.

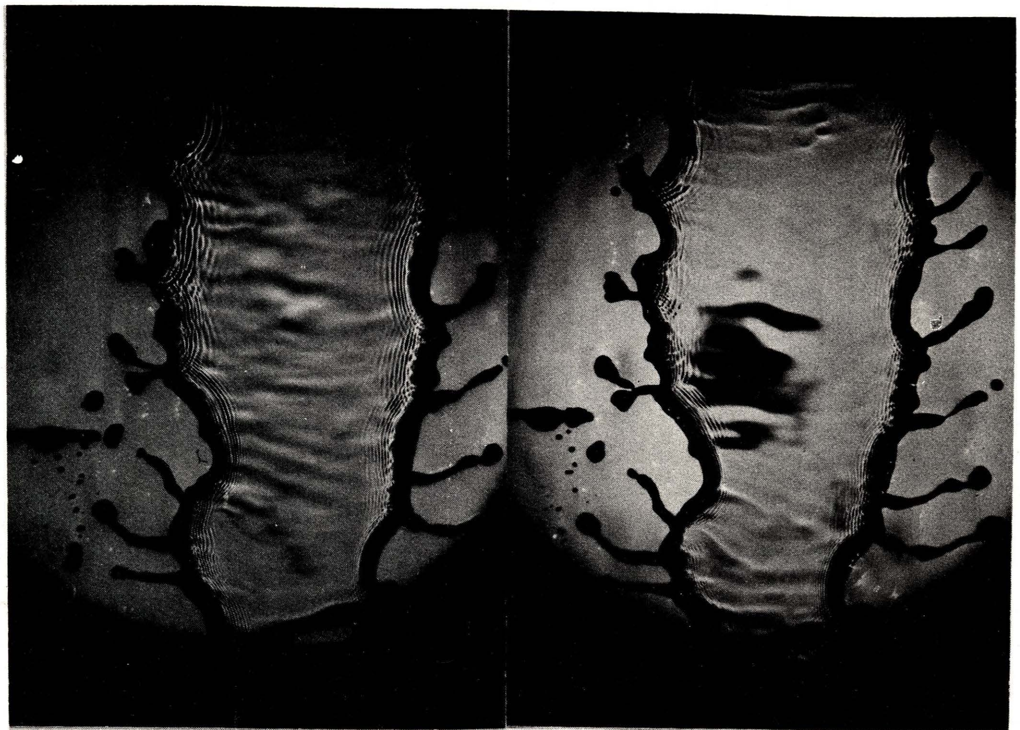

NANO TWIN shot showing water curtain coming from a high pressure flat jet nozzle.
The pointer at the left serves to indicate and to permit measuring of movement and velocities.
Time interval between the two shots : 500 microsecs.

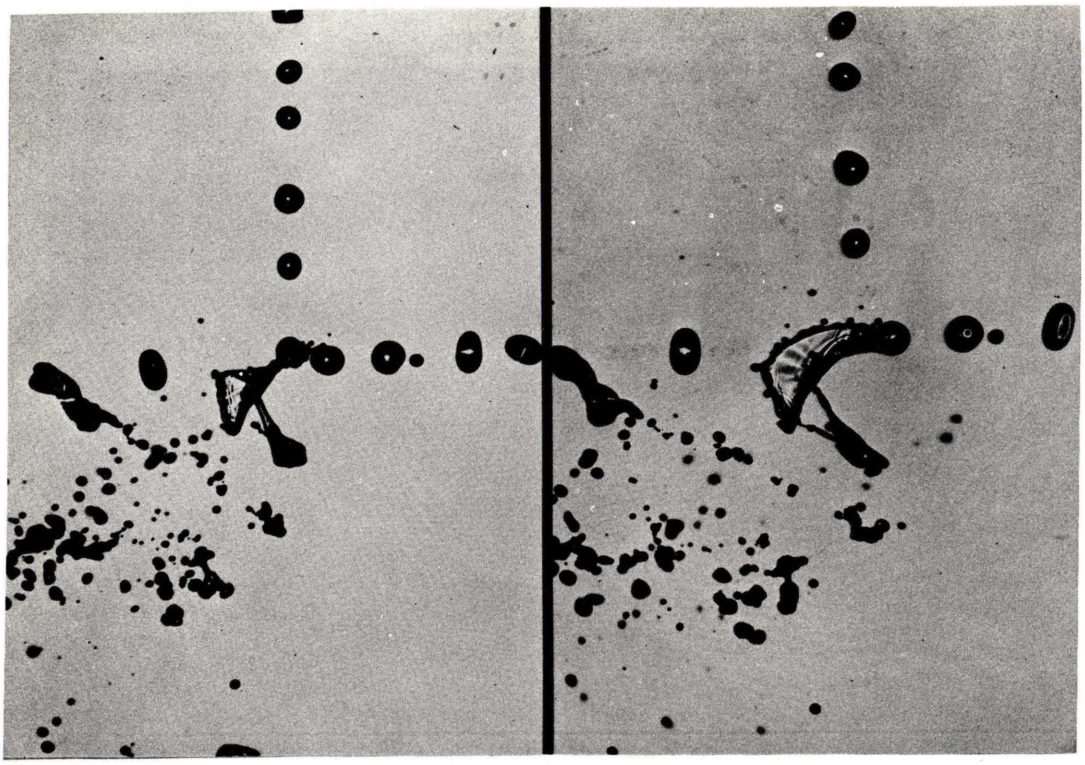

Droplet collision between a vertical and a horizontal squirt.
On impact the liquids coagulate under considerable change of shape and eventually resulting in very fine atomisation.
Such phenomena occur e. g. in fuel injection and are of great interest for fuel research scientists.
Photographed with NANO TWIN, interval between the two shots : 80 microsecs., image magnification on the negative : 8 times natural size.

VIBRATION OF ROTATING MACHINERY

R. L. Eshleman
IIT Research Institute
Chicago
Ill., U.S.A.

SUMMARY - Recent technology on the vibration of rotating machinery as reported in the international technical literature is reviewed. The review is limited to significant contributions with emphasis on 50 papers published within the last 3 years.

INTRODUCTION

Engineers have been concerned with the generation and transmission of power for centuries; however, in recent times (the last 25 years) the demand for power by society has increased to the extent that very high-speed rotating machinery is a necessity. In fact turbine speeds in the range of 20,000 rpm are not uncommon, and, for highly specialized equipment, rotors have been designed that operate at speeds of over 100,000 rpm. The realization of machinery which successfully functions at these speeds was made possible by a technology based on the invariant fundamentals of physics, numerical methods of computation, testing techniques and instrumentation, and good engineering practice. In the pursuit of developing the technology involved in the design and development of rotating machinery, many problems involving vibration have been solved through analysis and testing.

A typical rotating machine is composed of various components -- a rotor, disks, support bearings, foundations, and housings. These massive and flexible components absorb and dissipate energy, when subjected to internal and external disturbances, and produce a unique pattern of motions called response. Response is related to the design of the rotating machine; i.e., it is an indication of the system's deflections and stresses. The state of the machine is established by comparing response with a design specification.

The undamped natural frequencies of a system provide a measure of the nonrotating system's mass and elasticity, both of which are useful in identifying potential areas; e.g., vibration resonant conditions that may exist when a vibratory disturbance occurs at a system natural frequency. System natural frequencies change with rotor speed due to the rotor's mass acceleration (spin-rotor whirl interaction, called the gyroscopic effect). Critical speeds correspond to resonant frequencies of the machine system. The basic identification of critical speeds is made from the natural frequencies of the rotating system and a knowledge of the forcing phenomena.* If the frequency of any harmonic component of a periodic forcing phenomenon is equal to, or approximates, the frequency of any mode of rotor vibration, a condition of resonance may exist; if resonance exists at a specific speed, that speed is called a critical speed. The calculated critical speeds of a machine system, although useful, constitute incomplete design data and serve as indicators of potential trouble in machine operation; thus, design engineers should concern themselves with system response.

* Forcing phenomena are not used in classical lateral critical speed calculation where the system critical speeds are defined to be equal to its natural frequencies. However, a more complete description of the system's critical speeds is obtained through the use of associated forcing phenomena.

Self-excited vibrations and instabilities, which occur frequently in machine systems, develop through a mechanism whereby a rotor will perform nonsynchronous speed whirl at (or near) one or more of its natural frequencies. The rotor draws energy from its rotational motion and supports rotor whirling up to destructive amplitudes. Self-excited vibrations are potentially more destructive than vibration due to mass unbalance because they induce alternating stresses in the rotor which can lead to fatigue failures and/or catastrophic fracture, whereas synchronous frequency forced vibration does not involve alternating stresses but rather psuedostatic stresses.

In this paper, the recent technology on the vibration of rotating machinery as reported in the international technical literature will be reviewed. Since comprehensive survey papers now exist in this technical area, no attempt will be made to discuss all the literature on the vibration of rotating machinery. In fact, this would be a Herculean task because today over 750 technical publications on critical speeds, response, and stability of rotating machinery exist. Significant contributions with emphasis on over 50 papers published in the last 3 years to this technology are reviewed herein.

ROTOR STABILITY

Unexpected instabilities, created by the inadvertent combination of physical factors, have plagued rotor designers for years. Ehrich (1) has categorized rotor and rotor associated instability phenomena in three distinct classes and has described their working mechanisms in detail using graphical depiction of the force balance in the rotor. Figure 1 is a typical illustration from Ehrich's paper showing the force condition for hysteretic whirl. Ehrich's classical paper "Identification and Avoidance of Instabilities and Self-Excited Vibrations in Rotating Machinery" reviews the literature in this area up to the year 1971.

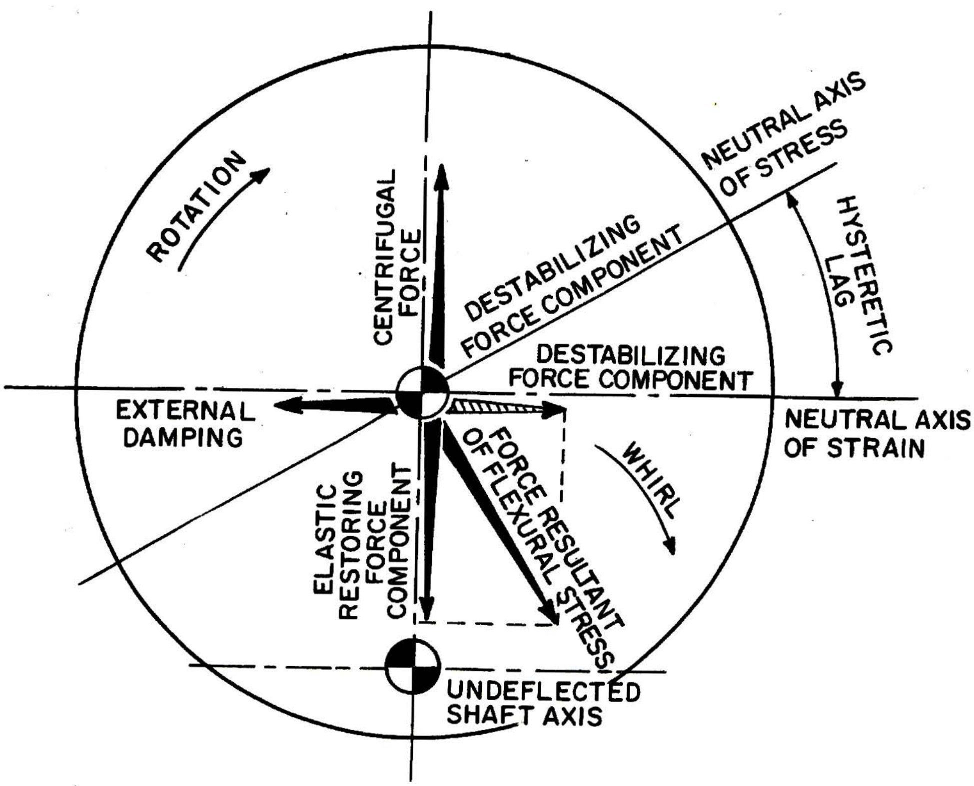

Figure 1. Hysteretic Whirl (1)

In the most frequently encountered category of instability (generally termed "whirling" or "whipping"), the unifying generality is the generation of a tangential force, normal to an arbitrary radial deflection of a rotor, whose magnitude is proportional to that deflection. At some "onset" rotational speed, such a force system will overcome the stabilizing external damping forces which are generally present, and induce a whirling motion of ever-increasing amplitude, limited only by nonlinearities which ultimately limit deflections. The most important examples of this category are:

- hysteretic whirl,
- fluid trapped in the rotor,
- dry friction whips,
- aeroelastic tip-clearance effect, and
- fluid bearing whip.

All these self-excitation systems involve friction or fluid energy dissipation mechanisms to generate the destabilizing force.

A second general category of instability is "parametric excitation" where instability is induced by the effective periodic variation of the system's parameters (stiffness, speed, torque, inertia, natural frequency, etc.). Two particular instances of interest in the field of rotating machinery are:

- lateral instability due to asymmetric shafting and/or bearing characteristics, and
- lateral instability due to pulsating torque.

A final important phenomenon which constitutes a category into itself is:

- stick-slip rubs and chatter.

Recent contributions to the topic of rotating machinery stability deal with computational methods for the prediction of the threshold of instability. A general method for calculating threshold speed of instability and damped critical speeds of a general flexible rotor in fluid-film journal bearings has been developed by Lund (2). This method is analogous to the Holzer-Myklestad-Prohl method for calculating critical speeds and is readily programmed for numerical computation. The rotor model can simulate any practical shaft geometry and support configuration. The bearings are represented by their linearized dynamic properties, also known as the stiffness and damping coefficients of the bearing, and the calculation includes hysteretic internal damping in the shaft and destabilizing aerodynamic forces. To demonstrate the application of the method, Lund shows the results for an industrial, multistage compressor.

Small linear and angular displacements are assumed in De Choudhury's (3) model which includes the effects of external and internal damping, aerodynamic coupling and gyroscope effects. Routh stability criteria for different parametric conditions is used on the characteristic equation. Gasch (4) achieves similar results using the principle of virtual work to derive the energy equations of a vibrating shaft. These equations are transformed into a set of ordinary differential equations and further into the classical eigenvalue formulation rather than using transmission matricies.

Using a more general model, necessary and sufficient conditions for the stability of motion of whirling shafts were established by Mingori (5) using the direct method of Lyapunov. The nonlinear mathematical model employed is based on the work of V. V. Bolotin and includes the effects of both internal and external damping. A coordinate transformation is used to facilitate the analysis. In effect, this transformation establishes a mathematical equivalence between the governing equations for a whirling shaft with both internal and external damping, and the governing equations for a whirling shaft with internal damping only.

Pedersen (6) recently conducted a study of the nonsynchronous, self-excited whirl of continuous rotors caused by internal damping forces and by hydrodynamic bearing-film forces. Taking into account gyroscope effects, the effect of shear on bending, and external damping, the equations of motion are derived by the variational principle. By means of two-mode expansions simple expressions are obtained for the limit of stability and the corresponding whirling frequency that are valid for small values of the velocity dependent forces. Numerical methods are used to obtain better approximations to the limits of stability and the whirling frequencies. Pedersen's results show that for large values of internal and external damping forces and gyroscopic moments, the widely used two-mode approximation may be greatly in error. It is found that if the limit of stability is raised by adding external damping to the rotor system, then even a small amount of internal damping may considerably reduce the limit of stability. In accordance with experimental work done by other authors, it is found that for certain damping conditions a second stability region exists.

Recently Black et al (7, 8, 9) published several papers on centrifugal pump rotor vibrations. These papers deal specifically with the theoretical and practical aspects of stability of centrifugal pumps and are design oriented. Problems dealing with close internal clearances retaining pressure to act as powerful hybrid bearings, large hydraulic forces depending on the ratio of flow to optimum flow in vane diffuser type pumps, and high pressure ring seals are addressed. Kramer (10) presented a paper intended to bridge the gap between theory and practice at the recent conference on "Vibrations in Rotating Systems" held in London. Bousso (11) reports on the stability of an inertia mounted on a rotating flexible shaft. In contrast to the Routh-Hurvitz stability criterion for which linearization of the equations of motion is required, this perturbation method is based on direct analysis of forces and moments acting on the inertia when it precesses at any of its natural frequencies as a result of a random disturbance. A realistic nonlinear internal friction law is assumed in setting up the stability criterion. The influence of load moment, hitherto neglected in stability considerations, is explained. The method used is based on a physical approach to the problem and leads to a deeper understanding of the stability problems through its direct analysis of the operating forces.

Vance (12) has used mathematical methods to determine the stability speed threshold of non-synchronous whirl instability for an unbalanced flexible rotor on a rigid foundation. This threshold of instability is shown to be the same as the threshold for balanced rotors established by previous investigations. The location of the external damping (foundation or rotor) is shown to be important in determining stability when the foundation is made very rigid.

Ehrich (13) noted that in the technical literature axial flow turbomachines are sometimes subject to whirling instability when subject to high mass flow. His paper hypothesizes an instability model, where destabilizing forces are induced on the turbomachine's blading as a result of its incremental motions when elastically deflected in the internal stream of working fluid. The model bears some analytical resemblance to the instability which propellers can experience when they are elastically deflected in an external stream.

Recent papers on self-excited rotor instabilities caused by assymetric rotors and bearings have been published by Iwatsubo (14), Arnold (15) and Messal (16). All papers utilize a distributed parameter rotor model. Iwatsubo used Galerkin's method and the perturbation method to determine changes in the main instability regions whereas Messal used a perturbation analysis based on Hsu's method.

Yamamoto, Ota, and Kono (17) determine unstable regions in the neighborhood of both the major critical speed and the rotating speed at which the sum of two natural frequencies of the system is equal to twice the rotating speed of the shaft for a rotating shaft system carrying an unsymmetrical rotor, as in a rotating shaft system with inequality in stiffness. The unstable vibrations appearing in these unstable regions are treated for the system consisting of a rotor with unsymmetrical inertia and a shaft with unequal stiffness which rotates with the rotor. Finally, Begg (18) addresses the problem of self-excited rotor whirl induced by rubbing friction between stator and rotor in close clearance rotating machines. He determines stability regimes dependent on the damping and stiffness characteristics of a simple flexible overhung rotor.

CRITICAL SPEEDS

Critical speed evaluation, once the forte of the rotating machinery designer, no longer is sufficient to ensure smooth functioning machines. However, much valuable information is gained from a true critical speed evaluation because many potentially troublesome situations can be avoided.

Determination of critical speeds of rotating machinery required the calculation of the system natural frequencies (a function of mass, elasticity, rotor speed, external force and external torque) utilizing an appropriate mathematical model. In addition, system disturbing frequencies, usually a multiple of rotor speed, are often used in the critical speed identification process. Presently two principal methods are utilized to calculate system natural frequencies: (1) the controlled searching technique of Holzer, Myklestad and Prohle, where the independent variable is frequency, from which the sytem mode shape is calculated -- if the mode shape fits the boundary conditions, the assumed frequency is a natural frequency; and (2) the matrix iteration technique in which the mode shape is assumed and the frequency is calculated. The iteration process proceeds until convergence to the natural frequency occurs. Many other techniques are available for critical speed calculation including:

- Exact methods
- Rayleigh's method
- Ritz's method
- Stodola's method
- Dunkerley's method
- Polynomial methods
- Galerkin's method
- Impedance matching

A description of these methods is contained in a survey of "Critical Speeds and Response of Flexible Rotor Systems" by Eshleman (19).

In simple cases, the forcing phenomena are synchronous with rotor speed; when the rotor speed matches a system natural frequency, therefore, it is labeled a critical speed. In systems such as an internal combustion (I. C.) engine, in which forcing phenomena are nonsynchronous, the critical speed is the speed at which the forcing frequency is equal to a system natural frequency. For an I. C. engine, the formula for critical speed is

$$\text{Critical Speed} = \frac{\text{natural frequency}}{\text{order number}}$$

The order number is an integer because gas and inertia forces can be expanded in a Fourier series whose period corresponds to twice the engine speed. The determination of critical speeds is further complicated when system gyroscopic effects are strong, and the natural frequencies depend on the rotor speed. In this case, two critical speeds are obtained for each mode (backward and forward whirl). The ratio of the rotor speed Ω to the whirl frequency is plotted against the whirl frequency as shown in Figure 2. It is obvious that the rotor speed, Ω, alters the system natural frequencies. Rotor induced nonsynchronous periodic disturbance may induce whirling if the disturbance frequency equals one of these "dynamic" natural frequencies.

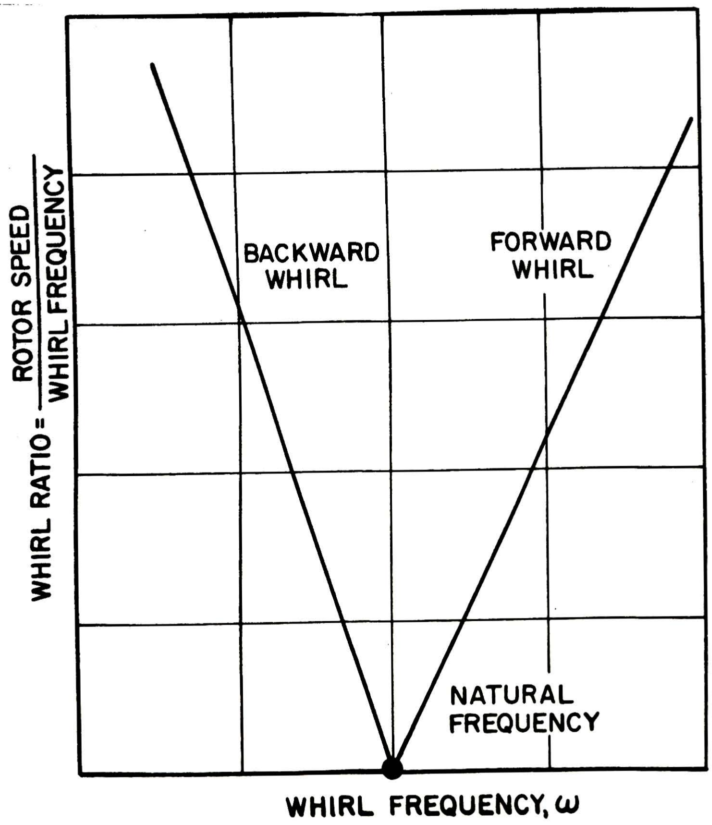

Figure 2. The Effect of Rotor Speed on Whirl Frequency (19)

Recent advances in critical speed determination are concerned with governing physical phenomena and computational techniques. Dopkin (20) reports a general analysis to predict the natural frequencies of vibration of a rotating shaft on linear, undamped bearings including any number of flexible disks. A limited parametric study of six different rotor geometries with a range of disk flexibilities is presented.

Using Galerkin's method, Dubigeon (21) analyzed the natural frequencies and mode shapes of long vertical shafts. Experimental results from a laboratory model are reported in this paper.

A theoretical study of the whirling of a cantilever elastic shaft subjected to external pressure was reported by Newland (22). The whirling speeds are shown to depend on the variation of pressure and area along the shaft and the lowest critical speed is solved approximately by an energy method for a number of cases. When the external pressure is high enough, its effect may be important and the critical speed may be raised or lowered, depending on the pressure distribution.

Porat and Niv (23) formulated the rotating shaft problem including the effects of shear, rotatory inertia and gyroscopic moments. Two interesting conclusions were drawn from this investigation; namely, that only forward resonance could be caused by rotation and that at high speeds, the high-level natural frequencies are identical for all modes. However, it must be recognized that torque, the cause of backward whirling in the experiments of Lowell (24, 25) and Eshleman and Eubanks (26), was not included in this mathematical model.

Palmer and Mc Callion (27) describe a method for the evaluation of natural frequencies and mode shapes of a general system of shafts linked by general interconnections. A detailed description is given of the particular case where a connection is made by two meshing spur gears; transverse displacement of gear centers as well as torsional displacement being taken into account. This method can be applied to any type connection for which a linear relation exists between the displacements. Satisfactory identification was obtained for the lower frequency modes of a gearbox rig.

Ramamurti (28) recently devised a simultaneous iteration method of obtaining the natural frequencies and mode shapes of torsional systems. Shaikh (29) reports another technique applicable to torsional vibration problems in which an analysis of branched systems is performed using transfer matrices in Holzer type solutions. Unlike other methods, no matrix inversions (or equivalent operations) are required to account for branches at a junction. A single determinant giving natural frequencies is arrived at irrespective of the number of branches and junctions. Thus the method is straightforward, compact, and economical for computer solutions.

A method for the analysis of critical speeds using the modified transfer matrix and dynamic stiffness techniques was applied to practical problems by McLean (30). The dynamic stiffness concept is applied to separate a complete structure into its components parts, each of which can be evaluated independently. The dynamic stiffnesses derived for each subsystem are superposed to give the dynamic response of the complete structure. This has an added advantage in that for complex structures the problem can be reduced to the evaluation of the dynamic stiffness of a simpler system to obtain the critical speeds of the complete assembly. Parszewski (31) developed a critical speed calculation procedure oriented to the digital computer which utilizes experimentally determined support structure characteristics.

Finally, Gilbert (32) presented a new method for calculation of torsional natural frequencies of branch systems. His solution consists of writing the potential and kinetic energies of the system, employing Lagrange's equation to write the equations of motion. These equations of motion and the equation of the moment of momentum are written in matrix notation for iteration for frequency (which will appear as a dominant root of the dynamic matrix) and the modal column which is the normal mode of deflection. A typical example illustrates a numerical method (a form of matrix iteration) which simplifies the solution.

ROTOR RESPONSE

Current techniques allow the calculation of rotor response as a function of speed, geometry, and space. The digital computer and numerical techniques are practical tools for solving large system problems. Critical operating speeds are determined through evaluation of response, which is a measure of the state of a machine.

During the past 5 years rotor response calculation techniques have undergone much refinement and development; however, accurate response prediction is still at the mercy of damping force characterization. Rotor response methodology and experience published prior to the year 1972 has been surveyed and documented by Eshleman (19). The prediction of flexible rotor system response is dependent upon the characterization of external and internally generated forcing phenomena. Each phenomenon is classified according to its mathematical description, which is a function of time. Response calculation methods that utilize these phenomena are listed.

- harmonic linear ⟶ Modified Holzer-Myklestad-Prohl
- periodic/aperiodic linear ⟶ Modal
- nonlinear ⟶ Direct Integration

This classification is used because response techniques are associated with each type of function. Any analytical technique is capable of handling any function adjacent to or above it. Harmonic functions model phenomena (e.g., mass unbalance, gear inaccuracies) that have a once per revolution frequency. Periodic functions composed of harmonic components are used to model engine gas forces and disturbances caused by rolling element bearings. Aperiodic functions are required for suddenly applied loads of a nonperiodic nature; e.g., external shock loading. Nonlinear models may be used for bearing characterization.

Some frequently occurring forcing phenomena associated with rotating machinery are listed below.

- mass unbalance
- shaft eccentricity
- coupling misalignment
- universal joints
- bearings ball movement
- gears
- propeller, fan, pump, turbine, impeller and blade passing
- slider crank mechanisms
- electrical motor pulsations
- liquid pulsations
- shock loading
- frictional surface variations

Recent efforts to refine the popular modified Holzer-Myklestad-Prohl method for rotor response calculation were published by Lemke and Trumpler (33) and Doyle (34). Lemke and Trumpler conducted an analytical investigation of the effect of coupling characteristics on the response of axially coupled sets of turborotors. The results of this investigation are based on transfer matrix techniques which utilize a generalized machine element matrix and coupling fixity matrix. Disk inertia, gyroscopic effects, and both shaft and coupling orthotropy are included in the model. An example, utilizing two axially coupled modified Prohl rotors, demonstrates that the nature of the couplin g has a significant effect on the response characteristics of the rotor set. This is accomplished by varying coupling fixity from zero to infinite in an isotropic and orthotropic manner. As a consequence, this result implies that the coupling must be taken into account throughout the entire mechanical design effort devoted to the rotor system. In particular, the coupling must be considered when writing balancing specifications and during actual balancing of the rotor set. Finally, it is shown that the axial coupling of turborotors can result in the unloading of particular bearings of the turborotor set at discrete speeds. Such unloading may initiate journal instabilities that are known to be associated with light loading conditions.

Doyle has provided the foundation and basic structure of a new highly generalized lumped parameter (Holzer-Myklestad-Prohl type) method for predicting the steady-state transverse dynamical behavior of actual multispan rotor bearing support systems. By employing 17 x 17 real matrices, the problem of finding critical speeds, three-dimensional mode shapes, damped unbalance response, and phase relations is readily handled in cases involving forward or backward synchronous or nonsynchronous elliptic whirl. Each fluid-film bearing support system is assumed to be anisotropic and is described in terms of 27 parameters, 16 of which are direct and cross-coupling film coefficients for treating both translatory and conical journal whirl. The mass, stiffness, and damping properties of each support are included, as are the effects of thrust, torque, shear deflection, and gyroscopic moments on the rotor.

The modal analysis technique for flexible rotor response calculation was originally published by Gladwell and Bishop (35) in 1959. Even though this computational technique is more powerful than the Holzer-Myklestad-Pohl method, it has not been utilized as frequently. Recent applications of the modal analysis technique include rotating machine-structure interaction response by Lee (36), flexible rotor (lateral motion) - fluid-film bearing response by Lund (37), crankshaft-end item torsional response by Eshleman (38), and rotating shaft response in fluid medium by

Prodonoff (39). Lee (34) developed a coupled modal method for solving the problem of dynamic interaction between flexible rotating machines and the elastic supporting structure. A special feature of the problem considered is that the rigid-body displacements of the rotor are identified with the structure modes; therefore, the customary component mode synthesis techniques are not directly applicable. The present approach combines the free-free modes of the rotating machine directly with the structure modes. An example problem is solved for the case of a harmonic excitation. Interaction effects, including gyrocopic coupling, are investigated and discussed.

Lund (37) recently published an analysis for calculating the response of a general flexible rotor in fluid-film bearings to forced and transient excitation. The governing system equations are transformed by means of normal coordinates into a set of decoupled, first-order equations which are solved in closed form. The transformation is based on the orthogonal complex modal functions ("mode shapes") associated with the eigenvalues of the system. The method has been applied to an industrial multistage compressor. Numerical results are given for the response to selected unbalance distributions and, also, the transient response to a shock pulse.

A digital simulation technique for determining the torsional response of internal combustion engines subject to constant and pulsating end item torques is described by Eshleman (38). A refined mathematical model of the engine and end item power shafts is utilized to determine their natural frequencies, mode shapes, torsional motions and stresses using a digital computer. The mathematical model is composed of a finite number of elements which simulate lengths of continuous, massive, elastic shaft with end-attached lumped masses and springs. Forcing functions, obtained by Fourier series expansion of the engine pressure-crank angle curve, are applied at the lumped masses. The technique is applied to a small gasoline engine attached to a reciprocating compressor and to a large diesel engine with a constant torque end item.

Using Euler-Bernoulli beam theory, Prodonoff (39) investigates the dynamic behavior of an eccentric rotating shaft, subject to linearly varying or constant tension. The shaft has distributed mass and elasticity and is suspended in a fluid. Initial lack of straightness is also included in the analysis. The local mass eccentricity is assumed to be a deterministic function of the axial coordinate. For the variable tension case the response is determined for a vertical shaft simply supported at the top and vertically guided at the bottom. The constant tension case is analyzed for a shaft simply supported as its end. Results are given in graphical form for several values of the tension and different eccentricity functions.

Ruhl (40) utilized the recently popular direct element matrix method with a finite element model to study turborotor system stability and unbalanced mass response. The finite element model characterizes the shafting section mass and elasticity as uniformly distributed along its length and allows mass, elasticity, and damping discretely lumped at the rotor ends.

The most general and most costly technique for flexible rotor-bearing-structural response is direct integration. The advent of large digital computers has allowed the solution of transient nonlinear rotor response problems. Shen and Mogil (41) pioneered in this area. Kirk and Gunter (42, 43, 44), Breed and Castelli (45) and Childs (46) have recently published in this area.

Kirk and Gunter (42) examine the transient response of the single-mass Jeffcott rotor in elastic bearings mounted on damped, flexible supports by integrating the equations of motion numerically using a modified fourth order Runge-Kutta procedure.

Kirk (43) derived nonlinear journal bearing force expressions from the short bearing approximation to study the stability and transient response of the floating bush squeeze damper support system in his doctoral work. Both rigid and flexible rotor models are studied and results indicate that the stability of flexible rotors supported by journal bearings can be greatly improved by the use of squeeze damper supports. Results from linearized stability studies of flexible rotors indicate that a tuned support system can greatly improve the performance of the units from the standpoint of unbalance response and impact loading.

Kirk and Gunter (44) recently published the equations of motion (derived from energy principles) necessary to calculate the transient response of a multimass flexible rotor supported by nonlinear, damped bearings. Rotor excitation may be the result of internal friction, rotor acceleration, nonlinear forces due to any number of bearing or seal stations, and gyroscopic couples developed from skewed disk effects. The method of solution for transient response simulation is discussed in detail and is based on extensive evaluation of numerical methods available for transient analysis.

Breed and Castelli (45) present a method for rotor dynamic analysis which has sufficient generality to treat nonlinearities, time transients, steady states, dynamic responses and critical speeds for unbalanced, nonuniform shafts on any type of bearing suspension. The technique consists of integrating the transient equations forward in time.

Childs (46) published a transient flexible rotor formulation based on a representation previously employed to simulate the motion of flexible spinning spacecraft. The distributed parameter characteristics of the rotor are approximated by modeling the rotor as an elastically connected group of nonrigid bodies. The elastic rotor deflections of the component rigid bodies are defined in terms of a rotor-fixed frame of reference; hence, during constant synchronous whirling the elastic deflections appear to be constant. The model is initially simplified by the traditional small deflection assumptions of the theory of elasticity, and is additionally simplified by the use of modal coordinates. Modal coordinates dramatically reduce the dimensionality of the model, and significantly clarify the dynamic analysis of the problem.

The influence of bearings on rotor dynamics analyses has been surveyed and documented by Shapiro and Rumbarger (47) in 1972. Fluid film and rolling element bearing representation is covered in detail.

Recent papers on the effects of bearings on rotor response have been published by Holmes (48) and Nakagawa and Aoki (49). Holmes sets up the nonlinear equations which govern the vibration of shafts supported on hydrodynamic sleeve bearings. Solutions are presented for two categories of application: (1) reciprocating engine crankshafts, and (2) steam turbine, alternator and gas turbine rotor shafts. These solutions are compared with experimental and practical evidence to assess applicability. An analytical solution for floating-ring journal bearings and a theoretical analysis of unbalance vibration of a rotor bearing system is presented by Nakagawa and Aoki. Theoretical solutions for fluid film force, friction coefficient and stiffness and damping coefficients are derived. The effect of a floating-ring journal bearing on unbalance vibrations of a symmetrical rotor-bearing system and some design recommendations for optimum bearing dimensions are discussed.

Recent papers involved in the calculation of rotor response while passing through critical speeds were published by Yanabe et al, (50) Iwatsubo et al, (51) and Schweitzer et al(52). Yanabe studied the problem of passage through a critical speed with regard to the maximum deflection of a shaft. The deflection of a shaft, the angular velocity of whirling motion and the phase angle between the unbalance and the whirling motion, under a uniform angular acceleration over the wide range of the angular velocity of a shaft were examined. From the numerical solutions and the experiments on a simple system with one disk, it is clarified that the amplitude of the whirling motion causes a beat after running through the critical speed. In case of acceleration the maximum (minimum) amplitude of beat occurs when the angular velocity of the whirling motion becomes maximum (minimum) and the phase angle becomes $n\pi + \pi/2$ radians when the angular velocity of whirling is equal to the angular frequency corresponding to the critical speed of the system. The nonstationary vibration of an asymmetric rotor with limited power supply was studied by Iwatsubo, et al (51) using the asymptotic method. The many factors which affect the transient vibrating behavior of the asymmetric rotor in passing through critical speed are studied in relation to the amplitude of motion, phase angle, energy, etc. by numerical calculation; that is, stiffness ratio of the asymmetric rotor, damping coefficients, and driving torque (during both acceleration and deceleration). The experimental study using a simple model is added.

Finally Schweitzer, et al (52) examined the motion of high speed rotors as influenced by gyroscopic forces and by the elasticity and damping of their suspension. Starting with the equations of motion, Schweitzer et al investigate the rotor's natural and disturbance behavior. When the rotors are run at critical speeds, instationary motions appear. Axial forces lead to parametric excited vibrations. Optimal parameters of a rotor are determined. Experiments were conducted to verify the theoretical results. The published results of several practical and experimentally oriented studies provide much good design information. Hancock (53) reports on a study to produce empirical vibration data for the process pump according to its design and severity of service. The published vibration norms are represented in clear graphical form according to process pump design, service temperature, and revolutions per minute. The data are directed toward the refinery maintenance engineer who is faced daily with decisions regarding corrective/preventive maintenance of process pumps under his command.

Comprehensive investigations by Schwirzer (54) on existing plants of different design and at various rotational speeds showed that existing available criteria for the valuation of bearing and shaft vibrations are not universally applicable to water power engines. This holds for machines with vertical axis of rotation running at low speeds and for machines with special bearing designs. However, the existing experiences allowed the derivation of valuation criteria which are valid for all types of water power engines. These criteria hold only if the existing oscillatory forces and not the exciting vibrations are submitted to a valuation. The specific unbalance which is equivalent to the exciting forces can be taken as a measure. A valuation diagram based on this characteristic parameter is proposed for discussion. Furthermore, some special requirements are reviewed which vibration surveillance facilities for water power machines must satisfy.

Giberson (55) discusses the advantages of using film-damper bearings to control rotor response. He notes that film-damper bearings can be used on practically any size machine; however, they require "tuning" to optimize the design of an entire rotor-bearing system.

The practical aspects of ship line shafting vibration are discussed by Toms and Martyn (56) in a recent paper. The longstanding problems of whirling due to first order (unbalance) and propeller blade order excitations are discussed. The source of the blade order harmonic components and the close correlation with alignments and the resulting bearing loadings are traced. Problems associated with frequency calculations are outlined and a computer program is described.

CONCLUSIONS

The abundance of technical literature (over 50 significant papers, reports, etc. published in the past 3 years) on vibration in rotating machinery indicates the continuing concern for performance structural integrity, safety and life aspects of rotating machinery. Despite this continuous activity much important work remains. The physical phenomena that govern rotor behavior are, in general, well understood; however, characterization of damping phenomena still lags the other technology. In fact, this is due to the requirement that damping force descriptions be harmonic and/or periodic because of existing analytical techniques. The advent of more general computational tools capable of handling nonlinearties and time varying descriptions will lead to more activity involving damping force characterization.

REFERENCES

1. Ehrich, F.F., "Identification and Avoidance of Instability and Self-Excited Vibrations in Rotating Machinery", ASME 72-DE-21 (1972).

2. Lund, J.W., "Stability and Damped Critical Speeds of a Flexible Rotor in Fluid-Film Bearings", To be published in Trans. ASME, J. Engr. for Indus.

3. De Choudhury, P., "Dynamic Stability of Flexible Rotor-Bearing Systems", Univ. Va., 258 pp (1971).

4. Gasch, R., "Running Stability of Rotating Shafts", Ing. Arch. 42 (1), 58-68 (1972).

5. Mingori, D.L., "Stability of Whirling Shafts with Internal and External Damping", Intl. J. Nonlinear Mech. 8(2), 155-159 (Apr. 1973).

6. Pedersen, P.T., "On Self-Excited Whirl of Rotors", Ing. Arch. 42 (4), 267-283 (1973).

7. Black, H.F.; Brown, R.D.; France, D.; and Jenssen, D.N., "Theoretical and Experimental Investigations Relating to Centrifugal Pump Rotor Vibrations", Conf. on "Vibrations in Rotating Systems", Inst. Mech. Engr., pp 198-212, (Feb. 14-15, 1972).

8. Black, H.F., "Calculation of Forced Whirling and Stability of Centrifugal Pump Rotor Systems", To be published in Trans. ASME, J. Engr. for Indus.

9. Black, H.F. and Jenssen, D.N., "Effects of High-Pressure Ring Seals on Pump Rotor Vibrations", ASME Paper No. 71-WA/FE-38 (1971).

10. Kramer, E., "Instabilities of Rotating Shafts", Conf. on "Vibrations in Rotating Systems", Inst. Mech. Engr. pp 230-246, (Feb. 14-15, 1972).

11. Bousso, D., "A Stability Criterion for Rotating Shafts", Israel J. Tech. 10(6), 409-423 (1972).

12. Vance, J. M., "Stability of High-Speed Rotors with Internal Friction", To be published in Trans. ASME, J. Engr. for Indus.

13. Ehrich, F. F., "An Aeroelastic Whirl Phenomenon in Turbomachinery Rotors", To be published in Trans. ASME, J. Engr. for Indus.

14. Iwatsubo, T.; Tomita, A.; and Kawai, R., "Vibrations of Asymmetric Rotors Supported by Asymmetric Bearings", Ing. Arch. 42 (5), 416-432 (1973).

15. Messal, E. E. and Bonthron, R. J., "Subharmonic Rotor Instability Due to Elastic Asymmetry", J. Engr. Indus., Trans. ASME 94 (1), 185-192 (Feb. 1972).

16. Arnold, R. C. and Haft, E. E., "Stability of an Unsymmetrical Rotating Cantilever Shaft Carrying an Unsymmetrical Rotor", J. Engr. Indus., Trans. ASME 94 (1), 243-249 (Feb. 1972).

17. Yamamoto, T.; Ota, H.; and Kono, K., "On the Vibrations of a Rotor with Rotating Inequality and with Variable Rotating Speed", Mem. Fac. Engr., Nagoya Univ. 24 (1), 1-80 (May 1972).

18. Begg, I. C. "Friction Induced Rotor Whirl -- A Study in Stability", To be published in Trans. ASME J. Engr. for Indus.

19. Eshleman, R. L., "Flexible Rotor-Bearing System Dynamics -- Part I: Critical Speeds and Response of Flexible Rotor Systems", ASME Publication No. H42, New York, N.Y. (1972).

20. Dopkin, J. A., "The Effect of Disk Flexibility on Rotor Dynamics", Rutgers Univ., State Univ. N.J., PhD Thesis, 160 pp (1972).

21. Dubigeon, S., "The Movement of Long Vertical Shafts", J. Sound Vib. 26 (3), 337-352 (Feb. 1973).

22. Newland, D. E., "Whirling of a Cantilever Elastic Shaft Subjected to External Pressure", J. Mech. Engr. Sci. 14 (1), 11-18 (Feb. 1972).

23. Porat, I. and Niv, M., "Vibration of a Rotating Shaft by the Timoshenko Beam Theory", Israel J. 9 (5), 535-546 (1971).

24. Lowell, C. M., "Lateral Vibrations in Reciprocating Machinery", ASME Paper No. 58-A-79 (1958).

25. Lowell, C. M., "Whirl in Reciprocating Engine Flywheel-Crankshaft Systems", ASME Paper No. 67-VIBR-59 (1967).

26. Eshleman, R. L. and Eubanks, R. A., "On the Critical Speeds of a Continuous Shaft-Disk System", Trans. ASME 89 (4), p 645 (1967).

27. Palmer, N. S. and McCallion, H., "Natural Frequencies and Mode Shapes of Systems of Generally Interconnected Shafts", Instn. Mech. Engr. Proc. 187 (8/73), 63-70 (1973).

28. Ramamurti, V., "Application of Simultaneous Iteration Method to Torsional Vibration Problems", J. Sound Vib. 29 (3), 331-340 (Aug. 8, 1973).

29. Shaikh, N., "A Direct Method for Analysis of Branched Torsional Systems", To be published in Trans. ASME, J. Engr. for Indus.

30. McLean, R. F., "The Analysis of Critical Speeds Using the Modified Transfer Matrix and Dynamic Stiffness Techniques", Conf. on "Vibrations in Rotating Systems", Inst. Mech. Engr. pp 72-85 (Feb. 14-15, 1972).

31. Parszewski, Z., "Critical Speeds of Shaft Bearing Foundation Systems", Conf. on "Vibrations in Rotating Systems", pp 247-271 (Feb. 14-15, 1972).

32. Gilbert, A. C., "A Note on the Calculation of Torsional Natural Frequencies of Branch Systems", J. Engr. for Indus., Trans. ASME 94(1), 279-283 (Feb. 1972).

33. Lemke, D. G. and Trumpler, P. R., "On the Dynamic Response of Axially Coupled Turborotors", J. Engr. Indus., Trans. ASME 94 (2), 507-516 (May 1972).

34. Doyle, R. E., "A Generalized Matrix Solution for Elliptic Whirl of Elastic Rotors", Univ. Wisc., 130 pp (1971).

35. Gladwell, G. M. L. and Bishop, R. E. D., "The Vibration of Rotating Shafts Supported in Flexible Bearings", J. Mech. Engr. Sci. 1(195) (1959).

36. Lee, T. H., "A Dynamic Analysis for Elastic Structures Interacting with Rotary Machines", AIAA/ASME/SAE 13th Structure, Structural Dynamics and Materials Conf., San Antonio, Tex. (Apr. 10-12, 1972) AIAA Paper 72-375, 8 pp.

37. Lund, J.W., "Modal Response of a Flexible Rotor in Fluid-Film Bearings", To be published in Trans. ASME, Engr. for Indus.

38. Eshleman, R.L., "Torsional Response of Internal Combustion Engines", To be published in Trans. ASME, J. Engr. for Indus.

39. Prodonoff, V., "The Effect of Tension on the Dynamic Behavior of Eccentric Shafts Rotating in Fluid Medium", Houston Univ., Tex., Rept. No. 72-27514 134 pp (1972).

40. Ruhl, R.H. and Booker, J.F., "Finite Element Model for Distributed Parameter Turborotor Systems", J. Engr. for Indus., Trans. ASME 94(1), 126-132 (Feb. 1972).

41. Shen, F.A. and Mogil, E., "Flexible Rotordynamic Analysis", NASA Lewis Res. Ctr., NASA CR72740 (1970).

42. Kirk, R.G. and Gunter, E.J., "The Effect of Support Flexibility and Damping on the Synchronous Response of a Single-Mass Flexible Rotor", J. Engr. Indus., Trans. ASME 94(1), 221-232 (Feb. 1972).

43. Kirk, R.G., "Nonlinear Transient Analysis of Multimass Flexible Rotors", Univ. Va., Charlottesville, Va., PhD Thesis, 539 pp (1972).

44. Kirk, R.G. and Gunter, E.J., "Transient Response of Rotor-Bearing Systems", To be published in Trans. ASME, J. Engr. for Indus.

45. Breed, D.S. and Castelli, Va., "Time Transient Approach to the Solution of Shaft Dynamics Problems", Columbia Univ., New York, N.Y., PhD Thesis, 340 pp (June 1972).

46. Childs, D.W., "A Rotor-Fixed Modal Simulation Model for Flexible Rotating Equipment", To be published in Trans. ASME, J. Engr. for Indus.

47. Shapiro, W. and Rumbarger, J.H., "Flexible Rotor-Bearing System Dynamics -- Part II: Bearing Influence and Representation in Rotor Dynamics Analysis", ASME Document No. H46 (1972).

48. Holmes, R., "The Effect of Sleeve Bearings on the Vibration of Rotating Shafts", Conf. on "Vibrations in Rotating Systems", Inst. Mech. Engr., pp 185-197 (Feb. 14-15, 1972).

49. Nakagawa, E. and Aoki, H., "Unbalance Vibration of a Rotor Bearing System Supported by Floating-Ring Journal Bearings", Bull. JSME 16(93), 503-512 (Mar. 1973).

50. Yanabe, S. and Tamura, A., "Vibration of a Shaft Passing Through a Critical Speed -- 1st Report: Experiments and Numerical Solutions", Bull. Japan Soc. Mech. Engr. 14(76), 1050-1058 (Oct. 1971).

51. Iwatsubo, T.; Kanki, H.; and Kawai, R., "Vibration of Asymmetric Rotor Through Critical Speed with Limited Power Supply", J. Mech. Engr. Sci. 14(3), 184-194 (June 1972).

52. Schweitzer, G.; Schiehlen, W.; Müller, P.C.; Hubner, W.; Luckel, J.; Sandweg, G.; and Lautenschlager, R., "Gyroscopic Response of Elastically Mounted Rotors", Ing. Arch. 41(2), 110-140 (1972).

53. Hancock, W.P., "Practical Considerations on the Control of Vibration Levels of Refinery Process Pumps", To be published in Trans. ASME, J. Engr. for Indus.

54. Schwirzer, T., "Valuation and Surveillance of the Vibrational State of Large Water Power Machines, Parts I and II", VDI-Z 114(1), 28-32 (Jan. 1972); 114(2), 137-140 (Feb. 1972).

55. Giberson, M.F., "Taming Rotor Whirl with Film-Damper Bearings", Mach. Des. 45(7), 176-181 (Mar. 1973).

56. Toms, A.E. and Martyn, D.K., "Whirling of Line Shafting", Inst. Marine Engr., Trans. 84(6), 176-191 (1972).

Noise, Shock & Vibration Conference, 1974 Monash University, Melbourne

ON THE INTERACTION BETWEEN SELF-EXCITED AND FORCED VIBRATIONS IN ONE-MASS SYSTEMS

A. Tondl
Prague, Czechoslovakia

SUMMARY

The paper presents an analysis of a one-mass system with two degrees of freedom described by a single vector differential equation of the second order; the system can perform self-excited vibration and is excited by the whirling vector of the excitation force. The solution to the problem is obtained analytically as well as by analogue computer modelling. In the analytical solution the steady vibration is approximated by a component of forced vibration and by a component of self-excited vibration. As the analysis shows, the interaction between the two components can be substantial; in resonance the component of self-excited vibration is even apt to be completely suppressed.

1. INTRODUCTION

In a number of systems which can perform self-excited vibration due consideration must be given to the action of external excitation forces. Little attention has so far been accorded to this problem; a systematic analysis of a class of such systems with one degree of freedom was first undertaken by C. HAYASHI [1] who examined the Van der Pol oscillator taking into account external harmonic excitation. He treated the resonant cases when the excitation frequency is close to the natural frequency of the linearized undamped system or to an integral multiple or sub-multiple thereof. He assumed that the frequency of self-excited vibration was equal to the excitation frequency or to that sub-multiple or multiple. In the present paper we have adopted another approach: the steady solution is approximated by both a component of forced vibration and a component of self-excited vibration, and the frequencies of these components are required to meet no assumptions imposed in advance.

The subject of our analysis is a system whose motion can be described by a single vector differential equation of the second order where the deflection vector has two components. Such an equation expresses, for example, the motion of a highly simplified rotor system idealised as a mass in a plane.

The most frequent cause of self-excited vibration of rotors is the presence of viscous forces in the bearings and glands, or of forces produced by flow through the slot around a disk or rotor body (the so-called slot effect), or of forces of internal damping arising either through material hysteresis as the shaft distorts or through dry friction on contact surfaces in consequence of unequal deformations of the various parts of the rotor such as between the shaft and the disk hub. All those forces can be included in one class because in the simplified linearized description they can be represented identically. Denote by z the vector of the disk deflection in the plane at right angles to the rotor axis, so that $z = x + iy$ where x, y are the Cartesian coordinates or the angular deflections about two mutually perpendicular axes. We may then write the linearized expression of those forces in the form

$$P = -K(\alpha\dot{z} - i\omega z) \qquad (1)$$

where K is a constant of proportionality and ω is the angular velocity of rotation of the rotor (for other expressions see [2]). The form of the first term is identical to that of linear viscous damping (so that to this term we can also add the external viscous damping proper). The second term has a destabilizing effect, and is a component proportional to the magnitude of the deflection vector but having a direction normal to the deflection vector in the sense of rotor rotation (as though the vector z were turned 90° in the sense of rotor rotation). If the elastic restoring force is of a central type, that is it acts in the direction opposite to that of the deflection vector z, then the force component $iK\omega z$ is a tangential component with respect to the elastic restoring force.

Let us now write the equation of motion of our system taking into consideration also the gyroscopic effect, any external linear damping which, as already mentioned, can be included in the component $K\alpha\dot{z}$, the nonlinearity of elastic restoring force and rotor unbalance. Following rearrangement and time transformation we obtain the equation of motion

$$\ddot{z} - ig\eta\dot{z} + \kappa\dot{z} - i\beta\eta z + (1 + \mu z\bar{z})z = \eta^2 exp(i\eta t) \tag{2}$$

where for simplicity dots are again used for denoting the derivatives. Here g, κ, β, μ, are dimensionless coefficients of which: $g > 0$ is the coefficient of the gyroscopic term, $\kappa > 0$ includes both external viscous damping and the term $K\alpha\dot{z}$, β is the coefficient of the tangential component (although $\beta > 0$ for the above-mentioned cases, we shall consider for the sake of completeness also $\beta < 0$), and μ is the coefficient of the nonlinear term of the restoring force Further, z is the dimensionless deflection vector referred to the eccentricity of the centroid from the rotor axis, and η is the reduced velocity of rotor rotation

$$\eta = \frac{\omega}{\omega_0} \text{ where } \omega_0{}^2 = \frac{c}{m} \ ;$$

c is the stiffness of the linearized restoring force (or moment) and m is the rotor mass (or the rotor equatorial moment); $\bar{z} = x - iy$. We shall call the system described by the differential equation (2), System I.

In gyroscopic systems we sometimes come across forces which - as in the preceding case - act like a tangential component to the elastic central force. This tangential component is not, however, proportional to the velocity of rotor rotation. In gyroscopic theory such forces are termed circulatory (or follower) forces. Following manipulations analogous to those of the former case, we then get the equation of motion

$$\ddot{z} - ig\eta\dot{z} + \kappa\dot{z} - i\beta z + (1 + \mu z\bar{z})z = \eta^2\exp(i\eta t) \ . \tag{3}$$

We shall call this system, System II. In what follows we shall first carry out an analytical solution and then present the results of analogue computer modelling. The latter were obtained by Mrs. M. Stuchlikova using a MEDA 41T analogue computer. Her assistance in this matter is gratefully acknowledged.

2. ANALYTICAL SOLUTION OF SYSTEM I

We shall now seek the steady state solution of equation (2). To aid this we note that on displacing the origin of time by ϕ/η (where ϕ is the phase angle between the deflection vector and the excitation force vector) we get on the right-hand side of equation (2) the expression $\eta^2\exp[i(\eta t + \phi)]$. We shall now approximate the solution of equation (2) by the form

$$z = r\ exp(i\eta t) + R\ exp(i\Omega t) \tag{4}$$

where r is the amplitude of the component of forced vibration, R is the amplitude of the component of self-excited vibration, and Ω is the reduced frequency of the component of self-excited vibration. On substituting (4) into equation (2) (with the right-hand side rearranged as shown above), and upon comparing the coefficients of terms $exp(i\eta t)$ and $exp(i\Omega t)$ we get the following equations for the determination of r, R, ϕ, Ω:

$$r[1 - \eta^2(1 - g) + \mu(r^2 + 2R^2) - i\eta(\beta - \kappa)] = \eta^2 exp(i\phi) \ ,$$

$$R[1 - \Omega^2 + g\eta\Omega + \mu(2r^2 + R^2) - i(\beta\eta - \kappa\Omega)] = 0 \ .$$

The separation of the real parts from the imaginary ones gives

$$r[1 - \eta^2(1 - g) + \mu(r^2 + 2R^2)] = \eta^2\cos\phi \ , \tag{5}$$

$$r\eta(\kappa - \beta) = \eta^2\sin\phi \ , \tag{6}$$

$$R[1 - \Omega^2 + g\eta\Omega + \mu(2r^2 + R^2)] = 0 \ , \tag{7}$$

$$R(\kappa\Omega - \beta\eta) = 0 \ . \tag{8}$$

As the above equations imply, there may exist a non-trivial solution ($r \neq 0$, $R \neq 0$) as well as a semi-trivial solution ($r \neq 0$, $R = 0$). (In the absence of excitation, when the right-hand sides of the first two equations are zero, there will exist the solution $R \neq 0$, $r = 0$). We shall now establish under what circumstances the various solutions have a meaning. First turn to the simpler semi-trivial solution. For $R = 0$ equations (5) and (6) take on the form

$$r[1 + \mu r^2 - \eta^2(1 - g)] = \eta^2\cos\phi \ , \tag{5a}$$

$$r\eta(\kappa - \beta) = \eta^2\sin\phi \ . \tag{6a}$$

On setting in equation (5a) $\phi = \frac{\pi}{2}$ (which is identical with the case of a perfectly balanced rotor) we get the equation of the *skeleton curve* (refer to [3] for details of this and of the so-called *limit envelope*)

$$r_{so} = \{\frac{1}{\mu}[\eta^2(1 - g) - 1]\}^{\frac{1}{2}} \ . \tag{9}$$

Subscript s denotes the skeleton curve, subscript o the semi-trivial solution.

On setting in equation (6a) $\sin\phi = 1$ (theoretically also $\sin\phi = -1$) we get the equation of the limit envelope

$$r_L = (\kappa - \beta)^{-1}\eta \ . \tag{10}$$

Since it always holds for the cases stated in the Introduction that $\kappa - \beta \geq 0$, it will also always hold that $\sin\phi \geq 0$, that is the phase angle ϕ lies in the interval $(0 - \pi)$. The equation of the limit envelope is the equation of a straight line passing through the origin. The curve $r_o(\eta)$ is always found on one side of the limit envelope which it touches at a point that is simultaneously the point of intersection of the skeleton curve and of the limit envelope. The solution corresponding to that point is that in which $\phi = \frac{\pi}{2}$. In our case the limit envelope is directly a tangent to the curve $r_o(\eta)$. The latter is determined from the equation which results from squaring and adding euqations (5a) and (6a), namely,

$$r\{[1 + \mu r^2 - \eta^2(1 - g)]^2 + \eta^2(\kappa - \beta)^2\} = \eta^4 \ .$$

After some rearrangement the above yields a biquadratic equation in η which is

$$\eta^4[(1 - g)^2 - \frac{1}{r^2}] - 2\eta^2[(1 - g)(1 + \mu r^2) - \frac{1}{2}(\kappa - \beta)^2] + (1 + \mu r^2)^2 = 0 \ . \tag{11}$$

For prescribed r we establish the corresponding η, and thus also obtain the inverse function $r_o(\eta)$. (Subscript o refers to the semi-trivial solution). So long as there applies the inequality

$$1 - \eta^2(1 - g) + \mu r^2 >> \eta(\kappa - \beta) \ ,$$

that is, so long as the points involved do not lie in the vicinity of the resonant peak, we can determine the function $r(\eta)$ from the approximate relation

$$\eta = (1 + \mu r^2)^{\frac{1}{2}}(1 - g \pm \frac{1}{r})^{-\frac{1}{2}} \ . \tag{12}$$

On dividing equation (6a) by (5a) we get the relation for establishing the phase angle :

$$\tan\phi = \eta(\kappa - \beta)[1 + \mu r^2 - \eta^2(1 - g)]^{-1}. \tag{13}$$

Let us now tackle the determination of the non-trivial solution. As equation (8) implies, it is

$$\Omega = \frac{\beta}{\kappa}\eta \ . \tag{14}$$

Since $\kappa > 0$, it is always the case that $\Omega > 0$ for $\beta > 0$. And as we have already pointed out, the systems of interest have $\beta > 0$. But in the interest of completeness and because of the peculiarity of the solution we shall also consider the case $\beta < 0$. If $\Omega > 0$, precession of the vector of the component of self-excited vibration is of the same sense as rotor rotation; for $\Omega < 0$, it is of opposite sense. We shall first assume that $\beta > 0$ and then give separately a comprehensive review of the case $\beta < 0$.

The substitution for Ω from equation (14) into (7) enables us to express

$$R^2 = \frac{1}{\mu}\left[\frac{\beta}{\kappa}(\frac{\beta}{\kappa} - g)\eta^2 - 1\right] - 2r^2 \ . \tag{15}$$

Only a positive value of R has a meaning. For η for which R becomes negative, only the semi trivial solution has a meaning. The boundary can be determined by setting $R = 0$ which step gives the dependence

$$^*r = \left(\frac{1}{2\mu}\{\frac{\beta}{\kappa}(\frac{\beta}{\kappa} - g)\eta^2 - 1\}\right)^{\frac{1}{2}} \ . \tag{16}$$

The points of intersection of curves $r(\eta)$ and $*r(\eta)$ mark out the limit of validity of the non-trivial solution - see Fig. 1 in which the portion of $r(\eta)$ corresponding to $R^2 < 0$ is shown as a dotted line.

The substitution for R^2 from equation (15) into (5) gives the following equations for the determination of r and ϕ :

$$r\left[\eta^2\{\frac{\beta^2}{\kappa^2} - 1 - g(2\frac{\beta}{\kappa} - 1)\} - 1 - 3\mu r^2\right] = \eta^2\cos\phi \ , \tag{17}$$

$$r\eta(\kappa - \beta) = \eta^2\sin\phi \ .$$

The second of these equations is identical with equation (6a). It follows from this fact that the resonance curves $r(\eta)$ and $r_o(\eta)$ have a common limit envelope (see Fig. 2), a straight line passing through the origin with slope $(\kappa - \beta)^{-1}$. The points of intersection of curves $r_o(\eta)$ and $r(\eta)$ must simultaneously be the points of intersection of curves $r(\eta)$ and $*r(\eta)$. We shall not examine the stability of the solution. We shall assume that the rule of vertical tangents applies - the contact points form a division between the portions of curves $r(\eta)$ and $r_o(\eta)$ to which correspond stable and unstable solutions. The analogue solution will show whether or not this assumption is correct.

Upon eliminating ϕ from equation (17) we get

$$r^2\left[\{\eta^2[2\frac{\beta^2}{\kappa^2} - 1 - g(2\frac{\beta}{\kappa} - 1)] - 1 - 3\mu r^2\}^2 + \eta^2(\kappa - \beta)^2\right] = \eta^4$$

and after rearrangement, the equation

$$\eta^4[(2\frac{\beta^2}{\kappa^2} - 1 - 2g\frac{\beta}{\kappa} + g) - \frac{1}{r^2}] - 2\eta^2[(2\frac{\beta^2}{\kappa^2} - 1 - 2g\frac{\beta}{\kappa} + g)(1 + 3\mu r^2) - \frac{1}{2}(\kappa - \beta)^2] + (1 + 3\mu r^2)^2 = 0 \ . \tag{18}$$

This equation makes it possible to find η for a given r and thus also to establish the dependence $r(\eta)$. Similarly, as in the semi-trivial solution, the portion of curve $r(\eta)$ not in the close vicinity of the resonant peak can be obtained from the approximate formula

$$\eta = (1 + 3\mu r^2)^{\frac{1}{2}}\left(2\frac{\beta^2}{\kappa^2} - 1 - 2g\frac{\beta}{\kappa} + g \pm \frac{1}{r}\right)^{-\frac{1}{2}} \ . \tag{19}$$

The angle of phase displacement is determined from the relation

$$\tan\phi = \eta(\kappa - \beta)\left[\eta^2(2\frac{\beta^2}{\kappa^2} - 1 - 2g\frac{\beta}{\kappa} + g) - 1 - 3\mu r^2\right]^{-1} \ . \tag{20}$$

To complete our discussion we may also write the equation of the skeleton curve of the non-trivial solution, namely

$$r_s = \left[\frac{1}{3\mu}\{(2\frac{\beta^2}{\kappa^2} - 1 - 2g\frac{\beta}{\kappa} + g)\eta^2 - 1\}\right]^{\frac{1}{2}} \ . \tag{21}$$

As a comparison shows, the relations defining $r_{so}(\eta)$, $r_s(\eta)$ and $*r(\eta)$ - equations (9), (21) and (16) - are analogous to one another. For $\frac{\beta}{\kappa} = 1$ all three curves start from the same point on the axis η ; for $\frac{\beta}{\kappa} < 1$ and $\frac{\beta}{\kappa} + 1 > g$ (the most usual case)

$$\eta_{so} < *\eta < \eta_s \ ; \tag{22}$$

and for $\frac{\beta}{\kappa} > 1$ and $\frac{\beta}{\kappa} + 1 > g$

$$\eta_{so} > *\eta > \eta_s \ , \tag{23}$$

where η_{so} , $*\eta$, η_s are the respective abscissae on the axis η from which the curves $r_{so}(\eta)$, $*r(\eta)$ and $r_s(\eta)$ start. These curves, however, differ in curvature. If inequality (22) applies it is always the curve $r_s(\eta)$ that is most deflected, and the curve $r_{so}(\eta)$ that is least deflected - see the schematic representation in Figs. 3a $(\frac{\beta}{\kappa} < 1)$ and 3b $(\frac{\beta}{\kappa} > 1)$ for $\mu > 0$. The three curves, the limit envelope and the approximate relations defining $r_o(\eta)$ and $r(\eta)$ provide prompt and comparatively accurate information on the system behaviour.

For the purposes of comparison we shall also carry out the solution for perfect balancing, when the right-hand side of equation (2) is zero. In this case, the equation of motion is satisfied by the particular solution

$$z = R\ \mathit{exp}(i\Omega t) \ . \tag{24}$$

The substitution of solution (24) into the homogeneous equation (2) yields the following equations for the determination of R and Ω :

$$R(1 - \Omega^2 + g\eta\Omega + \mu R^2) = 0 \ , \qquad (25)$$
$$R(\kappa\Omega - \beta\eta) = 0 \ .$$

As the second of the above equations implies, so long as $R \neq 0$,

$$\Omega = \frac{\beta}{\kappa}\eta \ .$$

On substituting into the first of equations (25) we get the following relation for the determination of the amplitude of the non-trivial solution:

$$R = \left[\frac{1}{\mu}\left\{\frac{\beta}{\kappa}\left(\frac{\beta}{\kappa} - g\right)\eta^2 - 1\right\}\right]^{\frac{1}{2}} \ . \qquad (26)$$

This expression differs from that of $^*r$ - see equation (16) - only in that it contains μ in place of 2μ . The curve of $R(\eta)$ therefore starts from the same point on the axis η but the amplitude of $R(\eta)$ is greater by a factor of $\sqrt{2}$ than that of $^*r(\eta)$. Applying the procedure outlined in monograph [4] and also used in [2] and [5], we can readily ascertain whether or not solution (24) is stable.

We know that the term with coefficient κ represents positive damping. The substitution for Ω from the second into the first of equations (25), and some manipulations, give

$$\kappa^2 + g\kappa\beta\eta^2 + \kappa^2\mu R^2 = \beta^2\eta^2 \ .$$

The left-hand side of the above equation represents the component of positive damping, the right-hand one that of negative damping. The two components are equilibrated for an $^*R$ satisfying the above equation. $^*R$ will continue to be stable so long as the following inequalities hold good for $\varepsilon > 0$:

$$\kappa^2 + g\kappa\beta\eta^2 + \kappa\mu(^*R + \varepsilon)^2 > \beta^2\eta^2 \ ,$$
$$\kappa^2 + g\kappa\beta\eta^2 + \kappa\mu(^*R - \varepsilon)^2 < \beta^2\eta^2 \ .$$

As to the trivial solution $R = 0$, so long as

$$\kappa^2 + g\kappa\beta\eta^2 > \beta^2\eta^2$$

it is stable; for the opposite inequality, it becomes unstable. It can readily be shown that the trivial solution is stable within the interval

$$0 < \eta < \left[\frac{\beta}{\kappa}\left(\frac{\beta}{\kappa} - g\right)\right]^{-\frac{1}{2}}$$

where the upper bound is given by that value of η which is the abscissa of the starting point of curve $R(\eta)$ on the axis η - see equations (26). It is equally easy to see that the non-trivial solution $R(\eta)$ is stable for $\mu > 0$ and unstable for $\mu < 0$. Both cases are illustrated in Figs. 4a ($\mu > 0$) and 4b ($\mu < 0$), with the dependence $R(\eta)$ drawn in dashed lines. This is what the last findings mean for a perfectly balanced rotor: so long as the reduced frequency of rotation η stays below the value

$$\left[\frac{\beta}{\kappa}\left(\frac{\beta}{\kappa} - g\right)\right]^{-\frac{1}{2}} ,$$

the centroid is at rest; once that value is exceeded, self-excited vibration with a finite amplitude arises for $\mu > 0$ while the deflection continually grows for $\mu < 0$. For $\mu > 0$ and

$$\eta < \left[\frac{\beta}{\kappa}\left(\frac{\beta}{\kappa} - g\right)\right]^{-\frac{1}{2}} ,$$

the position at rest is absolutely stable, that is to say, the transient vibration will tend to the position at rest for any disturbance. For $\mu < 0$ and

$$\eta < \left[\frac{\beta}{\kappa}\left(\frac{\beta}{\kappa} - g\right)\right]^{-\frac{1}{2}} ,$$

the situation will, however, depend on the disturbance or, possibly, on the initial conditions. For some initial conditions the transient vibrations will converge to the equilibrium position, for others divergent vibrations occur. There exist two regions of initial conditions - the *domains of attraction*; the initial conditions inside one of them lead to a state of rest whereas inside the other, they induce divergent vibrations. In view of the fact that the system is defined by four initial conditions, the separatrix that divides the two domains of attraction is a surface in four-dimensional space. We shall not tackle here the problem of determining the separatrix surface; the solution to it may be obtained by the method described in monograph [4], and for self-excited systems by the procedure outlined in monograph [5]. As discussed in detail in [2], the value of R corresponding to the unstable solution may be used for estimating the limiting magnitudes of disturbances which must not be exceeded in order to prevent divergent vibrations from taking place. This follows from the fact that to the unstable steady solution with amplitude R corresponds the unstable limit cycle which lies on the separatrix surface. Accordingly, the smaller is the value of R the smaller are the limiting disturbances which must not be exceeded in order to preclude divergent vibrations. This analysis enables us to make at least an estimate as to the stability in the case of the non-trivial solution of an excited system.

Let us now take up an illustrative example. Fig. 5 shows the dependences $r_o(\eta)$, $r(\eta)$, $*r(\eta)$ and $R(\eta)$ for the following values of the coefficients:

$$g = 0.3 \ ; \quad \kappa = 0.1 \ ; \quad \beta = 0.08 \ ; \quad \mu = 0.002 \ .$$

So long as no self-excited vibration is initiated, the course of the vibration is harmonic; after it is initiated, the course becomes generally aperiodic. The result obtained for a slow continuous increase of the excitation frequency (rotor speed) differs from that for a slow continuous decrease. In the stated range of $0 < \eta < 2$, self-excited vibration will not arise at all for an increasing η. As to η decreasing from the initial value of $\eta = 2$, since there exist two steady locally stable solutions for this value of η, the situation depends on the initial conditions. For initial conditions (for example, zero) for which there occurs the non-trivial steady solution, the amplitude of the component of forced vibration follows the curve of $r(\eta)$ with η decreasing to $\eta = 1.62$; thereafter it follows the curve of $r_o(\eta)$ - namely, its non-resonant branch with η decreasing to 1.405 at which value it passes over to the resonant branch.

Because the system is symmetric, the extreme values of z, x, y are the same. When plotting, for example, the local maxima of x (denoted by $[x]$) we see that for the non-trivial solution this value ranges between the limits $r \pm R$ (for $R < r$) and $R \pm r$ (for $R > r$). Diagrams of $[x]$ as a function of η according to the analytical results are presented later - for the purposes of comparison - together with the results of the analogue solution.

Let us now analyze the alternative $\beta < 0$. So far as the formal expression is concerned, most of the results continue to apply because the assumption that $\beta > 0$ was taken only in the derivation of inequalities (22) and (23). But we shall have to modify some of our conclusions. Although the expressions for $r_o(\eta)$, $r(\eta)$, $R(\eta)$, $r_{so}(\eta)$, $r_s(\eta)$ and $*r(\eta)$ are wholly identical we must bear in mind that, for example, for the same absolute values of κ, β of the two alternatives, the values of $\kappa - \beta$ are additive for $\beta < 0$ and the limit envelope is a straight line with a tangent smaller than in the case $\beta > 0$. It is always inequality (23) that holds for $\beta < 0$ and

$$-\frac{\beta}{\kappa} > 1 \ ;$$

for

$$g > 1 + \frac{\beta}{\kappa}$$

inequality (23) applies even for arbitrarily small ratios $-\beta/\kappa$.

To illustrate, we have drawn in Fig. 6 the dependences $r_o(\eta)$, $r(\eta)$, $*r(\eta)$, and $R(\eta)$ for the following coefficients:

$$g = 0.3 \ ; \quad \mu = 0.001 \ ; \quad \kappa = 0.039 \ ; \quad \beta = -0.031 \ .$$

3. RESULTS OF THE ANALOGUE SOLUTION FOR SYSTEM I

The various alternatives modelled on the analogue computer were solved for the following values of the coefficients:

Alternative	g	μ	κ	β
Ia	0.3	0.002	0.1	0.08
Ib	0.3	0.002	0.1	0.09
Ic	0.3	0.002	0.1	0.1
Id	0.3	0.001	0.039	-0.031
Ie	0.3	0.001	0.039	-0.0312
If	0.3	0.001	0.039	-0.0315

The first three alternatives differ only in the value of β, which is positive. The next three alternatives also differ in the value of β which, however, is negative. Alternatives

Ia and Id were solved analytically (see Figs. 5 and 6).

The equations of motion in x, y coordinates were naturally used for the analogue solution and they are as follows:

$$\begin{aligned} \ddot{x} + g\eta\dot{y} + \kappa\dot{x} + \beta\eta y + [1 + \mu(x^2 + y^2)]x &= \eta^2\cos\eta t \,, \\ \ddot{y} - g\eta\dot{x} + \kappa\dot{y} - \beta\eta x + [1 + \mu(x^2 + y^2)]y &= \eta^2\sin\eta t \,. \end{aligned} \tag{27}$$

The solution was carried out in the interval $0 < \eta < 2$ by slowly varying the frequency η in both directions (possibly with dwells in the transitions from one steady solution to another). The values of [x] and [y], that is, the local maximum values of coordinates x, y were recorded by an automatic plotter. Since it was fully confirmed that [x] = [y] = [z], we shall show only the results established for [x]. Whenever there existed a component of self-excited vibration in addition to the component of forced vibration, the stylus - instead of tracing a smooth curve - drew parallel lines (hatching) over an area whose width represented the double amplitude of the component of either forced or self-excited vibration, depending on whether $R \gtrless r$.

The solution obtained for alternative Ia is shown in Fig. 7a; the curve drawn there in heavy dashed lines pertains to the case without excitation (perfectly balanced rotor) when only the self-excited vibration exists. Fig. 7b represents a corresponding diagram plotted on the basis of the approximate analytical solution. Comparing the two figures we see that their qualitative agreement is very good and that the quantitative differences are only of minor importance. The only major deviations can be noted in the transition from the resonant vibration to the vibration with a self-excited vibration component which - for an increasing η - occurs earlier in the analogue solution. Raising the coefficient β (Figs. 8 and 9) produces a transition from the resonant vibration with zero value of the amplitude of the self-excited vibration component to vibration in which there exists a self-excited vibration component with a large amplitude. The solution is unique for any $0 < \eta < 2$.

Although for $\beta < 0$ the three alternatives examined differ only slightly in coefficient β , the results obtained for them are at considerable variance. The analogue solution of alternative Id is shown in Fig. 10a and the corresponding diagram drawn on the basis of the analytical treatment, is in Fig. 10b. Fig. 11 represents the records of vibration developed along the axis x (vibration in axis y is the same, but displaced in phase by $\frac{\pi}{2\eta}$) for various values of η ; the upper record belongs to an increasing, the lower to a decreasing η . The corresponding records of whirling motion in the x, y plane are shown in Fig. 12. It is seen that in the presence of self-excited vibration whose amplitude is larger than that of forced vibration, the sense of whirling is opposite to that of rotor rotation. The results of the solution of alternatives Ie and If, shown in Figs. 13 and 14, agree very well with the analytical solution (Fig. 10b). Resonance with backward precession of small amplitude is observable in all alternatives having a negative β in the neighbourhood of $\eta = 0.85$. This resonance is absent in the case of positive β .

4. ANALYTICAL SOLUTION FOR SYSTEM II

We shall again introduce a ϕ/η - displacement of the time origin - and approximate the solution to equation (3) by the form (4). Using the procedure outlined in Section 2 we get the following algebraic equations for the determination of r, R, ϕ, Ω :

$$r[1 + \mu(r^2 + 2R^2) - \eta^2(1 - g)] = \eta^2\cos\phi \,, \tag{28}$$

$$r(\kappa\eta - \beta) = \eta^2\sin\phi \,, \tag{29}$$

$$R[1 - \Omega^2 + g\eta\Omega + \mu(2r^2 + R^2)] = 0, \tag{30}$$

$$R(\kappa\Omega - \beta) = 0 \,. \tag{31}$$

As for System I, there can exist here both the semi-trivial and the non-trivial solution. Let us first turn to the semi-trivial solution ($R = 0$, $r \neq 0$). For $R = 0$ equations (28) and (29) lead to the same dependence describing the skeleton curve as for System I. For the same values of coefficients g, the skeleton curves of Systems I and II are identical for the semi-trivial solution, and the conclusions drawn for System I are equally applicable to System II. The limit envelope is different, however; it is determined from the equation

$$r_L = \eta^2(\kappa\eta - \beta)^{-1} \,. \tag{32}$$

Since only $r_L > 0$ has a meaning, it is enough - so long as $\beta > 0$ - to establish the course of this curve for $\eta > \frac{\beta}{\kappa}$ only. In the interval $\frac{\beta}{\kappa} < \eta < \infty$ the character of curve $r_L(\eta)$ is such that on the boundaries of the interval r_L grows beyond all limits. For large η , r_L grows practically linearly with growing η because the straight line $r = \frac{\eta}{\kappa}$ forms an asymptote. Thus, r_L reaches its minimum for $\eta = \frac{2\beta}{\kappa}$ when $r_{Lmin} = 4\frac{\beta}{\kappa^2}$.

Amplitude r is established from the equation

$$r^2\{[1 - \eta^2(1 - g) + \mu r^2]^2 + (\kappa\eta - \beta)^2\} = \eta^4 \tag{33}$$

which is not as simple as for System I, so that it becomes necessary to use a digital computer. For small values of κ, β and for points remote from the resonant peak we can use the approximate relation

$$\eta = (1 + \mu r^2)^{\frac{1}{2}}(1 - g \pm \frac{1}{r})^{-\frac{1}{2}}$$

which is identical to equation (12). From this fact follows the conclusion that for equal values of g, μ the course of curves $r_o(\eta)$ is roughly the same for Systems I and II except for the portion near the resonant peak. The phase angle is found from the equation

$$\tan\phi = (\kappa\eta - \beta)[1 + \mu r^2 - \eta^2(1 - g)]^{-1}. \tag{34}$$

Let us now determine the non-trivial solution and the limit of validity of this solution. As equation (31) implies, it is

$$\Omega = \frac{\beta}{\kappa}. \tag{35}$$

In this case the frequency of self-excited vibration is constant, independent of the excitation frequency, that is, of the rotor speed. For $\beta > 0$ the sense of precession of the component of self-excited vibration is the same as that of rotor rotation; for $\beta < 0$ it is opposite. On substituting for Ω into equation (30) we get

$$R = \{\frac{1}{\mu}[(\frac{\beta}{\kappa})^2 - g\eta\frac{\beta}{\kappa} - 1] - 2r^2\}^{\frac{1}{2}} \tag{36}$$

and on substituting the above into equation (28) we can find from equations (28) and (29) both r, ϕ and the skeleton curve and the limit envelope. Since equation (29) does not contain R, the limit envelope described by equation (32) applies to the semi-trivial as well as to the non-trivial solution. The equation for the determination of the skeleton curve is

$$r_s = \{\frac{1}{3\mu}[2(\frac{\beta}{\kappa})^2 - 1 - 2g\frac{\beta}{\kappa}\eta - \eta^2(1 - g)]\}^{\frac{1}{2}}. \tag{37}$$

As this equation suggests, the skeleton curve of the non-trivial solution is deflected in a direction opposite to that of the semi-trivial solution. The equations for establishing r, ϕ turn out to be

$$r^2\{[2(\frac{\beta}{\kappa})^2 - 1 - 2g\frac{\beta}{\kappa}\eta - \eta^2(1 - g) - 3\mu r^2]^2 + (\kappa\eta - \beta)^2\} = \eta^4, \tag{38}$$

$$\tan\phi = (\kappa\eta - \beta)[2(\frac{\beta}{\kappa})^2 - 1 - 2g\frac{\beta}{\kappa}\eta - \eta^2(1 - g) - 3\mu r^2]^{-1}. \tag{39}$$

The dependence $r(\eta)$ cannot be obtained as readily as in the preceding case; for specified values of the coefficients we must employ a digital computer. In the regions remote from the resonant peak and for small β, κ we can use the approximate relation

$$\eta^2(1 - g \pm \frac{1}{r}) + 2g\frac{\beta}{\kappa}\eta + 1 + 3\mu r^2 - 2(\frac{\beta}{\kappa})^2 = 0. \tag{40}$$

Similarly, as in Section 2, we can establish the dependence $*r(\eta)$ which delimits the validity of the non-trivial solution, using the formula

$$*r(\eta) = \{\frac{1}{2\mu}[(\frac{\beta}{\kappa})^2 - g\eta\frac{\beta}{\kappa} - 1]\}^{\frac{1}{2}}. \tag{41}$$

Whenever $\beta > 0$, the curve $*r(\eta)$ has a meaning only for $\beta > \kappa$. With increasing η the dependence $*r(\eta)$ decreases and takes on a zero value for

$$\eta = \frac{\kappa}{\beta g}[(\frac{\beta}{\kappa})^2 - 1].$$

For $\beta < 0$, $*r(\eta)$ is an increasing function of η and starts either from the point with abscissa

$$\eta = \frac{\kappa}{\beta g}[1 - (\frac{\beta}{\kappa})^2]$$

on the axis η (for $-\beta < \kappa$) or from the point with

$$*r(0) = \{\frac{1}{2\mu}[(\frac{\beta}{\kappa})^2 - 1]\}^{\frac{1}{2}}$$

on the axis $*r$ (for $-\beta > \kappa$).

The character of curve $*r(\eta)$ is analogous to that of curve $R(\eta)$ for zero excitation, that is, for a perfectly balanced rotor, when

$$R = \{\frac{1}{\mu}[(\frac{\beta}{\kappa})^2 - 1 - g\eta\frac{\beta}{\kappa}]\}^{\frac{1}{2}} . \quad (42)$$

The values of $*r(\eta)$ and $R(\eta)$ - in the case without excitation - depend on η only, because of the gyroscopic effect. For $g = 0$ they are constant, that is, independent of the frequency of rotor rotation.

We can also show, as for System I, the displacement of the starting points of curves $r_{so}(\eta)$, $r_s(\eta)$ and $*r(\eta)$ from the axis η. Inequality (22) always holds for $\beta < 0$ while for $\beta > 0$ it holds so long as

$$[2(\frac{\beta}{\kappa})^2 + 2\frac{\beta}{\kappa} - 1]g < 2[(\frac{\beta}{\kappa})^2 - 1] ,$$

that is, for smaller values of g.

To illustrate we have drawn in Fig. 15 the curves $r_o(\eta)$, $r(\eta)$, $*r(\eta)$, and $R(\eta)$ for the following values of the coefficients: $\beta = -0.045$, $\kappa = 0.05$ (Fig. 16), $\beta = -0.05$, $\kappa = 0.05$ (Fig. 17), and $g = 0.3, \mu = 0.001$.

5. RESULTS OF THE ANALOGUE SOLUTION FOR SYSTEM II

The analogue solution was obtained for the same examples for which we have carried out the approximate analytical solution. The values of the coefficients are reviewed in the Table below:

Alternative	g	μ	κ	β
IIa	0.3	0.002	0.1	0.13
IIb	0.3	0.001	0.05	-0.045
IIc	0.3	0.001	0.05	-0.05

The solution proceeded in the way outlined for System I. Since here, too, it holds that $[x] = [y] = [z]$ we show only the dependence of $[x]$ on η. For the purposes of comparison we present the results obtained on the basis of the approximate analytical solution in corresponding figures numbered sub *b*. Alternative IIa is represented in Fig. 18. The qualitative agreement between the analogue and the analytical solution is seen to be good. The two solutions differ quantitatively in that in the former the transition from the semi-trivial resonance solution to the non-resonant solution at increasing η occurs earlier than in the latter. Some difference is also observed in the magnitude of the amplitude of the self-excited vibration component and in the dependence of this amplitude on η at decreasing η. Alternatives IIb and IIc are reviewed in figs. 19 and 20. In both cases the qualitative agreement is very good and the quantitative differences are smaller than in the preceding case.

CONCLUSION

The most important results may be reviewed as follows:

In systems capable of self-excited vibration, and subject to external periodic force, the component of forced vibration interacts to a considerable degree with the component of self-excited vibration. In a certain interval of the excitation frequency, η, and especially in the region of resonance, the component of self-excited vibration is apt to be completely suppressed. The interaction between the two components is substantially enhanced by the nonlinearity of restoring force. This effect manifests itself by both the distortion and the displacement of the curve representing the dependence of the amplitude of the forced vibration component on the excitation force frequency (rotor unbalance) as compared with its dependence in the absence of the self-excited vibration component. The action of self-excited vibration is likely to cause the character of the amplitude-frequency curve of the component of excited vibration to differ importantly from that of a corresponding system with the same characteristics of the restoring force nonlinearity but without self-excitation. In System I curve $r_o(\eta)$ is of the same sense as curve $r(\eta)$, but of different magnitude of curvature of the resonant peaks. In System II even the sense of curvature of the two curves is different. Thus, for example, for a symmetric hardening characteristic of the restoring force when the resonant peak of curve $r_o(\eta)$ is deflected towards higher values of the excitation frequency η, the peak of curve $r(\eta)$ is bent in the opposite direction, as though the characteristic of the nonlinearity were a softening one. The interaction between the two components is influenced not only by the restoring force nonlinearity but also by the coefficient of the gyroscopic term. The displacement of curve $r_0(\eta)$ relative to the curve $r(\eta)$ may be estimated qualitatively with the aid of the skeleton curves and of the starting points of the curves themselves on the axis of the excitation frequency η . It is affected by the ratio of the coefficients of the self-excitation and the damping term, β/κ , and by the magnitude of the coefficient of the gyroscopic term.

Owing to the effect of the restoring force nonlinearity there may exist two (and possibly, even more) steady, locally stable solutions for a certain excitation frequency. In such a case the steady vibration that arises following the attenuation of transient phenomena depends on the initial conditions. For the same frequency there may exist, for example, vibration with zero amplitude as well as vibration with non-zero amplitude of the self-excited vibration component. This is evidenced by the circumstance that the response for increasing frequency is not the same as that for decreasing frequency, with different results obtained in certain intervals of the excitation frequency.

A comparison of systems with and without excitation enables us to draw the following conclusions: the amplitude of the self-excited vibration component is always smaller for systems with forcing; it does not hold, however, that the amplitude of the forced vibration component for non-zero amplitude of the self-excited vibration component is always smaller than the corresponding amplitude of forced vibration for zero amplitude of the self-excited vibration component.

The results of the approximate analytical solution are found to differ only very slightly qualitatively from those of the analogue solution, and the two sets of data agree comparatively well, even quantitatively.

REFERENCES

[1] C. Hayashi, Nonlinear Oscillations in Physical Systems, McGraw-Hill Book Co., New York, 1964.

[2] A. Tondl, Some Problems of Self-Excited Vibration of Rotors, Monographs and Memoranda, National Research Institute for Machine Design, Bechovice, No. 17, in print.

[3] A. Tondl, Some Properties of Nonlinear System Characteristics and their Application to Damping Identification, Acta technica, CSAV, 18, No. 2, 166-179, 1973.

[4] A. Tondl, Domains of Attraction for Nonlinear Systems, Monographs and Memoranda, National Research Institute for Machine Design, Bechovice, No. 8, 1970.

[5] A. Tondl, Self-Excited Vibrations, Monographs and Memoranda, National Research Institute for Machine Design, Bechovice, No. 9, 1970.

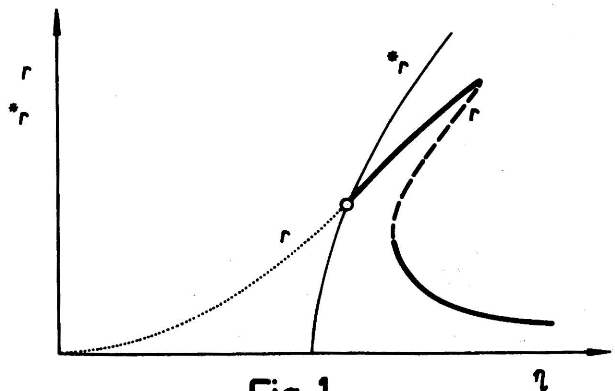

Fig 1

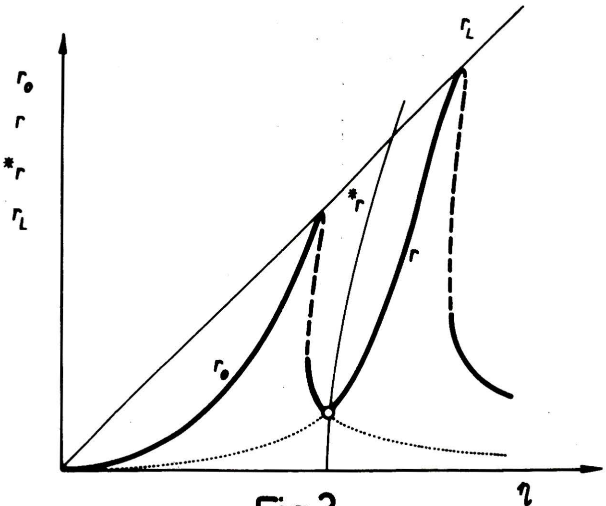

Fig 2

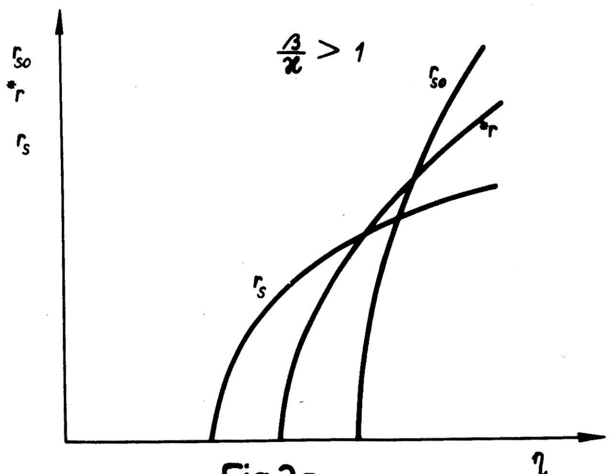

Fig 3a

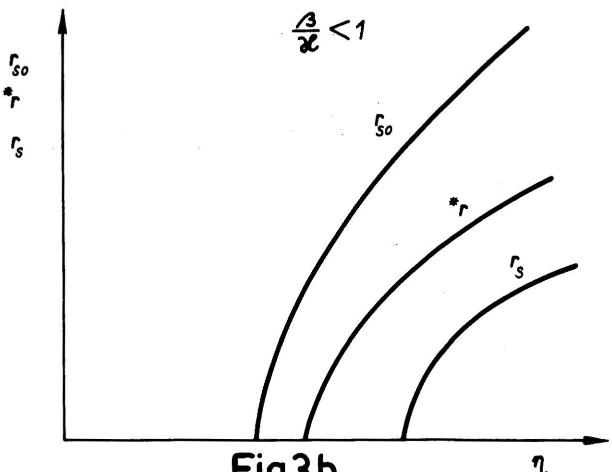

Fig 3b

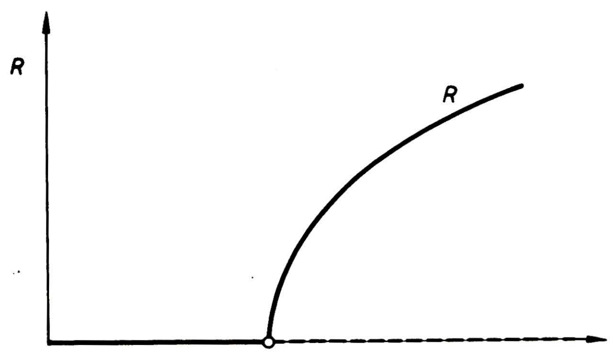

Fig 4a

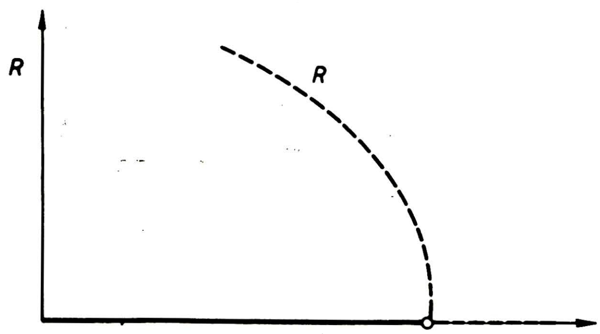

Fig 4b

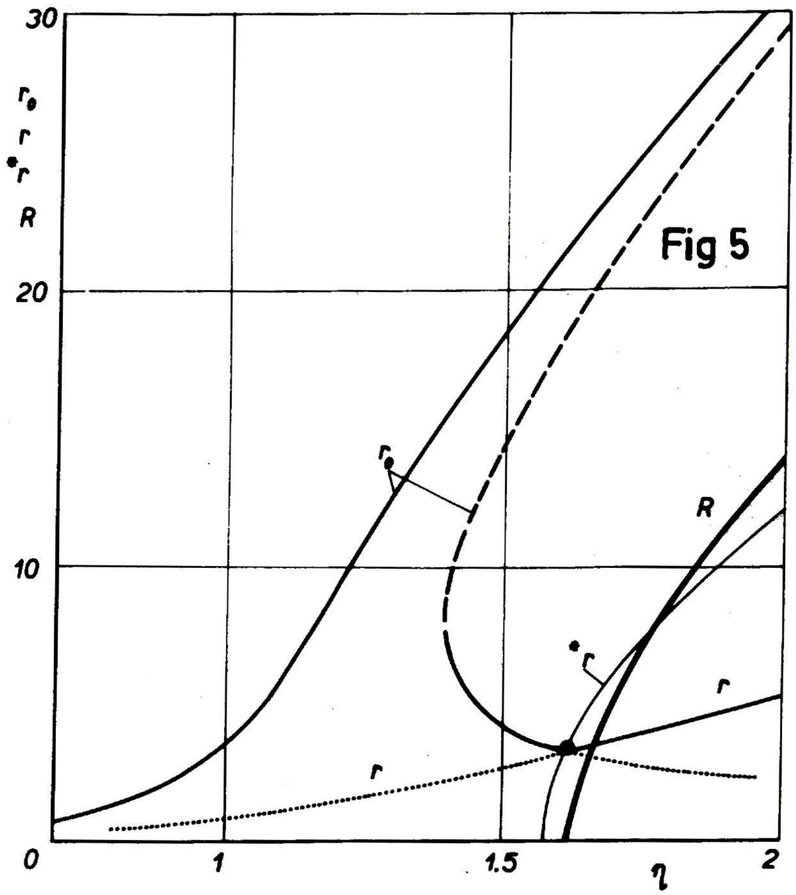

Fig 5

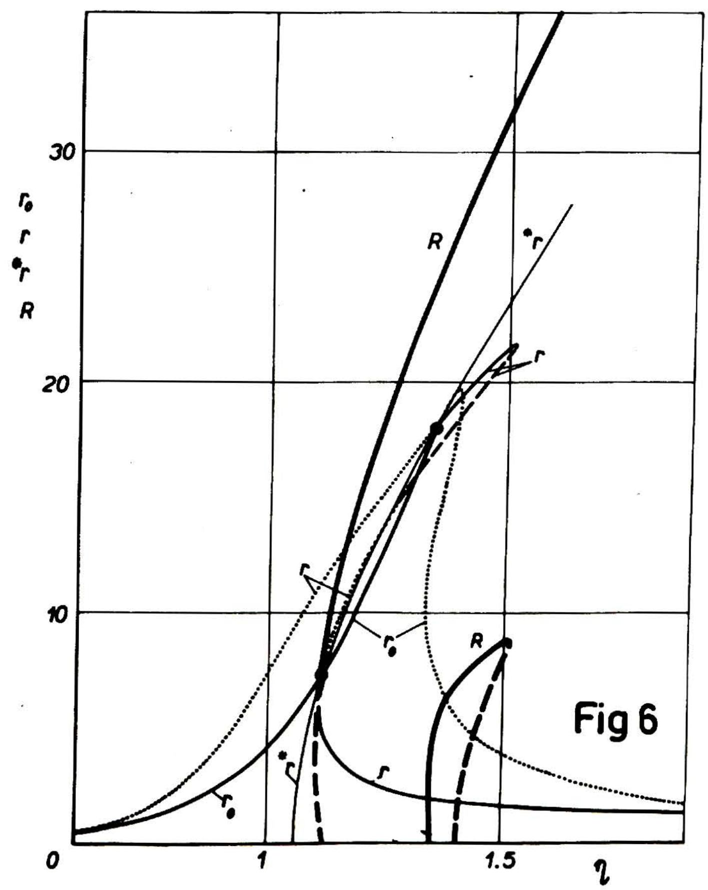

Fig 6

Fig7a

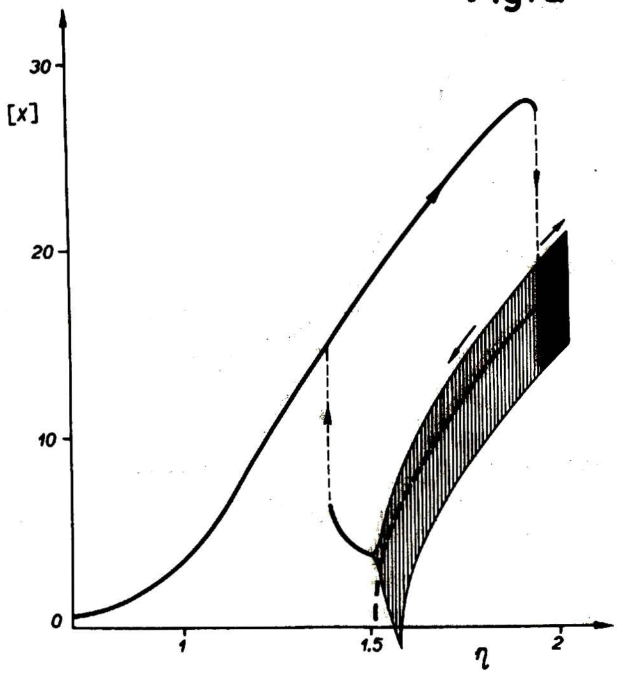

Fig7b

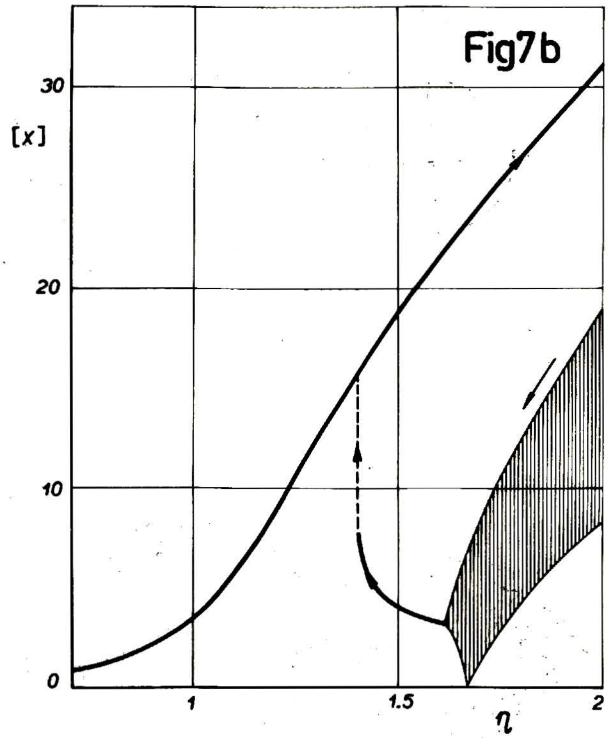

Fig 8

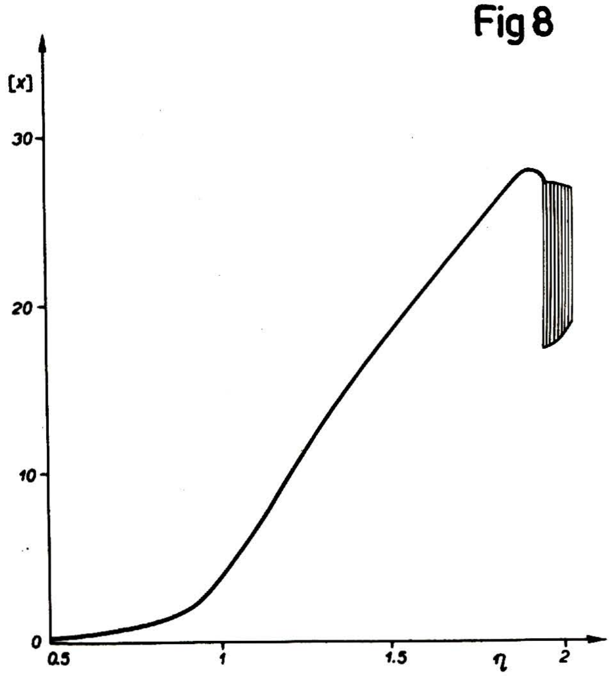

Fig 9

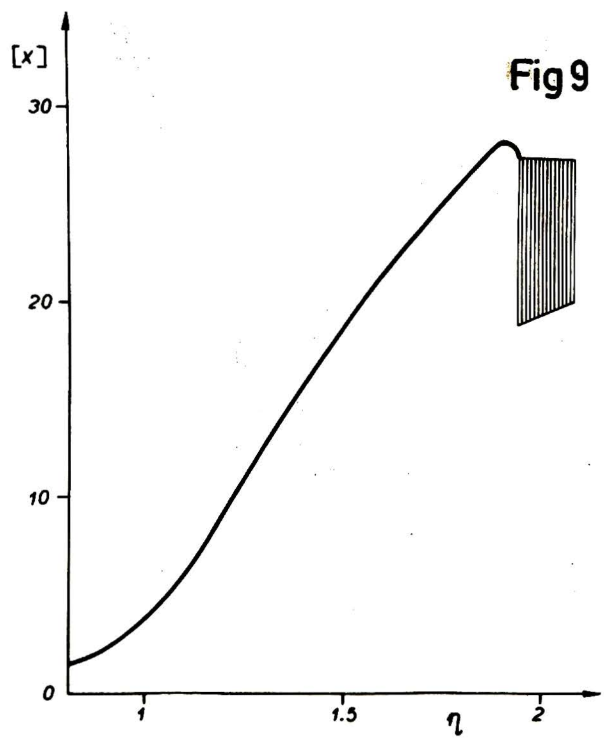

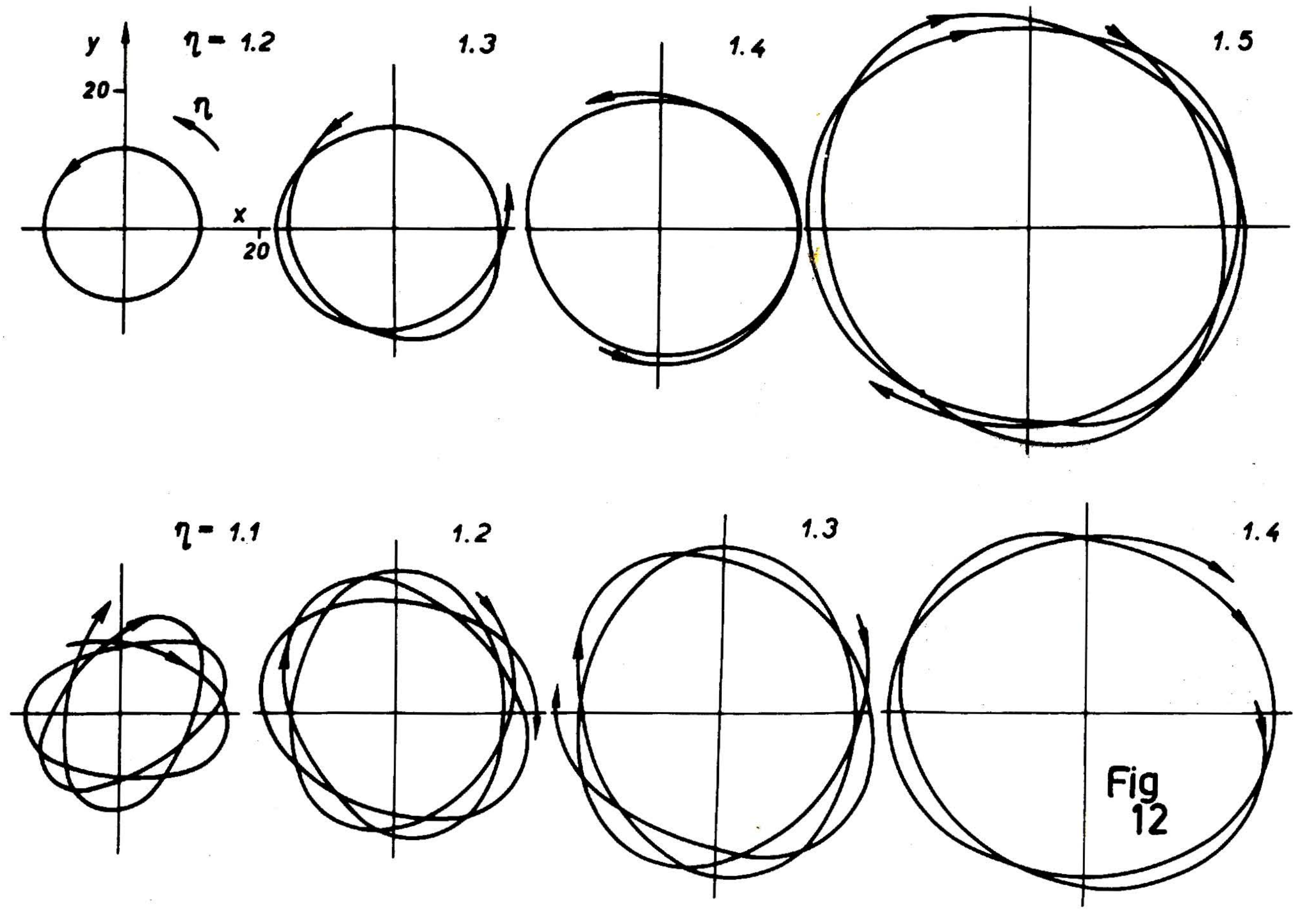

Fig 12

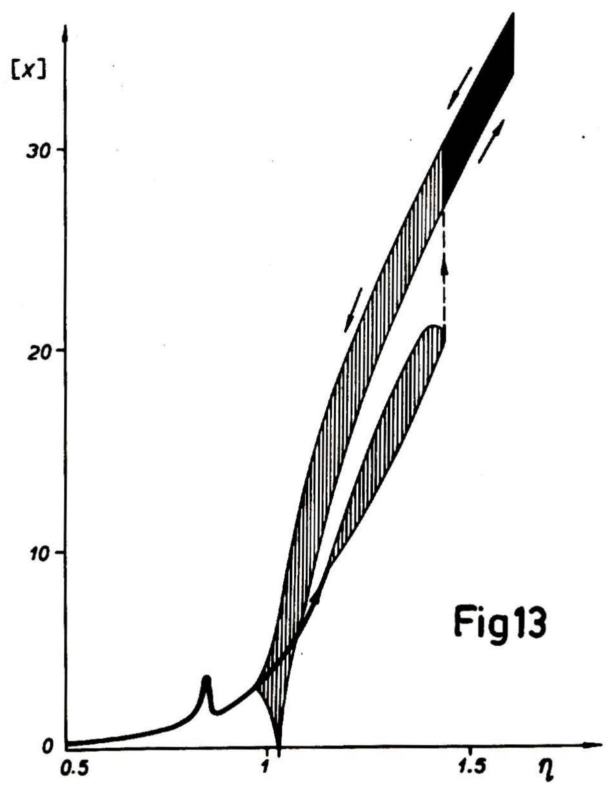

Fig13

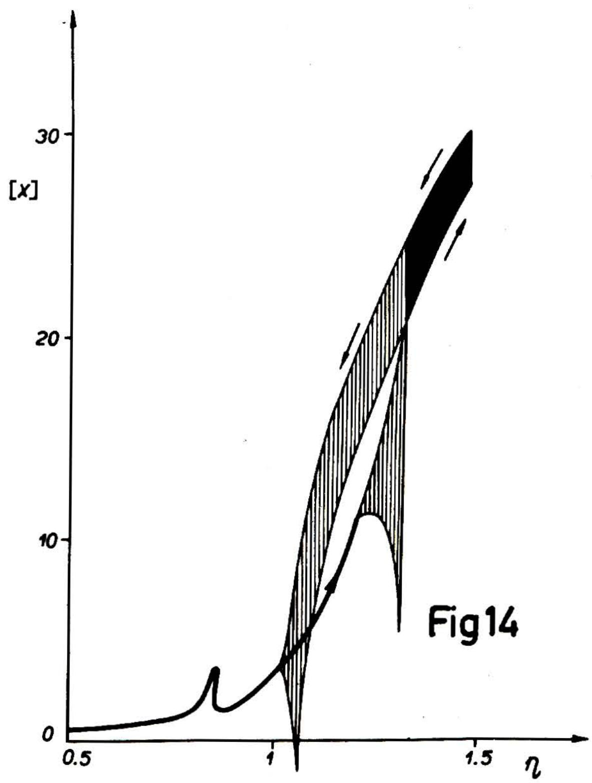

Fig14

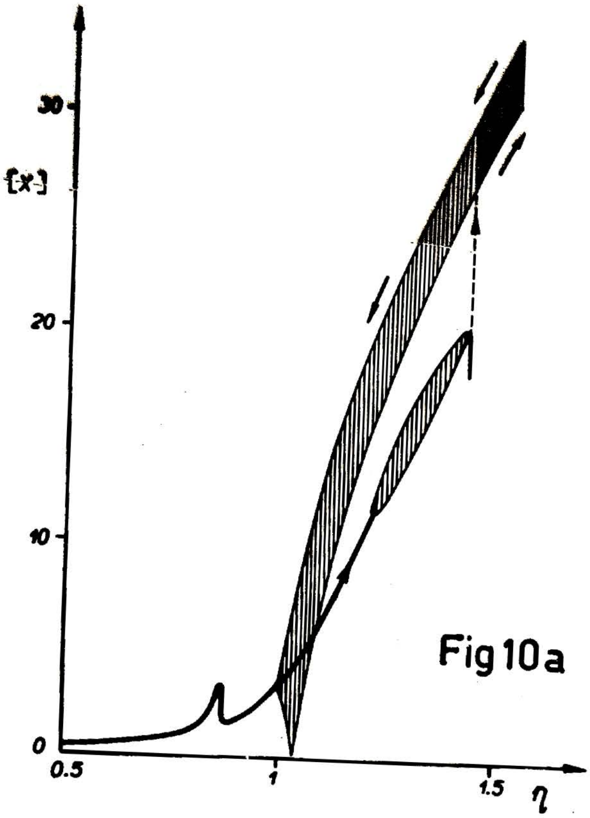

Fig 10a

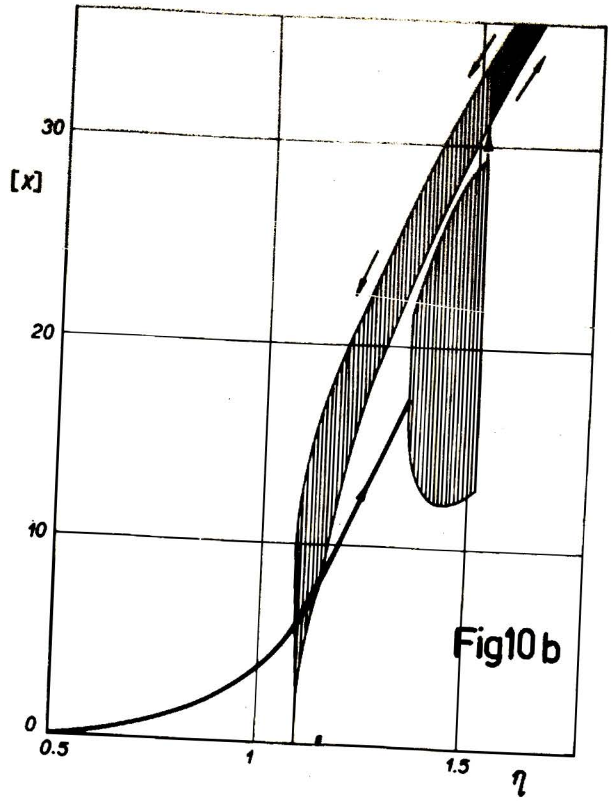

Fig 10 b

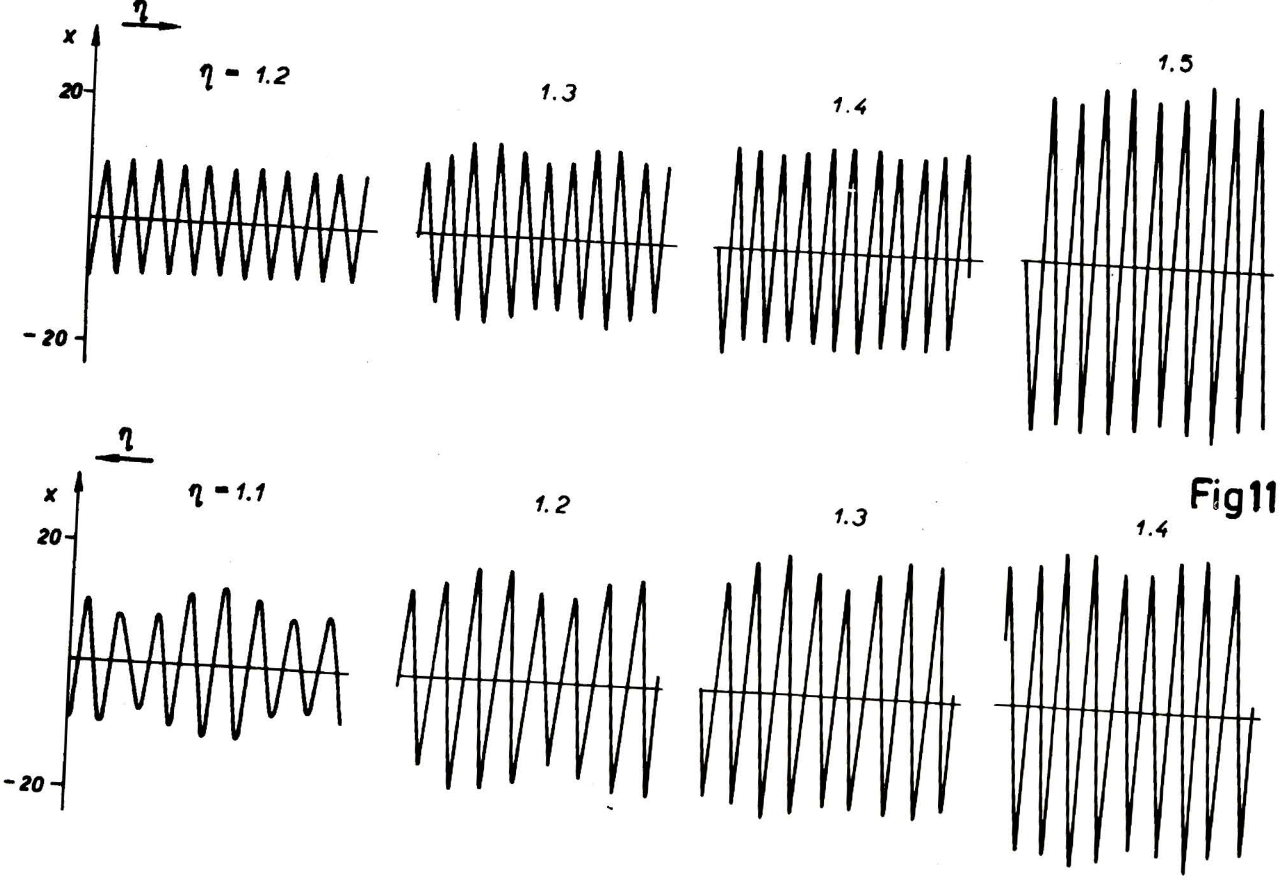

Fig 11

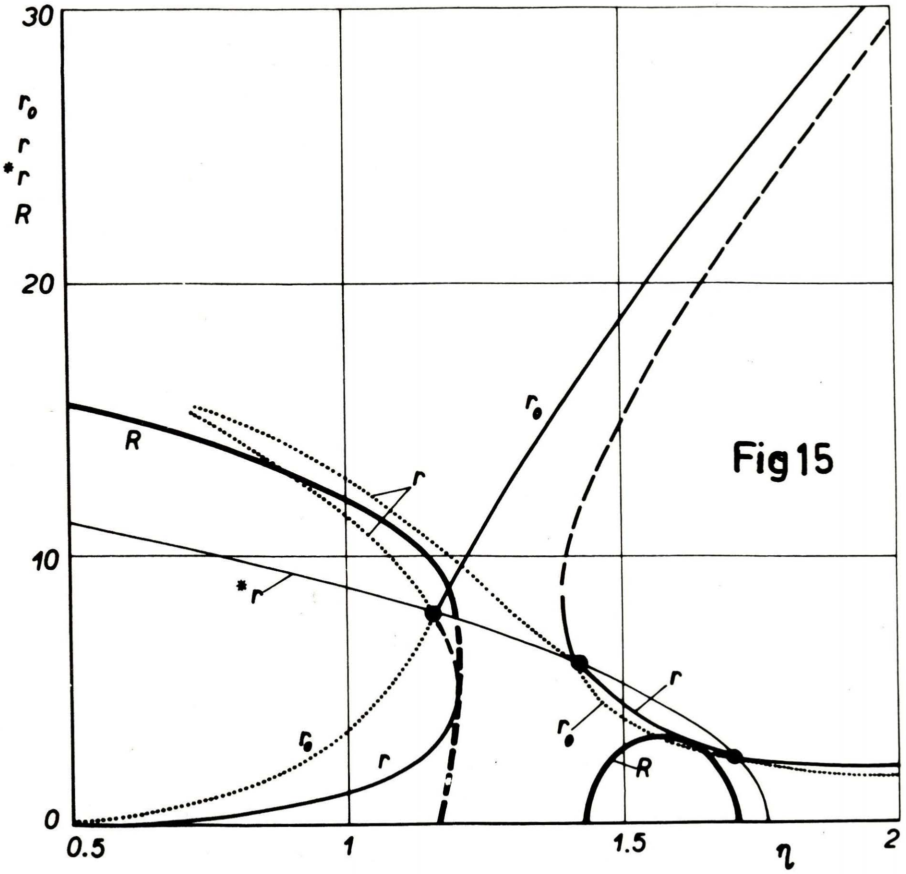

Fig 15

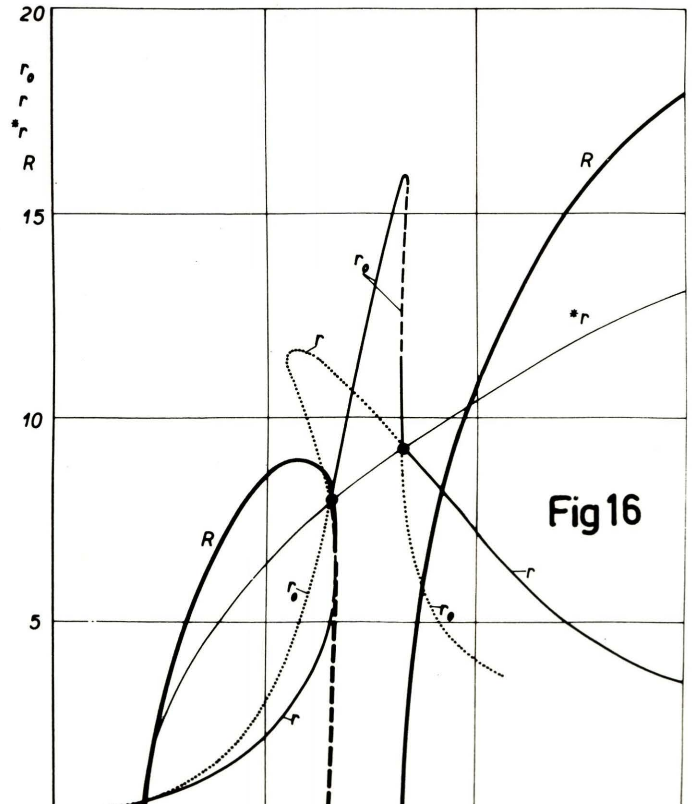

Fig 16

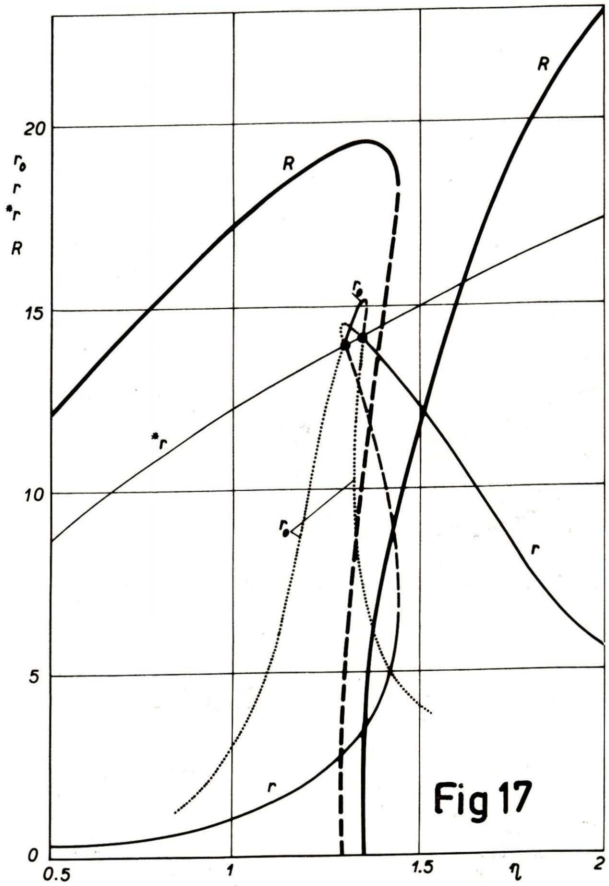

Fig 17

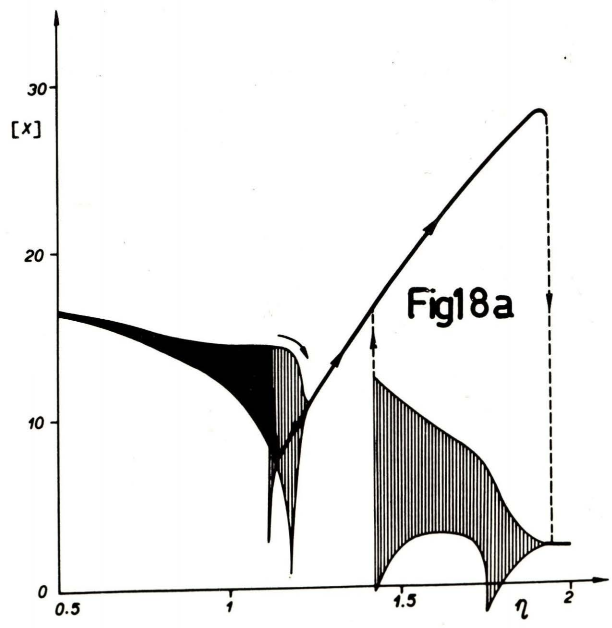

Fig18a

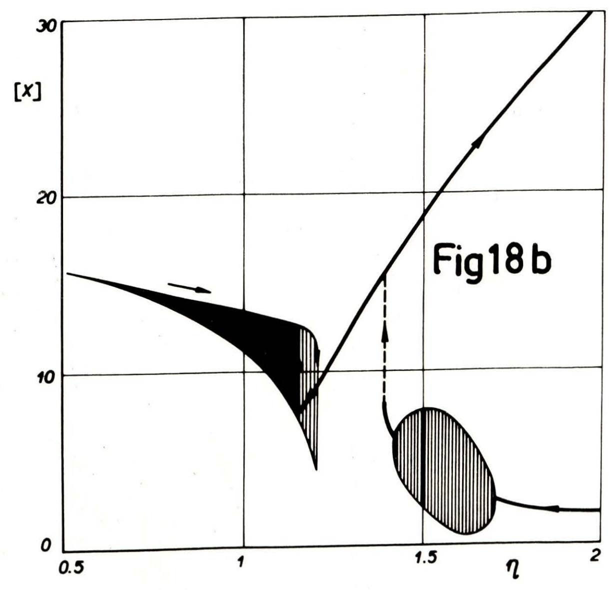

Fig18b

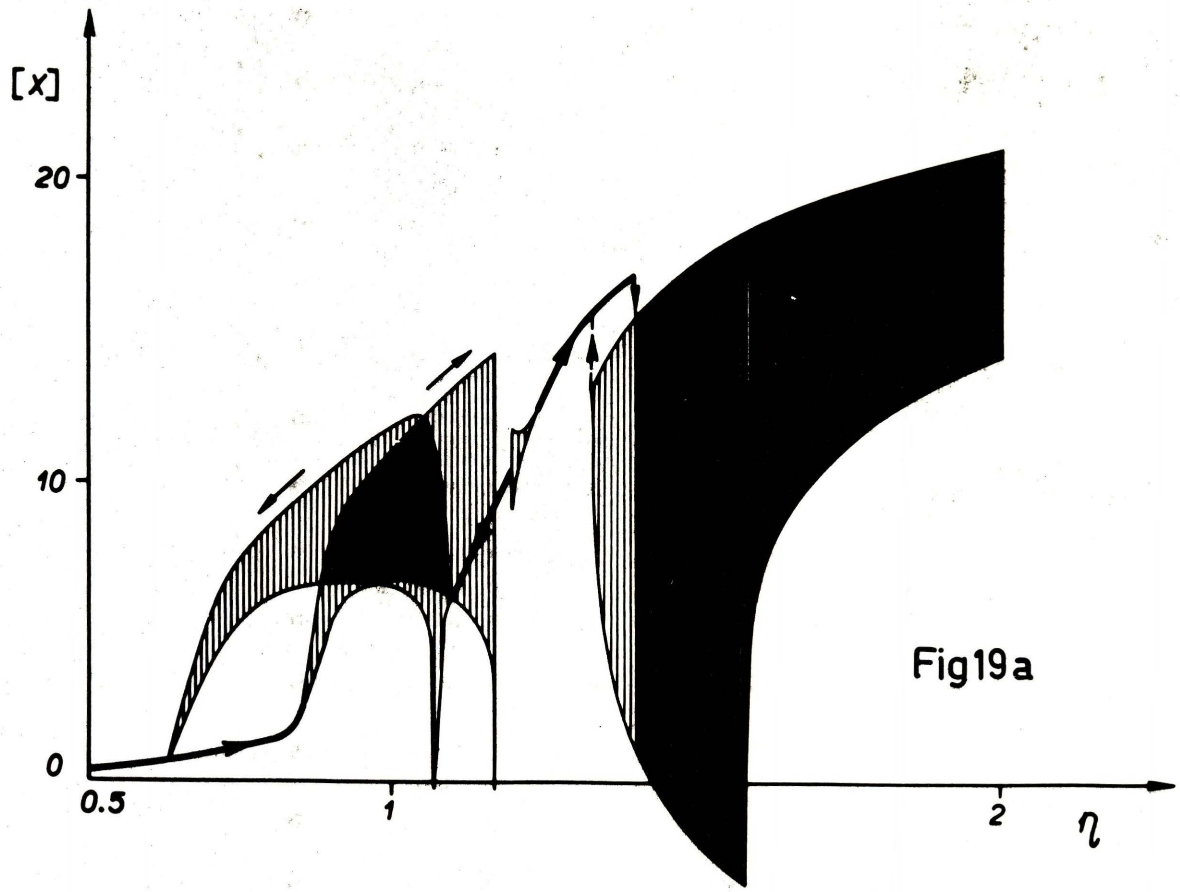

Fig19a

Fig 19b

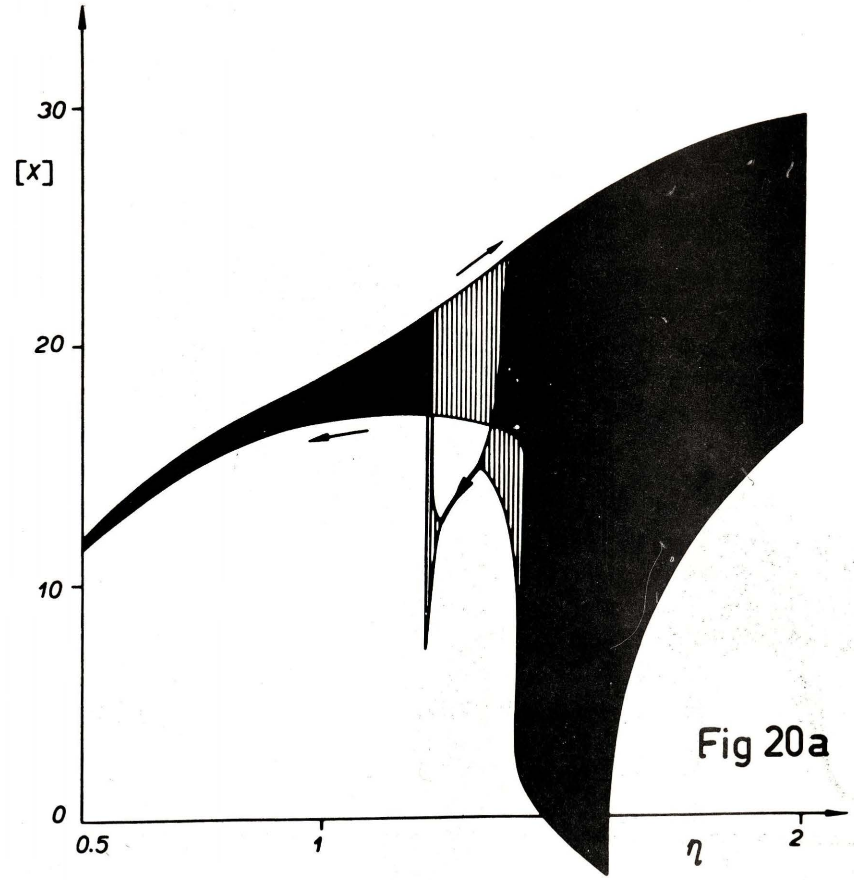

Fig 20a

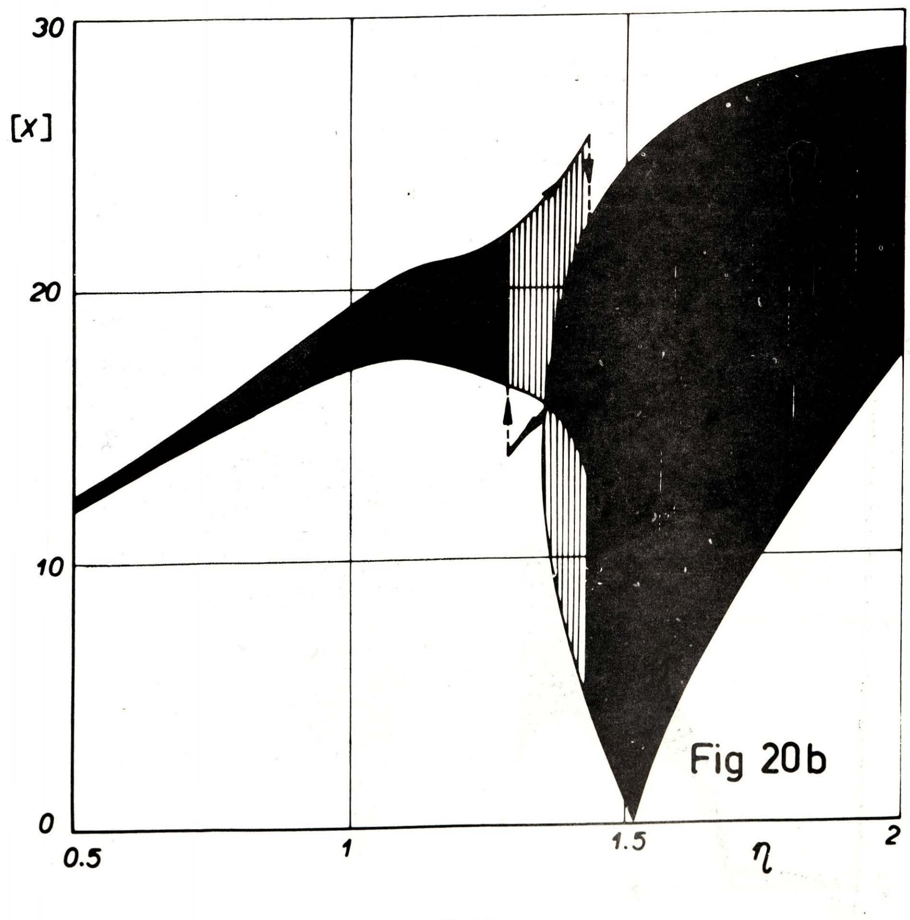

Fig 20b

DEVELOPMENTS IN ABSOLUTE CALIBRATION OF ACCELEROMETERS AT THE NATIONAL STANDARDS LABORATORY

N. H. Clark
CSIRO Division of Applied Physics
National Standards Laboratory
Sydney, N.S.W.

SUMMARY

Accelerometers which are to be used as standards are calibrated in terms of national standards of length and time. In measuring the displacement, precautions are taken to avoid error from disturbance of the "fixed" reference frame. Methods are described of isolating the reference, and of controlling drift of the centre of oscillation. Various scales and techniques are described for absolute determination of displacement. A simple technique of absolute displacement measurement is described, utilising a wide-screen oscilloscope display of the photoelectric signal from a multiple-beam interferometer.

1. INTRODUCTION

Accelerometers used for day-to-day measurements in engineering laboratories are usually calibrated at regular intervals by comparison with a good quality accelerometer maintained as a secondary standard. In principle the procedure is to compare the output of the test accelerometer with that of the standard when both are subjected to rectilinear motion applied in the direction of their sensitive axes. In such transfer calibrations it is difficult to reduce the error below about one per cent (Ref.1), and in less careful comparison calibrations the error may range from a few per cent to a hundred per cent or more at certain frequencies.

However, in no case can the transfer process yield calibration factors to greater accuracies or narrower uncertainty limits than those given for the standard. Furthermore, valid results can not be assumed when the transfer is performed outside the ranges of frequency or amplitude, or other relevant parameter, within which the properties of the standard have been adequately determined and are known to exhibit no spurious effects.

A standard accelerometer is generally calibrated by measuring its electrical output whilst it is subjected to an acceleration which is precisely known in terms of displacement and time. If voltage (or charge), displacement and time are measured in terms of national standards, this is defined as constituting an absolute calibration. Such a calibration is generally steady-state, i.e. excitation consists of sinusoidal oscillation at each of a number of discrete frequencies and displacement amplitudes. An absolute calibration should cover the whole range of amplitudes and frequencies in which it is anticipated that the accelerometer will be used.

2. ABSOLUTE CALIBRATION

In an absolute calibration, frequency is generally measured with a frequency counter, using as reference a calibrated crystal oscillator. At the National Standards Laboratory the frequency counter may also be checked at any time during a calibration against the atomic frequency standard, which has an uncertainty of only a few parts in 10^9. The practical limit to the accuracy of the calibration frequency measurement is in the stability of the oscillator which supplies the drive system for the vibrator; the oscillator used at NSL has a frequency stability of ± 0.02 per cent over the duration of a calibration at one frequency.

If an accelerometer is to be used as a standard, it is preferable to use it always with the same amplifier; the combination may then be considered as the standard. In an absolute calibration, the output of such an accelerometer-amplifier combination is measured with an a.c. millivoltmeter which has been calibrated against a standard e.m.f. source, for example by thermal transfer methods. When another accelerometer is subsequently calibrated by comparison with the standard, the two outputs may be compared using an appropriate instrument of reasonable quality; the absolute calibration of the readout instrument is of secondary importance in this case.

An alternative approach is to calibrate a standard system consisting of standard accelerometer, charge amplifier and millivoltmeter, without regard to the absolute calibration of the meter. In a subsequent comparison, an unknown accelerometer system including readout may be calibrated using the meter of the standard system as an indicator of the applied acceleration. Voltage standards need not be referred to when this method is applied.

At the NSL a combination of the above two methods is used. A standard system is calibrated in absolute terms of frequency and displacement, and the true-r.m.s. millivoltmeter of the system is calibrated by thermal transfer. The standard system is then used to calibrate secondary standards by a comparison method. Secondary standards may also be calibrated by direct methods, but this is time consuming and costly. Only accelerometers of the highest quality are accepted for calibration as secondary standards, and preferably they are calibrated with the particular amplifiers with which they will subsequently be used.

A major difficulty in carrying out an absolute calibration is in obtaining oscillatory motion which is truly rectilinear and undistorted over the whole desired range of frequencies. No commercially available vibration generator meets this ideal; some may approach it over parts of the frequency range. Experience at NSL and elsewhere (Ref.2) indicates that defects in the motion are a serious source of inaccuracy in both absolute and comparison calibrations.

Another major difficulty lies in measuring the small displacement amplitudes at high frequencies; for example, to calibrate an accelerometer at 1 g (where $g = 9.8\ ms^{-2}$) at 1000 Hz requires a displacement amplitude of 0.24 µm to be measured. Such amplitudes are comparable to wavelengths of visible light, so optical interferometry methods have been developed to establish precise scales of displacement, (Ref.3-7). In an absolute calibration, the dominant component of the total uncertainty arises from the measurement of displacement amplitude, particularly at the higher frequencies, therefore the rest of this paper is concerned mainly with the practical problems involved in setting up such displacement scales.

3. MEASUREMENT OF DISPLACEMENT

International standards of length are now defined in terms of wavelengths of light, primarily the orange line associated with the $^2p_{10}$ $^5d_5$ transition in a krypton 86 discharge. From spectroscopy, other lines are precisely known in terms of the krypton line, and may therefore be validly used to set up a scale for length measurement, using interferometric techniques. For vibration metrology it is convenient to use the brightest line in the mercury spectrum, that is the green line of nominal wavelength $\lambda = 546.078 \times 10^{-9}$m. This line is readily obtained from a low pressure mercury arc lamp, and has adequate stability and coherence length.

Briefly, the principle of the NSL vibration interferometer is as follows. Two aluminised optically flat glass surfaces are separated by a small air gap and are arranged with a small wedge angle between the surfaces (Fig.1). A collimated beam of mercury green light is projected onto the surfaces, the light undergoes multiple reflections and a system of fringes of high contrast is formed. The fringes, which have the appearance of fine dark bands against a bright background, are focused by a lens system to form a real image in the plane of an adjustable slit aperture, which can be aligned parallel to the image of the fringes. The accelerometer to be calibrated is attached to the first of the glass flats, the other flat is seismically supported to form an inertial reference. If the first flat S_1 is moved normally to its surface through a distance, relative to the reference, equal to one half wavelength, the set of fringes will move through a distance of one fringe spacing. If the first flat, with the accelerometer, is oscillated through a displacement equal to many wavelengths, the displacement may be measured by counting the number of fringes which pass the slit aperture during one peak-to-peak excursion of the oscillation. This is accomplished electronically by placing behind the slit a photomultiplier, to convert the light signal to an electrical analogue.

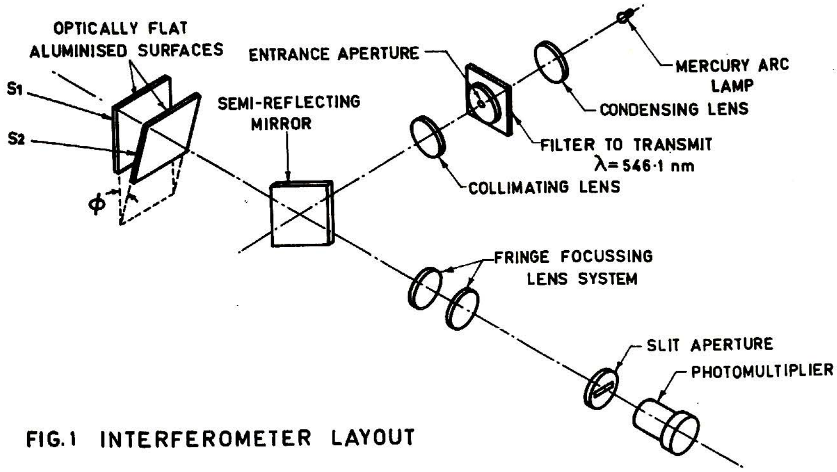

FIG. 1 INTERFEROMETER LAYOUT

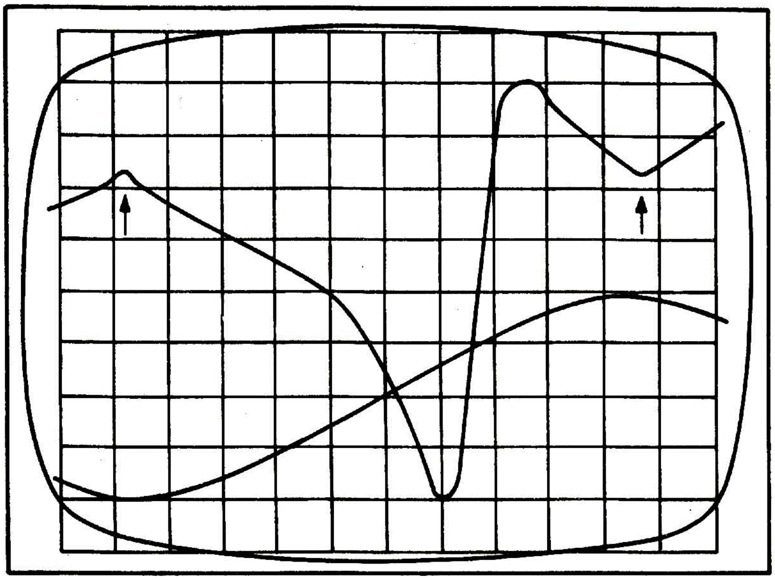

FIG. 2 (a) SIGNAL WITH DISPLACEMENT AMPLITUDE = $\frac{\lambda}{4}$

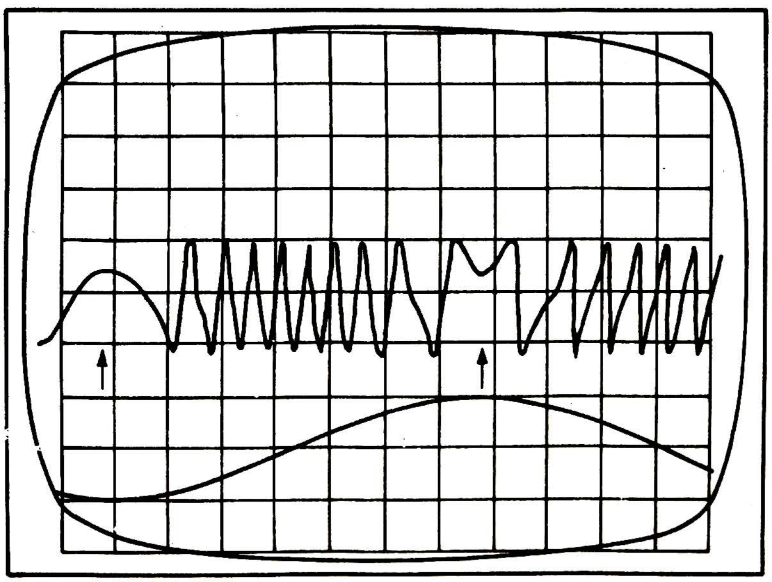

FIG. 2 (b) SIGNAL WITH DISPLACEMENT AMPLITUDE = $\frac{9\lambda}{4}$

If conventional electronic counting is used with the above system, the uncertainty of the displacement measurement may be an appreciable fraction of a fringe, thus the overall precision of measurement may be acceptable only at large amplitudes. Furthermore, as the velocity increases, the signal-to-noise ratio of the photoelectric signal decreases, hence the likelihood of a miscount becomes progressively greater at larger amplitudes.

An improvement in precision has been attained at NSL by the very simple expedient of connecting the photomultiplier output to a wide-screen display oscilloscope, controlling the time base by a signal from the vibration drive oscillator. Provided the ratio of the slit aperture size to the spatial period of the image of the fringes is small enough, say of the order of 0.05, the photoelectric signal is a reasonable analogue of the intensity distribution across the fringe pattern. If the drive amplitude is adjusted so that the oscilloscope shows exactly one cycle of this signal during one half period of the vibration, (Fig.2a), then the peak-to-peak displacement is $\lambda/2$, and the displacement amplitude equals $\lambda/4$, i.e. one quarter of a wavelength. With the mercury green light source, the displacement is 0.136 μm; with care this can be established with an accuracy of approximately two per cent, and multiples of this displacement can be established with similar accuracy. Figure 2b shows the oscilloscope display of the photoelectric signal with displacement amplitude equal to $9\lambda/4$; nine fringe cycles are traversed in one peak-to-peak excursion, whole numbers being attained by ensuring that the level of the photoelectric signal is equal at the two turning points (shown by arrows in the Figure). The 30 cm wide screen of the display oscilloscope improves the resolution for direct visual counting at larger displacements. From photographs of the oscilloscope display, one hundred fringes peak-to-peak have been counted, with an uncertainty of approximately one fringe, i.e. the displacement is 13.6 μm plus or minus one per cent. These visual methods have been used to supplement the second harmonic method (Ref.7) which is discussed in Section 7. Although more accurate, the harmonic method is time consuming; the visual methods give quick results which are often sufficiently accurate.

4. REFERENCE FRAME FOR DISPLACEMENT MEASUREMENT

In any measurement of displacement some "fixed" reference or inertial frame is generally assumed. If displacement is measured with a microscope, the microscope is assumed to be attached to this frame; in interferometric methods, the reference mirror is assumed to be so attached. Should the reference be disturbed during a measurement, error may result. In measuring oscillatory displacements, such disturbances may be of two types: either at the frequency of the oscillation being measured, resulting in possible systematic error, or composed of quasi-random vibrations originating outside of the measuring equipment. The latter could be expected to contribute random error, and a reduced signal-to-noise ratio resulting in poorer resolution. There is also the possibility of disturbance due to slow thermal drift; this is discussed in the next Section. Whatever the type of disturbance, some form of monitoring and/or isolation of the reference is mandatory for accurate measurements.

Disturbing vibrations of external origin transmitted through the supporting structure can be effectively reduced by a seismic suspension. In the NSL vibration interferometer the optical components are mounted in a massive cast iron body to which the vibrator also is attached; the whole is supported by a concrete block. The total mass of about one tonne is mounted on four air springs (Ref.8). The natural frequency of this system in the vertical mode is about 2 Hz, thus providing adequate attenuation of the floor vibrations which have their main frequency components in the vicinity of 20 Hz.

Disturbances at the frequency of the oscillation which is being measured come from the reaction of the shaker support structure. As the mass of the oscillating mirror assembly is less than one kg, the displacement of the concrete block and cast iron body, if together they react as a rigid body, should be less than 0.1 per cent of the motion of the oscillating mirror. The reference mirror of the NSL interferometer was originally firmly attached to the cast iron body; the relative phase and amplitude of the reaction of the reference mirror were measured using three accelerometers, and a correction was applied to the measured displacement. However, this was unacceptable where the reaction exceeded about one per cent, and indeed reaction reached 30 per cent at certain frequencies where structural resonances were excited. The solution chosen was to mount the mirror on a brass block of 1.5 kg, radially supported by three rubber-in-shear isolators (Fig.3). The combination gives a measured natural frequency of 20 Hz in a translational mode normal to the mirror surface, and rotational modes at approximately 25 Hz and 28 Hz. As the instrument is used for calibrations at 200 Hz and higher, this provides adequate attenuation of the reaction, and gives an effective seismic reference for the displacement measurements.

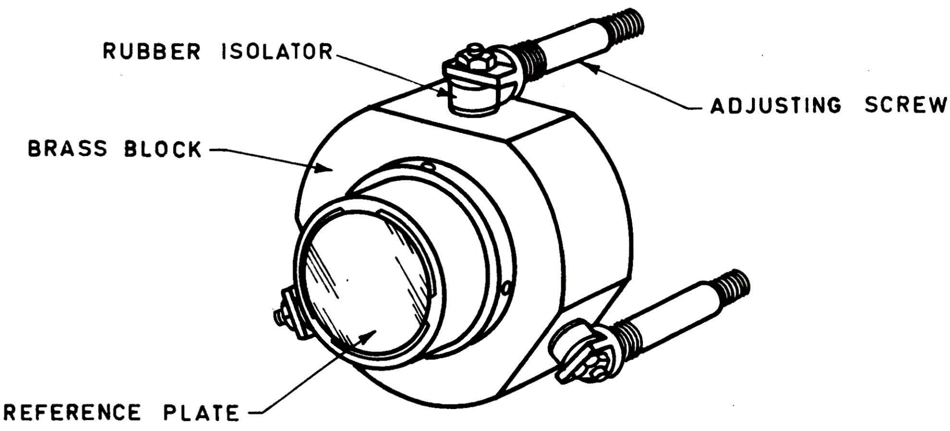

FIG. 3
SEISMIC REFERENCE PLATE

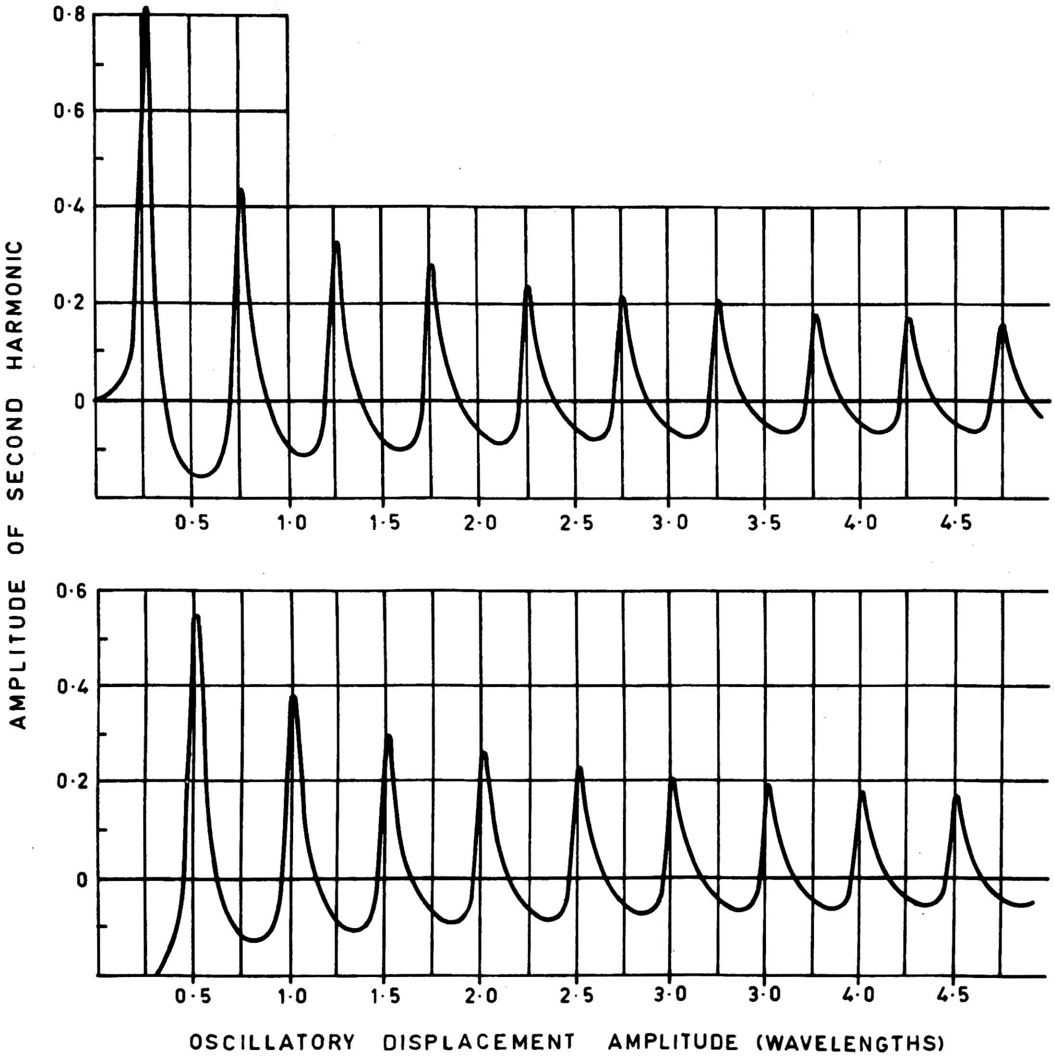

FIG. 4
SECOND HARMONIC FUNCTION

5. DRIFT OF THE CENTRE OF OSCILLATION

Accurate displacement measurements are rendered more difficult, if there is appreciable rate of drift of the oscillation centre relative to the seismic reference. Thermal expansion and contraction of the components of the interferometer and of the vibrating systems produces such drift, and in the NSL instrument, a principal source of this was found to be the cycling of the room air conditioner. With a large rigid polymer foam box placed over the entire interferometer to act as a thermal shield, the rate of drift was reduced by a factor of more than 10, to approximately 0.002 μm per minute.

A further source of thermal drift is the mercury lamp, the housing of which is bolted onto the interferometer. The lamp is of low power, however, and it has been found that near equilibrium is attained after a few hours warmup with the thermal shield in place.

Resistive heating of the vibrator drive coil is another drift source. The problem became more serious when the shaker assembly was re-designed to remove some unwanted resonances and permit operation at higher frequencies; in the new design, the drive coil is required to be much closer to the mirrors and to the metal diaphragms which support the oscillating assembly. To remedy this the coil is now thermally insulated from the rest of the assembly by a ceramic disc, and a simple heat exchanger has been designed to remove excess heat from the system. At the time of writing the performance has not been evaluated with the modified coil assembly.

6. CONTROLLING THE CENTRE OF OSCILLATION

The method of adjusting the centre of oscillation, and compensating for drift, is to inject direct current into the shaker drive coil. Alternatively the position of the reference could be adjusted, for instance by using an electromagnetic transducer; an adjustable reference such as this is incorporated in a new vibration interferometer being designed at NSL. In either case it is first necessary to know the magnitude and direction of the drift of the centre from the desired position.

One approach has been to monitor the time-averaged value of the photocurrent. For a fringe pattern having a symmetrical intensity distribution, the mean photocurrent will be a minimum if the centre of a dark fringe oscillates symmetrically past the exit slit of the interferometer. This method does not show the sign of any shift of centre, and allowance must be made for possible random changes in the total light flux.

An easier method makes use of the wide-screen oscilloscope (Fig.2). Provided the time base is stable and phase-locked to the shaker drive signal, the centre of oscillation may be monitored by aligning the photoelectric fringe pattern with the oscilloscope graticule. By this means the centre of oscillation is controllable to approximately ± 2 per cent of the displacement amplitude, that is, for an amplitude of 0.136 μm the centre can be controlled to within 0.003 μm. By expanding the oscilloscope trace it is possible to achieve a similar precision of control at larger displacement amplitudes. It is not necessary for the fringe pattern to be symmetrical.

Another method which has been developed for asymmetric fringes utilises the thin metallic films on the glass optical flats; these have been made to function as capacitor plates as well as optical surfaces. The capacitor is connected in one arm of an a.c. bridge, which is balanced after the centre of a dark fringe has been aligned with the exit slit, with the system at rest. Using standard reference capacitors and a good quality bridge with a 10 kHz carrier, it has been possible to resolve a static change in capacitance of 10^{-5} pF, equivalent to approximately 0.002 μm when the mean gap between the plates is approximately 1000. μm. When the system is vibrated, the unbalance signal at the bridge output unfortunately has a relatively large modulation at the frequency of vibration, and this reduces resolution. To improve this condition, the conventional tuned null detector has been replaced by a lock-in amplifier incorporating a narrow bandpass filter, with which it has been possible to resolve shifts of centre of approximately 0.002 μm even when the oscillatory displacement is as large as 30 μm. The d.c. output of the null detector could be used as error signal for a servo to automatically control the centre of oscillation; at the time of writing this has not been done. Provided the drift rate is not too great, the centring can be adjusted by manual control of the d.c. injected into the coil.

7. DISPLACEMENT SCALE USING SECOND HARMONIC DETECTION

If the centre of oscillation is specified such that the centre of a dark fringe oscillates symmetrically past the exit slit of the interferometer, then the photoelectric signal contains only even harmonics of the vibration, provided the fringe pattern has a symmetrical intensity distribution. Similarly, only even harmonics are present if the centre of oscillation is the mid-point between two dark fringes. For each of these cases it has been shown (Ref.6) that the amplitude of the second harmonic will undergo a series of abrupt changes as the oscillatory displacement is increased. The functional relationships are shown in Fig.4, in which the two graphs correspond to the two symmetrical positions of the centre of oscillation. The functions are independent of the frequency of oscillation, and the turning points are used to provide convenient scales of oscillatory displacement.

Monitoring the centre of oscillation of such a system consists in simply ensuring that the fundamental component of the photoelectric signal is always zero. An unfortunate complication arises from the necessity to maintain a large mean gap (approx. 1 mm) between the glass flats and from other practical considerations which combine to produce a fringe intensity distribution which is not symmetrical (Ref.7). The effect can be noticed in Fig.2a. Because of this it has been considered desirable to measure the intensity distribution directly. The distribution is then expressed as a Fourier series, and the centre of oscillation is arbitrarily specified as such that the fundamental component of the photoelectrical signal is always zero. The specified centre thus varies with amplitude, and it is necessary to evaluate the zeroes of the function which describes the fundamental for every value of displacement for which the second harmonic function is to be calculated. The resulting second harmonic functions are very similar to those of Fig.4, but the abscissae are shifted by approximately 0.01λ.

The smallest displacement which can be established by this method using mercury green light is 0.135 μm. This has been measured with an uncertainty of ± 0.001 μm. The uncertainty is similar at larger amplitudes; a displacement of approximately 5.0 μm has been established with an uncertainty of ± 0.001 μm, that is, ± 0.02 per cent.

The method is supplemented by the wide-screen oscilloscope display described in Section 3. From the oscilloscope display the centre of oscillation is readily seen, and hence the appropriate second harmonic function can be chosen (Fig.4). The visual display also gives the integral number of the turning point of the function. Before carrying out a full calibration by the second harmonic method, a quick calibration, to approximately 2 per cent accuracy, is performed using the oscilloscope display alone. In case of the calibration factor of an accelerometer being thereby shown to have changed markedly since a prior absolute calibration, no further time need be spent on the calibration.

8. OTHER DISPLACEMENT SCALES

The centre of oscillation need not be specified as above. If instead some centre, fixed relative to the inertial reference, is specified, the second harmonic function differs from that of Fig.4 and the peaks of this new function provide another scale of displacement. A convenient centre is the minimum intensity position on the fringe pattern. With this choice, further displacement scales are available due to the asymmetry of the pattern; the fundamental and higher harmonics all vary with displacement in a fashion similar to the second harmonic function shown in Fig.4. With the centre of oscillation effectively controlled as earlier described, scales of displacement may be set up using the peaks and zeroes of the various harmonics.

Interpolation between the discrete values of displacement amplitude is possible by utilising the capacitor plates (see Section 6) as a transfer. The main advantage of the technique, first mentioned in Ref.9, lies in the possibility of extrapolation to displacement amplitudes smaller than $\lambda/4$. A fixed centre of oscillation is necessary, and the capacitor is calibrated dynamically by measuring the fundamental component in the bridge output at each of a number of discrete amplitudes using the scales already described.

9. CONCLUDING REMARKS

The work described in this paper is part of a continuing programme, at the National Standards Laboratory, of development of techniques for the absolute calibration of reference standard accelerometers. The accent so far has been on the 200 Hz - 1 kHz range of frequencies. The existing equipment is being modified to make possible calibrations to 1.5 kHz. Other work in progress is concerned with ensuring rectilinearity of the calibrating motion, and with extending the range of displacement which can be measured in absolute terms. Projected developments include a new vibration interferometer which should permit the Laboratory to undertake calibrations over a much wider range of frequencies.

10. REFERENCES

(1) BOUCHE, R.R. - *Proc.22nd Annual I.S.A. Conference,* Vol.22, (Paper No.M18-3-MESTIND-67), (1967).

(2) JONES, E., LEE, D. and EDELMAN, S. - *J.Acoust.Soc.Am.,* Vol.41, pp.354-7, (1967).

(3) THOMAS, H.A. and WARREN, G.W. - *Phil.Mag.,* Vol.5, p.1125, (1928).

(4) OSTERBERG, H. - *J.Opt.Soc.Am.,* Vol.22, p.19, (1932).

(5) SCHMIDT, V.A., EDELMAN, S., SMITH, E.R. and JONES, E. - *J.Acoust.Soc.Am.,* Vol.33, No.6, (1961).

(6) GOLDBERG, J.L. - *J.Acoust.Soc.Am.,* Vol.36, p.1922, (1964).

(7) GOLDBERG, J.L. - *Metrologia,* Vol.7, No.3, pp.87-103, (1971).

(8) DORIEN-BROWN, B. - *Proc.The Harold Armstrong Conference on Production Science in Industry,* (1971).

(9) GOLDBERG, J.L. - *J.Scient.Instrum.,* Ser.2, Vol.1, p.481, (1968).

VIBRATIONAL ANALYSIS OF A PUNCH PRESS

L. L. Koss
Department of Mechanical Engineering
Monash University
Clayton, Victoria

SUMMARY: - The difficulties in obtaining frequency response data for a punch press from conventional vibrational shaker techniques will be discussed. The main difficulty in shaker simulation was the creation of a force internal to the punch press system similar to the force which acts during a punch operation. Experimental results for frequency response information obtained from a shaker analysis, and a blanking operation for mild and stainless steels will be compared.

1. Introduction

The purpose of this paper is to present experimental results on the vibration response of a punch press. The response is given in the form of transfer functions obtained from vibration shaker tests and from blanking tests on mild and stainless steels. These functions are valuable for the purposes of shock isolation of the press and for identification of possible modes of acoustic radiation.

2. Analysis

The transfer function, H(f), of a position of interest on the surface of a machine is usually obtained by exciting another position on the machine with a vibration shaker and measuring the acceleration at the position of interest. The method of beating through the important frequencies [1] or the swept sine wave technique [2], [3], [4] can be used to obtain the frequency dependence of this function. The same techniques can be utilized to measure the transfer functions of positions on a punch press when the vibration shaker is located at the same position as a punch and die set.

During a punch press operation a force, F(t), is generated between the punch and die which can cause accelerations A(t) on the body of the press. In the above expressions t represents time. The Fourier transform of F(t) is given by

$$F(f) = \int_0^\infty F(t)\, e^{-j2\pi ft} dt \qquad \ldots(1)$$

and the Fourier transform of A(t) is given by

$$A(f) = \int_0^\infty A(t)\, e^{-j2\pi ft} dt \qquad \ldots(2)$$

where $j = \sqrt{-1}$, and f is frequency.
An operational transfer function, Ho(f), can be defined as

$$Ho(f) = \frac{A(f)}{F(f)} \qquad \ldots(3)$$

or

$$|Ho(f)| = \frac{|A(f)|}{|F(f)|} \qquad \ldots(4)$$

when no noise is present in the measuring system.

Many differences exist between the conditions under which the shaker tests are performed and the actual operating situation so that H(f) may not be equal to Ho(f). The differences in conditions are attributable to the following.

1. The shaker is attached to the base plate of the punch press as is shown in Figure 1. The shaker force is transmitted to the press via the base of the shaker as the piston is not attached to the body of the press. The force in a punch press operation, see Figure 2 for typical force time traces, is transmitted to the press both through the base plate and by the ram connecting rod, see Figure 3. The ram connecting rod is attached to the crankshaft eccentric by bearings. The flywheel shaft is also attached to the crankshaft. This shaft is supported by bearings in the C frame. The force thus transmitted by the connecting rod has to pass through bearings to the top of the C frame. The transmitted force causes the shafts to move through clearances in the bearings and it is possible for forces to be transmitted through lubricant. Thus, the force transmission paths are different for the shaker test and an actual operation which may lead to the excitation of different modes in each case.

2. A friction force exists between the punch and die for a blanking process which could add damping to some of the vibratory modes.

3. The punch press "C" frame deflection may be non linear with load so that a shaker test is only valid for small load conditions.

4. During a punch operation the ram is in its lowered position while during a shaker test it would be in its upper position, so that any acceleration measurements taken on the top of the ram due to shaker excitation may be misleading.

A comparison will be made between H(f) obtained from shaker analyses and Ho(f) obtained from blanking operations for three measurement positions on the press.

The blanking operations consisted of blanking a 2.54 centimeter (cm) diameter circular hole in mild steel sheet of 0.152 cm thickness and in stainless steel sheetof 0.168 cm thickness. In Figure 3 are shown the three measurement positions.

3. Shaker Test Results

The acceleration response of the EA1500 MB shaker is shown in Figure 3b. The response is flat from ≃ 100 Hz to 10 KHz. The response of the accelerometer attached to the shaker piston is also shown in Figure 3b. The response is flat from ≃ 200 Hz to 2000 Hz thus indicating that a constant root mean square force is being transmitted to the baseplate of the punch press. The flat position of the accelerometer response was 30 to 40 db above that for accelerations on the base plate which indicated that the press did not load the shaker to any great extent. The transfer functions for the press obtained from the shaker tests are given in decibels as a logrithmic potentiometer was used in the level recorder.

The shaker tests were performed by automatically scanning through the audible frequencies as described in [1]. The transfer function for position 2 on the support plate is shown in Figure 4a Major frequency peaks exist at ≃ 960 Hz and 1200 Hz, other peaks exist but are of lower amplitude. In Figure 5b is shown the transfer function for position 1 on the top of the ram, the ram being in its upper position. Important response peaks exist at 400, 650, 950 and at 1200 Hz. In Figure 5a is shown the transfer function for position 4 on the base plate. Five spectral peaks are prominent, they exist at 650, 900, 1200, 1700 and at 2100 Hz.

4. Results from Blanking Experiments

The experimental force time and acceleration time curves were recorded simultaneously on a Precision Instrument model 6200 tape recorder. The amplitude frequency response of the recorder was verified to be flat from 20 Hz to 10 KHz. Bruel & Kjaer type 4333 accelerometers were used to measure the accelerations.

Kistler dual mode amplifiers mode 504D3 with 10 KHz low pass notch filters were used to amplify the signals. The force time curves were measured with the use of strain gauges located on diametrically opposite sides of the punch. A high common mode rejection type amplifier was used to amplify the force time signals. The tape recorded signals were digitized at an effective 20 KHz rate and a fast Fourier transform routine was used to transform the data into the frequency domain. The results presented here are given at approximately ever 40 Hz.

It is important to note that the blanking tests results were not repeatable, from shot to shot and the results for $|Ho(f)|$ presented here are for an average of two shots. The operational transfer functions for position 2 are shown in Figure 6. The $|Ho(f)|$ for mild and stainless steels qualitatively agree in shape and both results qualitatively agree with the shape obtained from the shaker tests, Figure 4a. The peak response at ≃ 1000 Hz and 1200 Hz do differ in

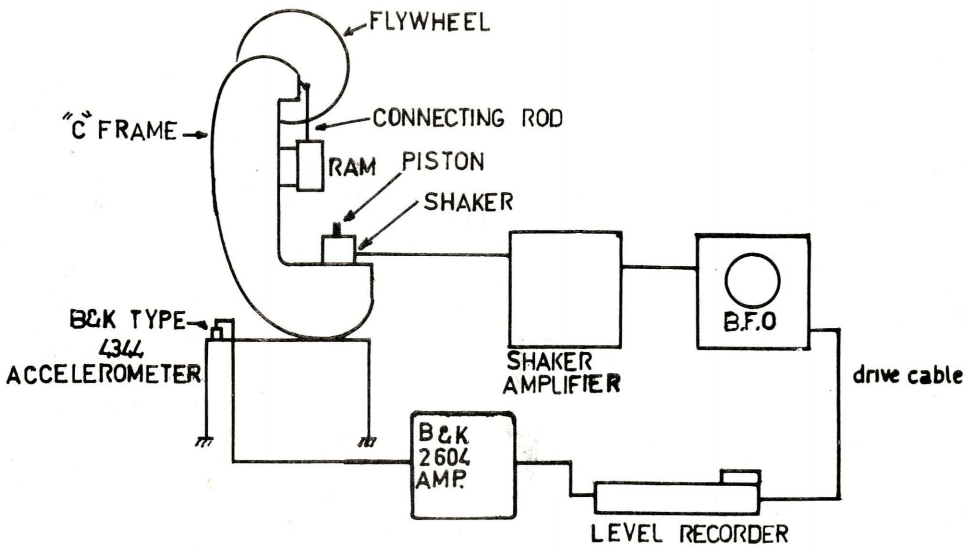

Figure 1 . Schematic diagram of shaker test .

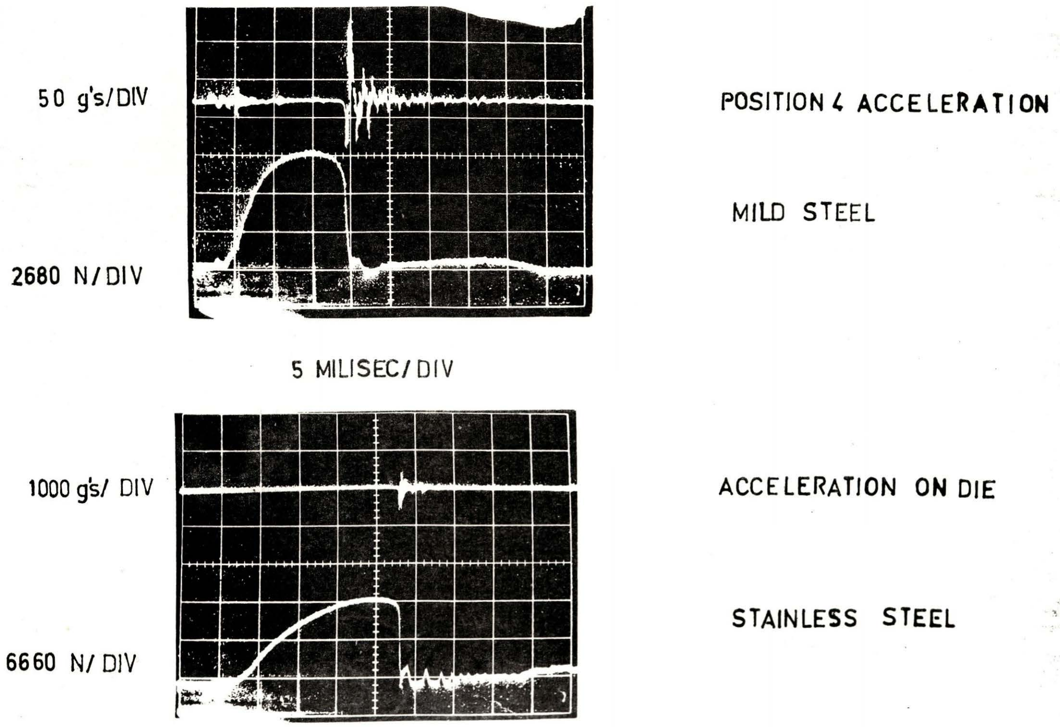

Figure 2 , Sample force time traces.

Figure 3. Punch press in anechoic chamber.

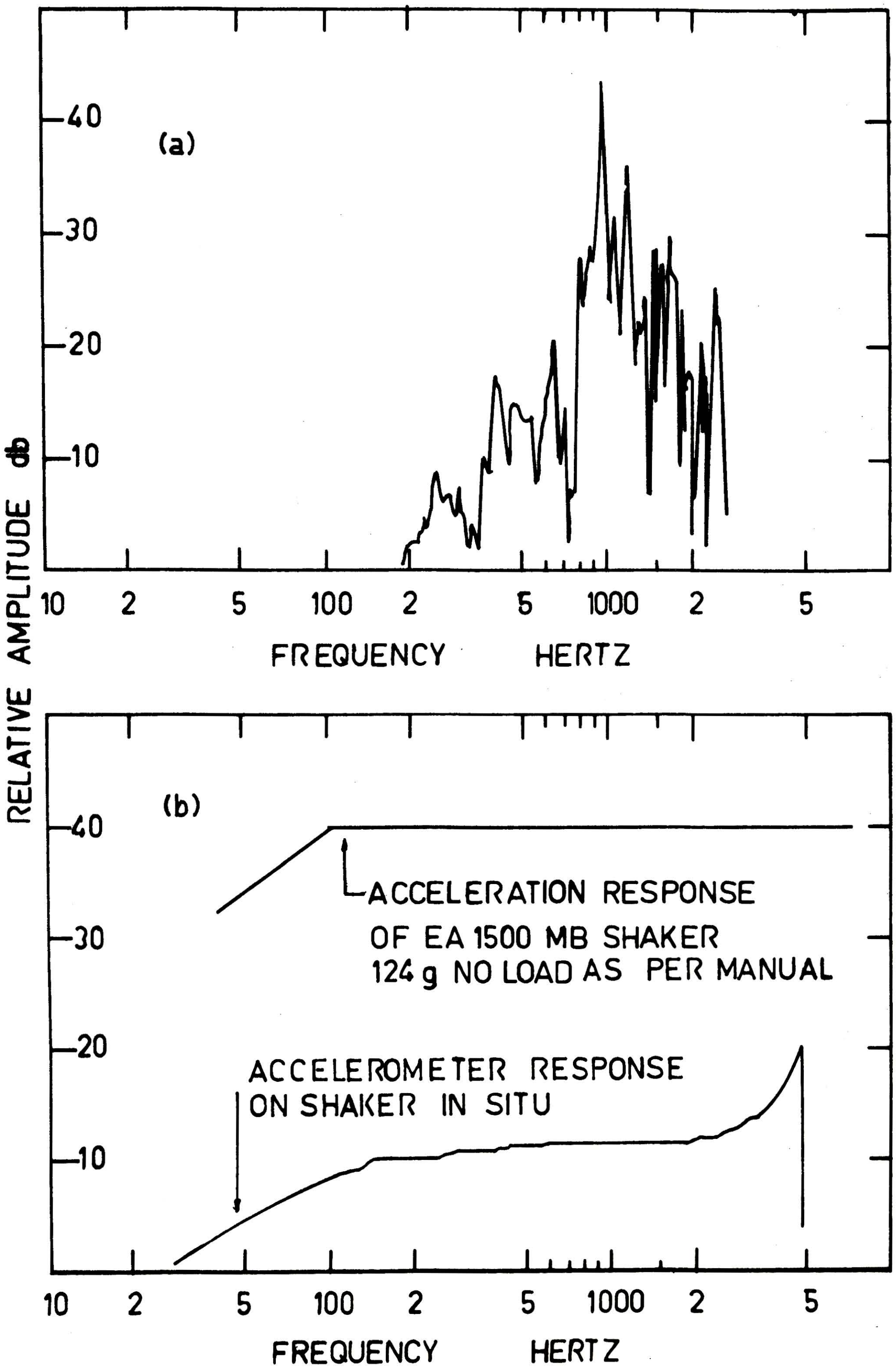

Figure 4. a. |H(f)| for position 2 on the support plate.
b. Shaker response.

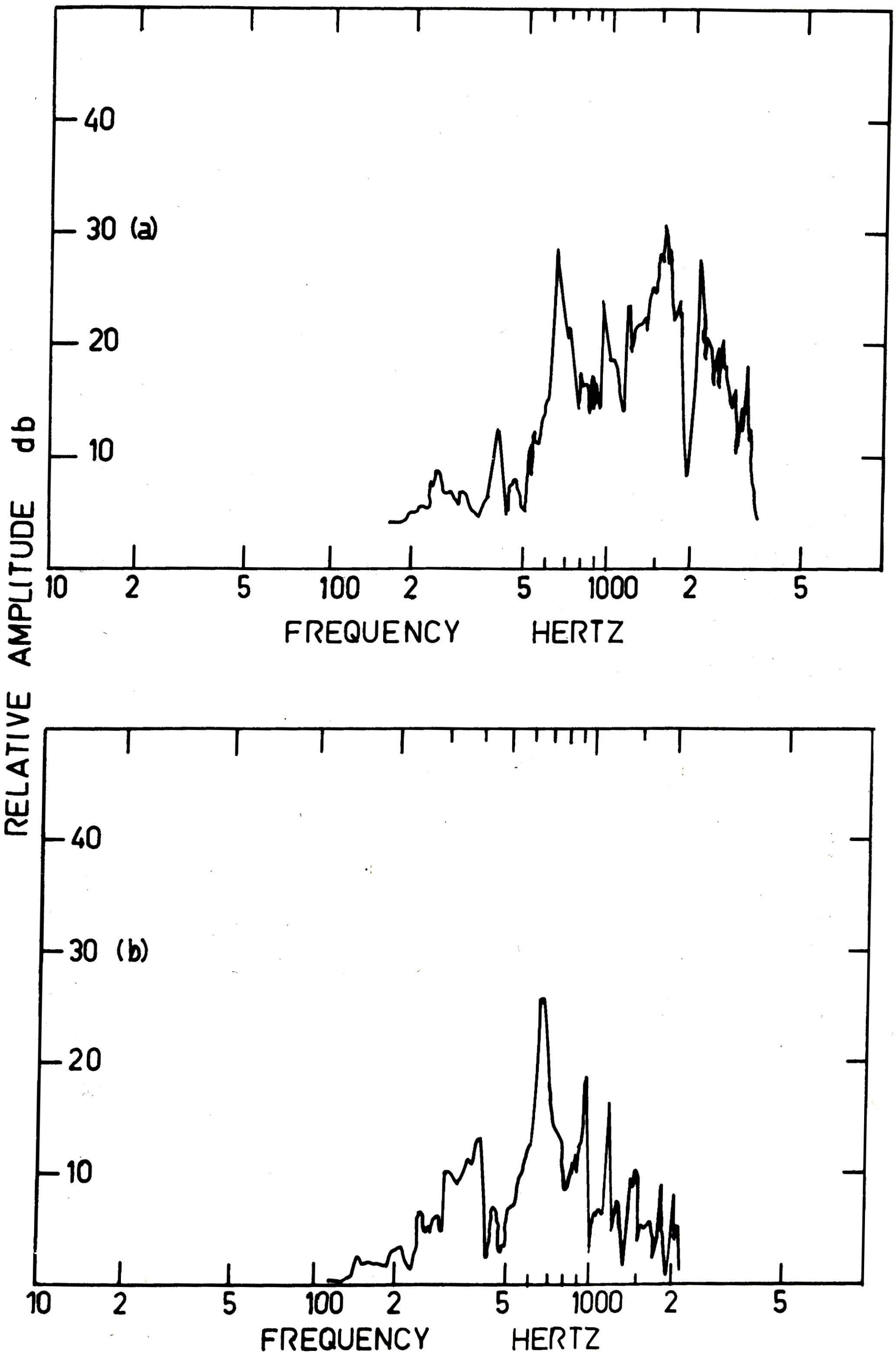

Figure5. a. |H(f)| for position 4 on base plate.
b, |H(f)| for position 1 on top of the ram.

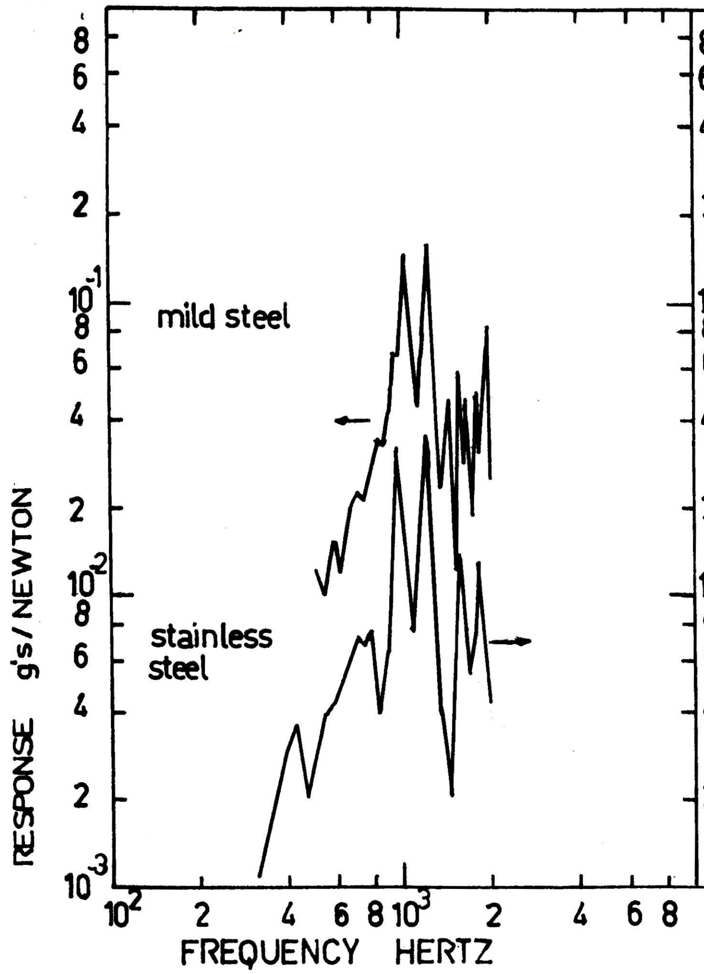

Figure 6. $|H_o(f)|$ for position 2 on the support plate.

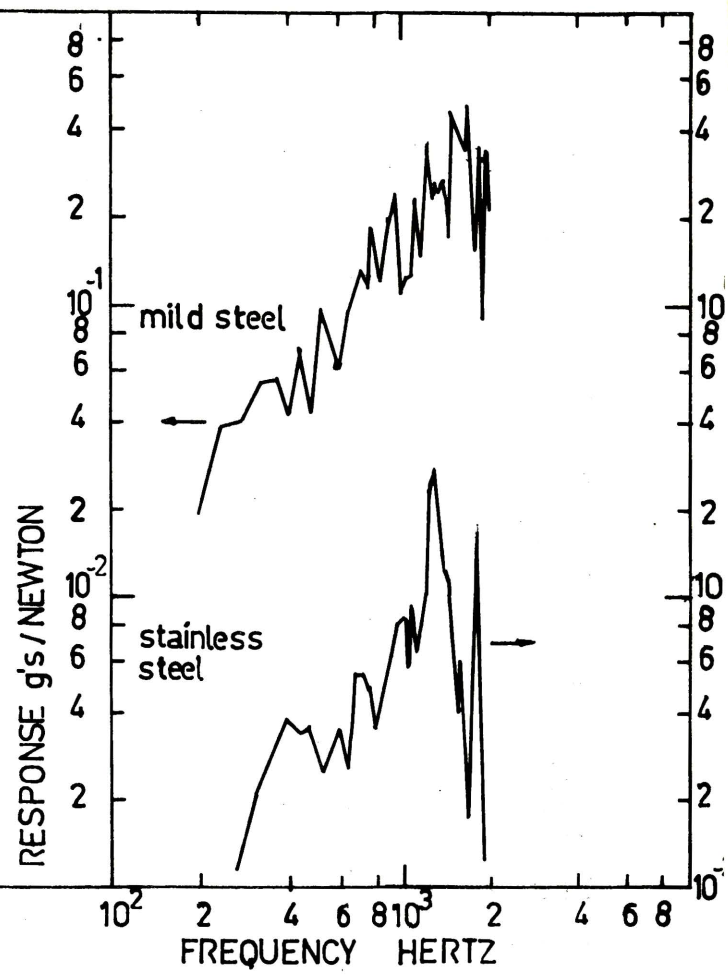

Figure 7. $|H_o(f)|$ for position 1 on the ram.

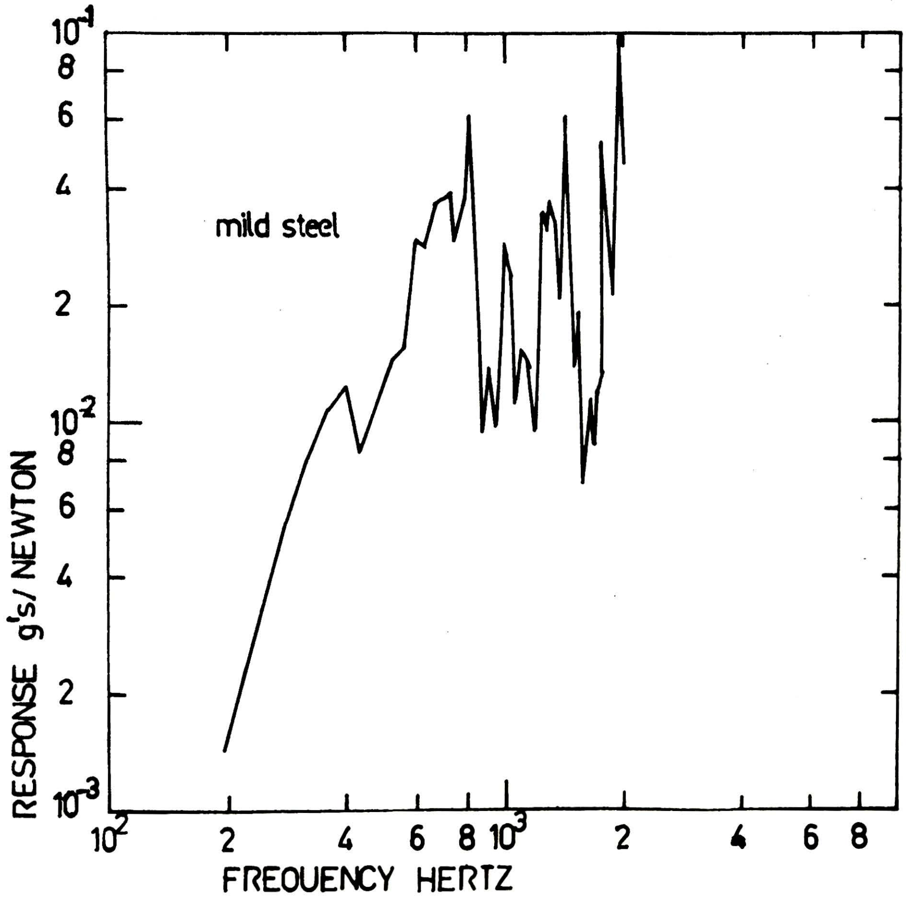

Figure 8. $|H_o(f)|$ for position 4 on the base plate.

amplitude between the shaker results and the blanking results. In Figure 7 the results for |Ho(f)| for mild and stainless steels for position 1 are compared. The |Ho(f)| are qualitatively similar but the mild steel result tends to be of higher value than the stainless steel result. Also, a region of very high response exists between 1200 and ˙300 Hz for the stainless steel result. At first glance the position 1 shaker test result, Figure 5b, does not resemble the |Ho(f)| obtained from the punch press. However, there are similar frequency peaks at ≃ 700 Hz, 900 Hz and resembles qualitatively the shaker test results fiven in Figure 5a. Similar frequency peaks exist at ≃ 400 Hz, 650 Hz, 950 Hz, 1400 Hz and 2000 Hz. The |Ho(f)| for position 4 on the base plate is shown in Figure 8. Major spectral peaks exist at 650 Hz, 800 Hz, 950 Hz, 1200 Hz, 1500 Hz, 1800 Hz and 1900 Hz. The shaker test result for position 1 shown in Figure 4a has similar spectral characteristics.

5. Discussion and Conclusion

The |H(f)| obtained from shaker tests and the |Ho(f)| obtained from blanking tests are qualitatively similar for position 4 on the base plate and position 2 on the support plate. The results for position 1 on top of the ram gave similar frequency peaks but did not have a similar response form. As explained previously, the ram was in its upper postion during the shaker tests but during the blanking operation it was in its lowered position, so that apriori similar results for the transfer functions could not be expected. Thus, it would seem that the transfer functions for positions 4 and 2 are less sensitive to load and ram position than position 1.

The differences between the |Ho(f)| and |H(f)| could be explained by the four factors mentioned previously. For position 2 and position 4 the shaker analysis gave a reasonable prediction of the |Ho(f)|. However, for position 1 the shaker analysis only gave important frequencies and did not give a good prediction of the |Ho(f)|. Overall, the shaker analysis was a good first test to determine the vibrational response of the punch press.

References

1. Bruel & Kjaer 1970 - Application of B & K equipment to mechanical vibration and shock measurements.

2. R.G. White 1971 - Journal of Sound and Vibration 15, 147-161. Evaluation of the dynamic characteristics of structures by transient testing.

3. F. Kandianis 1971 - Journal of Sound and Vibration 15, 203-215. Frequency response of structures and the effects of noise on its estimates from the transient response.

4. P. Holmes and R. White 1972 - Journal of Sound and Vibration 25, 217-243. Data analysis criteria and instrumentation requirements for the transient measurement of mechanical impedance.

RECENT DEVELOPMENTS IN ACCELEROMETER CALIBRATION

J. A. Macinante
CSIRO Division of Applied Physics
National Standards Laboratory
Sydney, N.S.W.

SUMMARY

The object of this paper is to review the developments that have taken place since about 1960 in methods of calibrating small transducers of the types generally used for vibration and shock measurements. The basic methods and recent advances in rectilinear steady-state calibration are outlined and discussed. Steady-state methods and calibrators described include those recently developed at the Australian National Standards Laboratory for absolute calibration by optical interferometry, for comparison and transverse calibrations, and for calibrations at large displacements and low frequencies. The basis of shock calibration is indicated and recent developments discussed. The paper concludes with some general comments on accelerometer calibration requirements in Australia.

1. INTRODUCTION

Over the past few decades there have been marked changes in the nature and ranges of calibration required, in the techniques and equipment used, and in the appreciation of the importance of calibrating vibration measuring instruments. During this period small transducers have been developed to meet nearly all vibration and shock measurement requirements. With few exceptions the readings or records produced by the large and cumbersome instruments formerly used were interpreted on the assumption that the instrument, regardless of the complexity of its seismic suspension and its amplification and recording system, would behave as an ideal single-degree-of-freedom system. Its 'calibration factor' was simply calculated or based on a static magnification test. Recent dynamic calibrations of some of these instruments have indicated serious discrepancies between actual and calculated calibration data.

Today nearly all vibration measurements are made with small piezoelectric accelerometers, servo-accelerometers and electromagnetic velocity-type transducers, used with suitable electrical amplification, signal conditioning and recording equipment. The calibration of such transducers is the subject of the present paper. Much of the discussion will have some relevance to the calibration of larger transducers such as portable seismographs, and to proximity and other non-seismic transducers, but unless the context indicates otherwise the discussion refers to small seismic transducers. For brevity we shall use the term 'accelerometer' to denote any small acceleration-type transducer.

Vibration measurements may be made in a wide range of environments, hence it may be necessary to determine the influence of such factors as temperature, pressure, strain, acoustic and electrical fields on the sensitivities of the accelerometers used. An environmental factor that is commonly overlooked is transverse motion. For example, in vibration testing the accelerometer measuring the nominally rectilinear input motion is often subjected to trans components, likewise the accelerometers on the test object will almost certainly experienc some transverse excitation. Hence the transverse sensitivity of accelerometers must be determined so that correction may be made or uncertainties assessed.

The acceptance or rejection of a costly consignment of merchandise may depend on the behaviour (function, damage, survival) of a representative sample during or after shock testing. When the test results appear to call for rejection a dispute can be expected about the validity of the calibration of a piezoelectric accelerometer used under impact conditions.

At present there is active interest in the specification, for commercial purposes, of acceptable levels of vibration of rotating machinery, and consequently in the specification of calibration requirements for the instruments to be used for the measurements (Ref.1). Even where there is no contract or client involved, calibration may be of critical importance. For example, in using vibration analysis to diagnose the condition of machinery with the object of obtaining early warning of malfunction, so that unscheduled shut-down may be avoided, the clue to impending failure could be a small increase in the amplitude of a particular frequency component, and this increase may have occurred over an appreciable period of time. Uncertainty about the calibration and long term stability of the vibration measuring system could conceal the vital information.

As part of the world-wide concern for the environment, vibration pollution is beginning to attract more attention. A great deal of published information on the effects of vibration on human health, performance and comfort is of questionable value because of uncertainty about the validity of the measurements. In a recent critical review of the published work on human response to vibration, the authors (Ref.2, p.38) emphasise that the worth of measurement results cannot be appraised without adequate information about the equipment and its manner of use, and the method and range of its calibration.

The object of this paper is to describe the developments in accelerometer calibration since about 1960 when two comprehensive surveys of the available methods were published (Ref.3 and 4). Although accelerometers are not designed for specifically steady-state or shock measurement, the methods of calibration for the two types of measurement are best considered separately. The developments in steady-state calibration are reviewed in Sections 2 and 3, the latter describing methods developed at the Australian National Standards Laboratory (NSL). The important developments in shock calibration are outlined in Section 4, and the paper concludes with some general comments on the provisions for calibration in Australia.

2. DEVELOPMENTS IN STEADY-STATE CALIBRATION

The object of the calibration is to determine the relationship between the electrical output and the mechanical vibratory input, and to determine how that relationship varies over the frequency and amplitude ranges of interest, and over the ranges of the environmental factors that may be encountered when the equipment is used in practical situations. The output may be that of the accelerometer only, or that of a system comprising accelerometer, signal conditioning equipment and a meter or other output indicator. In this paper we are primarily concerned with the methods of generating the input motion and determining its characteristics.

A recent American National Standard (Ref.5) is a valuable guide to the selection of calibrations and tests that may be used to provide the technical information necessary to judge the suitability of a particular transducer for a specific measurement application.

2.1 Static Calibration in Earth's Field

An accelerometer that is capable of measuring an unvarying ('zero-frequency') acceleration can be calibrated in the range $\pm$ 1 g ($g = 9.8\ ms^{-2}$ = acceleration due to gravity) by supporting it with its sensitive axis in the vertical plane at angles in the range 0-180 deg. from the vertical. The usefulness of this form of calibration has been enhanced (Ref.6) with the development of servo accelerometers having a 'flat' frequency range extending from 0-100 Hz. This has made it possible for piezoelectric accelerometers to be compared dynamically in an overlapping frequency range (eg. 10-100 Hz) with servo accelerometers that have been calibrated in the earth's gravitational field.

2.2 Static Force Calibration

An accelerometer having a seismic element that is accessible can be calibrated statically by supporting the accelerometer with its sensitive axis vertical and loading the seismic mass with calibrated weights. The change in output of the accelerometer, which must be capable of measuring zero-frequency acceleration, is related to the acceleration calculated as the applied force divided by the seismic mass. This method has been applied (Ref.6) to the calibration of quartz accelerometers featuring near dc response. As the method calls for direct loading of the seismic element which is inaccessible to the normal user of the accelerometer, the method is of value primarily to the manufacturer.

2.3 Centrifugal Calibrators

The accelerometer is supported on a balanced horizontal table which can be rotated about a vertical axis with uniform angular velocity. The sensitive axis of the accelerometer is aligned radially so that the accelerometer is subjected to a constant acceleration determined by its radial position and the angular velocity. Again the method is applicable only to accelerometers having zero-frequency response. The development of precision centrifuges and associated calibration techniques has been stimulated by the demands of space exploration programmes. Recent publications describe precision centrifuges (Ref.7) and discuss improved techniques for the reduction of the test data (Ref.8). The important sources of error, apart from errors in the primary quantities radius and angular velocity, are concerned with the alignment of the sensitive axis and the radial positioning of the sensitive element of the accelerometer (Ref.9).

2.4 Steady-state Vibration Calibrators

Most calibration is done by imparting to the accelerometer a steady-state vibration which is defined by the amplitude (of displacement, velocity or acceleration) and the frequency. The frequency can be measured with more than adequate accuracy for calibration purposes with commercially available equipment and is not discussed further. The present Section is mainly concerned with methods of generating the input vibration; methods of determining its amplitude are discussed in Sections *2.5, 2.6*.

Ideally the input is an undistorted sinusoidal motion having no transverse components. Vibrators of the kinds designed for vibration testing purposes are commonly used to provide calibrating motion in those ranges where the performance of the vibrator has been found by appropriate measurements to be acceptable. Alternatively a vibrator may be modified or specifically designed to meet the more stringent requirements for use as a calibration input generator: recent examples are the replacement of a mechanical suspension with air bearings (Ref.10), the use of a ceramic moving element guided in air bearings (Ref.11), a calibrator (Ref.12) having two moving coils 1 m apart on a stiff rod and incorporating a magnetic suspension.

The United States National Bureau of Standards (NBS) has recently installed a computer-controlled calibration system (Ref.13) using Dimoff-type exciters (Ref.10,11) for steady-state calibrations at selected frequencies and acceleration levels. Electrodynamic vibrators designed as calibration input generators and incorporating calibrated reference accelerometers are now commercially available.

Another approach has been to use a commercial vibrator to drive a calibrating table or fixture designed to improve the quality of the motion and, if used at resonance, to increase the amplitude in the vicinity of a resonance frequency. The use of flexural elements for this purpose at frequencies below 1 kHz is mentioned in Section 3. At higher frequencies longitudinal resonances are preferable (Ref.14) because of undesirable twisting and rotational effects with flexural systems vibrating in modes higher than the fundamental. A uniform rod excited in longitudinal vibration offers a succession of discrete resonance frequencies which can serve as calibration points. In Ref.15 a method is described in which resistance strain gauges are bonded on the side of a bar electromagnetically excited in a longitudinal mode. The end displacement amplitude is measured by interferometry and subsequently an accelerometer is calibrated by attaching it to the end of the bar and using the calibrated strain gauges to determine the displacement. In Ref.16 a vibrator is described in which several materials (tungsten carbibe, butyl rubber, alumina) have been combined and driven by piezoelectric material so that the resonances of the component elements overlap to provide good motion over a wide frequency range. The displacement is measured by interferometry.

2.5 Optical Methods of Measuring Displacement Amplitude

In the well established methods a reference line (mark, feature) on the vibrating surface is observed through a microscope having an eyepiece scale or micrometer. With continuous illumination the line is seen as a band representing the peak-to-peak displacement. With intermittent illumination the line moves slowly across the scale if the light interruption frequency differs slightly from the vibration frequency (f). With light interruption frequency 2f and phase adjustment, an image of the line at each extremity of the displacement can be observed on the scale. Alternatively by fixing a scale on the accelerometer being calibrated (Ref.17) the displacement is read on a double image of the scale.

Recent developments have included an electro-optical device (Ref.18) which tracks and measures the displacement of a suitable target on the vibrating object, and an image-shearing eyepiece (Ref.19) in which rotation of a prism separates the image of the object into red and green components: the rotation is calibrated so that displacements in the object plane, corresponding to the separation of the two images, may be determined.

In a new calibrator (Ref.20), attached to the accelerometer is a slit assembly which forms a light image that is transmitted through an optical system and arranged to fall centrally on a position-sensitive photo cell. The slit image oscillates across a central dividing line. The photo current is proportional to the area of illumination of each side of the central line and is calibrated in terms of known static displacements of the accelerometer.

Oscillating moire fringes, which are produced by relative motion of finely spaced lines on gratings, have a spacing much larger than the grating line spacing thereby providing optical magnification. Refs. 21, 22 describe the application of moire fringes in vibration measurement and accelerometer calibration.

2.6 Interferometric Methods

In accelerometer calibration at the higher frequencies (above say 1 kHz) very small displacements, of the order of light wavelengths, must be determined. For this reason there has been continuing interest in methods in which the surface whose displacement amplitude is to be measured is incorporated in one or other of the classical forms of interferometer. As the vibration amplitude is varied, changes take place in the interference fringe pattern; by applying optical theory the changes can be interpreted to measure the amplitude in terms of the wavelength (λ) of the light used. A useful review of methods developed up to 1964 is given in Ref. 23.

'Full field' extinction techniques using two-beam interferometry are suitable for measuring amplitudes of a few λ at frequencies of some kHz. This method was used for many years at the United States NBS for primary calibrations at high frequencies (Ref.4), and is used in Russia (Refs.12,23) and Germany (Ref.24). Fringe disappearance techniques have also been applied at larger displacement amplitudes : observations were made beyond the 40th disappearance so that the amplitude range covered by interferometry would overlap that of observations using the microscope/stroboscope technique (Ref.14); satisfactory agreement was indicated.

When a multiple beam system is used the vibration of one of the surfaces in the interferometer causes a corresponding vibration of a family of narrow, clearly defined fringes. At first observational techniques were simply carried over from the earlier optical methods: with continuous illumination the broadening of the fringes in relation to the fringe spacing was used to measure amplitudes up to $\lambda/4$, and with intermittent illumination the fringes could be counted visually as they moved slowly past a reference line (Ref.25).

More recently the variations in light flux as the fringes pass a slit aperture are detected photoelectrically and the fringes counted by electronic methods. Ref. 26 proposes an interesting alternative to counting the total number of fringes generated in the peak-to-peak displacement (2A) of a surface oscillating with motion $A \sin \omega t$. The maximum velocity (v) of the surface is derived from the least time interval between the occurrence of two fringes, and the displacement amplitude is calculated using $v = A\omega$.

A quite different approach is to use a calculated characteristic relating the displacement amplitude with a selected component frequency of the photo current that is harmonically related to the vibration frequency. This is discussed further in Section *3.1*.

2.7 Reciprocity Method

This is an indirect and rather complicated method of primary calibration applicable only to transducers satisfying certain criteria (reversibility, linearity). The theory and experimental procedure are well documented (Refs.3,4). The method has been used for many years by NBS to calibrate velocity transducers incorporated in primary vibration calibrators. During recent years the method is being applied to acceleration transducers, for example Refs. 11, 27.

2.8 Comparison Calibration

The method most widely used in vibration laboratories is comparison calibration, in which the test and reference accelerometers are subjected to the same vibration and their outputs compared. A group of five papers published in 1967 (Ref.28) describes developments in equipment and techniques for comparison calibration, a noteworthy advance being the development of reference accelerometers designed so that the test accelerometer can be attached directly to the reference accelerometer.

In practice, to avoid errors from distortion of the axial motion and from the influence of unwanted transverse motion, the comparison is made only in those frequency ranges where the calibrator is known, from supplementary experimental investigations, to provide satisfactory input motion. A new approach, in which a resonance fixture is interposed between the vibrator and the back-to-back pair of accelerometers is described in Section *3.2*.

2.9 Transverse Calibration

The transverse sensitivity ratio is the ratio of the output of the accelerometer when oriented with its sensitive axis transverse to the direction of the input motion to the output when the sensitive axis is aligned in the direction of the same input motion (Ref.3). In the method generally used (Ref.4) it is first necessary to determine the transverse motion of the calibrator, e.g. with proximity probes; transverse calibrations are then made only in ranges of frequency where transverse motion of the vibrator would introduce small error.

An interesting alternative to this is a technique (Ref.29) which identifies the components of the test accelerometer output that are caused by input motion in other than the desired direction. If certain idealizing assumptions are made about the nature of the transverse response, this technique provides a full polar plot of transverse sensitivity from observations at only four orientations of the accelerometer around the sensitive axis while subjected to vibration normal to that axis.

The transverse sensitivity of an accelerometer can be determined by comparison with the known transverse characteristics of a reference accelerometer. For example (Ref.30), the two accelerometers are fixed at opposite ends and coaxial with an octagonal prism driven normal to its axis, and the accelerometer outputs are compared at the eight angular settings. A new method in which excitation can be applied in any transverse direction without resetting is described in Section *3.3*.

2.10 Calibration in Various Environments

Calibrations and tests may be necessary in special environments to verify the environmental extremes to which the accelerometer may be exposed without permanent change of its characteristics, or to evaluate the error that could arise when the accelerometer is operated in a particular environment. At present there are no generally accepted methods covering all the environmental factors: methods are proposed in Ref. 5 for temperature sensitivity, strain sensitivity, magnetic sensitivity, transient temperature effects on piezoelectric accelerometers, acoustic sensitivity and cable effects.

3. NSL DEVELOPMENTS IN STEADY-STATE CALIBRATION

During the period of review beginning about 1960 the following new techniques and calibrators have been developed in the CSIRO Division of Applied Physics, National Standards Laboratory.

3.1 Interferometric Methods

The peak-to-peak displacement of the vibrating plate in a multiple beam interferometer can be determined by counting interference fringes passing across a slit aperture. Although visual counting of stroboscopically slowly moving multiple beam fringes had been used at NSL for the calibration of a vibrometer (Ref.25), electronic counting obviously was preferable. J. L. Goldberg investigated the frequency spectrum of the photoelectric signal from an oscillating fringe pattern (Ref.31), and drew attention to the basic difficulty: the vibration velocity determines the minimum bandwith of the photo-detector output circuit that is necessary to ensure that satisfactory pulses are produced for counting, and this conflicts with the requirement of restricted bandwith to mitigate the effects of 'noise' in the photo detector circuit.

Goldberg later (Ref.32) devised a method of overcoming this difficulty by using an interferometer in which the surfaces that produce the optical interference effects are designed to function also as the electrodes of an electrical capacitor. Sinusoidal displacement is imparted to one surface and a waveform representing the corresponding capacitance change recorded on a chart. The capacitance change is then calibrated in terms of the light wavelength by slowly moving the surface and recording on the chart the pulses corresponding to passage of fringes past the photo-detector.

Concurrently with the foregoing studies Goldberg had been investigating a new form of calculated characteristic (Ref.33) relating the vibratory displacement with the signal from a photoelectric detector exposed, through a slit aperture, to the optical field across which the multiple beam fringe pattern is vibrating. As the vibration amplitude is continuously increased from zero the amplitude of a selected component frequency in the photo current (e.g. the second harmonic of the vibration frequency) passes through a succession of well defined maxima. These can be observed with a pointer-on-scale meter and are directly related to the vibration amplitude. This calculated characteristic is illustrated and its application discussed in another paper at this Conference (N.H. Clark, Ref.34).

In an interferometer in which two metal coated surfaces function both as a capacitor and as the optical surfaces of the interferometer, correction may be necessary for the effects of air compression, which can produce changes in both the dielectric constant and the refractive index of the air between the plates. Investigations by Goldberg (Ref.35) have shown that the effects are unimportant in steady-state oscillatory conditions, but could be significant for transient motions.

The way in which the foregoing basic studies of vibration measurement by interferometry have been implemented in a calibrator for the absolute calibration of reference accelerometers has been described by Goldberg, (Ref.36). The further development of this interferometer and in the techniques of its use since the work described in Ref. 36 is the subject of the abovementioned paper by N.H. Clark. The vibrating head of this calibrator is shown schematically in Fig. 1.

3.2 Comparison Calibrator

When a comparison calibration is made with the test and reference accelerometers back-to-back on the table of an electrodynamic vibrator, transverse motion of the table can introduce errors. A calibrator has been developed (Ref.37) in which transverse motion is restrained by using annular spring diaphragms to support a capsule carrying the two accelerometers (Fig.2). The rectilinearity of the driving vibrator thereby becomes of secondary importance. By varying the material, thickness and outer clamping diameter of the diaphragms a large number of resonance frequencies is provided: in the prototype described in Ref. 37 more than 200 discrete frequencies are available for calibrations in the range 98 - 520 Hz. With this design, if the maximum peak-to-peak displacement is limited to 0.25 mm, the total harmonic distortion does not exceed one per cent. This displacement limit, applied in the frequency range 98 - 520 Hz, corresponds to an acceleration range of 50 - 1350 ms^{-2} (or 5 - 138 g). In this range the transverse displacement as observed with a proximity probe is less than one per cent of the axial displacement. A further development now in progress is expected to increase the frequency range to about 1 kHz which is probably the practical limit for this design.

A simpler and portable version of this type of calibrator is being developed for use at test sites for spot-check comparison calibrations at a few particular frequencies.

3.3 Transverse Calibrator

A new method of transverse calibration has been devised (Ref.38) which allows the transverse response characteristics of an accelerometer to be determined without the resetting that is necessary in methods currently used. The test accelerometer is attached to the upper end surface of a vertical cantilever beam of circular cross section clamped near its lower end (Fig.3). The beam is driven in transverse flexural vibration by two small electromagnetic vibrators as shown. These are driven through a dual amplifier from a single oscillator adjusted to the frequency of resonance of the mechanical system. By adjusting the relative amplitudes of the two driving forces the test accelerometer can be subjected to a transverse acceleration of constant magnitude in any direction in the plane of its mounting face.

The amplitude of the transverse acceleration, typically 200 ms^{-2} (20 g) at 100 Hz, is determined from its two orthogonal components which are measured with a pair of monitoring accelerometers fixed as shown near the test accelerometer. The outputs of these two accelerometers are connected to an oscilloscope screen so that an analogue of the transverse motion is displayed as a Lissajous figure. Errors arising from the fact that the transverse motion is not strictly rectilinear and that the monitoring accelerometers are themselves subject to transverse excitation have been shown to be relatively unimportant. Further development in progress will provide a more convenient method of clamping and extend the frequency range.

3.4 Calibrators for Large Displacements at Low Frequencies

The following calibrators have been designed for the calibration of relatively large transducers, or sets of transducers as used in multi-channel measurements of the vibrations of large structures at frequencies below 10 Hz and displacement amplitudes up to 10 mm.

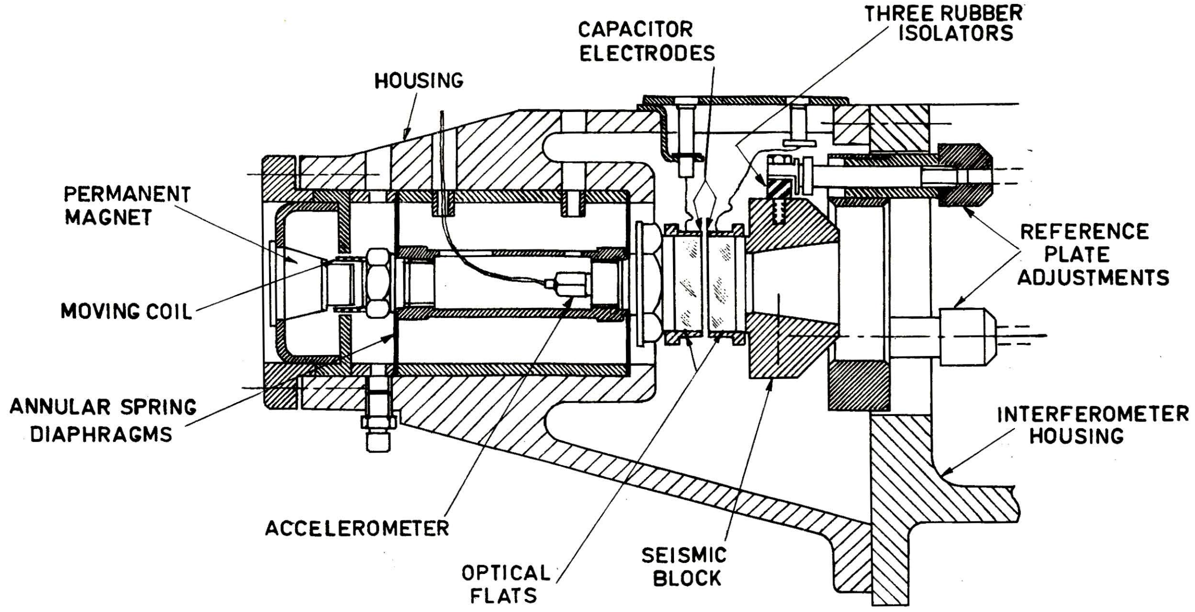

FIG. 1
VIBRATING HEAD OF INTERFEROMETRIC CALIBRATOR

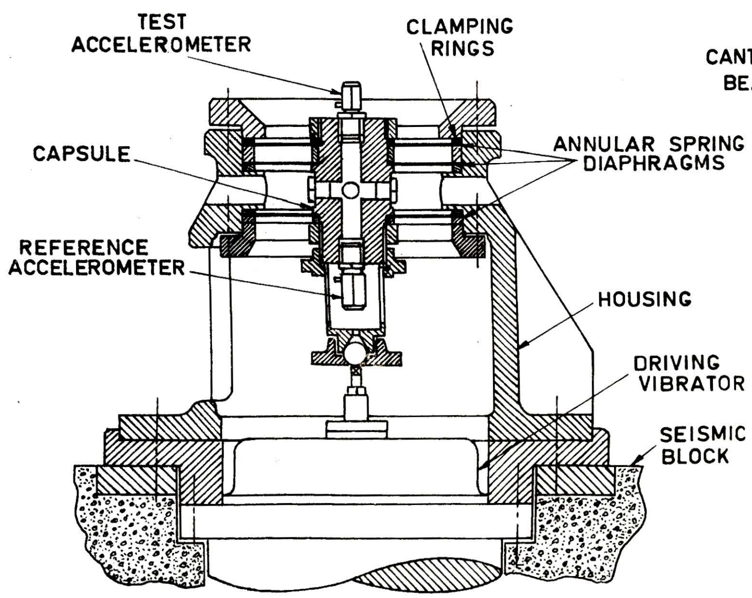

FIG.2
COMPARISON CALIBRATOR

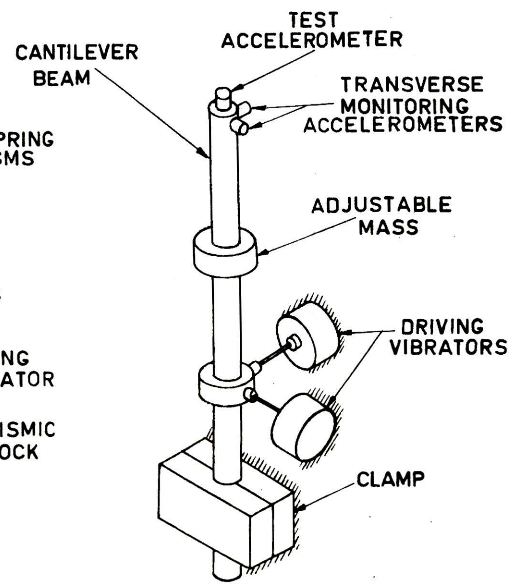

FIG. 3
TRANSVERSE CALIBRATOR

A vertical motion table (Ref.39) is supported on a helical tension spring and guided in air bearings. The displacement in free vibration is determined with a variable-area type of capacitance transducer which is calibrated in situ by a static displacement method. This system provides a rectilinear calibrating motion of large displacement and good waveform which, over small intervals of time, is quasi steady-state. For horizontal calibrations in a similar range a table 60 × 30 cm, supported and guided in air bearings is being developed for a test load of mass 50 kg. The input motion is determined with reference accelerometers or by direct optical methods.

4. SHOCK CALIBRATION DEVELOPMENTS

The results of steady-state calibration of accelerometers are commonly used in the reduction of shock test data. Even if the frequency range of the steady-state calibration is wide enough to cover the Fourier components of the shock pulse to be measured the validity of applying the steady-state calibration data is not assured, because the loading and stressing of the sensitive element of the accelerometer under shock conditions differs from that applied in the steady-state calibration. Hence there has been continuing investigation of methods of calibrating accelerometers under impact conditions.

The two basic methods of generating the input for shock calibration are the ballistic pendulum and the drop impact tester. In each, although the configurations and details differ, the test accelerometer is attached to a mass which strikes or is struck by another mass. The shape, peak value and duration of the acceleration pulse are varied by changing the masses, materials and geometry of the impacting bodies.

More recent methods of generating the input pulse include: an electrodynamic method (Ref.40) in which energy stored in a bank of capacitors is discharged through a coil so that the time-varying magnetic field causes rapid acceleration of a conductor (projectile) carrying the test accelerometer; an air gun (Ref.41) which ejects a projectile to impact an anvil carrying the test accelerometer which experiences shock acceleration of the order 10^5 g. Another method of generating shock acceleration in this high range makes use of mechanical amplification of a stress wave travelling in a bar having an exponentially decreasing cross section (Ref.42). There is growing interest in the use of electromagnetic and hydraulic vibrators as pulse generators (Ref.43), and the use of on-line digital computers in conjunction with electrodynamic exciters to produce specific transient waveforms (e.g. Refs.44, 45).

4.1 Velocity Change Method

In the 'velocity change' method of shock calibration the impact imparts to the accelerometer plus its supporting mass a velocity change which is measured usually with photo-detectors arranged at known spacings. The magnitude of the acceleration pulse is deduced by equating the velocity change to the time integral of the acceleration over the duration of the pulse; the integral is usually derived from a recorded trace, or by electrical integration, of the test accelerometer output.

This procedure involves the usually tacit assumption of amplitude linearity, i.e. that the sensitivity of the accelerometer is constant throughout the range of acceleration involved in the calibration. The error that can arise from amplitude non-linearity of the accelerometer is discussed in Refs. 40, 41.

In any method that makes use of the output of the test accelerometer as part of the data for determining the input calibrating motion the question arises: is the output pulse shape presented by the accelerometer a true replica of the acceleration input pulse? Brennan (Ref.46) investigated this in 1958 by delivering the impulse through an elastic bar on which resistance strain gauges were bonded to gain an independent record of the pulse shape. With this approach suspicion shifts to the strain gauges; the validity of the correlation of surface strain with the motion of the end of the bar must be established. In a similar more recent study (Ref.47) it was claimed that satisfactory correlation was obtained between the surface strain measured with resistance strain gauges on the bar and the end-plane acceleration.

4.2 Impact Force Measurement

An alternative to the velocity change method involves measurement of the force associated with the impact. In Kistler's drop impact calibrator (Refs.6,40) a small carriage carrying the accelerometer falls onto a piezoelectric force transducer; the peak deceleration is calculated as the peak force divided by the total impacting mass. Ref. 40 describes the use of a strain gauge force transducer which is impacted by a ballistic pendulum carrying the test accelerometer. With methods involving the measurement of the impact force, uncertainty arises concerning the validity of applying static load calibration data when the force cell is used under impact conditions.

4.3 Comparison Calibration

A method of comparison calibration of shock accelerometers made possible by the availability of high speed digital computers is that of Favour (Ref.48) in which the test accelerometer and a shock calibrated reference accelerometer are subjected to an impulse, and a digital computer calculates the ratio of the Fourier integral transforms of the output signals.

4.4 Doppler-Interferometric Method

A new method developed at NBS (Ref.49) is the most important of the recent developments because the relevant input, which is a purely kinematic quantity, is determined directly in terms of length and time units; that is, without dependence on intermediary determinations of other physical quantities (such as mass, force, velocity change subsequent to the impact) and quite independently of the output of the accelerometer that is being calibrated. The surface on which the accelerometer is mounted is the moving reflector in a laser-Doppler interferometric system. When the surface is subjected to a shock motion the velocity-time history of that motion is determined from the Doppler shift of the system frequency.

5. CONCLUDING REMARKS

Developments in steady-state calibration since 1960 have produced new electrodynamic calibrators having wider frequency ranges and reduced transverse motion, 'pick-a-back' reference accelerometers to which the test accelerometer can be directly attached for comparison calibration, new interferometric techniques for absolute calibration, and new types of comparison calibrator and transverse calibrator.

In shock calibration the velocity-change method has been re-examined because of dissatisfaction with the practice of accepting the output of the test accelerometer as data for determining the input pulse shape. In the alternative approach involving the direct measurement of the force/time history of the calibrating impact, there is concern about the validity of relating the force that is effective in the dynamic event with the statically determined standard of force. In the face of the abovementioned difficulties the new method of shock calibration developed at the United States NBS, which determines the velocity/time history of the calibrating impulsive motion directly in terms of the light wavelength and frequency standards, is of major importance.

In Australia the various vibration laboratories and consultants generally use reference accelerometers of overseas manufacture, mostly having calibration traceability to NBS. While this is satisfactory in principle, it does involve considerable inconvenience for the user if the accelerometer must be returned overseas periodically for recalibrations. For this reason NSL has been developing the necessary facilities in Australia.

Some two years ago NSL made its first interferometric calibration of a reference accelerometer for an Australian laboratory. The range covered was 200 Hz - 1 kHz with accelerations in the range 3.9 - 16.6 ms^{-2}. The comparison calibrator mentioned in Section *3.2* will be in service in 1974 for the calibration of reference accelerometers in the range 100 - 500 Hz. Transverse calibrations can be made with the prototype calibrator mentioned in Section *3.3*. Continued development is in progress to extend the frequency and amplitude ranges of steady-state calibration and to provide facilities for the calibration of accelerometers under impact conditions.

(40) KELLEY, R.W. - Calibration of shock accelerometers. *Instrum.Soc.Am.22nd Ann.ISA Conf.* Preprint No. M18-2-MESTIND-67, 16 p., 1967.

(41) DOVE, R.C., DUGGIN, B.W. and BUTLER, R.I. - Calibration and evaluation of accelerometers in the 10 000 g to 100 000 g range. *Instrum.Soc.Am.20th Ann.ISA Conf.* Preprint No. 17.3-1-65, 13 p., 1965.

(42) BELL, R.L. - Development of 100 000 g test facility. *Shock and Vib.Bull.* 42, Pt.2, pp.205-14, 1969.

(43) OTTS, J.V. and HUNTER, N.F. - Shock reproduction on shakers. *Instrum.Soc.Am.24th Ann. ISA Conf.* Preprint No. 69-561, 6 p., 1969.

(44) FAVOUR, J.D., LEBBRUN, J.M. and YOUNG, J.P. - Transient waveform control of electromagnetic test equipment. *Shock and Vib.Bull.* 40, Pt.2, pp.157-71, 1969.

(45) MOSER, J.R. and GARNER, D. - An improved electrodynamic shaker shock technique. *Shock and Vib.Bull.* 40, Pt.2, pp.173-81, 1969.

(46) BRENNAN, J.N. and NISBETT, J.S. - Direct method of accelerometer calibration. *J.Acous.Soc.Am.* Vol.30, No.1, pp.41-46, 1958.

(47) CANNON, J.E. and RIMBEY, D.H. - Transient method of calibrating a piezoelectric accelerometer for the high g-level range. *Am.Soc.Mech.Engrs.* Paper 71-Vibr.-43, 7 p., 1971.

(48) FAVOUR, J.D. - Calibration of accelerometers by impulse excitation and Fourier integral transform techniques. *Shock and Vib.Bull.* 37, Pt.2, pp.17-27, 1968.

(49) BALLARD, L.D., EPSTEIN, W.S., SMITH, E.R. and EDELMAN, S. - Optical FM system for measuring mechanical shock. *J.Res.Natn.Bur.Stan.-C.Engng. and Instrum.* Vol.73C, Nos.3,4, pp.75-78, 1969.

Noise, Shock & Vibration Conference, 1974 Monash University, Melbourne

ACOUSTIC RADIATION FROM PIPES WITH INTERNAL TURBULENT GAS FLOWS

M. K. Bull
Department of Mechanical Engineering
University of Adelaide
Adelaide, S.A.

D. C. Rennison
Department of Mechanical Engineering
University of Adelaide
Adelaide, S.A.

SUMMARY -

A procedure is developed for calculating the dynamic response of a thin-walled cylindrical shell to the random pressure field generated by an internal turbulent flow (either a boundary layer or fully-developed pipe-flow). In particular a general expression is obtained for the power spectral density of the surface displacement of the vibrating structure averaged over the vibrating surface. Expressions are given for the joint acceptance of a cylindrical shell, which are consistent with a statistically homogeneous response around the circumference of the cylinder. Conditions under which hydrodynamic coincidence of turbulent pressure excitation and structural response can occur are discussed and illustrated by appropriate joint acceptance curves. An expression is derived for the spectral density of the acoustic power radiation on the assumption that the radiation originates from only supersonic resonant shell modes, and that for these modes the radiation ratio is unity. The roles of the structural parameters (ratios of shell length and radius to thickness, elastic properties of the shell) and both hydrodynamic and acoustic coincidence frequencies are illustrated. Some typical radiation spectra are given.

1. INTRODUCTION

To estimate the acoustic power radiation from a pipe through which turbulent fluid is flowing, it is necessary to consider first the vibrational response of the pipe to the random fluctuating pressure field which a turbulent boundary layer or fully developed turbulent pipe-flow produces on the pipe wall, and second the sound field generated in the fluid outside the pipe by vibration of the pipe walls. Clearly, the acoustic power radiation will depend both on how well the properties of the turbulent pressure field match the vibrational properties of the pipe (that is, the efficiency of the pressure field in producing vibration) and on how well this vibration of the pipe wall couples with the external fluid (that is, the radiation efficiency of the vibrating surface). Both these aspects of the sound generation process will be examined.

For the purposes of analysis the pipe is modelled as a thin cylindrical shell with simply supported ends. The calculation of the statistical properties of the vibrational response is based on the normal mode method of generalised harmonic analysis as developed by Powell[1] in particular. This approach has been quite widely used previously to obtain the vibrational response of both flat plates and, to a lesser extent, cylindrical shells to acoustic and hydro-dynamic pressure fields. The calculation procedures are lengthy, and in previous work various approximations have been made to make them more tractable. This has frequently led to short-comings, many of which we believe are avoided in the present work.

For the calculation of the acoustic power radiated from the vibrating pipe wall a statistical approach is used. It is assumed that the only significant contribution to the acoustic power will come from resonant modes, and, further, that it will be dominated by the supersonic modes (that is, those modes for which the wave speed in the shell is greater than the acoustic wave speed in the fluid surrounding the shell). In fact the calculations are made on the basis that only the supersonic modes produce acoustic radiation, and that for these modes the radiation ratio (defined later) is unity. This procedure requires a modification of the overall vibrational response calculation; for this purpose it is necessary to calculate the mean square response of the shell for supersonic modes only.

2. GENERAL THEORY OF THE DYNAMIC RESPONSE OF A STRUCTURE TO A RANDOM PRESSURE FIELD

For a structure with N independent normal modes (uncoupled and orthogonal), the total displacement of the structure at a point $\underset{\sim}{r}$ on it at time t, $\zeta(\underset{\sim}{r},t)$, is given by

$$\zeta(\underset{\sim}{r},t) = \sum_{\alpha=1}^{N} \zeta_\alpha(t)\psi_\alpha(\underset{\sim}{r}), \tag{1}$$

where ζ_α is the generalised co-ordinate (the displacement amplitude of vibration at the reference point) corresponding to the α th mode, and $\psi_\alpha(\underset{\sim}{r})$ the mode shape. In these circumstances the Lagrange equations yield N independent equations of the form

$$M_\alpha\ddot{\zeta}_\alpha + C_\alpha\dot{\zeta}_\alpha + K_\alpha\zeta_\alpha = Q_\alpha(t), \tag{2}$$

one for each mode, where M_α, C_α, K_α, and Q_α are, respectively, the generalised mass, damping, stiffness and force associated with the α th mode. The undamped natural (radian) frequency of the α th mode is $\omega_\alpha = (K_\alpha/M_\alpha)^{\frac{1}{2}}$.

The Fourier transform of equation (2) leads to the relation between the Fourier spectra of the displacement amplitude and the generalised force (Powell[1]), and consequently to the following expression (see Powell [1] and Richards and Mead[2], chapter 14) for the power spectral density, $\phi_\zeta(\underset{\sim}{r},\omega)$, of the displacement amplitude:

$$\phi_\zeta(\underset{\sim}{r},\omega) = \sum_\alpha \frac{\psi_\alpha^2(\underset{\sim}{r})}{|Z_\alpha(\omega)|^2} \int_S dS(\underset{\sim}{r}_1)\psi_\alpha(\underset{\sim}{r}_1) \int_S dS(\underset{\sim}{r}_2)\psi_\alpha(\underset{\sim}{r}_2)\phi_p(\underset{\sim}{\xi},\omega)$$

$$+ \sum_\alpha \sum_{\substack{\beta \\ \alpha\neq\beta}} \frac{\psi_\alpha(\underset{\sim}{r})\psi_\beta(\underset{\sim}{r})}{Z_\alpha(\omega)Z^*_\beta(\omega)} \int_S dS(\underset{\sim}{r}_1)\psi_\alpha(\underset{\sim}{r}_1) \int_S dS(\underset{\sim}{r}_2)\psi_\beta(\underset{\sim}{r}_2)\phi_p(\underset{\sim}{\xi},\omega). \tag{3}$$

Here S is the area of the vibrating surface, Z_α is given by

$$Z_\alpha(\omega) = M_\alpha(\omega_\alpha^2 - \omega^2 + iB_\alpha\omega), \tag{4}$$

where $B_\alpha = C_\alpha/M_\alpha$, and ϕ_p is the cross spectral density of the pressure field. The pressure field is assumed to be homogeneous and stationary, with a space-time covariance

$$Q_p(\underset{\sim}{\xi},\tau) = \overline{p(\underset{\sim}{r},t)p(\underset{\sim}{r}+\underset{\sim}{\xi}, t+\tau)}, \tag{5}$$

where the bar indicates a time average. Its cross spectral density is therefore

$$\phi_p(\underset{\sim}{\xi},\omega) = \frac{1}{2\pi}\int_{-\infty}^{\infty} Q_p(\underset{\sim}{\xi},\tau)e^{-i\omega\tau}d\tau. \tag{6}$$

[Note that in this work power spectral densities are defined for both positive and negative frequencies. So, for example,

$$\overline{\zeta^2(\underset{\sim}{r},t)} = \int_{-\infty}^{\infty} \phi_\zeta(\underset{\sim}{r},\omega)d\omega. \quad] \tag{7}$$

Since the narrow-band space-time correlation coefficient of the pressure field at frequency ω is given by

$$R_p(\underset{\sim}{\xi},\tau;\omega) = \frac{|\phi_p(\underset{\sim}{\xi},\omega)|\cos(\omega\tau + \delta)}{\phi_p(\omega)}$$

(see Bull, Wilby and Blackman[3]), equation (3) can be re-written as

$$\phi_\zeta(\underset{\sim}{r},\omega) = \phi_p(\omega)S^2\Big[\sum_\alpha \frac{\psi_\alpha^2(\underset{\sim}{r})j^2_{\alpha\alpha}(\omega)}{|Z_\alpha(\omega)|^2} + \sum_{\substack{\alpha\ \beta\\ \alpha\neq\beta}}\sum \frac{\psi_\alpha(\underset{\sim}{r})\psi_\beta(\underset{\sim}{r})j^2{}_{\alpha\beta\tau}(\omega)}{|Z_\alpha(\omega)||Z_\beta(\omega)|} \Big] , \qquad (8)$$

where the power spectral density of the pressure field $\phi_p(0,\omega)$ has been written simply as $\phi_p(\omega)$. Of the two joint acceptances $j^2{}_{\alpha\beta\,\tau}$ we need define only the first; it is

$$j^2{}_{\alpha\alpha}(\omega) = \frac{1}{S^2}\int_S dS(\underset{\sim}{r}_1)\psi_\alpha(\underset{\sim}{r}_1) \int_S dS(\underset{\sim}{r}_2)\psi_\alpha(\underset{\sim}{r}_2)R_p(\underset{\sim}{\xi},0;\omega). \qquad (9)$$

If equation (8) is averaged over the whole surface of the structure and account taken of the orthoganality of the resonant modes, the average of the second term is zero and we obtain

$$[\phi_\zeta(\omega)]_{AV} = \phi_p(\omega)S^2\sum_\alpha \frac{[\psi_\alpha{}^2(\underset{\sim}{r})]_{AV}\ j^2{}_{\alpha\alpha}(\omega)}{|Z_\alpha(\omega)|^2} \quad . \qquad (10)$$

If equation (7) is also averaged over the surface of the structure, the result is

$$[\overline{\zeta^2}]_{AV} = \int_{-\infty}^{\infty} [\phi_\zeta(\omega)]_{AV}d\omega = S^2\sum_\alpha[\psi_\alpha{}^2(\underset{\sim}{r})]_{AV} \int_{-\infty}^{\infty} \frac{\phi_p(\omega)j^2{}_{\alpha\alpha}(\omega)}{|Z_\alpha(\omega)|^2}\, d\omega. \qquad (11)$$

From equation (10) a more convenient approximate expression for $[\phi_\zeta(\omega)]_{AV}$ can be obtained. For a narrow frequency-band, of width $\Delta\omega$, centred on ω, we can write

$$[\phi_\zeta(\omega)]_{AV} \simeq \frac{1}{\Delta\omega} \int_{\omega-\Delta\omega/2}^{\omega+\Delta\omega/2} [\phi_\zeta(\omega')]_{AV}d\omega'$$

$$= \frac{S^2}{\Delta\omega} \int_{\omega-\Delta\omega/2}^{\omega+\Delta\omega/2} \phi_p(\omega')\sum_\alpha \frac{[\psi_\alpha{}^2(\underset{\sim}{r})]_{AV}j^2{}_{\alpha\alpha}(\omega')}{|Z_\alpha(\omega')|^2}\, d\omega' \qquad (12)$$

The response of a lightly damped structure in this frequency band will be dominated by those resonant modes whose natural frequencies are within the band. For each of these modes $1/|Z_\alpha|^2$ rises from a small value to a large peak and again falls off to a small value within the band. On the other hand, for a given mode, we can expect ϕ_p and $j^2{}_{\alpha\alpha}$ not to vary significantly over the small bandwidth. We therefore make the approximation

$$\frac{1}{|Z_\alpha(\omega)|^2} \simeq \delta(\omega_\alpha) \int_0^\infty \frac{d\omega}{|Z_\alpha(\omega)|^2} = \frac{\pi Q_\alpha\delta(\omega_\alpha)}{2M_\alpha{}^2\omega_\alpha{}^3}\ , \qquad (13)$$

where $Q_\alpha = \omega_\alpha/B_\alpha$ is the damping factor for the α th mode, and the value of the integral is that given by Crandall[4]. Thus,

$$[\phi_\zeta(\omega)]_{AV} \simeq \frac{\pi S^2\phi_p(\omega)}{2\omega^3\Delta\omega} \sum_{\alpha(\Delta\omega)} \frac{[\psi^2{}_\alpha(\underset{\sim}{r})]_{AV}j^2{}_{\alpha\alpha}(\omega)Q_\alpha}{M_\alpha{}^2} \qquad (14)$$

where $\alpha(\Delta\omega)$ indicates that the summation is confined to modes with natural frequencies in the band being considered.

The joint acceptance is completely defined by either the mode number α or the wave vector; or, equivalently, by θ, the angle the wave vector for a particular mode makes with the co-ordinate axes, and the frequency. For a structure which has a very large number of resonant modes in any frequency band we can regard $j^2{}_{\alpha\alpha}$ as a continuous function $j^2(\omega,\theta)$ of θ and ω.

In this case we can also introduce a continuous modal density function $n(\omega,\theta)$ representing the number of resonant modes per unit frequency and per unit wave vector angle. The parameters $[\psi^2_\alpha(\underset{\sim}{r})]_{AV}$ and Q_α can be treated similarly. This allows the summation in equation (14) to be replaced by an integral and we obtain

$$[\phi_\zeta(\omega)]_{AV} \simeq \frac{\pi S^2\phi_p(\omega)}{2\omega^3}\int_\theta \frac{[\psi^2_\alpha(\underset{\sim}{r})]_{AV}Q(\omega,\theta)j^2(\omega,\theta)n(\omega,\theta)}{M_\alpha^2}\,d\theta, \tag{15}$$

where the integration is to be taken over all possible θ values for a particular ω. Integratio of equation (15) over ω will give the result for $[\zeta^2]_{AV}$ corresponding to equation (11).

3. DYNAMIC RESPONSE OF A CYLINDRICAL SHELL TO INTERNAL TURBULENT FLOW

We consider a cylindrical shell of length ℓ and radius a. The x co-ordinate is along the shell surface and parallel to the axis; the y co-ordinate is in the circumferential direction around the shell surface. Since the results for shells with simply supported and fixed ends will not be significantly different, except perhaps at low frequencies, we confine attention to the former.

In order to make use of equation (15) to evaluate the mean square displacement of the shell averaged over its surface, we require the mode shapes, the undamped natural frequencies of the shell modes, and the power spectral density and narrow band space-time correlations (or, what amounts to the same thing, the cross spectral density) of the turbulent pressure field.

3.1 The pressure field

Many studies have been made of the statistical properties of the fluctuating wall pressure field associated with a turbulent boundary layer and fully-developed turbulent pipe flow, for example Willmarth and Woolridge[5], Bull[6] and Corcos[7]. In general these indicate that the cross spectral density, for both types of flow can be fairly well represented (except perhaps at very low frequencies) by

$$\phi_p(\underset{\sim}{\xi},\omega) = \phi_p(\xi,\eta,\omega)$$

$$= \phi_p(\omega)\exp\left(-c_x\frac{\omega|\xi|}{U_c} - c_y\frac{\omega|\eta|}{U_c} + i\frac{\omega\xi}{U_c}\right), \tag{16}$$

where ξ and η are spatial separations in the x-direction (the flow direction) and y-direction respectively and U_c is the convection velocity of the pressure field at frequency ω. The corresponding narrow band correlation coefficient $R_p(\xi,\eta,\tau;\omega)$ at $\tau=0$ is

$$R_p(\xi,\eta,0;\omega) = \exp\left(-c_x\frac{\omega|\xi|}{U_c} - c_y\frac{\omega|\eta|}{U_c}\right)\cos\frac{\omega\xi}{U_c} \tag{17}$$

This can also be written as

$$R_p(\xi,\eta,0;\omega) = R_{px}(\xi,0;\omega)R_{py}(\eta,0;\omega), \tag{18}$$

where

$$R_{px}(\xi,0;\omega) = e^{-c_x\omega|\xi|/U_c}\cos\frac{\omega\xi}{U_c} \tag{19}$$

and

$$R_{py}(\eta,0;\omega) = e^{-c_y\omega|\eta|/U_c} \tag{20}$$

These forms are used in the present analysis.

3.2 Modes and mode shapes

For a cylindrical shell with simply supported ends, if the x-axis were to be a modal line, the appropriate mode shapes would be

$$\psi_\alpha(\underset{\sim}{r}) = \psi_{mn}(x,y) = \sin\frac{m\pi x}{\ell}\ \sin\frac{ny}{a}, \tag{21}$$

where m is the (integer) number of half-waves in the length ℓ and n is the (integer) number of full waves round the circumference. On the other hand, if the x-axis were to be an anti-nodal line the appropriate mode shapes would be

$$\psi_{mn}(x,y) = \sin\frac{m\pi x}{\ell}\cos\frac{ny}{a} \tag{22}$$

In the case of excitation by a homogeneous stationary internal pressure field, as Powell[8] has pointed out, the vibrational response must also be statistically homogeneous in the circumferential direction. This boundary condition can be satisfied by including both sine and cosine modes, as given by equations (21) and (22), with the same mean square displacement amplitude response in each. Equations (21) and (22) each represent a set of orthogonal modes and the two sets are mutually orthogonal; so the theory of section 2 will apply to the combined set of modes. Both mode shapes are included in the subsequent analysis.

3.3. Natural frequencies

Many analyses to obtain the natural frequencies of thin-walled circular cylinders have been made. Those of Lord Rayleigh[9], Kennard[10], Cremer[11], and Smith[12], which have been discussed and compared by Heckl[13], and Szechenyi[14, 15] might be cited.

These analyses lead naturally to a relation between the natural resonance frequencies and the ring frequency, ω_r, which is the frequency at which the wave-length of a longitudinal wave in the shell wall material is equal to the circumference of the cylinder. It is given by

$$\omega_r = \frac{c_{Lp}}{a} \quad , \tag{23}$$

where, if E, ρ_s and μ are respectively the Young's modulus, density, and Poisson's ratio of the shell material,

$$c_{Lp} = \left[\frac{E}{\rho_s(1-\mu^2)}\right]^{\frac{1}{2}} \quad . \tag{24}$$

Apart from a change of notation, Heckl's expression for the resonance frequencies of a shell with wall thickness h is

$$\nu_{mn}^2 = \frac{\omega_{mn}^2}{\omega_r^2} = \beta^2\left[k^4a^4 - \frac{k_n^2a^2(4-\mu)-(2+\mu)}{2(1-\mu)}\right] + (1-\mu^2)\left(\frac{k_m}{k}\right)^4, \tag{25}$$

where $\beta=h/(2\sqrt{3}a)$, and $k_m=m\pi/\ell$ and $k_n=n/a$ are the components in the x- and y- directions of the resultant wave number $k=(k_m^2+k_n^2)^{\frac{1}{2}}$. The natural frequencies are, of course, defined by integer values of the mode numbers (m,n). Equation (25) can be approximated by

$$\nu^2_{mn} = \beta^2k^4a^4 + (1-\mu^2)\left(\frac{k_m}{k}\right)^4 \tag{26}$$

Heckl's work (13) indicates that this is a good approximation except when the two terms in equation (26) are nearly equal. According to Szechenyi[15] the errors are significant only for small k_na. In any case, since the error appears to be confined to a relatively small number of modes, it is unlikely to introduce serious error into modal density calculations.

3.4 The joint acceptance

If the narrow-band space-time correlation can be expressed as the product of two functions, one x-dependent and one y-dependent, as in equation (18), and if the mode shapes can also be written in a form in which the variables are separated, that is as

$$\psi_{mn}(\underset{\sim}{r}) = \psi_m(x)\,\psi_n(y), \tag{27}$$

then the joint acceptance for the (m,n)th mode of a cylindrical shell excited by internal flow can be expressed as

$$j^2_{mnmn}(\omega) = j^2_{mm}(\omega)\,j^2_{nn}(\omega). \tag{28}$$

In this equation

$$j^2_{mm}(\omega) = \frac{1}{\ell^2}\int_0^\ell dx\psi_m(x)\int_0^\ell dx\; R_{px}(x'-x,0;\omega)\psi_m(x') \tag{29}$$

and

$$j^2_{nn}(\omega) = \frac{1}{(2\pi a)^2} \int_0^{2\pi a} dy\psi_n(y) \int_0^{2\pi a} dy' R_{py}(y'-y,0;\omega)\psi_n(y'). \tag{30}$$

For either of the sets of modes described by equations (21) and (22) and the narrow-band correlation of equation (19), equation (29) becomes

$$j^2_{mm}(\omega) = \frac{1}{\ell^2} \int_0^{\ell} dx \sin k_m x \int_0^{\ell} dx' e^{-a_x|\xi|} \cos k_c\xi \sin k_m x', \tag{31}$$

where $\xi = x'-x$, $a_x = c_x k_c$, and $k_c = \omega/U_c$.

Because of the symmetry of the pipe flow, the correlation function $R_{py}(\eta,0;\omega)$ must be an even function of η (as for boundary layer flow on a flat plate), and must also satisfy the condition $R_{py}(\pi a+\eta,\ 0;\omega) = R_{py}(\pi a-\eta,\ 0;\omega)$ It can be shown that, when both these conditions are taken into account, equation (30) reduces to

$$j^2_{nn}(\omega) = \frac{1}{2\pi a} \int_0^{\pi a} R_{py}(\eta,0;\omega)\cos k_n\eta d\eta \tag{32}$$

for both the sets of modes described by equations (21) and (22). With the range of η in equation (32) restricted to $0 \leq \eta \leq \pi a$, equation (20) for R_{py} can be substituted directly, whereas it could not be substituted directly in equation (30) without being modified to have the second of the required symmetry properties. We therefore obtain

$$j^2_{nn}(\omega) = \frac{1}{2\pi a} \int_0^{\pi a} e^{-a_y|\eta|} \cos k_n\eta d\eta, \tag{33}$$

where $a_y = c_y k_c$. The two sets of modes given by equations (21) and (22) also have identical values of both $[\psi_{mn}{}^2(r)](=\frac{1}{4}$for all modes in this case) and $n(\omega,\theta)$. Noting that for a pipe with an internal gas flow (virtual mass of fluid negligible), the generalised mass is $M_\alpha = \rho_s Sh/4$ for all modes, equation (15) then becomes

$$[\phi_\zeta(\omega)]_{AV} = \frac{4\pi\phi_p(\omega)}{\rho^2{}_s h^2\omega^3} \int_\theta Q(\omega,\theta)j^2(\omega,\theta)n(\omega,\theta)d\theta \tag{34}$$

where $n(\omega,\theta)$ now includes only the modes described by equation (21). This result is consistent with that of Rattayya and Junger[16] who also considered the two sets of modes, but with a somewhat different approach from that given here.

If $Q(\omega,\theta)$ is assumed to be independent of θ, equation (34) reduces to

$$[\phi_\zeta(\omega)]_{AV} = \frac{2\pi\phi_p(\omega)Q(\omega)J(\nu)}{\rho_s{}^2h^2\omega^3\omega_r}, \tag{35}$$

where

$$J(\nu) = \int_\theta j^2(\nu,\theta)N(\nu,\theta)d\theta \tag{36}$$

and $N(\nu,\theta) = \omega_r n(\omega,\theta)$.

The expression for j^2_{mm}, equation (31), is the same as that for a flat plate and has been evaluated by a number of authors. The results have been expressed in a variety of forms, not always equivalent. The results given by, for example, Bozich and R.W.White[17], P.H.White[18], and Bull, Wilby, and Blackman[5] are correct, and can be expressed as

$$\begin{aligned} j^2_{mm}(\omega) = \{&2[(A_{xl}{}^2+K_{ml}{}^2-K_{cl}{}^2)^2 - 4A_{xl}{}^2K_{cl}{}^2][1 - (-1)^m e^{-A_{xl}}\cos K_{xl}] \\ &+ 8A_{xl}K_{cl}(A_{xl}{}^2+K_{ml}{}^2-K_{cl}{}^2)(-1)^m e^{-A_{xl}}\sin K_{cl} + A_{xl}K_{ml}(A_{xl}{}^2+K^2_{ml}+K_{cl}{}^2)\Delta\}/K_{ml}{}^6\Delta^2 , \end{aligned} \tag{37}$$

where

$$\Delta = [(A_{xl}^2 + K_{ml}^2 + K_{cl}^2)^2 - 4K_{ml}^2 K_{cl}^2]/K_{ml}^4,\ A_{xl} = a_x \ell,$$

$$K_{ml} = k_m \ell (= m\pi),\ \text{and}\ K_{cl} = k_c \ell$$

From equation (33), the corresponding expression for $j^2{}_{nn}$ is

$$j^2{}_{nn}(\omega) = \frac{A_y[1-(-1)^n e^{-\pi A_y}]}{2\,(A_y{}^2 + K_n{}^2)} \tag{38}$$

where $A_y = a_y a$, and $K_n = k_n a$ $(=n)$. We also define here $K_m = k_m a (= m\pi a/\ell)$ and $K_c = k_c a$.

The form of the joint acceptance functions is shown in figures 1(a), (b), and (c). Figure 1(a) shows $j^2{}_{mm}$ according to equation (37) with $a_x = 0.1k_c (c_x=0.1)$, for m = 6 to 10, as a function of the ratio K_{cl}/K_{ml} of fluid wave number to axial component of structural wave number; figure 1(b) shows $j^2{}_{nn}$ according to equation (38), with $a_y = 0.7k_c (c_y=0.7)$, for n = 6 to 10, as a function of the ratio K_c/K_n of fluid wave number to circumferential component of structural wave number; and figure 1(c) shows the total joint acceptance $j^2{}_{mnmn}$, obtained from the preceding two figures, for n = 6 and m = 6 to 10, as a function of K_c/K_m for $\ell/a = 20$.

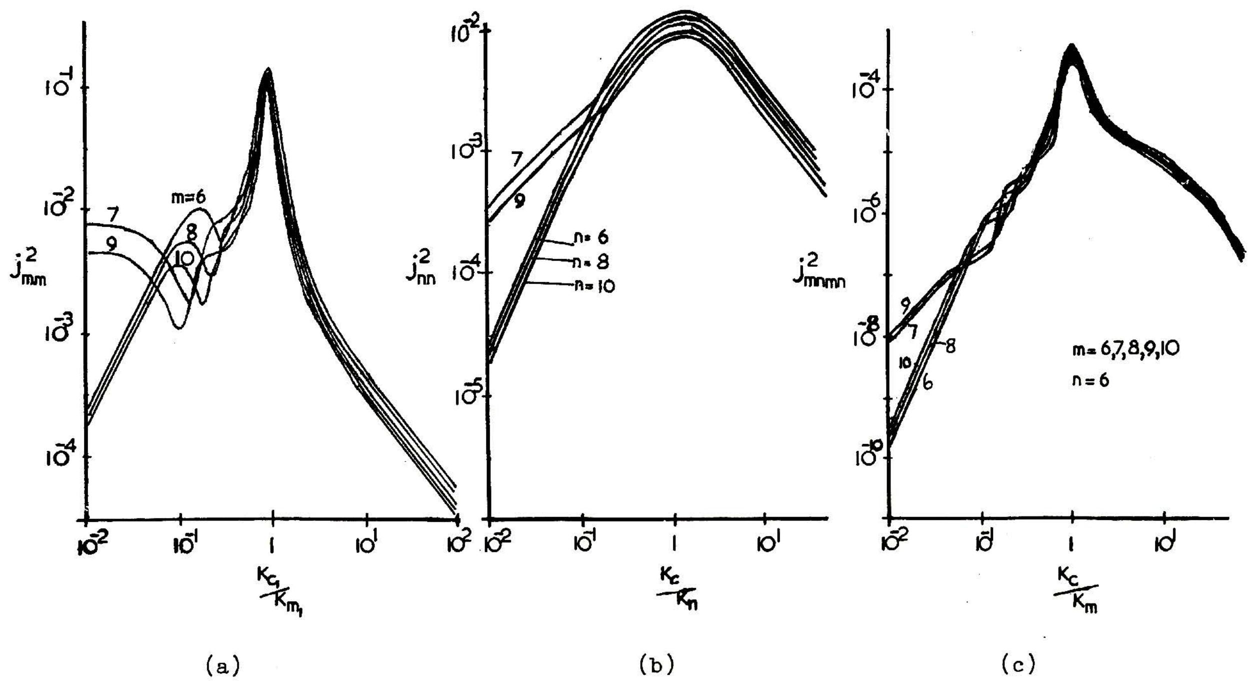

Figure 1 Joint acceptance functions: (a) axial, equation (37); (b) circumferential, equation (38); (c) total, equations (28), (37) and (38). $a_x = 0.1k_c$. $a_y = 0.7k_c$. $\ell/a = 20$.

3.5 Coincidence effects

The term "coincidence" is used here to describe the situation in which a structural wave has an axial wave number component equal to the fluid "wave number" $k_c = \omega/U_c$. This implies also that the trace velocity of the structural wave in the flow direction is equal to the convection velocity U_c of the turbulent pressure field.

For turbulent flow over a flat plate of thickness h, the highest frequency at which coincidence can occur, here termed the hydrodynamic coincidence frequency, ω_{hc}, is $2\sqrt{3}U_c^2/hc_{Lp}$

Expressed in terms of the ring frequency of a circular cylinder of radius a it is

$$\nu_{hc} = \frac{1}{\beta}\left(\frac{U_c}{c_{Lp}}\right)^2 \tag{39}$$

At this frequency the direction of structural wave propagation is the flow direction. For $\nu<\nu_{hc}$, the direction of propagation of the flexural wave which gives coincidence makes an angle $\cos^{-1}(\nu/\nu_{hc})^{\frac{1}{2}}$ with the flow direction.

For a flat plate with the same length as the cylinder we are considering, and with a width equal to the circumference of the cylinder, the resonance frequencies are given by $\nu^2=\beta^2(ka)^4$ (compare equation (26)); so that on a wave number diagram (k_m versus k_n) the lines of constant resonance frequency are quadrants of circles centred on the origin. The fluid wave number is represented on the diagram by the line k_m = constant = k_c, and the points at which this line intersects a line of constant resonance frequency represent coincidence conditions. In this case there is only one such intersection in the positive quadrant; and there is therefore only one flexural wave which will give coincidence at a given frequency.

In the case of a cylindrical shell the lines of constant resonance frequency on the wave number diagram are given by equation (26) and have the non-dimensional form shown in figure 2. For a given resonance frequency there may now be two, one, or no coincidence conditions. Solution of equation (26) with ν = constant and $K_m = K_c$ gives the following expression for the values of K_n at coincidence:

$$K_n = \left\{\frac{\nu}{\beta\sqrt{2}}\left[1 \pm \sqrt{1 - 4(1-\mu^2)/\nu^2_{hc}}\right]^{\frac{1}{2}} - \frac{\nu^2}{\beta\nu_{hc}}\right\}^{\frac{1}{2}} \tag{40}$$

For these values to be real and therefore for coincidence to occur at all, requires first that $\nu_{hc} \geq \nu_{hc}$ crit, where

$$\nu_{hc\ crit} = 2(1-\mu^2)^{\frac{1}{2}}. \tag{41}$$

If this condition is satisfied, there will be two real positive values of K_n (that is two coincidence conditions) if, in addition

$$\nu \leq \nu_{hc}\left[1-(1-\nu^2_{hc\ crit}/\nu^2_{hc})^{\frac{1}{2}}\right]^{\frac{1}{2}}/\sqrt{2} = \nu_1; \tag{42}$$

one real positive value (that is only one coincidence condition) if $\nu_1>\nu$ but

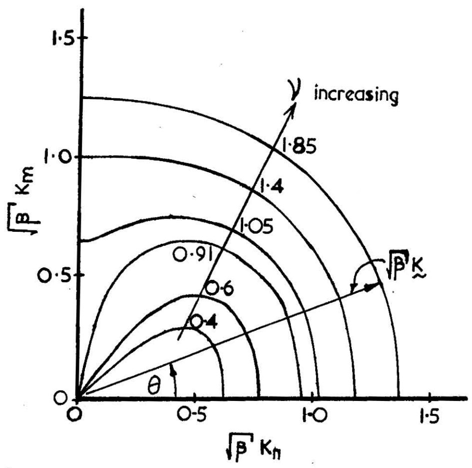

Figure 2 Wave number diagram showing constant resonance frequency curves

$$\nu \leq \nu_{hc}\left[1 + (1-\nu^2_{hc\ crit}/\nu^2_{hc})^{\frac{1}{2}}\right]^{\frac{1}{2}}/\sqrt{2} = \nu_2 ; \tag{43}$$

and no real roots if $\nu>\nu_2$.

Figure 1(a) which applies to both the flat plate and the cylinder, shows that, as might be expected, the joint acceptance for a particular mode (which is directly proportional to the mean square structural response in that mode) has a peak for $K_c/K_m \simeq 1$, that is, essentially, at coincidence.

The variation of $j^2_{mm}(\nu,\theta)$, $j^2_{nn}(\nu,\theta)$, are their product $j^2(\nu,\theta)$ with θ (= $\tan^{-1}K_m/K_n$ as shown in figure 2), at various constant values of ν, for a cylinder, for two values of $\nu_{hc}/\nu_{hc\ crit}$ (one>1 and one <1)) is shown in figures 3 and 4. For these figures we have set μ =0.3, giving $\nu_{hc\ crit}$ = 1.908. For figures 3(a), (b) and (c) ν_{hc}=2.50, $\nu_{hc}/\nu_{hc\ crit}$=1.31, ν_1=1.05, and ν_2=2.27. In figure 3(a) ν =0.6< ν_1, in which case there are two coincidence conditions; this is reflected in the variation of j^2 which shows two corresponding maxima. In figure 3(b) ν=1.4, and $\nu_1<\nu<\nu_2$ corresponding to one coincidence condition; as expected j^2 shows one maximum. In figure 3(c) ν=3.0>ν_2; coincidence does not occur and this is borne out by the absence of a maximum in j^2. The corresponding curves for the flat plate are also shown. For the plate coincidence occurs for $\nu<\nu_{hc}$, and hence for ν=0.6 and 1.4 here; but, as can be clearly seen from

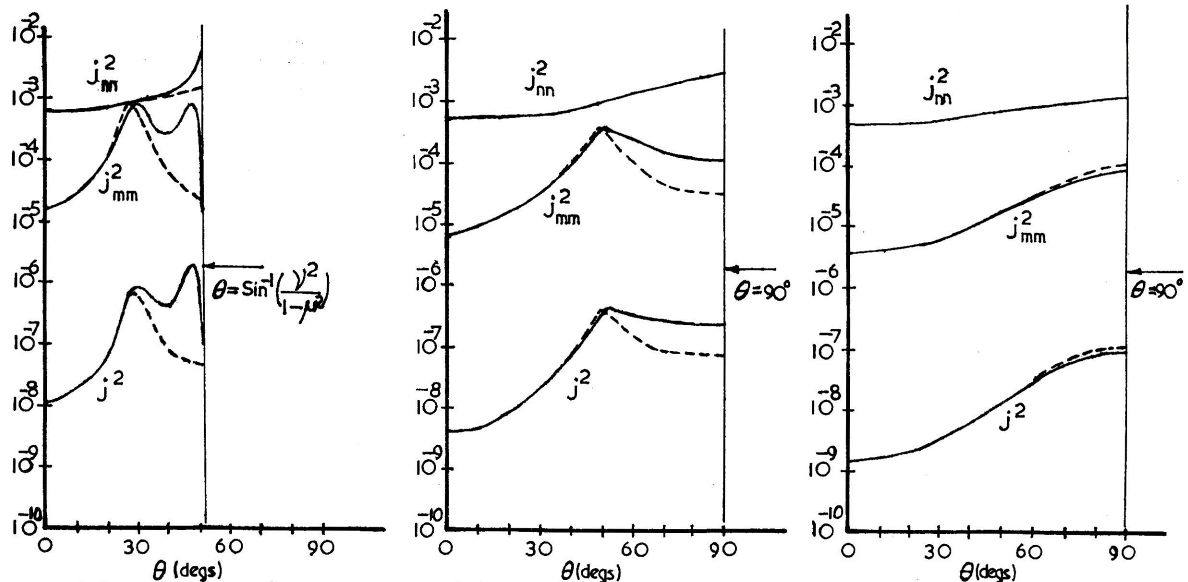

(a) ν=0.6 ($\nu<\nu_1$) (b) ν=1.4 ($\nu_1<\nu<\nu_2$) (c) ν=3.0 ($\nu>\nu_2$)

Figure 3 Joint acceptance functions. Variation of j^2_{mm}, j^2_{nn} and j^2 with wave angle for cylinder(———) and flat plate (– – – –). ν_{hc}=2.50(>$\nu_{hc\ crit}$); ν_1=1.05; ν_2=2.27

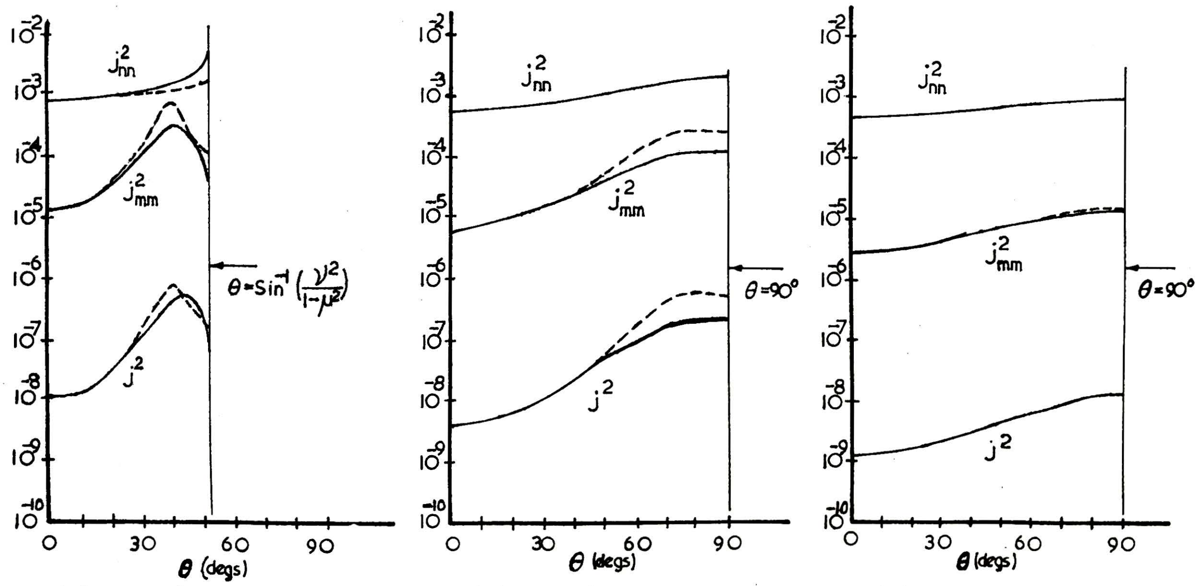

(a) ν=0.6 (b) ν=1.4 (c) ν=3.0

Figure 4 Joint acceptance functions. Variation of j^2_{mm}, j^2_{nn} and j^2 with wave angle for cylinder (———) and flat plate (– – –). ν_{hc}=1.50 (<$\nu_{hc\ crit}$).

the figures, there is only one coincidence condition for a given ν. The expression for j^2_{mm} for the plate is the same as that for the cylinder, namely equation (37); the expression for j^2_{nn} is not the same as for the cylinder, but can be obtained from equation (37) by substituting n for m, $2\pi a$ for ℓ, a_y for a_x, and putting $K_{cl}=0$.

Figures 4(a), (b), and (c) show the variation of the joint acceptance functions with θ, for the same values of ν as in figures 3(a), (b), and (c), for a value of $\nu_{hc}/\nu_{hc\ crit} < 1$ ($\nu_{hc} = 1.50$, $\nu_{hc}/\nu_{hc\ crit} = 0.786$). For this value of ν_{hc} coincidence cannot occur for any value of ν, and equations (42) and (43) do not yield real values of ν_1 and ν_2. The absence of coincidence is reflected in the variation of j^2 with θ - only at the lowest value of ν, for which there is the closest approach to coincidence, does j^2 show even one maximum in the θ range. Flat plate values are also shown in figure 4. Again coincidence occurs for ν=0.6 and 1.4, and its effect is shown by the values of j^2_{mm} for the plate being generally greater than those for the cylinder at these frequencies.

4. ACOUSTIC POWER RADIATION

The acoustic power, P, radiated from a vibrating surface can be expressed in terms of a radiation resistance, R_{rad}, and the average over the vibrating surface of the mean square velocity of vibration of the surface, $[\overline{v^2}]_{AV}$, by means of the relation

$$P = R_{rad}[\overline{v^2}]_{AV}. \tag{44}$$

The radiation resistance can be expressed in terms of that of an infinite piston (ρc per unit area) and the so-called radiation ratio, σ. By definition,

$$R_{rad} = \sigma\rho c S, \tag{45}$$

where ρ and c are respectively the density and speed of sound in the fluid surrounding the vibrating surface, and, as previously, S is the surface area.

As indicated in the introduction, it is assumed that the dominant contribution to the acoustic power radiation is made by supersonic resonant shell modes, that is by resonant modes whose wave speed is greater than c. For these modes we assume σ=1 (and σ=0 for subsonic resonant modes). The spectral density of the acoustic power radiation at frequency ω is therefore

$$\phi_P(\omega) = \rho c S[\phi_{vs}(\omega)]_{AV}, \tag{46}$$

where $\phi_{vs}(\omega)$ is the power spectral density of the vibrational velocity of the shell surface, associated with supersonic modes only. Thus, if $[\overline{v^2}_s]_{AV}$ is the surface average of the mean square velocity of the supersonic modes,

$$[\overline{v_s^2}]_{AV} = \int_{-\infty}^{\infty} [\phi_{vs}(\omega)]_{AV} d\omega. \tag{47}$$

The relation between the power spectral densities of the velocity and displacement for the supersonic modes is

$$[\phi_{vs}(\omega)]_{AV} = \omega^2[\phi_{\zeta s}(\omega)]_{AV} ; \tag{48}$$

so that equation (46) can be written as

$$\phi_P(\omega) = \rho c S\omega^2[\phi_{\zeta s}(\omega)]_{AV} . \tag{49}$$

Substitution of the equivalent of equation (35) for the supersonic modes gives

$$\phi_P(\omega) = \frac{2\pi\rho c S\phi_p(\omega)Q(\omega)J_s(\nu)}{\rho_s^2 h^2\omega\omega_r} , \tag{50}$$

where

$$J_s(\nu) = \int_{\theta_1}^{\theta_2} j^2(\nu,\theta)N(\nu,\theta)d\theta \tag{51}$$

and θ values in the range $\theta_1<\theta<\theta_2$ correspond to supersonic modes at a given frequency.

In section 3.5 we defined a hydrodynamic coincidence frequency ν_{hc} for a flat plate. An acoustic coincidence frequency ν_{ac} can be defined similarly, as the frequency at which a flexural wave in the plate has the same speed and wave-length as an acoustic wave propagating in a direction parallel to the plate surface. It is given by

$$\nu_{ac} = \frac{1}{\beta}\left(\frac{c}{c_{Lp}}\right)^2 . \qquad (52)$$

The resonant vibrational modes of the plate will be subsonic or supersonic according as ν is less or greater than ν_{ac}.

For any vibrating surface, the condition that a mode is supersonic is $\omega > kc$, or, written in terms of cylinder parameters, $\nu^2 > \beta K^2 \nu_{ac}$. In the case of the cylinder, this condition in conjunction with equation (26) leads to the result that for a given ν those modes for which

$$\theta \geq \theta_1 = \sin^{-1}\left[\frac{\nu^2}{1-\mu^2}\left(1-\frac{\nu^2}{\nu^2_{ac}}\right)\right]^{\frac{1}{4}} \qquad (53)$$

are supersonic. For $\nu_{ac} \leq 2(1-\mu^2)^{\frac{1}{2}}$ ($= \nu_{hc\ crit}$), θ increases with increasing ν to a maximum, and then falls to zero at $\nu=\nu_{ac}$; for $\nu \geq \nu_{ac}$ all modes are supersonic. Thus, in this case, the lower limit of integration in equation (51) is given by equation (53) for $\nu<\nu_{ac}$ and is zero for $\nu \geq \nu_{ac}$. For $\nu_{ac} > 2(1-\mu^2)^{\frac{1}{2}}$ there is a range of frequencies $\nu_B \leq \nu \leq \nu_A$ ($<\nu_{ac}$) for which equation (53) gives no real values of θ_1, and at these frequencies there are no supersonic modes (and, with the present assumptions, no power radiated). ν_A and ν_B are given by

$$\nu_{A,B} = \nu_{ac}\ \{1 \pm [1 - 4(1-\mu^2)/\nu^2_{ac}]^{\frac{1}{2}}\}^{\frac{1}{2}} \ / \ \sqrt{2}\ . \qquad (54)$$

Hence, in this case, the lower limit in equation (51) is given by equation (53) for $\nu \leq \nu_B$ and $\nu \geq \nu_A$, and $J_s(\nu)=0$ for $\nu_B \leq \nu \leq \nu_A$. Again, for $\nu \geq \nu_{ac}$, this lower limit is zero.

For $\nu<(1-\mu^2)^{\frac{1}{2}}$, modes with n=0 are not possible. In this case it is appropriate to take the upper limit of integration θ_2 as the value of θ corresponding to the n=1 mode at a given ν, that is as the root of equation (26) with $K_n=1$. For $\nu \geq (1-\mu^2)^{\frac{1}{2}}$, $\theta_2=\pi/2$.

The modal density $N(\nu,\theta)$ for resonance frequencies given by equation (26) is (see also Miller and Hart[19])

$$N(\nu,\theta) = \ell/[2\pi\beta a(1 - \frac{1-\mu^2}{\nu^2}\sin^4\theta\ )^{\frac{1}{2}}]. \qquad (55)$$

Equation (50) can be conveniently written in non-dimensional form. For a fully developed pipe flow let U_o be the centre-line velocity and $q = \frac{1}{2}\rho_f U_o^2$, where ρf is the fluid density. We take $\Phi_p = \phi_p U_o/q^2 a$, $\Phi_P = \phi_p/\rho c^2 Sa$, $u = U_c/U_o$, and denote the ratio ρ_f/ρ_s by ρ_{fs}. Then

$$\frac{\Phi_P}{(\Phi_p/u^3)} = \left(\frac{\pi\rho^2_{fs}}{24\beta\nu_{ac}^{\frac{1}{2}}}\right)\left(\frac{J_s\nu_{hc}^{3/2}}{\nu}\right)Q \qquad (56)$$

In this equation Φ_p/u^3 is determined entirely by the fluid flow; and the first group on the right hand side is fixed once the internal fluid, and the pipe material and geometry (ℓ/a and β) are chosen, and it is independent of frequency. For our present purposes we shall assume that the damping is the same for all modes. Then for fixed geometry, since $J_s=J_s(\nu,\nu_{hc},\ell/a,\beta)$, the term $(J_s\nu_{hc}^{3/2}/\nu)$ determines the frequency dependence of the spectral density ratio $\Phi_P/(\Phi_p/u^3)$. It also determines the dependence of the spectral density ratio on flow Mach number M (defined here in terms of the speed of sound in the fluid <u>outside</u> the pipe, as U_o/c) through $\nu_{hc}=u^2M^2\nu_{ac}$.

Figures 5(a), (b) and (c) show the variation of $(J_s\nu_{hc}^{3/2}/\nu)$ with frequency for a thin-walled steel pipe with ℓ/a=20, with air as both the internal and external fluid, for three different values of ν_{ac} (less and greater than $2(1-\mu^2)^{\frac{1}{2}}$). The value of ν_{ac} in conjunction with c for the external fluid and c_{Lp} for the pipe material determines the corresponding value of β. Curves are shown in each case for values of Mach number in the range $0.1 \leq M \leq 0.5$.

We might note at this point the limiting behaviour of ν_A and ν_B which determine the frequency range in which there are no supersonic modes when $\nu_{ac}>2(1-\mu^2)^{\frac{1}{2}}$. As $\nu_{ac}\to 2(1-\mu^2)^{\frac{1}{2}}$ from above, both ν_A and $\nu_B \to \sqrt{2}(1-\mu^2)^{\frac{1}{2}}$; and as $\nu_{ac}\to\infty$, $\nu_A\to\nu_{ac}$ and $\nu_B\to(1-\mu^2)^{\frac{1}{2}}$ (that is, essentially, the ring frequency).

Figure 5(a) represents the case where $\nu_{ac}<2(1-\mu^2)^{\frac{1}{2}}$; so that there are always some supersonic modes at a given ν (and all modes are supersonic for $\nu \geq \nu_{ac}$), and the power radiated is finite at all frequencies. The power radiation varies only slowly with frequency at frequencies below the ring frequency (ν=1), rises to a maximum value in the region of the ring frequency, and then falls off slowly with further increase in ν. For figure 5(b), $\nu_{ac}=2>2(1-\mu^2)^{\frac{1}{2}}$. There is now a range of frequency, $\nu_B=1{\cdot}18 \leq \nu \leq \nu_A=1.61$, for which there are no supersonic modes and no power radiated. For $\nu<\nu_B$ the power radiated is again almost independent of frequency, it again rises to a maximum for $\nu\sim 1$, and falls off slowly for $\nu>\nu_A$. The results in figure 5(c) are for $\nu_{ac}=20>>2(1-\mu^2)^{\frac{1}{2}}$, and apply to extremely thin-walled pipes. At M=0.5 hydrodynamic coincidence can occur (the corresponding ν_{hc} is $2.45>\nu_{hc\ crit}$), but for subsonic flow it is not possible for coincidence to be associated with supersonic modes, and the possibility of coincidence in this case is therefore not reflected in the values of $(J_S\nu_{hc}^{3/2}/\nu)$ or the power radiated. The behaviour of $(J_S\nu_{hc}^{3/2}/\nu)$ is, in fact, very similar to that shown in figure 5(b), except that now the frequency range for which there are no supersonic modes is larger, namely $\nu_B=0.96\leq\nu\leq\nu_A=19.98$.

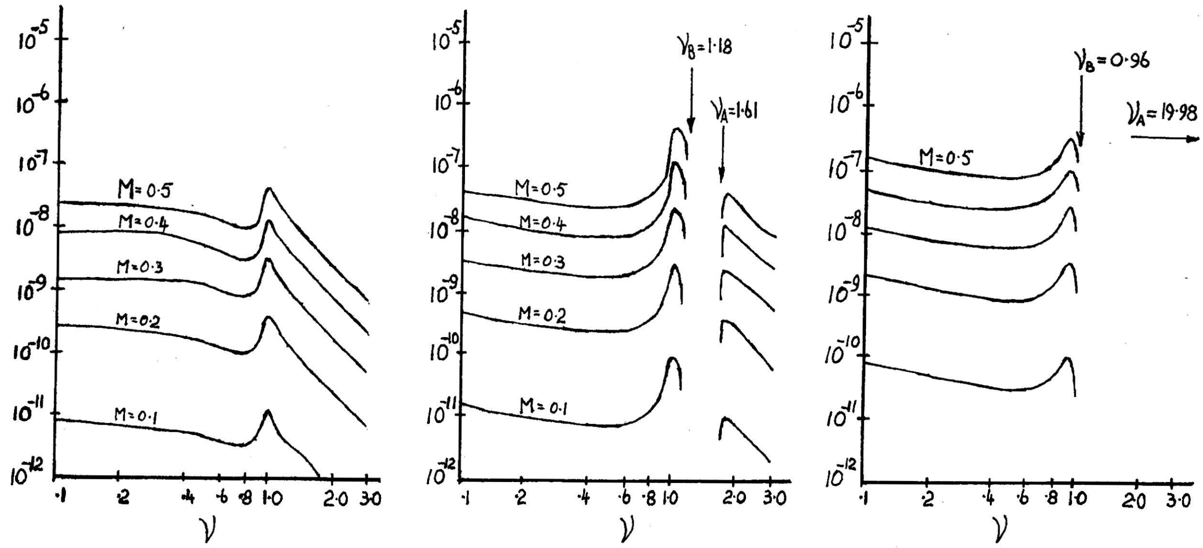

(a) $\nu_{ac}=0.5<2(1-\mu^2)^{\frac{1}{2}}$, $\beta=5.0\text{x}10^{-3}$

(b) $\nu_{ac}=2>2(1-\mu^2)^{\frac{1}{2}}$ $\beta=1.25\text{x}10^{-3}$

(c) $\nu_{ac}=20>2(1-\mu^2)^{\frac{1}{2}}$ $\beta=1.25\text{x}10^{-4}$

Figure 5 Variation of the power radiation parameter $(J\nu_{hc}^{3/2}/\nu)$ with frequency, flow Mach number, and acoustic coincidence frequency.

Finally, as an illustration, the calculated form of the spectrum of the acoustic power radiation is shown in figure 6 for M=0.5 and ν_{ac}=2.0 and 20. The curves shown are based on the power spectral density of pressure fluctuations given by Bull[6] and a value of u=0.7 at all frequencies; the frequency range is confined to $0.1<\nu<1.1$. Scales are also shown for the sound power levels corresponding to a pipe with a=50mm and ℓ=1.0m. It will be noted that for the two cases chosen the sound power levels are very low (33 and 49 dB/1pW).

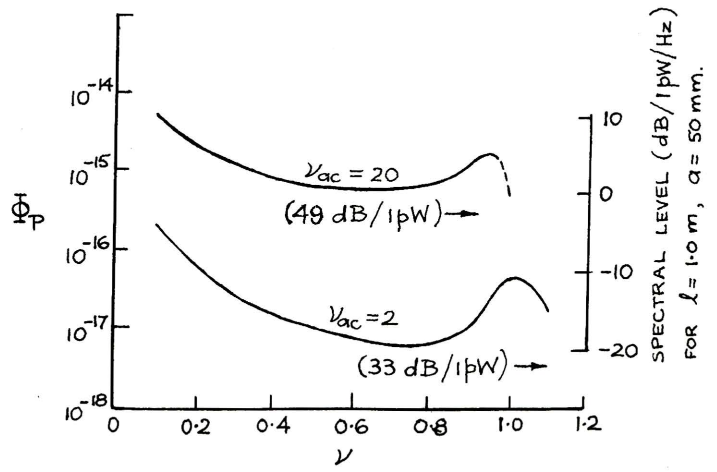

Figure 6 Acoustic power radiation from steel pipes with internal air flow at M=0.5, for ν_{ac}=2.0 and 20.

REFERENCES

1. GABOR, Dennis, Science 177, No.4046, 299-313 (28 July 1972)
2. BERANEK, L.L. editor, Noise and Vibration Control, McGraw-Hill Book Co. 1971, Ch.11
3. GABOR, Dennis, KOCK, Winston E., STROKE, George W., Science 173, Np.3991, 11-23 (July 1971)
4. BERANEK, L.L. editor, Noise and Vibration Control, McGraw-Hill Book Co. 1971, Chs. 4 & 6
5. BORN, M., and WOLF, E., Principles of Optics, Pergamon Press 1964, 453-458
6. APRAHAMIAN, R. and EVENSEN, D.A., TRW, Applications of Holography to High Frequency Vibrations and Transient Response, NASA - CR - 125413 (1972)
7. BERANEK, L.L. editor, Noise and Vibration Control, McGraw-Hill Book Co. 1971, Ch.6
8. Symposium on reverberant enclosures, J.Sound and Vib. 16 (1971)
9. LAWLER, Edward D., Sound & Vibration 2, (1968)
10. WILSON, Alan P., and STROPE, Douglas H., J.Opt.Soc.Am. 60, No.9, 1162-1165 (Sept.1970)
11. MORSE, P.M. and INGARD, K.U., Theoretical Acoustics, McGraw-Hill Book Co. 1968, Ch. 7
12. ALEKSOFF, C.C., Applied Optics, 10, No. 6, 1329-1341 (June 1971)

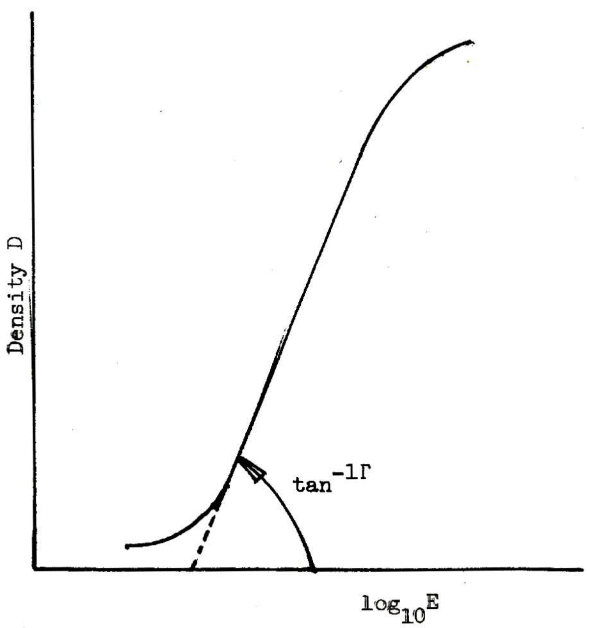

Figure 1

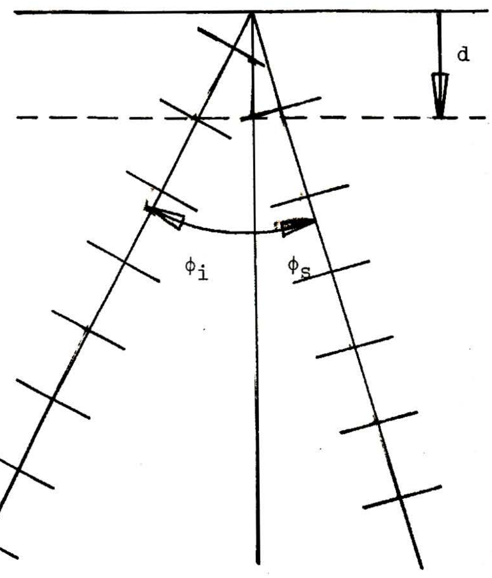

Figure 2

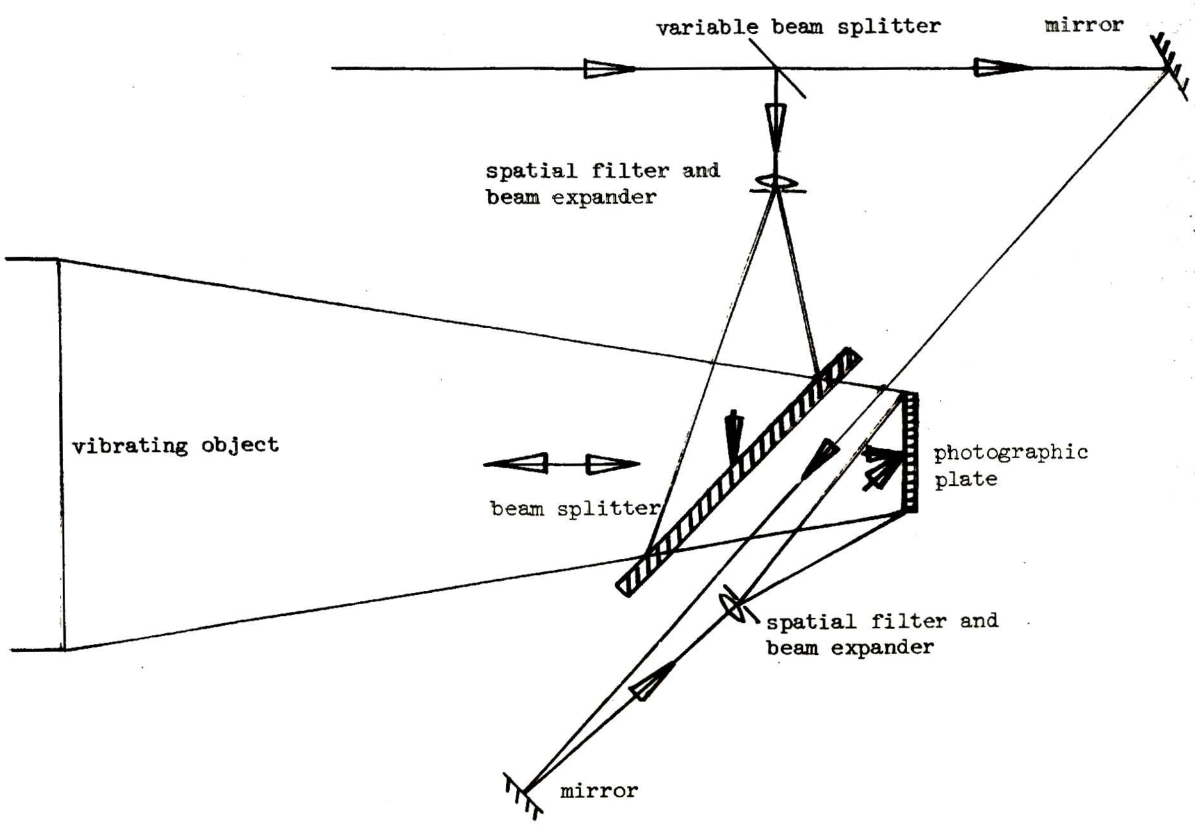

Figure 3

(a)

(b)

Figure 5

(a) Time lapse hologram of a pipe driven at one of its resonances.

(b) Time lapse hologram of a six cylinder engine block driven in its lowest order bending mode.

for liquids and hot gases in the pipe, for example, for which the wave velocity C_B is greater than the speed of sound in air, condition (4) may well not apply. Section 3.2 presents a more general discussion to include this case.

For the present, however, we assume the pipe diameter to be small and model the peristaltic displacement of the pipe by a distribution of point souces of strength per unit length

$$q = U(x,t)2\pi a$$

where U is the surface velocity of the pipe and a its radius. The velocity potential at $\underset{\sim}{r}$ (figure 2) for a distribution of these sources over a length L is

$$\phi(\underset{\sim}{r},t) = \int_{-\frac{1}{2}}^{\frac{1}{2}} \frac{U(x,t - \frac{R}{C}) \cdot 2\pi a}{4\pi R} dx \qquad \ldots (5)$$

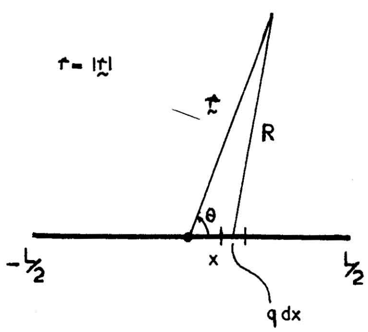

Fig. 2

Correspondingly the instantaneous sound pressure $p(\underset{\sim}{r},t)$ is

$$p(\underset{\sim}{r},t) = \rho\frac{\partial\phi}{\partial t} = -\rho\phi_t$$

so that the mean square pressure $\overline{p^2(\underset{\sim}{r})}$ will be given by

$$\overline{p^2(r)} = \frac{\rho^2 a^2}{4}\int_{-\frac{1}{2}}^{\frac{1}{2}}\int_{-\frac{1}{2}}^{\frac{1}{2}} \overline{U_t(x_1,t-\frac{R_1}{C})U_t(x_2,t-\frac{R_2}{C})}\frac{dx_1}{R_1}\frac{dx_2}{R_2}$$

Now for a propagating surface wave on the pipe for which the radial velocity is

$$U(x,t) = U \sin (k_B x - \omega t) \qquad \ldots (6)$$

the mean square pressure is evidently

$$\overline{p^2(r)} = \frac{\rho^2 a^2\omega^2 U^2}{4}\int_{-\frac{1}{2}}^{\frac{1}{2}}\int_{-\frac{1}{2}}^{\frac{1}{2}} \overline{\cos (k_B x_1-\omega(t-\frac{R_1}{C}))\cos(k_B x_2-\omega(t-\frac{R_2}{C}))}\frac{dx_1}{R_1} \cdot \frac{dx_2}{R_2}$$

which reduces to

$$\overline{p^2(r)} = \frac{\rho^2 a^2\omega^2 U^2}{8}\int_{-\frac{1}{2}}^{\frac{1}{2}}\int_{-\frac{1}{2}}^{\frac{1}{2}} \cos\{k_B(x_1-x_2) + \omega(\frac{R_1-R_2}{C})\}\frac{dx_1}{R_1} \cdot \frac{dx_2}{R_2} \qquad \ldots (7)$$

The total sound power, P, radiated by this distribution of sources is now easily found by integrating the energy flux $\frac{p^2}{\rho c}$ over a sphere of radius r. From figure 2, R_1 may be approximated by

$$R_1 \simeq r - x_1 \cos \theta \qquad \ldots (8)$$

for $r \gg \frac{L}{2}$ so that the total power radiated is (using (7) and (8))

$$P = \frac{2\pi\rho a^2\omega^2 U^2}{8C}\int_0^{\pi}\int_{-\frac{1}{2}}^{\frac{1}{2}}\int_{-\frac{1}{2}}^{\frac{1}{2}} \cos\{(k_B-\frac{\omega}{C}\cos\theta)(x_1-x_2)\}\sin\theta\, dx_1 dx_2 d\theta$$

By straightforward integration this reduces to

$$P = \frac{\pi\rho a^2\omega U^2 L}{2}\int_{Lk_B(1-\frac{C_B}{C})}^{Lk_B(1+\frac{C_B}{C})} \{\frac{1 - \cos\zeta}{\zeta^2}\} d\zeta \qquad \ldots (9)$$

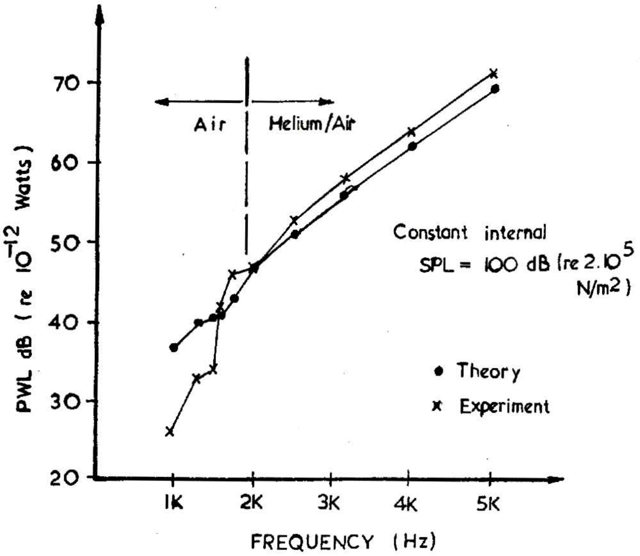

Fig. 9 Power radiated from pipe with internally propagating plane acoustic waves

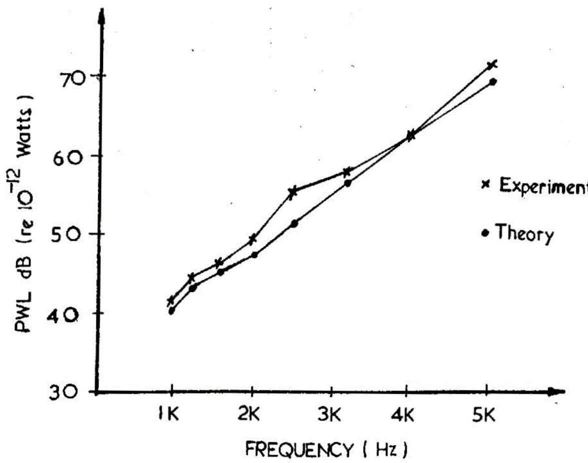

Fig. 10 Power radiated from pipe containing helium/air mixture. Excitation by 1/3 octave bands of random noise. Constant internal SPL = 100 db (re $2.10^{-5}N/m^2$). Plane propagating acoustic waves.

4.2.3 The effect of changes in end conditions

Having established a forced n = 0 pipe response to a plane propagating acoustic wave and agreement in this case between theory and experiment it is then of interest to examine, experimentally, the effects of changes to the end conditions. Firstly the mechanical termination was removed. Local measurements of pipe wall response showed much greater variations in amplitude (± 10 db) and the variations in phase suggested standing waves in the pipe. As shown in figure 11, however, only relatively small changes in the power radiated, occurred. Though further measurements are required this result supports the view that, though resonant pipe modes occur in this frequency range, the circumferential mode number, n, is, in this case, not zero but some even number and these modes therefore couple very poorly with the axi-symmetric pressure field and similarly radiate inefficiently. Because of the high radiation efficiency of the peristaltic displacement it therefore appears to remain the dominant source of sound radiation from long pipes (i.e. L>>λ). Similarly a local squeezing of the pipe produced marked changes in local accelerations but minor changes in sound power radiated. Somewhat to our surprise, removing the acoustic termination also had a relatively minor effect on the sound power radiated for the same r.m.s. pressure in the pipe, (figure 11). It appears to be straightforward to extend the discussion of section III to the case of waves of the same frequency travelling in opposite directions and this is planned.

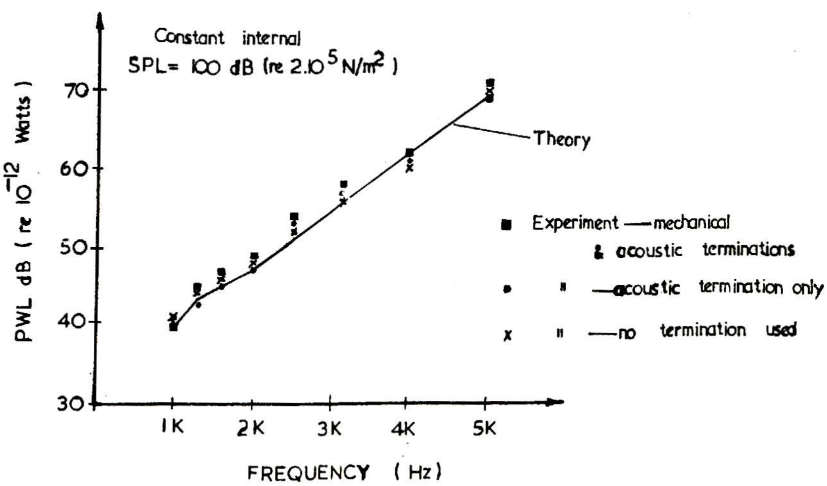

Fig. 11 Comparison of power radiation from different terminations

V DISCUSSION AND CONCLUSION

It is not surprising that these experiments and the theory presented agree closely. The theory is essentially simple and fundamental, and measurements confirmed that the experimental design achieved the idealization of the theory, namely a forced axi-symmetric peristaltic displacement. It does seem, however, important to confirm agreement in this case before comparing the same theory with a less well defined experiment. This, it seems to us, accounts for the present agreement and the discrepancy of up to 25 db which Morfey finds between theory and experiment. In the experiments of Heckl[5] which Morfey discusses the loud speaker is mounted in the pipe and it is not clear what is the contribution of the near field of the speaker to the pipe response. Our results suggest that the relatively larger sound powers which Heckl found confirm his view that the near field is a significant factor in the sound powers he measured in the plane wave frequency region. From our own results this appears likely to be the explanation for the discrepancy rather than either finite pipe length or departures from an exactly circular cross-section. This local source asymmetry is suggested by Morfey[7], more recently, as the probable explanation.

The present experiments in which the sound source is isolated from the pipe so far support the view that, for long isolated pipes ($L >> \lambda$) and plane acoustic waves, a useful lower bound for the sound power radiated can be obtained from the theory presented, considering the pipe ends to reflect no mechanical energy. The explanation, as discussed, lies in the efficiency with which the peristaltic displacement radiates acoustic energy and the poor coupling and correspondingly low radiation efficiency of the modes where resonant frequencies correspond with the frequency of the plane sound waves. Further measurements with various end conditions have yet to be made, however, particularly for the case in which the acoustic energy is partially reflected from the pipe end.

Finally it should be pointed out that the results presented are for frequencies between 1000 and 5000 c.p.s. There is little reason to doubt that similar results will be obtained at lower frequencies provided the pipe length remains large compared with the acoustic wavelength. It is planned to investigate this case with the existing apparatus in an analogous way to the high frequency case by using a gas with a speed of sound much less than air. This value of $\frac{C_B}{C}$ less than 1 will provide a further check on the applicability of the theoretical results of section III.

REFERENCES

1. MORFEY, C.L., 1971, 7th International Congress on Acoustics
2. MORSE and INGARD, 1968, Theoretical Acoustics (McGraw-Hill).
3. SMITH, P.W., 1957, J.Acoustical Society America, 29 (6).
4. CREMER, L., 1955, Acustica 5, p.245.
5. HECKL, M., 1958, Acustica 8, p.259.
6. BULL, M.K. and RENNISON, D.C., 1973, personal communication.
7. MORFEY, C.L., 1973, Personal communication.

Noise, Shock & Vibration Conference, 1974 Monash University, Melbourne

FREQUENCY RESPONSE CHARACTERISTICS OF MESHING GEARS FOR TRANSMISSION ERROR AND DYNAMIC LOADING

A. Bhattacharyya
Jadavpur University
Calcutta, India

G. S. Patki
Jadavpur University
Calcutta, India

S. R. Deb
Jadavpur University
Calcutta, India

B. K. Mullick
Jadavpur University
Calcutta, India

SUMMARY

Analytical and experimental investigations of the transmission error and the dynamic loading of two meshing gears under actual working conditions, clearly demonstrate that the dynamic loading is predominantly a forced vibration phenomenon in which certain resonance harmonics are active. A special new technique has been developed to secure the frequency response characteristics due to the transmission error as well as the dynamic loading, based on the dynamic signal level records and their analyses in 1/3rd octave band.

The results thus arrived at through the present investigations, have established the fact that the dynamic loading is a random phenomenon with a certain spectrum of frequency response having a correlation with the frequency spectrum of the transmission errors.

INTRODUCTION

When the gears are rotating, errors in spacing and form of the teeth together with elastic deformation under load act to change the relative velocity of the rotating members and produces varying load cycles, thus leading to 'Dynamic Load'. Though there have been some contradictory standards to evaluate the dynamic load, it is important to gear engineers that a more rational analysis of dynamic loading, based on experimental investigations is carried out.

Hence, the object of this paper is to analyse the experimental results of investigations conducted by the authors to demonstrate that dynamic loading is predominantly a forced vibration phenomenon in which certain spectrum of frequency response is dependant on the frequency spectrum of transmission error. It is also important to note the influence of tooth flexibility over a contact cycle, on the dynamic loading pattern so as to obtain a clearer picture of the phenomenon of the gearing action. However the results indicate that no such deterministic models for dynamic loading, as advocated by earlier research workers are sufficient for all typical applications.

SURVEY OF PREVIOUS RESEARCH

In general, the analysis of dynamic load attempted by various researchers can be put mainly into two categories: (i) analysis of isolated error; (ii) analysis of continuous motion.

Analysis of Buckingham(1), Tuplin(2), Reswick(3) fall in the group of isolated error which seems to be extreme simplification in the design problems. Their analyses are applicable to slow speed gears because of the assumption that pitch line velocities are equal even at the time of insertion of error. Further damping has not been considered. ASME Research Committee (4) was guided by the assumption that during operation, transient error causes the tooth separation followed by contact with impact. The analysis of Strauch(5) gives an idea of forced vibration of gears due to stiffness variation.

Experiments of Attia(6), Niemen and Rattig(7) and Utagawa(8) point towards direct measurement of dynamic loading. Harris(9) carried out measurements of dynamic stress pattern of gears made of photo-elastic materials. Gregory, Harris and Munro(10) attempted continuous measurement of transmission error of a pair of gears by optical method. Zeman(11) introduced a continuous sinusoidal error function which induced a forced vibration. In comparison with the above results and those of Houser(12) and Kohler(13), Buckingham's method of calculation of dynamic loading gives somewhat conservative results.

ANALYSIS OF TRANSMISSION ERROR AND DYNAMIC LOADING OF GEARS

TRANSMISSION ERROR

Transmission error for a gear pair is defined as a measure of instantaneous fluctuation from ideal output motion. The sources from which transmission error occurs, include: (a) position error in the individual gears, (b) installation errors, (c) other miscellaneous errors arising from the effect of misalignment of shaft couplings and bearings etc.

A large amount of transmission error comes from installation run-outs and eccentricity from ideal tooth positions. They cause a sinusoidal variation in the transmission error.

The frequency spectrum of transmission error contains two gear speeds and a few multiples of these as well as tooth meshing frequency and a few multiples of it. Because of its periodicity transmission error may be represented by the form,

$$\begin{aligned} e_t &= e_m + \sum (A_n \ \mathrm{Sin}\ n\,\bar{w}t + B_n \ \mathrm{Cos}\ n\,\bar{w}t) \\ &= e_m + \sum E_n \mathrm{Sin}(n\,\bar{w}t + \alpha_n) \qquad \ldots(1) \\ E_n &= \sqrt{A_n^2 + B_n^2} \quad \text{and} \quad \tan\alpha_n = \frac{B_n}{A_n} \end{aligned}$$

where e_m = constant mean transmission error; E_n = maximum value of nth order resultant harmonic component; n = order of harmonic; $\bar{w}$ = fundamental frequency; t = time measured from a specific instant; α_n = phase angle.

ANALYSIS OF DYNAMIC LOADING OF GEARS

Dynamic loading of gears is essentially a vibration problem and its contributing factors include: (a) flexibilities of gear teeth in contact, and of gear blank, shaft and bearing supports; (b) transmission error and elastic deformation under load; (c) mass effects of gear, shafts and other connected links and (d) damping effect.

For representation of the basic mechanism of dynamic loading of gears in a simplified form, an equivalent spring-mass system has been illustrated in Fig. 1. The equation of motion with displacement excitation may be written as,

$$M_e \ddot{x} + c(\dot{x} - \dot{e}) + K_e (x - e) = 0 \qquad \ldots(2)$$

Where, M_c = equivalent mass = $\frac{m_1 . m_2}{m_1 + m_2}$ in terms of individual masses of gears in mesh; and K_e = equivalent gear tooth stiffness = $\frac{K_1 K_2}{K_1 + K_2}$ in terms of tooth stiffness of the pair of gears in mesh; x = total displacement = $x_1 + x_2$ in terms of individual gear displacement x_1 and x_2; e = error function = $e_1 + e_2$ in terms of individual error e_1 and e_2 of gear pair.

With the substitution of Z = (x - e), equation 2 may be rewritten in the form,

$$M_e\ddot{Z} + C\dot{Z} + KZ = -M_e \ddot{e} \qquad \ldots(3)$$

Since, error is sinusoidal, $e = E \ \mathrm{Sin}\ \bar{w}t$

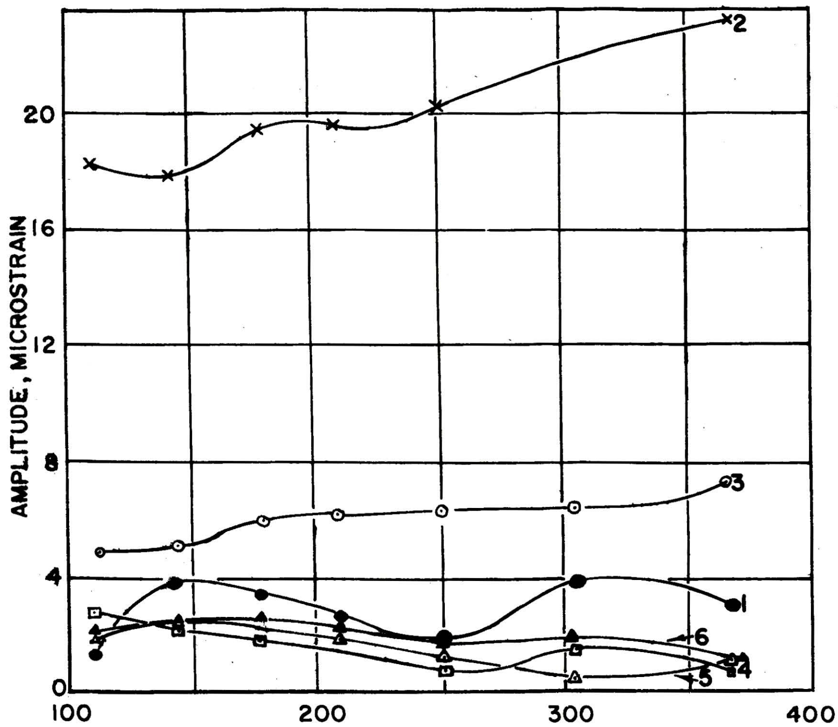

FIG. 9

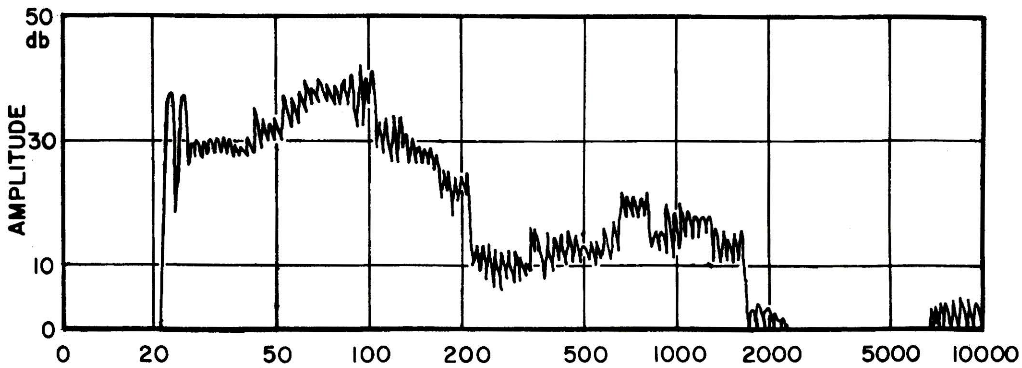

FIG. 10(a)

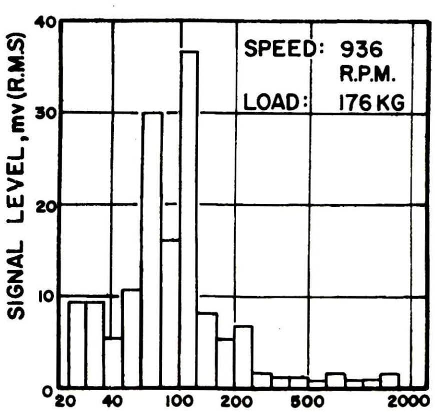

FIG. 10 (b)

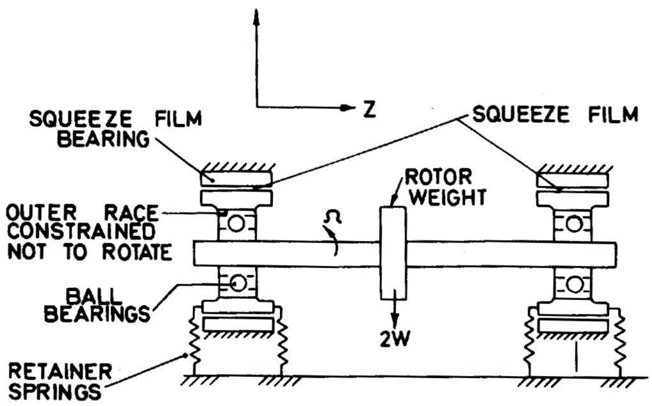

FIG. 1. Schematic diagram of a squeeze film damper support system.

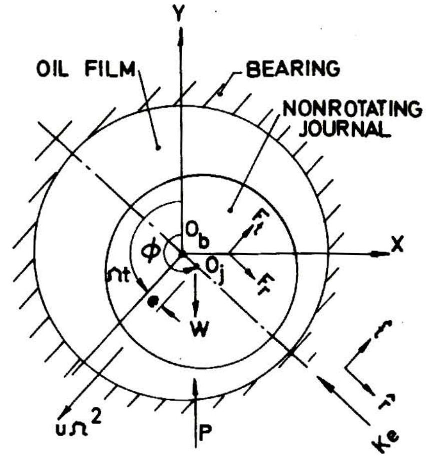

FIG. 2. External forces acting on squeeze film bearing.

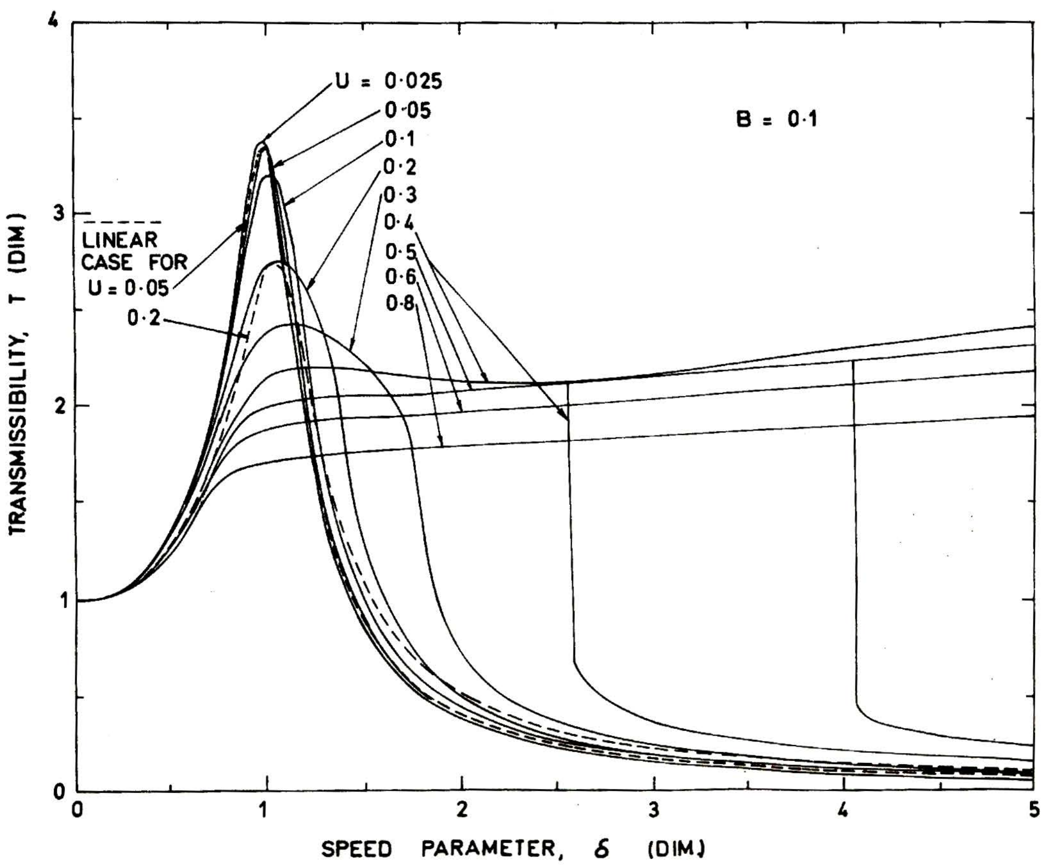

FIG. 3. Transmissibility frequency response for range of unbalance (B = 0·1)

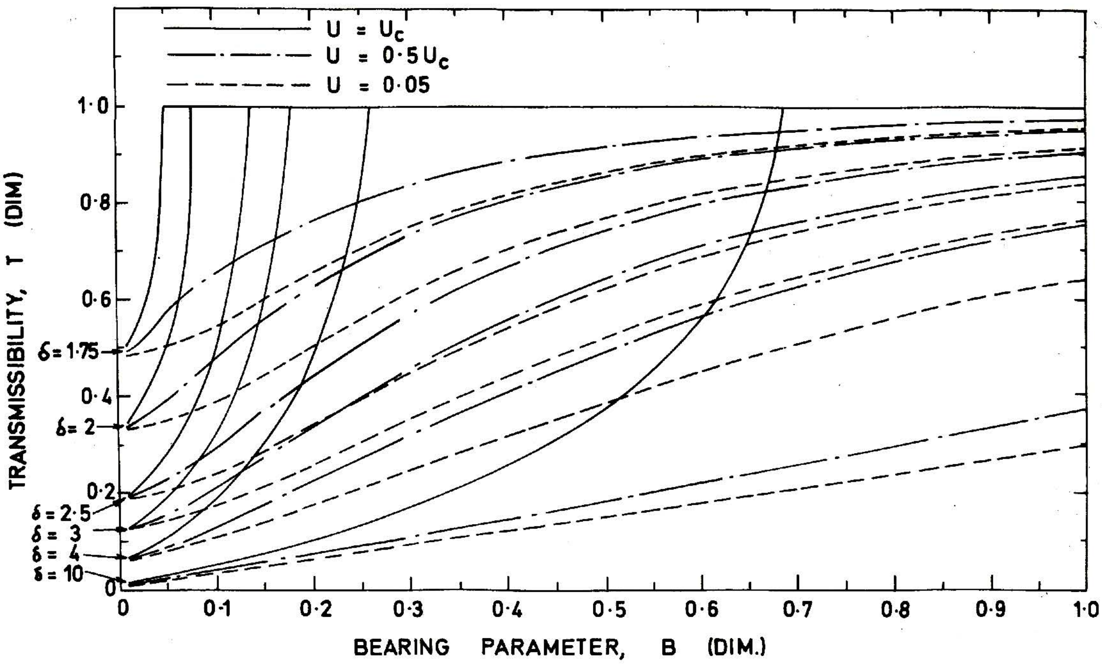

FIG. 9. Variation of transmissibility with bearing parameter, speed parameter and unbalance.

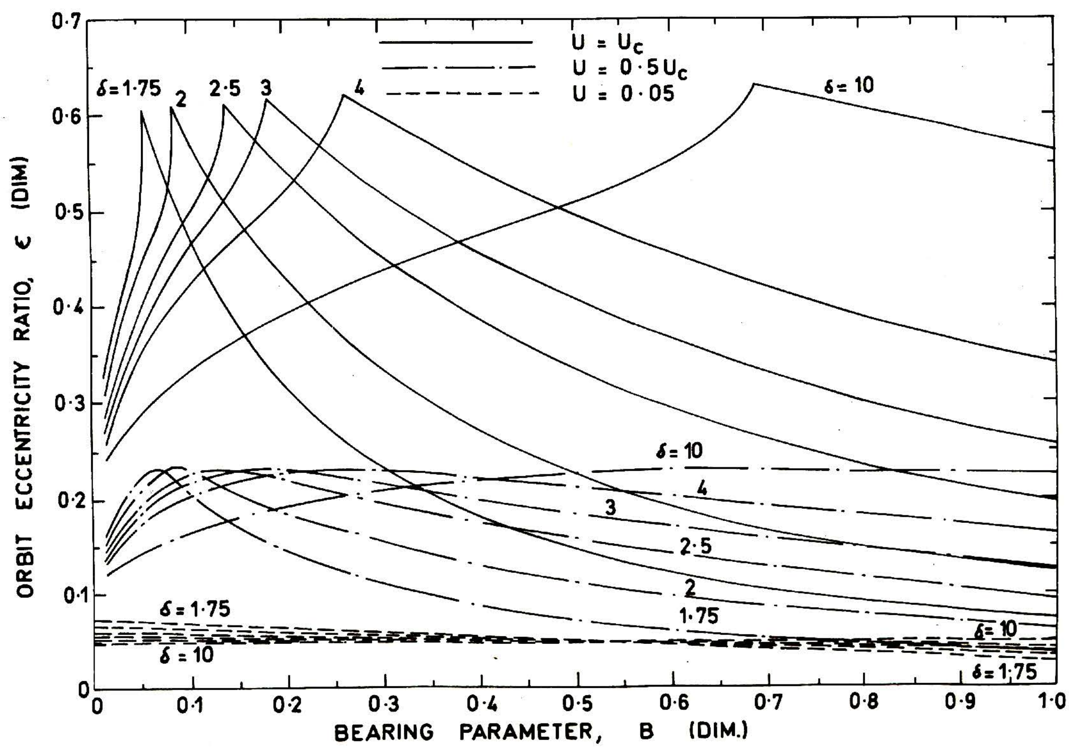

FIG. 10. Variation of rotor vibration amplitude with bearing parameter, speed parameter and unbalance

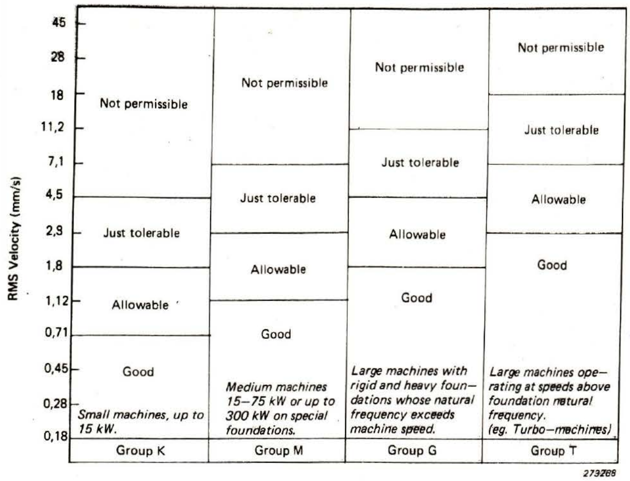

Fig.1 Vibration Criterion Chart (VDI 2056)

Fig. 2 Portable Vibration Set

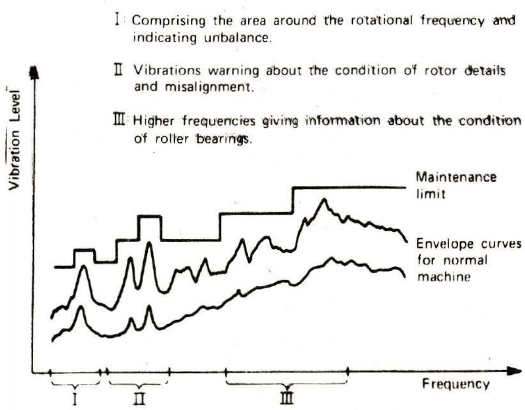

Fig.3 Vibration Spectrum Envelopes

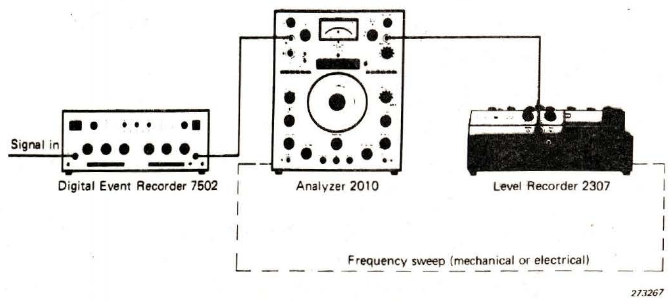

Fig.4 Instrument Set-up for High Speed Analysis

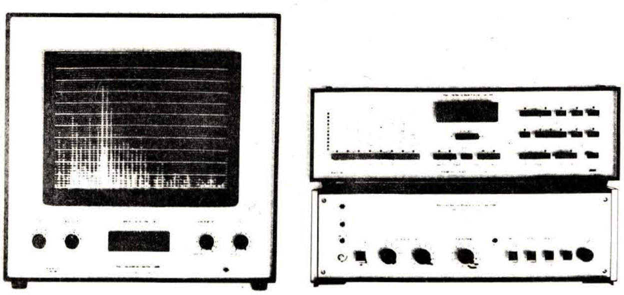

Fig.5 Time Compression Analyzer

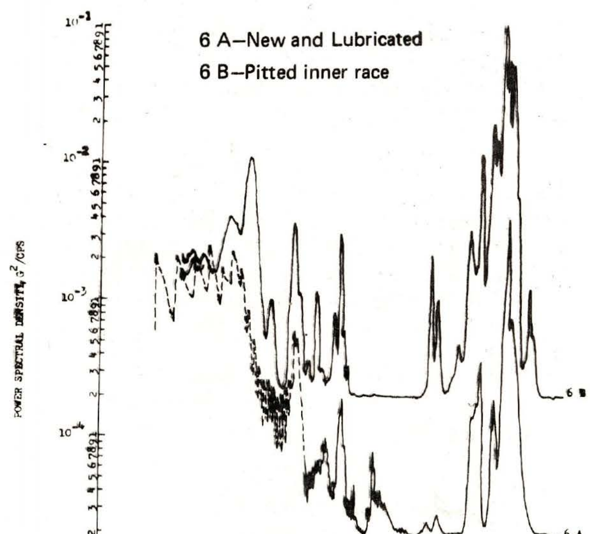

Fig.6 Ball Bearing Vibration Spectra (Ref.16)

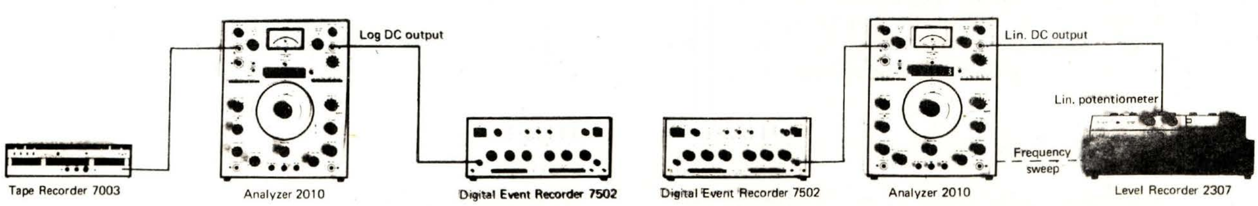

(a) Recording log power spectrum

(b) Cepstrum Analysis of recorded log spectrum

273269

Fig.7 Instrument Set-ups for Cepstrum Analysis


Meter Reading
Monitoring
Level
Delay
Test Function
Trip
Alarm
Minimum
%
Trip
Alarm
Min. Level
Vibration Monitor Type 5500
Brüel & Kjær
Copenhagen
Reset/Test Cycle
MONITORING POINT
F T 6

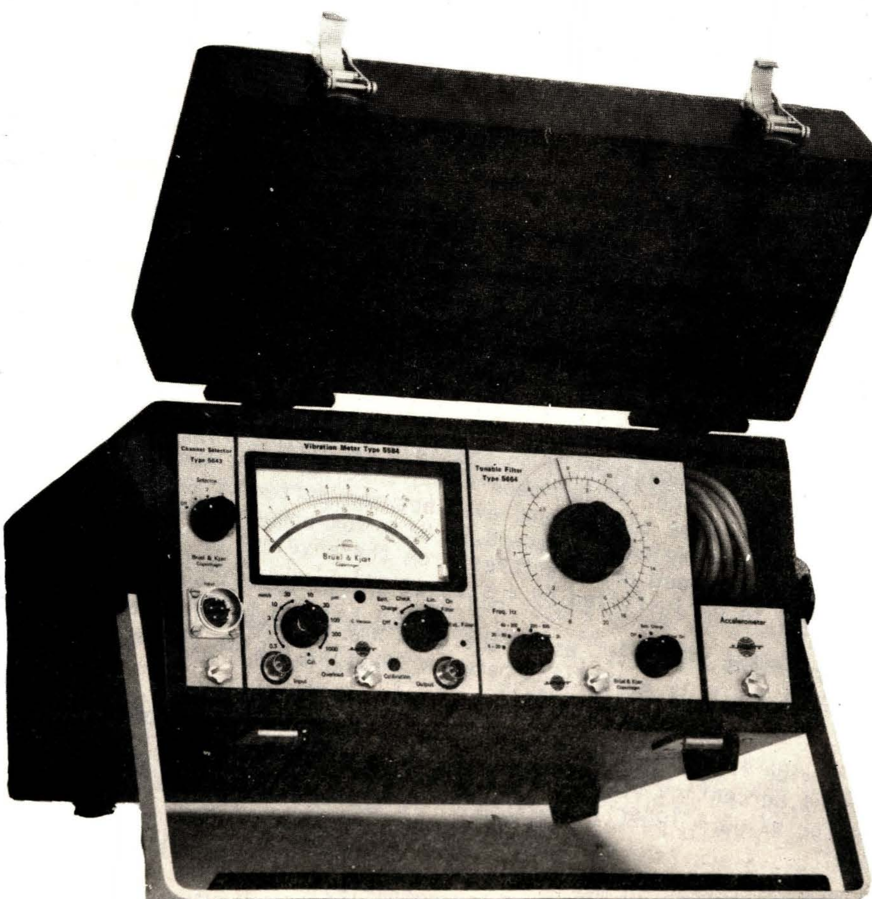
Vibration Meter Type 5584
Brüel & Kjær
Accelerometer

itself apparent. It is also hoped that it (and the references) will help to avoid pitfalls which lead to faulty conclusions and thus can do a great deal of harm.

REFERENCES

1. E. Downham & R. Woods, "The Rationale of Monitoring Vibration on Rotating Machinery in Continuously Operating Process Plant". ASME Paper No. 71-Vibr-96 Journal of Engineering for Industry.

2. J. Trampe Broch, "Mechanical Vibration and Shock Measurements" (May 1972) A/S Brüel & Kjær, Denmark.

3. VDI Richtlinien, "Beurteilungsmasstäbe für mechanische Schwingungen von Maschinen" VDI 2056, October 1964.

4. BS 4675:1971. "A Basis for Comparative Evaluation of Vibration in Machinery". British Standards Institute.

5. Deutsche Normen. "Schwingstärke von rotierenden elektrischen Maschinen der Baugrössen 80 bis 315. DIN 45 665. July 1968.

6. C.A.W. Glew, D.C. Watson, "The Octave Band Vibration Analyzer as a Machinery Defect Indicator", ASME Paper 71-DE-47.

7. R.N. Chapman, "Vibration Analysis applied to Machinery Maintenance", Naval Engineers Journal, June 1967 pp. 431-437.

8. R.B. Randall, "Frequency Analysis of Stationary Signals recorded on Tape Loops". B & K Application Note 12-036.

9. R.B. Randall, "High Speed Narrow Band Analysis using the Digital Event Recorder Type 7502" B & K Technical Review No. 2, 1973.

10. R.B. Randall, "Analysis Time for Swept Frequency Analysis" B & K Application Note 13-054.

11. R.L. Bannister & V. Donato, "Signature Analysis of Turbomachinery", Sound and Vibration, September 1971, pp. 14-21.

12. G.D. Bergland, "A Guided Tour of the Fast Fourier Transform", IEEE Spectrum, July 1969, pp. 41-52.

13. B. Weichbrodt and K.A. Smith, "Signature Analysis. Non-intrusive Techniques for Incipient Failure Identification. Application to Bearings and Gears". General Electric Co. Schenectady, N.Y., Report No. 70-C-364.

14. "Workshop in On-Condition Maintenance", I.S.V.R., Southhampton University 5-6 January 1972

15. "Acoustics as a Diagnostic Tool". Institution of Mechanical Engineers, London, Meeting 20th October, 1970.

16. H.L. Balderston, "The Detection of Incipient Failure in Bearings", Materials Evaluation, June 1969, pp. 121-8.

17. L.D. Mitchell & G.A. Lynch, "Origins of Noise", Machine Design, May 1, 1969.

18. R.B. Randall, "Cepstrum Analysis and Gearbox Fault Diagnosis". B & K Application Note 13-150.

19. R.B.Randall, "High Speed Narrow Band Analysis with Digital Output", B & K Application Note 12-192.

AUTOMATIC MEASUREMENT OF SOUND POWER LEVEL WITHOUT A COMPUTER

R. W. Raymond
General Radio Company
Concord, Massachusetts, U.S.A.

SUMMARY

The measurement of sound power level is becoming increasingly important. It is complicated, involving many measurements and computations. Performed manually with conventional instrumentation, it takes hours. Dedicating a computer to the task is expensive. This paper describes a new, economical approach utilizing standard electronic instrumentation without the need for a computer.

The measurement of sound power level is becoming increasingly important. For many years, standards organizations such as the American Society of Heating, Refrigerating and Air Conditioning Engineers and the Air Moving and Conditioning Association have been using radiated sound power as a means of characterizing the noise produced by their products. With increasing emphasis on standardization and a desire to obtain a universal description of product noise, sound power level measurements are becoming more common.

The sound power measurement provides a well-defined means of describing the acoustical output of the source without having to specify the acoustical environment. A knowledge of the sound power level and the characteristics of the ultimate environment will also permit you to predict the sound pressure level at various points in that sound field. In this manner, a manufacturer can rate his product in a controlled acoustical environment and predict the sound pressure levels that will result when the product is in use at its final destination.

The sound power radiated by a source is nearly independent of its acoustical environment. It is the total power flowing away from the source. It is this aspect of sound power level that makes its measurement valuable. Sound power level defines the acoustic output power of the source.

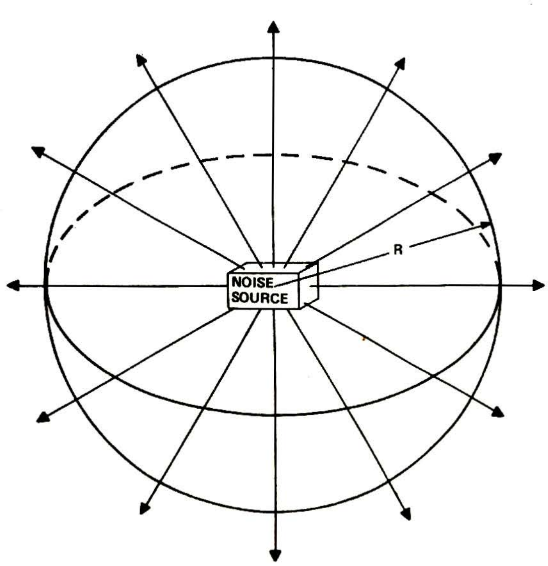

Figure 1.

Envision a hypothetical sphere of radius R which surrounds a noise source (see Figure 1); the sound power generated by that source is proportional to the average pressure at the surface of the sphere.

Sound power is usually expressed as sound power level in decibels referred to a reference power:

$$PWL = 10 \log \frac{W}{W_{REF}}$$

where PWL is the sound power level,
W is the sound power in watts,
W_{REF} is the reference power, usually 10^{-12} watt, or 1 picowatt.

Sound power level may be determined in an anechoic, semi-reverberant or reverberant environment.

Anechoic Environment

In a free-field area, the determination of PWL is relatively simple. Microphones are located at specified points on a hypothetical sphere or hemisphere at a radius R from the source (see Figure 2).

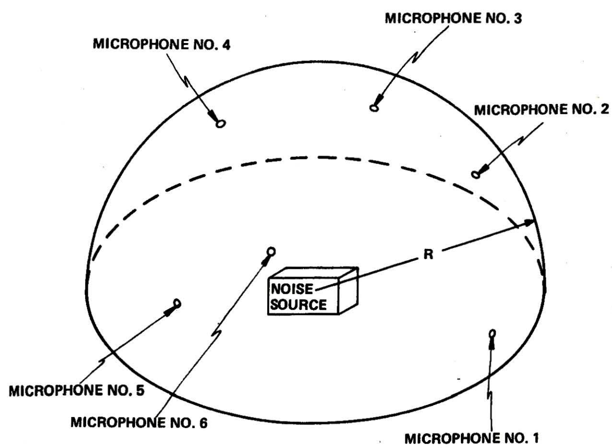

Figure 2.

The output of each microphone is usually measured in 1/3-octave or octave bands. PWL may be calculated from the following equation.

$$PWL = \overline{SPL} + 20 \log R + 0.5 \text{ dB}^{*}$$

where PWL is the sound power level in dB re 10^{-12} watt;

$$\overline{SPL} = 10 \log \frac{1}{n}\left(\text{antilog} \frac{SPL_1}{10} + \text{antilog} \frac{SPL_2}{10} + \text{antilog} \frac{SPL_n}{10}\right),$$

SPL_1 is the sound pressure level measured at point 1; SPL_2 at point 2; and SPL_n at point n,
R* is the distance in feet from the acoustic center of the source to the surface of the hemisphere.

Sound power level is usually determined on an octave or 1/3-octave basis. Therefore, the computation of $\overline{SPL}$ is required for each frequency band measured. Unless the levels from the microphones in each frequency band are very close together, the computation must be made by the following method.

*For R in meters:

$$PWL = \overline{SPL} + 20 \log R + 10.8 \text{ dB}.$$

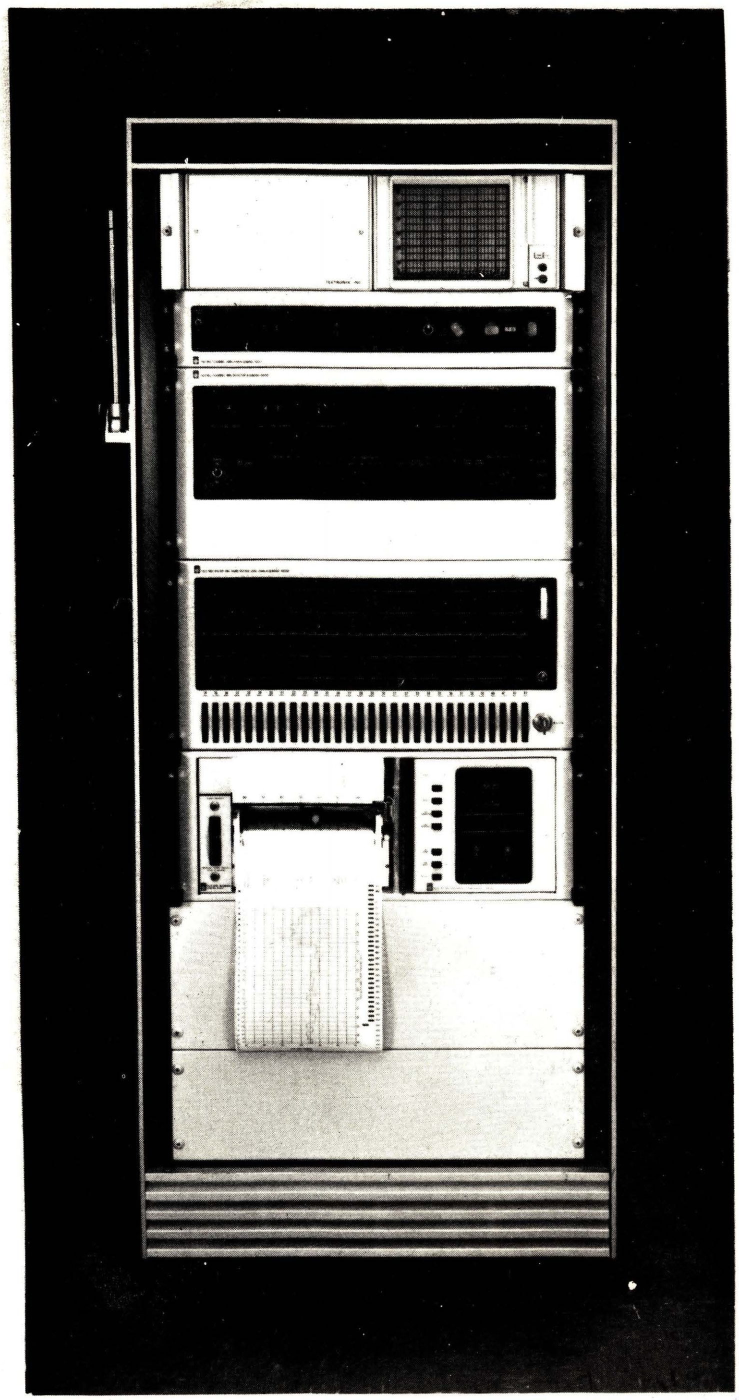

Figure 7. Automatic Sound Power Level Measurement System

AUTHOR INDEX